LIBRARY
Michigan State
University

This is to certify that the
dissertation entitled

INVESTIGATING THE FUNCTIONAL ROLES OF LIPIDS
IN MEMBRANE PROTEIN CYTOCHROME *C* OXIDASE
FROM *RHODOBACTER SPHAEROIDES*
USING MASS SPECTROMETRY AND LIPID PROFILE
MODIFICATION

presented by

XI ZHANG

has been accepted towards fulfillment
of the requirements for the

Ph.D. degree in Chemistry and Biochemistry &
Molecular Biology

S. Ferguson-Miller

Major Professor's Signature

11/13/2009

Date

MSU is an Affirmative Action/Equal Opportunity Employer

PLACE IN RETURN BOX to remove this checkout from your record.
TO AVOID FINES return on or before date due.
MAY BE RECALLED with earlier due date if requested.

DATE DUE	DATE DUE	DATE DUE
JAN 31 2012		

5/08 K:/Proj/Acc&Pres/CIRC/DateDue.indd

INVESTIGATING THE FUNCTIONAL ROLES OF LIPIDS IN MEMBRANE PROTEIN CYTOCHROME *C* OXIDASE FROM *RHODOBACTER SPHAEROIDES* USING MASS SPECTROMETRY AND LIPID PROFILE MODIFICATION

VOLUME I

BY

Xi Zhang

A DISSERTATION

Submitted to
Michigan State University
in partial fulfillment of the requirements
for the degree of

DOCTOR OF PHILOSOPHY

Chemistry and Biochemistry & Molecular Biology

2009

ABSTRACT

INVESTIGATING THE FUNCTIONAL ROLES OF LIPIDS IN THE MEMBRANE PROTEIN CYTOCHROME *C* OXIDASE FROM *RHODOBACTER SPHAEROIDES* USING MASS SPECTROMETRY AND LIPID PROFILE MODIFICATION

By

Xi Zhang

Recent successes in X-ray crystallography at high resolution have revealed that a number of lipid molecules remain bound to the membrane protein cytochrome *c* oxidase (C*c*O). These lipid binding sites are well conserved in C*c*O purified from different bacterial and bovine sources, in spite of differences in the membrane lipid composition and purification and crystallization procedures, suggesting important structural and functional roles. In particular, cardiolipin has been proposed to be essential for the functions of C*c*O in mammalian systems by *in vitro* lipid removal / replacement studies.

To test the hypothesis that specific lipids are required for C*c*O assembly or function, *in vivo* lipid profile modulation was achieved by using a series of specific lipid-deficient mutant strains of *Rhodobacter sphaeroides* (*R. sphaeroides*) to express C*c*O, including the specific glycerophosphatidylcholine (GPCho), sulfoquinovosyldiacyl-glyceride (SQDG) and cardiolipin (CL) deficient mutants. In addition, metabolic modification was used to collectively change the balance between phospholipids and non-phospholipids by the phosphate-limiting growth. The effects on cell growth, C*c*O expression, purification stability, subunit composition, activity, spectroscopic properties and crystallization of the C*c*O were evaluated, and the lipid profiles of the cell membranes, purified C*c*O and C*c*O crystals were quantitatively characterized by mass spectrometry with electrospray ionization or matrix-assisted laser desorption/ionization. None of the GPCho, SQDG and CL lipids was found to be essential for *R. sphaeroides*

C*c*O production, stability, or activity, indicating that each of these lipids could be functionally compensated by other lipids, despite the significantly depleted quantity of the specific lipid (< 5% of wild type) and altered membrane and C*c*O lipid profiles. The lipids in the purified C*c*O and C*c*O crystals reflected the species in the membrane though at different levels, but C*c*O did not display a significant accumulation of the depleted type of lipid. CL-deficient C*c*O could be crystallized under similar conditions to the wild type C*c*O, and produced 4-subunit and 2-subunit crystals that diffracted up to 3.2 Å and 2.8 Å respectively. Combination of CL-deficient mutation with phosphate-limiting growth created a five-fold cleaner CL-depleted mutant (< 1% CL), which displayed wild-type properties of the membranes and purified C*c*O, but the lipid profiles were drastically altered. It is concluded that the CL in bacteria ($CL(18:1)_4$) functions via mechanisms different from the previously reported CL in mammalian systems ($CL(18:2)_4$).

A novel type of non-phospholipid, glutamine lipid, was discovered and found to be increased in the phosphate-limiting growth. The quantification and identification of lipids were made possible by an in-depth investigation of the gas-phase fragmentation mechanisms of lipids in ion trap and triple quadrupole mass spectrometers. GPCho non-covalent anionic adducts, SQDG, diacylglycerol-N,N,N-trimethyl-homoserine (DGTS), ornithine lipids and glutamine lipids were characterized by using deuterium labeling, H/D exchange and multistage tandem mass spectrometry. The fingerprint ions for each type of lipid were proposed. The fragmentation mechanisms of these lipids were found to be highly dependent on the anion identity, charge state/site and ion conformation. The difficulties of detergent and lipid extraction from membrane proteins were also examined.

To

my grandparents

and parents

ACKNOWLEDGEMENT

The project is the product of the dual-degree program in Chemistry and Biochemistry & Molecular Biology under the joint guidance of Dr. Shelagh M. Ferguson-Miller and Dr. Gavin E. Reid, in close collaboration with Dr. Christoph Benning. Many people have helped me to make the program successful.

First and for most, I would like to give my deepest gratitude to my advisor Dr. Shelagh M. Ferguson-Miller, who is behind every step of progress and has made everything in this program become possible. Her ever-present encouragement, extraordinary scientific insight, enormous courage, perseverance and hard work to pursue untraveled path to find out the truth in scientific research have been the perpetual source of inspiration for me to proceed. She has led me through all of the difficult situations with extraordinary grace and courage, and demonstrated to me what is right. She would spend hours to drive me to gain the access to a functional mass spectrometer to obtain the confirmative experimental evidence, and she has made it possible for me to keep pursuing mass spectrometry. She has also taught me the importance of the efforts and ability to establish strategic collaborations in the new era of biological research.

Shelagh is not only an outstanding research advisor, she has also made a huge difference in a student's life and she is my mentor of life time. I am also very grateful to the Millers family for their warm encouragement and understanding throughout these years.

I sincerely thank Dr. Gavin E. Reid, who became my joint-advisor in the middle of my third year in the program, for guiding me through the exploration of the gas-phase fragmentations of lipids and for the rigorous training in mass spectrometry. His high

standards of requirements in understanding instrumentation and performing efficient experiments would also benefit my future scientific career. I sincerely thank him for allowing me the enormous amount of time to work on the mass spectrometers and providing me with his insightful comments and critiques. I am very thankful for the opportunity to start the lipid analysis using mass spectrometry in his lab, and I am also thankful for the invaluable opportunity to gain a glimpse of the challenges that a professor had to accomplish to launch a career.

Each of my committee members has gone out of his way to help me to accomplish this journey. Dr. Christoph Benning is also the joint principle investigator of the project, and has given me invaluable advice and critiques, which would benefit not only the research project but also my future career. Dr. Jack T. Watson, my second reader, has provided me with invaluable guidance, advice and discussions throughout the program, especially on the quantification of lipids during the interim of time when I didn't have a mass spectrometry advisor on board. I am very thankful to Dr. Gary Blanchard, who is also the graduate coordinator of the department of Chemistry, for being willing to go out of his way to help the journey of a graduate student's academic pursuit become successful.

I would like to thank Dr. John Allison, professor *emeritus* and my joint-advisor for the first two years of the program, for introducing me to the fascinating area of mass spectrometry. I also thank Dr. Julia Busik (Department of Physiology) and Dr. Walter J. Esselman (Department of Microbiology and Molecular Genetics) for the opportunity to start the application of the lipid analysis methods developed here to the investigation of diabetic retinopathy.

Even though all of the results presented in this dissertation are original and acquired independently, they wouldn't have been possible without the indispensible collaboration with Ms. Banita Tamot and Dr. Carrie Hiser. Ms. Banita Tamot from Dr. Benning's group not only created the CL-deficient mutant, but also taught me how to run the beautiful TLC analysis without reservation. Dr. Carrie Hiser expressed C*c*O in all of the strains examined in this dissertation, and she also shared with me the "perfect" protocols for the gel and oxygraph analyses.

The help and support from all of the Ferguson-Miller group members throughout these years have been invaluable. Dr. Ling Qin taught me how to perform the protein purification and crystallization, and has kindly served as the driver for the trips of crystallography data collection for the past two years. Together with Dr. Carrie Hiser, Dr. Denise Mills has always been willing to help me through, and they have spent valuable amounts of time to proof-read my entire dissertation. I am sincerely thankful to Dr. Carrie Hiser, Dr. Denise Mills, Dr. Ling Qin and Dr. Martyn Sharpe, for always making themselves available for my questions, and for the very helpful discussions throughout these years of study. I thank Namjoon Kim, Jian Liu and Leann for the helpful communications and warm encouragement. I also thank the former Allison group members, Anne, Jamie and Eric for their help in the first two years of the study.

I thank Kristy Lucien for preparing the cell cultures. I thank Todd Lydic for sharing the Advion autosampler settings during the SQDG analysis using the triple quadrupole mass spectrometer at Dr. Gavin Reid's lab. I thank MSU mass spectrometry facility for the access to the MALDI-TOF mass spectrometer for the first three years of the program.

Last but never the least, I am deeply thankful to my grandparents for their unreserved love and belief in me without conditions, and to my parents and sister for their complete understanding, encouragement and support from the other side of the Pacific.

TABLE OF CONTENTS

LIST OF TABLES xviii

LIST OF FIGURES xx

LIST OF SCHEMES xxxii

LIST OF ABBREVIATIONS xxxiv

CHAPTER 1 AN OVERVIEW OF THE STRUCTURAL AND FUNCTIONAL IMPACT OF MEMBRANE LIPIDS ON MEMBRANE PROTEINS, WITH A FOCUS ON CYTOCHROME *C* OXIDASE 1

1.1 INTRODUCTION: STRUCTURAL AND FUNCTIONAL ROLES OF LIPIDS IN MEMBRANE PROTEINS 1
1.2 LIPIDS IN CELL MEMBRANES 2
1.2.1 Lipids: the biological membrane environment 2
1.2.1.1 Basic structures of lipids 3
1.2.1.2 Dynamic modifications of lipid structures 10
1.2.1.3 Typical bacterial lipid structures 10
1.2.1.4 Cellular distribution of lipids 12
1.2.2 Biosynthesis of lipids and remodeling of cardiolipin 12
1.2.3 Structural /physical features underlying the functions of lipids 14
1.3 THE MEMBRANE PROTEIN CYTOCHROME *C* OXIDASE: STRUCTURE, FUNCTION, MECHANISM AND REGULATION 15
1.3.1 Oxidative phosphorylation and respiratory chain complexes 15
1.3.2 Structure of C*c*O 17
1.3.2.1 Electron transfer metal centers 18
1.3.2.2 Proton transfer pathways 19
1.3.2.3 Subunit characteristics 19
1.3.2.4 Bacterial *aa3*-C*c*O as a model for mammalian in mechanistic study 20
1.3.2.5 Lipid components in C*c*O and their significance 21
1.3.2.6 Function and mechanism of C*c*O and their analysis 24
1.3.3 Regulation of C*c*O 26
1.4 MEMBRANE BOUND SUPER-MOLECULAR COMPLEX ORGANIZATION 27
1.4.1 The "static" versus the "fluidic" model of organization 27
1.5 INTERACTIONS OF LIPIDS WITH MEMBRANE PROTEINS AND SUPER-MOLECULAR COMPLEXES 31
1.5.1 Interactions experienced by membrane proteins in a membrane environment 31
1.5.2 Effects of lipids on membrane proteins 34

1.5.2.1 Lipids interact with membrane proteins to maintain integrity of biological membranes 35
1.5.2.2 Lipids assist with membrane protein insertion, folding, assembly and topology 35
1.5.2.3 Lipids assist with assembly and stabilization of super-molecular complexes 37
1.5.2.4 Lipids affect or regulate membrane protein activities 37
1.5.2.5 Binding motifs of lipids in membrane proteins 37
1.5.3 Cardiolipin and OXPHOS complexes 41
1.5.4 Cardiolipin and CcO 42
1.6 MEMBRANE PROTEIN PURIFICATION AND CRYSTALLIZATION 44
1.6.1 Usage of detergent 45
1.6.2 Cubic phase technique: making lipids the medium 47
1.6.3 Optimization of crystallization using mass spectrometry as a tool 48
1.7 STRATEGIES USED TO INVESTIGATE MEMBRANE PROTEIN-LIPID INTERACTIONS 48
1.7.1 Biochemical extraction and phospholipase digestion 48
1.7.2 Spin-labeling combined with EPR 49
1.7.3 ^{31}P-NMR of lipids to monitor the lipid exchange 49
1.8 LIPID PROFILE MODIFICATION AS THE TOOL TO PROBE PROTEIN-LIPID INTERACTIONS *IN VIVO* 49
1.8.1 Genetic manipulation of lipid content as the probe *in vivo* 49
1.8.2 Phosphate limiting growth media 50
1.8.3 Growth temperature stress 51
1.8.4 Salt concentration (osmotic pressure) stress 51
1.9 SUMMARY 52

CHAPTER 2 AN OVERVIEW OF MASS SPECTROMETRY STRATEGIES EMPLOYED FOR LIPID ANALYSIS **53**

2.1 MASS SPECTROMETRY: THE ENABLING TOOL FOR LIPIDOMICS 53
2.2 SAMPLE PREPARATION FOR MASS SPECTROMETRIC ANALYSIS OF LIPIDS 54
2.2.1 Lipid extraction 56
2.3 TRADITIONAL METHODS FOR LIPID IDENTIFICATION AND QUANTIFICATION 58
2.4 MASS SPECTROMETRY 60
2.4.1 Ion source 61
2.4.1.1 MALDI 62
2.4.1.2 ESI 62
2.4.1.3 Direct imaging coupled with MALDI and DESI 63
2.4.1.4 Factors affecting the ionization of lipids 63
2.4.2 Mass analyzer 65
2.4.2.1 Quadrupole mass analyzer 65
2.4.2.2 CID MS/MS in triple quadrupole mass spectrometer 69
2.4.2.3 Quadrupole ion trap 72

2.4.2.4 MS/MS and MS^n in quadrupole ion trap 74
2.4.2.5 Factors affecting lipid analysis results using quadrupole ion trap 79
2.4.2.6 Other dissociation methods in the quadrupole ion trap 80
2.4.2.7 Other mass (m/z) analyzers 81
2.4.3 Ion detection 82
2.5 TOOLS TO UNRAVEL THE MECHANISMS OF MS^N FRAGMENTATION OF LIPIDS 82
2.5.1 Probing fragmentation mechanisms and product ion structures using MS/MS and MS^n experiments 83
2.5.2 Structural labeling 84
2.5.3 Isotopic labeling 84
2.5.4 Computation and theoretical modeling 85
2.6 FRAGMENTATION REACTIONS OF LIPIDS 85
2.6.1 Forms of lipids precursor ions 86
2.6.2 Characteristic MS/MS fingerprints for lipid class identification 87
2.6.3 Mechanistic aspects of the fragmentation of lipids in CID MS/MS and MS^n. 92
2.6.3.1 Charge state: positive vs negative 92
2.6.3.2 Fatty acid chain positions: *sn-1* vs *sn-2* 95
2.6.3.3 Head group: acidity 96
2.6.3.4 Conformational factors 96
2.6.3.5 Other factors 97
2.6.4 Identification of double bond position in CID MS/MS and MS^n 97
2.7 QUANTIFICATION OF LIPIDS USING MASS SPECTROMETRY 98

CHAPTER 3 MATERIALS AND METHODS **100**

3.1 MATERIALS 100
3.2 GROWTH AND EXPRESSION OF *Cc*O 102
3.2.1 Growth conditions 102
3.2.2 R. sphaeroides growth curves 103
3.2.3 Construction of CL-deficient mutant of *R. sphaeroides* 104
3.2.4 Engineering R. sphaeroides 2.4.1 and specific lipid-deficient strains to overproduce *Cc*O 104
3.3 PURIFICATION AND CHARACTERIZATION OF *Cc*O 110
3.3.1 Isolation of R. sphaeroides cell membrane pellets 110
3.3.2 Purification of *Cc*O using FPLC affinity chromatography 110
3.3.2.1 Detergent solubilization of membrane pellets 110
3.3.2.2 FPLC purification of *Cc*O 111
3.3.3 BCA protein assay 113
3.3.4 UV-Visible spectroscopy of membrane suspension and purified *Cc*O 114
3.3.5 Urea SDS-PAGE gel electrophoresis 114
3.3.6 Steady state activity assay of the *Cc*O based on oxygen consumption 115
3.3.7 Phosphorus analysis 116

3.4 CcO CRYSTALLIZATION 117
3.4.1 Four-subunit CcO crystallization 118
3.4.2 Two-subunit CcO crystallization 118
3.4.3 Flash-cooling of the CcO crystals 119
3.4.4 Harvesting CcO crystals for mass spectrometry analysis 120
3.4.5 X-ray diffraction data collection 120
3.5 LIPID EXTRACTION 120
3.5.1 Extraction of lipids from isolated membranes 120
3.5.2 Extraction of lipids from purified CcO 121
3.5.2.1 Acetone washing to remove detergent from purified CcO 122
3.5.2.2 Dilution-filtration (3 kDa) to remove detergent from purified CcO 123
3.5.3 Evaluation of extraction efficiency of lipids from purified CcO 123
3.6 THIN LAYER CHROMATOGRAPHY 124
3.6.1 1-D thin layer chromatography 124
3.6.2 Evaluation of cleavable detergent for potential application in lipids extraction from purified CcO using TLC 124
3.6.3 2-D thin layer chromatography 125
3.6.4 Quantitative TLC lipid analysis using ^{14}C-labeling 125
3.7 MASS SPECTROMETRY 126
3.7.1 Characterization of lipid extracts using ESI ionization sources 126
3.7.1.1 Identification of lipids by using ESI MS and CID MS^n on a linear quadrupole ion trap mass spectrometer 126
3.7.1.2 Pulsed-Q collision induced dissociation MS^n on a linear quadrupole ion trap 128
3.7.1.3 Analysis of lipid extracts using ESI MS and CID MS/MS on a triple quadrupole mass spectrometer 129
3.7.1.4 Extensive identification of lipids using ESI MS^n 130
3.7.2 Quantification of lipids using ESI MS and MS/MS 131
3.7.2.1 Internal standards for lipid quantification using ESI 131
3.7.2.2 Establishing the basis for quantification by using internal standards in ESI 132
3.7.2.3 Quantification of abundant species in lipid extracts using ESI MS 133
3.7.2.4 Quantification of low-abundance or overlapping species in lipid extracts using ESI CID MS/MS 134
3.7.2.5 "Purification" and relative quantification between molecular species of the SQDG using MS/MS 136
3.7.3 Direct lipid analysis using MALDI-LIT 136
3.7.3.1 Direct lipid identification analysis using MALDI-LIT MS and MS^n .. 136
3.7.3.2 Quantitative lipid comparison using MALDI-LIT MS 138
3.7.4 Optimizing the detection of lipids and subunits in purified CcO enzyme using MALDI-TOF MS 138

3.8 METHODS USED TO PROBE THE FRAGMENTATION MECHANISMS OF LIPIDS IN CID MS^N IN LINEAR ION TRAP MASS SPECTROMETER 140
3.8.1 Synthesis and fragmentation of structural analogues 140
3.8.2 H/D exchange of lipid extracts 140
3.8.3 Theoretical calculations 141

CHAPTER 4 MULTISTAGE TANDEM MASS SPECTROMETRY OF ANIONIC PHOSPHATIDYLCHOLINE LIPID ADDUCTS REVEALS NOVEL DISSOCIATION PATHWAYS **142**

4.1 SUMMARY 142
4.2 INTRODUCTION 144
4.3 RESULTS AND DISCUSSION 146
4.3.1 Dependence of the formation of anionic adducts on the phospholipid type.. 146
4.3.2 Negative ion CID MS/MS of anionic adducts of GPCho 16:0/16:0 and GPCho 16:0/18:1 147
4.3.3 CID MS^3 experiments to probe the structure of the product ions formed by neutral loss of (A+15) from the anionic adducts of GPCho 165
4.3.4 Deuterium isotope labeling and CID MS^3 experiments to probe the structure of the product ions formed by neutral loss of (A+60) from the anionic adducts of GPCho 171
4.3.5 Deuterium isotope labeling and CID MS^3 experiments to probe the structure of the product ions formed by neutral loss of (A+86) from the anionic adducts of GPCho 176
4.3.6 Deuterium isotope labeling and CID MS^3 and MS^4 experiments to probe the structure of the $[M+A-59]^-$ product ion formed from the $H_2PO_4^-$ adducts of GPCho 179
4.3.7 Deuterium isotope labeling and CID MS^3 experiments to probe the structure of the $[M+A-(A+1)]^-$ product ions formed from the anionic adducts of GPCho and isotope effect 182
4.3.8 Deuterium isotope labeling and CID MS^3 experiments to probe the structure of the $[M+A-(A+16)]^-$ product ions formed from MS/MS of anionic adducts of GPCho 189
4.3.9 Rationalizing the effects of anions on the gas-phase fragmentation behavior of anionic adducts of GPCho 190
4.3.10 Competitive formation of anionic adducts with GPCho 193
4.4 CONCLUSIONS 197

CHAPTER 5 CHARACTERIZATION OF ORNITHINE AND GLUTAMINE LIPIDS IN THE CELL MEMBRANES OF *RHODOBACTER SPHAEROIDES* **198**

5.1 SUMMARY 198
5.2 INTRODUCTION 200
5.3 RESULTS AND DISCUSSION 204
5.3.1 ESI-MS of wild type and GPCho-deficient *R. sphaeroides* 204
5.3.2 Identification and characterization of ornithine lipids in *R. sphaeroides* by using positive and negative ionization mode MS^n 208
5.3.3 Identification and characterization of glutamine lipids in *R. sphaeroides* by using positive and negative ionization mode MS^n 224
5.3.4 Summary of the ornithine and glutamine lipid species identified from wild type and GPCho-deficient *R. sphaeroides* cell membranes 240
5.4 CONCLUSIONS 243

CHAPTER 6 CHARACTERIZATION OF SULFOQUINOVOSYLDIACYL-GLYCERIDE (SQDG) AND DIACYLGLYCERYL-N, N, N-TRIMETHYL-HOMOSERINE (DGTS) LIPIDS EXTRACTED FROM *RHODOBACTER SPHAEROIDES* USING TRIPLE QUADRUPOLE AND LINEAR ION TRAP MASS SPECTROMETRY **244**

6.1 SUMMARY 244
6.2 INTRODUCTION 247
6.2.1 Biological interests in SQDG and DGTS lipids 247
6.2.2 Current status of structural studies of SQDG and DGTS 249
6.3 RESULTS AND DISCUSSION 253
6.3.1 Fragmentation behaviors of SQDG in MS/MS and MS^n 253
6.3.1.1 CID MS/MS of SQDG in a triple quadrupole mass spectrometer 253
6.3.1.2 PQD MS/MS fragmentation of SQDG lipids in a quadrupole linear ion trap 258
6.3.1.3 Collision energy dependence on fragmentation in a quadrupole linear ion trap 259
6.3.1.4 MS^n fragmentation of SQDG in a quadrupole linear ion trap 263
6.3.2 Fragmentation mechanisms of SQDG in CID MS/MS and MS^n 265
6.3.3 Relative quantification of SQDG in lipid extract using MS/MS 271
6.3.4 Fragmentation behaviors of DGTS in MS/MS and MS^n 275
6.3.4.1 CID MS/MS and MS^n fragmentation of DGTS in quadrupole linear ion trap 275
6.4 CONCLUSIONS 281

CHAPTER 7 MASS SPECTROMETRY IDENTIFICATION AND SELECTIVE QUANTIFICATION OF *RHODOBACTER SPHAEROIDES* MEMBRANE LIPIDS: PROBING THE EFFECTS OF LIPID SPECIFIC MUTANTS ON CYTOCHROME *C* OXIDASE PRODUCTION AND ACTIVITY **283**

7.1 SUMMARY 283
7.2 INTRODUCTION 285
7.2.1 Lipids and the membrane bound redox protein C*c*O 285
7.2.2 Lipid-deficient mutants as the tool to probe the functions of lipids for C*c*O 286
7.2.3 Properties of the C*c*O produced from the lipid-deficient mutants 288
7.2.3.1 Cell growth, C*c*O expression in membranes and purification stability from the specific lipid-deficient mutants 288
7.2.3.2 UV-Vis spectroscopic properties of the purified C*c*O from the four strains 290
7.2.3.3 SDS-PAGE analysis of the purified C*c*O from the four strains 290
7.2.3.4 Activity of purified C*c*O from the four strains 292
7.2.3.5 Activity stability of the purified C*c*O under temperature stress: WT and CL− 292
7.2.4 Lipidomics 295
7.2.5 Complete lipid structural identification by using MS^n 295
7.2.6 Membrane lipids of R. sphaeroides 296
7.3 RESULTS AND DISCUSSIONS 297
7.3.1 Identification of membrane lipids in the wild type and the mutants 297
7.3.1.1 Traditional TLC analysis of the lipid profiles of membranes from each mutant 297
7.3.1.2 Identification of lipids in the wild type membrane using MS/MS and MS^3 301
7.3.1.3 Ion overlapping in MS illustrated by MMPE and DMPE 311
7.3.1.4 Changes in the lipid species in the mutants 317
7.3.2 Basis for absolute quantification by MS and MS/MS using internal standards 318
7.3.3 Quantitative lipid profiles of membranes from each mutant 320
7.3.3.1 Quantitative lipid profiles of membranes: abundant membrane lipids using ESI MS 320
7.3.3.2 Summary of the quantification of membrane lipid species 325
7.3.3.3 Quantification of the CL-deficient mutant: the low-abundance cardiolipin using ESI MS/MS 332
7.3.4 Interpreting the physiological meaning of the specific lipid deficiency in membranes 335
7.3.5 Profiles of the lipids maintained in the purified C*c*O: WT and CL− 337
7.4 CONCLUSIONS 346

CHAPTER 8 LIPID EXTRACTION FROM MEMBRANE PROTEINS: EFFECTS OF DETERGENT AND DETERGENT REMOVAL PROCEDURES ON EXTRACTION EFFICIENCIES **349**

8.1 SUMMARY 349
8.2 INTRODUCTION 351
8.2.1 The need to remove detergent from membrane proteins for lipid analysis ... 351

8.2.2 The issue of incomplete extraction of lipids from membrane proteins 353
8.2.3 The variables that might affect the lipid extraction efficiency 354
8.2.4 Approaches to improve the lipid extraction efficiency from C*c*O 358
8.3 RESULTS AND DISCUSSIONS 360
8.3.1 Evaluation of the efficiency of detergent removal methods 360
8.3.1.1 Detergent removal by a dilution-filtration method 360
8.3.1.2 Acetone-washing method to remove detergent 367
8.3.2 What affects the extraction of lipids from membrane protein C*c*O 370
8.3.2.1 Lyophilization of C*c*O prior to extraction 371
8.3.2.2 Acetone washing of C*c*O prior to extraction 372
8.3.2.3 Partial digestion of C*c*O to assist with the lipid release during extraction 373
8.3.2.4 Addition of acid or base in the extraction solvent 373
8.3.2.5 Urea treatment of C*c*O 374
8.3.2.6 Usage of cleavable detergent for detergent removal 374
8.3.3 Future directions 375
8.4 CONCLUSIONS 375

CHAPTER 9 CRYSTALLIZATION OF CYTOCHROME *C* OXIDASE PRODUCED IN A CARDIOLIPIN-DEFICIENT MUTANT OF *RHODOBACTER SPHAEROIDES* AND ITS LIPID PROFILE CHARACTERIZATION **377**

9.1 SUMMARY 377
9.2 INTRODUCTION 378
9.2.1 Why the focus of interest on CL in C*c*O 378
9.2.2 Effect of CL deficiency on *R. sphaeroides* cell growth 381
9.2.3 Production of C*c*O in *R. sphaeroides* WT and CL− cells 384
9.2.4 Properties of C*c*O purified from wild type and *cls* mutant cell lines 386
9.3 RESULTS 388
9.3.1 MALDI analysis of the membrane lipids expressing C*c*O 388
9.3.2 Purification and crystallization of C*c*O from cls mutant and wild type 395
9.3.3 MALDI analysis of the lipids in the re-dissolved four-subunit C*c*O crystals 397
9.4 DISCUSSIONS 405
9.4.1 Residual CL in the cardiolipin deficient mutant 405
9.4.2 Molecular components of CL species in *R. sphaeroides* 406
9.4.3 CL and growth of *R. sphaeroides* 407
9.4.4 A role for CL in the function or assembly of C*c*O of *R. sphaeroides* 408
9.4.5 Lipid mutants of *R. sphaeroides* as tools for the study of membrane proteins 410

CHAPTER 10 CHARACTERIZATION OF A CARDIOLIPIN-DEFICIENT MUTANT OF *RHODOBACTER SPHAEROIDES*, UNDER PHOSPHATE-LIMITED AND

PHOSPHATE-RICH CONDITIONS, WITH REGARD TO CYTOCHROME *C* OXIDASE PRODUCTION, ACTIVITY AND LIPID PROFILE MODIFICATION...**412**

10.1 SUMMARY 412
10.2 INTRODUCTION 414
10.2.1 Lipid profile modulation using phosphate-limiting growth media 414
10.2.2 Combining specific lipid-deficient mutation with phosphate-limiting growth 415
10.3 RESULTS AND DISCUSSIONS 417
10.3.1 Cell growth, C*c*O expression in membranes and purification stability 417
10.3.2 Characterization of C*c*O purified from the four cell samples 420
10.3.2.1 UV-Vis spectroscopic properties of the purified C*c*O 420
10.3.2.2 SDS-PAGE analysis of the purified C*c*O 422
10.3.2.3 Activity analysis of the purified C*c*O 424
10.3.3 Quantitative analysis of the membrane lipids profile for low-phosphate growth 426
10.3.4 Quantitative analysis of the lipids in the membrane grown with low-phosphate using MALDI 445
10.3.5 Analysis of the lipids in the purified C*c*O grown with low-phosphate using MALDI 452
10.4 CONCLUSIONS 463

BIBLIOGRAPHY **465**

LIST OF TABLES

TABLE 1.1 Basic structures of lipids found in eukaryotes and bacteria **5**

TABLE 1.2 Amino acid residues that bind the head groups of negatively charged lipids resolved in membrane protein crystal structures **39**

TABLE 1.3 Amino acid residues that bind the fatty acid tails of lipids resolved in membrane protein crystal structures **40**

TABLE 2.1 Characteristic CID MS/MS fragmentations of lipids previously identified in the literature. **89**

TABLE 3.1 *R. sphaeroides* strains and C*c*O plasmids used in this work **107**

TABLE 4.1 Negative ion mode CID MS/MS of anionic adducts of GPCho 16:0/16:0 and GPCho 16:0/18:1 ..... **151**

TABLE 4.2 Summary of the negative ion mode CID MS^3 product ions of various anionic adducts of GPCho **154**

TABLE 5.1 Summary of the ornithine (OL) and glutamine (QL) lipid species extracted from the cell membranes of wild type and GPCho-deficient *R. sphaeroides* **242**

TABLE 7.1 Identification of the lipid ions in positive ion mode MS of the membrane extracts of the wild type *R. sphaeroides* **303**

TABLE 7.2 Identification of the lipid ions in negative ion mode MS of the membrane extracts of the wild type *R. sphaeroides* **305**

TABLE 7.3 Lipid species identified in the membrane extracts of the wild type *R. sphaeroides* **308**

TABLE 7.4 Summary of lipids extracted from the membranes of wild type (2.4.1+C*c*O) and CL-deficient mutant (CL3+C*c*O), using MS and MS/MS: CL-deficient membranes are significantly depleted in cardiolipin **335**

TABLE 7.5 Summary of the percentage of changes in the quantity of phospholipids from the lipid extracts of C*c*O purified from the wild type (2.4.1+C*c*O) and the CL-deficient strain (CL3+C*c*O), in comparison to the membranes **343**

TABLE 8.1 Potential approaches to improve the lipid extraction efficiency from membrane proteins at different stages of lipid extraction **359**

TABLE 8.2 Effects of freeze-drying (fre-d) and acetone washing (ace-w) on the lipid extraction efficiency from C*c*O Basic structures of lipids found in eukaryotes and bacteria **370**

TABLE 9.1 Spectral and enzymatic properties of C*c*O purified from *R. sphaeroides* wild-type and BC-m3 cell lines **387**

TABLE 9.2 Crystallography screening results of C*c*O crystals obtained from *R. sphaeroides* wild type and *cls* mutant at different crystal growth temperatures **397**

LIST OF FIGURES

FIGURE 1.1 Traditional fluid mosaic model of a biological membrane in mammalian cells constituted by lipid bilayers **3**

FIGURE 1.2 Major biosynthetic pathways for phospholipids, and the different cardiolipin synthetic pathway in eukaryotes **13**

FIGURE 1.3 The mitochondrial respiratory chain complexes and ATPase that are responsible for the oxidative phosphorylation in eukaryotic systems **16**

FIGURE 1.4 Comparison of *R. sphaeroides* and bovine mitochondrial C*c*O structures **21**

FIGURE 1.5 Membrane lipids resolved in the crystal structure of *Rs* C*c*O **23**

FIGURE 1.6 C*c*O crystal structures showing bound lipids, (A) bovine heart C*c*O showing the lipid content, and (B) superimposed structure showing the conserved sites for lipids in subunits I and II **24**

FIGURE 1.7 The oxygen chemistry cycle of the reaction catalyzed by C*c*O..... **25**

FIGURE 1.8 Fitting of atomic structures of the yeast cytochrome bc_1 complex (*red*) and the bovine heart cytochrome *c* oxidase or complex IV (*green*) into selected EM projection maps for assignment of the arrangement of the $III_2 + IV_2$ and $III_2 + IV_1$ supercomplexes **28**

FIGURE 1.9 Scheme for dimeric ATP synthase from mitochondria **29**

FIGURE 1.10 Interactions that determine the structure and stability of membrane proteins **32**

FIGURE 1.11 Liquid crystallographic structure of a fluid lipid bilayer and its computed polarity profile **33**

FIGURE 1.12 Difference in the topological organization of LacY from *E. coli* cells containing (top) and genetically lacking (bottom) GPEtn (PE) **36**

FIGURE 1.13 Pseudo-atomic model of the $III_2 + IV_2$ super-complex with attached cytochrome *c*, showing the interactions of cardiolipin with complexes III and IV..... **41**

FIGURE 1.14 Schematic of the isolation of membrane proteins from membranes using detergent dodecyl maltosides **45**

FIGURE 2.1 Schematic showing the general operation of a mass spectrometer **61**

FIGURE 2.2 Stability of ions at different m/z as a function of U (DC) and V (RF) amplitudes in the quadrupole electric field, and the three operation modes under different applications of U and V ($m_1 < m_2 < m_3$) **68**

FIGURE 2.3 Three types of CID MS/MS scans typically applied in a triple quadrupole mass spectrometer: product ion scan, precursor ion scan and neutral loss scan **70**

FIGURE 2.4 Stability diagram of ions of different m/z in the 3-D quadrupole ion trap (upper graph), and the trapping efficiency represented by the Dehmelt potential (D) in eV (lower graph, right axis) as a function of the q value **74**

FIGURE 2.5 Operation modes of quadrupole ion trap as a function of the drive RF and supplementary RF amplitudes in an MS/MS example **75**

FIGURE 3.1 Full length amino acid sequences of *R. sphaeroides* *Cc*O deduced from the genome **109**

FIGURE 3.2 Typical FPLC gradient profile used in the purification of subunit II his-tagged *Cc*O in this study **112**

FIGURE 3.3 Vapor diffusion crystallization using (A) hanging drop setup, and (B) sitting drop setup **118**

FIGURE 4.1 Negative ionization mode CID MS/MS product ion spectrum of the $[M+A]^-$ precursor ions of GPCho 16:0/16:0 formed by anionic adduction with (A) acetate (*m/z* 792) and (B) methylcarbonate (*m/z* 808) **150**

FIGURE 4.2 Negative ionization mode (A) CID MS^3 product ion spectrum of the *m/z* 718 product ion formed via the neutral loss of ($A+CH_3$) from the acetate adduct of GPCho 16:0/16:0 in Figure 4.1A. (B) CID MS/MS product ion spectrum of the $[M-H]^-$ precursor ion of N, N-dimethylphosphatidyl-ethanolamine 16:0/16:0 ..... **167**

FIGURE 4.3 Negative ionization mode CID MS/MS product ion spectra of the methyl-carbonate adducts of (A) d_4-GPCho 16:0/16:0 (*m/z* 812), (B) GPCho d_{31}-16:0/d_{31}-16:0 (*m/z* 870) and (C) d_{13}-GPCho 16:0/16:0 (*m/z* 821) **173**

FIGURE 4.4 Negative ionization mode (A) CID MS^3 product ion spectrum of the *m/z* 673 product ion formed via the neutral loss of $(AH+(CH_3)_3N)$ from the methylcarbonate adduct of GPCho 16:0/16:0 in Figure 4.1B. (B) CID MS/MS product ion spectrum of the $[M-H]^-$ precursor ion of phosphatidylethanol 16:0/16:0 (m/z 675) **175**

FIGURE 4.5 Negative ionization mode (A) CID MS^3 product ion spectra of the m/z 673 product ion formed via the neutral loss of $[A+(CH_3)_3NCH=CH_2]$ from the methylcarbonate adduct of GPCho 16:0/18:1 in Table 4.1. (B) CID MS/MS product ion spectrum of the $[M-H]^-$ precursor ion of phosphatidic acid 16:0/18:1 (m/z 673) **178**

FIGURE 4.6 (A) Negative ionization mode CID MS/MS product ion spectrum of the phosphate ($H_2PO_4^-$) adduct of GPCho16:0/18:1 (m/z 856). (B) CID MS^3 product ion spectrum of the m/z 797 product ion formed via the neutral loss of $(CH_3)_3N$ (59 Da) from Figure 4.6A **181**

FIGURE 4.7 Negative ionization mode CID MS^3 product ion spectrum of (A) the m/z 732 product ion formed via the neutral loss of (AH) from the methylcarbonate adduct of GPCho 16:0/16:0 in Figure 4.1B. (B) the m/z 793 product ion formed via the neutral loss of (AD) from the methylcarbonate adduct of GPCho d_{31}-16:0/d_{31}-16:0 in Figure 4.3B. (C) the m/z 794 product ion formed via the neutral loss of (AH) from the methylcarbonate adduct of GPCho d_{31}-16:0/ d_{31}-16:0 in Figure 4.3B .. **185**

FIGURE 4.8 Negative ionization mode CID MS/MS product ion spectra of the trifluoroacetate adducts of (A) d_4-GPCho16:0/16:0 (m/z 850), (B) GPCho d_{31}-16:0/d_{31}-16:0 (m/z 908) and (C) d_{13}-GPCho16:0/16:0 (m/z 859)... **188**

FIGURE 4.9 Negative ionization mode CID MS^3 product ion spectrum of the m/z 717 product ion formed via the neutral loss of (A+16) from the trifluoroacetate adduct of GPCho 16:0/16:0 in Table 4.1 ..... **190**

FIGURE 4.10 Most stable structure (calculated at the PM3 level of theory) for the anionic chloride adduct of the model phosphatidylcholine lipid GPCho 6:0/6:0 ..... **192**

FIGURE 4.11 Dependence of the ion abundance of anionic adducts formed from (A) formate (m/z 778), (B) acetate (m/z 792), (C) chloride (m/z 768) and (D)

methyl carbonate (m/z 808) on the concentration of ammonium formate, ammonium acetate, ammonium chloride and ammonium hydroxide, in the solution of chloroform: methanol (1:1, v/v) containing 5 μM GPCho 16:0/16:0, analyzed in negative ion mode ESI MS **195**

FIGURE 4.12 The ratio of ion abundances of anionic adducts formed from A) $[M+formate]^-$ and $[M+acetate]^-$ (at m/z 778 and m/z 792) against the ratio of concentrations of ammonium formate/ammonium acetate in solution, and B) $[M+chloride]^-$ and $[M+formate]^-$ (at m/z 768 and m/z 778) against the ratio of concentrations of ammonium formate/ ammonium chloride in solution, in negative ion mode ESI MS, while the concentration of GPCho 16:0/16:0 was maintained at 5 μM.. ..... **196**

FIGURE 5.1 Positive ESI MS of crude lipid extracts isolated from the cell membranes of (A) wild type and (B) GPCho-deficient mutant *R. sphaeroides* (both with C*c*O over-expression) **207**

FIGURE 5.2 Identification of ornithine lipid (OL 3–OH 20:1/20:2) at m/z 731 from Figure 5.1B by positive ion CID MS/MS and MS^n **211**

FIGURE 5.3 Identification of ornithine lipid (OL 3–OH 20:1/20:2) (m/z 729) from Figure 5.1D by negative ion CID MS/MS and MS^n **215**

FIGURE 5.4 The fragmentation of ornithine standard in positive and negative ion modes **218**

FIGURE 5.5 The fragmentation of N_α–acetyl ornithine standard in positive and negative ion modes **219**

FIGURE 5.6 Identification of ornithine lipids (OL 3–OH 18:0/20:2 and OL 3–OH 20:1/18:0) at m/z 705 from Figure 1B by (A) CID MS/MS and by (B) CID MS^n of the m/z 687 ion from panel A. (C) Negative ion CID MS/MS of the corresponding ion at m/z 703 from Figure 1D **223**

FIGURE 5.7 Identification of overlapping ornithine (OL 3–OH 20:1/19:1) and glutamine (QL 3–OH 20:1/18:1) lipids at m/z 719 by positive ion ESI CID MS/MS and MS^n **225**

FIGURE 5.8 Identification of overlapping ornithine (OL 3–OH 20:1/19:1) and glutamine (QL 3–OH 20:1/18:1) lipids at m/z 719 by positive ion ESI CID MS^n **227**

FIGURE 5.9 Comparison of the positive ion mode ESI CID MS/MS spectra of m/z 189, the $[M + H]^+$ ions generated from synthesized amino acid standards: A) N_α-Ac-Gln, B) N_α-Ac-Lys, C) N_ε-Ac-Lys, D) N_δ-Me-N_α-Ac-Orn and E) O-Me-N_α-Ac-Orn **229**

FIGURE 5.10 Comparison of the negative ion mode ESI CID MS/MS spectra of m/z 187, the $[M - H]^-$ ions generated from synthesized amino acid standards: A) N_α-Ac-Gln, B) N_α-Ac-Lys, C) N_ε-Ac-Lys, D) N_δ-Me-N_α-Ac-Orn and E) O-Me-N_α-Ac-Orn **231**

FIGURE 5.11 The fragmentation of N_α–propyl glutamine standard in positive and negative ion modes: A) MS/MS of $[M + H]^+$ ions at m/z 203, B) MS/MS of $[M - H]^-$ ions at m/z 201 ..... **233**

FIGURE 5.12 Identification of overlapping ornithine (OL 3–OH 20:1/19:1) and glutamine (QL 3–OH 20:1/18:1) lipids at m/z 717 by negative ion ESI CID MS/MS and MS^n **237**

FIGURE 6.1 Negative ionization mode ESI MS/MS of m/z 819 (SQDG 16:0/18:1) using CID on the triple quadrupole (QqQ) mass spectrometer **255**

FIGURE 6.2 Collision-energy-resolved CID of m/z 845 (SQDG 18:1/18:1) (A), and m/z 819 (SQDG 16:0/18:1) (B) in MS/MS when the collision energy is changed from 10 to 70 V **257**

FIGURE 6.3 Negative ion mode ESI MS/MS product ion analysis of m/z 819 (SQDG 16:0/ 18:1) from *R. sphaeroides*, using pulsed-Q dissociation (PQD) on the quadrupole linear ion trap (LIT) mass spectrometer **258**

FIGURE 6.4 Negative ionization mode MS/MS product ion spectrum of m/z 819 (SQDG 16:0/18:1) from *R. sphaeroides* *Cc*O lipid extract **259**

FIGURE 6.5 Normalized collision-energy-resolved relative abundance of each product ion generated from m/z 819 (SQDG 16:0/18:1) from *R. sphaeroides* by ESI-LIT using CID MS/MS (A), and PQD MS/MS (B) fragmentations, plotted as the percentage of the total abundance of all the major product ions **262**

FIGURE 6.6 Negative ionization mode MS^3 product ion spectra of m/z 819 (SQDG 16:0/18:1) from *R. sphaeroides* *Cc*O lipid extract shown in Figure 6.4. (A) MS^3 of m/z 537, (B) MS^3 of m/z 563, and (C) MS^3 of product ion m/z

225 generated from m/z 819, which is identical to MS^4 of 225, using collision-induced dissociation (CID) on the ESI-linear ion trap (LIT) mass spectrometer **264**

FIGURE 6.7 Negative ionization mode A) MS/MS product ion analysis of m/z 822 (d_3-SQDG 16:0/18:1) from *R. sphaeroides* membrane lipid extract after in-solution H/D exchange using CD_3OD. B) MS^3 of m/z 540 from A), and C) MS^3 of m/z 566 from A), and D) MS^3 of product ion m/z 227 generated from 822 in panel A, using CID on the ESI-LIT mass spectrometer (h.g.=head group) **267**

FIGURE 6.8 Negative ionization mode ESI A) MS and B) CID MS/MS precursor ion scan for m/z 225 using the QqQ mass spectrometer, to selectively identify all the SQDG lipid species in the membrane lipid extract from the *R. sphaeroides* 2.4.1+C*c*O strain **273**

FIGURE 6.9 Negative ionization mode ESI A) MS and B) CID MS/MS precursor ion mapping for m/z 225 using the LIT mass spectrometer, to selectively identify all the SQDG lipid species in the membrane lipid extract from the *R. sphaeroides* CL3+C*c*O strain **274**

FIGURE 6.10 MALDI MS spectrum (A), and the low energy CID MS/MS (B) and MS^n (C and D) fragmentation of the protonated ions ($[M + H]^+$) of diacylglycerol-N, N, N-trimethylhomoserine (DGTS) from the membrane of *R. sphaeroides* (with C*c*O over-expression) aerobically grown under phosphate-limited conditions, using the MALDI-quadrupole linear ion trap mass spectrometer **277**

FIGURE 7.1 Reduced-oxidized UV-Vis spectroscopy of dodecylmaltoside-solubilized membranes isolated from *R. sphaeroides* 2.4.1+C*c*O (wild type), and the specific CL-deficient (CL3+C*c*O), SQDG-deficient (SB1K1+C*c*O) and GPCho-deficient (CHB20+C*c*O) stains, grown under aerobic conditions **289**

FIGURE 7.2 Reduced UV-Vis spectroscopy of C*c*O purified from *Rhodobacter sphaeroides* 2.4.1+C*c*O (wild type), and the specific CL-deficient (CL3+C*c*O), SQDG-deficient (SB1K1+C*c*O) and GPCho-deficient (CHB20+C*c*O) stains grown under aerobic conditions **291**

FIGURE 7.3 Steady-state oxygen consumption activity analysis of purified C*c*O using Ni-NTA gravity column from *Rhodobacter sphaeroides* 2.4.1+C*c*O (wild type), and the specific single lipid type deficient strains CL3+C*c*O (CL deficient), SB1K1+C*c*O (SQDG-deficient) and CHB20+C*c*O (GPCho-

deficient), before and after the addition of asolectin lipids in the reaction mixture **293**

FIGURE 7.4 Oxygen consumption activities of the Ni-NTA-purified C*c*O from the CL-deficient mutant (CL3+C*c*O) and the wild type (2.4.1+C*c*O), as a function of temperature (enzymes are incubated at each temperature for 1 minute in 10 μL aliquots) **294**

FIGURE 7.5 TLC of lipid extracts from the isolated membranes of the wild type and the specific lipid-deficient mutants of *R. sphaeroides*, containing 2.3 μg membrane proteins determined by the BCA assay **299**

FIGURE 7.6 The ESI MS spectra of the lipid extract from the cell membranes of the 2.4.1 wild type *R. sphaeroides* in (A) positive, and (B) negative ion modes **301**

FIGURE 7.7 Positive ion mode ESI MS/MS and MS^3 spectra of m/z 758 in the MS of lipid extracts from the cell membranes of the wild type *R. sphaeroides* reveal that this isotopically isolated precursor ion contains multiple species lead by GPCho 34:2, GPEtn 18:1/19:1 and N-Me GPEtn 18:1/18:1 ..... **312**

FIGURE 7.8 ESI MS/MS (A), and MS^3 spectra of m/z 780 from Figure 7.6A) revealing the overlapping of the sodium adduct ions of GPCho 34:2 (B), N-Me GPEtn 18:1/18:1 (C) and GPEtn 18:1/19:1 (D) **313**

FIGURE 7.9 ESI MS/MS (A), and MS^3 spectra of m/z 756 from Figure 7.6B) in the negative ion mode, revealing the overlapping of the deprotonated ions of N-Me GPEtn 18:1/18:1 (B) and GPEtn 18:1/19:1 (C) **315**

FIGURE 7.10 Correlation between the peak abundance ratios in ESI MS and MS/MS spectra and the actual concentration ratios of GPEtn, GPGro, GPCho and CL lipid standards containing two 18:1 fatty acid chains and the lipid standards containing two 14:0 fatty acid chains, in the lipid mixture solutions prepared at random combinations of concentrations (0 – 12 μM) **319**

FIGURE 7.11 Positive ion mode ESI MS of lipids extracted from cell membranes of A) wild type (2.4.1+C*c*O) B) CL-deficient (CL3+C*c*O) C) SQDG-deficient (SB1K1+C*c*O) and D) GPCho-deficient (CHB20+C*c*O) mutants of *R. sphaeroides*, with the internal standards GPEtn, GPGro, GPCho and CL 14:0 at final concentrations of 4, 2, 2 and 1 μM, respectively **321**

FIGURE 7.12 Negative ion mode ESI MS of lipids extracted from cell membranes of A) wild type (2.4.1+C*c*O) B) CL-deficient (CL3+C*c*O) C) SQDG-deficient

(SB1K1+C*c*O) and D) GPCho-deficient (CHB20+C*c*O) mutants of *R. sphaeroides*, with the internal standards GPEtn, GPGro, GPCho and CL 14:0 at final concentrations of 4, 2, 2 and 1 μM, respectively **323**

FIGURE 7.13 Summary of the quantification of the major phospholipid ions observed in the MS spectra of the membrane lipid extracts from the wild type and the specific lipid-deficient mutant in positive ion mode, based on triplicate extractions (except for duplicate for the CHB20 samples) **326**

FIGURE 7.14 Summary of the quantification of the major lipid ions observed in the MS spectra of the membrane lipid extracts from the wild type and the specific lipid-deficient mutant in negative ion mode, based on triplicate extractions (duplicate for the CHB20 sample) **327**

FIGURE 7.15 Quantitative phospholipid compositions in the membranes of in the wild type and the mutant strains, from negative ion mode MS analysis **330**

FIGURE 7.16 The percentage change in the quantity of each type of membrane lipid with available internal standards, relative to the wild type **331**

FIGURE 7.17 Negative ion mode nanoESI MS and MS/MS of lipids extracted from membranes of wild type (2.4.1+C*c*O) and cardiolipin-deficient (CL3+C*c*O) *R. sphaeroides* cells **333**

FIGURE 7.18 Negative ion mode nanoESI MS and MS/MS of lipids extracted from C*c*O purified from the wild type (2.4.1+C*c*O) and cardiolipin-deficient (CL3+C*c*O) *R. sphaeroides* membranes using a Ni-NTA gravity column **339**

FIGURE 7.19 The ratio of the numbers of moles of the lipids extracted from the purified C*c*O to the numbers of moles of the original purified C*c*O (moles/ moles), which should indicate the stoichiometric relationship of the lipids in C*c*O, and the relative quantification of other types of lipids **341**

FIGURE 8.1 The efficiency of detergent removal by the dilution-filtration method (3k molecular weight cutoff) from the detergent-containing membrane samples, displayed by thin layer chromatography (TLC) of the lipids, extracted from the resuspended membranes (8.7 μL, 1.25 mg of total membrane proteins determined by BCA assay) of R. sphaeroides 169Δ4 strain, diluted with 104 μL of the FPLC buffer containing 0.05% DDM **361**

FIGURE 8.2 The efficiency of detergent removal by the dilution-filtration method (3 kDa molecular weight cutoff) from the purified C*c*O enzymes is displayed using TLC of the lipids extracted from the purified C*c*O enzymes from the

R. sphaeroides 169Δ4 strain, in buffers containing 0.05% DDM or 0.2% DM **364**

FIGURE 8.3 Negative ion mode ESI MS of lipids extracted from wild type C*c*O enzyme purified by Ni-NTA gravity column, after three repeats of the dilution-filtration steps to clean up the detergent **366**

FIGURE 8.4 The efficiency of detergent removal by the acetone-washing method from the purified C*c*O enzymes, displayed by TLC of the lipids extracted from 0.68 μg purified C*c*O enzymes from the *R. sphaeroides* 169Δ4 strain ... **368**

FIGURE 9.1 Growth curves of *R. sphaeroides* 2.4.1and BC-m3 strains under A) anaerobic photoheterotrophic growth, and B) aerobic chemoheterotrophic growth conditions, both in Sistrom's media at 30 °C **383**

FIGURE 9.2 Optical difference spectra of dithionite-reduced minus ferricyanide-oxidized solubilized membranes from *R. sphaeroides* strains 2.4.1 (wild-type, graph A) and 2.4.1+C*c*O (with C*c*O plasmid pYJ123H, graph B) . **385**

FIGURE 9.3 Negative ion mode MALDI-MS spectra of isolated membranes from CL−proficient and CL-deficient *R. sphaeroides* **390**

FIGURE 9.4 Positive ion mode MALDI-MS spectra of isolated membranes from *R. sphaeroides* strains: A) wild type (2.4.1+C*c*O), B) CL-deficient mutant (BC-m3+C*c*O), C) wild type with *cls* gene insertion (2.4.1+C*c*O+*cls*) and D) CL-deficient mutant with *cls* gene insertion (BC-m3+C*c*O+*cls*), analyzed at 0.25 mg/mL protein concentration. All strains produce C*c*O from pYJ123H **393**

FIGURE 9.5 Oxidized and reduced spectra of FPLC-purified C*c*O from A) 169WT (WT) and B) 169CL3 (CL−) strains grown aerobically at 30 °C **396**

FIGURE 9.6 Negative ion mode MALDI-MS spectra of isolated membranes and C*c*O protein crystals from CL-proficient and CL-deficient *R. sphaeroides* ... **399**

FIGURE 9.7 Positive ion mode MALDI-MS spectra of isolated membranes (A and B) and C*c*O crystals (C and D) from CL-proficient (169WT) and CL-deficient (169CL3) *R. sphaeroides* **402**

FIGURE 9.8 Identification of the cardiolipin molecular species in the four-subunit C*c*O crystals from CL-proficient (169WT) and CL-deficient (169CL3) *R. sphaeroides* using CID MS/MS in negative ion mode on a MALDI-linear ion trap mass spectrometer **403**

FIGURE 9.9 Identification of the major lipids ions in the C*c*O crystals from CL-proficient (169WT) and CL-deficient (169CL3) *R. sphaeroides* using CID MS/MS in positive and negative ion modes on a MALDI-linear ion trap mass spectrometer **404**

FIGURE 10.1 Reduced-oxidized UV-Vis spectroscopy of the resuspended membranes isolated from *R. sphaeroides* strains 169-2.4.1(WT) and 169CL3(CL−) grown under normal P (20 mM KH_2PO_4; P+), and low P (0.1 mM KH_2PO_4; P−) conditions **419**

FIGURE 10.2 Reduced UV-Vis spectroscopy of C*c*O purified from *Rhodobacter sphaeroides* strains: 169-2.4.1 grown under normal phosphate (WT/ P+); 169CL3 under normal phosphate (CL−/ P+); 169-2.4.1 under low phosphate (WT/ P−); and 169CL3 under low P (CL−/ P−) **421**

FIGURE 10.3 SDS-PAGE analysis of the C*c*O purified by Ni-NTA FPLC from the *Rhodobacter sphaeroides* strains 169-2.4.1 (WT) and 169CL3 (CL−) aerobically grown under normal P (20 mM KH_2PO_4) (P+), and low P (0.1 mM KH_2PO_4) (P−) conditions, using conditions described in Chapter 3 and Coomassie blue for the staining **423**

FIGURE 10.4 Steady-state oxygen consumption activity analysis of the C*c*O purified by Ni-NTA FPLC from *Rhodobacter sphaeroides* strains169-2.4.1 (WT) and 169CL3 (CL−) grown aerobically under normal P (20 mM KH_2PO_4) (P+), and low P (0.1 mM KH_2PO_4) (P−) conditions, before and after the addition of asolectin lipids in the reaction mixture **425**

FIGURE 10.5 Positive ion mode ESI MS spectra of the lipids extracted from the same amount of isolated membranes of *R. sphaeroides* 169-2.4.1 grown under normal phosphate (WT/ P+), 169CL3 under normal phosphate (CL−/ P+), 169-2.4.1 under low phosphate (WT/ P−), and 169CL3 under low P (CL−/ P−), with the presence of the lipid internal standards of GPEtn 14:0/14:0, GPGro14:0/14:0, GPCho 14:0/14:0 and CL $(14:0)_4$ at final concentrations of 4, 2, 2 and 1 μM in the chloroform: methanol (1:1, v/v) solvent containing 40 mM ammonium hydroxide. Experimental conditions are described in Chapter 3 section 3.7.2 .....**428**

FIGURE 10.6 Summary of the quantification results from Figure 10.5 using positive ion mode ESI MS **431**

FIGURE 10.7 Negative ion mode ESI MS spectra of the lipids extracted from the same amount of isolated membranes of *R. sphaeroides*: WT/ P+ and CL−/ P+

grown under normal phosphate, WT/ P− and CL−/ P−, grown under low phosphate, in the presence of the lipid internal standards of GPEtn 14:0/14:0, GPGro14:0/14:0, GPCho 14:0/14:0 and CL $(14:0)_4$ at final concentrations of 4, 2, 2 and 1 μM in the chloroform: methanol (1:1, v/v) solvent containing 40 mM ammonium hydroxide. The m/z range of 600-1000 is displayed **434**

FIGURE 10.8 Summary of the quantification results from Figure 10.7 using negative ion mode ESI MS **436**

FIGURE 10.9 Negative ion mode ESI MS spectra of the lipids extracted from the same amount of isolated membranes of *R. sphaeroides* 169-2.4.1 grown under normal phosphate (WT/ P+), 169CL3 under normal phosphate (CL−/ P+), 169-2.4.1 under low phosphate (WT/ P−), and 169CL3 under low P (CL−/ P−), in the presence of the lipid internal standards of GPEtn 14:0/14:0, GPGro14:0/14:0, GPCho 14:0/14:0 and CL $(14:0)_4$ at final concentrations of 4, 2, 2 and 1 μM in the chloroform: methanol (1:1, v/v) solvent containing 40 mM ammonium hydroxide. The m/z range of 1200-1600 is displayed for the cardiolipin **439**

FIGURE 10.10 Summary of the quantification results of CL using negative ion mode ESI MS/MS with wide band isolation and activation, and the quantification of GPGro and SQDG lipids by MS **441**

FIGURE 10.11 Positive ion mode MALDI MS spectra of the same amount of isolated membranes (1 μL at 0.25 mg/ mL final membrane protein concentrations determined by BCA assay) of *R. sphaeroides* 169-2.4.1 grown under normal phosphate (WT/ P+), 169CL3 under normal phosphate (CL−/ P+), 169-2.4.1 under low phosphate (WT/ P−), and 169CL3 under low P (CL−/ P−), with the presence of the lipid internal standards of GPEtn 14:0/14:0, GPGro14:0/14:0, GPCho 14:0/14:0 and CL $(14:0)_4$ at final concentrations of 10, 5, 1.25 and 1.25 μM, respectively, in the mono-phase mixture with the sample **446**

FIGURE 10.12 Negative ion mode MALDI MS spectra of the same amount of isolated membranes (1 μL at 0.25 mg/ mL final membrane protein concentrations determined by BCA assay) of *R. sphaeroides* 169-2.4.1 grown under normal phosphate (WT/ P+), 169CL3 under normal phosphate (CL−/ P+), 169-2.4.1 under low phosphate (WT/ P−), and 169CL3 under low P (CL−/ P−), with the presence of the lipid internal standards of GPEtn 14:0/14:0, GPGro14:0/14:0, GPCho 14:0/14:0 and CL $(14:0)_4$ at final concentrations of 10, 5, 1.25 and 1.25 μM in the mono-phase mixture with the sample. The m/z range from 600-1000 is displayed **448**

FIGURE 10.13 Negative ion mode MALDI MS spectra in the m/z range from 1200-1600, for the same amount of isolated membranes (1 μL at 0.25 mg/ mL final membrane protein concentrations determined by BCA assay) of WT and CL− *R. sphaeroides* grown under the same set of conditions as in Figure 10.12, with the lipid internal standards of GPEtn 14:0/14:0, GPGro14:0/14:0, GPCho 14:0/14:0 and CL $(14:0)_4$ at final concentrations of 10, 5, 1.25 and 1.25 μM in the mono-phase mixture with the sample, respectively **450**

FIGURE 10.14 Positive ion mode MALDI MS spectra of the same amount of purified C*c*O (1 μL at 0.5 mg/ mL final C*c*O concentrations determined by UV-Vis spectroscopy) of WT and CL- *R. sphaeroides* grown under normal phosphate (WT/ P+), (CL−/ P+), and low phosphate (WT/ P−), (CL−/ P−), with the presence of the lipid internal standards of GPEtn 14:0/14:0, GPGro14:0/14:0, GPCho 14:0/14:0 and CL $(14:0)_4$ at final concentrations of 10, 5, 1.25 and 1.25 μM in a mono-phase mixture with the sample, respectively. The relative abundance in the m/z range of 706-830 is expanded 4 fold in all four panels for a clearer display of the lipids peaks **454**

FIGURE 10.15 Negative ion mode MALDI MS spectra of the same amount of purified C*c*O (1 μL at 0.5 mg/ mL final C*c*O concentrations determined by UV-Vis spectroscopy) from WT and CL− *R. sphaeroides* grown as described previously, with the presence of the lipid internal standards of GPEtn 14:0/14:0, GPGro14:0/14:0, GPCho 14:0/14:0 and CL $(14:0)_4$ at final concentrations of 10, 5, 1.25 and 1.25 μM in the mono-phase mixture with the sample, respectively. The relative abundances in the m/z ranges of 700-850 and 660-670, are expanded 4 fold in all four panels for a clearer display of the lipids and the internal standards peaks **457**

FIGURE 10.16 Negative ion mode MALDI MS spectra in the m/z range from 1200-1600, of the same amount of purified C*c*O (1 μL at 0.5 mg/ mL final C*c*O concentrations determined by UV-Vis spectroscopy) of *R. sphaeroides* 169-2.4.1 grown under normal phosphate (WT/ P+), 169CL3 under normal phosphate (CL−/ P+), 169-2.4.1 under low phosphate (WT/ P−), and 169CL3 under low P (CL−/ P−), with the presence of the lipid internal standards of GPEtn 14:0/14:0, GPGro14:0/14:0, GPCho 14:0/14:0 and CL $(14:0)_4$ at final concentrations of 10, 5, 1.25 and 1.25 μM in the mono-phase mixture with the sample, respectively. In panel D, The relative abundance in the m/z range of 1300-1600 is expanded 1.5 fold for a clearer view of the CL region. **460**

Images in this dissertation are presented in color.

LIST OF SCHEMES

SCHEME 1.1 The overall reaction catalyzed by cytochrome *c* oxidase **17**

SCHEME 1.2 Electron transfer pathway in *aa3*-type cytochrome *c* oxidase **18**

SCHEME 2.1 General structure of phospholipids **89**

SCHEME 2.2 Fragmentation of GPCho $[M+H]^+$ in CID MS/MS in positive ion mode **93**

SCHEME 2.3 Potential fragmentation pathways of phospholipids in negative ion mode **94**

SCHEME 3.1 The overall reaction catalyzed by C*c*O, which is also the reaction used to evaluate the steady state activity of C*c*O **116**

SCHEME 4.1 Formation of methyl carbonate anion **165**

SCHEME 4.2 Proposed MS/MS fragmentation pathway of $[GPCho+A]^-$ to lose $(A+CH_3)$ **167**

SCHEME 4.3 Proposed MS^3 fragmentation pathways of $[GPCho+A-(A+CH_3)]^-$ to form $RCOO^-$ or neutral RCOOH **170**

SCHEME 4.4 Proposed MS^3 fragmentation pathways of $[GPCho+A-(A+CH_3)]^-$ to form ketene neutral loss **171**

SCHEME 4.5 Proposed MS/MS fragmentation pathway of $[GPCho+A]^-$ to lose $(AH+(CH_3)_3)N)$ **174**

SCHEME 4.6 Proposed MS/MS fragmentation pathway of $[GPCho+A]^-$ to lose $(A+(CH_3)_3)NCH=CH_3)$ **176**

SCHEME 4.7 Proposed fragmentation pathways of $[GPCho+H_2PO_4]^-$ **182**

SCHEME 4.8 Proposed fragmentation pathways of $[GPCho+A]^-$ to lose AH and MS^3 of $[GPCho+A-AH]^-$ **186**

SCHEME 4.9 Proposed fragmentation pathways of $[GPCho+A]^-$ to lose alternative AH and MS^3 of $[GPCho+A-AH]^-$ to form radical anions **187**

SCHEME 5.1 Schematic structure of an ornithine lipid (OL) **202**

SCHEME 5.2 Proposed pathways for the multistage gas-phase fragmentation reactions of protonated ornithine lipids **213**

SCHEME 5.3 Proposed pathways for the multistage gas-phase fragmentation reactions of deprotonated ornithine lipids **217**

SCHEME 5.4 Proposed pathways for the multistage gas-phase fragmentation reactions of protonated glutamine lipids **235**

SCHEME 5.5 Proposed pathways for the multistage gas-phase fragmentation reactions of deprotonated glutamine lipids **239**

SCHEME 6.1 General structures of SQDG and DGTS **248**

SCHEME 6.2 Proposed fragmentation pathways of SQDG $[M-H]^-$ in MS/MS and MS^3 ..... **269**

SCHEME 6.3 Proposed fragmentation pathway of forming m/z 81 from m/z 225..... **270**

SCHEME 6.4 Proposed fragmentation pathway of forming m/z 95 from m/z 225..... **270**

SCHEME 6.5 Proposed fragmentation pathway of forming m/z 207 from m/z 225.... **271**

SCHEME 6.6 Proposed fragmentations of DGTS $[M+H]^+$ in MS/MS and MS^3 in positive ion mode **278**

SCHEME 10.1 Possible functional interchangeability between different types of lipids..... **416**

LIST OF ABBREVIATIONS

$[M+H]^+$	protonated ion
$[M-H]^-$	deprotonated ion
2,5-DHB	2,5-dihydroxyl benzoic acid
A	anion
Ac	acetate
AC	alternating current
Ace-w	acetone-washing
ADP	adenosine diphosphate
AGC	automatic gain control
ATP	adenosine triphosphate
ATT	6-aza-2-thiothimin
BCA	bicinchroninic acid, used in protein assay
BSA	bovine serum albumin
CcO	cytochrome c oxidase
CHCA	α-cyano-4-hydroxycinnamic acid
CI	chemical ionization
CID	collision induced dissociation
CL	cardiolipin
CL−	specific cardiolipin-deficient mutant
cls	cardiolipin synthase gene
CMC	critical micelle concentration

CRM	charge residue model
DC	direct current
DDM	dodecyl maltoside
DEAE	diethylaminoethyl, packing material for ion exchange chromatography column
DESI	desorption electrospray ionization
DGHS	diacylglycerolhomoserine
DGTS	diacylglyceryl-N, N, N-trimethylhomoserine
Dil-f	dilution-filtration
DM	decyl maltoside
DMPE	N, N-dimethyl phosphatidylethanolamine, N,N-Me_3 GPEtn
E2	bimolecular elimination
EI	electron impact ionization
ESI	electrospray ionization
ETD	electron transfer dissociation
FAB	fast atom bombardment
FADH2	reduced flavin adenine dinucleotide
Fm	formate
FPLC	fast protein liquid chromatography
Fre-d	freeze-drying (lyophilization)
FT-ICR	Fourier-transform ion cyclotron resonance mass spectrometer

GC-MS	gas chromatography-mass spectrometry
GGDG	glucosylgalactosyldiacylglyceride
GPCho	phosphatidylcholine
GPCho−	specific GPCho-deficient mutant
GPEtn	phosphatidylethanolamine
GPGro	phosphatidylglycerol
GPIns	phosphatidylinositol
GPInsP	phosphorylated phosphatidylinositol
GPSer	phosphatidylserine
h.g.	head group
HPLC	high performance liquid chromatography
i.s.	internal standard
IEM	ion evaporation model
kDa	kilo Dalton
LIT	quadrupole linear ion trap mass spectrometer
LMCO	low-mass-cutoff
LPS	lipopolysaccarides
LTQ	linear trap quadrupole, instrument model by Thermo Fisher Scientific
m.c.	methyl carbonate
MALDI	matrix-assisted laser desorption/ionization
MES	2-(N-morpholino)ethane-sulfonic acid
MMPE	N-monomethyl phosphatidylethanolamine, N-Me GPEtn

MS	mass spectrometry
MS/MS	tandem mass spectrometry
MSA	5-methoxysalicylic acid
MSn	multistage tandem mass spectrometry
NAD+	nicotinamide adenine dinucleotide
NADH	reduced nicotinamide adenine dinucleotide
nanoESI, nESI	nanoelectrospray ionization (most of the time ESI is used for nESI)
Ni-NTA	nickel-nitrilotriacetic acid, packing material for affinity chromatography column
NL	neutral loss
NMR	nuclear magnetic resonance
N-phase	negative side of the lipid bilayer membrane of mitochondria
OL	ornithine lipid
Orbi-Trap	Orbi-trap mass spectrometer, instrument model by Thermo Fisher Scientific
OXPHOS	oxidative phosphorylation
P–	phosphate-limiting growth
P+	phosphate-abundant growth, normal
PEG-400	polyethylene glycol, with average molecular weight 400 Da
Pi	phosphate
pPE	plasmalogen GPEtn
P-phase	positive side of the lipid bilayer membrane of mitochondria

PQD	pulsed-Q collision induced dissociation
PSD	post source decay
QL	glutamine lipid
QqQ	triple quadrupole mass spectrometer
RF	radio frequency
Rs, R. sphaeroides	*Rhodobacter sphaeroides*
SDS-PAGE	sodium dodecyl sulfate poluacrylamide gel electrophoresis
SM	sphingomyelin
S_N2	bimolecular nucleophilic substitution reaction
SQDG	sulfoquinovosyldiacylglyceride
SQDG–	specific SQDG-deficient mutant
TLC	thin layer chromatography
TMHS	N, N, N-trimethylhomoserine
TOF	time of flight mass analyzer
TSQ	triple quadrupole, instrument model by Thermo Fisher Scientific
UV-Vis	ultraviolet-visible spectroscopy
WT	wild type

Chapter 1

An Overview of the Structural and Functional Impact of Membrane Lipids on Membrane Proteins, with a Focus on Cytochrome *c* Oxidase

1.1 Introduction: Structural and functional roles of lipids in membrane proteins

The recently sequenced human genome revealed that 20% to 35% of the genome encodes putative membrane proteins, many of which have key functions [1]. Recently emerging experimental evidence suggests that, in addition to providing the hydrophobic environment, lipids can assist with the insertion and folding of membrane proteins, and are involved in specific interactions, in the regulation of super-molecular organization formation among membrane protein complexes, in the control of molecular transport across cell membranes and in mediating the signaling responses of cells to their environment.

1.2 Lipids in cell membranes

1.2.1 Lipids: the biological membrane environment

Lipid bilayers constitute the biological membrane environment (Figure 1.1), and provide specialized permeability barriers for cells and cell organelles, in which the basic processes of respiration, photosynthesis, protein and solute transport, signal transduction, and movement can take place [1]. A fluid -mosaic model has been proposed for the structure of biological membranes constituted by lipid bilayers (Figure 1.1). In the fluid-mosaic model, the lipids and proteins can move about relatively randomly to adjust to the changes in conditions and activity of the membrane bound proteins, while keeping the membrane sealed. However, recent experimental evidence increasingly suggests that membranes are actually more mosaic than randomly fluidic, and are packed with patches of microdomains [2]. The thickness of the hydrophobic region of the lipid bilayer is about 32 Å (GPCho 18:1/18:1 bilayer), but thinning and thickening of the membrane adjacent to membrane proteins have been reported to occur [2].

Lipids have been broadly defined as biological compounds with predominantly hydrophobic character including the diversity of fats (triglycerides), oils, waxes, cholesterol, sterols, hydrophobic vitamins, monoglycerides, diglycerides, and phospholipids. However, the lipids with the most interest for research are the amphiphilic group of molecules that typically contain a hydrophilic moiety with either a charged or polar head group, and a hydrophobic moiety often consisting of long fatty acyl or ester chains. The polar and hydrophobic interactions make the lipids tend to self-assemble into

a bilayer membrane or curved micelle structures in an aqueous environment, depending on the relative sizes of the polar head group and the hydrophobic tails (Figure 1.1).

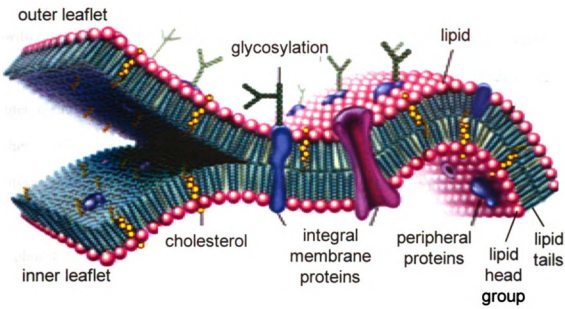


Figure 1.1 Traditional fluid mosaic model of a biological membrane in mammalian cells constituted by lipid bilayers. The insertion of cholesterol increases the rigidity of the membrane (adapted from http://media-2.web.britannica.com/eb-media/74/53074-004-9F65D813. jpg). Recent models depict more crowded membranes with patchiness, maintained with the assistance of cytoskeletons.

1.2.1.1 Basic structures of lipids

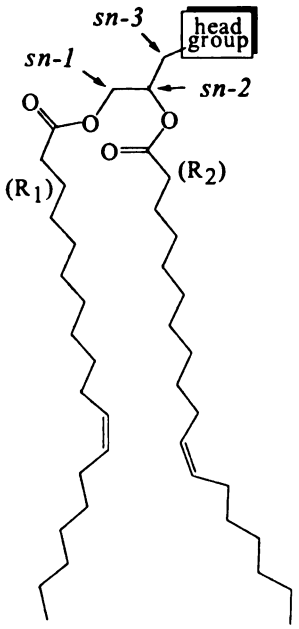
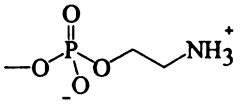
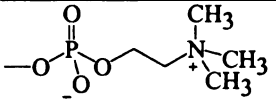
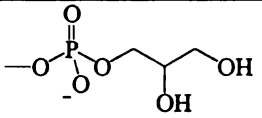
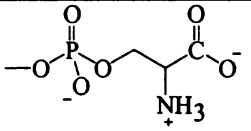
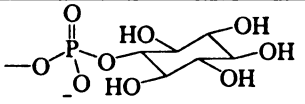
Several common nomenclature systems have been adopted for the classification of lipids [3,4]. Lipids can be categorized into glycerol-lipids and non-glycerol-lipids. Within the non-glycerol lipids, a particular group of lipids that contain amino acids or simple peptides in the head group and an amide bond in the backbone are termed "lipo

amino acids". Based on the presence of phosphate in the head group, lipids are also divided into phospholipids and non-phospholipids, the latter of which may contain a negatively-charged sulfate or sulfite group. Based on the total charge state of the lipid molecule under physiological conditions, lipids are divided into neutral lipids (including zwitterionic lipids), anionic lipids (negative lipids) and cationic lipids (positive lipids). A group of lipids with more complicated structures often found in the outer leaflet of the outer membrane of gram-negative bacteria formed through various glycosylation and other modifications, based on the basic structure of lipid A, are termed lipo-polysaccharides (LPS) [5], but it is not the central focus of interest in the current study.

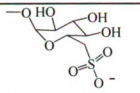
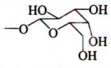
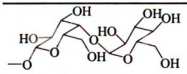
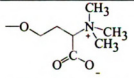
The most common group of lipids found in mammalian and bacterial membranes is phospholipids containing a phosphate in the head group and a glycerol backbone (Table 1.1). Whereas phosphatidylcholine (GPCho) and phosphatidylglycerol (GPGro) are close to rectangular in molecular shape and are prone to form bilayers, the phosphatidylethanolamine (GPEtn) head group is relatively small and is known for its tendency to form a curved structure [6].

Non-bilayer-forming steroid lipids, such as cholesterol, nevertheless are incorporated into membranes and are involved in important regulatory mechanisms.

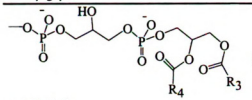
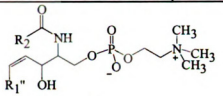
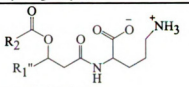
Table 1.1 Basic structures of lipids found in eukaryotes and bacteria

Backbone and tails	Head group	Abbre-viation*	Alter-native abbr.	Glycerol -lipid	Phospho -lipid	Glyco -lipid	Charge state**	Sources
	 phosphatidylethanolamine	GPEtn	PE	yes	yes	no	Zwitter-ionic	mammal, plants, bacteria
	 phosphatidylcholine	GPCho	PC	yes	yes	no	Zwitter-ionic	mammal, plants, bacteria
	 phosphatidylglycerol	GPGro	PG	yes	yes	no	anionic	mammal, plants, bacteria
	 phosphatidylserine	GPSer	PS	yes	yes	no	anionic	mammal, some bacteria
	 phosphatidylinositol	GPIns	PI	yes	yes	no	anionic	mammal

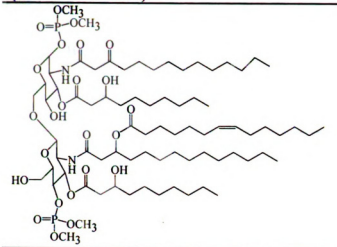
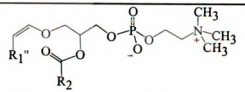
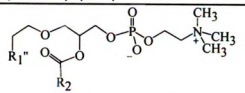
(Table 1.1 continued)

 sulfoquinovosyl diacylglyceride	SQDG	SL	yes	no	yes	anionic	plants, photosyn -thetic bacteria
 monogalactosyl diacylglyceride	MGDG	MGlc-DAG	yes	no	yes	neutral	plants, photosyn thetic bacteria
 glucosylgalactosyl diacylglyceride	GGDG		yes	no	yes	neutral	plants, photosyn thetic bacteria
 diacylglyceryl-N, N, N-trimethylhomoserine	DGTS		yes	no	no	Zwitter-ionic	photosyn thetic bacteria
 triacylglyceride	TG	TAG	yes	no	no	neutral	mammal, plants, yeast

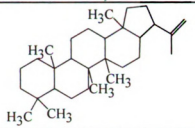
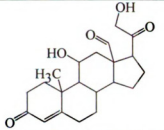
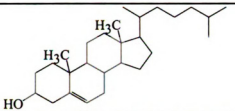
(Table 1.1 continued)

 diacylglyceride	DG	DAG	yes	no	no	neutral	mammal, plants, yeast
 cardiolipin	CL	CDL	yes	yes	no	anionic	mammal, bacteria
 sphingomyelin	SM		no	yes	no	Zwitter-ionic	mammal
 ornithine lipid	OL		no	no	no	Zwitter-ionic	hotosynthetic bacteria

(Table 1.1 continued)

	lipid A [#] *R. sphaeroides*		no	no	yes	neutral	Gram-negative bacteria
 plasmenyl phosphocholine	GPCho plasmalogen	pPC	yes	yes	no	Zwitter-ionic	mammal
 plasmanyl phosphocholine	GPCho alkyl-ether	ePC	yes	yes	no	Zwitter-ionic	mammal

(Table 1.1 continued)

	hopanoid	no	no	no	neutral	bacteria
	steroid	no	no	no	neutral	mammal, plants
	cholesterol	no	no	no	neutral	mammal, plants

* Abbreviation recommended by the LIPIDMAPS in 2005 [4].

** Charge state under physiological conditions (pH 6.8-7.4).

\# Lipid A can have variable structures, and the structure shown is from reference [5].

1.2.1.2 Dynamic modifications of lipid structures

In addition to the major basic structures described above, varied structures of lipids are formed as a consequence of dynamic modification processes [7,8]. The modification can target either the head group or the hydrophobic chains. For example, cardiolipin head groups have been found to be modified with a lysine amino acid which forms an acyl bond with the hydroxyl in the glycerol head group, during a specific cell growth phase of bacteria. Lysine modification of the glycerol head group in GPGro has also been well characterized in the bacterium *Sinorhizobium meliloti* to occur under acidic growth conditions or when they get in contact with their host plants [7]. Phosphorylation of the lipid A head group at the hydroxyl group can switch the non-toxic mono-phosphate state into the toxic di-phosphate state. In apoptosis of mammalian cells, the matured form of cardiolipins, containing four 18:2 poly-unsaturated fatty acyl chains, are modified by reactive oxidative species into peroxidized cardiolipins with addition of peroxide to the double bonds, allowing them to bind to cytochrome *c,* which is thought to trigger the massive release of cytochrome *c* from mitochondria, causing cell apoptosis [8-10] . The composition of membrane lipids in bacteria is also very dependent on the nutrients in the growth media, such as the availability of phosphate [7,11] and even the presence of Tris in the buffer [12].

1.2.1.3 Typical bacterial lipid structures

Bacterial membranes differ from mammalian and yeast cell membranes in that the Gram-negative bacteria have an outer membrane bilayer, the outer leaflet of which is predominantly composed of tightly packed lipo-polysaccharides (LPS). It plays a key role

in the bacteria's interaction with their host during infection, in addition to the cytoplasmic membranes, where the respiratory enzymes reside, which is also the focus of the current study.

Photosynthetic purple bacteria that are also capable of aerobic growth through respiration, such as *Rhodobacter sphaeroides,* make a rich variety of lipids, including phospholipids, some of which are not commonly found in bacteria, such as phosphatidylcholine [13], glycolipids which are typically found in photosynthetic plant chloroplasts, as well as the phosphate-free amino acid-containing betaine lipids (see Chapter 6), ornithine lipids and the more recently discovered glutamine lipids (see Chapter 5). However, sphingolipids and plasmalogen GPEtn/ GPCho lipids are typically not reported for purple bacteria.

The major types of fatty acyl chains in bacterial glycerol-backbone lipids (including the typical phospholipids) are 18:1, 16:0, 18:0, 16:1, 20:0, 20:1, 20:2, and the odd-carbon numbered cyclic propane-containing fatty acids19:1 and 21:1 [13,14]. A note on the nomenclature: in 18:1, for example, 18 represents the total number of carbon in the fatty acyl chain, and 1 represents the number of ring or double bond in the fatty acyl chain (other than the carbonyl group). Shorter chain fatty acid 14:0 can be detected but at very low levels [14]. Ornithine and glutamine lipids also contain the 3-hydroxyl fatty acids. The first site of unsaturation is often reported to be Δ^{11} in 18:1 fatty acid chains [15]. Polyunsaturated fatty acids common in mammalian cells such as 18:2, 20:4 (arachidonic acid), 22:5 and 22:6, are typically not found in purple bacteria [13,14]. The double bonds in the fatty acid chains are rarely conjugated.

1.2.1.4 Cellular distribution of lipids

Not all areas of the membranes are the same. Since the membrane proteins are each different from the other, they have individual requirements for their ligands and complements, such as lipids, to carry out their functions. In fact, patches of lipids and membrane proteins in the membranes formed with the assistance of cytoskeletons, termed detergent-resistant membrane microdomains, or lipid rafts, are being increasingly recognized to contain unique lipid compositions [2], and are often found to be enriched in cholesterol, sphingomyelin and plasmalogen GPEtn/GPCho. In eukaryotic cells, cardiolipin is found almost exclusively in the mitochondria, where the oxidative phosphorylation complexes reside. Phosphorylated GPIns lipids and long chain polyunsaturated lipids are found to be highly enriched in retina and brain cells, where signal transduction is highly active. To accommodate the physical surface curvature, the triangular-shaped GPEtn lipids are often found more enriched in the inner leaflet of membranes.

1.2.2 Biosynthesis of lipids and remodeling of cardiolipin

The major biosynthetic pathways of lipids in bacteria have been elucidated by using genetic approaches over the past decades (Figure 1.2) [14,16-18]. Under extreme conditions, alternative and minor synthetic pathways can also be turned on. The final synthesis of membrane lipids mainly occurs in ER membranes of eukaryotic cells, and cytoplasm membranes of bacterial cells.

While similar synthetic strategies were adopted by eukaryotic and bacterial systems, some routes are significantly different. For instance, in the bacterial system, the

cardiolipin is made from two molecules of GPGro by cardiolipin synthase [7], whereas in the eukaryotic system (including yeast and mammalian cells), the cardiolipin is made from one molecule of GPGro and one molecule of CDP-diacylglycerol (Figure 1.2) [9,10,19]; furthermore, in mammalian cells (but not yet reported for yeast [20]), it was recently found that the initial products of cardiolipin lipids are further remodeled into the mature functional form of $CL(18:2)_4$ by the enzyme tafazzin [9,21].

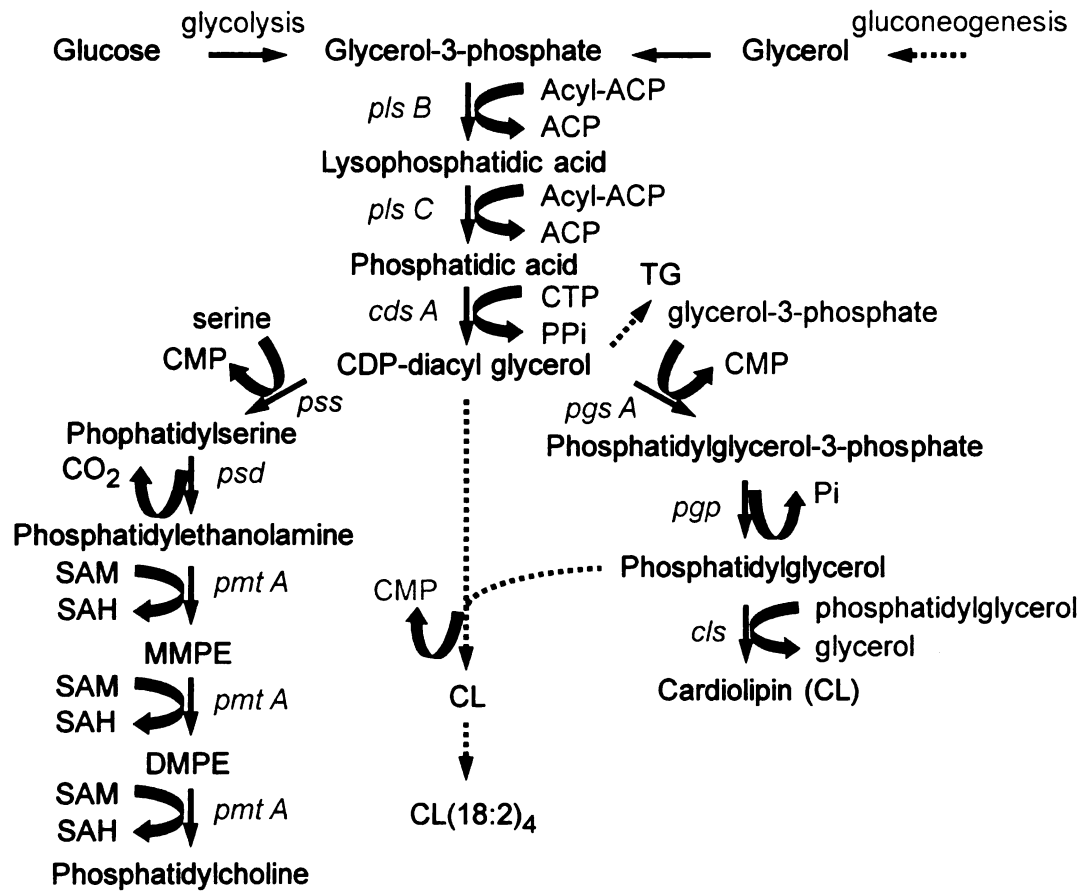


Figure 1.2 Major biosynthetic pathways for phospholipids, and the different cardiolipin synthetic pathway in eukaryotes (yeast and mammalian cells, shown in dashed arrows). The genes identified in bacteria to be responsible for the reactions are represented in italics (adapted from [7]).

1.2.3 Structural /physical features underlying the functions of lipids

The potential functions of lipids are underlined by the physical and structural features of these molecules. One feature is the molecular shape of the lipid. The relative size of the head group and the tails determine if the lipids adopt a rectangular or a triangular shape, and are thus prone to form a bilayer or a curved micelle surface instead [6]. Non-bilayer forming lipids might replace each other. Recently the non-bilayer forming glycodiacylglyceride lipids were found to be able to replace the functions of GPEtn, but GPGro, GPCho or CL could not [22].

Another feature is the head group charge state. It has been well established that anionic lipids GPGro and SQDG are inter-replaceable due to their anionic head groups [14]. GPGro was also often proposed to replace the function of CL in mammalian and yeast cells, due to the negative charges as well as similarity in their structures [23]. Via electrostatic interactions, the charge state of the lipids might also assist with the binding of positively charged substrates and protein residues [1] .

A third issue is the fatty acid chain composition. The unsaturation sites in fatty acid chains are often found to adopt the *cis* conformation, and introduce "kinks" in the tails making them more flexible and less tightly packed. Furthermore, the polyunsaturation of the fatty acid chain can serve as the target for peroxidation as a part of the signaling cascade, such as the recently solved case of cardiolipin 18:2 lipids in mammalian mitochondria [8].

A fourth feature relates to the metabolism of lipids, a process that can release second messengers via breaking down the membrane lipids by highly structure-selective

phospholipase or sphingomyelinase. The high selectivity is often directed toward the backbone structure, and distinguishes between the glycerol and non-glycerol backbones. Sphingomyelin lipids do not have the glycerol backbone, and their decompositions are tightly controlled to release ceramides, an important group of signaling molecules. Ornithine lipids are resistant to phospholipases, and lipid A, sharing chemical bond similarity to ornithine lipids, play important roles in the bacterial infection mechanism.

1.3 The membrane protein cytochrome *c* oxidase: structure, function, mechanism and regulation

1.3.1 Oxidative phosphorylation and respiratory chain complexes

As an important part of maintaining the balance of energy, living cells funnel most of the metabolic energy obtained from food into the stock of NADH and $FADH_2$ through oxidation-reduction reactions, which they can cash into the currency of ATP to spend for cellular activities such as biosynthesis, membrane transport and movement. Although ATP is also made in glycolysis and TCA cycle via substrate-level phosphorylation, the majority of ATP synthesis is the result of oxidative phosphorylation (OXPHOS), where the electrons in the reduced coenzymes NADH and $FADH_2$ are passed through a highly synchronized chain of proteins and coenzymes, called the electron transport chain, to reach and get consumed by molecular oxygen, the terminal electron acceptor, concomitantly establishing a proton gradient across the membrane

embedding these proteins to drive the next step of ATP synthesis from ADP (Figure 1.3)[24] .

The machinery of oxidative phosphorylation in most eukaryotic organisms is composed of F_1F_o-ATPase (complex V) and the four electron transport chain complexes, namely, NADH: ubiquinone reductase (complex I), succinate: ubiquinone reductase (complex II), ubiquinol: cytochrome *c* reductase (also called cytochrome bc_1 complex, complex III) and cytochrome *c* oxidase (complex IV), all embedded in the inner mitochondrial membranes (Figure 1.3). These oxidative phosphorylation complexes are also found in the cytoplasmic membranes of many aerobic bacteria.

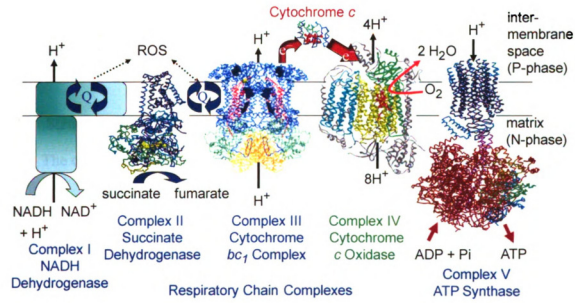


Figure 1.3 The mitochondrial respiratory chain complexes and ATPase that are responsible for the oxidative phosphorylation in eukaryotic systems (showing the structures of complexes III and IV from bovine heart, V from yeast, II from *E. coli* and cytochrome *c* from horse heart) (adapted from [25]).

The arrangement of these complexes in units of electron transfer super-molecular complexes, rather than as free and independent players, is emphasized by accumulating experimental evidence [26]. The charge distribution on the two sides of the membrane is asymmetric due to the storage of energy as an electrochemical/pH gradient; the matrix side is electronegative and also called the negative side of the membrane (N-phase).

The electron transport and oxidative phosphorylation are membrane-associated processes, not only in that the proteins responsible for these reactions are membrane bound, but also because they rely on the membrane barrier as an efficient capacitor to build up the potential of the proton and electrochemical gradient across the membrane to drive the reactions to proceed, emphasizing the interactive nature of the relationship of these proteins with the membrane lipids. In addition, lipids with steroid structures, such as deoxycholate, are also emerging as potential regulators of the complex by binding at specific sites in the complex [27].

1.3.2 Structure of C*c*O

The overall reaction that cytochrome *c* oxidase catalyzes is shown in Scheme 1.1. During each catalytic cycle, a total of eight protons are taken from the matrix side (N-phase) of the membrane, four of which are consumed in the reduction of oxygen into water and the other four are transferred across the membrane to the inter-membrane space (P-phase) of the membrane to generate a proton gradient.

$$\underset{\text{(Reduced)}}{4\ \text{cyt}\ c\ (Fe^{2+})} + 8\ H^{+}_{(in)} + O_2 \xrightarrow{CcO} \underset{\text{(Oxidized)}}{4\ \text{cyt}\ c\ (Fe^{3+})} + 2\ H_2O + 4\ H^{+}_{(out)}$$

Scheme 1.1 The overall reaction catalyzed by cytochrome *c* oxidase

The mammalian C*c*O purified from bovine heart is found to contain thirteen subunits, two irons, two copper centers, one zinc, one magnesium and one calcium per molecule of C*c*O [28,29]. The mitochondrial DNA-encoded subunits I, II and III are the biggest in size and also constitute the catalytic core for both proton pumping and electron transfer activities. The other ten subunits are encoded by the nuclear genome and can have varied forms (isoforms) in different tissues, with as yet unknown functional significance.

1.3.2.1 Electron transfer metal centers

Cytochrome *c* oxidase carries out the oxidation reaction by virtue of four redox active metal sites, namely the six- coordinate heme *a* (subunit I), the five- coordinate heme a_3 (subunit I), Cu_A (two mixed-valence copper ions $Cu^{1.5+} - Cu^{1.5+}$, subunit II) and Cu_B (subunit I). The electron transfer pathway is shown in scheme 1.2. This aa_3-type cytochrome *c* oxidase is found in mitochondria, and is also found in some aerobic bacteria including *Paracoccus denitrificans* and *Rhodobacter sphaeroides* in the cytoplasmic membranes under aerobic growth conditions, along with several other types of oxidases containing different types of heme centers. However, bacterial C*c*Os have only one more subunit in addition to subunits I, II and III, one magnesium, one calcium, but no zinc.

$$\text{cyt } c \rightarrow Cu_A \rightarrow \textit{heme a} \rightarrow \textit{heme } a_3 \rightarrow Cu_B \rightarrow O_2$$

Scheme 1.2 Electron transfer pathway in aa_3-type cytochrome *c* oxidase [30]

1.3.2.2 Proton transfer pathways

A series of specifically aligned residues and water molecules identified as the D-pathway and the K-pathway were found to be responsible for the uptake of protons from the matrix side of the membrane [25]. Exit and backflow pathways for proton transfer are also suggested by experimental evidence [31,32]. The mechanism of coupling between electron transfer and proton pumping remains unresolved.

1.3.2.3 Subunit characteristics

The amino acid sequence of *Rhodobacter sphaeroides* aa_3-type C*c*O displays 52% homology in subunit I, 39% in subunit II and 49% in subunit III to the bovine heart C*c*O sequence [33] Subunit I of C*c*O contains twelve transmembrane helices forming three four-helix bundles in an anticlockwise arrangement as viewed from the periplasmic side [30]. Being the most conserved in sequence and structure, it provides the scaffold for heme *a*, heme a_3 and Cu_B to reside, and contains the two proton uptake pathways (D and K pathways).

Subunit II contains one hydrophobic loop at the N-terminus, two transmembrane helices that interact with subunit I, and one hydrophilic extra-membrane globular domain at the C-terminus mainly composed of a ten-stranded β-barrel which harbors the Cu_A metal center [30]. This domain forms a tightly integrated cap on top of subunit I and also serves as the binding sites for the substrate, soluble cytochrome *c*.

Subunit III contains seven transmembrane helices. Subunit IV of *Rhodobacter sphaeroides* contains only one transmembrane helix. Several proteolytic forms of subunits II and IV (*Rhodobacter sphaeroides*) are also found to exist in the final purified C*c*O. Seven of the other ten subunits in mammalian C*c*O also contain hydrophobic transmembrane helix structures but none have homology to the bacterial subunit IV nor do they sit in the same position relative to the three core subunits.

1.3.2.4 Bacterial aa_3-C*c*O as a model for mammalian C*c*O in mechanistic study

The recent success in the crystallization of the membrane protein C*c*O has led to two types of C*c*O structures, the mammalian version of C*c*O from bovine heart, and the bacterial C*c*Os from *Paracoccus denitrificans* and *Rhodobacter sphaeroides [28,34,35]*. In the bovine heart C*c*O crystal, all 13 subunits are resolved. The bacterial C*c*O contained only 4 subunits, and the subunits I, II, and III are highly analogous to the structures of the mammalian subunits (Figure 1.4). Structures of a 2 subunit *Thermophilic* version of C*c*O have also been reported. A lower resolution structure of bo_3 oxidase has also been determined. Due to the high similarity to the bovine C*c*O in the catalytic core, but simpler subunit composition, a spectrally accessible catalytic center, and the ease of site-directed amino acid mutagenesis and lipid manipulation, *Rhodobacter sphaeroides* C*c*O is a good model in which to study the mechanism of the mammalian C*c*O, including the key aspects of electron transfer and proton pumping, enzyme regulation and the effects of lipids on the enzyme.

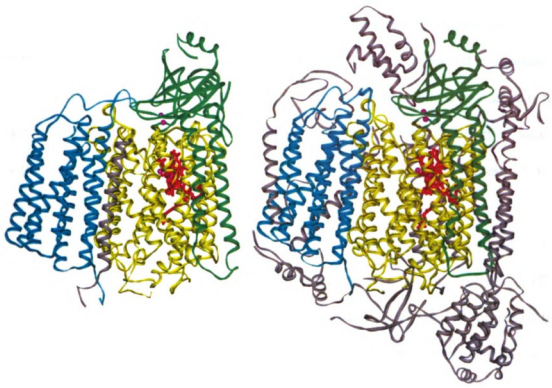


Figure 1.4 Comparison of *R. sphaeroides* and bovine mitochondrial C*c*O structures. The three core subunits I (yellow), II (green), and III (cyan) are highly homologous, as well as the redox active centers (hemes *a* and a_3 are shown in red, and coppers are shown in purple). The non-homologous subunits, including subunit IV of *Rs* C*c*O and the additional 10 subunits from bovine C*c*O are shown in gray [30].

1.3.2.5 Lipid components in C*c*O and their significance

Membrane proteins are highly hydrophobic and contain a significant percentage of α-helical and β-barrel structures. What holds the α-helical bundle structure together remains to be elucidated. Whereas membrane proteins are embedded in the membrane for various reasons, C*c*O sits in the membrane for an additional reason: to develop a potential gradient. It is using the membrane as a storage device for the potential gradient developed

by its proton pumping function. The membrane potential is its product, and the membrane is an integral partner for C*c*O to function. Therefore, the interaction of C*c*O with the membrane is likely to be more complicated than in some other membrane proteins. A tight interaction with the phospholipid bilayer is required to maintain the diffusion barrier and keep it sealed. The lipid bilayer hinders the diffusion of ions, a prerequisite for the generation of electrochemical potentials utilized for synthesis of ATP or active transport [1].

The crystal structure of the four-subunit *R. sphaeroides* C*c*O resolved at the resolution of 2.3-2.8 Å revealed a total of six lipid molecules, all interpreted as GPEtn lipids [34], four of which surround subunit IV, one fills the V-shaped cleft formed by the helix bundles in subunit III, and the other one binds at the interface between subunits III and I. Subunit IV displays no direct contact with the other subunits, but is stabilized and associated with the rest of the complex via the layer of lipid molecules in between (Figure 1.5).

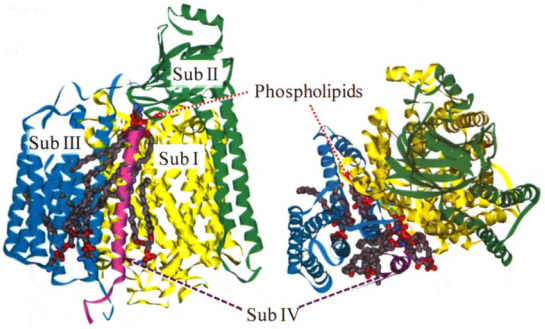


Figure 1.5 Membrane lipids resolved in the crystal structure of *Rs* C*c*O. The two figures represent a side view on the left and a top view on the right [30,34].

The crystal structure of bovine heart C*c*O resolved at the resolution of 1.8 Å revealed 13 lipid molecules bound to the C*c*O including two cardiolipins, four phosphatidylglycerols, three phosphatidylethanolamines, one phosphatidylcholine and three triacylglycerols (Figure 1.6 A) [28,36], and their fatty acid chains were further identified by mass spectrometry following lipid extraction. It was observed that each lipid head group has a specific binding site, and proposed that the flexibility of the fatty acid chains are also critical in creating an effective space-filling function. Furthermore, the palmitate (16:0) fatty acid chains from phosphotidylglycerol were proposed to control the O_2 transfer process through binding and blocking the O_2 transfer pathway. The selective binding of cis-vaccenate near the O_2 transfer was also used to suggest that the vaccenate

plays a critical role in the O_2 transfer mechanism [28]. The two cardiolipin lipids from each *Cc*O monomer were proposed to be critical in forming *Cc*O dimers [36].

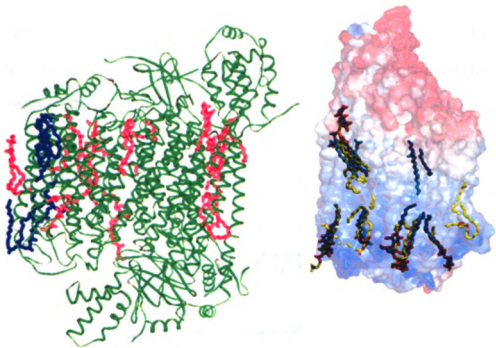


Figure 1.6 *Cc*O crystal structures showing bound lipids, (A) left, bovine heart *Cc*O showing the lipid content [36], and (B) right, superimposed structure showing the conserved sites for lipids in subunits I and II [35].

The two-subunit *R. sphaeroides* *Cc*O structure resolved at 2.0 Å was also recently obtained [35], and a number of lipid fatty acid chains and dodecyl maltoside molecules were identified in the structure (Figure 1.6 B). When superimposed onto subunits I and II of bovine heart *Cc*O and *P. denitrificans* *Cc*O, the lipid binding sites precisely overlapped, in spite of different purification methods and detergents [35].

1.3.2.6 Function and mechanism of C*c*O and their analysis

Because the activity of cytochrome oxidase is dependent on very fast electron transfer reactions, it is usually measured using rapid-kinetic methods as well as steady-state methods.

The intermediate states of the oxygen chemistry in C*c*O are illustrated in Figure 1.7 [30]. For each catalytic cycle, four electrons are transferred to the binuclear center and combined with dioxygen and four protons are taken from the inside of the membrane to form 2 waters. Four additional protons are transported across the membrane, but are not shown in the figure since the proton pumping mechanism is unknown [30].

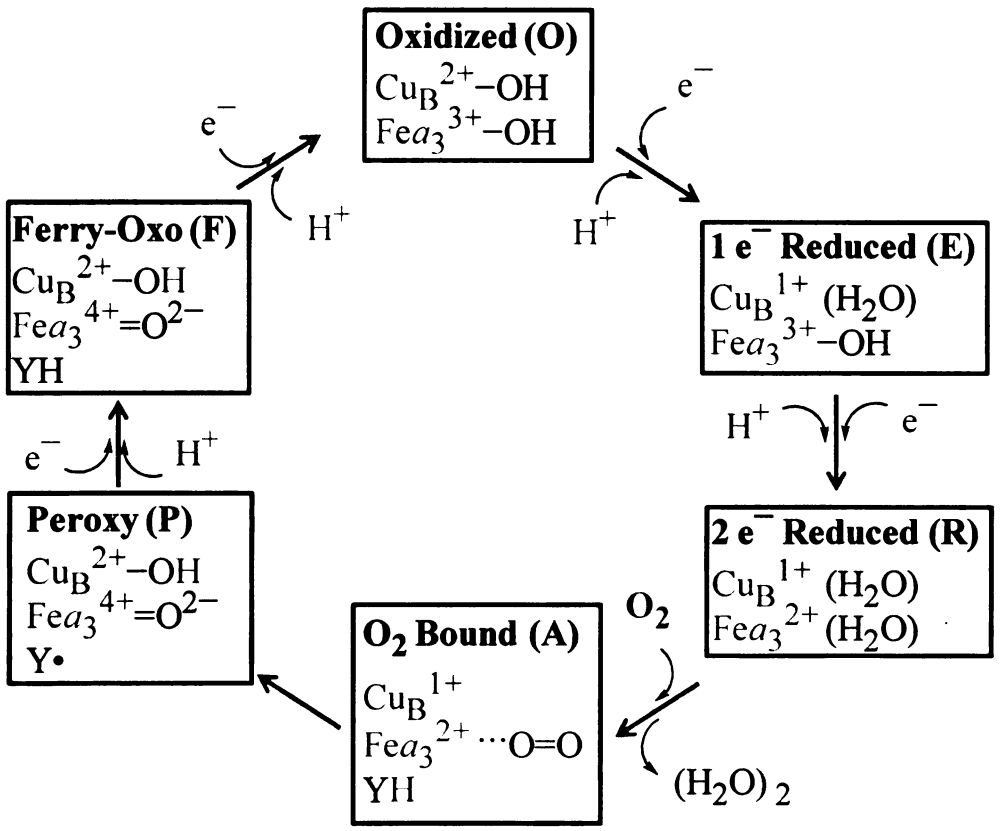


Figure 1.7 The oxygen chemistry cycle of the reaction catalyzed by C*c*O [30].

The complexity in the composition of the multi-subunit protein C*c*O, containing hemes, lipids, detergents and various forms of subunits, makes mass spectrometry a very important tool to map both its lipid and protein composition [37].

1.3.3 Regulation of C*c*O

Several mechanisms are emerging regarding the regulation of the redox proton pumping machine of C*c*O, as suggested by recent findings of multiple sites of phosphorylation, the binding of deoxycholate in a proton pathway [27], and the evidence for backflow as a mechanism to control the proton pumping efficiency [31,38].

Nucleotides have long been considered to have important regulatory effects on the activity of C*c*O. The cholate binding sites discovered in bovine C*c*O were considered to resemble the binding sites for nucleotides, suggesting potential regulatory sites by nucleotides [27]. The identification of the resolved bound deoxycholate molecule in *Rs*C*c*O can potentially be further characterized by using mass spectrometry analysis and computational analysis of the properties and specificity of the binding site.

Spanning across the membrane, and responding to the lipid molecules, regulation of trans-membrane C*c*O could also involve the concerted effects of lipids, along with phosphorylation and steroid interactions. Some lipids molecules, particularly those in the mitochondrial membrane, have been found to be actively involved in the regulation of protein and cellular activity [1]. For instance, cardiolipin appears to participate in formation of supercomplexes of respiratory chain components (see below).

1.4 Membrane bound super-molecular complex organization

1.4.1 The "static" versus the "fluidic" model of organization

Regarding the arrangement of the complexes that carry out oxidative phosphorylation in the membrane, a "fluidic" model and a "static" model have been proposed over the history [26,39]. In the "fluidic" model, each individual complex was depicted as being free and structurally independent, which is supported by the observation that each complex can be individually purified in its fully active form, and that the electron carriers ubiquinone and cytochrome *c* can diffuse at much faster rates than the protein complexes [26].

However, the "static" model, where these complexes are assembled into a unit of super-molecular complex, is being reinforced by recently accumulating experimental evidence using single particle electronic microscopy as well as native gel analysis and the use of mild detergent such as digitonin during purification [39-41]. Further mutations in specific subunits of the complexes were also shown to affect the assembly of these super-complex organizations.

It is more likely that the actual arrangement of these complexes is a dynamic combination of both the "fluid" and the "static" aspects, containing both monomers and various forms of super-complexes that are assembled dynamically to perform certain cellular functions as proposed by Ferguson-Miller et al [42].

The most well examined supercomplexes are III_2+IV_1, III_2+IV_2 (Figure 1.8) [41], and oligmers of ATP synthase (V_2) (Figure 1.9) [43]. Furthermore, complex V was found to affect the assembly of III and IV [44], and an introduction of a regulatory region in

complex V was also found to affect complex IV [45]. Complex I was recently found be involved in forming I+III+IV+cytochrome *c* and I+III supercomplexes as well [39].

The assembly of these super-complexes was found to act as the driving force to form local curvature of the membrane, and dynamically alter the cristae membrane and the inner boundary membrane regions of the inner membrane of the mitochondria [46].

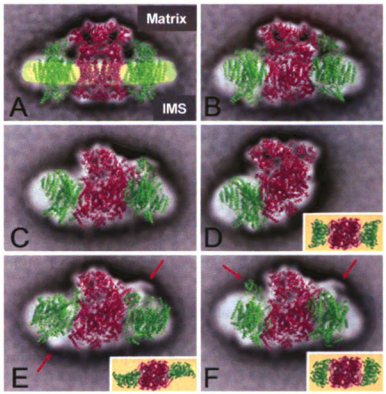


Figure 1.8 Fitting of atomic structures of the yeast cytochrome bc_1 complex (*red*) and the bovine heart cytochrome *c* oxidase or complex IV (*green*) into selected EM projection maps for assignment of the arrangement of the $III_2 + IV_2$ and $III_2 + IV_1$ supercomplexes. One common pseudo-atomic model was constructed (presented in the membrane plane in the *inset* of *D*) and used for generating different overlays closely matching the $III_2 + IV_2$ (*A-C*) and $III_2 + IV_1$ (*D*) supercomplex maps, respectively [41].

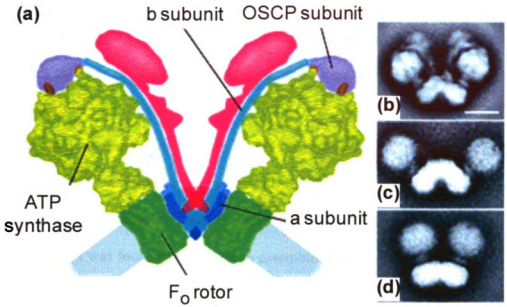


Figure 1.9 Scheme for dimeric ATP synthase from mitochondria. Each ATP synthase monomer consists of the F_1 headpiece and a central stalk region (yellow) connected to the membrane-embedded F_o rotor (green). Rotation of the complete headpiece is prevented by the b subunit of the peripheral stalk (blue), which is connected to the top of F_1 by the OSCP subunit (purple) and to the rotor by subunit a (dark blue). Other dimer-specific subunits that do not have direct functional importance for the monomers are depicted in red. **(b)** Projection map of *Polytomella* ATP synthase dimers. Scale bar = 10 nm. **(c)** Projection map of *Saccharomyces cerevisiae* ATP synthase true-dimers. **(d)** Projection map of *Saccharomyces cerevisiae* ATP synthase pseudo-dimers [43].

The organization of the respiratory-chain supercomplexes has been proposed to have fundamental functional implications [39,47-50], including 1) allowing enhanced electron transfer rates through electron channeling, 2) forming regulatory units of respiration, 3) determining the ultrastructure of the inner mitochondrial membrane, 4) increasing the stability of OXPHOS complexes, and 5) enhancing he protein insertion capacity of the inner mitochondrial membrane [39].

There are at least two aspects to the significance of the supermolecular organization, in addition to its regulatory possibilities. On the one hand, some complexes seemed to act as chaperones to assist the assembly of the other complexes [44]. For example, complex I was found to be unable to assemble without the presence of complex IV (C*c*O). In the yeast respiratory chain, ATPase is also required for the assembly of complex IV and the assembly of the supercomplex of III and IV [44,45].

On the other hand, the organization of super-molecular complexes was able to control the shape of the membranes [43,46]. Rather than solely relying on the reorganization of the lipid distribution in the membrane to alter the curvature, reshaping of the membrane is now emerging as a process that is more actively modulated by the formation of super-complexes. The formation of the supercomplex is found to follow a well controlled specific orientation and conformation. For instance, recent Electron Microscopy studies revealed that in the mitochondrial membrane, two ATPase molecules can join to form a well-defined curved dimer via their transmembrane domains, dragging along with them the lipid bilayer, and subsequently creating a curvature of the membrane as well [43,46,51]. The alteration in the membrane curvature is an important preceding step for the following interactions [39].

1.5 Interactions of lipids with membrane proteins and super-molecular complexes

Lipid molecules are resolved in the crystal structures of many membrane proteins, implying a significant role in protein structure and function. In fact, it has been shown that specific lipids are required for correct folding and assembly of some membrane proteins, such as the plant light harvesting complex and bacterial lactose permease. Other studies on bovine and yeast cytochrome bc_1, bovine cytochrome *c* oxidase, and bacterial KcsA K^+ channel, indicate a requirement for specific lipids for full activity [52,53]. In some cases, complete removal of bound lipid is found to abolish protein function, an effect that is reversible by adding back lipids [54,55].

In addition to their influence on assembly and function, bound lipids also stabilize the protein structure. A number of lipid molecules co-purify with C*c*O from *R. sphaeroides*, and the lipid binding sites in the core subunits of C*c*O are highly conserved from bacteria to mammals, emphasizing the importance of lipids in the protein structure [35].

The interactions between the membrane protein and lipids can be examined from two different perspectives; the chemical nature of the interactions, and the functional consequence of the interactions.

1.5.1 Interactions experienced by membrane proteins in a membrane environment

The assembly, folding and stability of the hydrophobic transmembrane proteins are fundamentally determined by the interactions surrounding the proteins. Besides

interactions of the polypeptide chains with themselves, water, neighboring lipids, cofactors, and with the membrane interface (Figure 1.10), the thermodynamic and electrostatic properties of the lipid bilayer itself are important. Like proteins, the lipid bilayer also sits at a state of minimum free energy as the result of the equilibrium of numerous interactions. Disturbance of this equilibrium by the introduction of proteins or other solutes, or by anisotropic motion and chemical heterogeneity can result in so-called bilayer effects (Figure 1.11) [56].

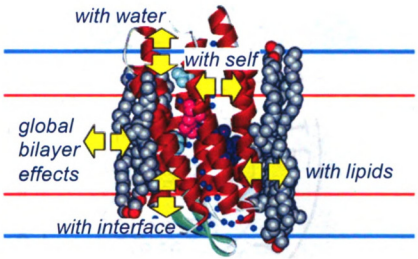


Figure 1.10 Interactions that determine the structure and stability of membrane proteins. The *blue lines* represent schematically the total thickness of the lipid bilayer, and the *red lines* the central hydrocarbon core bounded by the interfacial regions. The *pink* molecule is the cofactor retinal in bacteriorhodopsin [56].

The lateral pressure exerted by the lipid bilayer can affect the structural integrity of membrane proteins. Solubilization using detergent caused destabilization in general, decreasing the lateral pressure and increasing conformational freedom of the protein,

which might also explain why membrane proteins are so sensitive to their buffer conditions, and why it has been so much more challenging to obtain high-resolution crystal structures from membrane proteins than from the soluble proteins.

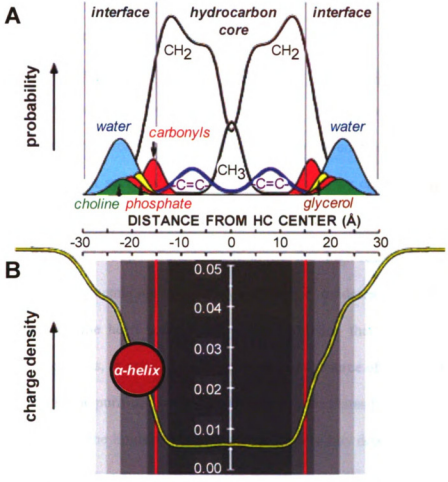


Figure 1.11 Liquid crystallographic structure of a fluid lipid bilayer and its computed polarity profile. *A*, structure of a GPCho bilayer (5.4 waters/lipid) determined by joint refinement of x-ray and neutron diffraction data ; *B*, polarity profile (*yellow curve*) of the GPCho bilayer computed from the absolute values of atomic partial charges [56].

1.5.2 Effects of lipids on membrane proteins

In membranes, lipids do far more than just statically build the environment for the organization and activities of membrane bound proteins and protein complexes. Lipids also provide an interactive platform for them to communicate with other proteins and other molecules, and are likely to be actively involved in these processes as suggested by emerging experimental evidence.

Membrane lipids generally contain a hydrophilic head group and a long hydrophobic tail, but both parts have been increasingly found to have a vast diversity in terms of their specific structures, enabling the potentially diversified functions of different lipid species. Recent successes in membrane protein X-ray crystallography at high resolution have discovered that many lipid molecules remain bound in the crystals of membrane proteins [28,34-36]. Superimposition of the high-resolution crystal structures of multi-subunit membrane protein cytochrome *c* oxidases purified from different bacterial and bovine heart sources led to the revelation that there are well conserved sites of bound lipids, in spite of the differences in the source of the membrane lipid compositions, and in the purification and crystallization procedures [35]. Although the sites are well conserved, the lipids at some sites were replaced by detergents, raising the question of lipid specificity requirements for the binding sites. One straightforward way to address these questions is to "remove" a particular type of lipid, and examine the consequences of the missing lipids on various aspects of the system.

Previous studies removed CL from purified bovine heart C*c*O, and found that the integrity and activity of C*c*O were destroyed [57]. Similarly, reversible inactivation resulted when the bound CL was removed using phospholipase digestion from purified

cytochrome bc_1 complex [54], suggesting an essential role of cardiolipin in maintaining the integrity of the super-molecular organization.

1.5.2.1 Lipids interact with membrane proteins to maintain integrity of biological membranes

Lipids bilayers provide the physically continuous and sealed compartmentalization of different cellular organelles, which is essential for cellular processes. Through interactions with membrane proteins, lipids bilayers also manage to maintain a tightly electrochemically sealed membrane for mechanisms that require the generation and maintenance of electrochemical potentials across the membrane, such as ATP synthesis and active transport, to occur.

1.5.2.2 Lipids assist with membrane protein insertion, folding, assembly and topology

It was found that anionic phospholipids are important in determining the membrane protein topology. A genetic deficiency in GPEtn lipids affects the topology of LacY from *E. coli.* (Figure 1.12) [19]. In the GPEtn-deficient mutant, transmembrane helix VII was found on the "out" side of the membrane, causing the lactose permease to malfunction. The lipid monogalactosyldiacylglycerol (MGlcDAG, also called MGDG) was found to fully replace GPEtn to create the correct topology, whereas neither CL nor GPCho could restore the proper activity and topology of LacY, an effect that the authors rationalized to originate from the non-bilayer prone structural feature of both GPEtn and

MGlcDAG, and the neutral charge state of MGlcDAG head group that would not disturb the charge balance of the membrane surface, according to the "positive inside rule" [19].

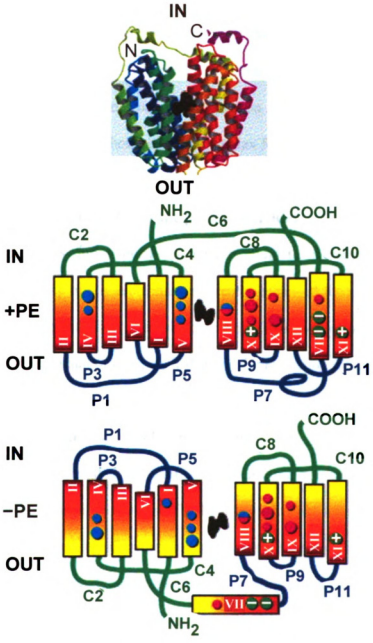


Figure 1.12 Difference in the topological organization of LacY from *E. coli* cells containing (top) and genetically lacking (bottom) GPEtn (PE) [1].

1.5.2.3 Lipids assist with assembly and stabilization of super-molecular complexes

For the light-harvesting complex II, it has been shown that the assembly depends on defined phospholipid and glycolipid species. In bacteriorhodopsin, a single lipid has been observed at every contact site of adjacent monomers [1]. Although the head group was not unequivocally assigned, tight interactions of the phosphate with Lys-40 were proposed based on its important role in purple membrane formation. It was concluded that this specific lipid acts as the glue in trimerization of bacteriorhodopsin [1]. The importance of cardiolipin in mitochondrial supercomplex formation is discussed below.

1.5.2.4 Lipids affect or regulate membrane protein activities

Harsh delipidations during purification were found to decrease the activity of C*c*O, whereas the presence of soy asolectin consistently enhanced the activity of C*c*O *in vitro* by 20-40% [27]. The addition of arachidonic acid (20:4) was also found to protect D132A, a suicide-prone mutant of C*c*O, against suicidal inactivation [58].

1.5.2.5 Binding motifs of lipids in membrane proteins

Lipid binding was found to be stabilized by multiple non-covalent interactions involving both the lipid head groups and the hydrophobic tails with protein residues [1,58]. The recently resolved atomic structures of membrane proteins with tightly bound lipids, as well as the structure-directed mutagenesis studies, provided new insights into protein–lipid interactions [1]. Distinct motifs in the amino acid residues have been identified for stabilizing the interactions with the phospholipids head groups and side chains from resolved membrane protein structures [1].

Based on the sites of binding, the resolved tightly bound lipids are classified into three general categories [1]: 1) the annular shell of lipids that surround the membrane protein like the bilayer and are presumably important for the perpendicular insertion of the protein, 2) the non-annular lipids that fill in the cavities, clefts or pores between subunit or oligomeric interfaces, and 3) the integral lipids that bind in unusual sites or orientations and might play roles in protein assembly and folding [1].

The head group is stabilized by strong interactions with basic residues such as arginine and lysine by forming ion pair and hydrogen bonds, as well as with aromatic residues (Table 1.2) [1], whereas the resolved lipids tails are stabilized by alanine, leucine, phenylalanine, isoleucine, serine and histidine residues (Table 1.3), likely through hydrophobic interactions [58].

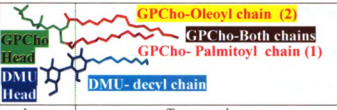
Table 1.2 Amino acid residues that bind the head groups of negatively charged lipids resolved in membrane protein crystal structures [1].

PL	AA	Protein	Comment	Species	PDB	Res. [Å]
PE	KT	BC1	*n*, annular	*G. gal.*	1BCC	3.2
PE	YQT	BC1	*n*, same binding site as L4	*G. gal.*	1BCC	3.2
PE	YNYQK	BC1	*n*, annular, L4	*S. cer.*	1KB9	2.3
PE	N	BC1	*n*, dimer interface, L2	*S. cer.*	1KB9	2.3
PE(4)	RHS; RW; R; K	COX	*n*	*R. sph.*	1M56	2.3
PE(2)	R; KR	COX	*n*	*B. tau.*	1V54/1V55	1.8/1.9
PE	YKR	RC	*n*, thermophilic bacteria	*T. tep.*	1EYS	2.2
PE	KK	SDH	*n*	*E. col.*	1NEK	2.6
PE(2)	QHK; YQ	COX	*p*	*R. sph.*	1M56	2.3
PE(1)	T	COX	*p*	*B. tau.*	1V54/1V55	1.8/1.9
PC	S	BC1	*n*, cavity at dimer interface, L1	*S. cer.*	1KB9	2.3
PC	RHE	COX	*n*	*P. den.*	1QLE	3.0
PC	H	COX	*n*	*B. tau.*	1V54/1V55	1.8/1.9
PC(3)	T	AC	*n*	*B. tau.*	1OKC	2.2
PC	HS	BC1	*p*	*S. cer.*	1P84	2.5
PC	RD	COX	*p*	*P. den.*	1QLE	3.0
PI	KST	BC1	*p*, integral protein lipid, L3	*S. cer.*	1KB9	2.3
PG(3)	RHS; RW	COX	*n*	*B. tau.*	1V54/1V55	1.8/1.9
PG(3)	RNRD; RS	PSI	*n*	*S. elo.*	1JBO	2.5
CL	K, RH	BC1	*n*, cavity at dimer interface, L7	*S. cer.*	–	2.5
CL	KYK, YHN	BC1	*n*, near Qi site (proton uptake), L5	*S.cer.*	1KB9	2.3
CL	RKYD, HKK	COX	*n*	*B. tau.*	1V54/1V55	1.8/1.9
CL	HR, KW	RC	*n*	*R. sph.*	1M3X	2.55
CL	HRN, WH	RC	*n*, lipidic cubic phase	*R. sph.*	1OGV	2.4
CL(2)	S	AC	*n*	*B. tau.*	1OKC	2.2
CL	NDY, HN	COX	*p*	*B. tau.*	1V54/1V55	1.8/1.9
CL	NT, NS	FDH	*p*, interface of adjacent monomers	*E. col.*	1KQF	1.6
DG	KS	BR	*n*, important for trimer formation	*H. hal.*	1BM1	3.5
SL	RKN	B6F	*n*, sulfolipid, cavity at dimer interface, same position as L1 and L4	*C. rei.*	1Q90	3.1

Table 1.3 Amino acid residues that bind the fatty acid tails of lipids resolved in membrane protein crystal structures [58].

KEY:

Color coding and location of GPCho or DMU



Species	*a.a. No.*	Inner loop	Transmembrane region	Outer loop	*a.a. No.*
E. Coli	304	→TFSRKR	LFGYTSLVWATVCITVLSFIVWLHHFFTMG	A ↵	340
	376	←VIRGQ	YMTFLWNFIKVGTPIAIIMTTIGFFANVNA	G ↵	341
T. Thermus	254	→KQAGGK	LVSDPMARLAFLLFLLLSTPVGFHHQFADP	GI ↵	290
	327	←RLRGAF	ELSAAVTFATMLSPVAVFLTLVSHIMKWTP	D ↵	291
Cyanobacter	286	→KP	LFGYRVVAISTVAIGVIGFTVWAHHMFTSG	T ↵	318
	352	←KGG	WMTAVWNFVKIGTPVAITMSTIMFFLRLWD	P ↵	319
Rhodobacter	308	→KP	IFGYLPMVYAMVAIGVLGFVVWAHHMYTAG	L ↵	340
	374	←SGG	WMTAIWSFIKIGTPVAIVMTAMMFYSQQTL	S ↵	341
Rickettsia	284	→KP	IFGYQGMVGAMVIIGFVGFIVWAHHMFTVG	L ↵	316
	350	←SGG	WMTAIWSFIKIGTPVAIIMTGATFYILANY	S ↵	317
Coral	266	→KQH	IFGYLGMVYAMISIGVLGFIVWAHHMFTVG	M ↵	299
	333	←SGG	YITALWSFIKIGTPVAIIMTAATFYARTDV	D ↵	300
Choanoflagulla	267	→KP	VFGYLGMVYAMLSIGLLGFIVWAHHMYTVG	M ↵	299
	333	←SGG	FMTAVWSFIKIGTPVAIIMTAATFYARTDV	D ↵	300
Coelacanth	264	→KKE	PFGYMGMVWAMMAIGLLGFIVWAHHMFTVG	M ↵	297
	331	←VGG	HLTALWSFVKVGTPIAIIMTASTFYARTDV	D ↵	298
Frog	264	→KKE	PFGYMGMVWAMMSIGLLGFIVWAHHMFTVD	L ↵	297
	331	←TGG	HMTALWSFVKVGTPIAIIMTASTFYARTDV	N ↵	298
Platypus	264	→KKE	PFGYMGMVWAMMSIGFLGFIVWAHHMFTVG	M ↵	297
	331	←DGG	HLTALWSFVKVGTPIAIIMTASTFYARTDV	D ↵	298
Bovine	264	→KKE	PFGYMGMVWAMMSIGFLGFIVWAHHMFTVG	M ↵	297
	331	←NGG	HLTALWSFVKVGTPIAIIMTASTFYARTDV	D ↵	298
Slow loris	264	→KKE	PFGYMGMVWAMMSIGFLGFIVWAHHMFTVG	M ↵	297
	331	←NGG	HLTALWSFVKVGTPIAIIMTASTFYARTDV	D ↵	298
Human	264	→KKE	PFGYMGMVWAMMSIGFLGFIVWAHHMFTVG	M ↵	297
	331	←NSG	HLTALWSFVKVGTPIAIIMTASTFYARTDV	D ↵	298

1.5.3 Cardiolipin and OXPHOS complexes

Lipids, in particular cardiolipin with its two phosphates and one glycerol in the head group and four hydrophobic fatty acid chains, is found to be essential for the assembly of supercomplexes from III and IV [59], and is proposed to act as a glue to assist with maintaining the integrity of these super-complexes (Figure 1.6) [41]. Figure 1.13 shows the position of cardiolipin in the supercomplex of III_2 + IV_2 with attached cytochrome *c* from yeast.

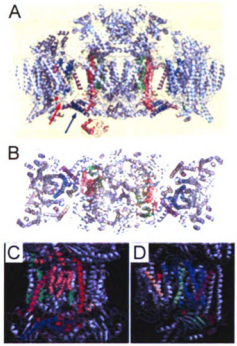


Figure 1.13 Pseudo-atomic model of the III_2 + IV_2 supercomplex with attached cytochrome *c*, showing the interactions of cardiolipin with complexes III and IV. *Salmon*, cardiolipin and GPEtn molecules of the complex III and subunits Cox I (***navy blue***), Cox II (***green cyan***), Cox III (***hot pink***), Cox IV (*purple*), Cox VIc (*brown*), Cox VIIa (***yellow orange***), and Cox VIIc (***green yellow***) of the complex IV, respectively. (A) side view, (B) top view, and (*C*) and (*D*) detailed views of the III_2 + IV_2 supercomplex [41].

Cardiolipin (CL) is one lipid whose requirement has been established by biochemical studies on the function of several membrane proteins from bacterial and mitochondrial sources [1,8,9,57,59-64]. Due to its unique structure, having four rather than two hydrophobic fatty acid chains, cardiolipin can bind more strongly to membrane proteins and is perceived to act as a "super glue" to help maintain the integrity of multi-protein super-complexes [65].

Digestion of tightly bound phospholipids inactivates the cytochrome bc_1 complex, without disturbing its spectral properties, and reactivation depends on addition of cardiolipin [54]. Two cardiolipin molecules have been identified in the structure of the yeast cytochrome bc_1 complex [1,52]. One cardiolipin is bound close to the site of ubiquinone reduction and is proposed to be of importance for the stability of the catalytic site and to be involved in proton uptake [52].

1.5.4 Cardiolipin and C*c*O

Cardiolipin has also been found to be specifically essential for the full activity of mammalian heart C*c*O [57]. However, the molecular basis of its function in C*c*O is not understood.

Although cardiolipins are involved in the respiratory chain complexes [8,28,59,65,66], particularly C*c*O, in both bacterial and eukaryotic systems, the last step of cardiolipin biosynthesis from GPGro, and the following remodeling reactions, are totally different between the systems, and the final composition of cardiolipin molecular species are also very different. Therefore it is conceivable that the mechanism through

which cardiolipin exerts its functional roles might be different as well, between the bacterial and mammalian systems.

In mammalian cells, cardiolipin can get peroxidized at its double bonds and form a complex with cytochrome *c*, which then triggers the release of cytochrome *c* from mitochondria under stress stimuli, and leads to cell apoptosis [8,9,67]. Further investigation of the cardiolipin molecular species revealed that healthy mammalian systems mainly contain cardiolipin with unsaturated 18:2 chains, particularly $CL(18:2)_4$ (L_4-CL) [8,9,21,68-70]. Although CL containing 18:1 and 16:0 are also found at much lower abundances, at least some of the critical roles of cardiolipin seem to involve the unsaturated $CL(18:2)_4$ species which has the potential for oxidation of its double bonds. Decreased fraction of $CL(18:2)_4$ leads to decreased activity of C*c*O down to 50% [68], and causes mitochondrial dysfunction [69]. When adding back cardiolipins, $CL(18:2)_4$ is more effective in stimulating C*c*O than other cardiolipin species. However, $CL(18:2)_4$ is not produced directly from the biosynthesis of lipids in mammalian cells, but it is formed through modification by acyltransferases on the initial cardiolipin species [9]. On the other hand, mutations in the assembly, but not in the catalytic functions of C*c*O, were found to decrease the biosynthesis of cardiolipin down to 50% to 60%, whereas mutations in complex III or complex V did not display such effects on cardiolipin synthesis [69].

In marked contrast, the bacterium *R. sphaeroides* makes mainly $CL(18:1)_4$ (Chapters 7, 9 and 10). No detectable levels of $CL(18:2)_4$ are seen even when they are

grown under aerobic conditions and survive via the respiratory chain complexes (Chapters 7, 9 and 10). Likewise, yeasts predominantly produce cardiolipin containing 18:1 and 16:1 fatty acyl chains but not 18:2 [20]. Several studies using genetic mutagenesis in bacterial and yeast systems found that the deficiency in cardiolipin did not significantly affect the activity of C*c*O, nor did it alone cause the dysfunction of the mitochondria in yeast [71], but the double deficiency in GPGro and CL resulted in very little C*c*O production and severely dysfunctional mitochondria, suggesting CL is not essential for C*c*O or mitochondria in yeast, but is functionally replaceable by GPGro lipids [71].

1.6 Membrane protein purification and crystallization

Since structural stability is a crucial factor for membrane protein crystallization, retention of lipid molecules during the purification steps has been emphasized for successful protein crystallization [35,72]. Supporting evidence for the role of lipids in the crystallization of membrane proteins includes the observation that the quality of *E. coli* lactose permease crystals can be controlled by changing the phospholipid levels [1]. A similar observation was made regarding the crystallization behavior of the cytochrome b_6f complex, in which addition of lipids improved the crystallizability of the protein [73,74]. Such efforts to obtain high resolution structures of membrane proteins have led to the need for closer scrutiny of the role of protein-associated lipid molecules.

1.6.1 Usage of detergent

Detergents are needed in the purification of most membrane proteins to form a micelle around the protein and pull it out of the lipid bilayer membrane into the solution [6,75,76] (Figure 1.14). Membrane proteins sometimes can also be isolated utilizing their existing lipids and lysolipids. This mechanism was adopted by using cobra phospholipase A2 to cleave the *sn-2* fatty acid chain from phospholipids and turn them into lysophospholipids, which then act as detergents to dissolve the membranes [24].

In the purification of bovine heart C*c*O, the membranes are disrupted with cholate [28,29], a steroid detergent that tends to initially create membrane patches. In the purification of C*c*O from cytoplasmic membranes of bacteria, detergents are used throughout the process to solubilize the membrane pellets, to keep the protein from deformation or aggregation, and to keep it in the active form [35,75,77].

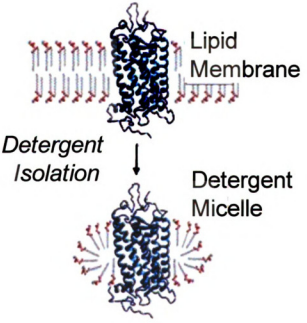


Figure 1.14 Schematic of the isolation of membrane proteins from membranes using detergent dodecyl maltosides (adapted from www.science.uottawa.ca).

The effects of the detergent closely depend on their structural and physical properties and differ significantly between detergents [6,78,79]. Compared to lipids, detergents have molecular shapes that tend to form micelles rather than bilayers. The most commonly used types of detergents have relatively small tails (12 carbons or less) and a large head group so that they can form micelles with the head groups pointing out into the aqueous solution [6]. The charge state, potential hydrogen bonding sites, head group size, chain length and the molecular shape are critical factors that determine the ability of detergents to form micelles (critical micelle concentration, CMC) and the aggregation number in the micelle, which can translate into the overall power to remove proteins from the membrane. The solubilization of the protein from the membrane starts to occur when the concentration of the detergent approaches 1 CMC [80]. The detergents are evaluated by their abilities to assist with the solubilization, maintaining activity (non-inactivating), and crystallization of the membrane proteins [30,75].

While ionic detergents, such as sodium dodecyl sulfate (SDS), usually solubilize the membrane efficiently, they almost always destabilize membrane proteins, causing precipitation and significant inactivation. Zwitterionic detergents often cause inactivation as well, and their charge states are sensitive to the pH. Non-ionic detergents such as maltosides are generally characterized as milder and cause less disruption to the proteins' structures and activities [75]. Steroid-based detergents such as cholic acid and deoxycholic acid (bile acids) have high CMC values and low and ionic-strength-dependent aggregation numbers, making them easier to remove for reconstitution. They

are mild and often lead to less inactivation, but have been found not helpful in crystallization [80].

The chain length of the detergent causes differences in the protein activity and stability, even with the same head group [75,79]. The chain length that can best mimic the membrane layer thickness seems to maintain the highest activity of the protein. Shorter chains (C7-C10) cause more inactivation of the proteins than longer chains (C12-C14) [75,80]. Although decyl maltosides (C10) leads to lower protein activity and stability [75], exchanging into it from dodecyl maltosides (C12), the detergent that can maintain the highest activity of C*c*O [75], was found to produce C*c*O protein crystals with higher resolution [30].

In general, the non-ionic detergent dodecyl maltoside has been found to be applicable to most membrane proteins, not only in efficient solubilization and maintaining activity, but also in crystallization [6,30,75,80].

1.6.2 Cubic phase technique: making lipids the medium

To maintain the lateral pressure exerted by lipid bilayers, minimizing both the disturbance and disordering of the membrane protein, the cubic phase crystallization method was recently developed to crystallize membrane proteins in a lipid environment [72,81-83]. In this method, a bicontinuous membrane formed by mixing lipids and water is used as a support matrix for nucleation and crystal growth. This method has been particularly successful with a class of membrane proteins with seven robust transmembrane helices including bacteriorhodopsin, halorhodopsin, and sensory rhodopsin II [72,81-83].

1.6.3 Optimization of crystallization using mass spectrometry as a tool

Mass spectrometry has emerged as a useful tool in assisting with the optimization of membrane protein crystallization [84]. Directed by the mass spectrometry detection of the heterogeneous forms of the subunits and the degradation of the protein over time, molecular biology methods can be applied to engineer more stable and homogeneous forms of protein that could produce crystals that diffract at higher resolution. Mass spectrometry has also been applied to identify the components in the protein crystals that could not be completely resolved by the crystallography due to limited resolution [84], such as the molecular structures of the lipids and detergents in the membrane protein C*c*O crystals [28] (earlier findings presented in [30]). The extensive usage of detergents in membrane protein purification, however, often poses as a challenge in mass spectrometry analysis [85], particularly in the lipid analysis by ESI through interfering with the ionization process, and has to be addressed by using various approaches (Chapter 8).

1.7 Strategies used to investigate membrane protein-lipid interactions

1.7.1 Biochemical extraction and phospholipase digestion

Previous studies removed CL from purified bovine heart C*c*O with detergent, and it was found that the integrity and activity of C*c*O was destroyed [54,57]. Similarly, reversible inactivation resulted when the bound CL was removed using phospholipase digestion from the purified cytochrome bc_1 complex [54]. These types of *in vitro* biochemical approaches could potentially disturb the enzyme structure and do not address the possible adaptability of the membrane proteins with their lipid components.

1.7.2 Spin-labeling combined with EPR

EPR coupled with spin-labeling has been applied to monitor the change in the metals at the influence of the surrounding ligands as a result of the changes in lipids components of the membrane proteins [86,87]. It is also combined with ^{1}H-NMR tomonito the dynamics of the protein change as a result of the altered lipids [86,87].

1.7.3 ^{31}P-NMR of lipids to monitor the lipid exchange

Since the phosphorus atoms from different types of phospholipids have distinctive positions of chemical shift in ^{31}P-NMR and the NMR methods can be quantitative, ^{31}P-NMR can be applied to monitor the change in the quantity of phospholipids [88,89].

1.8 Lipid profile modification as the tool to probe protein-lipid interactions *in vivo*

1.8.1 Genetic manipulation of lipid content as the probe *in vivo*

The development of strains of microorganisms in which membrane lipid composition can be genetically manipulated in viable cells has provided a set of reagents to probe lipid functions. These mutants have uncovered previously unrecognized roles for lipids and provided *in vivo* verification for putative functions described *in vitro* [19].

Specific lipid-deficient mutants of yeast and bacteria have been created by mutating the lipid synthase genes to probe the effects of the particular type of lipids on

the activities of yeast mitochondria, and the respiratory complexes, including discussions on cytochrome *c* oxidase [59,69,71].

Several specific lipid deficient strains of *R. sphaeroides* have also been developed to examine the effect of the particular lipid on the overall bacterial viability, growth and behavior. The mutant GPCho-deficient *R. sphaeroides* strain CHB20 (selected from chemically-induced mutant forms), containing no measurable GPCho beyond the background level, and accumulating the precursor GPEtn, was found to behave similarly to the wild type strain 2.4.1 under normal growth conditions, in spite of the significantly altered membrane lipid properties [90]. The mutant SQDG-deficient *R. sphaeroides* strain SB1K1 also grew normally like the wild type 2.4.1, but when both SQDG and GPGro are deficient, the cells could not survive [14].

Specific lipid "removal" via genetic manipulation provides a more natural context to observe the consequences of lipid substitutions to the system, by allowing the membrane proteins to develop and adapt to the altered lipid environment from the beginning.

In this thesis, through genetic manipulation of the lipid composition of *R. sphaeroides*, the analysis of a variety of strains that are each intrinsically deficient in a specific type of lipid was reported (see Table 3.1 in Chapter 3 for detailed descriptions of the strains). These strains provided a tool to probe the function of each type of lipid in the overall bacterial cellular processes and the effects on the specific membrane protein *R. sphaeroides* Cc*O*, *in vivo* and in the purified state.

1.8.2 Phosphate limiting growth media

The lipid composition of bacteria and yeast was found to respond to the growth media by developing certain mechanisms to adapt to the nutrition sources [11,12,91-93]. Phosphate-limiting media growth has been performed on *R. sphaeroides* and other photosynthetic bacteria [11,93]. Manipulation of the lipid profile, via the metabolic approach, provided another tool to probe the functions of the lipids and their functional substitution *in vivo*.

1.8.3 Growth temperature stress

Deviation from the comfortable growth temperature for bacteria has been found to cause a change in the lipid composition, in both types of lipids and the lipid fatty acid chain compositions [94-96]. Therefore it can be used as another metabolic tool to modulate the lipid profile. For instance, higher growth temperatures induced an increase in ornithine lipid and lipids containing 2-OH fatty acid chains [95]. On the other hand, the increase of growth temperature can also be introduced as a source of stress, to probe the stability of the protein complexes and the super-complex organizations under a stressed condition.

1.8.4 Salt concentration (osmotic pressure) stress

Increase in salt concentrations in the growth media was also found to enhance the production of cardiolipin, as a mechanism to cope with the high osmotic pressure stress, and such a high salt stress-induced increase in cardiolipin has been used to probe its functions [97,98].

1.9 Summary

Membrane proteins play important roles in many physiological processes and are often key targets for pharmacological intervention. However, membrane proteins have been found difficult to study, both structurally and functionally. This thesis reports advances in the analysis of the membrane protein C*c*O, using mass spectrometry approaches and genetic manipulation of lipid content to better define the requirement and specificity of lipid interactions.

Chapter 2

An Overview of Mass Spectrometry Strategies Employed for Lipid Analysis

2.1 Mass Spectrometry: the enabling tool for lipidomics

Accurate identification of the enormously diversified structures of lipids and further quantification of each lipid molecular species, over a wide range of abundance, has remained a challenge until mass spectrometry (MS), with its high sensitivity and multistage tandem mass spectrometry capability, became available. A lot of our current knowledge about the lipid composition of various bacteria has been achieved over the past decades, when the identification of the type of lipids used to rely mainly on the selective spray of the thin-layer-chromatography (TLC) plate with reagents that selectively react with specific functional groups, and the quantification of each of the lipids relied on radioactive labeling followed by TLC separation, or phosphorus analysis for the quantification of phospholipids [11,14,90]. More details of the lipid structure would be derived from gas chromatography-mass spectrometry (GC-MS) analysis following saponification of the re-extracted lipid bands scraped from a TLC plate, or nuclear magnetic resonance (NMR) analysis of purified lipid [11,14,90,99]. Electron impact ionization, field desorption, plasma desorption, chemical ionization had been used to attempt the analysis of lipids [100,101]. Fast atom bombardment (FAB)-collision induced dissociation (CID) tandem mass spectrometry (MS/MS) was later used to

confirm the lipid structures [11,102-109]. With the recent advent of modern techniques in mass spectrometry, such as the "soft" matrix assisted laser desorption/ionization (MALDI), electrospray ionization (ESI) and desorption electrospray ionization (DESI) ionization methods, coupled with low-energy CID dissociation methods, and increasingly more versatile and sensitive mass analyzers including the quadrupole ion trap, triple quadrupole, time of flight (TOF), Fourier transform-ion cyclotron resonance (FT-ICR) and Orbi-trap, strategies can be developed for most of the lipids to be quickly and accurately identified with structural details directly in the complicated mixture, without the requirement of previous purification and using a minimum sample amount [101,110-118]. At the same time, quantification of individual lipid species can be achieved by incorporating lipid internal standards in mass spectrometry analysis.

2.2 Sample preparation for mass spectrometric analysis of lipids

As will be discussed below, lipid sample preparation is heavily dependent on the analytical methods to be applied. The high structural resolution, sensitivity, and tandem MS versatility of modern mass spectrometry often makes elaborate pre-analysis separation of different types of lipids unnecessary, and can be applied with only a minimum amount of sample compared to other traditional methods. MALDI can be directly used with developed TLC plates [119,120] membrane pellets (Chapters 9 and 10), membrane proteins containing lipids (Chapters 9 and 10), tissue slices for lipid-distribution imaging [121-125], even whole plankton or bacterial cells [126,127], as well as lipid extract solutions [5,114,128-130]. The ESI ion source often requires that the

lipids are extracted and solubilized for the spray, but it does not require the chromatographic separation of lipid extracts. Although whole cell suspension has also been electrosprayed [131], the information obtained was very limited. However, due to the high sensitivity of mass spectrometry methods, several considerations have to be taken into account during the lipid sample preparation that might affect the analysis.

General considerations of sample preparation include: keeping the lipid molecules intact if lipid extraction is performed; the pH of the sample, which can affect the ionization efficiency of the lipids and the charge state of lipid ions and cause hydrolysis of some types of lipids such as the plasmalogen at acidic pH [117,132]; the presence of detergents, which can significantly suppress the ionization of lipids in ESI more than in MALDI due to the ESI ionization mechanism [85] (discussed below); the presence of salt (from buffers) which can form non-covalent alkali or anionic adducts with lipids and can suppress efficient ionization (Chapter 4); contamination from the containers such as plasticizers [133]; and additives that can promote ionization in ESI such as volatile ammonium salts and ammonium hydroxide [134] (also see Chapter 4).

For quantitative profiling of lipid extracts, the chemical extraction efficiency and proper quantification control are the upstream key factors that determine the validity of quantification. Depending on the purpose of the analysis, well-calibrated internal lipid standards should be properly chosen and incorporated into the sample at the specific step of sample preparation at optimal concentrations. Compared to the highly reproducible mass spectrometry analysis itself, the biological sample preparation contributes to the majority of the deviation. Therefore, at least triplicate independent biological sample preparations should be performed, in order to obtain valid quantification results. The

basis of lipid quantification can be tissue or cell wet weight, dry weight, cell number, cell culture plate number or protein concentration.

Although not always required, the coupling of liquid chromatography with ESI mass spectrometry does provide an extra dimension for lipid separation and can assist with the lipid identification and quantification. Reverse-phase liquid chromatography can separate lipids in the mixture by their hydrophobic tails, while normal-phase liquid chromatography can separate the lipids by head-group polarity [115,135]. Liquid chromatography is particularly useful, and is probably the most efficient method, in removing the contaminating detergents from the lipid extracts, which is often an issue with lipid extracts from lipid rafts and detergent-solubilized membrane proteins (Chapter 8).

2.2.1 Lipid extraction

Identification and quantification of lipids using ESI mass spectrometry have recently become more extensively applied to the lipid mixture extracted from tissues, cells, cellular organelles, lipid rafts and lipid-containing membrane proteins. Several systems have previously been developed to extract lipids from tissues. Among them are the Folch extraction [136], and the one-phase based Bligh and Dyer method [137] which were initially developed for lipid extraction from fish tissue with high water content, using chloroform and methanol as the solvents, and could achieve extraction yields of ~ 90% [137-139]. These methods have been widely applied in mass spectrometry-based analysis with slight modifications [111,140,141], yet the efficiency of extracting the lipids from these various systems have not been discussed in detail in these recent

applications. The essential principle of the Bligh and Dyer extraction method is to maximize the contact of the lipids in the tissue with the extraction solvent by dispersing the tissue into the one-phase mixture formed by chloroform, methanol and water, followed by addition of a certain amount of water or chloroform to drive the mixture to separate into two phases, and the lower chloroform-rich phase contains the lipids [137]. Tissue and mammalian cells can be directly subjected to chemical lipid extraction, but Gram-negative bacteria such as *Rhodobacter sphaeroides* have tightly packed lipopolysaccharide (LPS) cell walls and often require cell lysis and membrane pellet isolation prior to lipid extraction, or the incorporation of KH_2PO_4 buffer (pH 4.7) and extensive vibrant shaking to assist with cell-breaking in the chloroform and methanol extraction solvent [15]. In addition to the extraction by using organic chemical solvents, microwave [142], liquid CO_2 superfluid extraction [142], and "in-cell fractionation" using fixed silica-based sorbents on sequential pressurized liquid extraction [143] have also been applied in the lipid extraction from tissues or cells.

In addition to the polarity of lipids and the extraction solvents, a number of variables have been reported to affect the efficiency of the chemical lipid extraction. In the Rose extraction [144], using chloroform: iso-propanol (7:11, v/v) instead of chloroform: methanol (2:1, v/v) is found to extract the hydrophobic lipid components (cholesterols) more efficiently and minimize heme extraction from red blood cells. Less-toxic t-butyl methyl ether can replace chloroform with a similar extraction yield, and make the operation easier by concentrating the lipids in the top layer during the phase separation step [145]. The extraction of charged lipid is often assisted by the addition of counter ions [146]. Acid or base is also applied, in order to adjust the pH to neutralize the

lipids with different charge states in solution and increase their solubility in hydrophobic solvents [53]. In the traditional analysis of lipids, total lipids are often separated into the general types of neutral, positive, and negative lipids, using solid-phase extraction, by adjusting the pH of the eluting solvents with strong acid and base to neutralize the charge of the lipids. Generally, extraction efficiency is often higher with smaller sample size in a larger solvent volume and at higher extraction temperature [138,147-149].

However, lipid extraction from purified membrane proteins is known to be much more difficult than from bulk tissue or membrane pellets, because the lipids that remain in the purified membrane proteins are more tightly bound to, or buried inside, the hydrophobic portion of the proteins. The extraction yield is often low and requires additives to help remove the lipids through ionic pairing, hydrophobic replacing (detergent), protein denaturing, or preventing protein scaffolds from denaturing and aggregating (detergent and ionic buffer) (see Chapter 8 for a detailed discussion).

In the recent applications of quantitative lipid analysis, even though the lipid extraction yield is not directly evaluated, the lipid internal standards are often chosen to be added to the tissue or cells, prior to lipid extraction, assuming that the extraction efficiency of the added internal standards is the same as that of the endogenous lipids.

2.3 Traditional methods for lipid identification and quantification

Traditionally the identification and structural characterization of lipids are carried out using a time-consuming multi-step procedure on a relatively large scale. It often requires the lipids to be extracted and separated using thin-layer chromatography (one-

dimensional and two-dimensional), solid-phase extraction, or liquid chromatography. The identification of the lipid class is based on comparison of the migration position with known standards, and the presence or absence of specific functional groups is determined by using functional-group-selective colorimetric spray: molybdate for phosphate, ninhydrin for free amino groups, and α-naphthol for sugar groups [11,14,15,90]. The identification of the fatty acyl chains often employs generic saponification reactions to release the fatty acid chains, which are further derivatized, typically by methylation, for gas chromatography analysis. Highly structure-selective lipolytic enzymes, such as a series of region-selective enzymes, were also applied to relate the specific fatty acid to the *sn-1* or *sn-2* positions on the glycerol backbone [150]. Note that the methods described above also required the availability of well characterized lipid standards and fatty acid standards for the comparison. The definitive structural identification of an unknown lipid requires ^{1}H-NMR and ^{13}C-NMR structural analysis following lipid purification using TLC, and scraping the specific bands off the plate and re-extraction.

The traditional methods of analysis often show the quantification of each general type of lipid and the quantification of overall fatty acyl chain composition separately. In ^{31}P-NMR, the chemical shift of phosphorus is dependent on its chemical environment and is found to differ between the general types of phospholipids. It is non-destructive, and theoretically quantitative based on the intensity of each peak, but the ^{31}P-NMR of the biological samples takes a long resonance time, and requires a relatively large lipid sample size (eg. 2 mg -100 mg lipids) [89,151] in order to obtain useful spectra. To make it more complicated, multiple peaks are often observed to be generated from each type of

lipid, which are variable, and dependent on the concentration of the lipid. The most sensitive and reliable way to quantify the lipids is to use the metabolic radioactive labeling methods by incorporating ^{14}C-acetate or ^{14}C-labeled head group precursors in the growth media, and comparing the radioactivity of the corresponding bands after TLC separation. However, this method is time-consuming and expensive, and the reading of the quantification is still restricted by the resolution of the TLC separation.

The traditional methods have been extensively applied for lipid analysis in past decades. However, they take a long time with multiple steps, risk oxidation due to a lengthy exposure in air, have relatively lower sensitivity, and require a large sample size. Modern mass spectrometry based methods can overcome all of these problems.

2.4 Mass Spectrometry

Mass spectrometry is emerging as a powerful tool for large scale lipid analysis, both in extensive identification based on detailed structural characterization, and in quantification of molecular species, with little or no requirement for pre-analysis lipid extraction or the separation of the lipid extracts. Mass spectrometry can not only be applied to quickly confirm the structure of complicated lipids, which were previously very difficult to analyze, such as lipid A, but most importantly, it can be used to independently elucidate the total chemical structures of lipids (including novel lipids), which are essential in understanding the structural/functional interactions of lipids with membrane proteins, but are typically difficult, if not impossible, to be obtained from other methods at high sensitivity.

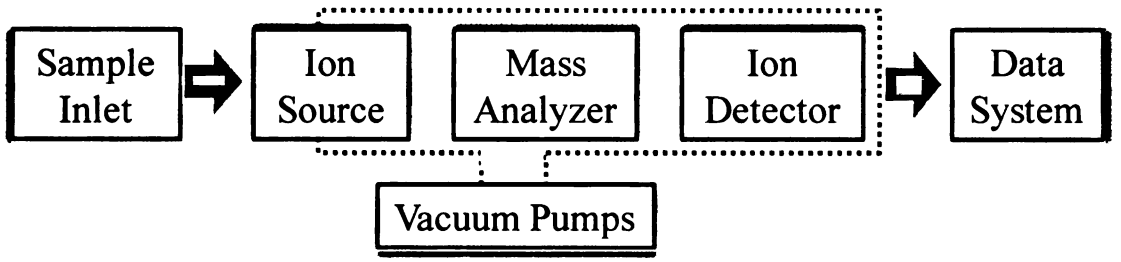


Figure 2.1 Schematic showing the general operation of a mass spectrometer

The operation of a mass spectrometer (Figure 2.1) includes: 1) creation of gas-phase ions, 2) separation of the ions in space or time by their mass-to-charge ratio (m/z), 3) fragmentation of ions at a selected m/z to obtain structural information (optional), and 4) measurement of the quantity of ions at each m/z.

2.4.1 Ion source

Mass spectrometry measures the mass to charge ratio (m/z, often used in the unit of Da), and the analyte can be converted into a charged form through various methods in the ionization stage. In addition to the earlier fast atom bombardment (FAB) [102] and chemical ionization (CI) [100,101], the softer and more biomolecule-amenable electrospray ionization (ESI) [110,117], matrix-assisted laser desorption/ionization (MALDI) [115], and more recently desorption electrospray ionization (DESI) [112] are finding increasingly important applications in the fast, sensitive, accurate and direct analysis of biomolecules, including lipids, present in different sample states.

2.4.1.1 MALDI

MALDI includes a laser source (typically UV) and UV-absorbing small organic molecules as the matrix to form co-crystals with the analyte deposited on a sample plate surface. Upon UV laser radiation, the matrix molecules absorb the UV light and form a plume of ions and neutrals, meanwhile desorbing and ionizing the analyte molecules, likely through gas-phase proton transfer [152,153]. Acidic matrices are therefore often chosen with the intention to increase the formation of positive ions [101,115]; however, negative ions are also formed during the MALDI process, even under highly acidic pH conditions [118] (see also Chapters 9 and 10). The ions formed by MALDI are generally singly charged [154]. The ions are then separated and analyzed by an appropriate electric field or magnetic field in the mass analyzer. The matrix can be deposited using solution based or non-solution based methods [122,155]. In the solution based method, due to the difference in solubility, the various components in the mixture are likely to form heterogeneous distributions in the co-crystals. Obtaining more homogenous sample spots requires empirical optimization of the concentration and the matrix solvent compositions.

2.4.1.2 ESI

Electrospray ionization was first applied by Fenn et al. in 1989 in mass spectrometers, where ions of the analytes are formed by spraying the sample solution under an electric field [156-158]. The charge residue model (CRM) [159] and the ion evaporation model (IEM) [160,161] have been proposed to explain the mechanism of ESI, suggesting that the ions are formed by generating small charged droplets through Coulombic fission, and by continuous evaporation of the droplet solvent, respectively.

The ESI process involves very little internal energy transfer and is shown to be the softest ionization technique that is amenable for the analysis of large labile biomolecules, such as lipids. By using a lower flow rate, down to tens of nanoliters per minute, nanoelectrospray ionization (nanoESI) can have a higher sensitivity with less contamination, partially due to a higher desolvation efficiency compared to conventional ESI [162].

While a pulse-type ion source such as MALDI is sensitive to the total number of ions generated in each pulse of laser ablation, the signal abundance in ESI is sensitive to the concentration of the sample ions which are generated in a continuous flow.

2.4.1.3 Direct imaging coupled with MALDI and DESI

DESI employs a stream of charged solvent to spray on the sample to desorb and ionize the surface molecules for analysis [163]. Both MALDI and DESI can be used to directly analyze solid-phase samples without solubilization, and have been recently applied in the molecular imaging of tissue slices for the distribution of lipids, proteins or metabolites [121-125,163,164].

2.4.1.4 Factors affecting the ionization of lipids

The ionization of lipids in ESI is highly dependent on the structure of the lipids. In addition, several general factors contribute to their ionization characteristics, including the solvent composition, the pH value of the solution, the presence of additives such as acids, bases and ammonium salts, and the presence of other cations or anions [165]. Based on the ion evaporation model of ESI, the gas-phase charge state should be largely

dependent on the ionization of the lipids in the solution, but the solution pKa values are shown to be insufficient to explain the formation of protonated or deprotonated ions observed in the positive or negative ion mode [166]. The addition of low concentrations of ammonium salt or ammonium hydroxide could enhance ion formation of lipids in both positive and negative ion modes [134]. Alkali ions such as lithium and sodium, and anions such as chloride and acetate can easily form non-covalent adduct ions with lipids [165], and are intentionally added to generate adduct ions from non-polar lipids, such as triacylglycerides and cholesterols [167], for more sensitive analysis.

In MALDI, the ionization efficiencies of different types of lipids are strongly dependent on the matrix selection, due to mechanisms that are not explained by comparison of pKa values [166]. Modulation of the matrix pH might affect the conformational changes of the sample molecules during the MALDI co-crystal formation, but typically does not appreciably enhance ionization efficiency. Instead, a change in the surface pH of the co-crystals can dramatically affect the ionization efficiency (previous findings not included in this dissertation). MALDI often induces prompt or fast fragmentations of the lipids in the source to a different extent [168], depending on the lipid structure and the matrix, and it has been found that GPEtn is the most labile type of phospholipid, and α-cyano-4-hydroxycinnamic acid (CHCA) is the most "hot" matrix that induces the most extensive in-source decomposition (previous findings not included in this dissertation). Since salts often end up being concentrated on the surface of the MALDI sample spots, due to the relatively larger solubility in aqueous solution, salt contamination significantly decreases the efficiency of forming protonated or deprotonated ions, and often causes the formation of adduct ions of lipids with

multiple alkali cations in both positive and negative ion modes (previous findings not included in this dissertation). A desalting step prior to analysis is often found to increase the ionization efficiency of lipids (previous findings not included in this dissertation), as well as peptides [169].

2.4.2 Mass analyzer

Mass analyzers measure the m/z values of the generated ions. The mass analyzers that are finding rapidly increasing applications in lipid analysis include: time of flight (TOF), triple quadrupole (QqQ), quadrupole ion traps (3-D Paul ion trap and 2-D linear ion trap), high-resolution Orbi-trap, and Fourier transform-ion cyclotron resonance (FT-ICR) mass analyzers.

2.4.2.1 Quadrupole mass analyzer

The quadrupole mass analyzer is composed of four hyperbolic-shaped rod electrodes assembled in pa $\Phi_0 = +(U - V\cos\omega t)$ rallel, and the combination of an alternating field radiofrequency (AC or RF) and a constant field (DC) voltage are imposed on the electrodes to form a quadrupole electric field. The stability and movement of ions in the quadrupole electric field are described by the solutions of the Mathieu equations [170] as discussed below.

The combined potentials applied on the opposite sets of electrodes are

$$\Phi_0 = +(U - V\cos\omega t) \qquad (1)$$

$$-\Phi_0 = -(U - V\cos\omega t) \qquad (2)$$

where U is the amplitude of the DC potential, V is the amplitude of the AC potential, ω is the angular velocity of the AC potential (equal to 2πυ, υ being the frequency), and t is time. The overall field potential Φ in the quadrupole is thus

$$\Phi_{x,y} = \Phi_0(x^2 - y^2)/r_0^2 = \frac{(x^2 - y^2)(U - V\cos\omega t)}{r_0^2} \qquad (3)$$

where x and y define the position from the center of the rods, and r_0 is the distance from the center of the space to the electrode.

The movement of an ion (m/z) in x and y dimensions as a result of the force experienced by the ion in the electric field is therefore:-

$$F_x = ma_x = m\frac{d^2x}{dt^2} = -ze\frac{\partial\Phi}{\partial x} \qquad (4)$$

$$F_y = ma_y = m\frac{d^2y}{dt^2} = -ze\frac{\partial\Phi}{\partial y} \qquad (5)$$

Substitution and rearrangement lead to the equations of motion that establish the relationship between the space coordinates of the ion and time, under the stability boundary conditions of $x < r_0$ and $y < r_0$.

$$\frac{d^2x}{dt^2} + \frac{2ze}{mr_0^2}(U - V\cos\omega t)x = 0 \qquad (6)$$

$$\frac{d^2y}{dt^2} - \frac{2ze}{mr_0^2}(U - V\cos\omega t)y = 0 \qquad (7)$$

They are similar to the equation solved by Mathieu in 1866 [170],

$$\frac{d^2u}{d\xi^2} + (a_u - 2q_u\cos 2\xi)u = 0 \qquad (8)$$

Therefore equations 6 and 7 can be described in the form of Mathieu equation, when

$$\xi = \frac{\omega t}{2} \qquad (9)$$

$$a_u = a_x = -a_y = \frac{8zeU}{m\omega^2 r_0^2} \qquad (10)$$

$$q_u = q_x = -q_y = \frac{4zeV}{m\omega^2 r_0^2} \qquad (11)$$

Parameter ξ is dimensionless, and a_u and q_u are dimensionless and known as the trapping parameters. Rearrangement of equations 10 and 11 leads to:-

$$U = a_u \frac{m\omega^2 r_0^2}{8ze} \qquad (12)$$

$$V = q_u \frac{m\omega^2 r_0^2}{4ze} \qquad (13)$$

which define the stability of the ion in the quadrupole field. The stability areas can be represented by a triangular area in an a_u-q_u diagram, or similarly a U-V diagram illustrated in Figure 2.2. Obviously, now the ability of an m/z to stably pass through the quadrupole without hitting the boundaries depends on the values of r_0, U, V and ω. Both r_0 and ω are typically fixed for a given instrument geometry. The stability of the ion is thus manipulated through suitable choices of U and V. U and V are the actual operating parameters for the quadrupole mass analyzer.

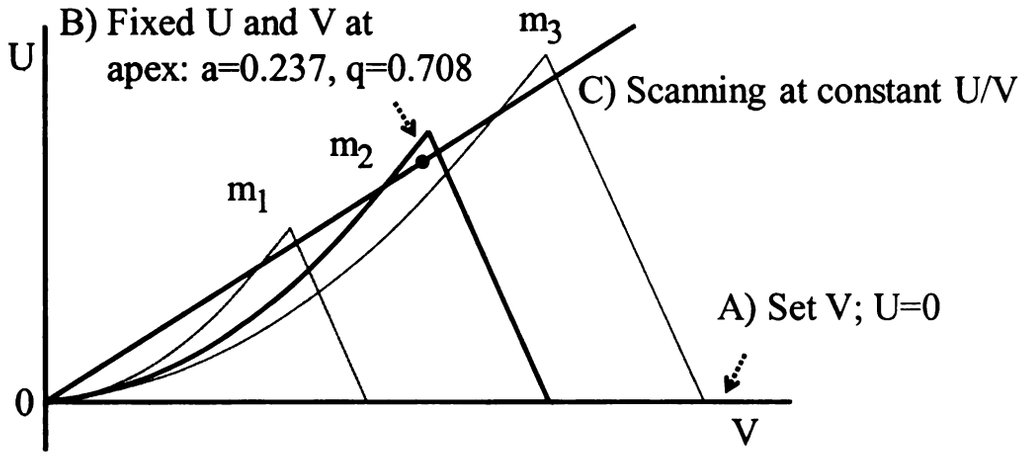


Figure 2.2 Stability of ions at different m/z as a function of U (DC) and V (RF) amplitudes in the quadrupole electric field, and the three operation modes under different applications of U and V ($m_1 < m_2 < m_3$) (adapted from [171]).

The quadrupole can operate in three major modes by setting U and V at different values, according to the stability diagram (Figure 2.2).

1) Operation as a high pass filter for ion transmission by setting U at zero and keeping V static (Figure 2.2A). All the ions with m/z higher than that corresponding to the lowest applicable V are stably transmitted and ions with lower m/z are lost.
2) Operation as a mass selective device by applying U and V at fixed amplitudes that put the given m/z at the apex of the stability diagram, at a=0.237 and q=0.708 (Figure 2.2B). Ions with all the other m/z are not stable and lost.
3) Operation as a mass analyzer by scanning U and V increasingly, while keeping the ratio of their amplitudes constant (Figure 2.2C). Stable trajectories can be obtained for ions with increasing m/z, and the ions are then sequentially mass

analyzed. The higher the U/V ratio of the operation line, the higher the mass resolution, since fewer m/z stability areas can overlap in the smaller area above the operating line. Ions that can stably pass through the mass analyzer are sequentially transferred to the next stage of ion manipulation or to the detector for ion abundance measurement.

2.4.2.2 CID MS/MS in triple quadrupole mass spectrometer

The triple quadrupole mass spectrometer is designed as three quadrupoles connected in series. Quadrupoles Q1 and Q3 are both supplied with DC and RF and can function as mass analyzers, whereas q2 has only RF and can confine a bath gas, thus it has no mass analyzing function but can act to focus the ions and serve as a reaction cell. Simple MS can be obtained by setting Q1 at mass analyzer operation mode, and both q2 and Q3 at high pass filter operation mode as described earlier. Tandem mass spectrometry (MS/MS) is achieved by setting quadrupoles Q1, q2 and Q3 at different combinations of operation modes, because in a triple quadrupole mass spectrometer MS/MS has to be "tandem in space", and a discrete mass analyzer is responsible for each stage of mass spectrometry.

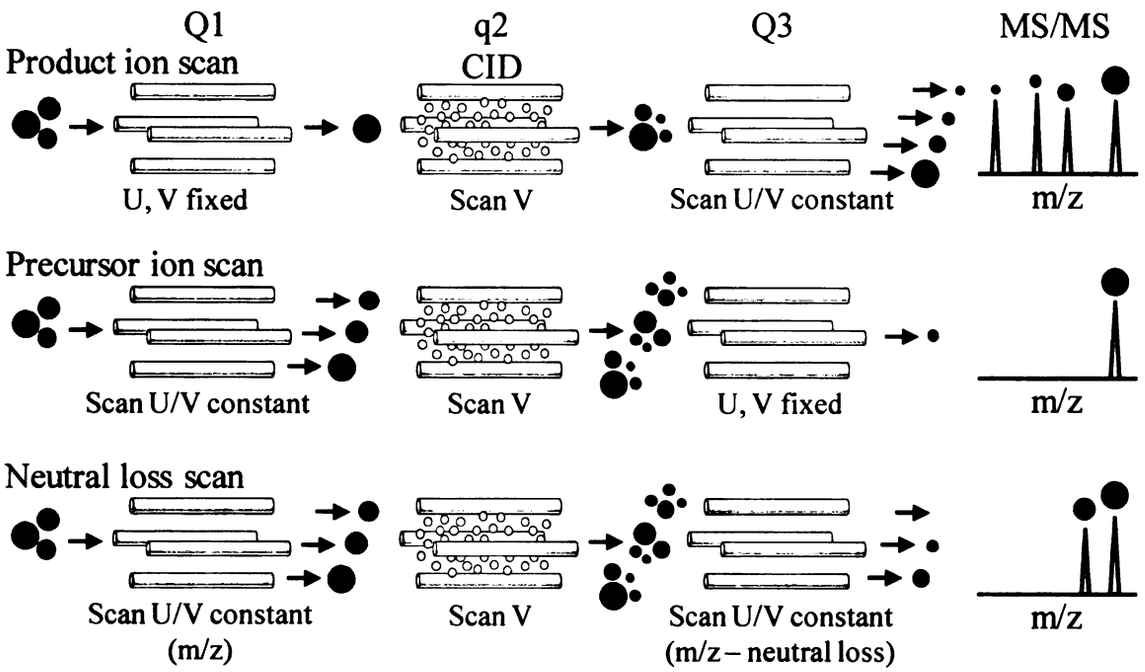


Figure 2.3 Three types of CID MS/MS scans typically applied in a triple quadrupole mass spectrometer: product ion scan, precursor ion scan and neutral loss scan.

In MS/MS, q2 is used as a collision cell for the collision-induced dissociation (CID) and is typically filled with Ar, and an offset DC voltage is applied to increase the kinetic energy of the ions for efficient CID dissociation, whereas Q1 and Q3 are set at different combinations of the operation modes. The three types of typically useful MS/MS scans, namely, the product ion scan, the precursor ion scan, and the neutral loss scan, are illustrated in Figure 2.3. In the product ion scan mode (the most common type of MS/MS), Q1 operates as a mass selective device, and selects only the precursor ions with the m/z of choice to pass to q2 for CID fragmentation, and then Q3 operates as a mass analyzer of the product ions. In the precursor ion scan, Q1 acts as a mass analyzer and scans all the precursor ions, while Q3 acts as a mass selective device and passes only

a given m/z product ion for detection, such that the resultant MS/MS shows all the precursor ions that give rise to the product ion at the given m/z. The x axis shows the m/z of the precursor ions, and the y axis displays the corresponding abundance of the given product ion. In the neutral loss scan, Q1 and Q3 act as coupled mass analyzers, and are scanned concomitantly with a constant offset of m/z between them, which corresponds to the given neutral loss, and all the precursor ions that fragment via the same neutral loss are displayed in the MS/MS spectrum.

Since the CID fragmentations of lipids are characteristic of the chemical structures of the lipid type, and often generate "fingerprint" product ions or neutral losses, the precursor ion scan and neutral loss scans are particularly useful in sorting out the molecular species of a specific lipid type from mixtures of complex lipid extracts as a way of "purification" and identification at improved sensitivity, and relative quantification between the molecular species of the same lipid type.

The configuration of the "triple" quadrupoles allows only tandem MS/MS to be performed. However, since the fragment ions are further reactivated by collision with the bath gas upon formation, the product ions observed often result from the combination of primary and secondary fragmentation reactions. The extent of CID MS/MS fragmentation in triple quadrupoles is a function of the pressure of bath gas and the collision energy (DC offset) applied in q2 with a given type of gas (Ar). The low mass limit in MS/MS is imposed by the minimally applicable RF amplitude, and is typically set at m/z 50 Da, but it is usually not a limitation issue for lipid analysis, because most lipid fingerprint fragment ions are observed at m/z values higher than 50 Da.

2.4.2.3 Quadrupole ion trap

A quadrupole ion trap is essentially a quadrupole in 3-D, but in contrast to a quadrupole, it achieves the quadrupole electric field through the configuration of a hyperbolic ring electrode and a pair of hyperbolic end caps with central holes for ion passage, and forms a 3-D trapping volume for the ions. Only a drive RF (0-20 kV, at secular frequency of ω) applied to the ring electrode is required to form the quadrupole electric field, while an additional low-amplitude variable-frequency supplementary RF (0-300 V) is applied to the end cap electrodes to facilitate ion manipulations. Therefore the ions in the quadrupole ion trap operate along the line of $a_u = U = 0$ in the stability diagram (Figure 2.4) according to the Mathieu equation. The solution of the Mathieu equation for the "ideal" ion trap ($r_0^2 = 2z_0^2$, r_0 and z_0 being the radial and axial distances from the center of the trapping volume to the end caps and the ring electrode, respectively) then becomes:-

$$q_u = \frac{4zeV}{mr_0^2\omega^2} \qquad (14)$$

In practice, the ion trap geometry is stretched (z_0 is stretched by 57% in quadrupole ion traps of Model LCQ manufactured by Thermo Fisher Scientific, San Jose, CA) to overcome the mass shift due to a finite field, thus Equation 14 turns to:-

$$q_u = -2q_r = \frac{8zeV}{m(r_0^2 + 2z_0^2)\omega^2} \qquad (15)$$

This is the equation that governs the motion for ions in a practical ion trap, and allows the determination of the ion stability parameters for ion storage, the ion frequencies for ion manipulation, the ion energetics for ion activation, and the ion storage capacity for

dynamic range. Since r_0, z_0 and ω are constant for a given instrument, V is the operating factor that controls the q value, hence the stability, of ions at a particular m/z in the ion trap (Figure 2.4). Equation 15 indicates that q is proportional to V for a given m/z, and inversely proportional to m/z for a given V. Ions at a particular m/z move at their own characteristic secular frequency under given V and q values. Note that equation 15 also applies to the supplementary RF.

The efficiency of ion trapping is represented by the Dehmelt pseudo well potential (D, in the unit of eV) which is a function of the q value (Equation 16). The potential well depth D decides the amount of kinetic energy that an ion may acquire through resonant excitation, before being destabilized and ejected from the trap.

$$D = \frac{qV}{8} \qquad (16)$$

The fundamental axial secular frequency for an ion at a given m/z in the trap is determined by Equation 17, where Ω is the main drive frequency, and β is the boundary value approximately determined by q as shown in Equation 18.

$$\omega = \frac{\beta\Omega}{2} \qquad (17)$$

$$\beta = \sqrt{q^2/2} \qquad (18)$$

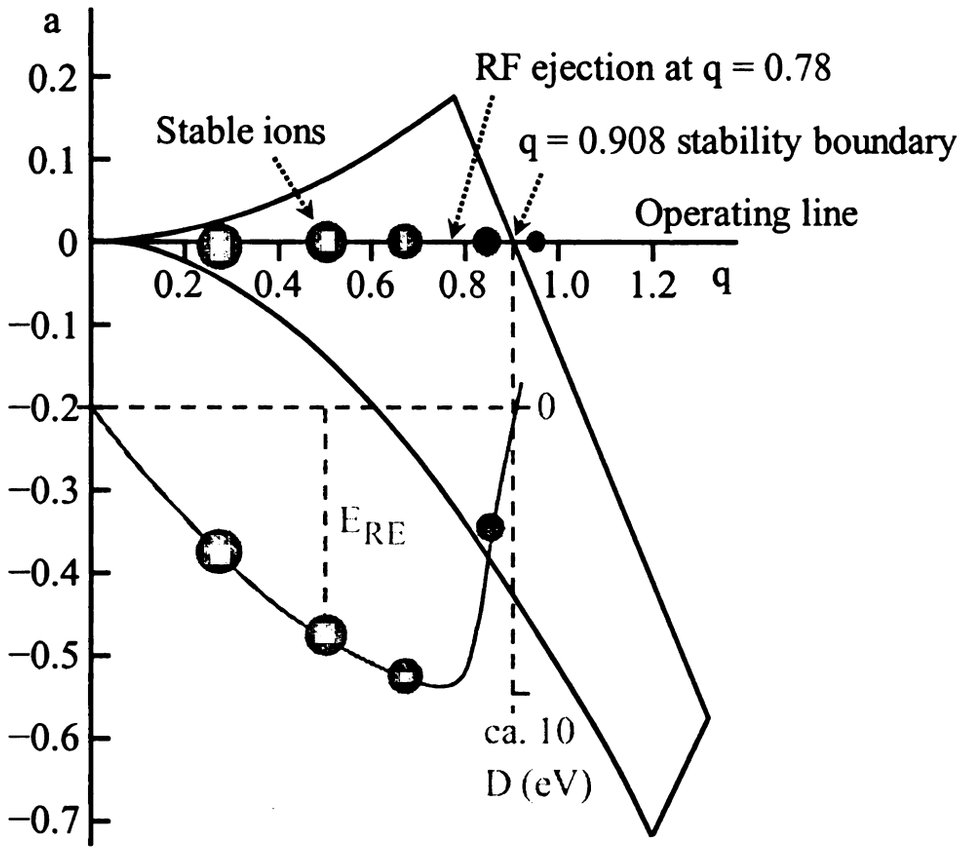


Figure 2.4 Stability diagram of ions of different m/z in the 3-D quadrupole ion trap (upper graph), and the trapping efficiency represented by the Dehmelt potential (D) in eV (lower graph, right axis) as a function of the q value. The balls of increasing size represent ions with increasing m/z. E_{RE} represents the energy required to destabilize and eject the ions (adapted from [171]).

2.4.2.4 MS/MS and MS^n in quadrupole ion trap

Tandem mass spectrometry MS/MS and MS^n in quadrupole ion trap is "tandem-in-time", and is achieved in the same trap space by operating at different modes as a

function of time (Figure 2.5). Successive multistage fragmentation can be carried out similarly to obtain MS^n spectra.

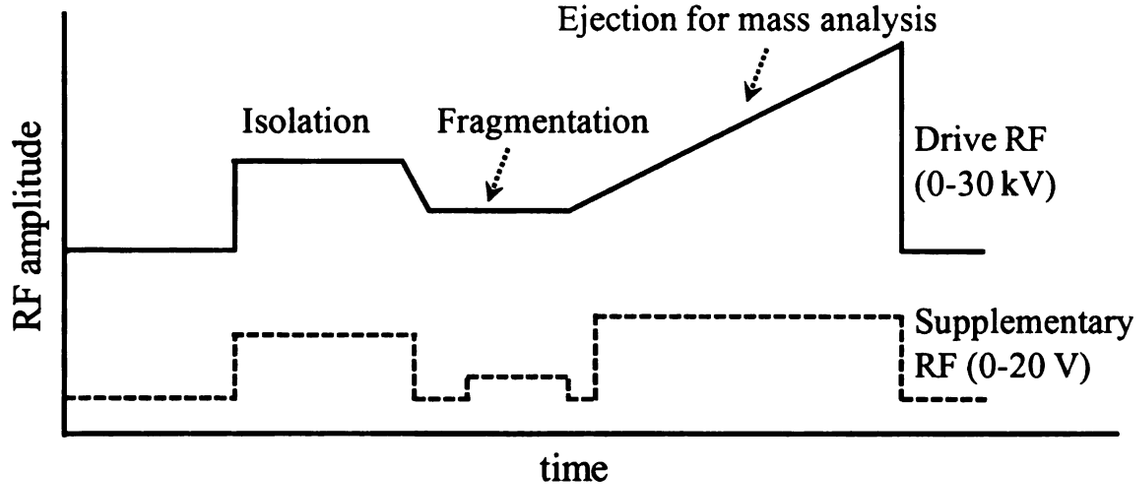


Figure 2.5 Operation modes of quadrupole ion trap as a function of the drive RF and supplementary RF amplitudes in an MS/MS example (adapted from [172]).

Ion motions in the ion trap are controlled by the settings of the drive RF and the supplementary RF. Based on the ion motions, the quadrupole ion trap can be operated in the following modes:

1) Trapping ions in the trap. Ions injected into the ion trap above a certain m/z value determined by the applied drive RF amplitude (corresponding to q = 0.908 stability limit), have stable trajectories (Figure 2.4 and Equation 15) and can be stored in the trap. Collision with the bath gas He (typically at 10^{-3} torr) removes excessive dynamic energy from the ions, dampens their trajectories, and helps to focus them into the center of the trap for more efficient trapping.

2) Isolation of the precursor ions. Among the variety of methods to isolate ions, the frequency notch isolation is adopted by the ion traps manufactured by Thermo Fisher Scientific. The drive RF amplitude is at first increased to move the ions of interest close to q = 0.78, then the supplementary RF containing the combination of a number of frequencies, except for the frequencies around the m/z of interest, is applied, so that all of the ions, other than the ions at the m/z of interest, are resonantly ejected out of the trap.

3) Fragmentation of isolated precursor ions. Selective resonant activation is often employed to fragment the precursor ions. A low-amplitude supplementary RF at the secular frequency of the precursor ions of interest is superimposed to increase the kinetic energy for the ions to energetically collide with the bath gas (He), resulting in internal energy deposition, and subsequent fragmentation The resultant product ions are cooled by colliding with the bath gas upon formation, and prevented from further dissociation, because their m/z values, and thus the secular frequencies, are now different from that of the precursor ion. Such CID dissociation in an ion trap is a slow-heating thermal, rather than dynamic, process in nature, and results in a Boltzman, or truncated Boltzman, energy distribution of ions prior to dissociation [173], which makes the lowest energy dissociation pathways dominate the fragmentation, and the tandem mass spectra easier to predict. Without the resonant excitation, collision of the ions with the bath gas (He) alone is not sufficient to cause the ions to fragment within a short time span.

4) Ejection of ions for mass analysis. For mass analysis, while the supplementary RF is applied at a certain amplitude and frequency, the amplitude of the drive RF is

increased to sequentially bring ions of increasing m/z into resonance with the supplementary RF (typically at q = 0.78), such that the rapid increase in kinetic energy due to resonance ejects the ions from the trap and sends them to the detector for ion abundance measurement (Figures 2.4 and 2.5). This is also how a MS spectrum is obtained. The boundary ejection at q=0.908 stability limit is not practically used, due to lower ion transfer efficiency.

Since the slow-heating mechanism for low energy CID fragmentation in quadrupole ion trap typically results in product ions formed from a single fragmentation with the lowest level of energy requirement [173], the product ions from multiple stages of fragmentation are typically not observed unless further MS^n is applied. The bath gas (He) pressure is usually set constant at 10^{-3} torr, and the percentage relative abundance of various product ions is not sensitive to the normalized collision energy applied in the ion trap once the fragmentation occurs. Such an instrumental property makes the MS/MS and MS^n spectra of lipids acquired from the quadrupole ion trap highly reproducible and informative in the study of lipids gas-phase fragmentation mechanisms, as well as for tandem mass spectrometry-based identification and quantification analysis.

However, a quadrupole ion trap has a limited product ion m/z range, originating from how the CID fragmentation is carried out. The lowest m/z limit for mass analysis, termed the low mass cut-off (LMCO) is a percentage of the precursor ion m/z, determined by the ratio of the activation q (typically 0.25) at which the precursor ion is activated over the stability boundary q (0.908), according to Equation 15 and Figure 2.4.

The activation q can be decreased to push the LMCO lower, but the lower the q, the shallower the potential well (Figure 2.4 and Equation 16), and more ions will become less stable and get lost during the activation. In lipid analysis, the precursor ions are often singly or doubly charged in the range of m/z 600-900. For example, when m/z 700 is activated at q=0.25, the LMCO is m/z 193. This is usually too high to detect most of the signature MS/MS fragment ions of the lipids. Decreasing activation q to 0.20, LMCO is then m/z 154, allowing some of the lipid head group fragment ions to be detected, but in combination with the slow-heating dissociation mechanism in the ion trap, considering the complicated compositions of a lipid mixture, it is often necessary to go to MS^n for further structural confirmation of the molecular species of the lipids in the mixture.

Another limitation in an ion trap is the space charge effect arising from the Coulombic repulsion between ions with the same charge type occupying the same space, making it necessary to limit the number of ions in the trap. Automatic gain control (AGC) is thus applied to control the number of ions in the trap and prevent the occurrence of the space charge effect, by incorporating a testing pre-scan, and then adjusting the ion injection parameters accordingly.

Nonetheless, the quadrupole ion trap mass spectrometer is marked with the versatility of carrying out gas-phase ion manipulations, including MS^n (typically n = 2 to 12), high MS/MS efficiency (50-95%) due to the continuous and mass selective activation of the precursor ions, rapid analysis (up to 13,000 Da/sec) and femtomole limits of detection, and is therefore particularly powerful in the identification and quantification of lipids in complex mixtures without previous separation. In addition to

the original 3-D Paul ion trap, the 2-D linear quadrupole ion trap has also been recently developed with much higher sensitivity and ion efficiency [170].

2.4.2.5 Factors affecting lipid analysis results using quadrupole ion trap

Several operating parameters of tandem MS directly affect the results of lipid analysis. Scanning the RF at a slower rate increases the resolution, but prolongs the analysis time. In the linear ion trap LTQ (Thermo Fisher Scientific), the enhanced scan mode is typically sufficient to obtain unit resolution of the lipid peaks, which are mainly singly or doubly charged, whereas the zoom and ultra-zoom scans take too long for the ESI lipid analysis, but their resolutions are still insufficient to resolve the overlapping species, which often differ only by a few hundredths of one Da.

The increase in the activation q value increases the trapping efficiency, represented by the pseudo-potential well depth, but also raises low-mass-cut-off, disabling detection of the signature lower mass fragment ions often observed. Typically an activation q of 0.20-0.25 enables both efficient trapping and the detection of common fragment ions from lipid head groups.

The longer the activation time, the more energy the precursor ions can receive in order to fragment, and 30 msec is applicable for most lipids ions, but it can be raised to potentially increase fragmentation efficiency.

Automatic gain control was adopted to control the number of ions in the trap, in order to prevent the space charge effects, which can skew m/z detection and quantitative properties and decrease resolution. The target number limits the number of ions stored in the trap before they are ejected, and for the enhanced scan mode in lipid analysis using an

ESI source, it is typically 1e4 for MS, and 3e4 for MS/MS in a Thermo linear ion trap. Maximum injection time defines the time allowed for the product ions to fill the trap before they are ejected for detection. Usually, a higher maximum injection time can significantly improve the detected tandem MS spectra of lower abundance precursor ions and less stable fragmentations. It works closely with the target number setting, and is particularly important when MS/MS is used for quantification analysis. If the maximum injection time is "maxed out" before the target number is reached, then the conversion algorithm of the ion abundance is different, and the resultant MS/MS spectrum cannot be directly used for a quantitative comparison.

The precursor ion scan and neutral loss scan MS/MS spectra results are similar to those from the triple quadrupole mass spectrometer but are obtained through different operation mechanisms, and can be obtained from the ion traps by incorporating specific data processing in the "ion mapping" options of the Thermo instruments.

2.4.2.6 Other dissociation methods in the quadrupole ion trap

The ion trapping function of a quadrupole ion trap allows a number of gas-phase reactions to be applied to the trapped ions in such a "reactor," including the fragmentation reactions, through several approaches. In addition to CID, selected precursor ions can also be fragmented or manipulated in the quadrupole ion trap using methods such as collision with a reactive gas (such as ozone or D_2O) [174,175], a laser beam (laser induced dissociation) [171] and potentially an electron beam (electron induced dissociation) [171], and electron transfer dissociation (ETD) [176].

The recent pulsed-Q dissociation (PQD) method was developed [177] to address the low mass cut-off issue in CID fragmentation by quickly activating the ions at q = 0.75, and the LMCO can be extended down to m/z 30 for lipid precursor ions. Although the trapping and fragmentation efficiency are often low and more sensitive to the collision energy choice, and higher energy fragmentation channels are potentially introduced, it can be a supplement to lipid CID analysis for quick low-mass fingerprint ion identification in MS/MS.

ETD, which can keep the post-translational modifications of peptides intact while inducing fragmentations at sites different from those of CID dissociation [176], has also been recently applied to sodium adducts of GPCho lipid standards in order to investigate the fragmentation characteristics [178].

2.4.2.7 Other mass (m/z) analyzers

In addition to triple quadrupole and quadrupole ion trap mass analyzers, medium to high resolution mass analyzers such as TOF, and high resolution mass analyzers such as FT-ICR and Orbi-trap, have also been applied in lipid identification by relying on the accurate measurement of m/z at high resolution in MS [179]. FT-ICR can carry out tandem-in-time MS/MS by incorporating CID, whereas TOF and Orbi-trap are restricted to only one stage of mass measurement, and tandem MS/MS can only be achieved in-space through coupling with a quadrupole ion trap (LIT-Orbi-trap), or a TOF (TOF-TOF) mass spectrometer.

2.4.3 Ion detection

Ion detectors measure the abundance of ions ejected at different m/z. Most of the modern mass spectrometers use an electron multiplier for the detection of ion abundance. For the negative ion mode, negative ions are at first converted to positive ions and then measured with the same instrument.

2.5 Tools to unravel the mechanisms of MS^n fragmentation of lipids

The fragmentation of lipids depends on the structure, polarity, charge state, and charge distribution of the lipid ions. Understanding how the lipids fragment is of essential importance to the application of determining the different types of lipids by tandem mass spectrometry (see Chapter 1 for lipid structures).

Because of their molecular composition and ionization characteristics, most lipids present in cell membranes fall in the narrow range between m/z 600 and 1600 resulting in significant overlapping of peaks in MS, and they are particularly crowded in the m/z 600-900 region. These regions are further complicated by the various cationic or anionic adducts formed by the lipids. Simply matching the m/z of the MS peaks with the calculated masses of possible lipids can lead to significant ambiguity, even with high resolution analyzers. In MS/MS or further MS^n, the precursor ions formed from different lipids, which fragment characteristically according to the individual lipid's molecular structure, makes possible the unambiguous identification of each lipid species, particularly those that overlap at the same m/z value. Tandem mass spectrometry is not only essential for lipid identification, but is also very useful in improving the sensitivity

and accuracy of lipid quantification using complex un-separated lipid mixtures at a minimum sample amount, by eliminating the interference from chemical noise in MS. It is therefore of pivotal importance to gain a solid understanding of the fragmentation process of lipids, and what factors might affect their fragmentation behavior.

However, the knowledge of gas-phase lipid fragmentation behavior in modern mass spectrometers is so far relatively limited compared to that of peptides. 'Soft' ionization sources such as MALDI and ESI can generate abundant intact lipid precursor ions, and in combination with low-energy CID MS/MS and MS^n, they provide powerful tools for probing the gas-phase behavior of lipid ions. Several tools that have been successfully applied in unraveling the gas-phase behavior of amino acid and peptide ions can also be applied to studying lipid ions.

2.5.1 Probing fragmentation mechanisms and product ion structures using MS/MS and MS^n experiments

Tandem mass spectrometry, particularly low-energy CID MS/MS in the triple quadrupole, and CID MS/MS and MS^n in the quadrupole ion trap, can not only provide signature fragmentation spectra of the precursor ions, but also construct a fragmentation tree to trace the origin of each of the product ions, either through the use of collision-energy-resolved CID MS/MS product ion abundance plots to reveal the first and second-generation product ions (triple quadrupole), or through sequential MS^n spectra (quadrupole ion trap). The structural identity of the product ions can be established by

further MS^n analysis and by comparison with the MS/MS fragmentation of independently synthesized target structures or structural analogs of the products.

2.5.2 Structural labeling

Elucidation of the mechanisms of fragmentation usually requires a revelation of the specific functional group or atoms involved in the fragmentation reactions. Chemical modification of a key functional group would significantly affect the fragmentation reaction channels, by shutting down the previous reaction, and sometimes by opening up new routes and generating new product ions. Typical chemical modification strategies include covalent methylation, acetylation or propylation of the hydroxyl, carboxyl or amino groups, to alter the nucleophilic propensity and eliminate the availability of the acidic OH or NH protons (Chapter 5). Guanidine modification which has been applied to peptides [180,181] can also be applied to switch the charge state propensity of lipids.

2.5.3 Isotopic labeling

Mobile proton transfer and deprotonation have been increasingly discovered to be critical steps in the gas-phase fragmentation of peptides and lipids using the slow-heating low-energy CID dissociation in positive or negative ion mode [182,183]. The involvement of protons at different locations can lead to different fragmentation channels. Isotopic labeling is an efficient way to locate the protons involved in these reactions. Typically solution-phase deuterium/ hydrogen exchange (CH_3OD or D_2O) is employed to label conventional active hydrogens such as those on OH and NH functional groups [184]. Gas-phase deuterium/hydrogen exchange in the trap, by introducing D_2O into the

bath gas at a certain pressure, has also been explored for amino acids ions [174]. However, since scrambling reactions can happen at a time-scale faster than that of ion dissociation via CID within the ion trap or quadrupole, caution has to be taken while interpreting the observed product ion spectra. On the other hand, unlike solution-phase reactions, transfers of non-exchangeable protons are often found to be actively involved in the gas-phase fragmentation of lipids, and these protons can be identified by labeling through synthetic incorporation [185]. Other stable isotopic labeling such as ^{13}C, ^{15}N, and ^{18}O labeling can also be potentially applied to elucidate the behavior of specific functional groups in the fragmentation reaction of lipids.

2.5.4 Computation and theoretical modeling

Ab initio calculation is a complementary tool to MS^n and labeling experiments, in order to gain insights into the most energy-favored reaction pathways by evaluating the energies of the potential structures of the reactants and products [186].

2.6 Fragmentation reactions of lipids

In the tandem mass spectrometry of lipids, a range of fragmentation channels can be observed, depending on the structure, polarity and charge state of the individual lipid precursor ions. For example, the characteristic CID fragmentation pathways of GPCho lipids in positive ion mode is the formation of m/z 184 corresponding to the phosphatidylcholine head group, but in negative ion mode GPCho lipids ionize by

forming non-covalent adduct ions with anions, and the fragmentation is highly dependent on the identity of the anions (see Chapter 4 for a detailed discussion). The phosphate-free non-glycerol-containing ornithine and glutamine lipids each produces different sets of head group specific fingerprint ions in CID MS/MS in both positive and negative ion modes (see Chapter 5 for detailed discussion).

The characteristic CID MS/MS fragmentations of the common types of phospholipids examined in recent studies have been comprehensively summarized in several reviews [117,187]. Therefore, only a brief summary on the key aspects of considerations in fragmentation mechanisms will be presented in this chapter.

2.6.1 Forms of lipids precursor ions

In ESI, most lipids form singly charged ions in positive and negative ion mode, in the form of protonated ions, deprotonated ions, non-covalent cationic adduct ions (alkali or ammonium), or anionic adduct ions. Multiple phosphate groups in the lipids can also lead to the formation of multiply charged negative ions. The observed ionization and charge state distribution of lipids are directly dependent on the lipid structures, spray voltage, instrument pressure and solvent desolvation conditions in the mass spectrometer, and play an important role in determining how the ion fragments in the subsequent MS/MS reactions. Although, due to the charge accumulation process in the droplets and charge modification through electrochemical process in the probe tip, the gas-phase ionization and charge state does not simply reflect the charge state in solution during ESI, the components in the solution such as an ammonium hydroxide additive, and various other cations and anions, significantly affect the charge state of the ions observed in the

gas phase (Chapter 4). However, ionization of lipids is not simply determined by the solution-phase pKa values, since negatively charged lipid ions can be observed at an ESI solution pH much lower than 7. Lipid ions generated by DESI were found to be very similar to those by ESI [112].

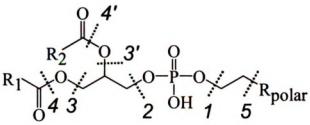
In MALDI, all of the lipids are observed as singly charged ions in positive or negative ion modes, including the protonated ions, alkali-adduct positive ions, and deprotonated ions, probably because the density of reactive species in MALDI can strip the multiple charges such that only the singly charged ions can survive.

2.6.2 Characteristic MS/MS fingerprints for lipid class identification

The most commonly observed characteristic MS/MS fragmentations of glycerophospholipids are summarized in Table 2.1 based on the major sites of cleavage shown in Scheme 2.1. It is clear that most cases of dissociation occur at the phosphatide bonds or acyl ester bonds, but due to differences in the charge state of the ion and the identity of the polar head group, the same moiety can be cleaved in different forms. For example, depending on the lipid type, in both positive and negative ion modes, the fatty acyl chains can be lost as a fatty acid or as a neutral ketene (equivalent to dehydrated fatty acid). In negative ion mode, it can also be cleaved as fatty acid anions.

It can also be seen from Table 2.1 that the formation of non-covalent adduct ions with an anion or cation, significantly change the fragmentation channels of the lipid ions. For instance, while the protonated GPCho is well characterized to fragment by forming the phosphatidylcholine head group ion at m/z 184, the adduction of GPCho by the sodium ion switches the reaction to result in the formation of the neutral loss of 59 Da

corresponding to trimethylamine, which is also highly characteristic to the head group [188].



Scheme 2.1

Table 2.1 Characteristic CID MS/MS fragmentations of lipids previously identified in the literature.

lipid type	positive ion	MS/MS neutral loss / product ion	bond cleavage*	reference	negative ion	MS/MS neutral loss / product ion	bond cleavage*	reference
GPA					$[M-H]^-$	m/z $RCOO^-$, NL RCOOH, m/z 153	*3, 3'* *3, 3'* *3+3'*	[189]
GPEtn	$[M+H]^+$	NL 141	*2*	[190]	$[M-H]^-$	m/z $RCOO^-$, NL RCOOH, m/z 153	*3, 3'* *3, 3'* *1+3+3'*	[190]
	$[M+Li]^+$	NL 147 (Li^+)	*2*	[191]				
	$[M+Na/K]^+$	NL 43	*5*					
	$[M-H+Ni]^+$	NL 123 (Ni^{2+})	*2*					

(Table 2.1 continued)

GPCho	$[M + H]^+$	m/z 184	*2*	[188]	$[M + Cl/Ac]^-$	NL CH3Cl/Ac (15+35/59), m/z 153	*5*	[185], Chapter 4
	$[M + Li]^+$	m/z 184	*2*				*1+3+3'*	
	$[M + 2Li]^+$							
	$[M + Na/K]^+$	NL 59	*5*					
SM	$[M + Na/K]^+$	NL 59	*5*	[192]	$[M + m.c.]^-$	multiple peaks		[185], Chapter 4
	$[M + H]^+$	m/z 184	*2*					
	$[M + Na/K]^+$	NL 59	*5*					
GPGro					$[M - H]^-$	$RCOO^-$, NL(RCOOH+glycerol), NL RCOOH, m/z 153	*3* *3'* *1+3, 1+3'* *1+3+3'*	[193]
CL	$[M + Na/K]^+$		*2* *3*	[194]	$[M - H]^-$	GPA-glycerol$^-$ (NL GPA) m/z 153		[195]
pPE	$[M + H]^+$	NL 18		[196]	$[M - H]^-$			
	$[M + Na/K]^+$							
GPSer	$[M + H]^+$	NL 185	*2*	[197]	$[M - H]^-$	NL 87 m/z 153	*1* *1+3+3'*	[197]
	$[M + Na/K]^+$	NL 88	*1*		$[M -2H +Na/K]^-$	NL 87	*1*	

(Table 2.1 continued)

GPIns					$[M - H]^-$	m/z 241 m/z 153	*2* *1+3+3'*	[198]
GPIns-P					$[M - 2H]^{2-}$	m/z 241 NL 98	*2*	[198]
SQDG					$[M - H]^-$	m/z 225 NL RCOOH	*2*	[108,199] Chapter 6
OL	$[M + H]^+$	NL H_2O NL (RCOOH+H_2O) NL RCOOH NL R'CH=C=O	*3* *4*	Chapter 5	$[M - H]^-$	NL R2COOH	*3, 3'*	
TG	$[M + Li]^+$ $[M + NH4]^+$		*3* *3'*	[200] [167]				
lysoGPCho	$[M + Na]^+$	(Na^+)	*1, 5*	[201]	$[M + Cl]^-$		*5*	[201]

* The numbers designate the sites of cleavage according to the illustration shown in Scheme 2.1.

2.6.3 Mechanistic aspects of the fragmentation of lipids in CID-MS/MS and MS^n

The final fragmentation product ion spectra are usually determined by the competition of several potential fragmentation pathways. Whether the fragmentation takes place via charge-driven or via charge-remote mechanisms is determined by the combination of several factors [202, 203]. Comparison of the fragmentation of phospholipids with that of the phosphate-free lipids indicated that the nucleophilic or negatively charged phosphate group plays a key role in dictating the fragmentation channels.

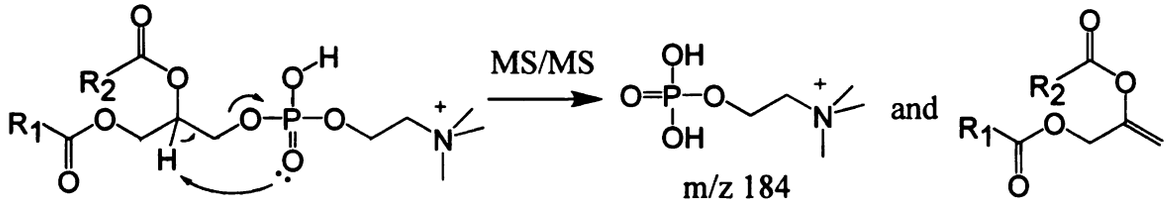
As an example to illustrate how the charged functional group and charge state could affect the fragmentation behavior of lipids in positive and negative ion modes, the introduction will focus on the GPEtn lipids [190], which can be detected in both ESI and MALDI (using appropriate matrix) both in positive and in negative ion modes, and are often the major components of membrane lipids and essential for some membrane proteins.

2.6.3.1 Charge state: positive *vs* negative

In ESI, GPEtn forms protonated ions that carry the positive charge at the amino group or carbonyl group in positive ion mode (note that amino protons can be mobile in the gas phase), and deprotonated ions that carry the negative charge at the phosphate group in negative ion mode. As shown in Table 2.1, in MS/MS the protonated GPEtn mainly fragments by losing the phosphatidylethanolamine head group as a neutral loss of 141 Da (cleavage site 2, Scheme 2.1 and Table 2.1), whereas deprotonated GPEtn

predominantly fragments by cleaving the fatty acid chains (cleavage sites 4 and 4', Scheme 2.1 and Table 2.1).

The fragmentation in positive ion mode is proposed to occur via nucleophilic attack on the *sn-2* proton initiated by the phosphate oxygen following a proton migration to put the positive charge on the carbonyl group of the fatty acid chains [117]. The contrast of GPEtn losing the head group as a neutral loss, to GPCho losing the head group as a positive product ion (Scheme 2.2), points to the key fact that GPCho head group has a fixed positive charge that cannot migrate. The comparison of GPEtn with GPCho suggests that the dissociation at site 2 is dominated by the nucleophilic phosphate group in positive ion mode, and appears independent of the positive charge site.

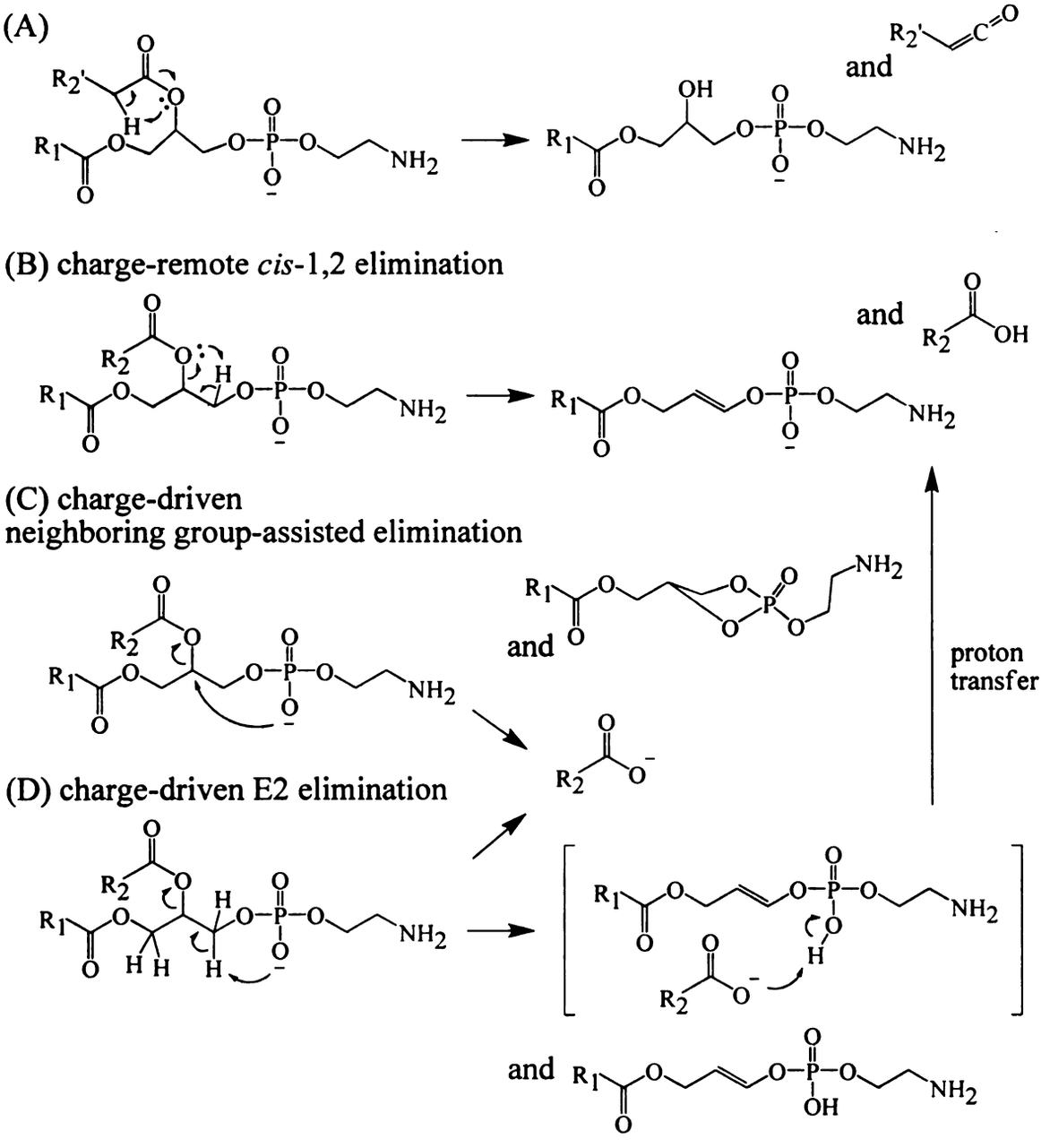


Scheme 2.2 Fragmentation of GPCho $[M+H]^+$ in CID MS/MS in positive ion mode

In negative ion mode, the neutral loss of ketene has been proposed to be formed via a charge-remote *cis*-1,2 elimination mechanism, initiated by nucleophilic attack of the acyl ester oxygen on the adjacent α-proton in the fatty acyl chain [117]. (Scheme 2.3A) Although the neutral loss of fatty acid RCOOH can also occur similarly via charge-remote elimination (Scheme 2.3B), its formation is often proposed as a phosphate negative charge-directed attack on the glycerol hydrogen or carbon, followed by an intra-ion-neutral-complex proton transfer step from the more acidic phosphate proton (Scheme

2.3C) [166,185]. Alternatively, it might also occur via a concerted one-step negative-charge-assisted *cis*-1, 2 elimination of the glycerol proton (Scheme 2.3D) [117]

The site of charge, especially the fixed negative charge, can also affect whether the fragmentation can occur through charge-directed, charge-assisted or charge-remote mechanisms via E2 elimination or neighboring group-assisted *cis*-elimination [203].



Scheme 2.3 Potential fragmentation pathways of phospholipids in negative ion mode

2.6.3.2 Fatty acid chain positions: *sn-1* vs *sn-2*

The negative ion mode fragmentations of deprotonated GPEtn lipids are found to form R_2COO^- more preferably than R_1COO^- in CID MS/MS, and the ratio of the two product ions are steady at about 2:1 in the ion trap and at optimal collision energies in triple quadrupole [190,204]. The observed differentiation between the abundance of *sn-1* and *sn-2* fatty acyl anion product ions or neutral losses can be understood in view of the statistics of the availability of critical targets, the conformational strain advantage for the reaction, the energy level of the product ions, and most importantly, the mechanism of fragmentation.

If the release of $RCOO^-$ fatty acid occurs via direct nucleophilic attack by the negative charge of the phosphate on the glycerol carbon backbone (S_N2 mechanism, Scheme 2.3C) [204], then the availability of the C target to form R_2COO^- and R_1COO^- is one for each (1:1); but the R_2COO^- channel forms a five-membered ring while the R_1COO^- channel forms a six-membered ring phosphatide, the relative energy level of which should then be the major determinant for the product ion abundance ratio of R_1COO^- and R_2COO^-.

If the fragmentation occurs by the charge-directed E2 fragmentation mechanism (Scheme 2.3D), initiated by the phosphate negative charge-directed deprotonation of the glycerol backbone protons, then the fatty acid anion R_2COO^- is formed via deprotonation of the *sn-1* and *sn-3* protons with the availability of four H, whereas the formation of R_1COO^- is formed by the deprotonation of an *sn-2* proton with only one H

available. The statistical ratio of available target protons, and thus the probability of occurrence between the two channels, is 4:1.

However, when the head group is changed, the relative tendency of the *sn-1* and *sn-2* to form fatty acid anion, fatty acid neutral loss or ketene neutral loss can be very different.

2.6.3.3 Head group: acidity

GPEtn, GPGro and GPA can all form deprotonated ions, but their fragmentation behaviors are very different [189,190]. The difference reflects the important involvement of the polar head group in the fragmentation reaction channels, and the mechanisms have been rationalized in terms of the lipid head group gas- phase acidity [166].

2.6.3.4 Conformational factors

In order for the fragmentation reactions to occur, the functional groups or atoms in the precursor ions have to be positioned in a favorable conformation. In contrast to the multiple cleavage sites in GPEtn and GPGro lipids with a flexible head group, the options of fragmentation channels are appreciably limited in glyco-lipids, which contain conformationally more rigid head group structures, such as the sugar ring. In SQDG that contains a sugar ring connected to the diacylglyceride moiety (see Table 1.1 Chapter 1 for structure), all of the fragmentations observed in MS/MS and MS^3 of the lysoSQDG product ions originate from the same and only site, of cleavage equivalent to site 2 in Scheme 2.1 (see Chapter 6 for a detailed discussion). The fragmentation involves proton transfer from specific sites on the sugar ring, and can potentially be applied, in turn, to

distinguish between conformational isomers. It also reinforced the active roles that the head group plays in lipid fragmentation. Conformational strain advantage, such as the formation of 5 or 6-member rings in the product ion might also affect the competition between fragmentation channels.

2.6.3.5 Other factors

In addition to the major factors discussed above, a few other structural factors also affect the lipid fragmentation. When the sn-1 fatty acid chain of GPEtn is changed into ester or vinyl ester (plasmalogen) tails, the fragmentation preference is altered and it can be used to distinguish plasmalogen GPEtn [132]. The number of charges also influences the fragmentation preference, which is illustrated by the different fragmentation spectra observed between singly and doubly deprotonated ions of cardiolipin (see Chapter 7). The formation of non-covalent adduction ions can drastically change the fragmentation behavior of lipids. The positive alkali-adduct ions have been discussed earlier (Table 2.1), and the negative anion adducts is examined in detail in Chapter 4 using GPCho as the example.

2.6.4 Identification of double bond position in CID-MS/MS and MS^n

Under EI, high energy CID or under low energy CID with slightly higher energy settings, lipid product ions corresponding to the fatty acid chains can sometimes further fragment in the next stage of tandem MS and generate fragment spectra characteristic for their double bond positions, but due to the higher energy required to break the fatty acid chains, the fragmentation tends to be not so efficient, and the abundance of the spectra

usually tends to be low [205]. Recently, the oxidation reactions of alkenes have been applied to assist with the facile identification of the double bond position in MS/MS or MS^3, by inducing cleavage at highly specific sites. In addition to in-solution treatment of the lipids with OsO_4 to form vicinal di-hydroxylation [206], in-source ozonolysis, or in-trap ozone-induced dissociation, have been shown to effectively and conveniently determine the double bond position in all of the common types of phospholipids [175,207].

The current study has advanced the understanding of the fragmentation mechanisms of GPCho as non-covalent anionic adduct ions, the lipo amino acid lipids, including ornithine lipids and novel glutamine lipids, and other phosphate-free lipids, such as SQDG and DGTS, and the results are discussed in detail in Chapters 4, 5 and 6.

2.7 Quantification of lipids using mass spectrometry

ESI MS and MS/MS can also be applied in the sensitive and accurate quantification of a particular molecular species of lipid in a complex lipid extract mixture by incorporating a single or a set of lipids as internal standards to the lipid extracts, or to the tissue prior to lipid extraction [110,208-210]. A linear relationship was typically found between the peak height and the concentration of a pure lipid standard between 0-50 μM by ESI MS (see also Chapter 7) , but the linearity is not valid at high concentrations [209]. However, in the actual sample, since the ionization efficiency of lipids in a mixture can be strikingly different depending on the head group but lipids of the same head group ionize with similar efficiency [165], ideally lipids of the same head

group, but with fatty acid chains typically not found in nature, are chosen as the internal standards [110] , and the quantification is achieved based on the linear relationship between the ratio of peak abundances and the ratio of concentrations of the sample and the internal standards.

Lipid quantification with higher sensitivity and accuracy can be achieved through CID MS/MS in precursor ion scan, or neutral loss scan mode on a triple quadrupole mass spectrometer [210,211], or by similar options in the quadrupole ion trap. MS/MS lipid quantification takes advantage of the lipid fragmentation characteristics, and can significantly improve the quantification sensitivity and accuracy by eliminating the interferences from overlapping precursor ions and from chemical noise [212-215]. It is therefore an ideal method for the analysis of complex small-amount lipid mixtures without elaborate pre-analysis separation. Quantitative analysis of lipid extracts using internal standards in MALDI instrument has also been described [115,129,130,216].

Chapter 3

Materials and Methods

3.1 Materials

Methanol (HPLC grade), polyethylene glycol (average mol wt 400, PEG-400), 1,3-bis[tris(hydroxymethyl)methylamino]-propane (BIS-Tris propane), benzenesulfonic acid, ammonium dihydrogen phosphate, L–ornithine, L–lysine, L–glutamine, N_{α}–acetyl L–ornithine, N_{α}–acetyl L–lysine, N_{ε}–acetyl L–lysine, soybean asolectin, MALDI matrices 2,5-dihydroxyl benzoic acid (2,5-DHB), α-cyano-4-hydroxycinnamic acid (CHCA), sinapinic acid (SA), 6-aza-2-thiothimin (ATT) and 5-methoxysalicylic acid (MSA), and isolated lipid standards from porcine brain phosphatidylinositol (GPIns) and phosphorylated phosphatidylinositol (GPIns-P) were purchased from Sigma-Aldrich (St. Louis, MO). Ethanol was purchased from the AAPER Alcohol and Chemical Co. (Shelbyville, KY). Isopropanol and ethyl ether were from Jade Scientific (Canton, MI). Ammonium acetate, ammonium fluoride, ammonium chloride, ammonium bicarbonate, KOH, HCl, deoxycholate, KCl, KH_2PO_4, acetic anhydride, ammonium bicarbonate, sodium citrate, anhydrous sodium bisulfate, glacial acetic acid, acetonitrile, chloroform (ACS and HPLC grades), and the thin layer chromatography plates (Si 250) were purhased from Mallinckrodt Baker (Phillipsburg, NJ). Ammonium iodide, formic acid and hydrobromic acid (48%) were from Spectrum Quality Products (Gardena, CA).

Ammonium thiocyanate was purchased from Fisher Scientific (Fairlawn, NJ). Ammonium hydroxide (28.0-30.0%), ammonium nitrate, L-ascorbic acid, sulfuric acid and hydrogen peroxide (30%, m/v) were from Columbus Chemical Industries (Columbus, WI). Trifluoroacetic acid (Sequanal grade) was obtained from Pierce (Rockford, IL). Propionic anhydride and iodomethane were purchased from EMD Chemicals (Gibbstown, NJ). CD_3OD (D, 99.8%) and $CDCl_3$ (D, 99.8%) were purchased from Cambridge Isotope Laboratories (Andover, MA). Ni^{2+}-NTA resin was from Qiagen (Santa Clarita, CA). High purity dodecyl maltoside (DDM), decyl maltoside (DM) and a switchable detergent (N'-dodecyl-N,N-dimethyl-acetimidamide bicarbonate) were from Anatrace Inc. (Maumee, OH). Protein assay reagents and gel protein ladder standards were from Bio-Rad (Hercules, CA). EDTA and Tris (≥99%) were purchased from Invitrogen Life Technologies (Carlsbad, CA). DNase I and RNase A (bovine pancreas) were from Calbiochem. Sodium chloride (GR ACS) was from Merck KGaA (Darmstadt, Germany). 2-(N-Morpholino)ethane-sulfonic acid (MES) was from Research Organics (Cleveland, OH). 1-amino-2-naphthol-4-sulfonic acid was from Eastman Kodak Company (Rochester, NY). The 200 μL contamination-free glass vials used for lipids extraction for mass spectrometry analysis were purchased from SUN-Sri Chromatography Accessories (Rockwood, TN).

N_α–acetylation and N_α–propylation of L–glutamine and O–methylation of N_α–acetyl L–ornithine were performed as previously described [217]. N_δ–methylation of N_α–acetyl L–ornithine was performed by reacting N_α–acetyl L–ornithine with a 100 fold

excess of CH_3I in 50 mM NH_4HCO_3 aqueous buffer at room temperature for up to 48 hours. Solvents were filtered with a sintered glass funnel (pore size 4-8 μm) prior to use.

Synthetic lipid standards GPCho(16:0/16:0), GPCho 16:0/18:1, d_4-GPCho 16:0/16:0, GPCho d_{31}-16:0/d_{31}-16:0, GPCho d_{31}-16:0/18:1, d_{13}-GPCho 16:0/16:0, GPA 16:0/18:1, GPEtn 16:0/16:0, 1,2-dipalmitoyl-*sn*-glycero-3-phosphoethanol-amine N,N-dimethyl, 1,2-dipalmitoyl-*sn*-glycero-3-phosphoethanol, hexadecyl phosphocholine, GPEtn 14:0/14:0, GPGro 14:0/14:0, GPCho 14:0/14:0, $CL(14:0)_4$, GPEtn 18:1/18:1, GPGro 18:1/18:1, GPCho 18:1/18:1, $CL(18:1)_4$ were purchased from Avanti Polar Lipids Inc. (Alabaster, AL). The nomenclature of the lipids adopted the system recommended by the LIPIDMAPS consortium in 2005 [4] (see Table 1.1).

3.2 Growth and expression of C*c*O

3.2.1 Growth conditions

All of the normal-phosphate *R. sphaeroides* strains were grown in Sistrom's succinate-basal salts medium at the KH_2PO_4 concentration of 20 mM (pH 7.0) with appropriate antibiotics as described earlier [218,219]. The cells were grown on agar-solidified medium or in liquid cultures at 30 °C under anaerobic photoheterotrophic [16] or aerobic chemoheterotrophic [220] condition, as previously described. When required, ampicillin (50 μg/mL), kanamycin (25 μg/mL), tetracycline (1 μg/mL), chloramphenicol (25 μg/mL), or streptomycin (50 μg/mL) plus spectinomycin (50 μg/mL) was added to

the media. For the phosphate-limiting growth, the 20 mM KH_2PO_4 in the Sistrom's media was replaced with 50 mM HEPES-KOH and 0.1 mM KH_2PO_4 (pH 6.8).

All the strains over-expressing C*c*O were grown aerobically on plates in Sistrom's media containing 50 μg/mL spectinomycin, 50 μg/mL streptomycin and 1 μg/mL tetracycline pH 7.0 at 30 °C for 3-5 days, then the cells were picked and inoculated into small flasks with 100 mL of Sistrom's media containing the same antibiotics and grown for two days at 30 °C with vigorous shaking at 250 rpm. Then 50 mL of starter culture was used to inoculate a 2.8 L Fernbach flask with 800 mL Sistrom's media containing 1 μg/mL tetracycline, 25 μg/mL streptomycin and 25 μg/mL spectinomycin. The Fernbach flasks were shaken at 250 rpm at 30 °C for 2-3 days until the UV-Visual absorbance at 650 nm exceeded 1.2 and the pH reached over 8.5.

Escherichia coli cells were grown in LB medium at 37 °C. When required, antibiotics were added to the solid media or liquid cultures at the concentration of 50 μg/mL of ampicillin, kanamycin or chloramphenicol.

3.2.2 *R. sphaeroides* growth curves

This part of the experiments was performed by collaborator Dr. Carrie Hiser from Dr. Shelagh Ferguson-Miller's group, and the results are included as introductions.

For photosynthetic growth curves, 2.4.1 (wild-type) [221] and BC-m3 (*cls* deletion, also called CL3) [15] strains were grown in 250 mL sidearm flasks filled completely with Sistrom's medium under approximately 30 μmol $m^{-2}s^{-1}$ light without shaking. For aerobic growth curves, strains 2.4.1 and BC-m3 were grown at 30 °C in 50

mL of Sistrom's medium in 250 mL side-arm flasks with vigorous shaking (250 rpm). In each case, cell densities were measured in a Klett photometer with a #66 filter.

3.2.3 Construction of CL-deficient mutant of *R. sphaeroides*

This part of the experiments was performed by collaborator Banita Tamot from Dr. Christoph Benning's group [15] and is not included as the results of the present dissertation. In essence, the gene for cardiolipin synthase (*cls*) was isolated from *R. sphaeroides* genomic DNA, and a mutant strain of *R. sphaeroides* with the *cls* gene deleted (called BC-m3 or CL3) was created [15].

3.2.4 Engineering *R. sphaeroides* 2.4.1 and specific lipid-deficient strains to overproduce C*c*O

This part of the experiments was performed by collaborator Dr. Carrie Hiser from Dr. Shelagh Ferguson-Miller's group, and is not included as the results of the dissertation.

The *R. sphaeroides* strains 2.4.1, BC-m3 (also called CL3) and BC-m2 (CL2) [15], SB1K1 and SB1K2 [16], and CHB20 [90] were generated as described earlier. To overproduce a subunit I C-terminal histidine-tagged version of the C*c*O enzyme, the pRK-pYJ123H plasmid [220] carrying the genes coding for a wild-type C*c*O was transferred by conjugation from *E. coli* S17-1 into *R. sphaeroides* strains 2.4.1, CHB20, SB1K1 (and SB1K2) and CL3 (also called BC-m3) (and CL2, another *cls* mutant clone produced in parallel) as described [220] to create strains 2.4.1+C*c*O CHB20+C*c*O SB1K1+C*c*O (and SB1K2+C*c*O) and CL3+C*c*O (and CL2+C*c*O), respectively. The

sequence SNHHHHHH was directly added to the C terminus in subunit I. These strains were grown aerobically in Sistrom's media containing 1 μg/mL tetracycline at 30 °C.

To add back the *cls* gene to the overproducing strains, the *cls* gene was sub-cloned into an altered version of pBBR1-MCS [222] which had the chloramphenicol resistance cassette replaced by the streptomycin/spectinomycin resistance cassette from pHP45Ω. This expression plasmid, which can co-exist with pRK-pYJ123H in the same cell, was transferred by conjugation from *E. coli* S17-1 into *R. sphaeroides* strains 2.4.1+C*c*O and CL3+C*c*O to create strains 2.4.1+C*c*O+*cls* and CL3+C*c*O+*cls*, respectively. These strains were grown aerobically in Sistrom's media containing 1 μg/mL tetracycline and 5 μg/mL each of streptomycin and spectinomycin. In addition, strains 2.4.1+C*c*O, CL3+C*c*O, 2.4.1+C*c*O+*cls* and CL3+C*c*O+*cls* were also grown under 37 °C as a high temperature stress while keeping all the other conditions identical.

To overproduce a version of C*c*O suitable for crystallization, placing a histidine tag on the C terminus of subunit II (pointing toward the outside of the membrane on the top) and a shortened version of subunit IV were found to improve molecular homogeneity [35], where the HHHHHH histidine tag was used to replace the C-terminal sequence ARGGTY after sixteen amino acids were cleaved from the C terminus of the genomic sequence of subunit II (Figure 3.1). Therefore, the pCH169 plasmid [35] carrying these versions of the C*c*O genes was transferred by conjugation into the BC-m3 (also called CL3) mutant strain to create strain 169CL3. The CL-proficient crystallography strain used as the control herein is 169-2.4.1, which is derived from a wild-type 2.4.1 strain to which the pCH169 plasmid was added [220].

The various *R. sphaeroides* strains used in the dissertation are described in Table 3.1.

Table 3.1 *R. sphaeroides* strains and CcO plasmids used in this work

***R. sphaeroides* strain * #**	**Description**		**Source @**	**Chapter**
	CcO plasmid	**Background genome**		
(WT) 2.4.1+CcO (30/ 37 °C)	**pRK-pYJ123H** His-tag cox I WT cox II WT cox III WT cox IV	**WT** WT cox I WT cox II WT cox III WT cox IV	[220]; [223]	5, 6, 7, 8, 9
(CL−) CL3+CcO (30/ 37 °C)	As above	As above except deletion of *cls* gene	[220]; [15]	6, 7, 8, 9
(SQDG−) SB1K1+CcO	As above	As WT except SQDG-deficiency by chemical mutation	[220]; [16]	7
(GPCho−) CHB20+CcO	As above	As WT except GPCho-deficiency by chemical mutation	[220]; [90]	5, 7
2.4.1+CcO+*cls* (30/ 37 °C)	As above	As WT except an additional plasmid for *cls*	[220]; Dr. Carrie Hiser	9
CL3+CcO+*cls* (30/ 37 °C)	As above	As WT except deletion of *cls* gene, and an additional plasmid for *cls*	[220]; Dr. Carrie Hiser	9
(WT) 169WT	**pCH169** WT cox I His-tag cox II WT cox III short cox IV	**YZ200** WT cox I no cox II no cox III WT cox IV	[220]	9
(WT) 169-2.4.1 (P+/ P−)	As above	**WT** WT cox I WT cox II WT cox III WT cox IV	Dr. Carrie Hiser	9, 10
(CL−) 169CL3 (P+/ P−)	As above	As above except deletion of *cls*	Dr. Carrie Hiser	9, 10
(WT) 169Δ4 (P+/ P−)	As above	no cox I WT cox II WT cox III no cox IV	[35]	8
(WT) 37Δ4 (P+/ P−)	**pCH37** WT cox I, His-tag cox II, WT cox III, no cox IV	As above	[35]	6

(Table 3.1 continued)

* Growth was under 30 °C with normal concentration of phosphate (20 mM) unless specified otherwise.

P+ represents normal phosphate concentration (20 mM); P− represents low phosphate concentration (0.1 mM) in growth medium.

@ Sources for the plasmid and the genome are separated by ";" if different.

Subunit I

MADAAIHGHEHDRRGFFTRWFMSTNHKDIGVLYLFTGGLVGLISVAFTVYMRMELMAPGV
QFMCAEHLESGLVKGFFQSLWPSAVENCTPNGHLWNVMITGHGILMMFFVVIPALFGGFG
NYFMPLHIGAPDMAFPRMNNLSYWLYVAGTSLAVASLFAPGGNGQLGSGIGWVLYPPLSTSESGY
STDLAIFAVHLSGASSILGAINMITTFLNMRAPGMTMHKVPLFAWSIFVTAWLILLALPVLAGAI
TMLLTDRNFGTTFFQPSGGGDPVLYQHILWFFGHPEVYIIVLPAFGIVSHVIATFAKKPIFGYLP
MVYAMVAIGVLGFVVWAHHMYTAGLSLTQQSYFMMATMVIAVPTGIKIFSWIATMWGGSI
ELKTPMLWALGFLFLFTVGGVTGIVLSQASVDRYYHDTYYVVAHFHYVMSLGAVFGIFAGIYFWI
GKMSGRQYPEWAGKLHFWMMFVGANLTFFPQHFLGRQGMPRRYIDYPEAFATWNFVSSLG
AFLSFASFLFFLGVIFYTLTRGARVTANNYWNEHADTLEWTLTSPPPEHTFEQLPKREDWERAPA
H + (SNHHHHHH)

Subunit II

MRHSTTLTGCATGAAGLLAATAAAAQQQSLEIIGRPQPGGTGFQPSASPVATQIHWLDGFILVII
AAITIFVTLLILYAVWRFHEKRNKVPARFTHNSPLEIAWTIVPIVILVAIGAFSLPVLFNQQEIP
EADVTVKVTGYQWYWGYEYPDEEISFESYMIGSPATGGDNRMSPEVEQQLIEAGYSRDEFLLAT
DTAMVVPVNKTVVVQVTGADVIHSWTVPAFGVKQDAVPGRLAQLWFRAEREGIFFGQCSELCGI
SHAYMPITVKVVSEEAYAAWLEQ**ARGGTY** *ELSSVLPATPAGVSVE*
(HHHHHHH)

Subunit III

MAHAKNHDYHILPPSIWPFMASVGAFVMLFGAVLWMHGSGPWMGLIGLVVVLYTMFGWWS
DVVTESLEGDHTPVVRLGLRWGFILFIMSEVMFFSAWFWSFFKHALYPMGPESPIIDGIFPPEGI
ITFDPWHLPLINTLILLCSGCAATWAHHALVHENNRRDVAWGLALAIALGALFTVFQAYEYSHAA
FGFAGNIYGANFFMATGFHGFHVIVGTIFLLVCLIRVQRGHFTPEKHVGFEAAIWYWHFVDVVWL
FLFASIYIWGQ

Subunit IV

MAETNKGTGPMADHSHPAHGHVAGSMDITQQEKTFAGFVRMVTWAAVVIVAALIFLALANA

Figure 3.1 Full length amino acid sequences of *R. sphaeroides* C*c*O deduced from the genome. The incorporation of the histidine tag attached to the C-terminus of subunit I or subunit II is shown in blue and red, respectively [30]. In subunit I, SNHHHHHH was added to the C terminus, whereas in subunit II, sixteen amino acids were cleaved from the C terminus, and ARGGTY was replaced with HHHHHH histidine tag.

3.3 Purification and characterization and C*c*O

3.3.1 Isolation of *R. sphaeroides* cell membrane pellets

R. sphaeroides cells were harvested by centrifugation in a GS-3 rotor at 14,000 g for 20 minutes and re-suspended in pH 6.5 buffer containing 50 mM KH_2PO_4 and 1 mM EDTA. After addition of DNase I and RNase, the re-suspended cells were homogenized and lysed by passing through French press twice under 20,000 psi at 4 °C. The mixture was then centrifuged at 30,000 g for 30 minutes at 4 °C to remove the precipitated unbroken cells and debris, and the supernatant was then subjected to ultracentrifugation at 200,000 g for 90 minutes at 4 °C to precipitate the membrane pellets [220]. The membrane pellets were then resuspended on ice in the buffer containing 40 mM KCl and 10 mM Tris pH 8.0 (or with additional 1 mM imidazole and 200 mM KCl for subunit II his-tag labeled versions), quick-frozen in liquid N_2 and stored at −80 °C for further use. A typical yield obtained from fifteen 2.8 L Fernbach flasks of 169-2.4.1 or 169CL3 cell cultures was approximately 40 mg C*c*O.

3.3.2 Purification of C*c*O using FPLC affinity chromatography

3.3.2.1 Detergent solubilization of membrane pellets

Prior to loading to the Ni^{2+}-NTA column, the membrane pellets were thawed, homogenized and diluted to final protein concentration of 10 mg/mL (based on a BCA protein assay of the membrane suspension) using the membrane resuspension buffer described above, and 1% (m/v) final concentration of dodecyl maltoside was added to the

membrane suspension followed by vigorous stirring at 4 °C for 30 minutes to solubilize the membrane pellets. The mixture was then subjected to ultracentrifugation at 200,000 g for 30 minutes at 4 °C to separate the unsolublized membrane pellet precipitants from the solublized membrane supernatant, which was immediately loaded to the FPLC column.

3.3.2.2 FPLC purification of C*c*O

To enable the purification of C*c*O protein using affinity chromatography as described in detail below, the C*c*O over-expressed in a variety of *R. sphaeroides* strains (Table 3.1) were histidine-tagged at the C-terminus of subunit I or subunit II (Figure 3.1). The subunit I his-tagged C*c*O enzymes were purified by using a home-packed Ni^{2+}-NTA gravity column and concentrated with a Centriplus YM100 filter unit (molecular weight cutoff 100 kDa; maximum volume 15ml, Millipore) by Dr. Carrie Hiser as described earlier [220], and the final purified C*c*O was in the buffer containing 50 mM KCl, 0.05% (m/v) dodecyl maltoside and 10 mM Tris at pH 8.0. The subunit II his-tagged C*c*O enzymes were purified by using a home-packed column of Ni^{2+}-NTA (typical column volume 20 mL) on an FPLC system (AKTA, Pharmacia) similarly to the methods described earlier [35]. The bound C*c*O was eluted by increasing the concentration of imidazole, which competes with histidine tag for Ni^{2+}-NTA.

FPLC buffer A contained 0.05% dodecyl maltoside, 220 mM KCl, 10 mM Tris pH 8.0 and 10 mM imidazole, and buffer B contained 0.05% dodecyl maltoside, 220 mM KCl, 10 mM Tris pH 8.0 and 150 mM imidazole. The column was equilibrated with 4 column volumes of buffer A before the solubilized membrane proteins were loaded to the

column at a typical flow rate of 0.25 mL/min. The loaded column was then washed with 11 column volumes of buffer A, after which the percentage of buffer B was raised to elute the bound proteins. The typically applied elution gradient profile of buffer B is shown in Figure 3.2. UV-Vis absorbance at wavelength 280 nm was recorded to monitor the elution of protein components.

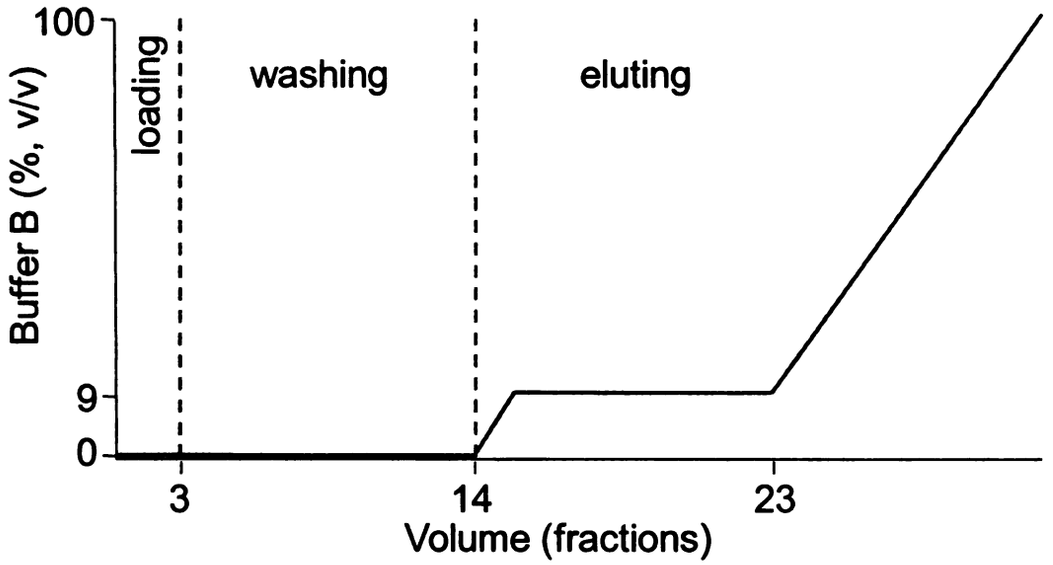


Figure 3.2 Typical FPLC gradient profile used in the purification of subunit II his-tagged C*c*O in this study [35].

All the peaks in the FPLC profile were examined using reduced minus oxidized UV-Vis spectroscopy from 500 to 700 nm to monitor the composition of protein and the purity of C*c*O. The flow-through fractions during sample loading were also examined to check for overflow of binding. All the fractions under the second peak of the elution profile, usually containing the pure C*c*O, were collected, diluted with buffer A to about 100 mL, and immediately concentrated to about 0.5 mL by using a N_2 pressure

concentrating unit at 4 °C to remove the imidazole. The sample was then diluted to 50 mL using the detergent exchange buffer containing 0.2% (m/v) decyl maltoside, 50 mM NaCl and 10 mM Tris pH 8.0, and concentrated to about 0.5 mL. This process was repeated one more time, and the final concentrated detergent-exchanged C*c*O was collected in centrifuge tubes, and kept at 4 °C for crystallization set up or quick-frozen in liquid N_2 and stored at −80 °C in aliquots for further analysis.

3.3.3 BCA protein assay

Total protein levels were determined by using the BCA^{TM} Protein Assay Kit (Thermo Fisher Scientific) using 1-20 μg BSA (2 mg/mL in 0.9% saline and 0.05% sodium azide) as the standard for membrane samples. However, the BCA assay is based on the reduction reaction of Cu^{2+} into Cu^{+} by proteins in alkaline medium, where each one Cu^{+} can then be chelated by two bicinchroninic acid (BCA) molecules to develop the purple-color. The effects of the structure of the protein, the sequence length and the four residues of cysteine, cystine, tryptophan and tyrosine on the color formation with BCA require a calibration curve to be established using standards as close to the sample as possible. Therefore, purified C*c*O with a UV-Vis spectroscopically determined concentration was used as the standard for the redissolved/ resuspended C*c*O crystal samples.

The protein samples and standards were diluted to 100 μL using a solution containing 0.25% (m/v) deoxycholate, 40 mM KCl and 10 mM Tris pH 11.2. Such a diluting solution was developed to optimize the reaction efficiency for membrane

proteins, and to minimize the interference from detergent. 2 mL of the freshly mixed solution of reagent A and reagent B at 50:1 (v/v) was added to each sample test tube, mixed well and incubated in 60 °C water bath for 30 minutes. Then the samples were quickly chilled in ice-water bath and let stand in room temperature, and the absorption at 562 nm was recorded using 1 cm-thick cuvette on the UV-Vis spectrophotometer within 10 minutes. Each of the standards and samples was analyzed in triplicate.

3.3.4 UV-Visible spectroscopy of membrane suspension and purified C*c*O

UV-Visible optical spectra were recorded on a Perkin-Elmer Lambda 40P UV-visible spectrophotometer. For the crude membrane samples, dithionite-fully-reduced minus ferricyanide-fully-oxidized spectra were collected from 500 to 700 nm wavelengths and the level of C*c*O was quantified by using the extinction coefficient $\Delta\varepsilon_{606\text{-}630} = 24\ cm^{-1}mM^{-1}$ [220]. For the purified C*c*O samples, a UV-Visible profile was directly collected from the original sample with and without reduction with sodium dithionite from 250 to 700 nm, and the level of C*c*O was quantified by using the extinction coefficient $\Delta\varepsilon_{606\text{-}640} = 40\ cm^{-1}mM^{-1}$ [220]. To counteract the acidity of the reducing agent, the samples were diluted with the buffer containing 1 mM EDTA, 0.1% dodecyl maltoside and 100 mM HEPES pH 7.4 prior to the analysis. At least triplicate spectra were collected for each sample.

3.3.5 Urea SDS-PAGE gel electrophoresis

Sodium dodecyl sulfate polyacrylamide gel electrophoresis (SDS-PAGE) was applied to monitor the protein compositions of the two eluted peaks from FPLC, and the

subunit composition of purified C*c*O. A broad range molecular weight protein marker standard (2-212 kDa) and 10 μg (5 μL of 2 μg/ μL C*c*O) protein diluted in buffer containing 40% glycerol, 25 mM Tris pH 6.5, 8% (m/v) SDS and 0.08% (m/v) bromophenol blue were loaded onto an 8% (m/v) acrylamide stacking gel (pH 6.8) on top of the urea-containing 18% (m/v) acrylamide separating gel (pH 8.8), and were electrophoresed at 100 V at room temperature for about two hours until the dye front ran off the gel. The gel was then stained with Coomassie blue and destained with 7.5% (m/v) acetic acid for 2-3 times [77], sealed in cellophane films, dried overnight and scanned for the image.

3.3.6 Steady state activity assay of the C*c*O based on oxygen consumption

The steady state activity of C*c*O was evaluated in view of its rate of oxygen consumption with cytochrome *c* as the electron donor according the reaction shown in scheme 3.1. The reaction mixture contained 30 μM cytochrome *c*, 1 mM TMPD, 2.8 mM ascorbic acid, 0.05 % dodecyl maltoside in 50 mM KH_2PO_4 pH 6.5 buffer which had been fully pre-saturated with atmospheric oxygen under room temperature. Asolectin lipids (1.1 mg/mL final concentration of soybean asolectin and 0.02% (m/v) final concentration of cholate) were also added to the mixture for comparison. The consumption of oxygen was recorded polarographically in a Gilson oxygraph with a Clark-type electrode. The phosphate-free buffer Bis-Tris propane pH 7.4 was used instead of KH_2PO_4 for the experiments of comparing 169-2.4.1 and 169CL3 C*c*O purified form the normal-phosphate/low-phosphate growth conditions. The turnover

number of the enzymatic activity was calculated as moles of cytochrome *c* oxidized per mole of enzyme per second (i.e. sec^{-1}).

$$4\ \text{cyt}\ c^{2+} + 8\ H^{+}_{(in)} + O_2 \xrightarrow{CcO} 4\ \text{cyt}\ c^{3+} + 2\ H_2O + 4\ H^{+}_{(out)}$$

Scheme 3.1 The overall reaction catalyzed by C*c*O, which is also the reaction used to evaluate the steady state activity of C*c*O.

3.3.7 Phosphorus analysis

To quantitatively measure the phosphorus content in the purified C*c*O, lipid extracts, and membrane samples, several previously reported phosphorus analysis methods were evaluated, and the method developed by Bartlett *et al* in 1959 [224] was chosen to use with a few adaptations due to its robustness and reproducibility.

In a typical assay, 20 μL of 200 μM C*c*O was diluted with H_2O to a final volume of 2 mL in a new glass test tube, and mixed with 0.2 mL of 10 M H_2SO_4. The buffer of the enzyme was used as the blank control. Non aqueous samples such as the lipid extracts in methanol: chloroform and the remains from lipid extraction were dried under vacuum prior to the addition of 2 mL H_2O, and appropriate buffer or organic solution was used as the background control and processed identically. KH_2PO_4 in aqueous solutions or $CL(18:1)_4$ lipid standard in methanol: chloroform solutions containing 0, 0.02, 0.04, 0.06, 0.08 and 0.10 μmole of equivalent phosphorus were used as the standards for phosphorus quantification, and treated identically to the unknown samples.

Ashing of the samples was performed by incubation at 150-160 °C for at least 3 hours, followed by addition of 50-200 μL of phosphorus-free hydrogen peroxide (30%, m/v) to each sample tube and another 1.5 hours of heating at the same temperature, until the solutions became clear. Then the samples were cooled to room temperature, and diluted with 4.4 mL of H_2O, followed by the addition of 0.2 mL fresh Fiske-SubbaRow reagent [224], prepared by mixing 15 g anhydrous sodium bisulfite, 0.25 g 1-amino-2-naphthol-4-sulfonic acid and 0.5 g anhydrous sodium sulfite in 100 mL water (filtered through 0.22 μm filter and kept in dark at 4 °C), and 0.2 mL 5% ammonium molybdate. The samples were mixed thoroughly and heated for 10 minutes in a boiling water bath, then the test tubes were quenched in ice-water bath and the absorbance at 830 nm was recorded. Each of the samples and standards were run in triplicate.

3.4 *Cc*O crystallization

To obtain *R. sphaeroides* *Cc*O crystals, a hanging drop crystallization set-up was used for initial condition screening and then a sitting drop set-up was used to obtain the crystals for further examination (Figure 3.3).

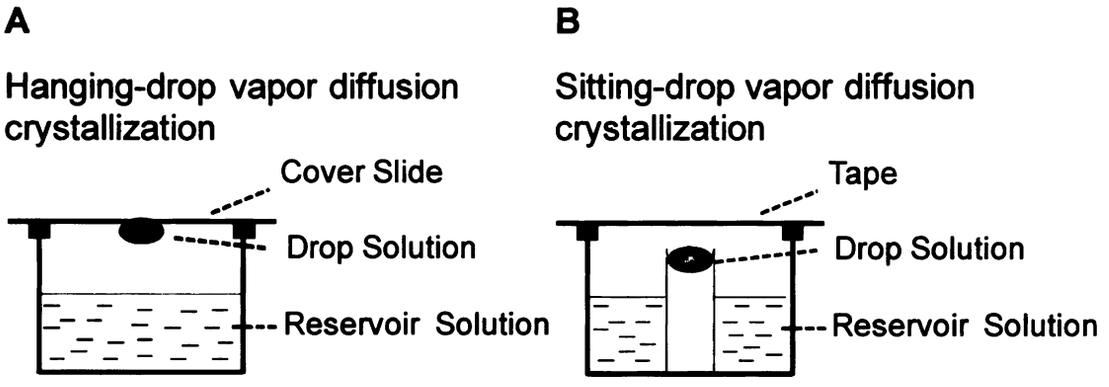


Figure 3.3 Vapor diffusion crystallization using (A) hanging drop setup, and (B) sitting drop setup (adapted from [30]).

3.4.1 Four-subunit C*c*O crystallization

In the sitting drop setup, typically 10 μL of 80 μM C*c*O in buffer containing 50 mM NaCl, 0.20% decyl maltoside and 10 mM Tris pH 8.0 was mixed with 5 μL of the reservoir solution containing 100 mM sodium citrate pH 5.7 (or 100 mM MES pH 6.3), 100 mM NaCl and 18-22.5% PEG-400, and 5 μL of the crystallization additive solution containing 5% heptanetriol, 33 mM $MgCl_2$, and 0.026% dodelcyl maltosides [30]. After incubating the crystallization drop at 4 °C for one week, triangular or hexagonal crystals usually started to appear, but the crystals were not harvested until after four to five weeks of growth when they had reached the size of approximately 0.2 × 0.2 × 0.1 mm to 0.7 × 0.7 × 0.3 mm. In the hanging drop initial screening, the volume of sample sizes was decreased by 5 fold.

3.4.2 Two-subunit C*c*O crystallization

By changing the concentration of C*c*O to 120 μM, increasing PEG-400 concentration to 24-26% in the reservoir solution, and using 32 mM $MgCl_2$ and 1.3 mM $CdCl_2$ in the additive solution, C*c*O crystals containing only subunits I and II can be obtained [30]. For the 169-2.4.1 and 169CL3 strains, however, these crystals were only able to be obtained at 20 °C, but not at 4 °C. Heavy protein precipitation occurred immediately after mixing of the drop contents, from which football-shaped or flower petal cluster-shaped two-subunit crystals gradually appeared after about two weeks and reached full size of approximately 0.2 × 0.2 × 0.1 mm in three to four weeks.

3.4.3 Flash-cooling of the C*c*O crystals

Picking and freezing of the crystals were performed in an environment of minimized-humidity at 4 °C or 20 °C depending on the crystal growth temperature, using the procedures developed earlier [30].

Before harvesting the crystals from the crystallization drop using cryoloops, the drop was equilibrated with 30 μL stablizing solution and gradually with 100 μL cryoprotection solution. The stablizing solution was designed to mimic the final composition in the crystallization drop and contained 91 mM sodium citrate pH 5.7 (or 91 mM MES pH 6.3), 91 mM NaCl, 18 mM Tris pH 8.0, 30 mM $MgCl_2$, 2.5% heptanetriol, 0.16% decyl maltoside, 0.016% dodecyl maltoside and 18-20% PEG-400, depending on the specific drop. The cryoprotection solution contained a higher concentration of PEG-400 (32%), with all the other components identical to the stablizing

solution. The crystals were immediately immersed into liquid N_2 and stored until x-ray data collection.

3.4.4 Harvesting C*c*O crystals for mass spectrometry analysis

For the mass spectrometry analysis, about a hundred of the crystals grown under similar conditions were each transferred, by using a clean cryoloop under a microscope, from the crystallization well into a clean well containing fresh 4 °C Milli-Q water. The crystals were then rinsed briefly, and collected in a new well containing typically 10 μL Milli-Q water or the exchange buffer without the detergent. The crystal mixture was then transferred into an Eppendorf centrifugation tube, vortexed vigorously, and the protein concentrations were determined by the BCA assay using BSA and purified C*c*O of known concentration (determined by UV-Vis) as the standards. The redissolved/resuspended crystal mixtures were then diluted to the same protein concentration for mass spectrometric analysis.

3.4.5 X-ray diffraction data collection

X-ray diffraction data were collected at LS-CAT and GM/CA-CAT at the Advanced Photon Source of the Argonne National Laboratory (Argonne, IL), using MARCCD-M165 detector and rotation data collection method.

3.5 Lipid extraction

3.5.1 Extraction of lipids from isolated membranes

For the results described in Chapters 5 and 7, triplicates of 10 μL of the suspended membranes from either wild type or mutant *R. sphaeroides* cells (diluted with water to approximately 1.4 mg/mL protein concentration determined by BCA assay) were freeze-dried, and lipids extracted by the sequential addition of 2 x 50 μL chloroform: methanol (2:1, v/v), 1 x 50 μL ethyl ether: ethanol (1:1, v/v), and 2 x 50 μL chloroform: methanol: ammonium hydroxide (100:50:2, v/v/v) followed by vigorous vortexing and removal of the solution at each step [53]. The extracts were combined, then dried under vacuum and re-dissolved in 50 μL chloroform: methanol (1:1, v/v) prior to mass spectrometry analysis. For 1-D TLC analysis, about 20-40 μL of the total 50 μL extracts would be used, but the same amount was applied for each sample in comparison.

For the experiments of the normal-phosphate and low-phosphate growth comparison (Chapter 10), triplicates of 20 μL of the membrane suspensions diluted with water to 1 mg/mL protein concentration were subjected to the lipid extraction using the same procedures as described above, except that the solvent ethyl ether: ethanol (1:1, v/v) was changed to ethyl ether: methanol (1:1, v/v).

For comparison, simple extractions using only 3 x 50 μL chloroform: methanol (1:1, v/v) or only 3 x 50 μL chloroform: methanol: ammonium hydroxide (100:50:2, v/v/v) were also performed on the freeze-dried membrane samples. All of these extractions were carried out in 250 μL glass vials shown to contain no contamination.

3.5.2 Extraction of lipids from purified C*c*O

Extraction of lipids from 10 μL of C*c*O enzyme (approx. 140 μM in the buffer containing 50 mM KCl and 0.05% w/v dodecyl maltoside for the subunit I his-tagged

version, or in the buffer containing 50 mM NaCl and 0.2% decyl maltoside for the subunit II his-tagged version) purified from the wild type and mutant *R. sphaeroides* cells, was carried out using the same procedure described above, following initial washing of the freeze-dried enzymes three times with 1 mL anhydrous acetone at 4 °C, or dilution and filtration using a membrane with a 3 kDa molecular weight cutoff (Millipore) (Chapter 8).

Other extraction methods were also evaluated to improve the lipid extraction efficiency from purified C*c*O. Using the modified Bligh & Dyer extraction [28,137], 100 μL of diluted enzyme at 50 μM was directly mixed with 2 mL of chloroform: methanol (1:1, v/v) in a 10 mL glass test tube with a teflon-lined screw cap to form a one-phase mixture. The mixture was vigorously vortexed for 5 min and let stand in ice or in room temperature for about 20 min, followed by the addition of 1 mL detergent-free aqueous buffer containing 50 mM NaCl and 10 mM Tris pH 8.0, and centrifugation 4 °C for 20 minutes to drive the separation of phases, where the chloroform-rich lower phase and the methanol/water-rich upper phase were separated with a thin film of protein formed in between. The film was carefully pierced with a glass pipette and the bottom layer was pooled in a clean test tube and washed once more with 1 mL detergent-free aqueous buffer, while the top layer and the protein film were extracted twice more with 2 mL of chloroform: methanol (1:1, v/v) by vigorous vortexing for 5 min and centrifugation for 20 min. The combined bottom layers were then dried under vacuum for further phosphorus analysis. These extraction experiments were done in triplicate.

3.5.2.1 Acetone washing to remove detergent from purified C*c*O

Typically 10 μL of the purified C*c*O was freeze-dried and washed with 1 mL cold anhydrous acetone [225] in Eppendorf centrifuge tubes at 4 °C followed by vortexing and sonicating for 3 min and centrifugation at 5000 rpm for 5 min to remove the acetone solution, for three times. The washed enzyme in the form of a green powder was transferred to a new glass vial, dried again under vacuum and subjected to lipid extraction using the procedures described above.

3.5.2.2 Dilution-filtration (3 kDa) to remove detergent from purified C*c*O

Typically 10 μL of the purified C*c*O was diluted with 500 μL of the detergent-free buffer containing 50 mM KCl and10 mM Tris pH 8.0, vortexed for 3 min, and centrifuged at 14k rpm (in a centrifugal filter unit with a 3K molecular weight cutoff filter) at 4 °C for about 20-30 min until the final volume of solution on top of the filter reached 50 μL. The filtrate was removed and collected separately, and 500 μL of detergent-free buffer was added again to dilute the enzyme, and the process was repeated twice more. The final washed enzyme was transferred to glass vial, dried again under vacuum and subjected to lipid extraction using the procedures described above.

3.5.3 Evaluation of extraction efficiency of lipids from purified C*c*O

Phosphorus analysis as described above was applied to the lipid extracts, the remains after extraction, and the enzyme without extraction in triplicate to obtain the percentage yield of extraction. To evaluate how the enzyme pre-extraction treatments affected the extraction efficiency, the same amounts of purified C*c*O, purified C*c*O after being freeze-dried, and purified C*c*O after being freeze-dried followed by anhydrous

acetone washing, were each subjected to the lipid extraction procedures described earlier in triplicate, and phosphorus analysis was applied to the extracts, the remains from extraction, and the protein without extraction.

3.6 Thin layer chromatography

3.6.1 1-D thin layer chromatography

Silica TLC plates with or without the concentrating band were soaked with 2M $(NH_4)_2SO_4$ solution and incubated at 120 °C for 3 hours to make the plates acidic. Typically the lipids extracted from 8.7 uL membrane (at about 140 mg/mL protein concentration) or 0.67 mg purified C*c*O (at about 20-40 μL volume) using the solvents described above were loaded to the plates, which were developed by acetone: toluene: water (91:30:7, v/v/v) for about 50-60 minutes to reach about 90% of the plate length (Chapters 7 and 8) [90]. The lipids were then visualized by iodine vapor stain. For the spots to be scraped off the plate and re-extracted for mass spectrometry identification analysis, the area over the spots was covered with aluminum foil during the iodine vapor staining, followed by extraction using chloroform: methanol (1:1, v/v).

3.6.2 Evaluation of cleavable detergent for potential application in lipids extraction from purified C*c*O using TLC

To explore the potential of removing the interference of detergent for MS and improving extraction efficiency of lipids from purified C*c*O, a structurally switchable type of detergent from Anatrace (bicarbonate salt, $C_{17}H_{36}N_2O_3$, m.w. 316.48) containing

a Schiff base bond linkage cleavable by argon gas bubbling at 60 °C was tested. However, it was not further investigated in the current study, because at 5 mM (i.e., 10 cmc) it caused instant precipitation of C*c*O (at final concentrations of 5 μM and 15 μM), its N, N-dimethyl-amino head group predominantly ionized even in MALDI MS using 2, 5-DHB as the matrix such that no lipids peaks were observable in either positive or negative ion mode except for its protonated ion at m/z 225 (+ve), and adjusting the pH of the buffer from 8.0 to 9.0 made no difference.

3.6.3 2-D thin layer chromatography

2-D TLC was performed by Banita Tamot from Dr. Benning's group [15], and the results are not included as part of the present dissertation. Lipid extracts were prepared and loaded onto activated Silica TLC plates as previously described [14]. The lipids were separated by two-dimensional TLC using chloroform-methanol-water (65:25:4, v/v/v) for the first dimension and chloroform-methanol-acetic acid-water (170:25:25:4, v/v/v/v) for the second dimension. Lipids were visualized by charring with 50% H_2SO_4 [14].

3.6.4 Quantitative TLC lipid analysis using ^{14}C-labeling

^{14}C-labeling quantification was performed by Banita Tamot from Dr. Benning's group [15], and the results are not included as part of the present dissertation. Lipids from aerobically-grown overnight cultures were then labeled by incubating the cultures with [1-^{14}C]-acetate as previously described [226]. Lipid extracts were prepared and separated by two-dimensional TLC as described above. The plates were exposed to a

phosphoimager (GE Healthcare, Piscataway, NJ) to obtain an image of the labeled lipids. The lipids on the TLC plates were then visualized by iodine staining and the radioactivity in the individual spots was measured by using a liquid scintillation counter [226]. The relative amount of each lipid was calculated as the percentage of total radioactivity present in the lipid sample.

3.7 Mass spectrometry

3.7.1 Characterization of lipid extracts using ESI ionization sources

3.7.1.1 Identification of lipids by using ESI MS and CID MS^n on a linear quadrupole ion trap mass spectrometer

Most of the mass spectrometry analysis of lipid extracts was performed using a linear quadrupole ion trap mass spectrometer (Thermo Fisher Scientific model LTQ, San Jose, CA), equipped with a nanoelectrospray ionization source (nanoESI), although traditional ESI and static nanoESI sources were also applied for comparison in the early stages of experiments. Total lipid extracts from each membrane sample obtained using the procedures described above were diluted 4 fold (20 fold for the individual specific-lipid-deficient mutant membrane lipid extracts) using $CHCl_3$:CH_3OH (1:1, v/v) containing 40 mM ammonium hydroxide, immediately prior to introduction to the mass spectrometer by direct infusion through non-coated silica tips with internal diameters of 30 μm (New Objective, Inc. Woburn, MA), at a flow rate of 0.3 or 0.5 μL/min. NanoESI

conditions were optimized to maximize the sensitivity and stability of the precursor ions of interest while minimizing 'in-source' fragmentation. Typical nanoESI conditions were: heated capillary temperature 180 °C, spray voltage 1.8 kV, capillary voltage 20 V and tube lens voltage 75 V. Mass spectra (MS) were acquired from m/z 150 to 2000 using enhanced scan mode.

Collision-induced dissociation (CID) MS/MS and MS^n experiments were performed using helium as the collision gas using an activation time of 30 ms. Collision energies were optimized for each precursor ion of interest. Typically, an activation q value of 0.2 was used in order to achieve a reasonable low-mass-cutoff while still maintaining good sensitivity, and depending on the activation q values, the corresponding optimal collision energies applied were 20%, 25% or 30% for the phospholipids, ornithine lipids and glutamine lipids, and had to be increased to 35% or 40% for the SQDG lipids. The isolation width required to obtain isotopical isolation of precursor ions was typically 1.2 Da for protonated and deprotonated ions, and 1.5-2.0 Da for non-covalent cationic or anionic adduct ions [185]. The spectra shown were typically the average of 50-300 scans. Each scan was typically an average of three microscans. The target number was set at 1e4 for MS and 3e4 for MS^n. The maximum injection time was typically set at 50 ms for MS and MS^n for the identification analysis, but increased to 100 ms or 500 ms for quantification purpose to prevent max out which is going to be specified below.

For the study of anionic adduct ions of synthesized phospholipids standards in Chapter 4, mass spectrometry experiments were performed using the Thermo model LTQ

linear quadrupole ion trap mass spectrometer equipped with nanospray ionization source. Synthesized phospholipids standards (5 μM) in $CH_3OH/CHCl_3$ (1:1, v/v) containing 0.1-20 mM ammonium salts were introduced to the mass spectrometer at a typical flow rate of 0.2 μL/min. Spectra were acquired in negative ionization mode. Typical nESI conditions were: spray voltage 1.5 kV, heated capillary temperature 200 °C, capillary voltage –20 V, tube lens voltage –75 V. Unless otherwise specified, CID-MS/MS and MS^n spectra were acquired at an activation q value of 0.2 using an isolation width of 2.0 Da to obtain stable isolation of the non-covalent anionic adducts precursor ions, a normalized collision energy of 30% and an activation time of 30 ms. The spectra shown were the average of 80 scans.

For the SQDG analysis shown in chapter 6, CID MS/MS experiments were performed in negative ion mode using a collision energy of 40% for a duration of 30 ms and an activation q value of 0.2. Each spectrum was the average of 100 scans containing three microscans for each scan. Ion mapping experiments to screen for the parent ions producing the SQDG signature product ion at m/z 225.08 were performed with a step size of 0.1 in centroid mode, over the MS range of m/z 150-2000.

3.7.1.2 Pulsed-Q collision induced dissociation MS^n on a linear quadrupole ion trap

In order to address the low mass cutoff issue delimited by the activation and detection methods of CID in linear quadrupole ion trap, an alternative quick Pulsed-Q Collision Induced Dissociation (PQD) fragmentation was used to extend the mass range for fragment ion detection to a much lower value, typically m/z 50 (or as low as m/z 30)

for lipid precursor ions, via an activation pulse of high q at 0.7 followed by a quick drop of q value down to 0.05 to trap the fragments ions for detection. The efficiency of fragmentation and trapping was more sensitive to the collision energy in PQD, which was optimized at around 20% for the duration of 0.01 ms. Nearly all useful lipid fingerprint fragment ions, not including sodium or potassium adducts, could be revealed above m/z 50 in PQD MS/MS.

3.7.1.3 Analysis of lipid extracts using ESI MS and CID MS/MS on a triple quadrupole mass spectrometer

For experiments on the Thermo TSQ triple quadrupole mass spectrometer (Thermo Fisher Scientific Model TSQ, San Jose, CA) equipped with the same nanoESI ion source through direct infusion, the only difference in sample preparation was that the lipid extract was about 4 fold more concentrated, due to the lower sensitivity in the TSQ triple quad instrument, but for the autosampler chip-based nanoESI source (Advion Biosystems nanomate 100 Robot, Ithaca, NY), the lipid extracts were finally diluted in methanol: chloroform: isopropanol (1:2:4, v/v/v) containing 40 mM ammonium hydroxide prior to the analysis, and the same lipid concentration could be used as in the linear quadrupole ion trap.

On the triple quadrupole mass spectrometer (TSQ), MS was performed using heated capillary temperature 150 °C, and spray voltage 1.5 kV using the autosampler nanoESI source. The flow rate in negative ion mode was estimated to be about 0.15 μL/min. Collision-energy-resolved fragmentation curves were obtained by varying the collision energy from 0 to 80 V at a step of 5 V on the isotopically isolated precursor

ions. Optimal MS/MS fragmentation spectra for SQDG were obtained under collision gas (Ar) pressure 1.5 mTorr (q2) and collision energy 60 V unless specified otherwise. Typically Q1 and Q3 peak widths were both set at 0.5 Da. Parent ion scans for predominant signature product ion at m/z 225.08 (−ve) were then performed under such settings over the MS range of m/z 300-1500 Da. Precursor ion scans for m/z 115 (+ve) and m/z 131 (−ve) were carried out similarly for identifying ornithine lipids, and m/z 147 (+ve), m/z 129 (+ve) and m/z 145 (−ve) for glutamine lipids. The samples were all complex lipid extracts without previous separation.

3.7.1.4 Extensive identification of lipids using ESI MS^n

For the comprehensive lipid identification results to be described in Chapters 7 and 9, lipid precursor ions that had normalized relative abundances higher than 1% in MS were further examined by MS/MS and MS^n both manually and in the data-dependent acquisition mode. Automatic acquisition of MS/MS and MS^3 using data dependent acquisition was applied to examine MS/MS spectra of typically the most abundant 40 peaks detected from m/z 600-950 in MS in both positive ion and negative ion modes, and further MS^3 spectra of the ten most abundant MS/MS fragment ions.

For those lipids for which synthesized lipid standards with the same head group were available, the molecular structure of the peaks was determined by comparing the fragment ion spectra with those from the standards. For those lipids without synthesized lipid standards available, the structures were rationalized based on our knowledge of the gas-phase fragmentation behaviors of the ions formed by lipids and other molecules. In

MS/MS and MS^n, the activation q value was optimized to achieve lower mass cut off while still maintaining good sensitivity. Pulsed-Q Dissociation (PQD) MS/MS was also applied to provide additional information on the low mass fragment ions.

3.7.2 Quantification of lipids using ESI MS and MS/MS

3.7.2.1 Internal standards for lipid quantification using ESI

A lipid internal standard mixture containing GPEtn 14:0/14:0, GPGro 14:0/14:0, GPCho 14:0/14:0, $CL(14:0)_4$ at final concentrations of 4 μM, 2 μM, 2 μM and 1 μM, respectively, was applied for the absolute quantification of these types of lipids in the extract samples. The ratio of concentrations of 4/2/2/1 μM was chosen based on the relative peak abundance of the corresponding types of lipids in the actual extract sample. When the concentration of lipids applied were higher than 5 μM, singly charged homo-dimers or hetero-dimers were often observed in the m/z range of 1400-1600, complicating the spectra and interfering with the detection of cardiolipin species.

Stock solutions of 1000 μM standard lipids in chloroform (typically 1-2 mL) were prepared by quickly weighing the standard powders on a balance of detection limit 0.01 mg, and stored at −80 °C. The 1000 μM stock solutions of GPEtn(14:0/14:0), GPGro(14:0/14:0), GPCho(14:0/14:0) and $CL(14:0)_4$ were then mixed and diluted to make a 25/ 12.5/ 12.5/ 6.25 μM internal standard mixture stock solution in chloroform: methanol (1:1, v/v, typically 1 mL) and stored at −80 °C for further usage. To make the sample for quantitative mass spectrometry analysis, a certain volume of the 25/ 12.5/

12.5/ 6.25 μM internal standards mixture was added to glass vials (16 μL for the preparation of 100 μL MS sample), mixed with a certain volume of the extracts (typically 25 μL for four fold diluted MS sample of final volume 100 μL), dried under vacuum, and kept at −80 °C. Directly prior to MS infusion, they were fully redissolved with 100 μL of chloroform: methanol (1:1, v/v) containing 40 mM ammonium hydroxide.

3.7.2.2 Establishing the basis for quantification by using internal standards in ESI

To establish the basis for lipid quantification using ESI, synthesized lipid standards GPEtn 18:1/18:1, GPGro 18:1/18:1, GPCho 18:1/18:1, and $CL(18:1)_4$ were mixed at random individual concentrations from 0 to 20 μM, with the internal standard mixture of GPEtn 14:0/14:0, GPGro 14:0/14:0, GPCho 14:0/14:0 and $CL(14:0)_4$ at final concentrations of 4 μM, 2 μM, 2 μM and 1 μM, in the solvent of $CHCl_3$:CH_3OH (1:1, v/v) containing ammonium hydroxide at a final concentration of 40 mM, and the ratio of the abundance of the monoisotopic peaks of the ions formed from the 18:1 lipids over the corresponding 14:0 standards in the form of deprotonated ions, anionic adduct ion, doubly charged deprotonated ion, were plotted against the ratio of the concentrations of 18:1lipids versus the 14:0 lipids introduced in the solution to generate the calibration curve.

For the cardiolipin standards, the ratio of the isolation and corresponding fragment ions of $CL(18:1)_4$ (m/z 699) over $CL(14:0)_4$ (m/z 591) in MS/MS was also examined in automatic acquisition mode with alternative scanning of the fragment ions

of the two precursor ions under identical settings, and it was used to establish the basis for quantification using fragment ions in MS/MS.

For quantitative comparisons between the wild type and the mutants, the relative changes in the lipids were represented by the ratio of these phospholipids species to the corresponding 14:0 standards. The absolute amount of the GPEtn 18:1/18:1, GPGro 18:1/18:1, GPCho 18:1/18:1, and $CL(18:1)_4$ lipids could be calculated from slope of the calibration curve and the known concentration of the internal standards. The isotopic distribution of different type of lipids with various chain lengths were also calculated, although this level of correction was contained in the slope of the experimental calibration curve for the 18:1 lipids.

3.7.2.3 Quantification of abundant species in lipid extracts using ESI MS

Quantitative mass spectrometry experiments on lipid extracts were performed using a Thermo LTQ linear quadrupole ion trap mass spectrometer equipped with a nanospray ionization source (nanoESI). Total lipid extracts from each membrane sample were diluted by 4 fold, using $CHCl_3$:CH_3OH (1:1, v/v) containing ammonium hydroxide at a final concentration of 40 mM, and internal standards GPEtn 14:0/14:0, GPGro 14:0/14:0, GPCho 14:0/14:0, $CL(14:0)_4$ at final concentrations of 4 μM, 2 μM, 2 μM and 1 μM, respectively, prior to introduction to the mass spectrometer by direct infusion through non-coated silica tips with internal diameters of 30 μm (New Objective, Inc. Woburn, MA) at a typical flow rate of 0.3 μL/min unless specified otherwise.

Typical nanoESI conditions for quantification were: heated capillary temperature 180 °C, spray voltage 1.8 kV, capillary voltage 20 V (−20 V for negative ion mode) and tube lens voltage 75 V (−75 V for negative ion mode). Quantitative analysis of the lipids extracted from each type of sample was performed on three independent extractions, each MS spectrum being an average of 100-250 spectra with 3 micro-scans acquired per spectrum from m/z 150 to 2000, in both positive and negative ion modes. Intensities of all the ions detected in each sample were first normalized to the internal standards observed in MS, and then converted into the quantity of each lipid using conversion factors previously determined from experiments using lipid standard mixtures.

3.7.2.4 Quantification of low-abundance or overlapping species in lipid extracts using ESI CID MS/MS

ESI CID MS/MS was applied to quantify the low-abundance species or the species overlapping at the same m/z in MS using the phospholipid internal standard mixture.

Quantification of low-abundance cardiolipin undetectable in the MS spectra was based on MS/MS in negative ion mode using internal standard $CL(14:0)_4$. MS and MS/MS spectra of cardiolipin lipids for each sample were acquired using an automatic sequential acquisition experiment, during which an initial MS scan was followed by CID MS/MS (He, collision energy 30%, isolation width 1.5, activation Q value 0.2) of precursor ions of $CL(14:0)_4$ internal standard at m/z 1239.80 and of $CL(18:1)_4$ in the lipid extract at m/z 1455.96. MS/MS was acquired from m/z 320 to 2000. Over 250 cycles of such a sequence were acquired for each sample. The abundance of the major fragment

from $CL(18:1)_4$ at m/z 699 in the consequent spectrum averaged from 250 scans was normalized to that of the major fragment from internal standard $CL(14:0)_4$ at m/z 591, and the ratio was used for comparison between lipids extracted from enzyme and membrane samples from wild-type and cardiolipin-deficient *R. sphaeroides* cells.

For the normal-phosphate/low-phosphate growth experiments of 169-2.4.1 and 169CL3 strains (as well as the 37Δ4 strain) to be described with details in Chapter 10, extensive MS/MS quantification experiments were carried out using the automatic acquisition mode in both positive and negative ion mode for the regions of m/z 600-1600. For all the peaks with normalized relative abundance in MS higher than 10% including the peaks of the internal standards, the MS/MS spectra of isotopically isolated precursor ions (isolation width 1.2 Da; 0.8 Da for doubly charged ions) were collected with 50 ms maximum injection time under an MS/MS target number of 3e4 and activation q value of 0.2. For all the peaks above 1% but equal to or below 10% as well as all the internal standards again, the maximum injection time was increased to 100 ms, and the number of scans collected was increased to about four fold of those higher than 10% whenever possible. Each scan was the average of three microscans. The collision energy applied was 30% for positive ion mode and 25% for negative ion mode. One additional automatic scan was performed including the wideband isolation and activation of the cardiolipin regions using isolation width of 10 Da, and the MS/MS of all the SQDG species using collision energy of 35%, under maximum injection time of 100 ms regardless of the abundance in MS. These experiments were performed on triplicate extraction samples.

After it was found that the 100 ms maximum injection time was not sufficient for all the MS/MS below 10% to reach the target number of 3e4, these MS/MS experiments

were repeated once for each strain using maximum injection time setting of 500 ms, which was found to be sufficient for most identifiable peaks to reach the target number of 3e4 in CID MS/MS.

3.7.2.5 "Purification" and relative quantification between molecular species of the SQDG using MS/MS

A precursor ion scan mode MS/MS experiment on the triple quadrupole mass spectrometer and, similarly the various ion mapping scan options in the linear quadrupole ion trap, were applied to isolate all the SQDG molecular species from the other types of lipids in the lipids extracts, some of which overlapped at the same m/z in MS, based on the SQDG-characteristic m/z 225 (−ve) fragment ions in MS/MS. The relative abundance of these peaks in precursor ion scan MS/MS were also used to relatively quantify these SQDG molecular species containing different fatty acid chains, since these SQDG lipids fragment in CID MS/MS with similar efficiency in spite of the slight difference in the fatty acid chain composition. The experimental settings were the same as those specified above in the identification section.

3.7.3 Direct lipid analysis using MALDI-LIT

3.7.3.1 Direct lipid identification analysis using MALDI-LIT MS and MS^n

Mass spectrometry and tandem mass spectrometry analysis of isolated membranes, purified C*c*O and redissolved C*c*O protein crystals were performed using a linear quadrupole ion trap mass spectrometer equipped with a matrix-assisted laser

desorption/ionization source (model vMALDI-LTQ, Thermo Fisher Scientific, San Jose, CA).

Crystals were rinsed briefly in water at 4 °C to remove residual protein precipitate and other well-solution components loosely attached to the surface of the crystals before re-dissolving by extensive vortexing in water. One μL of either resuspended membrane (at a protein concentration of 0.25 mg/ml determined by the BCA assay using bovine serum albumin as the standard), 1 μL of purified C*c*O (25 μM), or 1 μL of redissolved C*c*O crystal solution (at a C*c*O concentration of 8.3 μM [i.e. 1.00 mg/mL] determined by the BCA assay using purified C*c*O solution with UV-Vis determined concentration as the standard) were applied to individual spots on the stainless steel sample plate and dried in air.

Subsequently, 1 μL of 0.1 M (for membrane samples) or 0.5 M (for purified enzyme and crystal samples) 2, 5-hydroxy benzoic acid dissolved in acetonitrile: water (2:1, v/v) was added. MS and MS/MS spectra were acquired in negative and positive ion modes using enhanced resonance ejection scan conditions. Typical optimal laser power setting was 20 for the positive ion mode and 30 for the negative ion mode using 2, 5-DHB as the matrix. The m/z range for MS acquisition was m/z 200-2000. MS/MS and MS^n spectra were acquired using collision induced dissociation (CID) at normalized collision energy of 30%, an isolation width of 1.2 or 1.5 Da to achieve isotopical isolation, and an activation q value of 0.2, or using PQD MS/MS fragmentation at activation q value of 0.7, isolation width 1.2 Da, collision energy around 23% optimized for individual types of lipids and the low mass limit setting at m/z 50. The spectra shown were the average of 250 scans.

3.7.3.2 Quantitative lipid comparison using MALDI-LIT MS

In order to make a relatively quantitative comparison of individual lipid contents between different strains directly using MALDI, an internal standard mixture containing GPEtn 14:0/14:0, GPGro 14:0/14:0, GPCho 14:0/14:0 and $CL(14:0)_4$ at final concentrations of 10 μM, 5 μM, 1.25 μM and 1.25 μM, respectively, in methanol was added to the membrane suspension (0.25 mg/mL final protein concentration), or the purified C*c*O solution (4.2 μM final C*c*O concentration, i.e. 0.5 mg/mL protein concentration) to form one-phase mixtures. Then 1 μL of the mixture was applied to the vMALDI plate, and dried in air, followed by the application of 1 μL of 0.1 M (for membrane samples) or 0.5 M (for purified enzyme samples) of 2, 5-DHB dissolved in acetonitrile: water (2:1, v/v). The data acquisition settings were the same as described above.

3.7.4 Optimizing the detection of lipids and subunits in purified C*c*O enzyme using MALDI-TOF MS

MALDI-TOF MS experiments on enzyme solutions without extraction were performed by MALDI delayed-extraction time-of-flight mass spectrometry (model Voyager-DE STR, PerSpective Biosystems, Framingham, MA) equipped with nitrogen laser (337 nm, 3 ns pulse). 0.8 μL of resuspended membrane or 5 μM C*c*O purified from different strains of *R. sphaeroides* was applied onto the 100-well gold coated steel MALDI plate, followed by addition of 0.8 μL 1 M 2, 5-hydroxy benzoic acid dissolved in acetonitrile: water (1:1, v/v). Adjusting the pH of the matrix solution to 7-8 by using

ammonium hydroxide was also tested. The MALDI-TOF mass spectra were collected under delayed extraction linear negative ion mode, each being an average of 100 shots.

As one method to enhance the detection of cardiolipin lipids in negative ion mode, particularly in the purified enzyme samples in MALDI-TOF, 1 μL of ammonium acetate 0.1 M solution at 4 °C was applied on top of the cocrystalized sample spots, and instantly removed with a kimwipe tissue. Ammonium chloride, ammonium citrate, ammonium hydrozide were also tested, and they were also tested by premixing them with the analyte or the matrix solutions, or letting the 1 μL solution dry on top of the cocrystal spots, but the only method found to give obvious enhancement of the detection of cardiolipin was the procedure of cold ammonium acetate washing described above.

Detection of the subunit profile of the purified C*c*O enzymes and the re-dissolved crystals was applied to monitor the incorporation of the subunits, particularly the subunit IV which had alternative forms of different lengths and could introduce a significant degree of heterogeneity to the enzyme composition. These results were eventually used to optimize the construct of C*c*O plasmid to assist crystallization of higher diffraction resolution. Matrix 2, 5-DHB was used to monitor the subunits below molecular weight 15 kDa (in the case of *R. sphaeroides*, the various forms of subunit IV), as well as the lipids in both positive and negative ion modes. ATT and SA matrices were used to detect the bigger subunits I, II and III. The relative concentrations of C*c*O and detergent were optimized and found to be critical in improving the isolation and resolution of the detection of these big hydrophobic subunits. CHCA was not chosen as the optimal matrix because it was found that this was not as efficient in detecting the subunits of

higher molecular weight, and it induced higher degree of decomposition of lipids prior to detection even at minimum laser power.

3.8 Methods used to probe the fragmentation mechanisms of lipids in CID MS^n in linear ion trap mass spectrometer

3.8.1 Synthesis and fragmentation of structural analogues

Amino acid and N-acetylated and N-propylated amino acid standards were analyzed as 100 μM solutions in H_2O:CH_3OH (1:1, v/v) containing 40 mM ammonium hydroxide.

3.8.2 H/D exchange of lipid extracts

H/D exchange of the lipid extracts was achieved by drying the original lipid extracts under vacuum and redissolving in $CDCl_3$:CD_3OD (1:1, v/v) solvent. This process was repeated twice, and 90%-99% of each lipid species of different types of lipids was fully exchanged [184].

The examination of the H/D exchanged lipid extracts was performed by using the traditional ESI source in a solvent of $CDCl_3$:CD_3OD (1:1, v/v) containing 40 mM ammonium hydroxide under conditions optimized to minimize back exchange. For 1 μL/min sample infusion flow rate, typical ESI conditions were: heated capillary temperature 180 °C, spray voltage 4.0 kV, sheath gas (N_2) flow rate 12 arbitrary units,

auxiliary gas (N_2) flow rate 15 arbitrary units and sweep gas (N_2) flow rate 10 arbitrary units. Fully H/D exchanged precursor ions for ornithine lipids, glutamine lipids, GPEtn, GPGro and SQDG lipids were examined by MS/MS and MS^n with isotopic isolation.

3.8.3 Theoretical calculations

The lowest-energy conformation for GPCho anionic adducts in Chapter 4 was calculated using semi-empirical computations at the PM3 level of theory.

Chapter 4

Multistage Tandem Mass Spectrometry of Anionic Phosphatidylcholine Lipid Adducts Reveals Novel Dissociation Pathways †

4.1 Summary

The gas-phase fragmentation reactions of various anionic adducts of phosphatidylcholine lipids have been examined by electrospray ionization and multistage tandem mass spectrometry in a linear quadrupole ion trap mass spectrometer. The CID MS/MS and MS^n fragmentation reactions of the anionic adducts were found to be highly dependent on the identity of the anions. Consistent with previous reports, MS/MS of phosphatidylcholine lipid ions formed by anionic adduction with formate, acetate and chloride resulted in a dominant product ion corresponding to the loss of $(A+CH_3)$ from the $[M+A]^-$ precursor ions. In contrast, MS/MS of other anion-adducted precursor ions gave rise to multiple products, including $[M+A-(A+CH_3)]^-$, $[M+A-(AH)]^-$, $[M+A-(AH+CH_3)]^-$, $[M+A-(AH+(CH_3)_3N)]^-$, $[M+A-(A+(CH_3)_3NCH=CH_2)]^-$ and $[M+A-(CH_3)_3N)]^-$. In order to gain evidence for the structures of these product ions, and

† Part of the results described in this chapter were published in *Int. J. Mass Spectrom.***2006**; 252: 242-255 (Zhang X and Reid GE)

the mechanisms by which they were formed, each of the products formed by MS/MS were subjected to further analysis by MS^3 and MS^4. The MS/MS and MS^n fragmentation reactions of several deuterium isotope-labeled phosphatidylcholine lipid standards, as well as authentic or structurally analogous lipid standards corresponding to the proposed product ion structures were also examined to gain evidence to support the proposed mechanisms. The results from this study indicate that great care must be taken to control the identity of the anions employed during lipid isolation, purification and separation, in order to allow the development and application of sensitive and robust neutral loss scan methods for mass spectrometry based lipid identification and quantitative analysis.

4.2 Introduction

The identification, characterization and quantitative analysis of biologically important lipids is an important step toward the development of an improved understanding of the functional role of integral phospholipids in large multi-subunit membrane protein complexes [6,34,37,63,227,228] and lipid micro domains [229-232]. In previous studies employing mass spectrometry, the observation of neutral and acidic lipid species in either positive or negative ionization mode has been found to be highly dependent on the identity of the lipid head group [110,117,140,233-235]. For example, abundant precursor ions of phosphatidylcholine (GPCho) [188] and sphingomyelin (SM) [192] lipids are readily observed in positive ion mode, while phosphatidic acid (GPA) [189], phosphatidylglycerol (GPGro) [193], phosphatidylserine (GPSer) [197], phosphatidylinositol (GPIns) [198,236] and cardiolipin (CL) [195] are observed in negative ion mode; phosphatidyl ethanolamine (GPEtn) lipids can be observed in both positive and negative ion modes, albeit at significantly lower abundance when in the presence of other lipid species [190,234,235]. This variability in ion yield as a function of lipid structure may result in poor identification and quantitative analysis capabilities for MS methods applied to complex lipid samples, and often requires two separate analyses with different optimal sample preparation methods for each ionization mode [110,117,140,233-235]. Thus, the ability to observe both neutral and acidic lipids in a single ionization mode, with high sensitivity and reproducibility, would facilitate the development of more comprehensive methods for lipid identification and quantification,

with a reduced requirement for extensive sample extraction or purification prior to analysis.

Previously, cationic adduction (e.g., Li^+, Na^+) [110,116,140,188,192,208,237] has been applied to the analyses of lipid extracts containing GPEtn, SM, GPA, GPGro, GPSer, GPIns and CL in order to enhance the sensitivity of the GPEtn, GPA, GPGro, GPSer, GPIns, and CL lipid species in positive ionization mode. However, difficulties in reproducibly forming cationic adducts, due to competition between each of the phospholipid species for adduct formation, and the possibility of di-cationic adduction in addition to mono-cationic adduction, potentially limits the applicability of this approach. In contrast, adduction with formate (HCO_2^-), acetate ($CH_3CO_2^-$) and chloride (Cl^-) anions has previously been observed to result in the selective adduction of GPCho and SM lipid species in negative ionization mode [116,135,211,235]. Dissociation of these adducts (A) by either in-source dissociation [117,238-240], or by CID MS/MS [110,116,117,135,211,241-244] has resulted in the exclusive loss of (A+15) from these ions, enabling the use of neutral loss CID MS/MS scan methods in triple quadrupole mass spectrometers for the selective identification of GPCho and SM lipid species from within complex lipid mixtures [110,135,211,244,245].

Despite the great potential of employing anionic adduction for the selective analysis of GPCho or SM lipids in negative ion mode, together with most other lipids species, the negative ion fragmentation behavior of anionic adducts of GPCho lipids have not been explored in detail, in contrast to the detailed studies previously undertaken to elucidate the mechanisms responsible for the fragmentation reactions of protonated or cationic lipid ions in positive ion mode [116,117,188,191,192,197], or for deprotonated

lipid ions in negative ion mode [117,189,190,193,195,197,198,204,246-249]. Here, in order to develop an improved understanding of the characteristic ionization and fragmentation behaviors of anionic GPCho adducts, and to take advantage of this anionic adduction for developing improved methods for lipid identification and quantification in complex mixtures, a broad range of anions have been evaluated for the formation of anionic adducts of GPCho by electrospray ionization, and characterized their fragmentation reactions by multistage tandem mass spectrometry (MS^n) in a linear quadrupole ion trap mass spectrometer. Based on these results, together with those obtained by dissociation of D-labeled lipid standards and authentic or structurally analogous lipids, mechanisms for each of the observed fragmentation reactions are proposed.

4.3 Results and Discussion

4.3.1 Dependence of the formation of anionic adducts on the phospholipid type

The tendency to form non-covalent anionic adducts was here found to be dependent on the structure of the lipid. Here GPCho, GPEtn, GPGro and CL lipid standards were examined individually as well as in a mixture, in the presence of a variety of anions at given concentrations. Individually, GPCho is the type of lipid that tends to form anionic adducts in negative ion mode the most efficiently, due to the relatively strong electrostatic interactions with the fixed positive charge in the trimethyl amine head group. However, the formation of chloride adducts of GPEtn was also observed though at much lower efficiency of formation. Simple anionic adduct ($[M+A]^-$) formation of

GPGro and CL lipids was not observable in negative ion mode. In a mixture of these lipid standards at equal concentrations, the anionic adducts of GPCho was the predominant type of anionic adducts that was observed to form.

4.3.2 Negative ion CID MS/MS of anionic adducts of GPCho 16:0/16:0 and GPCho 16:0/18:1

In order to characterize the CID MS/MS and MS^n fragmentation behavior of various anionic (A) adducts of phosphatidylcholine lipids, ammonium salts (0.1 - 10 mM) of acetate ($CH_3CO_2^-$), formate (HCO_2^-), chloride (Cl^-), bromide (Br^-), iodide (I^-), fluoride (F^-), thiocyanate (SCN^-), nitrate (NO_3^-), phosphate ($H_2PO_4^-$), hydroxide (OH^-), bicarbonate (HCO_3^-), trifluoroacetate ($CF_3CO_2^-$), benzenesulfate ($C_6H_5SO_3^-$) or sulfate (HSO_4^-) salts were added to 5 μM solutions of GPCho 16:0/16:0 (molecular weight 733) or GPCho 16:0/18:1 (molecular weight 759), then introduced to the mass spectrometer by nESI. In positive ionization mode, protonated precursor ions $[M+H]^+$ for the GPCho 16:0/16:0 and GPCho 16:0/18:1 lipid species were readily observed at m/z 734 and m/z 760, respectively. As expected, in negative ionization mode, deprotonated precursor ions $[M-H]^-$ were not observed, consistent with the presence of the 'fixed positive charge' quaternary alkyl ammonium ion within the phosphocholine head group. Instead, abundant anionic $[M+A]^-$ adducts were observed as the dominant precursor ions. The m/z values observed by adduction of GPCho 16:0/16:0 and GPCho 16:0/18:1 with

each of the anions indicated above are listed in Table 4.1, and the major fragmentations observed by MS/MS and MS^3 are summarized in Tables 4.1 and 4.2, respectively.

The product ion spectrum obtained by CID MS/MS of the $[M+A]^-$ acetate adduct ion of GPCho 16:0/16:0 is shown in Figure 4.1A. It can be seen that a single product ion at m/z 718, formed by the neutral loss of 74 Da and corresponding to the loss of (A+15), was observed as the exclusive product, consistent with previously reported in-source fragmentation [117,238-240] and CID MS/MS [110,116,117,135,211,241-245] results using triple quadrupole and quadrupole ion trap mass spectrometry instrumentation. Identical product ion spectra were observed by CID MS/MS of the formate, chloride, bromide and iodide anionic adducts of GPCho 16:0/16:0 (neutral losses of 60 Da, 50 Da, 94/96 Da and 142 Da, respectively), and for the acetate, formate and chloride adducts of GPCho 16:0/18:1.

In contrast, when 10 mM ammonium hydroxide or ammonium bicarbonate was added to the GPCho 16:0/16:0 lipid containing solutions, an abundant precursor ion at m/z 808 (+75 Da) was observed, which did not correspond to either of the expected hydroxide (+17 Da, m/z 750) or bicarbonate (+61 Da, m/z 794) adduct ions (Table 4.1). Furthermore, in contrast to that observed from the acetate, formate and chloride adducts of GPCho 16:0/16:0, CID MS/MS of the m/z 808 adduct ions (Figure 4.1B) resulted in formation of the −(A+15) product ion at a relative abundance of only 1%. Instead, the major product ions corresponded to neutral losses of (A+1), (A+16), (A+60) and (A+86) from the precursor ion. Interestingly, precursor ions corresponding to $[M-15]^-$, $[M-60]^-$ and $[M-86]^-$ ions have also been observed previously for GPCho lipids formed by fast atom bombardment (FAB) in a sector or triple quadrupole mass spectrometer under

negative ionization mode conditions when $CH_3OH/CHCl_3$ was used as the solvent and triethylamine [202,250-252] or diethylamine [253] was used as the matrix. The structures of these ions were assigned to be $[M-CH_3]^-$, $[M-(CH_3)_3N]^-$, and $[M-(CH_3)_3NCH=CH_2]^-$, respectively, using sector FAB collision assisted dissociation (CAD) MS/MS [252].

Given that ammonium hydroxide and ammonium bicarbonate are commonly employed as a pH modifier in negative ionization mode MS analysis to promote the formation of abundant $[M-H]^-$ precursor ions from neutral and acidic phospholipids such as GPEtn, GPA, GPGro, GPSer, GPIns and CL [233,234] it is important that the identity of the anionic species responsible for adduction of the GPCho phospholipids in the presence of ammonium hydroxide and ammonium bicarbonate is determined. Furthermore, as the characteristic loss of (A+15) by CID MS/MS from acetate, formate and chloride adducts of GPCho and SM have been used previously for the selective identification of these lipid species by neutral-loss scan mode analysis, the formation of this product ion at only low relative abundance due to competitive adduction of GPCho or SM with other anionic species could severely limit the sensitivity of such approaches. Therefore, in order to determine the identity of the +75 Da anionic adduct of GPCho in the presence of ammonium hydroxide and ammonium bicarbonate, and to characterize the mechanisms and resultant product ion structures formed by CID MS/MS, the formation and fragmentation reactions of a range of anionic adducts of GPCho 16:0/16:0 and GPCho 16:0/18:1 were examined by MS/MS and multistage (up to MS^4) tandem mass spectrometry.

The product ions observed by CID MS/MS of the various anionic adducts of GPCho 16:0/16:0 and GPCho 16:0/18:1 are shown in Table 4.1. The appearance and relative abundance of these product ions were observed to vary considerably, depending on the identity of the anion. The major CID MS^3 product ions are shown in Table 4.2.

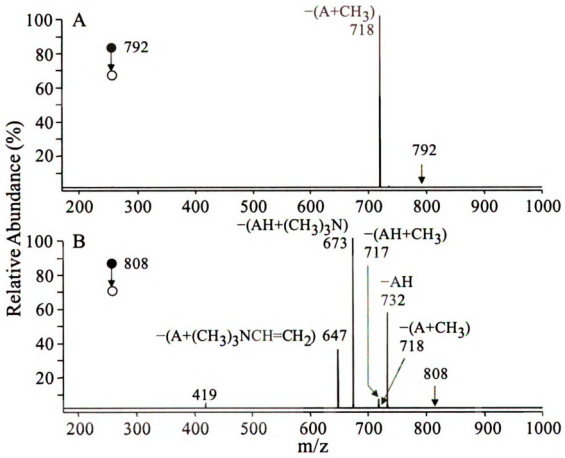


Figure 4.1 Negative ionization mode CID MS/MS product ion spectrum of the $[M+A]^-$ precursor ions of GPCho 16:0/16:0 formed by anionic adduction with (A) acetate (m/z 792) and (B) methylcarbonate (m/z 808).

Table 4.1 Negative ion mode CID MS/MS of anionic adducts of GPCho 16:0/16:0 and GPCho 16:0/18:1

GPCho Lipid	Anion (A)	Gas-Phase Acidity (kJ/mol)[a]	$[M+A]^-$ Precursor Ion (m/z)	Product Ions (% Relative Abundance)					
				$-AH$	Inter-molecular S_N2 $-(A+CH_3)$	$-(AH+CH_3)$	Inter-molecular E2 $-(AH+(CH_3)_3N)$	Intra-molecular E2 $-(A+(CH_3)_3NCHCH_2)$	Other[b]
				732	718	717	673	647	
16:0/16:0	$CH_3CO_2^-$	1427	792	—	100	—	—	—	—
	HCO_2^-	1419	778	—	100	—	—	—	—
	I^-	1293.7	860	—	100	—	—	—	—
	Br^-	1331.8	812/814	—	100	—	—	—	—
	Cl^-	1372.8	768	—	100	—	—	—	—
	F^-	1529.3	752	—	100	—	2	—	—
	SCN^-	1329	791	—	100	—	—	1	—
	NO_3^-	1329.7	795	—	100	—	1	11	$-(A+86+C_{15}H_{31}CO_2H)$ (391),1; $C_{15}H_{31}COO^-$, (255),1
	$H_2PO_4^-$	1351	830	—	100	—	3	21	$-(CH_3)_3N$,(771),1; (391),6; $C_{15}H_{31}COO^-$, (255),5
	OH^-/CH_3	ND[c]	822	64	49	2	100	40	$-(AH+59+C_{15}H_{31}CO_2$

(Table 4.1 continued)

	CH_2OH								H−2H),(419),1
	HCO_3^- / CH_3CH_2OH	ND[c]	822	65	33	5	100	41	−(AH+59+$C_{15}H_{31}CO_2$H−2H),(419),1
	OH^- / CH_3OH	ND[c]	808	62	1	6	100	36	−(AH+59+$C_{15}H_{31}CO_2$H−2H) , (419),60
	HCO_3^- / CH_3OH	ND[c]	808	61	1	7	100	34	−(AH+59+$C_{15}H_{31}CO_2$H−2H),(419),3
	$CF_3CO_2^-$	1328	846	81	1	47	100	18	−(AH+59+$C_{15}H_{31}CO_2$H−2H), (419),58; $C_{15}H_{31}COO^-$, (255),5
	$C_6H_5SO_3^-$	ND[c]	890	—	3	—	1	100	−(A+86+$C_{15}H_{31}CO_2$H),(391),1; $C_{15}H_{31}COO^-$, (255),1
				758	**744**	**743**	**699**	**673**	
16:0/ 18:1	$CH_3CO_2^-$		818	—	100	—	—	—	—
	HCO_2^-		804	—	100	—	—	—	—
	Cl^-		794	—	100	—	—	—	—
	$H_2PO_4^-$		856	—	100	—	2	19	**−$(CH_3)_3N$,(797),6**; (417),2; (391),2; $C_{15}H_{31}COO^-$, (255),2; $C_{17}H_{33}COO^-$, (281),2

(Table 4.1 continued)

	HCO_3^- / CH_3OH		834	55	1	6	100	35	−(AH+$(CH_3)_3N$+ $C_{17}H_{33}CO_2H$−2H) (419),2
	$CF_3CO_2^-$		872	79	45	57	100	18	−(AH+$(CH_3)_3N$+ $C_{17}H_{33}CO_2H$−2H) (419),24; $C_{15}H_{31}COO^-$, (255),1; $C_{17}H_{33}COO^-$, (281),2

a Gas-Phase Acidity data taken from the NIST database (http://webbook.nist.gov)

b Product ion, (m/z), % Abundance

c Not determined

Table 4.2 Summary of the negative ion mode CID MS^3 product ions of various anionic adducts of GPCho

MS^3 Precursor Ions $[M+A-(A+1)]^-$			MS^3 Product Ions m/z, relative abundance, identity
M	A^-	m/z	
GPCho 16:0/16:0	HCO_3^- / CH_3CH_2OH	732	224,<1,?; 255,100,$RCOO^-$; 269,30,R′CH=C(OCH_3)O^-; 435,4, −($N(CH_3)_3$+R′CH=C=O); 463,2,?; 476,1, −RCOOH; 494,12,−R′CH=C=O ; 717,1, $-CH_3$
	OH^-/CH_3OH	732	255,100,$RCOO^-$; 269,21,R′CH=C(OCH_3)O^-; 435,3, −(59+R′CH=C=O); 463,2,?; 476,1, −RCOOH; 494,14, −R′CH=C=O ; 717,1, $-CH_3$
	HCO_3^- / CH_3OH	732	224,<1,?; 255,100,$RCOO^-$; 269,23,R′CH=C(OCH_3)O^-; 435,4, −(59+R′CH=C=O); 463,1,?; 476,1, −RCOOH; 494,13, −R′CH=C=O ; 717,1, $-CH_3$
	$CF_3CO_2^-$	732	255,100,$RCOO^-$; 269,1,R′CH=C(OCH_3)O^-; 476,10, −RCOOH; 494,<1, −R′CH=C=O
GPCho 16:0/18:1	OH^-/CH_3OH	758	255,35,R_1COO^-; 269,6,R_1′CH=C(OCH_3)O^-; 281,100,R_2COO^-; 295,22, R_2′CH=C(OCH_3)O^-; 435,1,−(59+R_2′CH=C=O); 460,3, −(59+R_1′CH=C=O); 494,18, −R_2′CH=C=O; 520,1, −R_1′CH=C=O; 743,2,-CH_3
	HCO_3^- / CH_3OH	758	255,38,R_1COO^-; 269,10, R_1′CH=C(OCH_3)O^-; 281,100,R_2COO^-; 295,22, R_2′CH=C(OCH_3)O^-; 494,15, −R_2′CH=C=O; 520,1, −R_1′CH=C=O; 743,<1, $-CH_3$

(Table 4.2 continued)

	$CF_3CO_2^-$	758	255,32,R_1COO^-; 269,<1, $R_1'CH=C(OCH_3)O^-$; 281,100,R_2COO^-; 295,1, $R_2'CH=C(OCH_3)O^-$; 494,9,- $R_2'CH=C=O$; 520,2, $-R_1'CH=C=O$; 743,<1, $-CH_3$
GPCho d_{31}-16:0/ 18:1	OH^-/CH_3OH	789	281,100,R_2COO^-; 285,19, d_{30}-R_1COO^-; 286,54, d_{31}-R_1COO^-; 295,27, $R_2'CH=C(OCH_3)O^-$; 299,2,d_{30}-$R_1'CH=C(OCH_3)O^-$; 461,3,-328; 525,17, $-R_2'CH=C=O$; 774,2,-CH_3
GPCho d_{31}-16:0/ d_{31}-16:0	OH^-/CH_3OH	794	285,34,d_{30}-$RCOO^-$; 286,100,d_{31}-$RCOO^-$; 299,1,d_{30}-$R'CH=C(OCH_3)O^-$; 300,1, d_{30}-$R'CH=C(OCH_3)O^-$; 526,3, $-d_{30}$-$R'CH=C=O$
	OH^-/CH_3OH	793 -(AD)	285,100,d_{30}-$RCOO^-$; 286,85,d_{31}-$RCOO^-$; 299,14, d_{30}-$R'CH=C(OCH_3)O^-$; 525,5,$-d_{30}$-$R'CH=C=O$
	$CF_3CO_2^-$	794	286,100,d_{31}-$RCOO^-$; 295,1, d_{30}-$R'CH=C(OCH_3)O^-$; 526,2,$-d_{30}$-$R'CH=C=O$; 750,2, −43
d_4-GPCho 16:0/16:0	OH^-/CH_3OH	736	228,1,?; 255,100,$RCOO^-$; 269,24,$R'CH=C(OCH_3)O^-$; 438,3, $-(N(CH_3)_3+R'CH=C=O,298)$; 463,2, −273; 480,2, −RCOOH; 498,12, $-R'CH=C=O$; 721,4, $-CH_3$
	$CF_3CO_2^-$	736	255,100,$RCOO^-$; 269,2,$R'CH=C(OCH_3)O^-$; 480,2,-RCOOH; 498,19,-$R'CH=C=O$
$[M+A-(A+15)]^-$			
GPCho 16:0/16:0	$CH_3CO_2^-$	718	255,100,$RCOO^-$; 462,1, −RCOOH; 480,14, $-R'CH=C=O$
	Cl^-	718	255,100,$RCOO^-$; 462,2, −RCOOH; 480,15, $-R'CH=C=O$
	SCN^-	718	255,100,$RCOO^-$; 462,<1, −RCOOH; 480,9, $-R'CH=C=O$

(Table 4.2 continued)

	HCO_3^- /CH_3CH_2OH	718	255,100,$RCOO^-$; 462,<1, −RCOOH; 480,11, −R′CH=C=O
	HCO_3^- /CH_3OH	718	255,100,$RCOO^-$; 462,1, −RCOOH; 480,7, −R′CH=C=O
	$CF_3CO_2^-$	718	255,100,$RCOO^-$; 462,<1, −RCOOH; 480,10, −R′CH=C=O
	$H_2PO_4^-$	718	255,100,$RCOO^-$; 462,2, −RCOOH; 480,16, −R′CH=C=O
GPCho 16:0/18:1	$CH_3CO_2^-$	744	224,<1,?; 255,42,R_1COO^-; 281,100,R_2COO^-; 462,1,−R_2COOH; 480,18, −R_2′CH=C=O; 488,1, −R_1COOH; 506,4,−R_1′CH=C=O
	HCO_2^-	744	224,<1,?; 255,43,R_1COO^-; 281,100,R_2COO^-; 462,1, −R_2COOH; 480,18, −R_2′CH=C=O; 488,1, −R_1COOH; 506,4, −R_1′CH=C=O
	Cl^-	744	224,<1,?; 255,42,R_1COO^-; 281,100,R_2COO^-; 462,1,−R_2COOH; 480,17, −R_2′CH=C=O; 488,1,−R_1COOH; 506,3,−R_1′CH=C=O
	$CF_3CO_2^-$	744	255,26,R_1COO^-; 281,100,R_2COO^-; 462,1,−R_2COOH; 480,8,−R_2′CH=C=O; 488,1,−R_1COOH; 506,2,−R_1′CH=C=O
	$H_2PO_4^-$	744	224,<1,?; 255,37,R_1COO^-; 281,100,R_2COO^-; 462,1,−R_2COOH; 480,20,−R_2′CH=C=O; 488,1,−R_1COOH; 506,4,−R_1′CH=C=O
GPCho d_{31}-16:0/ 18:1	$CH_3CO_2^-$	775	281,100,R_2COO^-; 282,21,d_1-R_2COO^-; 285,16,d_{30}-R_1COO^-; 286,52,d_{31}-R_1COO^-; 511,21,−R_2′CH=C=O
	$H_2PO_4^-$	775	281,100,R_2COO^-; 282,18,d_1-R_2COO^-; 285,15,d_{30}-R_1COO^-; 286,51,d_{31}-R_1COO^-; 488,1,?; 493,2,?; 507,2,?; 511,25,−R_2′CH=C=O

(Table 4.2 continued)

GPCho d_{31}-16:0/ d_{31}-16:0	$CH_3CO_2^-$	780	285,21,d_{30}-$RCOO^-$; 286,100,d_{31}-$RCOO^-$; 512,2, $-d_{30}$-R′CH=C=O
	$CF_3CO_2^-$	780	286,100,d_{31}-$RCOO^-$; 512,2,$-d_{30}$-R′CH=C=O
	$H_2PO_4^-$	780	285,21,d_{30}-$RCOO^-$; 286,100,d_{31}-$RCOO^-$; 287,12,d_{32}-$RCOO^-$; 493,1,?; 512,9, $-d_{30}$-R′CH=C=O
d_4-GPCho 16:0/16:0	$CH_3CO_2^-$	722	255,100,$RCOO^-$; 466,2, −RCOOH, 484,18, −R′CH=C=O
	Cl^-	722	255,100,$RCOO^-$; 466,2, −RCOOH, 484,18, −R′CH=C=O
	$CF_3CO_2^-$	722	255,100,$RCOO^-$; 466,2, −RCOOH, 484,18, −R′CH=C=O
[M+A−(A+16)]$^-$			
GPCho 16:0/16:0	HCO_3^- /CH_3CH_2OH	717	255,4,$RCOO^-$; 419,23, −(RCOO+43); 462,100, −RCOO; 480,2, −RCOO; 673,21, $-CH_3NCH_3$; 728,22, $-CH_3$
	OH^-/CH_3OH	717	255,2,$RCOO^-$; 419,23, −(RCOO+43); 462,100, −RCOO; 480,1, −RCOO; 673,19, $-CH_3NCH_3$; 728,14, $-CH_3$
	HCO_3^-/ CH_3OH		255,4,$RCOO^-$; 419,25, −(RCOO+43); 462,100, −RCOO; 480,2, −RCOO; 673,22, $-CH_3NCH_3$; 728,15, $-CH_3$
	$CF_3CO_2^-$	717	255,3,$RCOO^-$; 419,28,-(RCOO+43); 462,100, −RCOO; 480,2, −RCOO; 673,26, $-CH_3NCH_3$; 728,17, $-CH_3$
GPCho 16:0/18:1	OH^-/CH_3OH	743	(low abundance) 462,100, $-R_2COO$; 699,22, $-CH_3NCH_3$; 728,67, $-CH_3$
	HCO_3^-/ CH_3OH	743	255,23,R_1COO^-; 281,43,R_2COO^-; 462,100, $-R_2COO$; 699,23, $-CH_3$-NCH_3; 728,57, $-CH_3$

(Table 4.2 continued)

	$CF_3CO_2^-$	743	255,23,R_1COO^-; 281,11,R_2COO^-; 462,100, $-R_2COO$; 480,18, −263; 699,28, $-CH_3NCH_3$; 728,18, $-CH_3$
GPCho d_{31}-16:0/ 18:1	OH^-/CH_3OH	774	281,10,R_2COO^-; 286,12,d_{31}-R_1COO^-; 493,100, $-R_2$ COO; 511,17,?; 730,20, $-CH_3NCH_3$; 764,19, $-CH_3$
GPCho d_{31}-16:0/ d_{31}-16:0	OH^-/CH_3OH	779	286,27, $RCOO^-$; 450,15, −(RCOO+43); 493,100, −RCOO; 735,36, $-CH_3NCH_3$; 764,32, $-CH_3$
	$CF_3CO_2^-$	779	286,14, $RCOO^-$; 450,27, −(RCOO+43); 493,100, −RCOO; 735,9, $-CH_3NCH_3$; 764,20, $-CH_3$
d_4-GPCho 16:0/16:0	OH^-/CH_3OH	721	255,7,$RCOO^-$; 423,27, −(RCOO+43); 466,100, −RCOO; 484,2, −RCOO; 677,6, $-CH_3NCH_3$; 706,27, $-CH_3$
	$CF_3CO_2^-$	721	255,7,$RCOO^-$; 423,25, −(RCOO+43); 466,100, −RCOO; 484,4, −RCOO; 677,5,$-CH_3NCH_3$; 706,23,$-CH_3$
$[M+A-(A+60)]^-$			
GPCho 16:0/16:0	HCO_3^-/ CH_3CH_2OH	673	255,100,$RCOO^-$; 417,1,−R′CH=C=O ; 435,6,−RCOOH
	OH^-/CH_3OH	673	255,100,$RCOO^-$; 417,1, −R′CH=C=O ; 435,6, −RCOOH
	HCO_3^- /CH_3OH	673	255,100,$RCOO^-$; 417,2, −R′CH=C=O ; 435,6, −RCOOH
	$CF_3CO_2^-$	673	255,100,$RCOO^-$; 417,2, −R′CH=C=O ; 435,6, −RCOOH
	$H_2PO_4^-$	673	237,1,(RCOOH-H_2O); 255,100,$RCOO^-$; 417,2, −R′CH=C=O ; 435,10, −RCOOH

(Table 4.2 continued)

GPCho 16:0/18:1	OH^-/CH_3OH	699	255,44,R_1COO^-; 281,100,R_2COO^-; 435,8, $-R_2'CH=C=O$; 443,1, $-R_1COOH$; 461,1, $-R_1'CH=C=O$
	HCO_3^-/ CH_3OH	699	255,43,R_1COO^-; 281,100,R_2COO^-; 417,<1,$-R_2COOH$; 435,9,$-R_2'CH=C=O$; 443,1,$-R_1COOH$; 461,1, $-R_1'CH=C=O$
	$CF_3CO_2^-$	699	255,40,R_1COO^-; 281,100,R_2COO^-; 417,<1,$-R_2COOH$; 435,3,$-R_2'CH=C=O$; 443,<1,$-R_1COOH$; 461,<1,$-R_1'CH=C=O$
	$H_2PO_4^-$	699	255,38,R_1COO^-; 281,100,R_2COO^-; 417,2,$-R_2COOH$; 435,11,$-R_2'CH=C=O$; 443,4,$-R_1COOH$; 461,2,$-R_1'CH=C=O$
GPCho d_{31}-16:0/ 18:1	OH^-/CH_3OH	730	281,100,R_2COO^-; 282,20,d_1-R_2COO^-?; 285,15,d_{30}-R_1COO^-; 286,56,d_{31}-R_1COO^-; 466,9,$-R_2COOH$
	OH^-/CH_3OH	729 -(AD+59)	281,100,R_2COO^-; 282,7,d_1-R_2COO^-?; 285,4,d_{30}-R_1COO^-; 286,55,d_{31}-R_1COO^-; 465,4,$-R_2COOH$
	$H_2PO_4^-$	730	281,100,R_2COO^-; 282,19,d_1-R_2COO^-?; 285,17,d_{30}-R_1COO^-; 286,44,d_{31}-R_1COO^-; 466,12, $-R_2COOH$; 461.9,5, $-R_1COOH$
GPCho d_{31}-16:0/ d_{31}-16:0	OH^-/CH_3OH	735	285,20,d_{30}-R_1COO^-; 286,56,d_{31}-R_1COO^-; 467,9, $-d_{30}$-$R'CH=C=O$
	OH^-/CH_3OH	734 −(AD+59)	285,100,d_{30}-R_1COO^-; 286,90,d_{31}-R_1COO^-; 466,1, $-d_{30}$-$R'CH=C=O$
	$H_2PO_4^-$	735	285,16,d_{30}-R_1COO^-; 286,100,d_{31}-R_1COO^-;287,13,d_{32}-R_1COO^- ?; 448,2,?; 467,4, $-d_{30}$-$R'CH=C=O$

$[M+A-(A+61)]^-$

(Table 4.2 continued)

d_4-GPCho 16:0/16:0	OH^-/CH_3OH	676 −(AD+59)	255,100,$RCOO^-$; 420,3, −RCOOH; 438,8, −R′CH=C=O
	$CF_3CO_2^-$	676 −(AD+59)	255,100,$RCOO^-$; 420,2, −RCOOH; 438,8, −R′CH=C=O
$[M+A-(A+59)]^-$			
GPCho 16:0/18:1	$CF_3CO_2^-$	700	255,13,R_1COO^-; 281,4,R_2COO^-; 419,100, $-R_2COO$; 437,20, −263; 445,7, $-R_1COO$
$[M+A-(A+86)]^-$			
GPCho 16:0/16:0	NO_3^-	647	153,4,$PO_4(CH_2)_2^-$; 255,43,$RCOO^-$; 391,100, −RCOOH; 409,10, −R′CH=C=O
	HCO_3^-/ CH_3CH_2OH	647	153,5,$PO_4(CH_2)_2^-$; 255,41,$RCOO^-$; 391,100, −RCOOH; 409,21, −R′CH=C=O
	OH^-/CH_3OH	647	153,7, $PO_4(CH_2)_2^-$; 255,44,$RCOO^-$; 391,100, −RCOOH; 409,23, −R′CH=C=O
	HCO_3^- /CH_3OH	647	153,6, $PO_4(CH_2)_2^-$; 255,42,$RCOO^-$; 391,100, −RCOOH; 409,23, −R′CH=C=O
	$CF_3CO_2^-$	647	153,2, $PO_4(CH_2)_2^-$; 255,30,$RCOO^-$; 391,100,−RCOOH; 409,15,−R′CH=C=O
	$H_2PO_4^-$	647	153,8, $PO_4(CH_2)_2^-$; 255,39,$RCOO^-$; 391,100, −RCOOH; 409,26, −R′CH=C=O
GPCho 16:0/18:1	OH^-/ CH_3OH	673	153,2, $PO_4(CH_2)_2^-$; 255,36,R_1COO^-; 281,12,R_2COO^-; 391,100, $-R_2COOH$; 409,18, $-R_2'CH=C=O$; 417,44, $-R_1COOH$; 435,1, $-R_1'CH=C=O$

(Table 4.2 continued)

	HCO_3^-/ CH_3OH	673	153,3, $PO_4(CH_2)_2^-$; 255,42,R_1COO^-; 281,13,R_2COO^-; 391,100, $-R_2COOH$; 409,30, $-R_2'CH=C=O$; 417,38, $-R_1COOH$; 435,2, $-R_1'CH=C=O$
	$CF_3CO_2^-$	673	153,2, $PO_4(CH_2)_2^-$; 255,41,R_1COO^-; 281,12,R_2COO^-; 391,100, $-R_2COOH$; 409,26, $-R_2'CH=C=O$; 417,29, $-R_1COOH$; 435,2, $-R_1'CH=C=O$
	$H_2PO_4^-$	673	153,6, $PO_4(CH_2)_2^-$; 255,36,R_1COO^-; 281,14,R_2COO^-; 391,100, $-R_2COOH$; 409,29, $-R_2'CH=C=O$; 417,42, $-R_1COOH$; 435,5, $-R_1'CH=C=O$
GPCho d_{31}-16:0/ 18:1	OH^-/CH_3OH	704	281,10,R_2COO^-; 284,5,d_{29}-R_2COO^-; 285,58,d_{30}-R_1COO^-; 286,37,d_{31}-R_1COO^-; 417,26, $-d_{31}$-R_1COOH; 420,7,$-d_1$-R_2COOH; 421,100,$-R_2COOH$; 422,96, $-R_2COOH$; 440,20,$-R_2'CH=C=O$
	OH^-/CH_3OH	703(−D)	281,7,R_2COO^-; 284,7,d_{29}-R_2COO^-; 285,35,d_{30}-R_1COO^-; 417,11, $-d_{31}$-R_1COOH; 420,37, $-d_1$-R_2COOH; 421,100, $-R_2COOH$; 439,27, $-R_2'CH=C=O$
	$H_2PO_4^-$	704	281,15,R_2COO^-; 282,7,R_2COO^-; 284,11,d_{29}-R_2COO^-; 285,44,d_{30}-R_1COO^-; 286,42,d_{31}-R_1COO^-; 417,35, $-d_{31}$-R_1COOH; 418,14, $-d_{32}$-R_1COOH; 420,15, $-d_1$-R_2COOH; 421,88,$-d_1$-R_2COOH; 422,100,$-R_2COOH$; 439,12,$-d_1$-$R_2'CH=C=O$; 440,44,$-R_2'CH=C=O$

(Table 4.2 continued)

GPCho d_{31}-16:0/ d_{31}-16:0	OH^-/CH_3OH	709	285,17,d_{30}-$RCOO^-$; 286,35,d_{31}-$RCOO^-$; 421,52,–d_{30}-RCOOH; 422,100,–d_{31}-RCOOH; 441,11,–d_{30}-R′CH=C=O
	$H_2PO_4^-$	709	285,35,d_{30}-$RCOO^-$; 286,52,d_{31}-$RCOO^-$; 421,53, –d_1-RCOOH; 422,100, –RCOOH; 441,26, –d_{30}-R′CH=C=O
$[M+A-(A+89)]^-$			
d_4-GPCho 16:0/16:0	OH^-/CH_3OH	648	153,11, $PO_4(CH_2)_2^-$;154,3, d_1-$PO_4(CH_2)_2^-$; 255,32,$RCOO^-$; 256,21,d_1-$RCOO^-$; 391,100, –RCOOH; 392,65, –d_1-RCOOH; 409,7, –d_1-R′CH=C=O; 410,45, –R′CH=C=O
	$CF_3CO_2^-$	648	153,13, $PO_4(CH_2)_2^-$;154,6, d_1-$PO_4(CH_2)_2^-$; 255,42,$RCOO^-$; 256,34,d_1-$RCOO^-$; 391,100, –RCOOH; 392,78, –d_1-RCOOH; 409,11, –d_1-R′CH=C=O; 410,56, –R′CH=C=O
$[M+A-59]^-$			
GPCho 16:0/16:0	$H_2PO_4^-$	771	255,4, $RCOO^-$; 391,16, –(RCOOH+$HPO_4CH_2CH_2$); 409,2, –(R′CH=C=O+$HPO_4CH_2CH_2$); 647,100, –$HPO_4CH_2CH_2$; 711,12,?
GPCho 16:0/18:1	$H_2PO_4^-$	797	255,4,R_1COO^-; 281,2,R_2COO^-; 391,11, –(R_2COOH+$HPO_4CH_2CH_2$); 409,2, –(R_2′CH=C=O+$HPO_4CH_2CH_2$); 417,6, –(R_1COOH+$HPO_4CH_2CH_2$); 647,100, –$HPO_4CH_2CH_2$

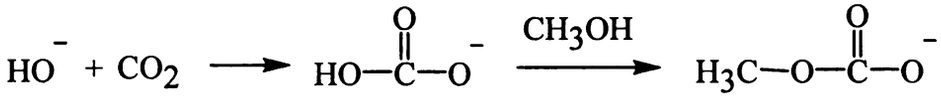
(Table 4.2 continued)

GPCho d_{31}-16:0/ 18:1	$H_2PO_4^-$	828	286,3,d_{31}-R_1COO^-; 281,1,R_2COO^-; 417,3, −(d_{31}-R_1COOH+$HPO_4CH_2CH_2$); 422,11, − (R_2COOH+$HPO_4CH_2CH_2$); 440,3, −($R_2'CH$=C=O+$HPO_4CH_2CH_2$); 704,100, −$HPO_4CH_2CH_2$; 768,2,?
GPCho d_{31}-16:0/ d_{31}-16:0	$H_2PO_4^-$	833	286,5,d_{31}-$RCOO^-$; 422,15, −(d_{31}-RCOOH+$HPO_4CH_2CH_2$); 440,1, −(d_{30}-R'CD=C=O+$HPO_4CH_2CH_2$); 709,100, −$HPO_4CH_2CH_2$; 773,1,?
d_4-GPCho 16:0/16:0	$H_2PO_4^-$	775	255,3,$RCOO^-$; 391,18,−(RCOOH+$HPO_4CD_2CD_2$); 409,2, −(R'CH=C=O+$HPO_4CD_2CD_2$); 647,100, −($HPO_4CD_2CD_2$); 715,5,?
[M+A−(AH+$N(CH_3)_3$+16:0COOH)]$^-$			
GPCho 16:0/16:0	HCO_3^-/ CH_3OH	419	125,25,?; 163,6,?; 255,28,$RCOO^-$; 363,100,−56
	$CF_3CO_2^-$	419	125,37,?; 163,9,?; 179,4,?; 255,50,$RCOO^-$; 363,100,−56
GPCho 16:0/18:1	OH^-/ CH_3OH	419	(low abundance)125,40,?; 255,100,R_1COO^-
	HCO_3^-/ CH_3OH	419	125,37,?; 163,8,?; 179,4,?; 255,50,R_1COO^-; 363,100,−56
	$CF_3CO_2^-$	419	125,21,?; 163,6,?; 179,4,?; 255,38,R_1COO^-; 363,100,−56
GPCho d_{31}-16:0/ 18:1	OH^-/CH_3OH	450	125,9,?; 126,8,?; 163,6,?; 224,4,?; 286,78,d_{31}-R_1COO^-; 394,100,−56

(Table 4.2 continued)

d_4-GPCho 16:0/16:0	OH^-/CH_3OH	423	129,44,d_4-?; 167,12, d_4-?; 255,31,$RCOO^-$; 367,100,−56
	$CF_3CO_2^-$	423	129,44,d_4-?; 167,9, d_4-?; 255,33,$RCOO^-$; 367,100,−56
$[M+A-(28+AH+N(CH_3)_3+R_1COOH)]^-$			
GPCho 16:0/18:1	$H_2PO_4^-$	417	153,30,$PO_4(CH_2)_2^-$; 281,100, R_2COO^-
GPCho d_{31}-16:0/ 18:1	$H_2PO_4^-$	417	153,17,$PO_4(CH_2)_2^-$; 281,100, R_2COO^-
$[M+A-(28+AH+N(CH_3)_3+16:0\ RCOOH)]^-$			
GPCho 16:0/16:0	$H_2PO_4^-$	391	97,<1,$H_2PO_4^-$; 153,28,$PO_4(CH_2)_2^-$; 255,100, $RCOO^-$
GPCho 16:0/18:1	$H_2PO_4^-$	391	153,30,$PO_4(CH_2)_2^-$; 255,100, R_1COO^-
GPCho d_{31}-16:0/ 18:1	$H_2PO_4^-$	422	153,12,$PO_4(CH_2)_2^-$; 286,100,d_{31}-R_2COO^-

When ethanol was employed in the lipid containing solutions, the $[M+A]^-$ adduct ions from GPCho 16:0/16:0 and GPCho 16:0/18:1 in the presence of ammonium hydroxide or ammonium bicarbonate were observed at m/z values 14 Da higher, i.e., an adduct mass of 89 Da, compared to 75 Da when methanol was used, indicating that the alcohol was involved in formation of the adduct. Thus, the +75 and +89 Da adduct ions observed in the presence of ammonium hydroxide or ammonium bicarbonate are proposed to be formed by the process shown in Scheme 4.1, involving reaction of the hydroxide anion with atmospheric CO_2 to initially form the bicarbonate anion, followed by reaction with methanol or ethanol in the solvent to yield a methylcarbonate (75 Da) or ethylcarbonate (89 Da) anion, respectively.



Scheme 4.1 Formation of methyl carbonate anion

4.3.3 CID MS^3 experiments to probe the structure of the product ions formed by neutral loss of (A+15) from the anionic adducts of GPCho

MS^3 of all the product ions formed by the loss of (A+15) from each of the anionic adducts were found to yield identical product ion spectra, indicating the formation of a common product ion in each case. Previous studies have proposed that the loss of (A+15) from the acetate, formate or chloride adducts of GPCho occurs via methyl group transfer from the quaternary alky ammonium ion on the phosphatidylcholine head group of the GPCho lipid to the anion, resulting in the formation of an N, N-dimethyl-

phosphatidylethanolamine lipid species [110,116,117,135,211,238,241-244] (Scheme 4.2). To confirm this here, the MS^3 spectra of the −(A+15) neutral loss product ion obtained by MS/MS of the GPCho 16:0/16:0 acetate anionic adduct (Figure 4.2A) was compared with the MS/MS product ion spectrum of an authentic N, N-dimethyl-phosphatidylethanolamine 16:0/16:0 lipid ion prepared in solution and introduced to the mass spectrometer by nESI (Figure 4.2B). It can be seen from Figure 4.2 that the product ion spectra are identical, indicating that the loss of (A+15) does correspond to formation of an $[M+A-(A+CH_3)]^-$ product ion as a result of methyl group transfer from the phosphocholine head group to the anion.

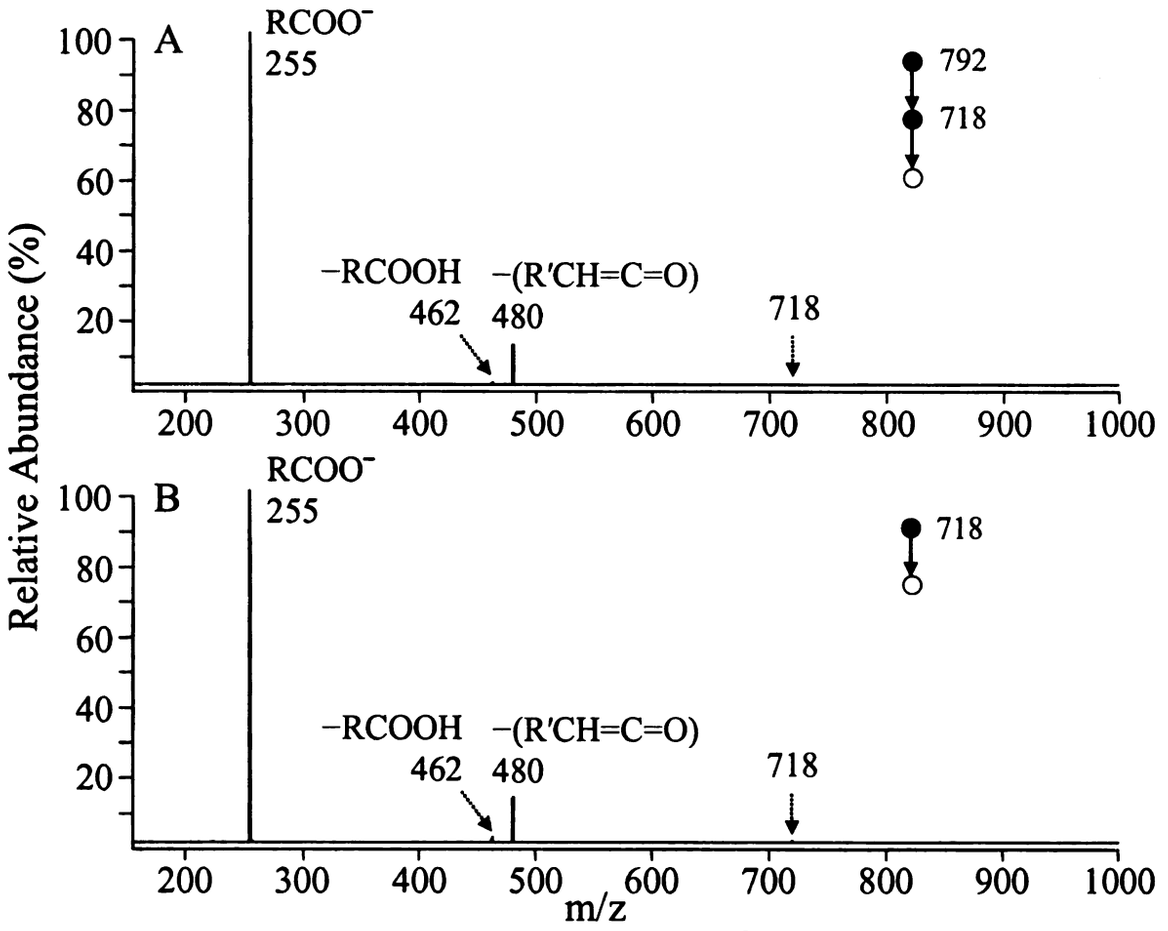
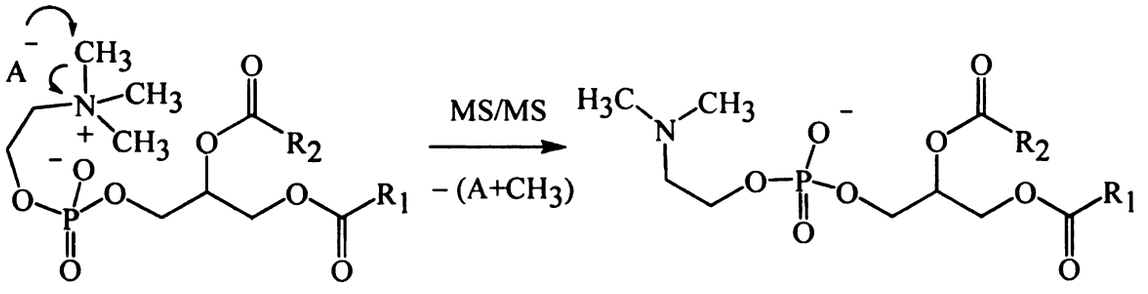


Figure 4.2 Negative ionization mode (A) CID MS^3 product ion spectrum of the m/z718 product ion formed via the neutral loss of ($A+CH_3$) from the acetate adduct of GPCho 16:0/16:0 in Figure 4.1A. (B) CID MS/MS product ion spectrum of the $[M-H]^-$ precursor ion of N, N-dimethylphosphatidylethanolamine 16:0/16:0.



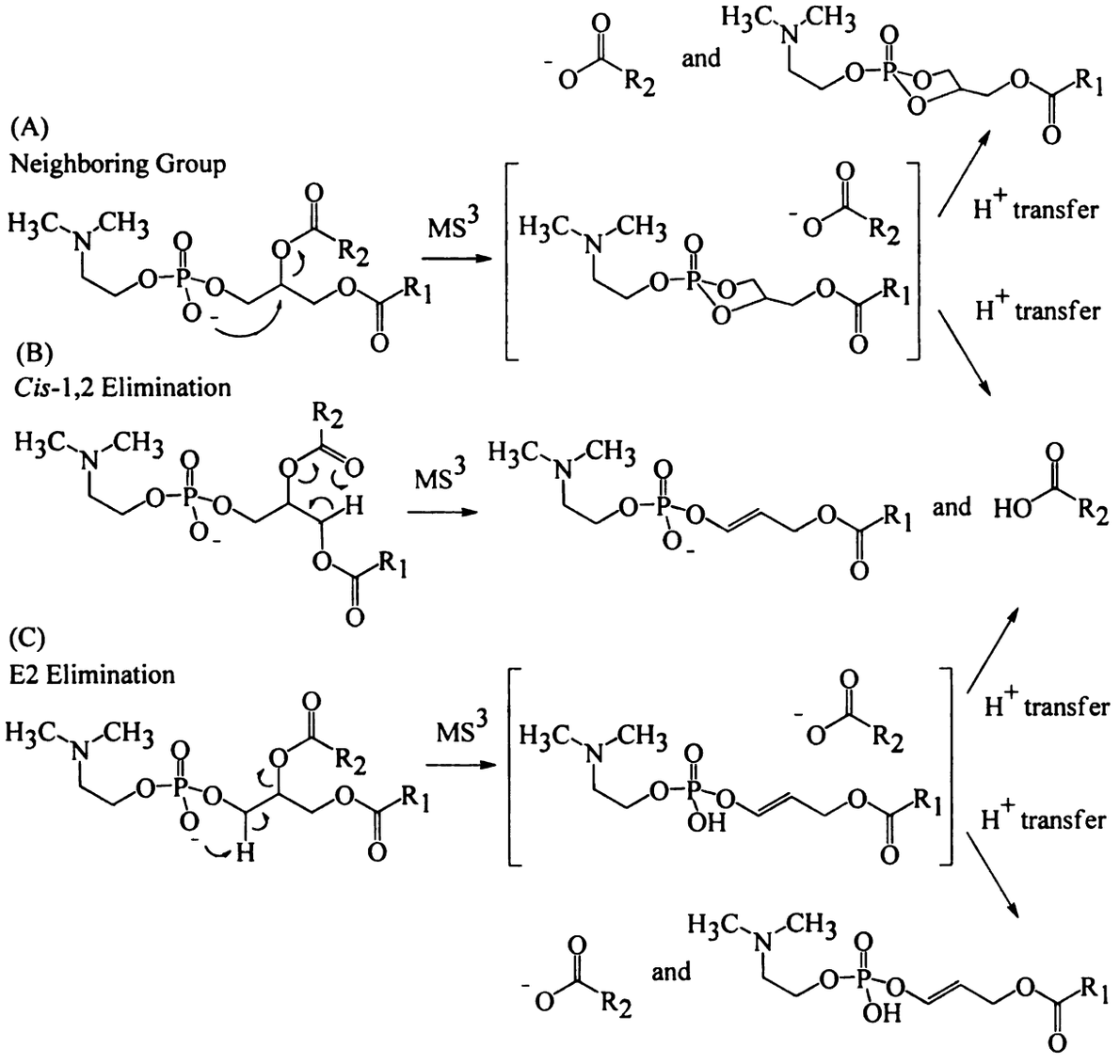
Scheme 4.2 Proposed MS/MS fragmentation pathway of $[GPCho+A]^-$ to lose ($A+CH_3$)

The major product ion (m/z 255) observed in Figure 4.2 corresponds to the formation of $RCOO^-$, by dissociation of one of the two ester linkages of the fatty acid chains within the 16:0/16:0 phospholipid ion. A product ion corresponding to the loss of the neutral fatty acid chain (−RCOOH, m/z 462) was also observed at low abundance. The R group is used here to indicate the fatty acid chain without specifying its origin from either the *sn-1* or *sn-2* position of the glycerol backbone, i.e., the $RCOO^-$ m/z 255 product ion in Figure 4.2 represents $C_{15}H_{31}COO^-$. For the 16:0/18:1 phospholipids, the origin of the fatty acid chain is specified by a subscript notation, i.e., R_1COO^- represents a fatty acid product ion formed by dissociation at the *sn-1* position of the glycerol backbone. A potential mechanism for formation of the $RCOO^-$ and − (RCOOH) product ions, via a 'charge-directed' neighboring group participation reaction mechanism involving nucleophilic attack from the phosphate oxygen anion at an electrophilic carbon adjacent to the fatty acid ester linkage on the glycerol backbone, resulting in the formation of an initial ion-neutral complex, is shown in Scheme 4.3A [117,189,190,198,204,247,249,254]. Simple dissociation of this ion-neutral complex would result in formation of the $RCOO^-$ product ion, and loss of an RCOOH neutral would be observed if intermolecular proton transfer within the complex occurs prior to its separation (note that only one of the possible pathways for proton transfer is shown). The relative abundances of the two product ions would therefore be expected to be dependent on the lifetime of the ion-neutral complex, and the relative gas-phase acidities of the two neutral species that may be formed. Note that only the pathway for the elimination of the *sn-2* fatty acid chain, via a 5-membered transition state is shown in Scheme 4.3.

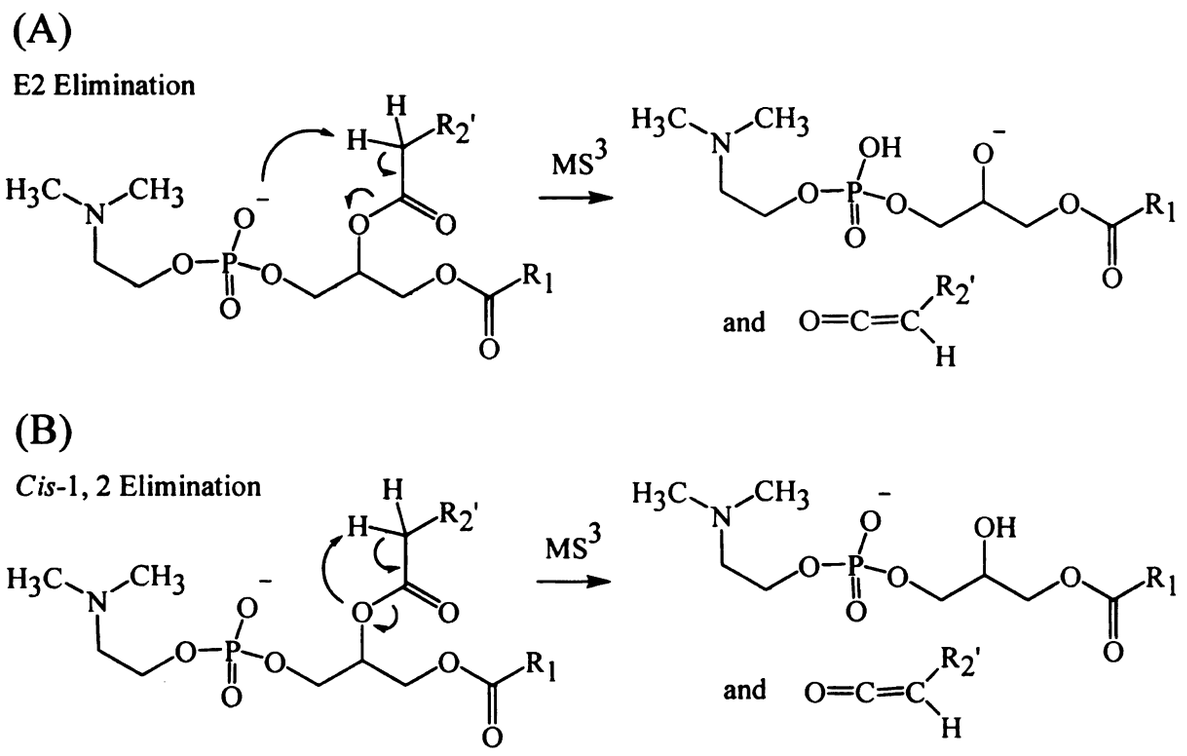
Fragmentation of the *sn-1* fatty acid chain would proceed via a similar mechanism, involving a 6-membered transition state. A 'charge-remote' mechanism involving a *cis*-1, 4 elimination pathway has also been proposed previously for formation of the −(RCOOH) product ions from the dissociation of deprotonated phospholipids (Scheme 4.3B) [190]. An alternative mechanism involving the formation of an ion-neutral complex following a 'charge-directed' E2 elimination reaction could also be used to explain the formation of these product ions (Scheme 4.3C). It is not possible from the studies performed here to distinguish between the neighboring group participation and E2 elimination reaction pathways, as the product ion structures in each case would be identical. It has been noted that a possible way of resolving this issue would be to examine the fragmentation reactions of a multiply charged precursor ion of the GPCho adduct, that contains an inert charge on the neutral species lost from the singly charged GPCho adduct, resulting in the formation of structurally distinct product ions amenable to further analysis [255]. The presence of the *cis*-1, 4 elimination pathway could potentially be determined via deuterium labeling of the glycerol backbone.

The product ion observed at m/z 480 in Figure 4.2 corresponds to loss of one of the 16:0 fatty acid chains as a neutral ketene $C_{14}H_{29}CHCO$ (labeled as −(R′CH=C=O)). Note that the R (or R_1 or R_2 for *sn-1* and *sn-2* specific fatty acid chain linkages) group is used here to indicate the presence of the alkyl chain. Formation of this ketene neutral-loss product ion may potentially occur via a 'charge-directed' E2 elimination reaction, initiated by nucleophilic attack from the phosphate oxygen anion to one of the α-hydrogens adjacent to the carboxyl group on the fatty acid chains (Scheme 4.4A), or by a 'charge-remote' 4-membered *cis*-1, 2 elimination reaction mechanism (Scheme 4.4B)

[189,193,246-248]. However, it is difficult to distinguish between these mechanistic possibilities, for example by the use of deuterium isotope labeling or further MS^n dissociation, due to the likelihood of intramolecular proton transfer occurring within the resultant product ions.



Scheme 4.3 Proposed MS^3 fragmentation pathways of $[GPCho+A-(A+CH_3)]^-$ to form $RCOO^-$ or neutral RCOOH



Scheme 4.4 Proposed MS^3 fragmentation pathways of $[GPCho+A-(A+CH_3)]^-$ to form ketene neutral loss

4.3.4 Deuterium isotope labeling and CID MS^3 experiments to probe the structure of the product ions formed by neutral loss of (A+60) from the anionic adducts of GPCho

In order to determine the structure of the product ion formed by loss of (A+60) from the anionic adducts of GPCho 16:0/16:0, the CID MS/MS fragmentation behavior of a d_4-labeled derivative of GPCho 16:0/16:0, where the deuterium labels are incorporated into the CH_2CH_2 positions of the phosphocholine head group, was examined. From the product ion spectrum obtained by CID MS/MS of the methylcarbonate adduct of d_4-GPCho 16:0/16:0 (m/z 812, Figure 4.3A) formed by

addition of 10 mM ammonium hydroxide to the lipid containing solution of $CH_3OH/CHCl_3$, the loss of (A+61) was observed at m/z 676, in contrast to the loss of (A+60) observed at m/z 673 for the GPCho 16:0/16:0 ion in Figure 4.1B, indicating that one of the deuterium labels in the phosphocholine head group of the d_4-GPCho 16:0/16:0 lipid was lost from the resultant product ion during the fragmentation reaction. Based on this, a mechanism for formation of the $[M+A-(AH+(CH_3)_3N)]^-$ vinyl phosphatidic acid product ion, by deprotonation of the methylene group adjacent to the phosphate via an E2 elimination reaction initiated by the anion, is proposed in Scheme 4.5.

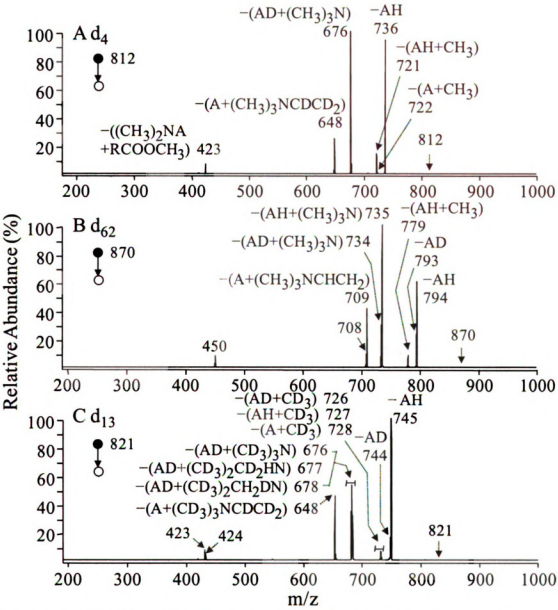
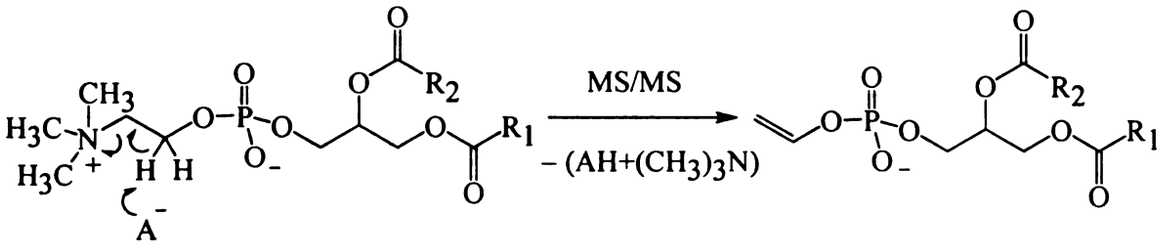


Figure 4.3 Negative ionization mode CID MS/MS product ion spectra of the methylcarbonate adducts of (A) d_4-GPCho 16:0/16:0 (m/z 812), (B) GPCho d_{31}-16:0/d_{31}-16:0 (m/z 870) and (C) d_{13}-GPCho 16:0/16:0 (m/z 821).



Scheme 4.5 Proposed MS/MS fragmentation pathway of $[GPCho+A]^-$ to lose $(AH+(CH_3)_3)N)$

MS^3 of all the product ions formed by the loss of $(AH+(CH_3)_3N)$ from each of the anionic adducts were found to yield identical product ion spectra, indicating the formation of a common product ion. To obtain further evidence to support the proposed vinyl phosphatidic acid product ion structure, the MS^3 spectrum obtained from the m/z 673 product ion of the GPCho 16:0/16:0 methylcarbonate adduct in Figure 4.1B (Figure 4.4A) was compared to the MS/MS fragmentation behavior of a structurally related lipid analog, phosphatidylethanol 16:0/16:0 (m/z 675) (Figure 4.4B). The difference of one double bond in the head group did not affect the fragmentation reactions observed for these structurally analogous ions. Indeed, aside from a 2-Da mass shift observed between the product ions containing the head group, the same fragmentation pathways and essentially identical product ion abundances were observed for both spectra, consistent with the proposed product ion structure. Furthermore, the product ions observed in Figure 4.4 correspond to the same fragmentation pathways, and similar product ion abundances, to those observed in Figure 4.2, indicating that neither of the head groups of the proposed

$-(A+CH_3)$ and $-(AH+(CH_3)_3N)$ neutral loss product ion structures are involved in their subsequent MS^3 fragmentation reactions.

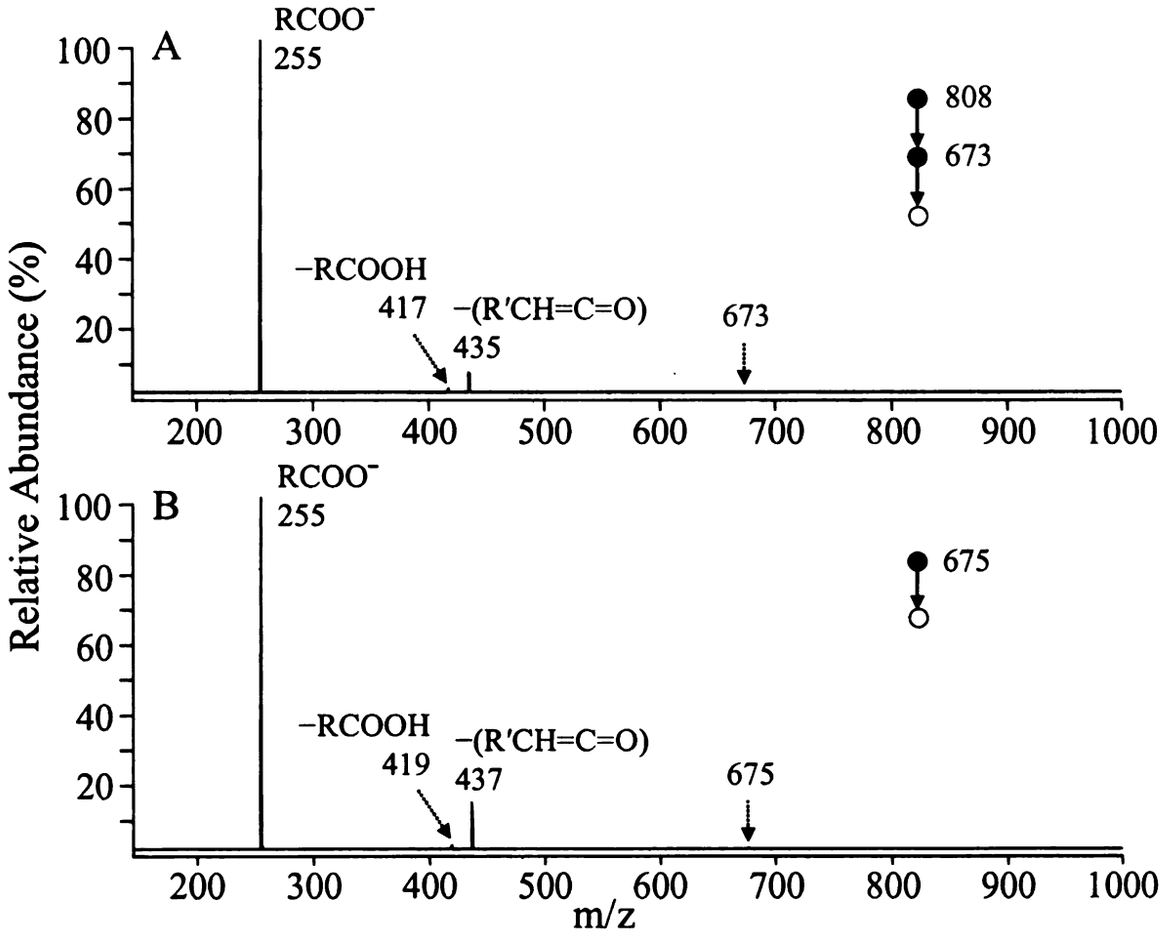
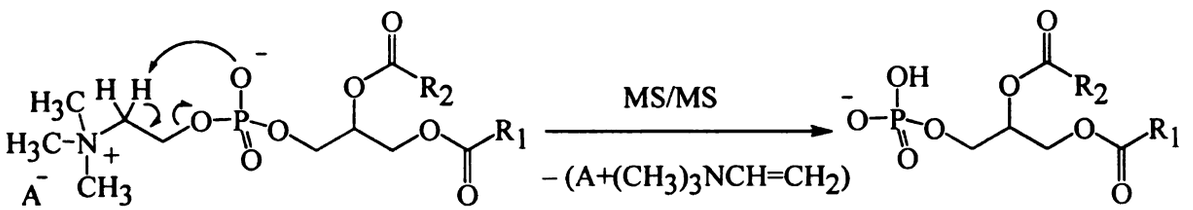


Figure 4.4 Negative ionization mode (A) CID MS^3 product ion spectrum of the m/z 673 product ion formed via the neutral loss of $(AH+(CH_3)_3N)$ from the methylcarbonate adduct of GPCho 16:0/16:0 in Figure 4.1B. (B) CID MS/MS product ion spectrum of the $[M-H]^-$ precursor ion of phosphatidylethanol 16:0/16:0 (m/z 675).

4.3.5 Deuterium isotope labeling and CID MS^3 experiments to probe the structure of the product ions formed by neutral loss of (A+86) from the anionic adducts of GPCho

To elucidate the structure of the m/z 647 product ions formed by neutral loss of (A+86) from the $[M+A]^-$ anionic adducts of GPCho 16:0/16:0, the CID MS/MS product ion spectrum obtained from the d_4-GPCho16:0/16:0 methylcarbonate lipid adduct was examined (Figure 4.3). It can be seen from Figure 4.3A that a product ion corresponding to the loss of (A+89) at m/z 648 was formed, in contrast to the loss of (A+86) observed at m/z 647 for the GPCho16:0/16:0 ion in Figure 4.1B, indicating that three deuteriums were lost as part of the neutral species upon dissociation of the adduct. Based on this behavior, a mechanism for formation of the $[M+A-(A+(CH_3)_3NCH=CH_2)]^-$ product ion, via a charge-directed E2 elimination reaction initiated by the deprotonated phosphate oxygen and resulting in loss of the choline head group to yield phosphatidic acid, is proposed in Scheme 4.6.



Scheme 4.6 Proposed MS/MS fragmentation pathway of $[GPCho+A]^-$ to lose $(A+(CH_3)_3)NCH=CH_3)$

The proposed phosphatidic acid structure of the $[M+A-(A+(CH_3)_3NCH=CH_2)]^-$ product ion from the GPCho anionic adducts was further supported by the observation that MS^3 fragmentation of the 16:0/18:1 lipid $-[A+(CH_3)_3NCH=CH_2)]$ neutral loss product ion (Figure 4.5A) was essentially identical to the MS/MS product ion spectrum obtained from the $[M-H]^-$ ion of the authentic phosphatidic acid 16:0/18:1 lipid ion prepared in solution and introduced to the mass spectrometer by nESI (Figure 4.5B). MS^3 of all the product ions formed by the loss of $[A+(CH_3)_3NCH=CH_2)]$ from each of the anionic adducts were found to yield identical product ion spectra, indicating the formation of a common phosphatidic acid product ion in each case.

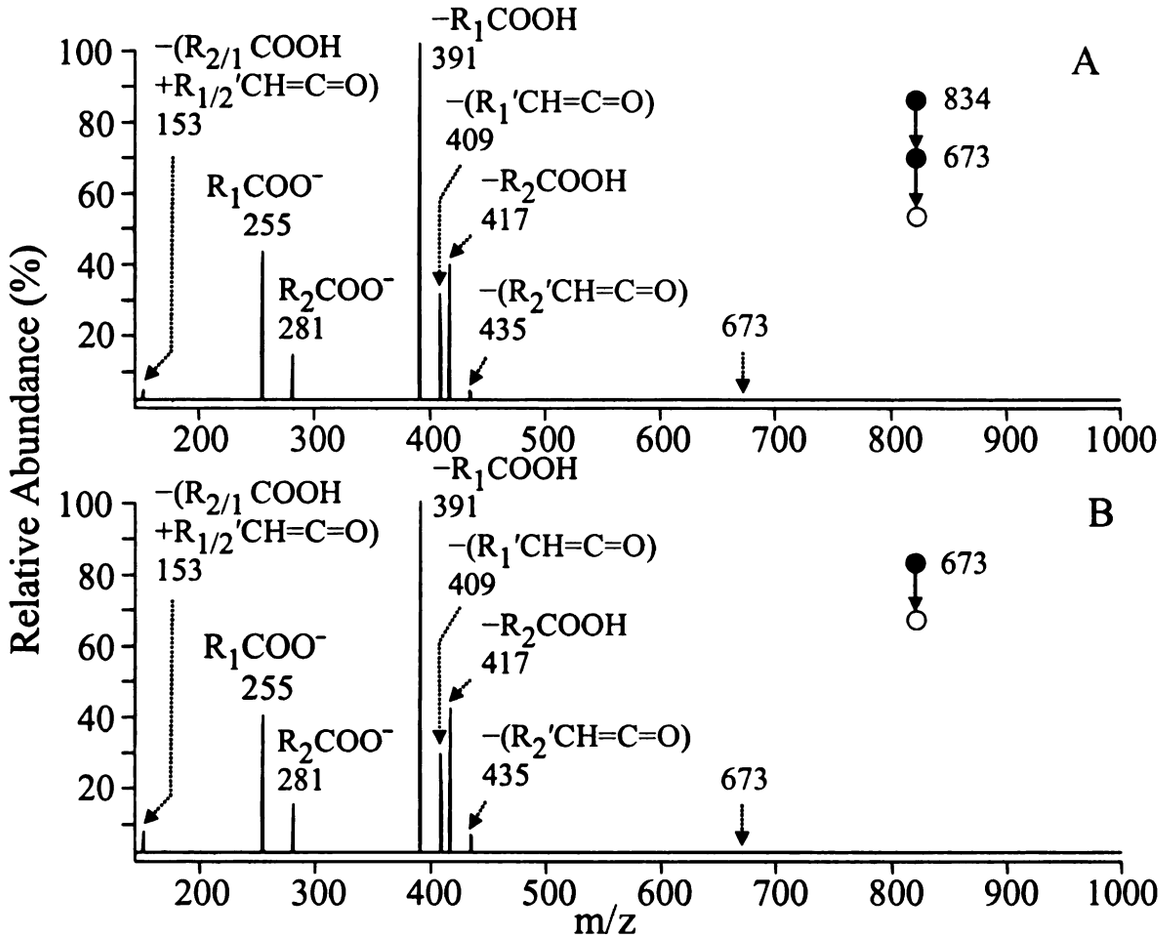


Figure 4.5 Negative ionization mode (A) CID MS^3 product ion spectra of the m/z 673 product ion formed via the neutral loss of $[A+(CH_3)_3NCH=CH_2]$ from the methylcarbonate adduct of GPCho 16:0/18:1 in Table 4.1. (B) CID MS/MS product ion spectrum of the $[M-H]^-$ precursor ion of phosphatidic acid 16:0/18:1 (m/z 673).

4.3.6 Deuterium isotope labeling and CID MS^3 and MS^4 experiments to probe the structure of the $[M+A-59]^-$ product ion formed from the $H_2PO_4^-$ adducts of GPCho

CID MS/MS of the dihydrogen phosphate $H_2PO_4^-$ anionic adduct of GPCho 16:0/18:1 (Figure 4.6A) resulted in formation of the $-(A+CH_3)$, $-(AH+(CH_3)_3N)$ and $-(A+(CH_3)_3NCHCH_2)$ neutral loss product ions described above, as well as a unique product ion at m/z 797 corresponding to the neutral loss of 59 Da from the $[M+A]^-$ precursor ion. A similar loss was also observed by MS/MS of the dihydrogen phosphate anionic adduct of GPCho 16:0/16:0 (Table 4.1). The formation of this 59 Da neutral loss product ion is consistent with the mechanism shown in Scheme 4.7, involving 'charge-directed' nucleophilic attack by the phosphate anion on an electrophilic carbon in the choline head group, resulting in elimination of $(CH_3)_3N$ and covalent incorporation of the anion. MS^3 of this product ion resulted in the loss of 124 Da, consistent with a composition of $C_2H_5PO_4$, as the major fragmentation pathway (Figure 4.6B). This loss could occur by an E2 elimination reaction pathway similar to that shown in Scheme 6 for the loss of $(A+(CH_3)_3NCH=CH_2)$, or by a neighboring group pathway following intramolecular proton transfer between the two phosphates within the product ion, to yield phosphatidic acid (Scheme 4.7). These two mechanisms can be readily distinguished from each other by examination of the MS^3 spectra obtained from the $[M+A-(CH_3)_3N]^-$ product ion of the d_4-GPCho 16:0/16:0 phosphate adduct.

Dissociation of the adduct by the E2 elimination pathway would result in the loss of 127 Da ($H_2PO_4CDCD_2$), whereas dissociation by the neighboring group pathway would result in the loss of 128 Da ($HPO_4CD_2CD_2$). The exclusive loss of 128 Da was observed from the d_4-GPCho 16:0/16:0 lipid (data not shown), indicating that the loss of 124 from the $[M+A-(CH_3)_3N]^-$ product ion of the GPCho 16:0/18:1 dihydrogen phosphate adduct corresponded to the cyclic $HPO_4CH_2CH_2$ neutral shown in Scheme 4.7. Finally, MS^4 of the $[M+A-((CH_3)_3N+HPO_4CH_2CH_2)]^-$ product ion at m/z 673 in Figure 4.6B was observed to yield an identical spectrum (data not shown) to that obtained by MS/MS of the phosphatidic acid 16:0/18:1 standard in Figure 4.5B, further confirming the structure of this product ion.

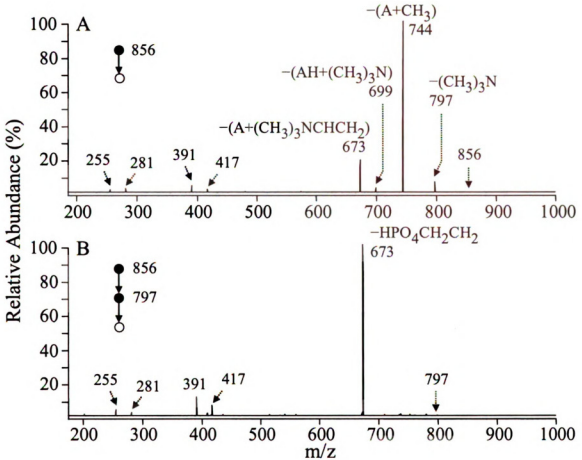
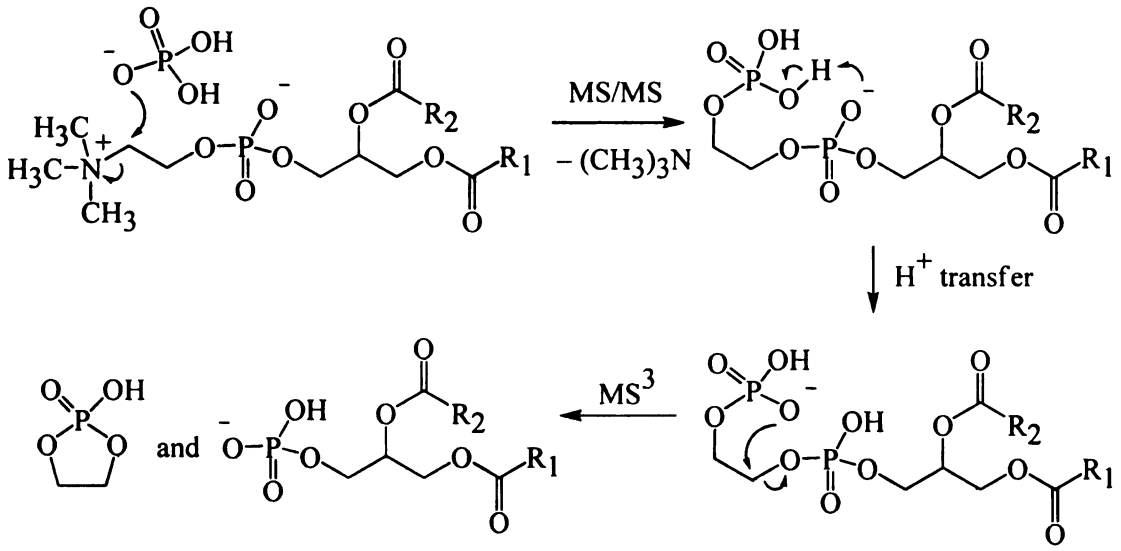


Figure 4.6 (A) Negative ionization mode CID MS/MS product ion spectrum of the phosphate ($H_2PO_4^-$) adduct of GPCho 16:0/18:1 (m/z 856). (B) CID MS^3 product ion spectrum of the m/z 797 product ion formed via the neutral loss of $(CH_3)_3N$ (59 Da) from Figure 4.6A.



Scheme 4.7 Proposed fragmentation pathways of $[GPCho+H_2PO_4]^-$

4.3.7 Deuterium isotope labeling and CID MS^3 experiments to probe the structure of the $[M+A-(A+1)]^-$ product ions formed from the anionic adducts of GPCho and isotope effect

CID MS/MS spectra of negatively charged GPCho ions formed by anionic adduction with ethyl carbonate, methylcarbonate and trifluoroacetate all resulted in the neutral loss of AH. The formation of these product ions requires either (i) deprotonation of the GPCho lipid to yield a product ion containing a single negative charge site i.e., neutralization of the quaternary alkyl ammonium ion within the choline head group, or (ii) deprotonation of the GPCho lipid at a site remote to the choline head group to yield a zwitterionic product ion. To determine the site of deprotonation for this neutral loss, the MS/MS product ion spectra obtained from the methylcarbonate anionic adducts of d_4-GPCho 16:0/16:0, d_{62}-GPCho 16:0/16:0, and d_{13}-GPCho 16:0/16:0 were examined. The

exclusive loss of AH (m/z 736) from the d_4-GPCho 16:0/16:0 methylcarbonate adduct ion (Figure 4.3A) indicates that the deprotonation reaction does not involve any of the CH_2CH_2 hydrogens within the phosphocholine head group. In contrast, the loss of AD (m/z 793) from the d_{62}-GPCho 16:0/16:0 methylcarbonate adduct ion (Figure 4.3B) indicates that the deprotonation reaction does involve a hydrogen from within the fatty acid. The loss of AH from the same precursor ion of d_{62}-GPCho 16:0/16:0 (m/z 794 in Figure 4.3B) and the loss of AD from the d_{13}-GPCho 16:0/16:0 lipid (m/z 744 in Figure 4.3C) indicated a second site for deprotonation, likely involving a hydrogen from an N-methyl group of the phosphocholine head group.

MS^3 of the AH neutral loss product ion from the GPCho 16:0/16:0 methylcarbonate adduct at m/z 732 in Figure 1B revealed a unique product ion at m/z 269, 14 mass units higher than the $RCOO^-$ ion at m/z 255 (Figure 4.7A). Likewise, a product ion at m/z 272, 17 mass units higher than the $RCOO^-$ ion was observed from the MS^3 of d_{13}-GPCho 16:0/16:0 (data not shown). Based on the data obtained from Figure 4.3B, which indicated that deprotonation can occur from the fatty acid chains, a mechanism for the formation of this m/z 269 product ion is proposed in Scheme 4.8 (pathway *b*). Deprotonation of a α-CH_2 group adjacent to either of the carbonyl groups in the fatty acid chains would initially yield an enolate anion, which may then undergo rearrangement by methyl group transfer from the quaternary alkyl ammonium ion of the choline head group. MS^3 of this rearranged product ion would give rise to the product ion

at m/z 269, corresponding to $R'CH=CO(OCH_3)^-$, via a similar neighboring group elimination reaction mechanism to that proposed earlier for formation of the $RCOO^-$ product ions. Evidence for this mechanism was provided by individually subjecting the −(AD) and −(AH) neutral loss product ions from the d_{62}-GPCho 16:0/16:0 lipid adduct, i.e, where the isomeric product ions formed by deprotonation at the two or more different sites within the GPCho lipid adduct ion are resolved from each other, to further dissociation by MS^3 (Figures 4.7B and 4.7C, respectively). From these spectra, it can be seen that an equivalent product ion to the one at m/z 269 in Figure 4.7A is only observed from the −(AD) neutral loss product (m/z 299 in Figure 4.7B), indicating that this ion is formed by deprotonation of the fatty acid chain.

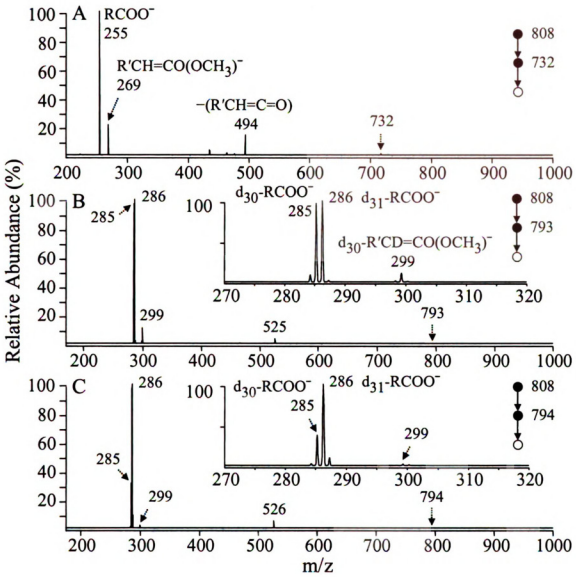
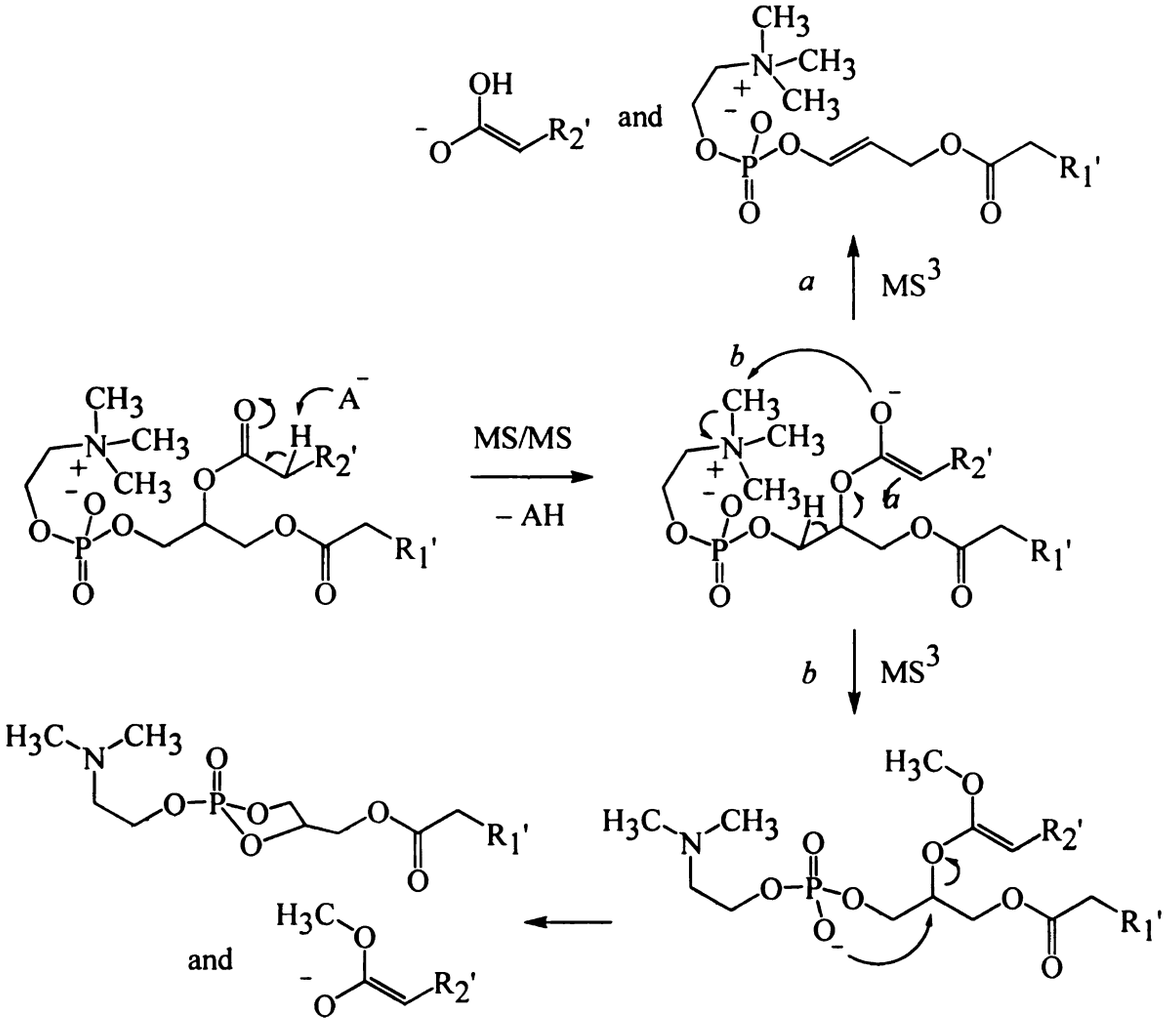


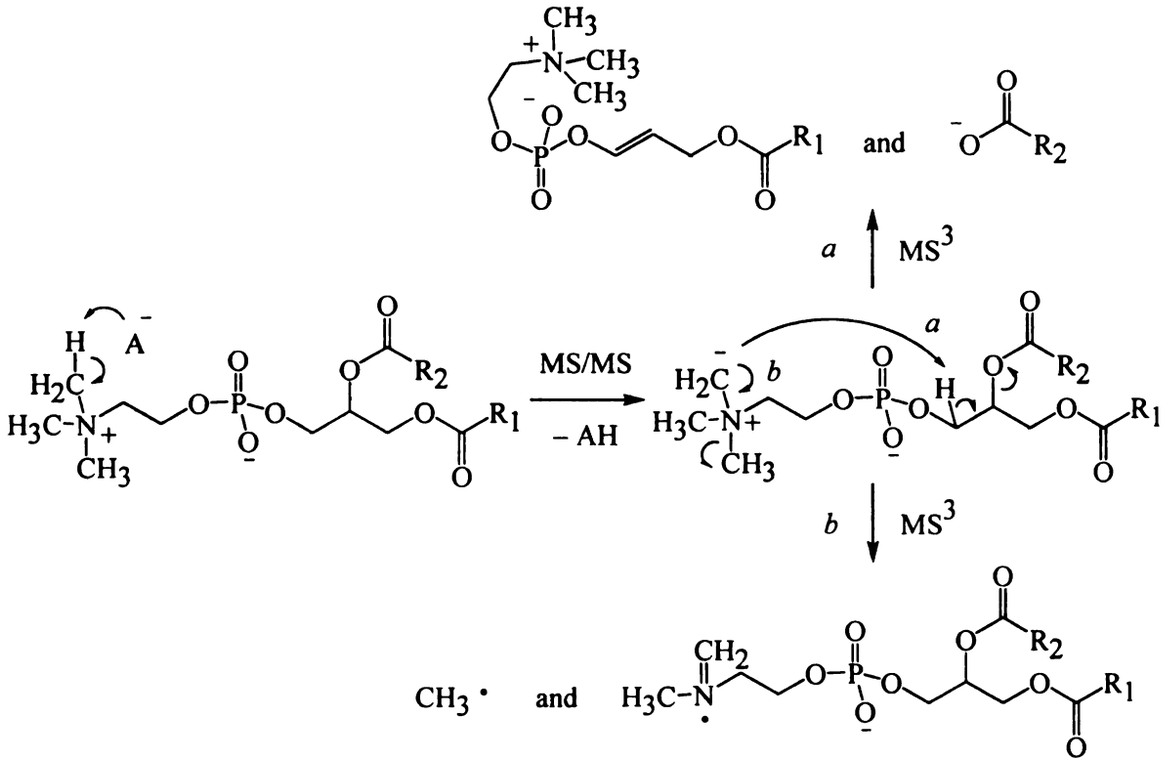
Figure 4.7 Negative ionization mode CID MS^3 product ion spectrum of (A) the m/z 732 product ion formed via the neutral loss of (AH) from the methylcarbonate adduct of GPCho 16:0/16:0 in Figure 4.1B. (B) the m/z 793 product ion formed via the neutral loss of (AD) from the methylcarbonate adduct of GPCho d_{31}-16:0/d_{31}-16:0 in Figure 4.3B. (C) the m/z 794 product ion formed via the neutral loss of (AH) from the methylcarbonate adduct of GPCho d_{31}-16:0/ d_{31}-16:0 in Figure 4.3B.



Scheme 4.8 Proposed fragmentation pathways of $[GPCho+A]^-$ to lose AH and MS^3 of $[GPCho+A-AH]^-$

Interestingly, CID MS/MS of the trifluoroacetate adduct of the d_4-GPCho 16:0/16:0 and d_{62}-GPCho 16:0/16:0 lipids resulted in exclusive AH loss (m/z 736 and m/z 794 in Figures 4.8A and 4.8B, respectively), while that of d_{13}-GPCho 16:0/16:0 produced only AD loss (m/z 744 in Figure 4.8C), indicating that the deprotonation reaction involved a hydrogen (or deuterium) from an N-methyl group of the

phosphocholine head group (Scheme 4.9, pathway *a*). Furthermore, MS^3 of each of these product ions indicated that the characteristic methyl group transfer product ion was almost absent in each case (data not shown), further indicating that the deprotonation reaction did not involve a hydrogen from the fatty acid chains. These differences observed by dissociation of the neutral loss product ions from the methylcarbonate and trifluoroacetate adducts indicate that the site of deprotonation, and therefore the structures of the −(AH) neutral loss MS/MS product ion at m/z 794, are highly dependent on the identity of the anion.



Scheme 4.9 Proposed fragmentation pathways of $[GPCho+A]^-$ to lose alternative AH and MS^3 of $[GPCho+A-AH]^-$ to form radical anions

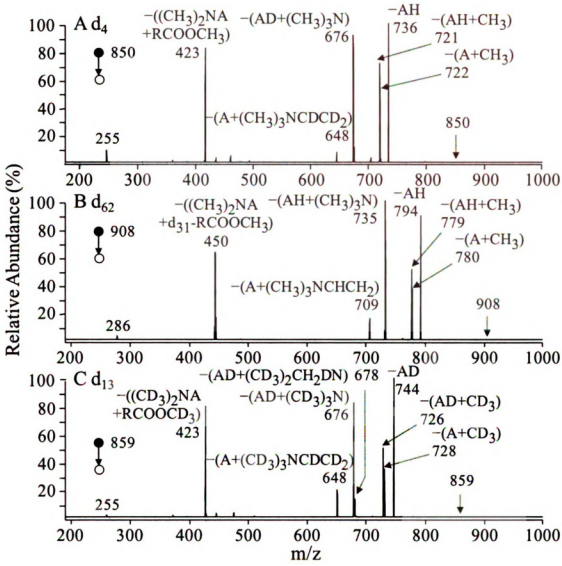


Figure 4.8 Negative ionization mode CID MS/MS product ion spectra of the trifluoroacetate adducts of (A) d_4-GPCho 16:0/16:0 (m/z 850), (B) GPCho d_{31}-16:0/d_{31}-16:0 (m/z 908), and (C) d_{13}-GPCho 16:0/16:0 (m/z 859).

4.3.8 Deuterium isotope labeling and CID MS^3 experiments to probe the structure of the $[M+A-(A+16)]^-$ product ions formed from MS/MS of anionic adducts of GPCho

The (A+16) neutral loss CID MS/MS product ion observed at m/z 717 from the methylcarbonate adduct of GPCho 16:0/16:0 (Figure 4.1B), should contain one nitrogen atom but has an odd mass, suggesting that it is an odd-electron species generated from the even-electron precursor ion $[M+A]^-$ via the combined losses of AH and a $CH_3\cdot$ radical. This neutral loss was found at particularly high abundance from the trifluoroacetate adduct of both the GPCho 16:0/16:0 and GPCho 16:0/18:1 lipid species (Table 4.1). MS/MS analysis of the $CF_3CO_2^-$ adducts of d_4-GPCho 16:0/16:0 and d_{62}-GPCho 16:0/16:0 (Figures 4.8A and 4.8B, respectively) both resulted only in the neutral loss of ($AH+CH_3\cdot$), while the d_{13}-GPCho 16:0/16:0 (Figure 4.8C) exclusively lost ($AD+CD_3\cdot$), indicating that the proton involved in such a neutral loss originates only from an N-methyl group of the phosphocholine head group (Scheme 4.9, pathway *b*).

MS^3 of the m/z 717 product ion generated by neutral loss of (A+16) from the trifluoroacetate adduct of GPCho 16:0/16:0 in Table 4.1 resulted in the spectrum shown in Figure 4.9. Neutral losses of 15 Da (m/z 702), 43 Da (m/z 673), 255 Da (m/z 462) and 298 Da (m/z 419) were observed, corresponding to even electron species generated via the loss of neutral radicals $CH_3\cdot$, $C_2H_6N\cdot$, $RCOO\cdot$ and $RCOOCH_2NCH_3\cdot$, respectively, in addition to a product ion at m/z 255 ($RCOO^-$). Similar losses of neutral radicals $CD_3\cdot$,

$C_2D_5HN^{\cdot}$, $RCOO^{\cdot}$ and $RCOOCD_2NCD_3^{\cdot}$ were observed from the MS^3 spectrum of the d_{13}-GPCho 16:0/16:0 lipid species.

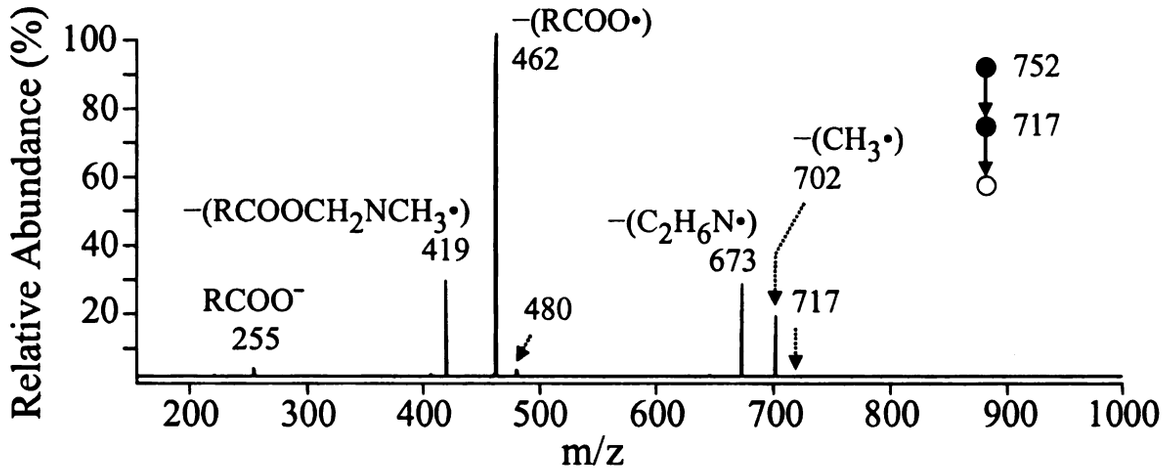


Figure 4.9 Negative ionization mode CID MS^3 product ion spectrum of the m/z 717 product ion formed via the neutral loss of (A+16) from the trifluoroacetate adduct of GPCho16:0/16:0 in Table 4.1.

4.3.9 Rationalizing the effects of anions on the gas-phase fragmentation behavior of anionic adducts of GPCho

A previous *ab initio* computational study on the gas-phase structure of zwitterionic GPCho has predicted that the phosphocholine head group adopts a cyclic conformation, stabilized by multiple *intramolecular* electrostatic interactions between the phosphate oxygens and the N-methyl groups within the choline head group [256]. Another study to examine the effect of hydration on the gas-phase structure of GPCho lipid molecules has found a strong interaction between water molecules and the phosphate oxygens, as well as with methyl and methylene moieties of the choline headgroup, resulting in a hydration driven conformational change of the GPCho head

group [257]. Extensive computational studies to determine the gas-phase structures of the various anionic GPCho lipid adducts described above were beyond the scope of this study. However, it is reasonable to expect that the fragmentation behaviors observed for the various GPCho lipid anionic adducts are likely to be highly dependent on the ability of the anion to disrupt these intramolecular electrostatic interactions, for example by forming multiple *intermolecular* electrostatic interactions with the N-methyl groups within the choline head group or by forming strong hydrogen bonds [257,258] with the phosphate oxygens of the phosphocholine head group, or due to the ability of the anion to form strong hydrogen bonds with the glycerol backbone or the ester linkage of fatty acid chains, hence opening up alternative dissociation pathways. In order to obtain a rudimentary picture of the major inter- and intra-molecular interactions associated with formation of the anionic GPCho adducts, a preliminary conformational search was conducted at the PM3 semi empirical level of theory of the chloride-GPCho anionic adduct, using the model phosphatidylcholine lipid GPCho 6:0/6:0. PM3 level calculations were performed due to the large size of the lipid structures, thereby making *ab initio* or density functional theory searches computationally prohibitive. Figure 4.10 shows the lowest energy conformation found for the GPCho 6:0/6:0 lipid with the chloride anionic adduct. It can be seen from Figure 4.10 that the chloride anion is exclusively associated with the lipid species via intermolecular electrostatic interactions with two of the choline methyl groups, while the remaining choline methyl group is involved in an intramolecular electrostatic interaction with the anionic phosphate oxygen. The two acyl fatty acid chains were found to be closely associated with each other by the formation of multiple intramolecular hydrophobic interactions. Overall, these interactions are

consistent with the experimentally observed fragmentation behavior for this adduct, involving the exclusive loss of ($A+CH_3$) via an intermolecular S_N2 reaction.

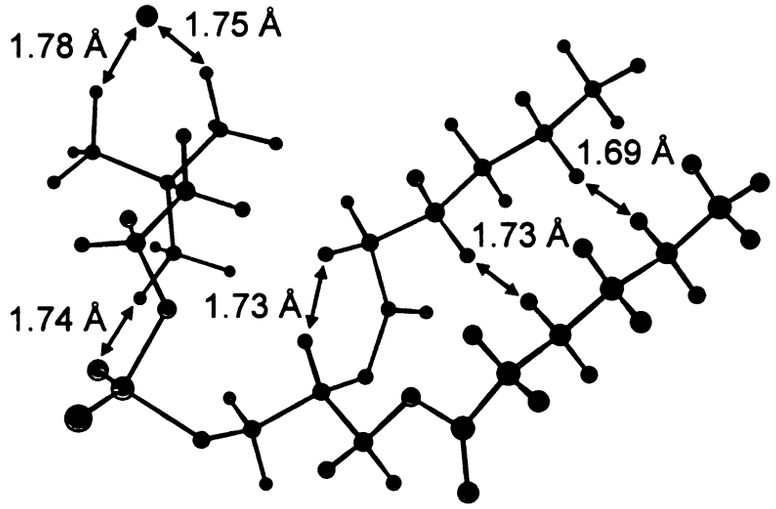


Figure 4.10 Most stable structure (calculated at the PM3 level of theory) for the anionic chloride adduct of the model phosphatidylcholine lipid GPCho 6:0/6:0.

The competition between S_N2 and E2 reactions in the gas-phase, such as those involving the loss of ($A+CH_3$), ($AH+(CH_3)_3N$) and ($A+(CH_3)_3NCHCH_2$) via intermolecular S_N2, intermolecular E2 or intramolecular E2 reactions in the work described here, respectively, have been the subject of several previous studies by Gronert *et.al.* [56]. Notably, Beauchamp and co-workers have recently observed competition between S_N2 and E2 pathways for reaction of the triphosphate dianion with choline, a closely related system to that examined here [57]. Also, O'Hair and co-workers have

recently described an S_N2 reaction for the fragmentation a GPCho dimer in positive ion mode MS/MS, resulting in gas-phase cross-linking via the loss of $N(CH_3)_3$ [259]. However, none of these studies have demonstrated a clear correlation between the observed gas-phase S_N2 or E2 fragmentation behaviors as a function of the gas-phase acidity (Table 4.1), nucleophilic strength [260], hard/soft acid base properties [261] or steric accessibility of the investigated species. Thus, it is likely that it is a combination of these factors, together with the respective activation barriers, that control the experimentally determined branching ratios for the observed fragmentation reactions. Further studies involving molecular dynamic simulations combined with molecular orbital calculations are currently underway to obtain more detailed insights into the nature of the various anion-GPCho lipid interactions, and their role in controlling the observed fragmentation reactions.

4.3.10 Competitive formation of anionic adducts with GPCho

The binding affinity of different anions with the GPCho lipids was also found to differ significantly depending on the identity of the anions. In solutions of chloroform: methanol (1:1, v/v) containing 5 μM GPCho 16:0/16:0, ammonium formate, ammonium acetate, ammonium chloride or ammonium hydroxide (forming methyl carbonate) were added individually from 0, 0.1 mM to 20 mM, and the consequent peak abundance of $[M+A]^-$ at m/z 778, m/z 792, m/z 768 or m/z 808, respectively, was plotted against the concentration of the anions in solution (Figure 4.11). In the case of formate and acetate (Figure 4.11A and 4.11B), the abundances of the anionic adduct ion increased rapidly

with the increase in anion concentration in the solution prior to 5 mM and 10 mM, respectively, but then slowly decreased as the anion concentration further increased. In the case of chloride, however, the highest abundance was reached at as early as about 1 mM chloride (Figure 4.11C), reflecting a higher affinity of chloride to GPCho lipids, but after 10 mM, serious clogging of the spray tip due to precipitation of the nonvolatile chloride salt prevented the formation of a stable spray. Even though the optimal abundance of chloride adducts was reached at much lower anion concentration, the optimal abundance of the adduct ion was much lower compared to those of the volatile formate and acetate in Figures 4.11A and 4.11B. When only ammonium hydroxide was added, the ion abundance of methyl carbonate adduct increased steadily until about 15 mM ammonium hydroxide (Figure 4.11D), and no adverse effects on the spray were observed. The speed by which these anionic adduction reached saturation (Figure 4.11), in the order of chloride>formate>acetate>methyl carbonate, also reflects the order of affinity of these anions to GPCho lipids.

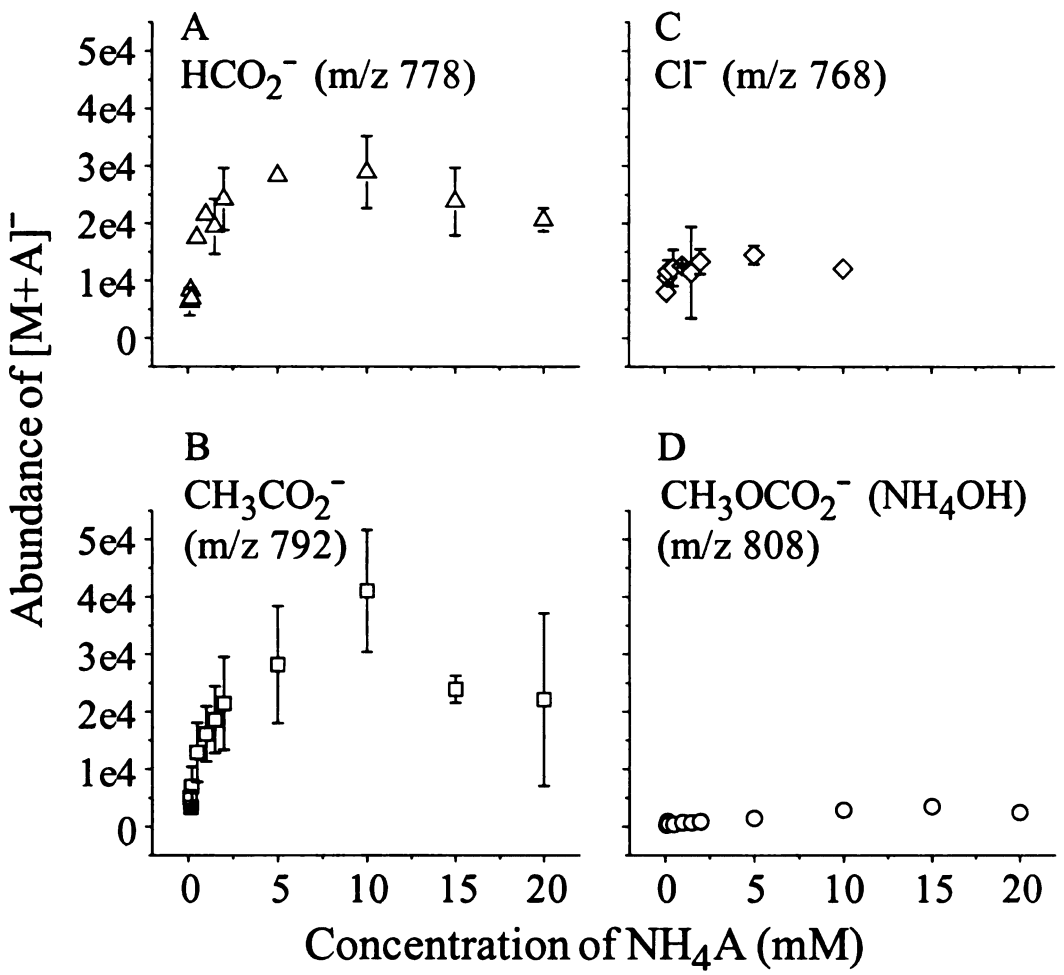


Figure 4.11 Dependence of the ion abundance of anionic adducts formed from (A) formate (m/z 778), (B) acetate (m/z 792), (C) chloride (m/z 768) and (D) methyl carbonate (m/z 808) on the concentration of ammonium formate, ammonium acetate, ammonium chloride and ammonium hydroxide, in the solution of chloroform: methanol (1:1, v/v) containing 5 μM GPCho 16:0/16:0, analyzed in negative ion mode ESI MS.

By keeping the concentration of GPCho 16:0/16:0 lipid constant at 5 μM, and varying the concentration of anion mixture containing formate and acetate, and the

mixture containing formate and chloride systematically, the ratio of the consequent anionic adduct ion abundances of $[M+formate]^-$ / $[M+acetate]^-$ was plotted against the ratio of [ammonium formate]/ [ammonium acetate] concentrations in solution (Figure 4.12A), and the similarly the ratio of $[M+chloride]^-$ / $[M+formate]^-$ against [ammonium chloride]/ [ammonium formate] was also plotted (Figure 4.12B). The results in Figures 4.12A and 4.12B showed that the ability to form adducts of these anions indeed follow the order of chloride>formate>acetate. The efficiency of formate to form adducts with GPCho is about five fold as great as that of the acetate (Figure 4.12A).

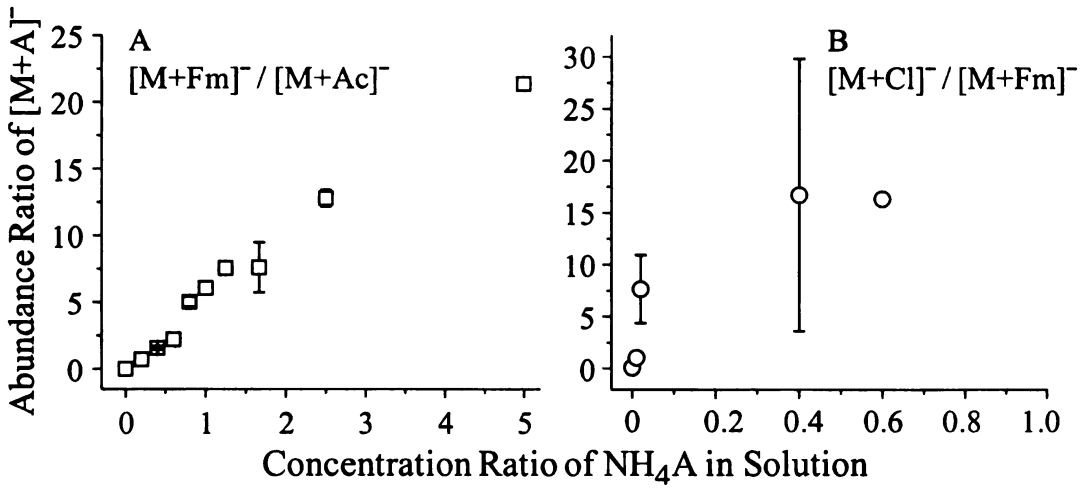


Figure 4.12 The ratio of ion abundances of anionic adducts formed from A) $[M+formate]^-$ and $[M+acetate]^-$ (at m/z 778 and m/z 792) against the ratio of concentrations of ammonium formate/ammonium acetate in solution, and B) $[M+chloride]^-$ and $[M+formate]^-$ (at m/z 768 and m/z 778) against the ratio of concentrations of ammonium formate/ ammonium chloride in solution, in negative ion mode ESI MS, while the concentration of GPCho 16:0/16:0 was maintained at 5 μM.

4.4 Conclusions

Phosphocholine containing lipids such as GPCho are readily observed in negative ion mode by adduction with a range of different anionic species. However, the observed MS/MS fragmentation reactions of the $[M+A]^-$ ions formed from these anionic adducts are highly dependent on the identity of the anions. Based on results of MS^n experiments of each of these adducts, as well as MS/MS and MS^n experiments using deuterium labeled lipids and authentic lipid standards, structures and mechanisms for the formation of each of the product ions have been proposed. The results from this study indicate that great care must be taken to control the identity of the anions employed during lipid isolation, purification and separation, in order to allow the development and application of sensitive and robust neutral-loss scan methods for mass spectrometry-based lipid identification and quantitative analysis.

Chapter 5

Characterization of Ornithine and Glutamine Lipids in the Cell Membranes of *Rhodobacter sphaeroides* ‡

5.1 Summary

The identification and structural characterization of a series of ornithine lipids extracted from the cell membranes of wild type *Rhodobacter sphaeroides*, as well as from a glycerophosphocholine-deficient strain, has been achieved by multistage tandem mass spectrometry of their protonated and deprotonated precursor ions in a linear quadrupole ion trap. Systematic examination of the multistage gas-phase fragmentation reactions of these ions, combined with the use of hydrogen/deuterium exchange, has enabled the pathways responsible for sequential losses of the 3-hydroxy linked fatty acyl chain (R_2) and the amide linked 3-OH fatty acid chain (R_1) from these lipids, as well as for the formation of the previously reported ornithine specific 'fingerprint' ion at m/z 115 in positive ion mode, to be determined. Additionally, the fragmentation pathways responsible for formation of a previously unreported product ion, specific for the ornithine lipid head group at m/z 131 in negative ion mode, have been examined. Based on these results, and by comparison with the fragmentation behavior of model lipoamino acid standard compounds, a series of novel glutamine containing lipids have also been

‡ Part of the results described in this chapter were published in *J. Am. Soc. Mass Spectrom.* **2009**; 20: 198-212 (Zhang X, Ferguson-Miller SM and Reid GE).

identified, with analogous structures, but with masses 14 Da higher than several of the ornithine lipids observed in this study. Characteristic 'fingerprint' ions indicative of these glutamine lipids were found at m/z 147, 130 and 129 in positive ion mode, and at m/z 145 and 127 in negative ion mode. The results from this study establish an experimental basis for future efforts aimed at the sensitive identification, characterization and quantitative analysis of ornithine and glutamine lipids in complex unfractionated cellular extracts.

5.2 Introduction

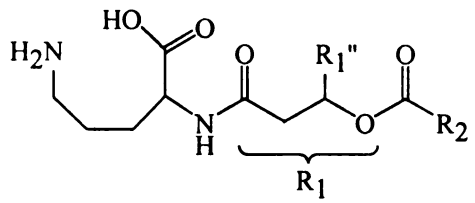
Ornithine lipids (OL) belong to a class of fatty acylated amino acids that do not contain either glycerol or phosphate. Since their discovery over 40 years ago [262-264], ornithine lipids have been found to be broadly distributed among a number of gram-negative bacteria and several gram-positive bacteria [7]. Ornithine lipids are also known to be predominantly located in the outer membranes [265] and resistant to phospholipases [266]. However, the function of the OL species in these bacteria remains unclear. Ornithine lipids constitute different proportions of the total membrane lipids depending on the individual bacterium and growth conditions, ranging from around 2 % in many bacteria grown under normal conditions, to being nearly the sole polar lipid present under phosphate-limited growth conditions in *Pseudomonas fluorescens* [267]. An increase in the abundance of OL under phosphate-limiting growth conditions, along with sulfoquinovosyldiacylglyceride (SQDG) and diacylglyceryl–N, N, N–trimethyl-homoserine (DGTS) lipids, has also been observed in *Rhodobacter sphaeroides* (*R. sphaeroides*), as revealed by TLC using ^{14}C-labeling quantification [11]. In *Sinorhizobium meliloti*, either OL or DGTS are required under phosphate-limiting conditions to ensure normal cell yields [93]. Also in *Sinorhizobium meliloti*, an OL genetic deficiency has been shown to be compensated for by increases in phosphatidylethanolamine (GPEtn)/ N–methyl GPEtn, phosphatidylcholine (GPCho) and phosphatidylglycerol (GPGro), and resulted in only subtle effects on the growth and delayed nodule formation [268]. OLs have also been implicated in high temperature tolerance in *Burkholderia cepacia* [95] and in acid tolerance in *Rhizobium tropici* [269].

OLs from *Bordetella pertussis* and *Flavobacterium meningosepticum* have been shown to have a number of biological functions, including hemagglutination, and stimulation of macrophages [266,270-272]. It is also known that OL is critical to obtaining the optimal biosynthetic yields of cytochrome *c* species in *Rhodobacter capsulatus* [273]. Finally, OL has recently been noted to be one of the lipid species that remain associated to the cytochrome *c* oxidase (C*c*O), after being purified and crystallized from *R. sphaeroides* (Chapter 9).

To date, ornithine is the only type of non-glycerol non-phosphate lipoamino acid reported to be present in *R. sphaeroides* [11,14,90,274]. However, lipids containing lysine, serine or serine-glycine dipeptides, with analogous backbone structures to OL have previously been observed in *Agrobacterium tumefaciens* [275] and *Flavobacterium meningosepticum* [270,272]. Unfortunately, little detail regarding the molecular structures of OL in *R. sphaeroides* is available, with prior work limited to their identification based on their migration position on TLC plates and the ninhydrin-positive (amino group) and molybdate-negative (no phosphate group) spray results [11,14,90,274].

Ornithine lipids typically contain an ornithine head group that is connected via its N_{α}–amino group to a 3–OH fatty acid (R_1), with a second fatty acid chain (R_2) esterified to the 3–OH group of the first fatty acid (Scheme 5.1) [7,95,102,106,107,263-272,276-282]. However, an increase in growth temperature from 25 to 40 °C has also been shown to promote the incorporation of a 2–OH fatty acyl group to the second fatty acid to OL in *Burkholderia cepacia*[95]. Furthermore, the incorporation of ^{14}C-labeled ornithine in

Rhizobium tropici revealed four different forms of ^{14}C-labeled lipid products, two of which were amino-negative in ninhydrin test [269].



Scheme 5.1 Schematic structure of an ornithine lipid (OL)

Mass spectrometry (MS) coupled with electrospray ionization (ESI) or matrix assisted laser desorption ionization (MALDI) has emerged as an attractive method to analyze intact, non-volatile, polar lipids, and is being increasingly applied to a wide range of lipid studies [117,187]. However, due to their molecular composition and ionization characteristics to mainly form ions of low charge states under the typically applied experimental conditions, the precursor ions for most membrane lipids fall into a relatively narrow m/z range between 600 – 1600 Da, resulting in significant crowding and potential overlapping of peaks in the resultant mass spectra, particularly in the region of m/z from 600 to 900. The mass spectra are further complicated by the presence of various cationic or anionic adducts from the lipids that may be present in the mixture (e.g., $[M+H]^+$ and $[M+Na]^+$ in positive ion mode, and $[M-H]^-$, $[M+Cl]^-$ or $[M+CH_3OCO_2]^-$ in negative ion mode) [117,187], as well as by the presence of multiple lipid isomers with identical elemental compositions at a given m/z value, undistinguishable even by high MS resolution. Therefore, the use of tandem mass spectrometry (MS/MS) or multistage

tandem mass spectrometry (MS^n) is generally required to unambiguously identify and characterize the individual lipid species that may be present, based on the characteristic product ions that are formed upon fragmentation.

Numerous previous studies have been carried out to examine the gas-phase fragmentation reactions of OL [102,106,107,268,273,280-282]. From these studies, a characteristic low mass product ion at m/z 115, resulting from the dissociation of protonated OL in positive ionization mode MS/MS, and corresponding to the formation of a 3–amino–2–oxopiperidinium ion, has been consistently observed [102,106,268,273,280,281]. This ion may therefore be considered a 'fingerprint' ion for ornithine lipid identification. However, this product ion is not generally observed due to the inherent low mass cutoff (LMCO) imposed on product ion detection when performing collision induced dissociation (CID)–MS/MS in quadrupole ion trap mass spectrometers under typical operating conditions. In this case, further dissociation (i.e., MS^n) of the high mass product ions that are initially formed during MS/MS may be required to provide information regarding the presence and identity of the OL species. With the exception of a single report in the literature [102], little information is available regarding the negative ionization mode CID MS/MS fragmentation behavior of OL species.

An improved understanding of the fundamental gas-phase fragmentation behavior of ornithine lipids using modern mass spectrometry instrumentation, in both positive and negative ionization modes, is therefore critical to the development of sensitive unequivocal identification, characterization and quantitative analysis strategies for this class of lipid molecule, and for subsequently determining their functional roles. The

results from these studies could also be applied to elucidation of the presence and structures of other lipoamino acid species that may be present.

Herein, the sequential fragmentation pathways responsible for formation of the diagnostic ornithine lipid specific product ion at m/z 115 in positive ionization mode, as well as for the formation of a related 'fingerprint' ion for ornithine lipids at m/z 131 in negative ionization mode, have been delineated. The identities of the major ornithine lipids isolated from the cell membranes of wild type *R. sphaeroides*, as well as from a GPCho deficient stain, have been determined using multistage tandem mass spectrometry in a linear quadrupole ion trap mass spectrometer, coupled with analysis of the fragmentation behavior of model lipoamino acid standards. Furthermore, several novel glutamine-containing lipids have been identified in each of these samples. Characteristic product ions, indicative of the glutamine lipid species, have been identified at m/z 129, 130 and 147 in positive ionization mode, and at m/z 127 and 145 in negative ion mode.

5.3 Results and Discussion

5.3.1 ESI-MS of wild type and GPCho-deficient *R. sphaeroides*

Mass spectra of membrane lipid extracts obtained from wild type *R. sphaeroides*, as well as from a GPCho-deficient mutant of *R. sphaeroides,* acquired in both positive and negative ionization modes are shown in Figures 5.1A and 5.1B, and in Figures 5.1C and 5.1D, respectively. As the lipid extracts examined here were comprised of complicated mixtures, and were introduced to the mass spectrometer without prior separation, the m/z values of individual ions could correspond to a number of different

molecular compositions. Thus, all lipids whose precursor ions had normalized relative abundances higher than 1% in the mass spectrum were subjected to analysis by using CID MS^n in order to determine their identities. The identities of several of the major lipids observed in the most abundant ions in these spectra are labeled in Figure 5.1.

The focus of the study described in this chapter however, was a series of odd m/z ions, including the italicized and underlined ions at m/z 705, m/z 719 and m/z 731 in positive ion mode, and at m/z 703, m/z 717 and m/z 729 in negative ion mode. According to the nitrogen rule, these ions should contain zero or an even number of nitrogen atoms, and therefore could correspond to putative protonated and deprotonated ions for various OL species, respectively. A comparison of the spectra obtained from the wild type and the GPCho-deficient mutant lipid extracts indicated an apparent increase of the relative abundances of various ions in the GPCho-deficient mutant, including the putative ornithine lipid ions. Previously, in the absence of over-expression of C*c*O, the GPCho-deficient mutant showed no increase in OL content, as quantified by TLC with ^{14}C labeling [90]. More recently, similar studies using mass spectrometry have been carried out to compare the wild type and GPCho-deficient strains when C*c*O is over-expressed in these systems (Chapter 7).

Here, it was not possible to determine if the observed changes in abundances for the putative ornithine lipid ions between the wild type and GPCho-deficient strains, obtained with C*c*O over-expression, was reflective of real changes in their concentrations, or whether the apparent increases were simply due to the removal of ionization suppression effects in the GPCho-deficient mutant, due to the unavailability of authentic ornithine lipid internal standards. Regardless of this limitation, it was of

particular interest to determine the presence and structural composition of the ornithine lipids in these samples, and to develop a comprehensive understanding of their fragmentation behaviors using MS^n for use in further identification and quantification applications. The higher ion abundances of these ions in the GPCho-deficient mutant made it the sample of choice in which to investigate these species. However, the corresponding ions in the wild type lipid extract were also examined in parallel.

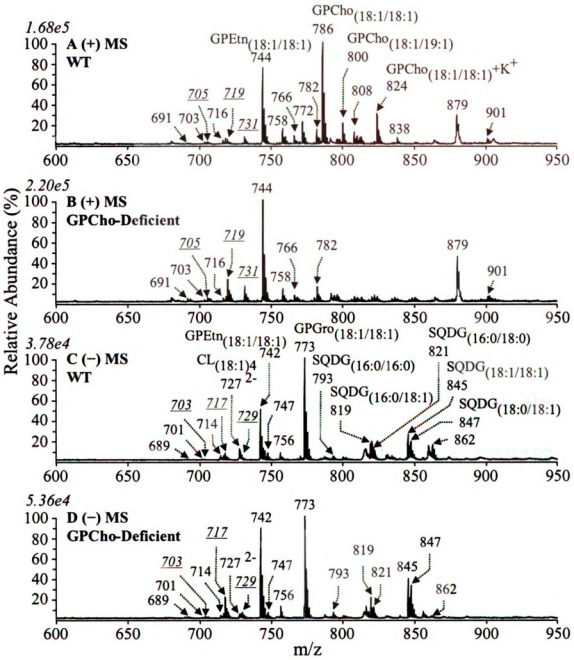


Figure 5.1 Positive ESI MS of crude lipid extracts isolated from the cell membranes of (A) wild type and (B) GPCho-deficient mutant *R. sphaeroides* (both with CcO over-expression). The negative ion mode ESI MS spectra are shown in panels (C) and (D), respectively. Only those ions within the selected m/z range of interest (600 – 950) are displayed. The italic underlined numbers represent ions of interest to this study.

5.3.2 Identification and characterization of ornithine lipids in *R. sphaeroides* by using positive and negative ionization mode MS^n

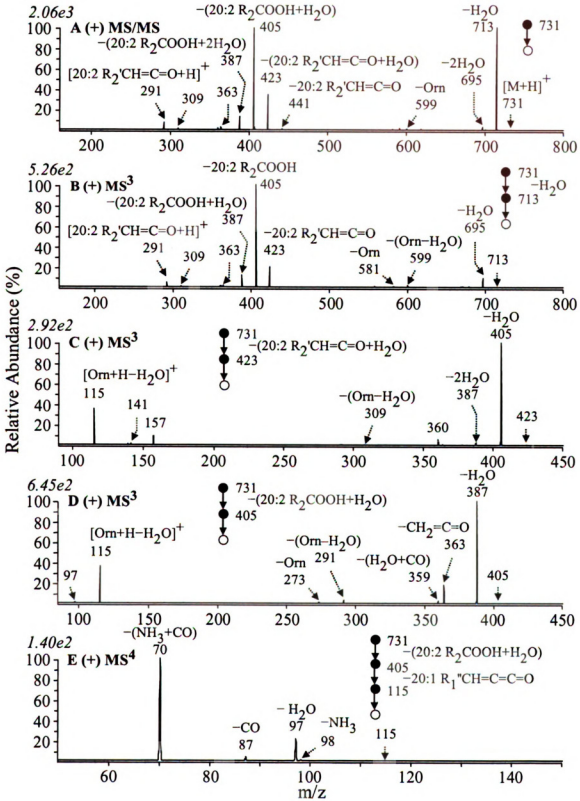
The MS/MS and MS^n spectra for the ion at m/z 731 in positive ion mode, and for the corresponding ion at m/z 729 in negative ion mode observed in the membrane lipid extract of the GPCho-deficient strain of *R. sphaeroides* are shown in Figures 5.2 and 5.3, respectively. Figure 5.2A shows the positive ion mode MS/MS for m/z 731. In this spectrum, the most abundant product ion observed above the low mass cutoff of m/z 160 (at an applied activation q value of 0.2) was m/z 713, formed via the loss of water from the protonated precursor ion (Scheme 5.1). The other abundant product ions in this spectrum provided information on the fatty acid composition of the precursor ion, which was more clearly revealed by MS^3 analysis of the $[M+H-H_2O]^+$ product ion. This ion underwent further fragmentation via (i) the loss of a 20:2 R_2 fatty acid chain as a neutral ketene ($-R_2'CH=C=O$, m/z 423), where 20 and 2 represent the number of carbons and the number of rings and double bonds respectively. (ii) the combined loss of $R_2'CH=C=O+H_2O$ or the loss of a neutral fatty acid (R_2COOH) (m/z 405), and (iii) the combined loss of $R_2COOH+H_2O$ (m/z 387) (Figure 5.2B). Further dissociation of the $[M+H-H_2O-R_2'CH=C=O]^+$ (m/z 423) product ion from Figure 5.2A led to the dominant loss of H_2O to yield the product ion at m/z 405 (Figure 5.2C). MS^3 of the m/z 405 product ion observed in Figure 2A was then used to demonstrate that this ion underwent further dissociation via the loss of a neutral ketene (20:1 $R_1"CH=C=C=O$) to yield the

characteristic 'fingerprint' ion for the ornithine lipid at m/z 115 (i.e., $[ornithine-H_2O+H]^+$) (Figure 5.2D). Thus, the structure of the ornithine lipid ion at m/z 731 is proposed to correspond to OL 3-OH 20:1/20:2 (note that the acyl chain designations for the OL (e.g., OL 3-OH 20:1/20:2) are listed in the order of R_1 and R_2).

To confirm its identity, the product ion at m/z 115 was subjected to further dissociation by MS^4 (Figure 5.2E), and was compared to the fragmentation behavior of the $[M+H-H_2O]^+$ or $[M+H-H_2O-CH_2CO]^+$ product ions formed by MS/MS or MS^3 of the $[M+H]^+$ precursor ions of authentic ornithine (Figure 5.4B) or N_α-acetyl-ornithine (Figure 5.5C) standards, respectively. The resultant spectra, revealing the losses of NH_3 (m/z 98), H_2O (m/z 97), CO (m/z 87) and NH_3+CO (m/z 70), were identical, thereby providing compelling evidence for its structure. Further evidence for the identity of this ornithine lipid was provided by observing the incorporation of five deuterium atoms upon H/D exchange and MS analysis of this ion (i.e., m/z 731 was observed to shift to m/z 736). However, as extensive deuterium scrambling of the deuterated precursor ion upon CID MS/MS, presumably resulting from exchange between the deuterium atoms in the amino and amide groups with the C_α hydrogen atoms in the backbone, was observed, as evidenced by the losses of H_2O, HOD, and D_2O, further mechanistic details regarding these losses could not be obtained. Thus, while Scheme 5.2 shows a potential pathway for formation of the ion at m/z 115, via the 'charge-directed' loss of water from the $[M+H]^+$ precursor ion, followed by the 'charge-remote' sequential losses of ketene

(−R_2'CH=C=O), water and ketene (R_1"CH=C=C=O), alternate charge-remote and charge-directed pathways cannot be ruled out.

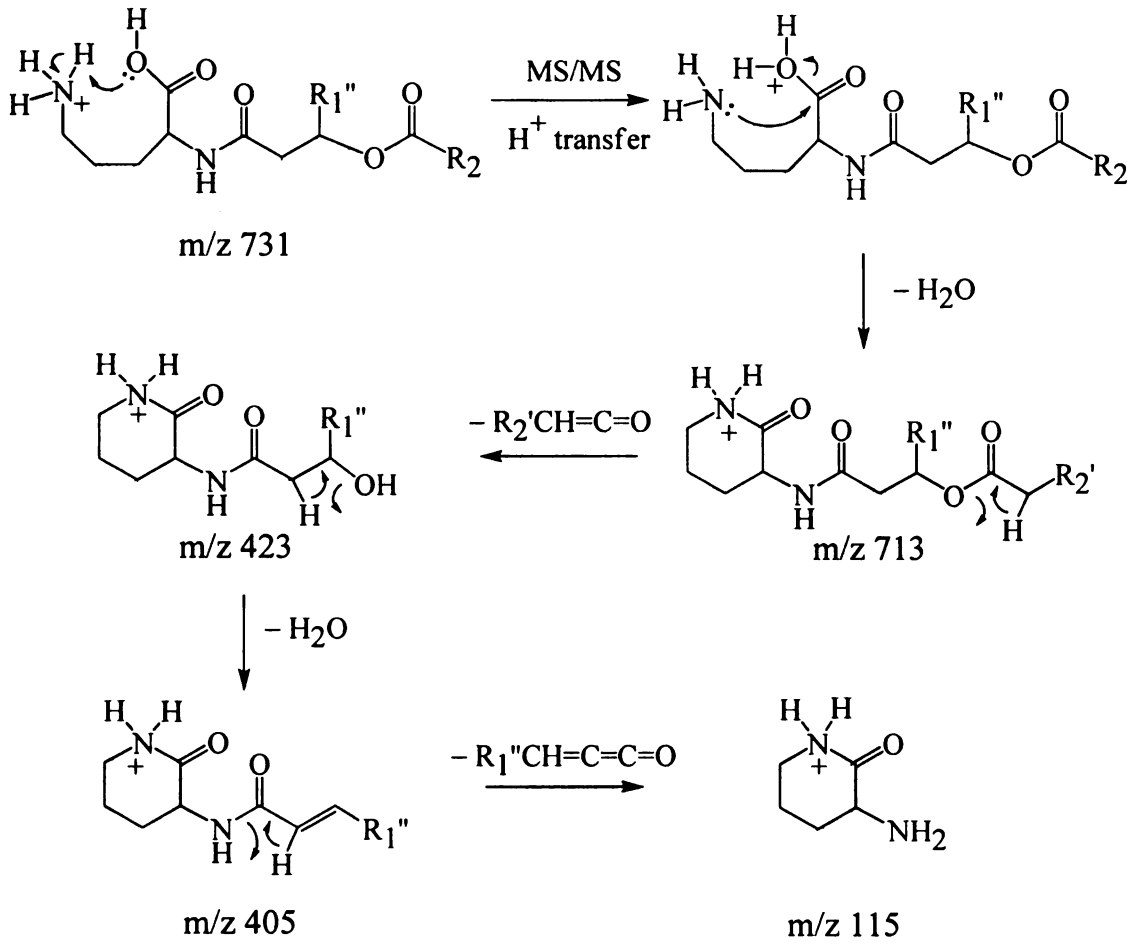
Figure 5.2 Identification of ornithine lipid (OL 3−OH 20:1/20:2) at m/z 731 from Figure 5.1B by positive ion CID MS/MS and MS^n. (A) MS/MS of m/z 731, (B) MS^3 of m/z 713 from panel A, (C) MS^3 of m/z 423 from panel A, (D) MS^3 of m/z 405 from panel A, and (E) MS^4 of m/z 115 from panel D.



t m/z 731 from

731, (B) MS^3 of

f m/z 405 from



Scheme 5.2 Proposed pathways for the multistage gas-phase fragmentation reactions of protonated ornithine lipids

Figure 5.3 shows the MS/MS and MS^3 spectra obtained by dissociation of the deprotonated $[M-H]^-$ precursor ion at m/z 729 from the GPCho-deficient strain of *R. sphaeroides*. The MS/MS spectrum (Figure 5.3A) was dominated by the loss of a neutral 20:2 fatty acid (R_2COOH, m/z 421), consistent with that observed from the positive ion mode data. This loss is proposed in Scheme 5.3 to occur via charged neighboring group-

assisted *cis*-1, 2 elimination reaction. This proposed mechanism was supported by the results from MS/MS of the fully H/D exchanged precursor ion (3 exchanges observed), where the loss of R_2COOH was predominantly observed, rather than R_2COOD (data not shown), indicating that it is the C_α-proton that is mainly involved rather than the exchangeable ones. Subsequent MS^3 of the m/z 421 product ion from the protonated precursor ion resulted in the loss of CO_2 (m/z 377), as well as the loss of a neutral ketene ($-R_1$"CH=C=C=O) originating from the 3–OH 20:1 fatty acid, thereby yielding a product ion at m/z 131 that corresponds to deprotonated ornithine (Figure 5.3B). A suggested pathway for these fragmentation reactions, consistent with previous reports in the literature describing the fragmentation reactions of deprotonated amino acids [183,283,284], is shown in Scheme 5.3. The formation of the m/z 131 ion in negative ion mode is also consistent with the sequential fragmentation reactions observed for the corresponding precursor ion in positive ion mode analysis. Also, MS^4 of the m/z 131 product ion (Figure 5.3C) resulted in identical spectra to those obtained by MS/MS or MS^3 of deprotonated ornithine or N_α–acetyl ornithine standards, respectively (Figure 5.4C and Figure 5.5E), thereby confirming its identity.

Analysis of the complementary pair of precursor ions observed at m/z 731 and m/z 729 in positive and negative ionization modes, as well as comparison of the fragmentation behavior of their characteristic 'fingerprint' ions observed at m/z 115 and m/z 131, respectively, with those of authentic ornithine or N_α–acetyl ornithine standards, provide insights into the multistage gas-phase fragmentation behavior of ornithine lipids,

thereby making possible the rapid and unambiguous assignment of these species in an unseparated complex lipid mixture, without requirement for independent synthesis of an entire OL lipid standard.

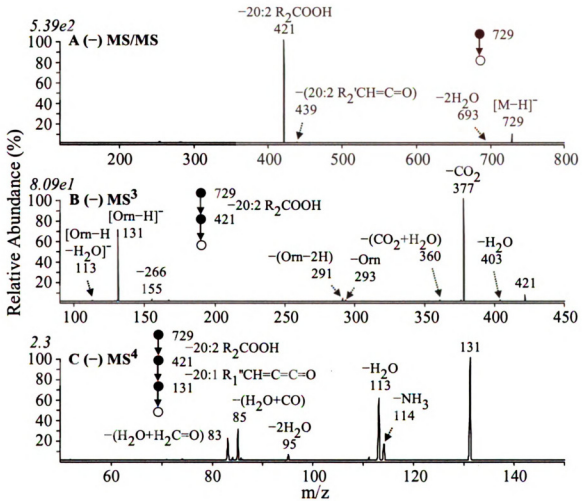
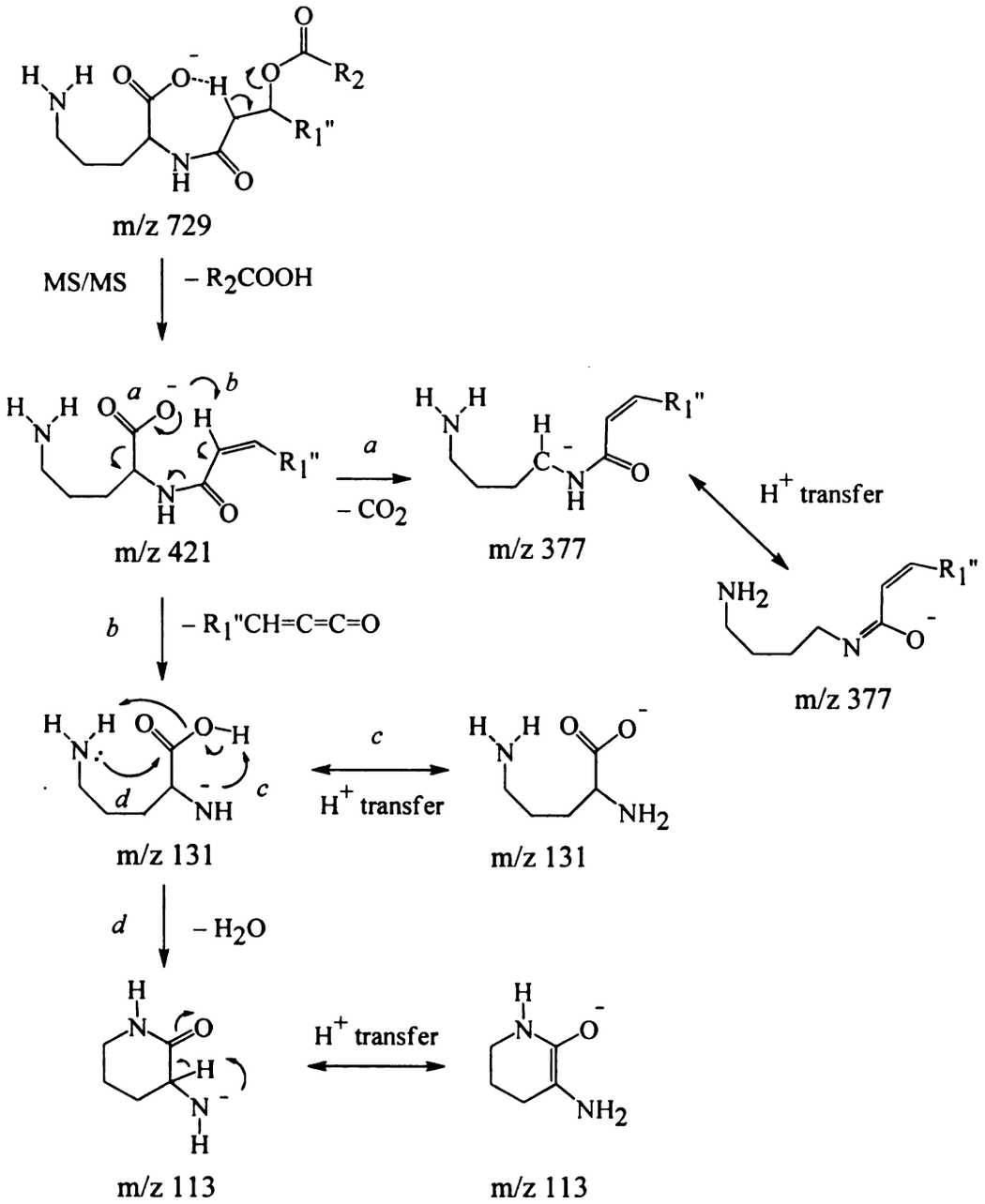


Figure 5.3 Identification of ornithine lipid (OL 3−OH 20:1/20:2) (m/z 729) from Figure 5.1D by negative ion CID MS/MS and MS^n. (A) MS/MS of m/z 729, (B) MS^3 of m/z 421 from panel A, and (C) MS^4 of m/z 131 from panel B.

The ornithine head group in the structures shown in Schemes 5.2 and 5.3 are linked to the fatty acid chain via an N_α amide bond, consistent with the structures of OL previously proposed for other bacteria. The linkage of the ornithine head group to the fatty acids could also potentially occur by forming an N_δ amide bond. However, dissociation of this species would not result in the same product ions observed here by MS/MS and MS^3 in either positive or negative ion modes. For example, CID MS/MS of protonated amino acids containing a free α–amino group are well known to result in the combined loss of H_2O and CO (46 Da), thereby allowing it to be disregarded.



Scheme 5.3 Proposed pathways for the multistage gas-phase fragmentation reactions of deprotonated ornithine lipids

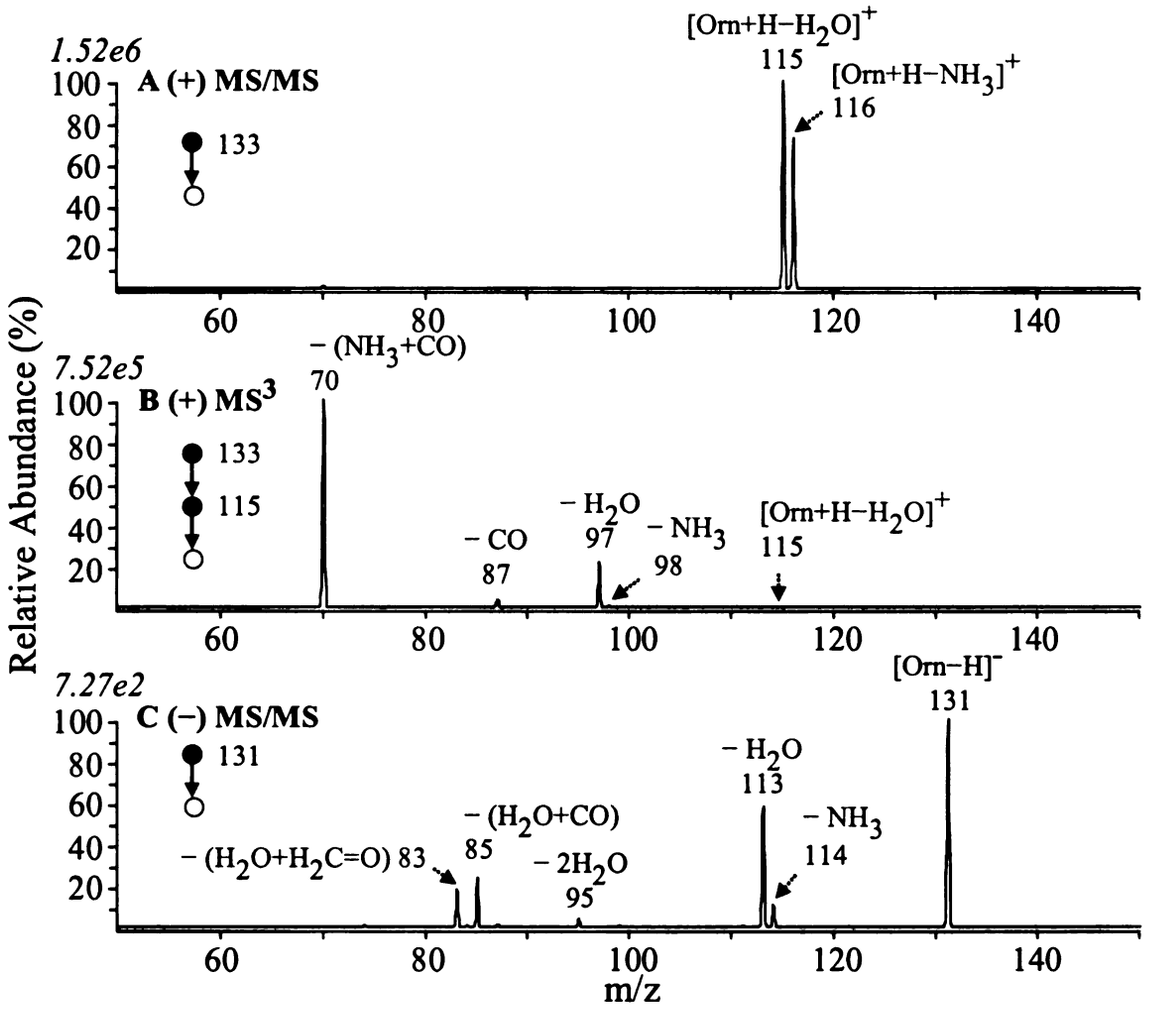
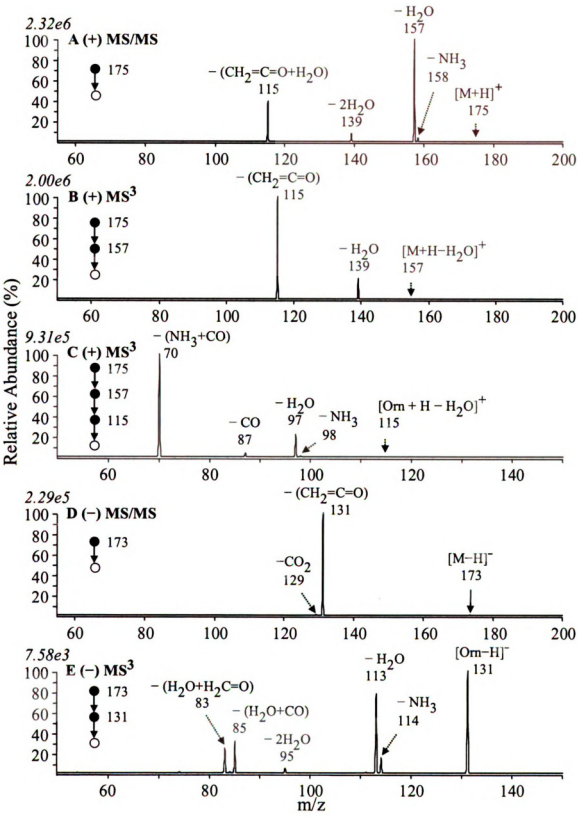


Figure 5.4 The fragmentation of ornithine standard in positive and negative ion modes: A) MS/MS of $[M + H]^+$ ions at m/z 133, B) MS^3 of m/z 115 generated in panel A, and C) MS/MS of $[M - H]^-$ ions at m/z 131.

Figure 5.5 The fragmentation of N_{α}–acetyl ornithine standard in positive and negative ion modes: A) MS/MS of $[M + H]^+$ ions at m/z 175, B) MS^3 of m/z 157 generated in panel A, C) MS^4 of m/z 115 generated in panel B, D) MS/MS of $[M - H]^-$ ions at m/z 173, and E) MS^3 of m/z 131 generated in panel D.


2.32e6
A (+) MS/MS
175
− (CH2=C=O+H2O)
115
− 2H2O
139
− H2O
157
− NH3
158
[M+H]+
175
2.00e6
B (+) MS3
175
157
− (CH2=C=O)
115
− H2O
139
[M+H−H2O]+
157
9.31e5
C (+) MS3
175
157
115
− (NH3+CO)
70
− CO
87
− H2O
97
− NH3
98
[Orn + H − H2O]+
115
Relative Abundance (%)
2.29e5
D (−) MS/MS
173
− (CH2=C=O)
131
−CO2
129
[M−H]−
173
7.58e3
E (−) MS3
173
131
− (H2O+H2C=O)
83
− (H2O+CO)
85
− 2H2O
95
− H2O
113
− NH3
114
[Orn−H]−
131
m/z

Elucidation of the fragmentation characteristics of different types of lipids is particularly useful when dealing with complicated lipid mixtures, since overlapping of multiple precursor ions at the same m/z frequently occurs. Figures 5.6A and 5.6B show the MS/MS and MS^3 spectra of the positive ion mode precursor ion observed at m/z 705 in Figure 5.1B and its $[M+H-H_2O]^+$ product ion, respectively. Similar to that observed in Figure 5.2A, the loss of water was observed as a dominant fragmentation pathway in the positive ion mode MS/MS spectrum, along with a seemingly complicated set of other product ions. However, MS^3 of the $[M+H-H_2O]^+$ ion at m/z 687 (Figure 5.6B) confirmed that these ions originated from the initial water loss product ion, indicative of the presence of 18:1 and 20:2 fatty acid chains. The product ions at m/z 423, 405 and 387 correspond to loss of the 18:1 fatty acid chain as a neutral ketene (18:1 $R_2'CH=C=O$), a neutral fatty acid (18:1 R_2COOH or 18:1 $R_2'CH=C=O+H_2O$) and a fatty acid + water (18:1 $R_2COOH+H_2O$), respectively, while m/z 397, 379 and 361 all correspond to the loss of the 20:2 fatty acid chain). This suggested the presence of two separate ornithine lipid species at similar relative abundances. Subsequent MS^3 analysis of the m/z 405 product ion (the resultant spectrum was identical to Figure 5.2D), as well as the m/z 379 product ion (data not shown), both led to formation of the m/z 115 ornithine 'fingerprint' ion via the loss of a 20:1 and 18:0 fatty acid, respectively, indicating that the identity of the two lipids present at m/z 705 corresponded to OL 3–OH 20:1/18:1 and OL 3–OH 18:0/20:2.

Confirmation of these lipids were obtained by MS/MS of the corresponding negative ion mode precursor observed at m/z 703 (Figure 5.6C). From this spectrum, two major product ions were formed, corresponding to the neutral losses of 18:1 R_2COOH (m/z 421) and 20:2 R_2COOH (m/z 395) fatty acid chains, respectively. MS^3 of these products both resulted in formation of the characteristic m/z 131 product ion via the loss of neutral 20:1 and 18:0 ketene molecules (R_1"CH=C=C=O), respectively (data not shown). They also displayed the same relative abundances as the two sets of product ions formed in positive ion mode MS/MS and MS^3.

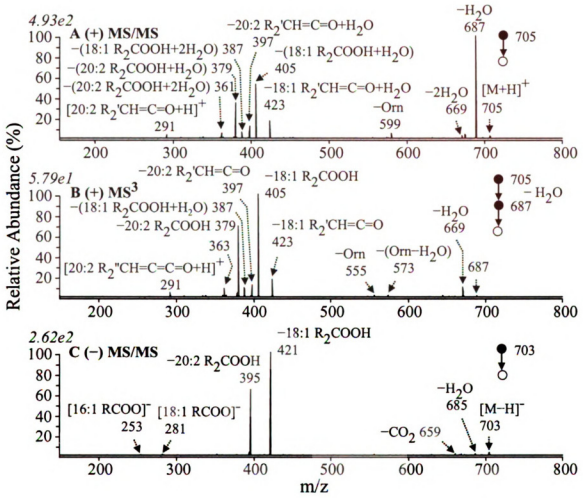


Figure 5.6 Identification of ornithine lipids (OL 3−OH 18:0/20:2 and OL 3−OH 20:1/18:0) at m/z 705 from Figure 1B by (A) CID MS/MS and by (B) CID MS^n of the m/z 687 ion from panel A. (C) Negative ion CID MS/MS of the corresponding ion at m/z 703 from Figure 1D.

5.3.3 Identification and characterization of glutamine lipids in *R. sphaeroides* by using positive and negative ionization mode MS^n

Similar to that seen in Figure 5.6A, MS/MS of the protonated precursor ion at m/z 719 from the membrane lipid extracts of both the wild type and GPCho-deficient strains of *R. sphaeroides* resulted in the dominant loss of water (m/z 701), along with multiple products corresponding to the loss of either a 19:1 (m/z 423, 405 and 387) or an 18:1 (m/z 455, 437, 420 and 419) fatty acyl chain (Figures 5.7A and 5.7B, respectively). However, MS^3 of the $[M+H-H_2O]^+$ product ion (Figure 5.7B) resulted in formation of only the 19:1 loss product ion series, suggesting that a non-ornithine containing lipid species was responsible for the 18:1 loss product ions. Subsequent fragmentation of the m/z 405 product ion in Figure 5.7C (the resultant spectrum was again identical to Figure 5.2D) resulted in the loss of a 20:1 fatty acid, allowing confirmation of the m/z 719 ornithine lipid that was present as being OL 3–OH 20:1/19:1. According to the nitrogen rule, the unknown lipid species that was also present at m/z 719 in addition to the OL 3–OH 20:1/19:1 lipid ion should contain an even number of nitrogen atoms.

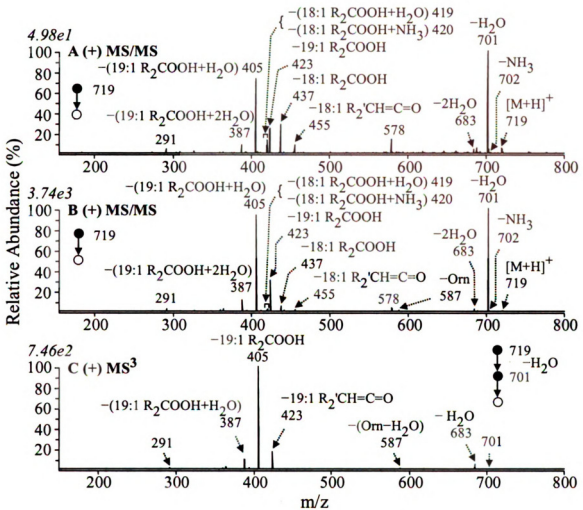


Figure 5.7 Identification of overlapping ornithine (OL 3−OH 20:1/19:1) and glutamine (QL 3−OH 20:1/18:1) lipids at m/z 719 by positive ion ESI CID MS/MS and MS^n. (A) MS/MS of m/z 719 from the wild type membrane lipid extract in Figure 5.1A, (B) MS/MS of m/z 719 from the GPCho-deficient mutant membrane extract in Figure 5.2B. (C) MS^3 of m/z 701 from panel B.

Figure 5.8A shows the MS^3 spectrum of the m/z 437 ion from Figure 5.7B. The most abundant product ions in this spectra were seen at m/z 420 and m/z 419, corresponding to the loss of water and ammonia, respectively. Notably, although the characteristic ornithine specific ion at m/z 115 was not observed, a series of product ions at m/z 147, 130 and 129 were formed, via the neutral loss of a 20:1 ketene ($-R_1$"CH=C=C=O) from the m/z 437 precursor ion or further from the m/z 420 and 419 product ions, respectively. Importantly, the ion at m/z 147 corresponds to the m/z of protonated ornithine with the addition of +14 Da, while the ions at m/z 130 and 129 correspond to the m/z of protonated ornithine with the addition of +14 Da, minus ammonia and water, respectively.

This +14 Da mass shift could potentially result from substitution of ornithine by lysine (analogous to incorporation of a methylene group into the ornithine amino acid side chain) [285], or via N– or O–methylation of ornithine to yield N–Me ornithine or ornithine–OMe, respectively. Alternatively, the +14 Da mass shift could result from substitution of the ornithine lipid by glutamine (analogous to oxidation of the δ methylene group of the ornithine amino acid side chain). N–methylation is a commonly observed process in lipid biosynthesis in *R. sphaeroides*. For instance, GPCho can be synthesized by consecutive N–methylation of GPEtn by the action of GPEtn N–methyl transferase [90], and both mono N–Me–GPEtn (+14 Da shift) and N, N–diMe–GPEtn (+28 Da shift) intermediates have been previously identified [90]. Similarly, the amino group in diacylglycerolhomoserine (DGHS) can be consecutively N–methylated to yield diacylglycerol–N, N, N–trimethylhomoserine (DGTS), a substitute for GPCho under phosphate-limiting growth conditions [274].

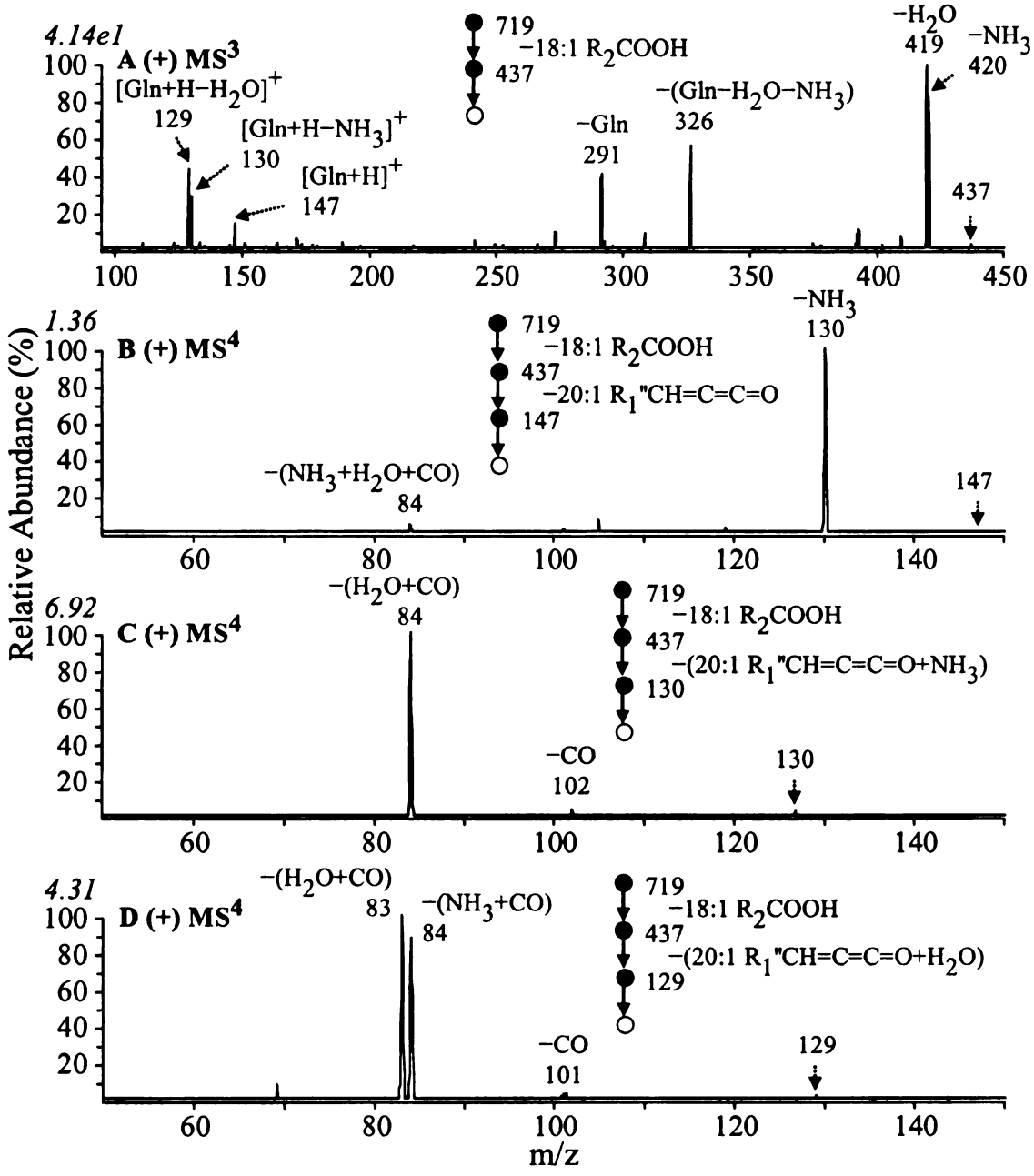
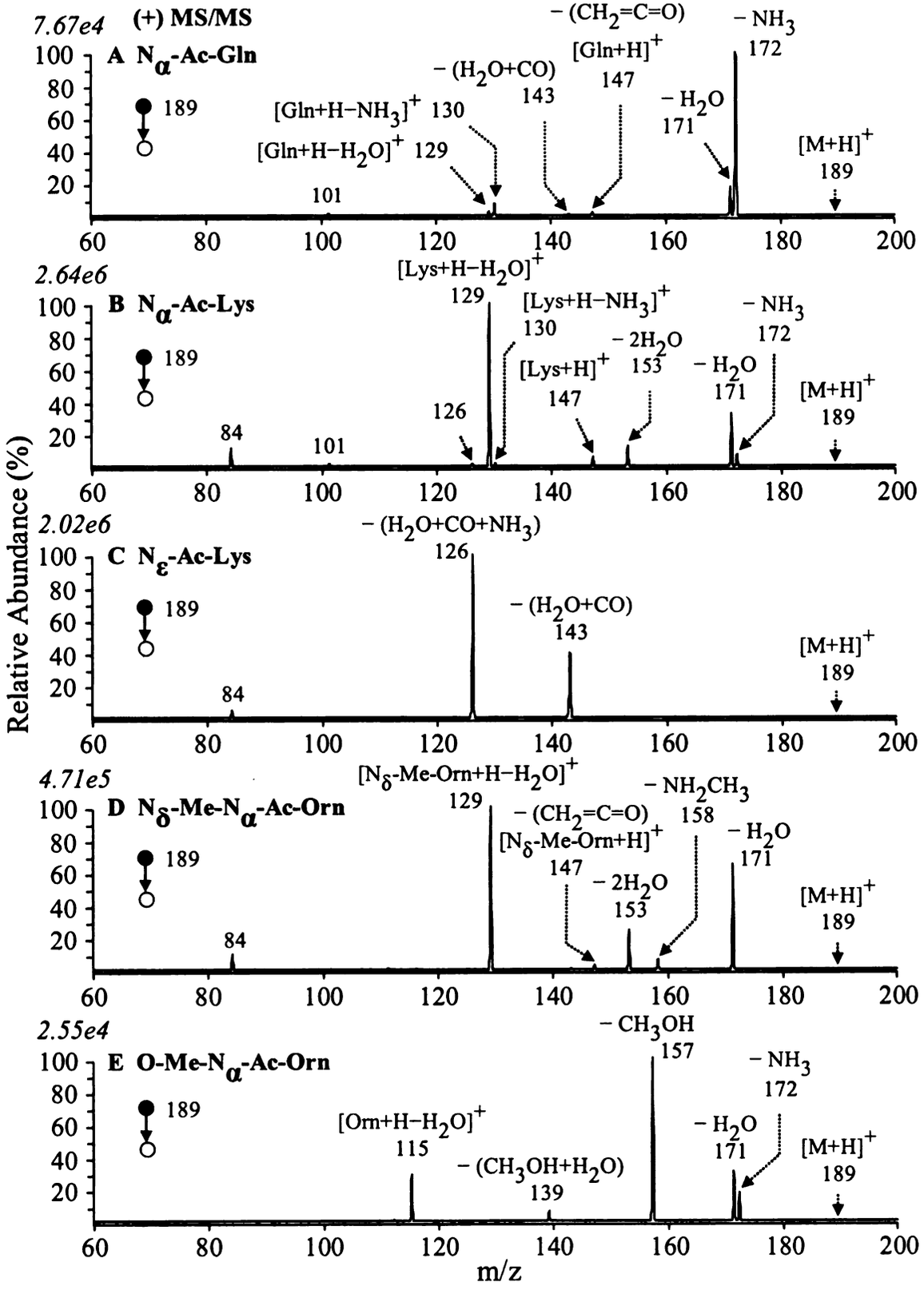


Figure 5.8 Identification of overlapping ornithine (OL 3−OH 20:1/19:1) and glutamine (QL 3−OH 20:1/18:1) lipids at m/z 719 by positive ion ESI CID MS^n. (A) MS^3 of m/z 437 from Figure 5.7B, (B) MS^4 of m/z 147 from panel B, (C) MS^4 of m/z 130 from panel B, and (D) MS^4 of m/z 129 from panel B.

Stark differences were observed however, between the product ions observed by MS^3 of m/z 437 (Figure 5.8A) with those formed by MS/MS of protonated N_α–acetyl lysine, N_ε–acetyl lysine, N_α–acetyl–N_δ–Me ornithine and N_α–acetyl ornithine–OMe (Figure 5.9), as well as between the MS^4 spectra obtained from the m/z 147, 130 and 129 product ions from Figure 5.8A (Figures 5.8B, 5.8C and 5.8D, respectively), and the MS/MS or MS^3 spectra obtained by dissociation of protonated lysine, N_δ–Me–ornithine and ornithine–OMe (data not shown), thereby ruling out these possible structures. In positive ion mode MS/MS (Figure 5.9), N_α–Ac–N_δ–Me–ornithine showed a distinct neutral loss of NH_2CH_3 (31 Da, Figure 5.9D) and N_α–Ac–ornithine–OMe predominantly fragmented by losing CH_3OH (32 Da, Figure 5.9E), whereas C_α, C_β, C_γ or C_δ–methyl ornithine should all tend to predominantly lose water (18 Da). The significant differences in the negative ionization mode MS^3 of m/z 435 (Figure 5.9B) from the MS/MS of these N–acetyl lysine or ornithine derived standards (Figure 5.10B–D) further denied these structures. Notably, the negative ion m/z 145 from all forms of lysine standards displayed predominantly the product ions at m/z 97 and m/z 99 via the neutral losses of H_2O + CH_2=O and H_2O + CO, respectively (data not shown), strikingly different from the m/z 145 of the unknown lipid.

Figure 5.9 Comparison of the positive ion mode ESI CID MS/MS spectra of m/z 189, the $[M + H]^+$ ions generated from synthesized amino acid standards: A) N_α-Ac-Gln, B) N_α-Ac-Lys, C) N_ε-Ac-Lys, D) N_δ-Me-N_α-Ac-Orn and E) O-Me-N_α-Ac-Orn.



spectra of m/z 189.

A) N_{α}-Ac-Gln. B)

c-Orn.

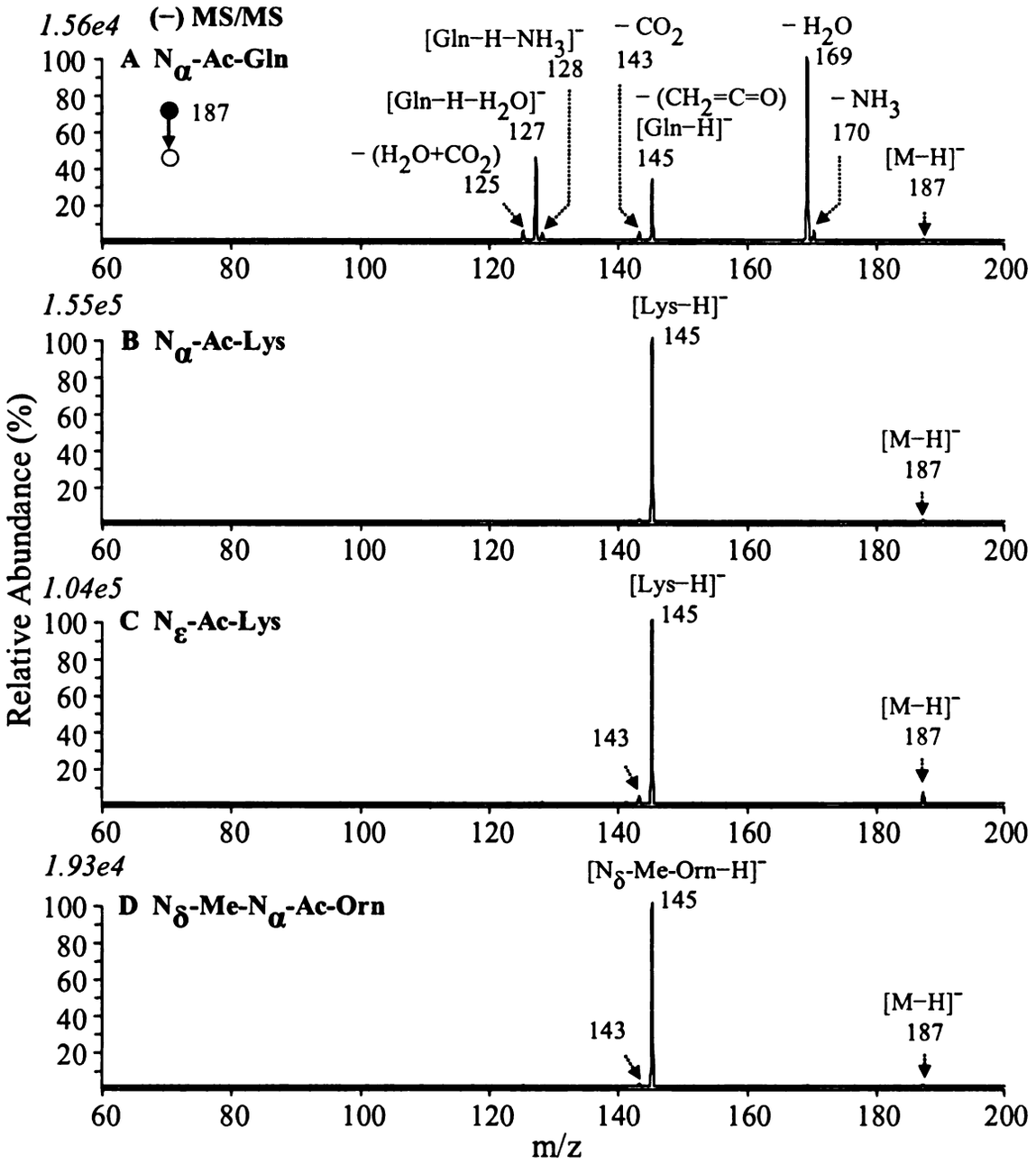


Figure 5.10 Comparison of the negative ion mode ESI CID MS/MS spectra of m/z 187, the $[M - H]^-$ ions generated from synthesized amino acid standards: A) N_α-Ac-Gln, B) N_α-Ac-Lys, C) N_ε-Ac-Lys, D) N_δ-Me-N_α-Ac-Orn and E) O-Me-N_α-Ac-Orn.

In contrast, the product ions observed by MS^3 of m/z 437 (Figure 5.8A) closely resembled those formed by MS/MS of N_α–acetyl or N_α–propyl glutamine (Figures 5.9A and 5.11A respectively), while the spectra shown in Figures 5.8B, 5.8C and 5.8D were found to be essentially identical to the spectra obtained by dissociation of the $[M+H]^+$, $[M+H-NH_3]^+$ and $[M+H-H_2O]^+$ ions from protonated glutamine (data not shown), indicating that the +14 Da mass shift had resulted from this substitution. The structure of the proposed glutamine lipid (QL) ion at m/z 719 therefore corresponds to QL 3–OH 20:1/18:1. Potential mechanisms to rationalize the product ion fragmentation pathways observed for this glutamine-containing lipid, and for formation of the m/z 147, 130 and 129 'fingerprint' ions, are shown in Scheme 5.4. Note that the pathway leading to the m/z 129 product ion in Scheme 5.4 is shown to occur via nucleophilic attack from the carbonyl oxygen of the glutamine amide side chain. This proposed pathway is consistent with previous mechanistic studies on the fragmentation reactions of protonated peptide ions. However, an alternative pathway involving nucleophilic attack from the amide nitrogen, resulting in the formation of a protonated 3–aminohexahydro–2, 6–pyridinedione product ion, can not be ruled out. The deamination fragmentation channel in MS^3 of m/z 437 (Figure 5.8A), seemed to be less favored with the increase in the length of the N–acyl chain (comparing with the MS/MS of N_α–acetyl or N_α–propyl glutamine in Figures 5.9A and 5.11A, respectively).

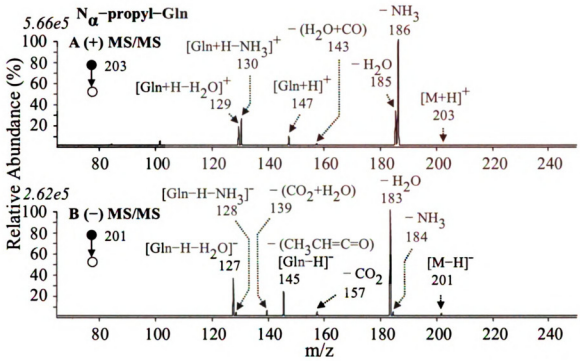
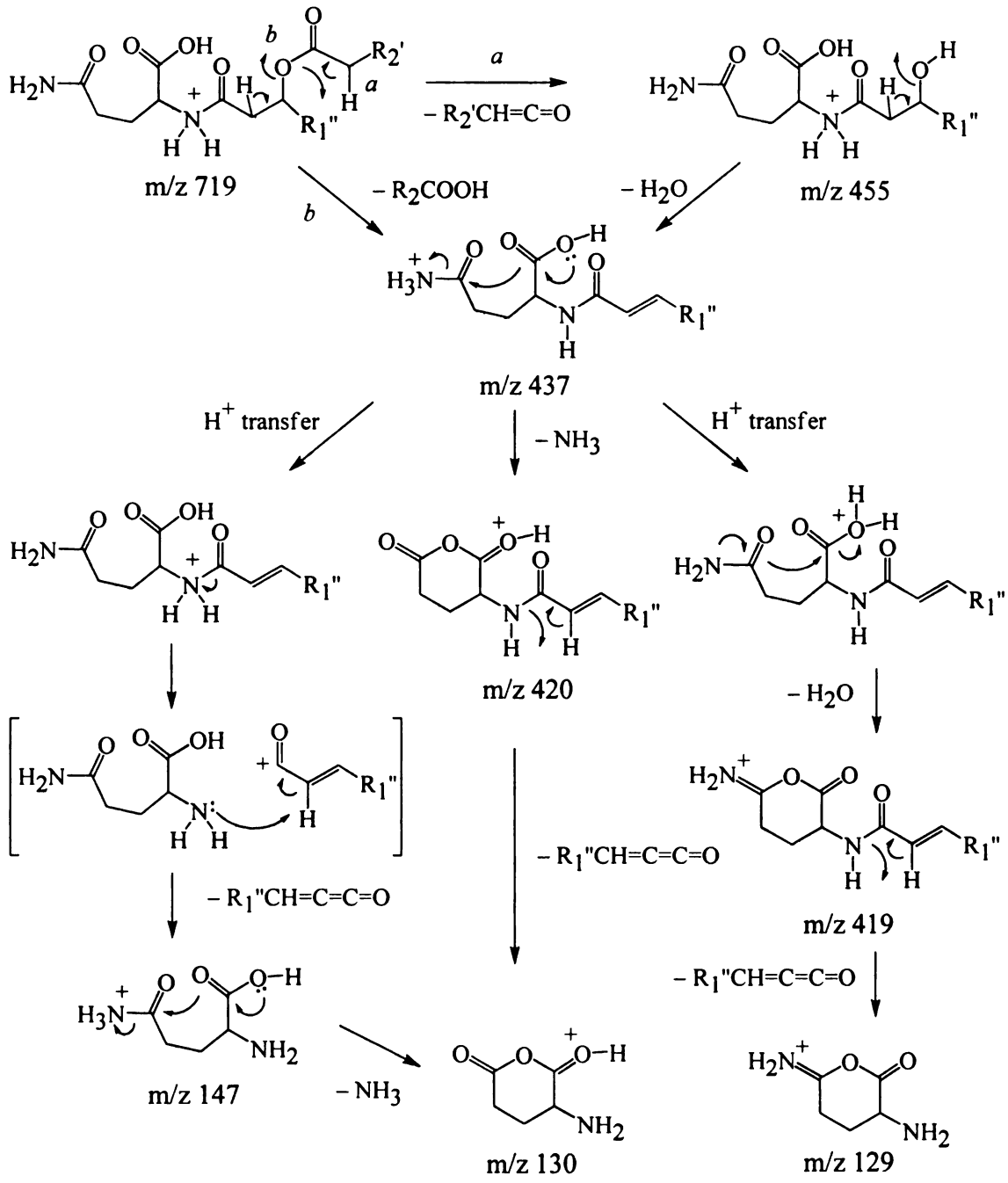


Figure 5.11 The fragmentation of N_α–propyl glutamine standard in positive and negative ion modes: A) MS/MS of $[M + H]^+$ ions at m/z 203, B) MS/MS of $[M - H]^-$ ions at m/z 201.

The fully H/D exchanged form of m/z 719 shifted to m/z 724 by incorporating five deuterium atoms. The product ion at m/z 455 in Figure 5.7B shifted predominantly to m/z 460 by losing $R_2'CH=C=O$, and when m/z 460 further fragmented in MS^3, HOD was observed as the predominant neutral loss, although H_2O and D_2O losses also occurred at much lower abundance. The loss of water containing one exchangeable proton and one non-exchangable C_α–proton supported the mechanism of sequentially losing ketene and water to form m/z 437 described in Scheme 5.4.



Scheme 5.4 Proposed pathways for the multistage gas-phase fragmentation reactions of protonated glutamine lipids

Further evidence for the presence of this QL 3–OH 20:1/18:1 glutamine containing lipid was obtained by inspection of the MS/MS, MS^3, MS^4 and MS^5 spectra obtained from the negative ion precursor at m/z 717 in Figure 5.1D. (Figures 5.12A–5.12D). Similar to that observed in the positive ion mode spectra, MS/MS of the negative ion precursor led to the neutral loss of either a 19:1 (m/z 421) or 18:1 (m/z 435) fatty acid ($-R_2COOH$) (Figure 5.12A). MS^3 of the m/z 421 ion resulted in loss of CO_2, as well as the loss of a 20:2 ketene to yield the 'fingerprint' ornithine specific product ion at m/z 131, confirming the presence of the OL 3–OH 20:1/19:1 ornithine lipid (data not shown). MS^3 fragmentation of the m/z 435 ion led to the losses of NH_3 (m/z 418), H_2O (m/z 417), CO_2 (m/z 391) and CO_2+H_2O (m/z 373), as well as the formation of product ions at m/z 145, 128 and 127 (Figure 5.12B). Similar to that observed in positive ion mode therefore, these ions correspond to the $[M-H]^-$, $[M-H-NH_3]^-$ and $[M-H-H_2O]^-$ ions of deprotonated glutamine. Indeed, the MS^4 spectra of the m/z 145 from Figure 5.12B (Figures 5.12C) and the further MS^5 spectra of its product ion at m/z 127 were found to be identical to the MS/MS and MS^3 spectra acquired from an authentic deprotonated glutamine standard (data not shown). Potential mechanisms to rationalize the formation of the m/z 145 and 127 glutamine specific 'fingerprint' ions are shown in Scheme 5.5. Note that the pathway for formation of the m/z 127 product ions from the m/z 435 product could also potentially occur via nucleophilic attack from the carbonyl oxygen of the glutamine amide side chain following initial proton transfer from the amide nitrogen to the carboxylate anion, analogous to that shown in Scheme 5.4.

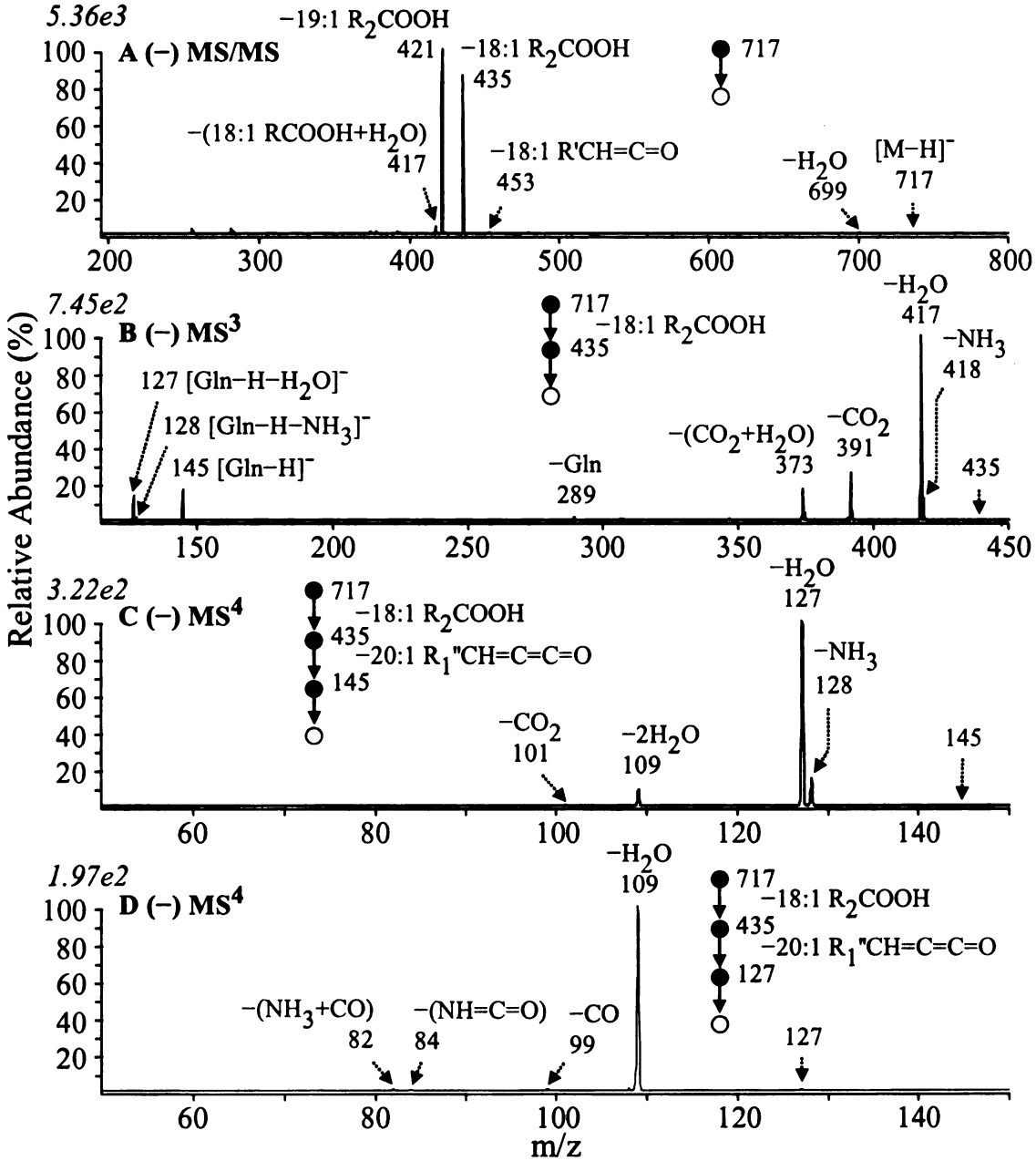
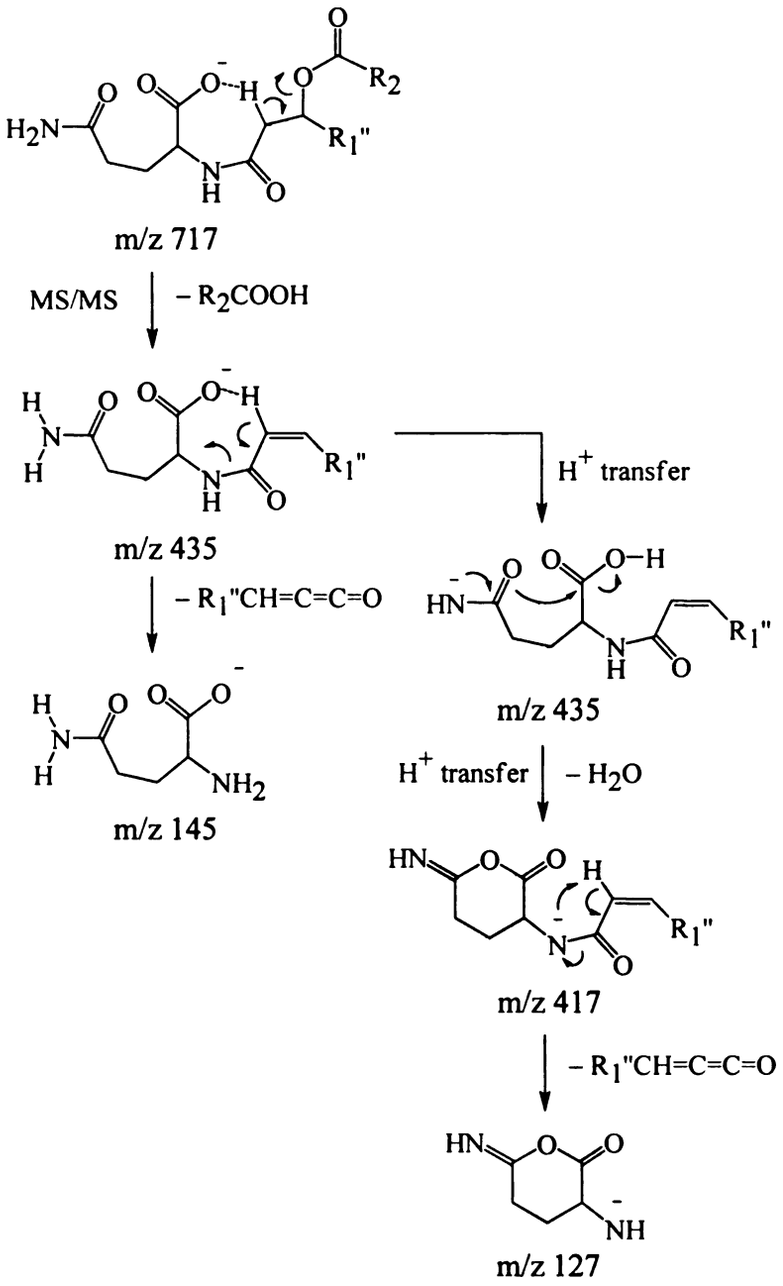


Figure 5.12 Identification of overlapping ornithine (OL 3−OH 20:1/19:1) and glutamine (QL 3−OH 20:1/18:1) lipids at m/z 717 by negative ion ESI CID MS/MS and MS^n. (A) MS/MS of m/z 717 from Figure 1D, (B) MS^3 of m/z 435 from panel A, (C) MS^4 of m/z 145 from panel B, and (D) MS^4 of m/z 127 from panel B.

Importantly, these proposed mechanisms were supported by the results from H/D exchange experiments. For example, MS/MS of the deuterated precursor ions at m/z 720 (three exchanges) resulted in loss of the 18:1 fatty acid as R_2COOH rather than R_2COOD, indicating that this loss mainly occurs by a *cis*-1, 2 elimination mechanism. MS^3 of m/z 435 resulted in formation of m/z 145 via loss of R_1"CH=C=C=O, consistent with the charge-directed fragmentation mechanism shown in the left branch of Scheme 5.5. In contrast, the loss of water was observed at m/z 418 (D_2O) and m/z 419 (HOD), at similar abundances, indicating that this loss could involve both exchangeable protons and the non-exchangeable C_α–proton.

Interestingly, the significantly increased abundance of the m/z 435 glutamine containing product ion in the negative ion mode MS/MS spectrum in Figure 5.12A relative to that of the m/z 421 ornithine-containing product ion, compared to the relative abundance of the corresponding ions in the positive ion mode spectrum (compare Figures 5.12A and 5.7B) is consistent with an expected improvement in the ionization efficiency for the glutamine lipid precursor ion in negative mode, due to the presence of its less basic amide functional group, compared to a primary amine in the ornithine lipid. In contrast, OL are expected to exhibit some preferential ionization in positive mode due to the presence of the more basic primary amine compared to the amide functional group.



Scheme 5.5 Proposed pathways for the multistage gas-phase fragmentation reactions of deprotonated glutamine lipids

5.3.4 Summary of the ornithine and glutamine lipid species identified from wild type and GPCho-deficient *R. sphaeroides* cell membranes

Using the characteristic multistage gas-phase fragmentation behaviors of the OL and QL lipids described above, all of the ions appearing above 1% normalized relative abundance in the positive and negative ion mode mass spectra for the wild type and GPCho-deficient *R. sphaeroides* cell membranes were examined here. The identities of all the lipids identified from this study are listed in Table 5.1. Interestingly, none of the major OL molecular species reported previously in bacteria *Sinorhizobium meliloti* [106] and *Rhodobacter capsulatus* [273] were found to be abundant in *R. sphaeroides*. The R_1 3–OH fatty acyl chains connected to the amino acid head group predominantly consist of 3–OH 18:0, 18:1, 20:0 and 20:1 chains. The R_2 second fatty acyl chain attached via the 3–OH group were found to primarily consist of 18:0, 18:1, 19:1, 20:2, 20:3 and 21:1 chains. Based on prior reports in the literature [107,187], the 19:1 and 21:1 chains are likely to contain a cyclopropane group, formed via the addition of CH_2 onto a double bond of an 18:1 or 20:1 fatty acid, rather than containing an odd number of carbons in the backbone [286].

Glutamine-containing lipids have not previously been reported in the literature, and their origin remains unknown. The presence of a side chain carbonyl group in glutamine lipids should make this lipid unreactive with the ninhydrin reagent. In fact, N_α–acetyl glutamine was found here to give a negative ninhydrin test result (data not shown). Thus, although evidence is lacking, it is intriguing to speculate that the ninhydrin-negative phosphate-free lipid species observed following incorporation of ^{14}C-

labeled ornithine as a substrate for a potential homolog of aspartyl/aspariginal β–hydroxylase in *Rhizobium tropici* [269], correspond to glutamine lipids.

The possibility of these glutamine lipids appearing as artifacts due to oxidation of ornithine lipid species during sample preparation cannot be ruled out. However, if this had occurred, it would be expected that the more susceptible double bonds in the fatty acid chains of the ornithine lipids would not be found intact. Efforts to chemically oxidize the δ–methylene group of N–acetyl–ornithine, using conditions previously demonstrated to result in the effective oxidation of methionine, cysteine, S–alkyl cysteine and tryptophan [287], did not yield N–acetyl–glutamine, indicating the stability of the ornithine head group to oxidative modifications. Furthermore, despite the wide variety of ornithine lipids observed here, only a limited number of glutamine lipids were observed, and the relative abundances of these lipids did not reflect those of the ornithine lipids. The artificial oxidation would not be expected to display such selectivity.

Table 5.1 Summary of the ornithine (OL) and glutamine (QL) lipid species extracted from the cell membranes of wild type and GPCho-deficient *R. sphaeroides*[a]

$[M+H]^+$ m/z	$[M-H]^-$ m/z	Ornithine Lipids (OL) (wild type)	Ornithine Lipids (OL) (GPCho-deficient)	Glutamine Lipids (QL) (wild type)	Glutamine Lipids (QL) (GPCho-deficient)
677	675		OL 3-OH 18:1/18:1 OL 3-OH 20:1/16:1 OL 3-OH 16:0/20:2		
691	689	OL 3-OH 18:1/19:1	OL 3-OH 18:1/19:1		
693	691	OL 3-OH 18:0/19:1	OL 3-OH 18:0/19:1		QL 3-OH 20:1/16:0 QL 3-OH 18:0/18:1
703	701	OL 3-OH 18:1/20:2 OL 3-OH 18:0/20:3	OL 3-OH 18:1/20:2 OL 3-OH 18:0/20:3		
705	703	OL 3-OH 18:0/20:2 OL 3-OH 20:1/18:1	OL 3-OH 18:0/20:2 OL 3-OH 20:1/18:1		
707	705	OL 3-OH 20:0/18:1 OL 3-OH 20:1/18:0	OL 3-OH 20:0/18:1 OL 3-OH 20:1/18:0		
719	717	OL 3-OH 20:1/19:1	OL 3-OH 20:1/19:1	QL 3-OH 20:1/18:1	QL 3-OH 20:1/18:1
721	719	OL 3-OH 20:0/19:1	OL 3-OH 20:0/19:1	QL 3-OH 20:0/18:1	QL 3-OH 20:0/18:1
731	729	OL 3-OH 20:1/20:2 OL 3-OH 20:0/20:3	OL 3-OH 20:1/20:2		
733	731		OL 3-OH 20:0/20:2		QL 3-OH 20:1/19:1
747	745	OL 3-OH 20:1/21:1	OL 3-OH 20:1/21:1		
749	747	OL 3-OH 20:0/21:1	OL 3-OH 20:0/21:1		

[a] Only those ions with relative abundance > 1% in the MS spectra were examined.

5.4 Conclusions

The molecular structures of ornithine lipid (OL) and novel glutamine lipid (QL) species extracted from the membranes of wild type *R. sphaeroides*, as well as from a GPCho-deficient mutant, have been determined by using multistage tandem mass spectrometry in a linear quadrupole ion trap. The glutamine lipids were found to share an analogous structure with the ornithine lipids, where the amino acid head group is connected to the first fatty acid via an amide bond at the N_{α}–position, and the second fatty acid is incorporated via an ester bond with a 3–OH group within the first fatty acid. Characteristic 'fingerprint' product ions for OLs are observed at m/z 115 in positive ion mode and at m/z 131 in negative ion mode, whereas analogous 'fingerprint' ions for QLs are observed at m/z 147, 130 and 129 in positive ion mode, and at m/z 145 and 127 in negative ion mode. The fundamental knowledge obtained here regarding the multistage gas-phase fragmentation behavior of both ornithine and glutamine lipids establishes the basis for future applications aimed toward the sensitive identification and quantification of these lipid species in complex lipid mixtures.

MICHIGAN STATE UNIVERSITY LIBRARIES
3 1293 03063 4079

THESIS
6
142
337
THS

LIBRARY
Michigan State
University

PLACE IN RETURN BOX to remove this checkout from your record.
TO AVOID FINES return on or before date due.
MAY BE RECALLED with earlier due date if requested.

DATE DUE	DATE DUE	DATE DUE

5/08 K:/Proj/Acc&Pres/CIRC/DateDue.indd

INVESTIGATING THE FUNCTIONAL ROLES OF LIPIDS IN MEMBRANE PROTEIN CYTOCHROME *C* OXIDASE FROM *RHODOBACTER SPHAEROIDES* USING MASS SPECTROMETRY AND LIPID PROFILE MODIFICATION

VOLUME II

BY

Xi Zhang

A DISSERTATION

Submitted to
Michigan State University
in partial fulfillment of the requirements
for the degree of

DOCTOR OF PHILOSOPHY

Chemistry and Biochemistry & Molecular Biology

2009

Chapter 6

Characterization of Sulfoquinovosyldiacylglyceride (SQDG) and Diacylglyceryl-N, N, N-trimethylhomoserine (DGTS) Lipids Extracted from *Rhodobacter sphaeroides* using Triple Quadrupole and Linear Ion Trap Mass Spectrometry

6.1 Summary

The polar non-phospholipids sulfoquinovosyl diacylglycerol (SQDG, negatively charged) and diacylglyceryl-trimethylhomoserine (DGTS, positively charged) were both found to be the major types of membrane lipids observed in *R. sphaeroides* under phosphate-limiting anaerobic [11] or aerobic growth conditions (see Chapter 10 for a detailed discussion). In contrast, under normal phosphate growth conditions, SQDG was present in the membrane at a much lower abundance compared to phospholipids, whereas DGTS was typically not detectable using either ^{14}C-radioactive labeling [11] or mass spectrometry (see Chapters 7, 9 and 10 for details). Since the drastically altered lipid profile still enables the survival of the bacteria, and even the unhampered expression of a fully active four-subunit membrane protein cytochrome *c* oxidase (see Chapter 10), and SQDG has been clearly detected in the C*c*O crystals even under normal phosphate growth (see Chapter 9), it was of importance to examine and understand the fragmentation characteristics of SQDG and DGTS, in order to be able to achieve an

accurate identification of their molecular structures, and the sensitive quantification of each molecular species using a minimum amount of sample, such as the purified protein and the C*c*O protein crystals (see Chapter 9 for a picture of crystal).

In spite of their potential physiological significance [288,289], SQDG and DGTS lipid structures and fragmentation mechanisms have not been examined systematically using modern mass spectrometry techniques, such as the low-energy CID tandem mass spectrometry coupled with "soft" ionization methods including MALDI and ESI, which have found increasingly extensive applications in the new areas of lipidomics and metabolomics [59,117,290]. The few previous cases of lipid biochemistry studies that have used mass spectrometry to help confirm SQDG and DGTS employed mass spectrometry with relatively higher energy, where the spectra can be different from those of low-energy mass spectrometry [11,99,106,108,291].

By using a combination of collision-energy-resolved tandem mass spectrometry (MS/MS), multistage tandem spectrometry (MS^n) and H/D exchange, the fragmentation characteristics of SQDG and DGTS lipids from complex mixtures (lipid extracts or membrane pellets) were examined. Without requirement for methods such as chromatography and NMR, identification could be achieved by using m/z 225 (−ve) for SQDG, and m/z 236 (as well as the lower-abundance m/z 144 if the low-mass-cutoff allows, +ve) for DGTS as the fingerprint product ions in tandem mass spectrometry (MS/MS). These fingerprint MS/MS product ions were then used to mass-spectrometrically "separate" SQDG lipids out of complex total lipids extracts, and at the same time quantify between all the SQDG molecular species with different fatty acids

chains by using a precursor ion scan in a triple quadrupole mass spectrometer, or by precursor ion mapping in a quadrupole linear ion trap mass spectrometer.

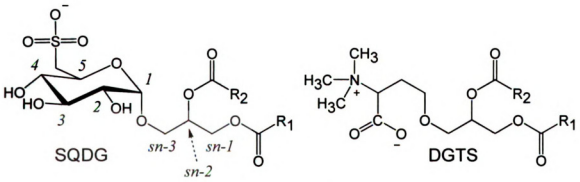
6.2 Introduction

6.2.1 Biological interests in SQDG and DGTS lipids

SQDG is a type of anionic, bilayer-forming, glycolipid that contains a negatively-charged quinovosylsulfite group instead of a phosphate group, and diacylglyceryl-trimethylhomoserine (DGTS) is a type of cationic phosphate-free lipid, composed of a diacyl-glyceride backbone connected to a positively-charged N, N, N-trimethyl homoserine head group (Scheme 6.1). SQDG is abundant in the membranes of most photosynthetic bacteria, higher plants, mosses, ferns and algae [14,289,292]. In contrast to phospholipids, SQDG contains a negatively charged sulfite linked via a S-C bond to the 6-C of the quinovose sugar ring attached to the glycerol backbone. SQDG has been found to be preferentially, though not exclusively, associated with photosynthetic organisms [14,289,292]. Although SQDG is found to be not essential for anoxygenic photosynthesis, and no evidence has suggested that SQDG has an essential role in the oxygenic photosynthesis [14], it does demonstrate conditional importance under phosphate-limiting conditions [289], and becomes essential when phosphatidylglycerol (GPGro) is depleted [289,292]. SQDG has also been found to inhibit DNA polymerases and to have antitumor and antiviral effects, probably due to its anionic detergent-like structure [293].

More recently, the polar non-phospholipids SQDG (negatively charged) and DGTS (positively charged) were both found to be the major types of membrane lipids in *R. sphaeroides* under phosphate-limiting anaerobic or aerobic conditions (see Chapter 10 for a detailed discussion). In contrast, under normal phosphate growth conditions, SQDG

was present in the membrane at an abundance much lower than the phospholipids, whereas DGTS was typically not detectable using either ^{14}C-radioactive labeling [11] or modern mass spectrometry (see Chapters 7, 9 and 10 for details). More importantly, however, despite a drastically altered lipid profile, the bacteria were still viable and resulted in the the unhampered expression of a fully active four-subunit membrane protein cytochrome *c* oxidase (see Chapter 10 for details). SQDG has also been clearly detected in CcO crystals, particularly in the cardiolipin-deficient version, even under normal phosphate growth conditions (see Chapter 9 for details).



Scheme 6.1 General structures of SQDG and DGTS

The major biosynthetic pathways of SQDG and DGTS in bacteria have been recently elucidated by using genetic approaches, but their functions still largely remain to be defined, in addition to the general proposition that SQDG can functionally replace GPGro due to the negatively charged head group, and DGTS can replace GPCho likely due to the fixed positive charge on the N, N, N-trimethyl head group [11,14]. Their physiological significance suggested by the recent findings outlined in Chapters 7 and 10, therefore, makes it very important to be able to accurately identify their molecular

structures and quantify each molecular species using a minimum amount of sample, especially when analyzing traces of lipids that remain bound in the purified C*c*O protein, and the micro-scale C*c*O protein crystals.

6.2.2 Current status of structural studies of SQDG and DGTS

Traditionally, the separation and identification of SQDG has relied on thin layer chromatography (TLC) combined with a series of functional-group-selective sprays, including a positive reaction with α-naphthol spray which can specifically react with the sugar structure to develop a color, and a negative reaction with phosphate and amino group tests [15] (see Chapter 2 for a detailed description). In order to obtain any convincing evidence of the new structure, NMR (^{1}H and ^{13}C) has mostly been a requirement [11,274,294,295], but typically requires a large amount of sample and rigorous lipid purification, often using TLC [11,274,295]. Recently, mass spectrometry-based methods have been applied to help confirm the presence of SQDG, once the lipid structure has been partially characterized using NMR methods, including FAB-sector high-energy collision-induced dissociation (CID) MS/MS [108,199,291,296], MALDI-TOF post-source decay (PSD) [99], ESI-CID MS/MS in triple quadrupole [150] , and more recently ESI-low-energy CID MS/MS in ion trap [296,297], and MALDI-trap TOF CID MS^{n} [298] in the negative ion mode. The quantification of this type of lipid has been dependent on silica gel TLC in combination either with metabolic radioactive labeling, or with gas chromatography-mass spectrometry (GC-MS), after scraping the identified spot off the plate followed by re-extraction, saponification and chemical derivatization [11,99,262,299].

Prior to the advent of highly sensitive multi-stage mass spectrometry (MS^n) experiments that can be carried out in quadrupole linear ion trap mass spectrometers, many cases of lipid biochemistry studies have relied on tandem mass spectrometry with relatively higher collision energies to assist with the confirmation of SQDG and DGTS. More recently, low-energy CID tandem mass spectrometry coupled with "soft" MALDI and ESI ion sources has found increasing extensive applications in the new eras of lipidomics and metabolomics [59,117,290]. A few recent cases that applied these methods have rationalized the formation of characteristic product ions from SQDG and DGTS lipids under low-energy CID conditions [93,199], but the mechanism for the formation of these ions has not been systematically investigated.

In most of these studies, SQDG lipids were identified by the observation of the characteristic product ions at m/z 81 (HSO_3^-) [150] or 80 (SO_3^- seen in FAB-CID MS/MS) [99,108,291] and the fragment ion at m/z 225 in some studies [99,108,150,291,296,298]. On the other hand, the DGTS lipids have been identified based on the observation of a group of multiple product ions consisting of m/z 58, 59, 83, 84, 102, 117, 130, 144, 162, 202 and 236, including both even-electron cations and radical cations, by using FAB-CID MS/MS [11,106]. More recently the product ions at m/z 144 and m/z 236 observed in ESI-CID MS/MS in a hybrid quadrupole-TOF mass spectrometer were proposed to come from DGTS [93]. However, the relative abundances of these product ions are highly dependent on the energy applied in the fragmentation reactions in these types of mass spectrometers, and the extent of different levels of fragmentation reactions are difficult to control (see Chapter 2 for a detailed explanation), such that the spectra can be quite different from those obtained by low-energy ion trap

tandem mass spectrometry, making it difficult to use these ions or these spectra as the reference for lipid identification in future studies. It is therefore important to understand more clearly the fragmentation characteristics of SQDG in modern mass spectrometry.

A good understanding of the fragmentation characteristics is critical for accurate identification and further quantification of SQDG lipid in complicated lipid mixtures. With the availability of collision energy resolved low-energy CID MS/MS in triple quadrupole mass spectrometer [300], and the CID MS^n experiments [173] in the quadrupole ion trap mass spectrometer together with the option of quick pulsed-Q dissociation (PQD), more abundant and reliable experimental information can be gained toward understanding the gas-phase fragmentation behavior of this anionic lipid, which points toward more accurate and sensitive identification and quantification of this type of lipid.

Most lipids primarily form singly charged precursor ions with the exception of lipids such as CL and phosphorylated phosphatidylinositol (GPIns-P_n), which form doubly or multiply charged precursor ions in the negative ion mode [117]. Structural information for their identification is often provided by the observation of characteristic neutral loss and/or low m/z product ions, such as the fatty acid chain ions and the ions formed from the head group such as $PO_4CH_2CHCH_2OH^-$ at m/z 153 from a few types of phospholipids [117,187], and $SO_3CH_2C_5H_7O_4^-$ at m/z 225 specifically from SQDG lipids (to be described in the following sections). The need to observe these lower-mass fragment ions poses a challenge for ion trap instruments due to the low mass cutoff issue [170]. The lowest product ion m/z value detectable in the quadrupole ion trap is limited

by the activation q value. In conventional low-energy CID on the quadrupole linear ion trap mass spectrometer, the activation of fragment ions is typically performed at a q value of around 0.25 (See Chapter 2 for a detailed description), corresponding to a low-mass-cutoff (LMCO) at around m/z 250 (for precursor ion at m/z 908), which is often higher than the m/z of fragment ions characteristic for the lipid head group. Complete identification of lipids often requires MS^n even in the negative ion mode. The ability of the instrument to detect these lower mass fragment ions can potentially enhance the accuracy of lipid identification in the MS/MS stage, which in turn makes MS/MS based ion mapping experiments, such as precursor ion mapping or the product ion mapping, more powerful for the rapid and accurate profiling of lipids in complex samples.

However, although decreasing the activation q value can extend the low mass cutoff, making ions at lower m/z more detectable, it also causes more precursor ions to become unstable in the activation step, leading them to be lost before they are fragmented. Alternatively, PQD fragmentation can be used to extend the mass range for fragment ion detection to a much lower value [177], typically m/z 50 for lipid precursor ions, which is achieved through applying a pulse at high q (0.7) for activation followed by a quick drop of the q value down to 0.05 to trap the fragment ions for detection. However, such a method can potentially open up more fragmentation channels due to the higher activation energy introduced to the precursor ion, and enhance the percentage of the precursor ions that undergo fragmentation, yet risk losing overall signals during activation at such a high q value. In order to perform sensitive and accurate lipid identification and quantification using the precursor ion scan, a higher abundance of the characteristic fragment ion is desired, which is a tradeoff between higher fragmentation

percentage and higher abundance of the ions that go to fragmentation. Nonetheless, PQD can potentially provide useful information complementary to that provided by CID, and it has never been reported in the application of lipid analysis, so the fragmentation of SQDG via PQD fragmentation was also examined in this chapter.

6.3 Results and discussion

6.3.1 Fragmentation behaviors of SQDG in MS/MS and MS^n

In order to understand the fragmentation behavior of SQDG, the SQDG lipids in a total lipid extract from *R. sphaeroides* isolated membrane pellets, or the purified C*c*O, were examined using ESI connected with triple quadrupole or quadrupole linear ion trap mass spectrometers, and low-energy CID fragmentations. PQD fragmentation in the ion trap was also characterized. The molecular species of SQDG in the membrane were found to be similar to those in the purified and crystallized enzymes (using both MALDI and ESI) based on the complete identification of each molecular species using MS^n (see Chapter 9 for some of the data). Also, the fragmentation behaviors of the SQDG species containing different fatty acid chains (16:0, 18:1 or 18:0) are very similar to each other. Here, SQDG 16:1/18:1 at m/z 819 is mainly shown as the example for the purpose of illustration.

6.3.1.1 CID MS/MS of SQDG in a triple quadrupole mass spectrometer

Figure 6.1 shows the negative ion mode ESI-CID MS/MS product ion spectra of m/z 819 from the membrane lipid extract of *R. sphaeroides* under optimized collision

energy (where the precursor ion is at about the same abundance level as the most abundant product ion) obtained on the triple quadrupole mass spectrometer, using isotopic isolation of the precursor ion. The predominant product ions observed in Figure 6.1 are m/z 225, corresponding to the dehydrated deprotonated sulfoquinovose head group, followed by m/z 537 and m/z 563, corresponding to the product ions formed via neutral losses of the 16:0 and 18:1 fatty acid chains, respectively, in the form of RCOOH. The fatty acid chains can also be observed as fatty acid anions at m/z 255 (16:0 $RCOO^-$) and m/z 281 (18:1 $RCOO^-$), albeit at relatively low abundance. Other less-abundant product ions that originate from the head group are also observed at m/z 81 and m/z 165. Observation of the most predominant ion at m/z 225 is in contrast with earlier reports that showed m/z 81 to be an abundant SQDG characteristic product ion in CID MS/MS in a triple quadrupole made by a different manufacturer [150]. Note that the CID in the triple quadrupole can involve both primary and secondary fragmentation reactions depending on the collision energy and gas pressure applied during the fragmentation (see Chapter 2 for a detailed explanation), thus the difference might arise from the difference in energy settings.

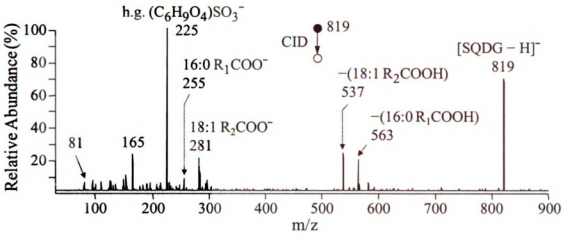


Figure 6.1 Negative ionization mode ESI MS/MS of m/z 819 (SQDG 16:0/18:1) using CID on the triple quadrupole (QqQ) mass spectrometer.

The collision-energy-resolved CID experiments were then performed in the triple quadrupole for m/z 819, as well as for m/z 845 (SQDG 18:1/18:1), by systematically increasing the collision energy at a fixed bath gas pressure (Figure 6.2). Each major product ion was plotted as a percentage fraction of the total abundance of all the observed major product ions and the precursor ion. As shown in Figure 6.2A, once the collision energy reached the threshold for fragmentation (at ~ 25 V in Figure 6.2A), the percentage of the precursor ion at m/z 845 gradually decreased, while the abundance percentages of the first- generation product ions started to increase. These ions mainly included m/z 563, the product ion formed via neutral loss of 18:1 RCOOH, and m/z 225, the head group product ion. A very low level (close to zero) of m/z 81 was observable. No ion at m/z 80 was observable.

When the collision energy increased to about 50 V (Figure 6.2A), the abundance percentage of m/z 563 started to drop, while the abundance percentage of m/z 225 kept increasing, suggesting that m/z 225 could also be generated from m/z 563 via secondary

fragmentation at a higher collision energy, in addition to being directly generated from m/z 845 as a first-generation product ion. Only after the collision energy reached 55 V, did the abundance percentage of m/z 225 start to decrease, and the abundance percentage of m/z 81 started to increase, exceeding that of m/z 225 and all other ions after the collision energy reached about 66 V. However as the collision energy approached 70 V (Figure 6.2A), the absolute abundance of the ions in the spectrum became too low to be of practical use.

Therefore, m/z 225, rather than m/z 81, appears to be a more robust fingerprint product ion for SQDG identification in CID MS/MS. Similar trends were observed from the collision-energy-resolved CID of m/z 819 shown in Figure 6.2B, using the autosampler ESI ion source under slightly different bath gas pressure settings.

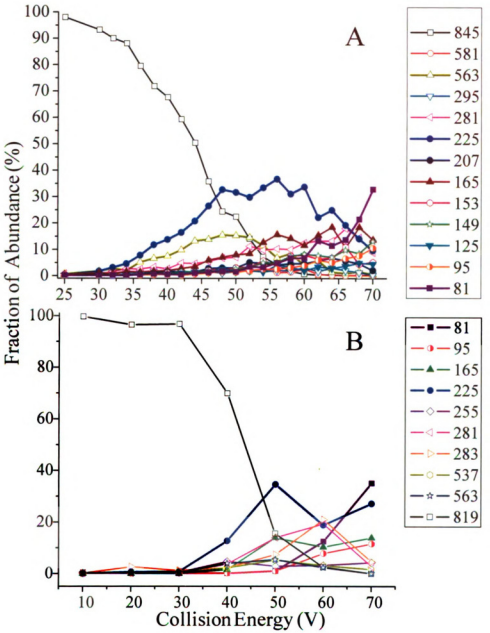


Figure 6.2 Collision-energy-resolved CID of (A) m/z 845 (SQDG 18:1/18:1), and (B) m/z 819 (SQDG 16:0/18:1) in MS/MS, where the collision energy was changed from 10 to 70 V. The relative abundance of the product ion was plotted as a percentage of the total abundances of all major ions. Experiments were performed in negative ion mode using ESI on a triple quadrupole mass spectrometer.

6.3.1.2 PQD MS/MS fragmentation of SQDG lipids in a quadrupole linear ion trap

Figure 6.3 shows the MS/MS spectrum of m/z 819 using PQD fragmentation in the quadrupole linear ion trap mass spectrometer in the m/z range of 50-1000. Similar to the spectrum in Figure 6.1, PQD fragmentation also revealed that the predominant fragmentation pathway was the formation of m/z 225, followed by loss of the two fatty acids as RCOOH neutrals. The product ion at m/z 81 was generated at very low abundance. Other product ions that originated from the head group including m/z 95, m/z 125, m/z 165 and m/z 207 were also observed at relatively low abundance. Also the free fatty acid $RCOO^-$ product ions were formed only at very low abundances (Figure 6.3).

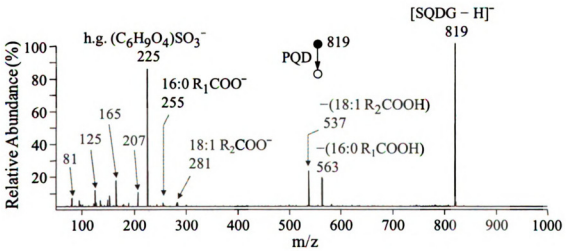


Figure 6.3 Negative ion mode ESI MS/MS product ion analysis of m/z 819 (SQDG 16:0/ 18:1) from *R. sphaeroides*, using pulsed-Q dissociation (PQD) on the quadrupole linear ion trap (LIT) mass spectrometer.

6.3.1.3 Collision energy dependence on fragmentation in a quadrupole linear ion trap

The CID MS/MS spectrum of the deprotonated ions for SQDG 16:0/18:1 at m/z 819 by using the quadrupole linear ion trap after isotopic precursor ion isolation is shown in Figure 6.4. For the precursor ion at m/z 819, the low-mass-cutoff was m/z 160 when the activation q value was set at 0.2. Figure 6.4 showed a very clean MS/MS product ion spectrum of m/z 819, and was dominated by two fragmentation channels involving formation of the characteristic m/z 225 head group ion and neutral loss of the RCOOH groups.

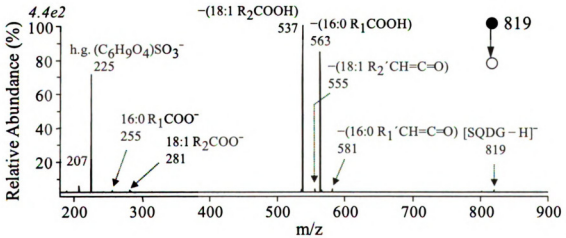


Figure 6.4 Negative ionization mode MS/MS product ion spectrum of m/z 819 (SQDG 16:0/18:1) from *R. sphaeroides* CcO lipid extract (h.g.=head group).

To examine how the collision energy affected the CID and PQD fragmentation behavior of SQDG on the quadrupole linear ion trap (note that the normalized collision energy is adopted by the Thermo LTQ instruments), normalized-collision-energy-

resolved CID and PQD experiments were performed for m/z 819 by steadily increasing the normalized collision energy settings from the threshold value of product ion generation to the point where the overall ion abundance was too low to be practically useful.

The normalized collision energy–resolved CID experiments of m/z 819 in the quadrupole linear ion trap confirmed a slight dependence of the fragmentation reaction degrees on the collision energy (Figure 6.5A) [173]. The relative abundance of the product ions at m/z 563, 537 and 225 increased steadily at a similar slope with an increase in collision energy using CID at an activation q of 0.2 on the linear ion trap, indicating that these three types of product ions were formed in parallel through one-step fragmentation reactions. They also remained the three major product ions throughout a normalized collision energy range of 18% to 31%. At a normalized collision energy of about 40%, the precursor ions were completely fragmented and these three ions became the most abundant product ions. Therefore at the normal low energy CID MS/MS, the productions of these three ions are the predominant low-energy fragmentation channels. The product ion at m/z 225 remains the predominant head group ion observed at any value of normalized collision energy above the fragmentation threshold. The ion at m/z 81 was not observable in the MS/MS spectrum due to the low mass cutoff in CID.

In the PQD fragmentation with low-mass cutoff at m/z 50, the product ion at m/z 81 remained at very low abundance regardless of the applied collision energy (Figure 6.5B).

Due to the slow-heating nature of the ion trap mass spectrometer (see Chapter 2 for a detailed explanation), the product ions observed are mainly the results of primary

fragmentation reactions and further secondary dissociation is prevented. Therefore, the reason why m/z 81 is not observed in the ion trap as a major product ion regardless of the collision energy, is probably because formation of m/z 81 requires a much higher energy than the other fragmentation channels. Therefore, m/z 81 is not a practically convenient fingerprint product ion for the identification of SQDG, but rather m/z 225 is demonstrated to be a clear and abundant fingerprint for the SQDG head group structure.

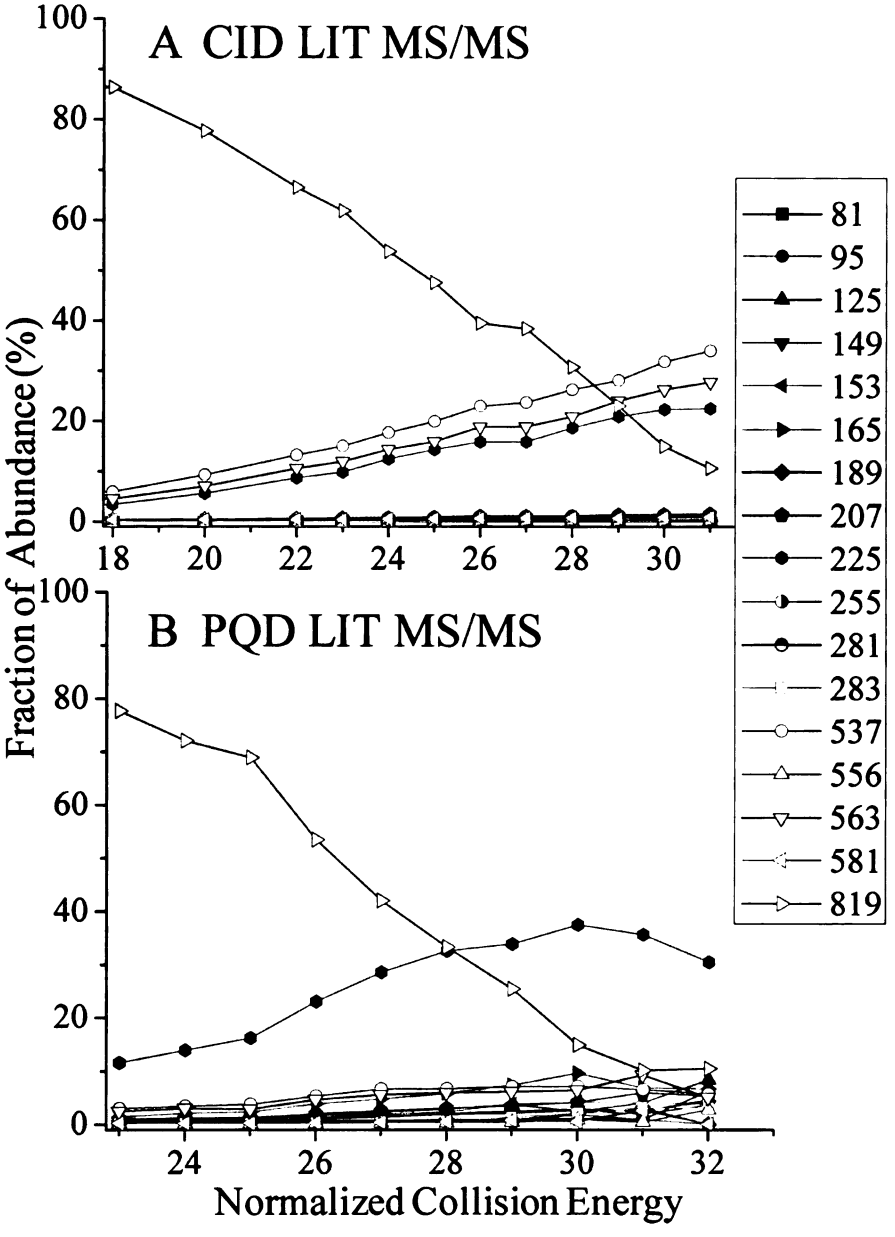


Figure 6.5 Normalized collision-energy-resolved relative abundance of each product ion generated from m/z 819 (SQDG 16:0/18:1) from *R. sphaeroides* by ESI-LIT using CID MS/MS (A), and PQD MS/MS (B) fragmentations, plotted as the percentage of the total abundance of all the major product ions.

6.3.1.4 MS^n fragmentation of SQDG in a quadrupole linear ion trap

MS^3 analyses of the m/z 563 (Figure 6.6A) and m/z 537 (Figure 6.6B) product ions from Figure 6.4 indicated that they both fragmented to generate m/z 225 as the only predominant product ion observed above the low-mass cutoff. MS^3 of m/z 225 (Figure 6.6C) showed that it is indeed a SQDG head group ion, and ruled out the possibility of it being a 14:1 fatty acid $RCOO^-$ ion which also has an m/z value at 225. More importantly, its product ion spectrum was highly specific to the SQDG head group structure. m/z 225 predominantly fragments by losing water to generate m/z 207; however, the product ion at m/z 81 is now observable, but still at much lower relative abundance. The order of CID product ion generations revealed by the ion tree constructed by the MS^n in the quadrupole linear ion trap is very consistent with the ion hierarchy suggested by the collision-energy-resolved CID in a triple quadrupole as discussed in the earlier section.

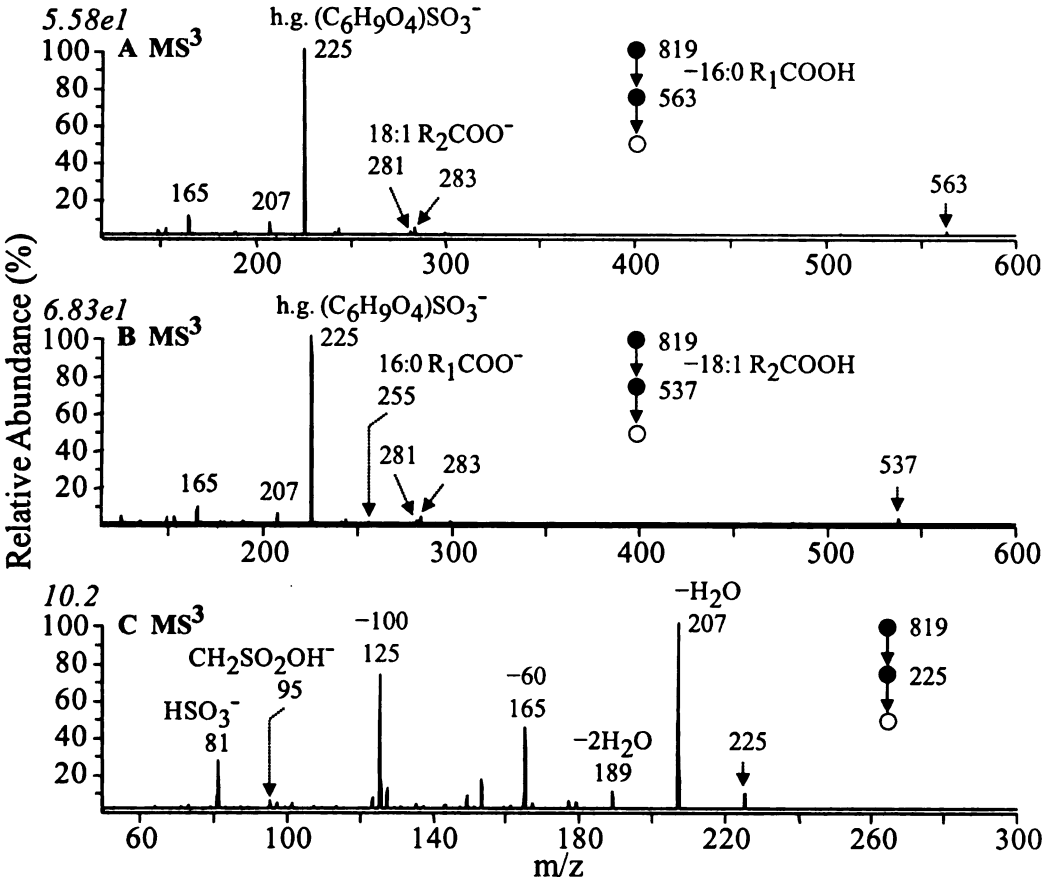


Figure 6.6 Negative ionization mode MS^3 product ion spectra of m/z 819 (SQDG 16:0/18:1) from *R. sphaeroides* CcO lipid extract shown in Figure 6.4. (A) MS^3 of m/z 537, (B) MS^3 of m/z 563, and (C) MS^3 of product ion m/z 225 generated from m/z 819, which is identical to MS^4 of 225, using collision-induced dissociation (CID) on the ESI-linear ion trap (LIT) mass spectrometer (h.g.=head group).

Both the collision-energy-resolved CID experiments in the triple quadrupole and the MS^n experiments in the quadrupole linear ion trap clearly show that the fragmentation of deprotonated SQDG ions predominantly yield a characteristic head group fingerprint ion at m/z 225, as well as the neutral loss of the fatty acid chains as RCOOH.

Thus, in both the triple quadrupole and the linear ion trap, the product ion of SQDG at m/z 225 is the ion to seek, because it is always the most abundant product ion, and it is much more abundant than m/z 81, and the m/z 80 product ion is not observed in low-energy CID.

6.3.2 Fragmentation mechanisms of SQDG in CID MS/MS and MS^n

The formation of RCOOH neutral losses from SQDG obviously requires a deprotonation reaction. The mechanisms of how the characteristic fragmentations of SQDG, described above, occur were then investigated by using H/D exchange experiments. H/D exchange should occur in the three OH groups of the sugar ring in the SQDG. After incubating the total membrane lipid extract with CD_3OD (99.9%) for three times and dried under vacuum, the exchange level into the fully exchanged precursor ion form of SQDG can reach over 90% of the total, using the typical nanoESI ion source under careful control. All the SQDG ions incorporated three deuterium atoms and displayed a 3 Da shift in the MS spectra (data not shown). The H/D exchange experiments can thus be used to distinguish between the hydroxyl OH protons and the C-H protons. The previous m/z 819 (SQDG 16:0/18:1) now shifted to m/z 822 (d_3-SQDG

16:0/18:1), and its CID MS/MS and MS^3 product ion spectra following isotopic isolation are shown in Figure 6.7.

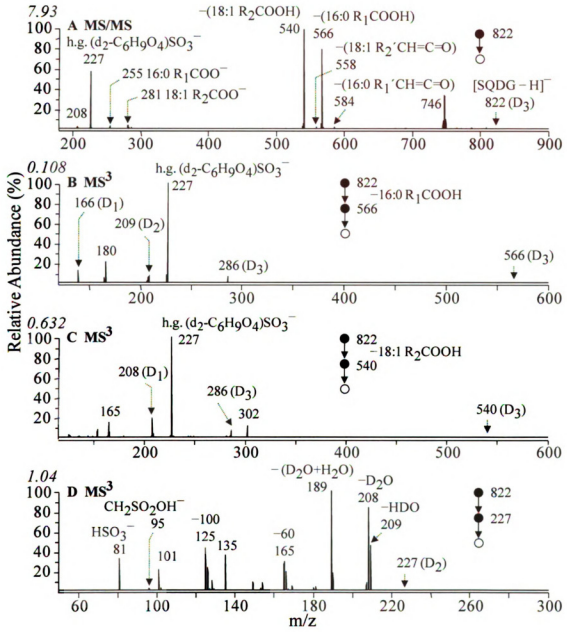
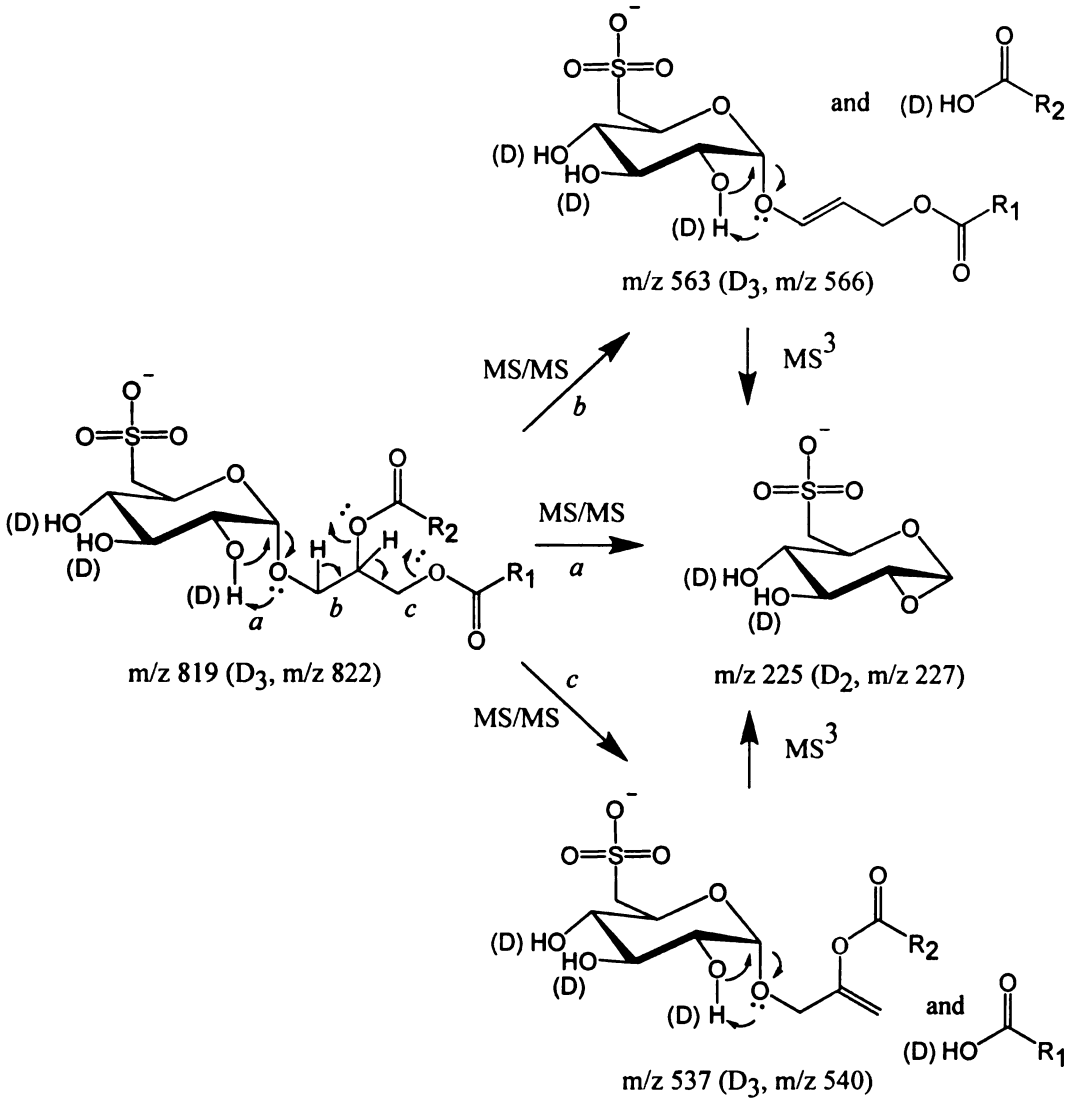


Figure 6.7 Negative ionization mode A) MS/MS product ion analysis of m/z 822 (d_3-SQDG 16:0/18:1) from *R. sphaeroides* membrane lipid extract after in-solution H/D exchange using CD_3OD. B) MS^3 of m/z 540 from A), and C) MS^3 of m/z 566 from A), and D) MS^3 of product ion m/z 227 generated from 822 in panel A, using CID on the ESI-LIT mass spectrometer (h.g.=head group).

The product ions now at m/z 540 and m/z 566 each displayed a 3 Da shift, indicating that the fatty acids are lost as neutral RCOOH and do not contain any deuterium. Therefore the formation of RCOOH is more likely to have occurred by deprotonating the glycerol backbone C-H protons (Scheme 6.2), and does not directly involve the hydroxyl groups in the head group. Four C-H protons are available for the formation of R_2COOH (*sn-1* and *sn-3*), and one C-H proton is available for R_1COOH (*sn-2*). However, such a population difference is not reflected in the actual relative abundances of this type of product ions from either m/z 819 (Figure 6.7A) or m/z 847 (SQDG 18:0/18:1, data not shown). It also raises the possibility that the precursor ions at m/z 819 contain a mixture of SQDG 16:0/18:1 and SQDG 18:1/16:0 isomers. On the other hand, the head group product ion is now observed at m/z 227, showing a 2 Da shift from m/z 225, and thus the incorporation of two deuteriums.

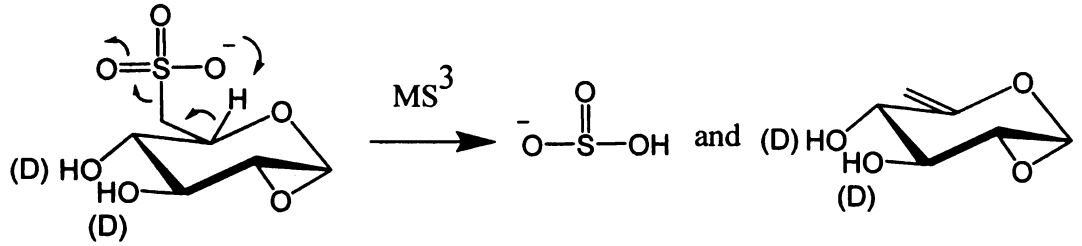
Such experimental evidence supports the fragmentation pathways proposed in Scheme 6.2, involving the generation of m/z 225 (pathway *a*) and RCOOH neutral losses (pathways *b* and *c*) via charge-remote *cis*-elimination processes [202,301]. The reason that the negative charge on the sulfite is not directly involved in these reactions is probably due to the conformational rigidity of the sugar ring. Note that the m/z 819 ion was also observed and fragmented in the MALDI-quadrupole linear ion trap, and no difference was found in the MS/MS (see Chapter 10) and MS^3 spectra, suggesting that such charge-remote fragmentation mechanisms also apply to the deprotonated SQDG ions generated in MALDI [302].



Scheme 6.2 Proposed fragmentation pathways of SQDG $[M-H]^-$ in MS/MS and MS^3

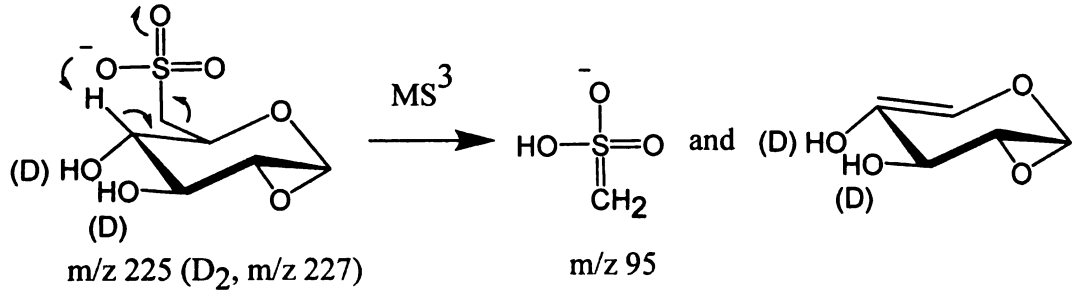
The fragmentation spectrum of m/z 225 generated directly from m/z 819 upon MS/MS (Figure 6.6C) was identical to that of m/z 225 generated from MS^3 (data not shown), suggesting that they have the same structure. Comparing the product ion spectrum of m/z 225 (Figure 6.6C) with that of the H/D exchanged version at m/z 227

(Figure 6.7D), also gives some clues of how the m/z 81 ion, which is observed in both versions, is formed. Since m/z 81 corresponds to the elemental composition of HSO_3^-, no hydroxyl proton is directly involved. A proposed mechanism of forming m/z 81 from m/z 225 via charge-driven process is shown in Scheme 6.3.

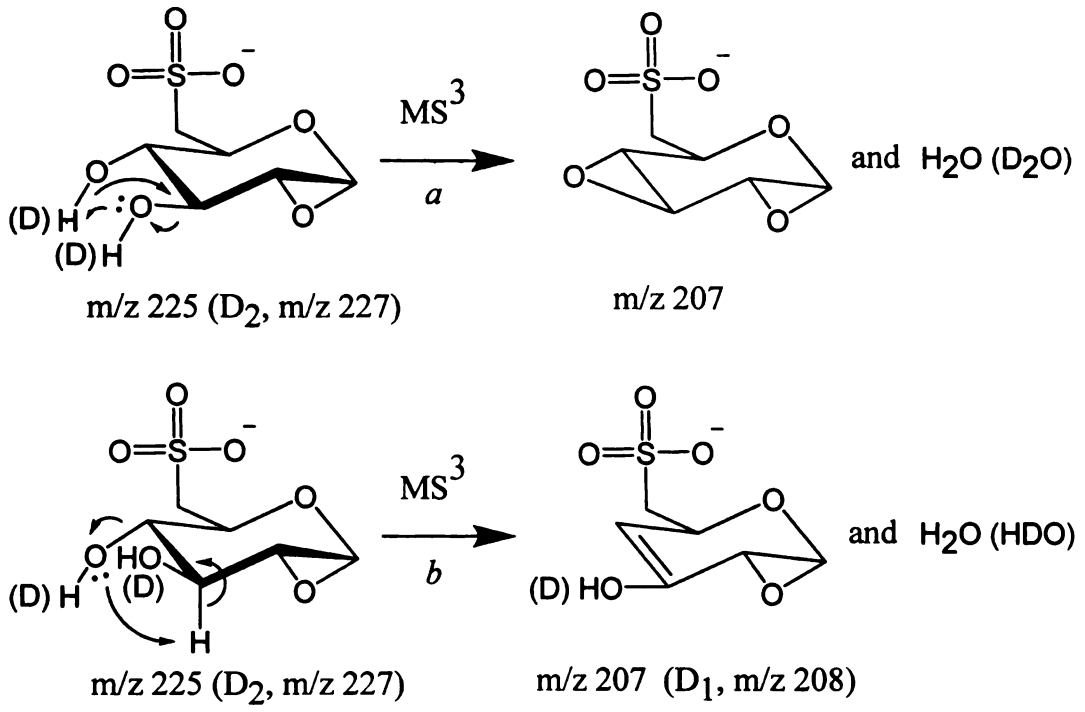


Scheme 6.3 Proposed fragmentation pathway of forming m/z 81 from m/z 225

In addition to m/z 81, the formation of m/z 95 from m/z 225 (Figure 6.6C) is also likely to be mainly through a charge-driven process (Scheme 6.4). The formation of m/z 207 from m/z 225 via water loss, however, seems to be able to occur via several pathways, led by the charge-remote pathways proposed in Scheme 6.5, since both D_2O (pathway *a*) and HDO (pathway *b*) losses are observed in Figure 6.6D.



Scheme 6.4 Proposed fragmentation pathway of forming m/z 95 from m/z 225



Scheme 6.5 Proposed fragmentation pathway of forming m/z 207 from m/z 225

The fragmentation behavior of the deprotonated SQDG ions demonstrated above suggested that, although charge-driven fragmentation mechanisms are often favored in the fragmentation of lipids in the negative ion mode, the rigidity of the sugar ring sitting between the negatively charged sulfite group and the rest of the molecule in SQDG poses a high price in energy, and significantly restricted the extent to which the negative charge could be involved in the cleavage of the ester or ether bonds.

6.3.3 Relative quantification of SQDG in lipid extract using MS/MS

Having gained an understanding of the fragmentation behavior of SQDG lipids, and recognized that the product ion at m/z 225 is a practical fingerprint for SQDG, such a

characteristic was then applied in the separation and relative quantification of SQDG molecular species from the membrane lipid extract of *Rhodobacter sphaeroides*.

Figure 6.8 shows the negative ion mode MS spectrum of *R. sphaeroides* membrane lipid extract (Figure 6.8A), and the precursor ion scan CID-MS/MS spectrum for the product ion at m/z 225 (Figure 6.8B), using the triple quadrupole mass spectrometer. Figure 6.7B clearly shows that the main SQDG lipids species are SQDG 18:1/18:1 (m/z 845), SQDG 16:0/18:1 (m/z 819), SQDG 18:0/18:1 (m/z 847), SQDG 16:0/18:0 (m/z 821) and SQDG 16:0./16:0 (m/z 793), in the order of decreasing relative abundance. The separation and relative quantification of SQDG is thus achieved at a high sensitivity in MS/MS and the chemical noise is significantly reduced compared to the MS [212-215].

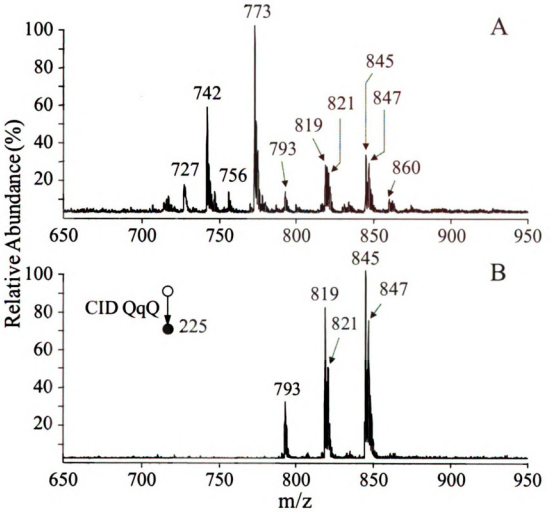


Figure 6.8 Negative ionization mode ESI A) MS and B) CID MS/MS precursor ion scan for m/z 225 using the QqQ mass spectrometer, to selectively identify all the SQDG lipid species in the membrane lipid extract from the *R. sphaeroides* 2.4.1+C*c*O strain.

The ion mapping option in the quadrupole linear ion trap mass spectrometer also demonstrated its applicability to generate similar functions by plotting all the precursor ions that give rise to m/z 225 and converting the horizontal axis from the time dimension

into the mass range (Figure 6.9). The resolution of the peaks in Figure 6.9B can be improved by selecting for smaller precursor ion m/z steps during the scanning.

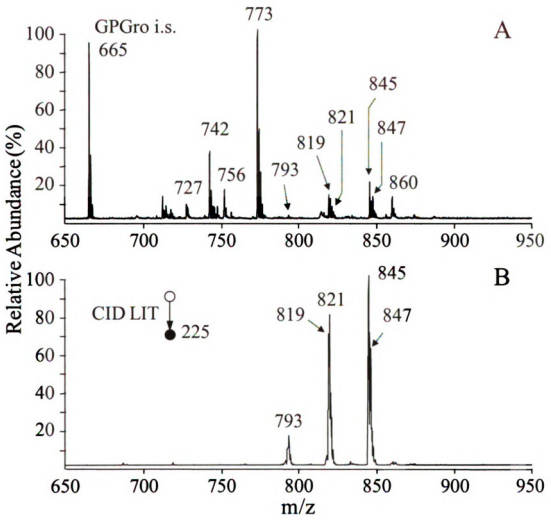


Figure 6.9 Negative ionization mode ESI A) MS and B) CID MS/MS precursor ion mapping for m/z 225 using the LIT mass spectrometer, to selectively identify all the SQDG lipid species in the membrane lipid extract from the *R. sphaeroides* CL3+C*c*O strain.

6.3.4 Fragmentation behavior of DGTS in MS/MS and MS^n

In combination with NMR analysis following TLC separation [11], DGTS has been confirmed to exist in *R. sphaeroides* under phosphate-limiting growth conditions by using FAB CID MS/MS, based on the observation of a complicated series of product ions in positive ion mode including m/z 236 and m/z 162 [11,106], which corresponds to the protonated ion of the trimethylhomoserine head group moiety. However, the fragmentation characteristics of DGTS under low-energy CID MS/MS and MS^n conditions have not been characterized in detail and the fragmentation mechanisms are not well understood, making it a challenge to quickly and accurately identify the DGTS molecular structures from a complex mixture by using only mass spectrometry without prior separation. Here the DGTS lipids from the membrane lipid extracts of *R. sphaeroides* grown under aerobic phosphate-limiting conditions were examined in detail using low energy CID MS/MS and MS^n, and PQD MS/MS, in a quadrupole linear ion trap, and the pathways for the origins of several characteristic product ions have been rationalized.

6.3.4.1 CID MS/MS and MS^n fragmentation of DGTS in quadrupole linear ion trap

The most abundant ion detected in the MS of *R. sphaeroides* membranes under phosphate-limiting growth conditions is at m/z 764, by using either ESI following lipid extraction or by MALDI directly on the membrane pellets (Figure 6.10A). Previous lipid genetics studies on *R. sphaeroides* [11] and *Sinorhizobium meliloti* [93,106,268] have reported that DGTS is a major membrane lipid component in phosphate-limiting growth

and its structure has been confirmed by TLC, NMR and FAB CID MS/MS, and its biosynthetic pathways in *R. sphaeroides* have been elucidated [11,274,303]. Since DGTS carries a fixed positive charge, it is expected to ionize at high efficiency in positive ion mode MALDI or ESI, and thus m/z 764 is possibly formed by DGTS lipids.

Based on its molecular weight, m/z 764 might be the protonated ion of DGTS 18:1/18:1. In order to find out the identity of m/z 764, MS/MS and MS^n analyses were carried out on the quadrupole linear ion trap (Figures 6.10B-6.10D). In MS/MS (Figure 6.10B), above the low-mass cutoff, m/z 764 mainly fragments by losing 18:1 RCOOH (m/z 482) and ketene 18:1 R'CH=C=O (m/z 500). The lower-abundance product ion at m/z 236 corresponds to the neutral loss of two 18:1 R'CH=C=O ketenes, suggesting that it might be a head group ion. In the MS^3 fragmentation, m/z 500 predominantly loses water to form m/z 482. It also forms m/z 236 via the neutral loss of the other 18:1 R'CH=C=O ketene, and m/z 144 which corresponds to the dehydrated protonated ion of trimethylhomoserine, both at low abundance (Figure 6.10C). The MS^3 fragmentation of m/z 482 opens up several fragmentation channels, and the spectrum contained a few product ions that contain the information on the head group identity (Figure 6.10D). The most abundant product ion from m/z 482 is m/z 144, the dehydrated trimethylhomoserine ion. Other product ions include the neutral loss of CO_2 (m/z 438), the loss of 18:1 RCOOH (m/z 200) and the loss of 18:1 R'CH=C=O ketene (m/z 218). These fragmentation characteristics can be explained by a DGTS 18:1/18:1 structure, through the fragmentation pathways proposed in Scheme 6.6. No radical cations were observed here upon low-energy CID in the quadrupole linear ion trap.

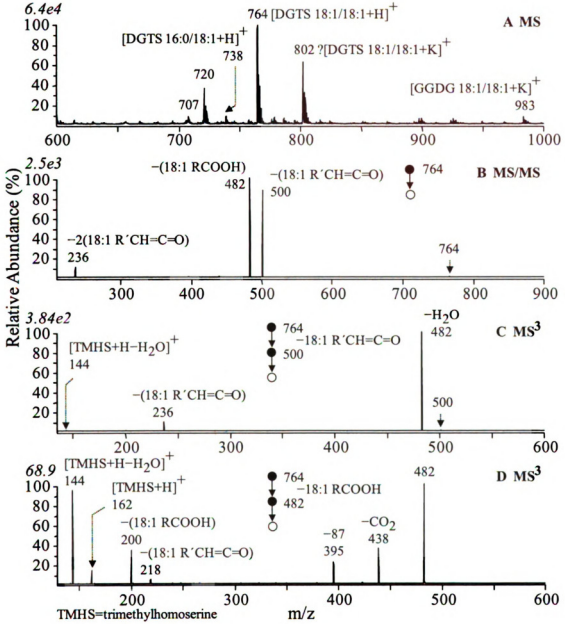
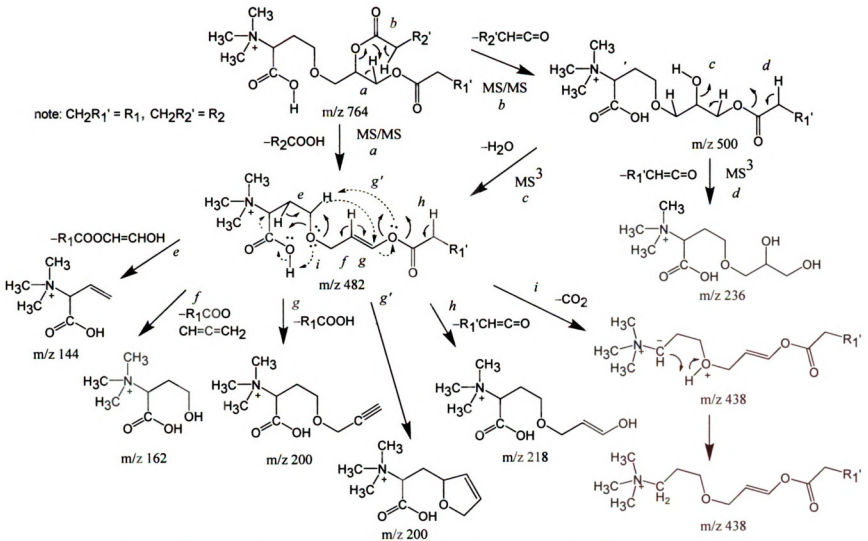


Figure 6.10 MALDI MS spectrum (A), and the low-energy CID MS/MS (B) and MS^n (C and D) fragmentation of the protonated ions ($[M+H]^+$) of diacylglycerol-N, N, N-trimethylhomoserine (DGTS) from the membrane of *R. sphaeroides* (with *Cc*O over-expression) aerobically grown under phosphate-limited conditions, using the MALDI-quadrupole linear ion trap mass spectrometer. TMHS represents trimethylhomoserine.



Scheme 6.6 Proposed fragmentations of DGTS $[M+H]^+$ in MS/MS and MS^3 in positive ion mode

The multiple channels in the fragmentation of m/z 500 are probably because of the flexibility of the ion structure. However, a common feature is that most of these pathways are initiated by nucleophilic attack on the relatively acidic OH proton, α-protons or C-H proton adjacent to a positive charge center by the electron pair on a hydroxyl, ester or ether oxygen.

In contrast to GPCho lipids, although DGTS has a similar N, N, N-trimethyl quaternary amine head group carrying a fixed positive charge, DGTS does not have the negatively charged phosphate group but has a carboxyl group as the nucleophilic center, and such a difference in the chemical structure switches DGTS into a very different set of fragmentation channels in CID MS/MS and MS^n by shutting off the fragmentation channels initiated or assisted by the strong nucleophilic group of phosphate, such as the formation of m/z 184 head group ion, a fingerprint for GPCho. Instead, most of the fragmentations of DGTS in MS/MS occur via charge-remote process because its positive charge is fixed and not mobile. Also due to the fixed positive charge, DGTS is expected to have a strong tendency to form non-covalent adducts with anions such as chloride and methyl carbonate, like GPCho, and the anionic adduct ions of DGTS can also be observed in negative ion mode ESI. In addition, DGTS strongly forms non-covalent alkali adduct ions with potassium present in the sample preparation similarly to GPCho in positive ion mode MALDI (Figure 6.9A), probably due to the carboxyl group.

In contrast to SQDG, DGTS has one positive charge center while SQDG has one negative charge center. However, the DGTS charge is fixed on the trimethylhomoserine and is difficult to become mobile, and the SQDG charge is restrained by the rigid sugar ring. Such comparisons in the fragmentation of DGTS with GPCho and SQDG also

provide insights into the chemical nature of the roles of charges in the gas-phase fragmentation reactions of lipids.

In summary, the MS/MS product ion at m/z 236 can therefore be applied as the fingerprint for the identification of DGTS lipids in positive ion mode, and the lower-abundance m/z 144 can be used as a supplementary evidence when the low mass cut-off permits.

6.4 Conclusions

Multistage tandem mass spectrometry combined with H/D exchange, and an energy-resolved-fragmentation plot, were employed to gain insights into the gas-phase fragmentation mechanisms of SQDG lipid ions. Under low-energy CID conditions, m/z 225 is a practical "fingerprint ion" for the identification of SQDG lipids. The improved understanding of the fragmentation behavior of SQDG also demonstrated its significance in enabling the application of quantification using MS/MS characteristic fragmentations in modern mass spectrometry.

Multistage tandem mass spectrometry of DGTS also elucidated its fragmentation behavior under low-energy CID conditions, and provided valuable guidance into the quick, sensitive and complete identification of the molecular species of this type of lipid by using mass spectrometry without having to resort to other time-and-sample-consuming methods. The CID MS/MS product ion at m/z 236 can thereby be used as the fingerprint product ion for the identification of DGTS, and it can be assisted by the lower-abundance ion at m/z 144, which has been discussed earlier [106], when low-mass-cutoff permits.

Although SQDG and DGTS have been recognized in traditional plant and bacterial lipid biochemical studies for over one decade, in the understanding of fragmentation reactions in mass spectrometry, both SQDG and DGTS belong to the less-studied polar non-phospholipids. Examination of the fragmentation behaviors of SQDG in negative ion mode, and DGTS in positive ion mode, also provided insights into how the chemical structure of lipids affect their gas-phase fragmentation behavior, which is

particularly valuable in recognizing and understanding future unknown lipids with new structures, or new modifications on lipid structure.

Chapter 7

Mass Spectrometry Identification and Selective Quantification of *Rhodobacter sphaeroides* Membrane Lipids: Probing the Effects of Lipid Specific Mutants on Cytochrome *c* Oxidase Production and Activity

7.1 Summary

MS and MS/MS and MS^n-based lipid identification and quantification methods have been developed and applied to the characterization of the membrane lipid profiles of the wild type and a series of specific lipid-deficient mutants of *R. sphaeroides*, including the GPCho-deficient, SQDG-deficient and CL-deficient mutants. These quantification results are consistent with previous ^{14}C-labeling quantification studies [15,16,91], and the differences in the membrane lipid profiles observed between these strains can be correlated with the lipid biosynthetic pathways, and are suggestive of the potential functional replacements between lipids. More importantly, these specific lipid-deficient mutants are used as an important set of tools to probe the functional role of the individual types of lipids in the membrane protein cytochrome *c* oxidase (C*c*O) *in vivo*. The changes in the membrane lipid profiles of these mutants, which set the background to examine the effects of lipids on the C*c*O produced and purified from these lipid environments, are

characterized in this chapter following a description of the consequent cell growth, C*c*O expression and C*c*O properties.

None of these single specific lipid deficiencies were found to be detrimental to the properties of C*c*O, including the cell growth, C*c*O expression yield, C*c*O purification yield, UV-Vis spectroscopic properties, subunit composition, steady state activity, or the temperature-dependence on the activity of the C*c*O purified from these strains, in spite of the significant changes in the lipids extracted from the purified C*c*O as revealed by mass spectrometry analysis.

7.2 Introduction

7.2.1 Lipids and the membrane bound redox protein C*c*O

In biological membranes, lipids do far more than statically provide the environment for the organization and activities of membrane bound proteins and protein complexes. Lipids also provide an interactive platform for them to communicate with other proteins and other molecules, and are likely to be actively involved in these processes, as suggested by emerging experimental evidence [1,19,22,34,35,52,54,55,59,304-307]. Membrane lipids generally contain a hydrophilic head group and a long hydrophobic tail, but both parts have been increasingly found to have vast diversity in terms of their specific structures, enabling the potentially diversified functions of different lipid species. Recent successes in membrane protein X-ray crystallography at high resolution revealed that lipid molecules remain bound in the crystals of membrane proteins [34-36]. Superimposition of the high-resolution crystal structures of the multi-subunit membrane protein cytochrome *c* oxidase, purified from different bacterial and bovine heart sources, led to the discovery of several well conserved sites of bound lipids, in spite of differences in the source membrane lipid compositions, and in the purification and crystallization procedures [35]. Although the binding sites were well conserved, the lipids at some sites were replaced by detergents, raising questions about the specificity requirements for lipids at these binding sites.

One straightforward way to address these questions is to "remove" a particular type of lipid, and examine the consequences of the missing lipids on various aspects of the system. Previous studies removed CL from purified bovine heart C*c*O using

phospholipase digestion, and found that the integrity and activity of C*c*O were destroyed [54]. Similarly, reversible inactivation resulted when the bound CL was removed using phospholipase digestion from purified cytochrome bc_1 complex [54]. These types of *in vitro* approaches could potentially disturb the enzyme structure, and could not examine the possibility of the adaptability/flexibility of the membrane proteins with their lipid components. Specific lipid "removal" via genetic manipulation, however, provides a more natural context to observe the consequences to the system, by allowing the membrane proteins to adapt to their altered lipid environment from the very beginning.

7.2.2 Lipid-deficient mutants as the tool to probe the functions of lipids for C*c*O

Several specific lipid deficient strains of *Rhodobacter sphaeroides* have been developed to examine the physiological effect of the particular lipid on the overall bacterial viability and growth [13]. The chemically mutated GPCho-deficient *R. sphaeroides* strain CHB20, in which the GPEtn methyl transferase is mutated, contains no measurable GPCho [90]. The strain accumulated the precursor, GPEtn, but behaved similarly to the wild type strain 2.4.1 under the normal anaerobic growth conditions [90]. The chemically mutated SQDG-deficient *R. sphaeroides* strain SB1K1 also grows normally compared to the wild type strain 2.4.1, but when both SQDG and GPGro are deficient, the cells do not survive [14,16]. More recently, a specific cardiolipin-deficient mutant of *R. sphaeroides* was also generated by deletion of the cardiolipin synthase gene [15].

These genetic manipulations of the lipid composition of *R. sphaeroides* thus provide a set of strains that are each intrinsically deficient in a specific type of lipid,

which can be used as a tool to probe the function of each type of these lipids with regard to the overall bacterial cellular processes and more specifically, to the expression and activity of the membrane protein *R. sphaeroides* C*c*O, *in vivo*. Characterization of the changes in the membrane lipid profiles of these mutants sets the background for further examination of the effects on the C*c*O grown and purified from these altered lipid environments.

The multi-subunit membrane-bound protein complex, cytochrome *c* oxidase (C*c*O), contains from 4 to 13 subunits, hemes, metal ions and several lipid species even after purification and crystallization steps [30]. The X-ray crystallography of C*c*O purified from bovine heart, *Paracoccus denitrificans* and *Rhodobacter sphaeroides* (*R. sphaeroides*) has revealed a number of conserved lipid binding sites [35]. Previous mass spectrometry analysis has also identified certain lipids which are retained within the purified enzyme and protein crystals, suggesting important roles for these lipids in the structure and function of C*c*O. Cardiolipin in particular has been reported to play an important role in the structure and function of C*c*O from mammalian mitochondria [10].

Increasing evidence suggests that the mammalian cardiolipin mainly functions in the form of $CL(18:2)_4$, rather than any other form of cardiolipin [8,21]. However, such a type of polyunsaturated cardiolipin species is not found in *R. sphaeroides*. It is therefore very important to determine the specific molecular structures of the lipids rather than just the general types of lipids, using methods such as mass spectrometry, if a clearer picture of how lipids functionally interact with C*c*O is to be gained.

To examine the potential structural and functional roles of lipids in *R. sphaeroides* C*c*O, the C*c*O proteins are expressed and purified from the series of specific lipid-

deficient mutants, including the CL-deficient, SQDG-deficient and GPCho-deficient mutants, as well as the wild type *R. sphaeroides* (see Table 3.1 in Chapter 3 for detailed descriptions of the strains). Such an approach of specific lipid "removal" via genetic manipulation provides a more natural context to observe the consequences to the C*c*O *in vivo*, as compared to the *in vitro* extraction or digestion processes. Here the properties of the C*c*O from these mutants have been characterized in terms of their expression, activity and spectroscopic properties, and the changes in the lipids in the C*c*O are determined by quantitative ESI MS and MS/MS (for the CL-deficient mutant) methods.

7.2.3 Properties of the C*c*O produced from the lipid-deficient mutants

7.2.3.1 Cell growth, C*c*O expression in membranes and purification stability from the specific lipid-deficient mutants

All of the specific lipid-deficient mutants are viable and can grow to similar optical density, and express C*c*O at yields similar to the wild type (data not shown). The heme *a* and *bc*1 absorption peaks did not display any shift from the wild type. The relative amounts of C*c*O compared to other complexes such as the *bc*1 complex in the mutants are also not significantly different from that of the wild type (Figure 7.1). The purification yield of C*c*O from these strains by using Ni-NTA gravity columns are also similar to that of the wild type (Dr. Carrie Hiser, data not shown), suggesting that the stability of the association of the subunits in the C*c*O is not significantly different from that of the wild type.

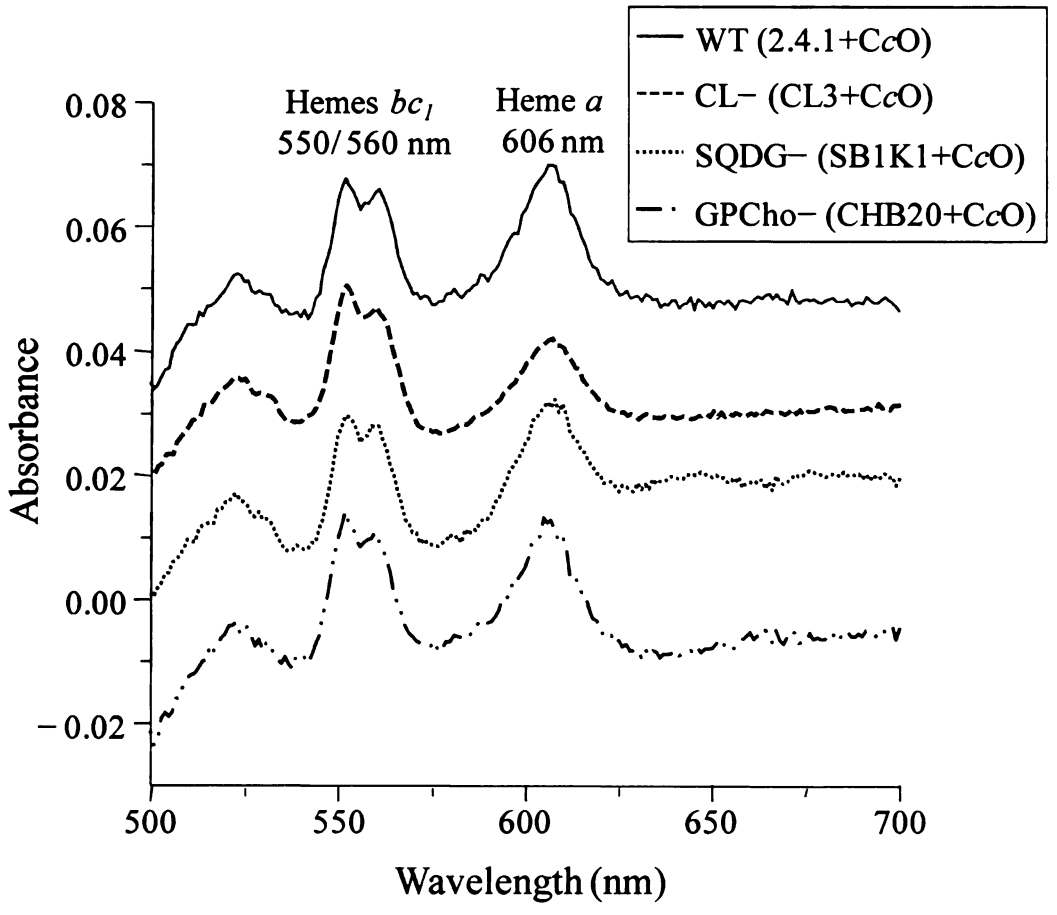


Figure 7.1 Reduced-oxidized UV-Vis spectroscopy of dodecyl maltoside-solubilized membranes isolated from *R. sphaeroides* 2.4.1+C*c*O (wild type), and the specific CL-deficient (CL3+C*c*O), SQDG-deficient (SB1K1+C*c*O) and GPCho-deficient (CHB20+C*c*O) stains, grown under aerobic conditions. The experiment was performed by Dr. Carrie Hiser.

7.2.3.2 UV-Vis spectroscopic properties of the purified C*c*O from the four strains

The reduced spectra of the C*c*O purified by using Ni-NTA chromatography from the four strains, including the wild type (2.4.1+C*c*O), and the specific single lipid deficient strains CL-deficient (CL3+C*c*O), SQDG-deficient (SB1K1+C*c*O) and GPCho-deficient (CHB20+C*c*O) stains, are shown in Figure 7.2. They display no appreciable differences in terms of the wavelength of the peaks, and the relative intensity between the Soret (445 nm) and alpha bands of heme *a* at 606 nm. The fact that no peak shift is observed suggests that the coordination state of the heme *a* catalytic center in the C*c*O is not disturbed in any of these mutants.

7.2.3.3 SDS-PAGE analysis of the purified C*c*O from the four strains

SDS-PAGE gel analysis of the purified C*c*O from *R. sphaeroides* 2.4.1+C*c*O (wild type), and the specific single lipid type deficient strains CL3+C*c*O (CL-deficient), SB1K1+C*c*O (SQDG-deficient) and CHB20+C*c*O (GPCho-deficient), using urea as the reducing reagent and blue Coomassie for the staining, shows no appreciable difference between the four samples of C*c*O in terms of subunit composition and the size of the subunits that are resolved by the SDS-PAGE method, and it is clear that each C*c*O contains four subunits (Dr. Carrie Hiser; data not shown). The specific lipid-deficiency in CL, SQDG or GPCho did not cause the subunits to be lost, particularly subunit IV, which is not directly connected to the rest of the enzyme, but is held via a layer of phospholipids [34].

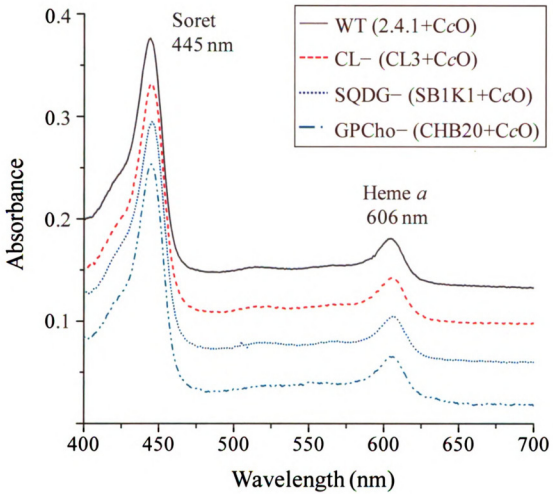


Figure 7.2 Reduced UV-Vis spectroscopy of C*c*O purified from *Rhodobacter sphaeroides* 2.4.1+C*c*O (wild type), and the specific CL-deficient (CL3+C*c*O), SQDG-deficient (SB1K1+C*c*O) and GPCho-deficient (CHB20+C*c*O) stains grown under aerobic conditions. The proteins were purified by using the Ni-NTA gravity columns. The experiment was performed by Dr. Carrie Hiser.

7.2.3.4 Activity of purified C*c*O from the four strains

The steady state activities of the C*c*O from these four strains were evaluated by oxygen consumption experiments in the presence of cytochrome *c* as the substrate, and the results are shown in Figure 7.3. The activities of these C*c*O enzymes do not differ greatly beyond what might be seen in the different batches of the wild type enzyme (Dr. Carrie Hiser, personal communication). The addition of asolectin lipids in the assay leads to an increase in activity by 20-30% in each case, the typical value observed for the wild type C*c*O [27]. Therefore the specific lipid deficiency in CL, SQDG or GPCho did not seriously hamper the C*c*O activity, and the C*c*O from these strains are not particularly more sensitive to the added lipids than that of the wild type C*c*O is.

7.2.3.5 Activity stability of the purified C*c*O under temperature stress: WT and CL−

Figure 7.4 shows the oxygen consumption activities of the Ni-NTA-purified C*c*O from the CL-deficient mutant (CL3+C*c*O) and the wild type (2.4.1+C*c*O), at increasing incubation temperature. Both C*c*O enzymes displayed steadily decreased activities with an increase in temperature from 20 to 85 °C, but the C*c*O from the cardiolipin-deficient mutant does not seem to be significantly more unstable to a temperature increase than the C*c*O from the wild type.

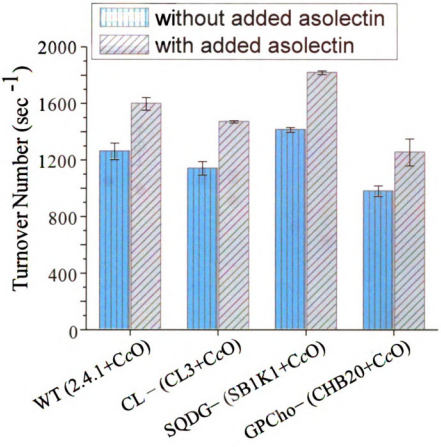


Figure 7.3 Steady-state oxygen consumption activity analysis of purified C*c*O using Ni-NTA gravity column from *Rhodobacter sphaeroides* 2.4.1+C*c*O (wild type), and the specific single lipid type deficient strains CL3+C*c*O (CL-deficient), SB1K1+C*c*O (SQDG-deficient) and CHB20+C*c*O (GPCho-deficient), before and after the addition of asolectin lipids in the reaction mixture. The data shown are the averages of triplicate assays, and the error bar is the standard deviation. The experiments were performed by Dr. Carrie Hiser.

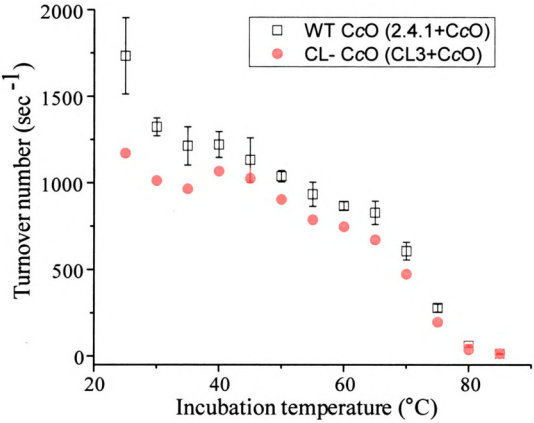


Figure 7.4 Oxygen consumption activities of the Ni-NTA-purified C*c*O from the CL-deficient mutant (CL3+C*c*O) and the wild type (2.4.1+C*c*O), as a function of temperature (enzymes are incubated at each temperature for 1 minute in 10 μL aliquots). The results shown are from the duplicate experiments for the CL-deficient strain and triplicates for the wild type. The error bar is the standard deviation (shown only for the wild type). The experiment was performed by Dr. Carrie Hiser.

7.2.4 Lipidomics

Accurate identification of the enormously diversified structures of lipids and further quantification of each lipid molecular species over a wide range of abundance has been a major challenge. With the availability of mass spectrometry with its high sensitivity and multistage MS/MS (i.e. MS^n) capability, approaches to this problem are now possible. The recent developments in mass spectrometry technologies are being increasingly applied to lipidomics and lipid biochemistry studies [59,111,112,117,140,207,290], where unprecedented details of the lipid structure and quantification are revealed at high sensitivity and versatility (see Chapter 2 for a detailed description).

7.2.5 Complete lipid structural identification by using MS^n

In the MS spectra of lipid mixtures, such as the lipid extracts from biological samples, a significant degree of mass overlapping is likely to occur, particularly in the m/z 600-900 region. These regions are further complicated by the formation of various non-covalent cationic or anionic adducts of the lipids. Simply matching the m/z of the MS peaks with the calculated masses of the possible lipids can lead to significant ambiguity, because often the overlapping species are structural isomers with exactly the same molecular weights. However, CID MS/MS (and MS^n experiments in quadrupole linear ion trap mass spectrometers) can potentially distinguish between these species by their fragmentation behaviors, which are highly sensitive to their chemical structures. These methods can also be used to achieve unambiguous structural characterization of

each of the lipid species even if they overlap at the same m/z value in MS, without the traditional requirement of independently synthesized standards or NMR following elaborate purifications. MS^n is a very important tool when dealing with biological samples, which often contain a lot of biologically significant lipids with unknown structures or structural modifications that could not be revealed by traditional methods. The high sensitivity of MS^n in both identification and quantification makes it an ideal tool to examine the lipids in the membrane pellets, in the purified C*c*O obtained at limited yield, and in the C*c*O crystals harvested at the size dimension of a few tenths of one millimeter.

7.2.6 Membrane lipids of *R. sphaeroides*

Previous studies based mainly on TLC analysis and ^{14}C-labelling have found that the membranes of wild type *R. sphaeroides* strain 2.4.1 contain phosphatidyl-ethanolamine (GPEtn), phosphotidylcholine (GPCho), phosphatidylglycerol (GPGro) and cardiolipin (CL), and the nonphospholipids sulfolipids (SQDG) and ornithine lipids (OL), when the growth media contained abundant phosphate, where phospholipids are the predominant components [16,90]. Under phosphate-limiting growth conditions, the novel phosphate-free glycolipids glucosylgalactosyl-diacylglyceride (GGDG) and diacylglyceryl-trimethyl homoserine (DGTS) are produced, and the SQDG and OL are increased [11] . DGTS is proposed to functionally compensate for GPCho, SQDG for GPGro and OL for GPEtn, based on the similarity of the charge state in the head group [11,14]. The characteristic fragmentation behaviors of GPCho and other phospholipids,

OL, glutamine lipids (QL) SQDG and DGTS have been discussed in previous chapters (see Chapters 2, 4, 5 and 6 for detailed descriptions).

That being said, there has not been any comprehensive detailed molecular structural information, or quantification, of the molecular species from either the wild type or any of these lipid-deficient mutants of *R. sphaeroides* prior to the current study. By taking advantage of the knowledge of the fragmentation characteristics of these lipids, the lipid compositions in the wild type and the individual lipid-deficient mutants that are specifically deficient in CL, SQDG and GPCho, all of which are viable and can produce C*c*O, have been extensively examined by using ESI following lipid extraction, for both the membrane and the purified C*c*O.

7.3 Results and discussions

7.3.1 Identification of membrane lipids in the wild type and the mutants

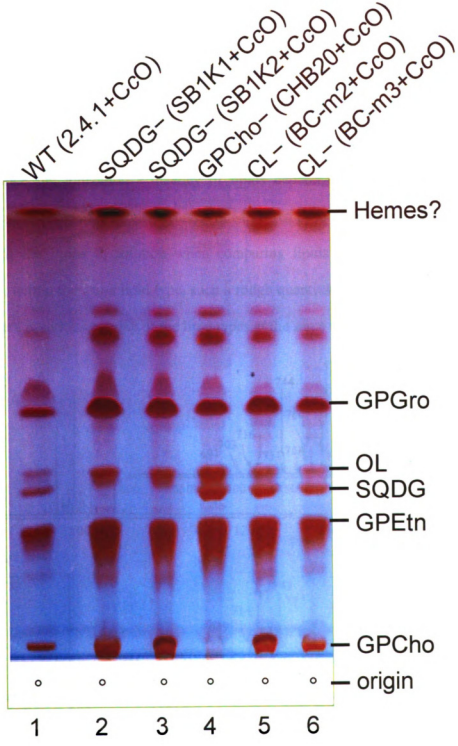
A detailed description of the specific strains studied in this chapter can be found in Table 3.1 in Chapter 3. The isolated membrane pellets were resuspended, measured for membrane protein concentrations, and then the lipids were extracted for ESI analysis using the methods described in Chapter 3.

7.3.1.1 Traditional TLC analysis of the lipid profiles of membranes from each mutant

Before applying the new methods of mass spectrometry analysis, traditional TLC analysis was applied to the analysis of membrane lipid extracts from the wild type and

the specific lipid deficient mutants (see Chapter 3 for a detailed description of methods). Although they can only show the general types of lipids including GPGro, GPEtn GPCho, SQDG and OL lipid as a migration band, and do not resolve CL well, using the conditions applied here, it does show the general feature that the GPCho-deficient mutant shows no GPCho, and the SQDG-deficient mutant shows no SQDG by the iodine vapor stain. However, the identification of specific lipid molecular species, and their changes in the mutants are not able to be provided by TLC.

Figure 7.5 TLC of lipid extracts from the isolated membranes of the wild type and the specific lipid-deficient mutants of *R. sphaeroides*, containing 2.3 μg membrane proteins determined by the BCA assay. Lane 1, wild type strain 2.4.1+C*c*O; lanes 2 and 3, SQDG-deficient strains SB1K1+C*c*O and SB1K2+C*c*O, respectively; lane 4, GPCho-deficient strain CHB20+C*c*O; lanes 5 and 6, CL-deficient strains BC-m2+C*c*O and BC-m3+C*c*O (also called CL3+C*c*O), respectively. The silica gel TLC plate containing a concentrating band was treated with $(NH_4)_2SO_4$, developed by using acetone: toluene: water (91:30:7, v/v/v), and visualized by iodine vapor strain. These conditions are not able to resolve the CL lipids.


WT (2.4.1+CcO)
SQDG− (SB1K1+CcO)
SQDG− (SB1K2+CcO)
GPCho− (CHB20+CcO)
CL− (BC-m2+CcO)
CL− (BC-m3+CcO)
Hemes?
GPGro
OL
SQDG
GPEtn
GPCho
origin
1
2
3
4
5
6

7.3.1.2 Identification of lipids in the wild type membrane using MS/MS and MS^3

The lipid extracts were then applied to systematic mass spectrometry analysis. Figure 7.6 shows the MS spectra of the membrane lipid extracts of the 2.4.1 wild type *R. sphaeroides* in positive and negative ion mode ESI. A first glance shows that the lipid ions observed in the positive ion mode are very different from those in the negative ion mode. Since the ionization efficiency of lipids depend heavily on head groups, the apparent abundance of the ions observed in MS often does not represent the true relative amount of the lipids in solution when comparing lipids with different head groups. However, within the same lipid type, such a rough quantitative comparison can be made, unless there is serious overlap of the lipid types at the same m/z value.

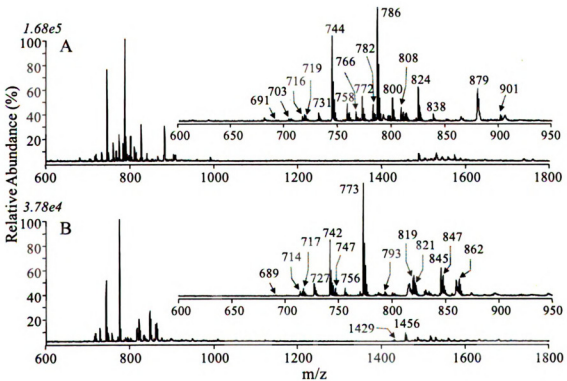


Figure 7.6 The ESI MS spectra of the lipid extract from the cell membranes of the wild type *R. sphaeroides* (2.4.1+CcO) in (A) the positive, and (B) the negative ion modes.

Only those peaks that had relative abundances higher than 1% in MS (Figure 7.6) were further examined by MS/MS and MS^n. Using both positive and negative ion mode MS/MS and MS^n, the molecular species of GPEtn, N-methyl-GPEtn (N-Me GPEtn; MMPE), N, N-dimethyl GPEtn (N, N-Me_2 GPEtn; DMPE), GPCho, GPGro, SQDG, CL and two series of lipids that were determined to be ornithine lipids and glutamine lipids were identified. The results reveal that these lipids include a wide spectrum of fatty acid compositions. The specific species identified by MS/MS and MS^n for the observed precursor ions in MS are presented in Table 7.1 for the positive ion mode, and in Table 7.2 for the negative ion mode. The combined identification results from both positive and negative ion modes are summarized in Table 7.3.

Table 7.1 Identification of the lipid ions in positive ion mode MS of the membrane extracts of the wild type* *R. sphaeroides*.

m/z	GPEtn	N-Me GPEtn	N,N-Me2 GPEtn	GPCho	OL	QL
691					OL 3-OH 18:1/19:1	
693					OL 3-OH 18:0/19:1	
703					OL 3-OH 18:1/20:2	
					OL 3-OH 18:0/20:3	
705					OL 3-OH 18:0/20:2	
					OL 3-OH 20:1/18:1	
707					OL 3-OH 20:0/18:1	
					OL 3-OH 20:1/18:0	
716	GPEtn 18:1/16:1			GPCho 28:2 +Na?		
	GPEtn 16:1/18:1					
718	GPEtn 18:1/16:0					
	GPEtn 16:0/18:1					
719					OL 3-OH 20:1/19:1	QL 3-OH 20:1/18:1
730	GPEtn 35:2			GPCho 32:2		
731					OL 3-OH 20:1/20:2	
					OL 3-OH 20:0/20:3	
744	GPEtn 18:1/18:1	N-Me GPEtn 35:2	N,N-Me2 GPEtn 34:2	GPCho 33:2		
746	GPEtn 18:0/18:1		N,N-Me2 GPEtn 34:1	GPCho 33:1		
				GPCho? +Na/K		
758	GPEtn 19:1/18:1	N-Me GPEtn 18:1/18:1	N,N-Me2 GPEtn 35:2	GPCho 34:2		
	GPEtn 18:1/19:1					
760	GPEtn 19:0/18:1?	N-Me GPEtn 18:0/18:1	N,N-Me2 GPEtn 35:1	GPCho 34:1		
766	GPEtn 18:1/18:1 +Na					
770	GPEtn 38:3					
	GPEtn 35:3 +K					
772	GPEtn 38:2	N-Me GPEtn 18:1/19:1?	N,N-Me2 GPEtn 18:1/18:1	GPCho 35:2		
774			N,N-Me2 GPEtn 18:0/18:1	GPCho 35:1		
780	GPEtn 18:1/19:1 +Na	N-Me GPEtn 18:1/18:1 +Na		GPCho 34:2 +Na		
782	GPEtn 39:4			GPCho 16:0/18:1 +Na		
	GPEtn 18:1/18:1 +K					
784	GPEtn 18:0/18:1 +K					

(Table 7.1 continued)

786	GPEtn 38:4+Na or 36:0+K		N,N-Me2 GPEtn 37:2	GPCho 18:1/18:1
792	GPEtn 20:2/18:1 +Na GPEtn 16:1/22:2? +Na GPEtn 16:1/18:1 +K+K?			
796	GPEtn 18:1/19:1 +K	N-Me GPEtn 18:1/18:1 +K	N,N-Me2 GPEtn 38:4	GPCho 34:2 +K GPCho 36:3 +Na
798	GPEtn 37:1 +K	N-Me GPEtn 36:1 +K	N,N-Me2 GPEtn 38:3	GPCho 34:1 +K
800	GPEtn 37:0 +K / ?+Na	N-Me GPEtn 36:0 +K / ?+Na	N,N-Me2 GPEtn 38:2	GPCho 18:1/19:1 GPCho 16:0/18:0 +K
808	GPEtn 38:3+ K / ?+Na GPEtn ?			GPCho 18:1/18:1 +Na
810	GPEtn ?+Na/K	N-Me GPEtn ? +Na/K	N,N-Me2 GPEtn18:1/18:1 +K	GPCho 18:0/18:1 +Na GPCho etc
812	GPEtn 41:3?		N,N-Me2 GPEtn 18:0/18:1+K	GPCho (20:2/18:1) GPCho 18:0/18:0 +Na GPCho 16:0/19:1? +K
879				GPCho ? GPCho ? +Na/K

* Wild type = strain 2.4.1+C*c*O, for Tables 7.1, 7.2 and 7.3.

Table 7.2 Identification of the lipid ions in negative ion mode MS of the membrane extracts of the wild type *R. sphaeroides*.

m/z	GPEtn	N-Me GPEtn	N,N-Me2 GPEtn	GPCho
689				
714	GPEtn 18:1/16:1			
	GPEtn 16:1/18:1			
716	GPEtn 18:1/16:0			
	GPEtn 16:0/18:1			
717				
719				
742	GPEtn 18:1/18:1			
744	GPEtn 18:0/18:1		N,N-Me2 GPEtn 16:0/18:1	
	GPEtn 18:1/18:0		N,N-Me2 GPEtn 18:1/16:0	
745				
747				
756	GPEtn 19:1/18:1	N-Me GPEtn 18:1/18:1		
	GPEtn 18:1/19:1			
770	GPEtn 18:1/20:1	N-Me GPEtn 18:1/19:1	N,N-Me2 GPEtn 18:1/18:1	
	GPEtn 20:1/18:1	N-Me GPEtn 19:1/18:1		
773				
775				
787				
793				GPCho 18:1/18:1+ Cl
800	GPEtn 18:1/18:1+ NaCl			
802	GPEtn 18:0/18:1+ NaCl			
818				GPCho 18:0/16:1+ Ac
				GPCho 16:1/18:0+ Ac
819				
820				GPCho 18:1/18:1+ Cl
821				
830	GPEtn 18:1/19:1+ KCl		N,N-Me2 GPEtn 18:1/18:1+	
	GPEtn 19:1/18:1+ KCl		formate	
831				
834				GPCho 18:1/19:1+ Cl
				GPCho 19:1/18:1+ Cl
845				
847				
860				GPCho 18:1/18:1+ m.c.
873				

(Table 7.2 continued)

m/z	GPGro	SQDG	OL	QL
689			OL 3-OH 18:1/19:1	
714				
716				
717			OL 3-OH 20:1/19:1	QL 3-OH 20:1/18:1
719			OL 3-OH 20:0/19:1	QL 3-OH 20:0/18:1
742				
744				
745	GPGro 16:1/18:1		OL 3-OH 20:1/21:1	
	GPGro 18:1/16:1			
747	GPGro 16:0/18:1		OL 3-OH 20:0/21:1	
	GPGro 18:1/16:0			
756				
770				
773	GPGro 18:1/18:1			
775	GPGro 18:0/18:1			
	GPGro 18:1/18:0			
787	GPGro 19:1/18:1		OL 3-OH 20:1/24:1	
	GPGro 18:1/19:1			
793		SQDG 16:0/16:0	OL 3-OH 20:1/25:5?	
800				
802				
818				
819		SQDG 16:0/18:1		
		SQDG 18:1/16:0		
820				
821		SQDG 16:0/18:0		
		SQDG 18:0/16:0		
830				
831	GPGro 18:1/18:1+ NaCl			
834				
845		SQDG 18:1/18:1		
847	GPGro 18:1/18:1+ KCl	SQDG 18:1/18:0		
		SQDG 18:0/18:1		
860		SQDG 19:1/18:1		
		SQDG 18:1/19:1		
873		SQDG 18:1/20:1		
		SQDG 20:1/18:1		

The major lipid types detected and identified in the positive ion mode between m/z 600 and 950 (Table 7.1) are GPEtn, MMPE, DMPE, GPCho, OL and QL. Both of the two fatty acid components in OL and QL lipids could be unequivocally assigned with the MS/MS, MS^3 and MS^4 data. Extensive Na^+/K^+ adduct ions of GPEtn and GPCho were also formed, but the Na^+/K^+ adducts of OL were probably formed as well. The Na^+/K^+ adducts assisted with further assignment of the individual fatty acid components in GPCho and GPEtn.

The major lipid types detected and identified in the negative ion mode between m/z 600 and 950 (Table 7.2) are GPGro, GPEtn, MMPE, DMPE, GPCho (in the forms of various anionic adducts), SQDG, CL, OL and QL. Both of the fatty acid components of these lipids were identified, but the position assignment based on comparison to the relative *sn-1/sn-2* ratios of the synthesized lipid standards showed that there was often a mixture of a *sn-1/sn-2* combination, although one of them often dominated. The exception is the SQDG species for which the standard *sn-1/sn-2* ratio is not available. But the two fatty acids in OL and QL lipids could be unequivocally assigned based on the MS/MS, MS^3 and MS^4 spectra because of the tandem connection of their two fatty acid chains, consistent with the corresponding spectra in positive ion mode.

Table 7.3 Summary of the lipid species identified in the membrane extracts of the wild type *R. sphaeroides* **.

GPEtn	N-Me GPEtn	N,N-Me2 GPEtn	GPCho
			GPCho 28:2
			GPCho 32:2
			GPCho 33:2
			GPCho 33:1
GPEtn 18:1/16:1		N,N-Me2 GPEtn 34:2	GPCho 34:2
GPEtn 16:1/18:1			
GPEtn 18:1/16:0		**N,N-Me2 GPEtn 16:0/18:1**	**GPCho 16:0/18:1**
GPEtn 16:0/18:1		**N,N-Me2 GPEtn 18:1/16:0**	**GPCho 18:1/16:0**
			GPCho 16:0/18:0
GPEtn 35:2	N-Me GPEtn 35:2	N,N-Me2 GPEtn 35:2	GPCho 35:2
		N,N-Me2 GPEtn 35:1	GPCho 35:1
GPEtn 18:1/18:1	**N-Me GPEtn 18:1/18:1**	**N,N-Me2 GPEtn 18:1/18:1**	**GPCho 18:1/18:1**
GPEtn 18:0/18:1	N-Me GPEtn 18:0/18:1	N,N-Me2 GPEtn 18:0/18:1	GPCho 18:0/18:1
GPEtn 18:1/18:0			
GPEtn 19:1/18:1	**N-Me GPEtn 18:1/19:1**	N,N-Me2 GPEtn 37:2	**GPCho 18:1/19:1**
GPEtn 18:1/19:1	**N-Me GPEtn 19:1/18:1**		**GPCho 19:1/18:1**
GPEtn 37:1			
GPEtn 18:1/20:1		N,N-Me2 GPEtn 38:2	
GPEtn 20:1/18:1			
GPEtn 20:2/18:1		N,N-Me2 GPEtn 38:3	GPCho 20:2/18:1
GPEtn 38:4		N,N-Me2 GPEtn 38:4	
GPEtn 41:3 ?			

(Table 7.3 continued)

GPGro	CL	SQDG	OL	QL
			OL 3-OH 18:1/19:1	
		SQDG 16:0/16:0	OL 3-OH 18:0/19:1	
			OL 3-OH 18:1/20:2	
			OL 3-OH 18:0/20:3	
			OL 3-OH 18:0/20:2	**QL 3-OH 20:1/18:1**
			OL 3-OH 20:1/18:1	
GPGro 16:1/18:1			OL 3-OH 20:0/18:1	QL 3-OH 20:0/18:1
GPGro 18:1/16:1			OL 3-OH 20:1/18:0	
GPGro 16:0/18:1	CL (18:1)3/16:0	SQDG 16:0/18:1	OL 3-OH 20:0/19:1	
GPGro 18:1/16:0		SQDG 18:1/16:0		
		SQDG 16:0/18:0	**OL 3-OH 20:1/19:1**	
		SQDG 18:0/16:0		
			OL 3-OH 20:1/20:2	
			OL 3-OH 20:0/20:3	
			OL 3-OH 20:1/21:1	
GPGro 18:1/18:1	CL (18:1)4	SQDG 18:1/18:1	OL 3-OH 20:0/21:1	
GPGro 18:0/18:1		SQDG 18:1/18:0		
GPGro 18:1/18:0		SQDG 18:0/18:1		
GPGro 19:1/18:1		SQDG 19:1/18:1		
GPGro 18:1/19:1		SQDG 18:1/19:1		
		SQDG 18:1/20:1		
		SQDG 20:1/18:1		

** Lipids shown in bold were identified by using both positive and negative ion modes.

Combining the experiments using both positive and negative ion modes, the identified molecular species of lipids detectable in the wild type (2.4.1+C*c*O) *R. sphaeroides* membranes, that were above 1% relative abundance in MS, are summarized in Table 7.3. Included were a series of phospholipids GPEtn, MMPE, DMPE, GPCho, GPGro and CL, and non-phospholipids SQDG, OL and QL. No species of phosphatidylserine (GPSer), phosphatidylinositol (GPIns), or sphingomyelin (SM) were detected above 1% normalized relative abundance in MS.

These resolved specific molecular species show that the hydrophobic chains identified in the glyceride lipids are mainly acyl fatty acids with one or zero unsaturation (ring or double bond), such as 16:1, 16:0, 18:1, 18:0 and 20:1. Odd carbon-number fatty acid 19:1 and 21:1, probably containing the cyclic propanyl functional groups (cyc), were also found to be present in most of these species, except for CL, likely due to its low abundance. Species containing two 18:1 fatty acid chains were the predominant species for all of the phospholipids. SQDG containing 16:0/18:1, 16:0/18:0 and 18:1/18:0 were found to be close to SQDG 18:1/18:1 in abundance. In OL and QL, the two fatty acids are not attached to the glycerol backbone but are linked via an ester bond formed between the 3-OH position of the first fatty acid and the carboxyl group of the second fatty acid. In these lipids, the first fatty acids were found to be mainly 3-OH 18:1, 3-OH 18:0, 3-OH 20:1 and 3-OH 20:0, and the second fatty acids were not only 18:1, 18:0, cyc19:1, and cyc21:1, but also 20:2 and possibly 20:3. The OL containing 3-OH 20:1 and 20:2 fatty acids was the most abundant OL species, and the QL containing 3-OH 20:1 and 18:1 was the most abundant species among this type.

All of the fatty acid combinations of MMPE and DMPE were also found in GPEtn and GPCho, confirming the previous finding that both MMPE and DMPE are the intermediates in the biosynthesis of GPCho from GPEtn by the enzyme methyl transferase in *R. sphaeroides* [90], and that these intermediates remain inserted in the membrane while the methyl transferase makes the sequential methylation modification on the head group [90].

7.3.1.3 Ion overlapping in MS illustrated by MMPE and DMPE

Although MMPE and DMPE are common intermediates in the biological synthesis of GPCho from GPEtn, the most abundant phospholipid components, the identification of MMPE and DMPE has not been largely described previously by mass spectrometry methods. The reason is probably that their precursor ions often sit at an m/z that contains an overwhelming number of overlapping ions. The 14 Da shift in the addition of one N-methyl group, can also correspond to the addition of one more carbon in the fatty acid chain in the GPEtn lipids, or one less carbon in the GPCho lipids. A third reason is that they do not have very distinctive fragmentation behaviors, but are more or less similar to GPEtn. However, the subtle difference between their fragment ions and those of the GPEtn in MS/MS and MS^3 enabled the unequivocal identification of the MMPE and DMPE lipids among all kinds of overlapping species.

Figure 7.7 demonstrates that the precursor ion at m/z 758 in positive ion mode MS contains N-Me GPEtn 18:1/18:1, in addition to GPCho 34:2, GPEtn 18:1/19:1. While GPEtn fragments by losing the head group as a neutral loss of 141 Da, the N-Me GPEtn loses the head group as a neutral loss of 155 Da.

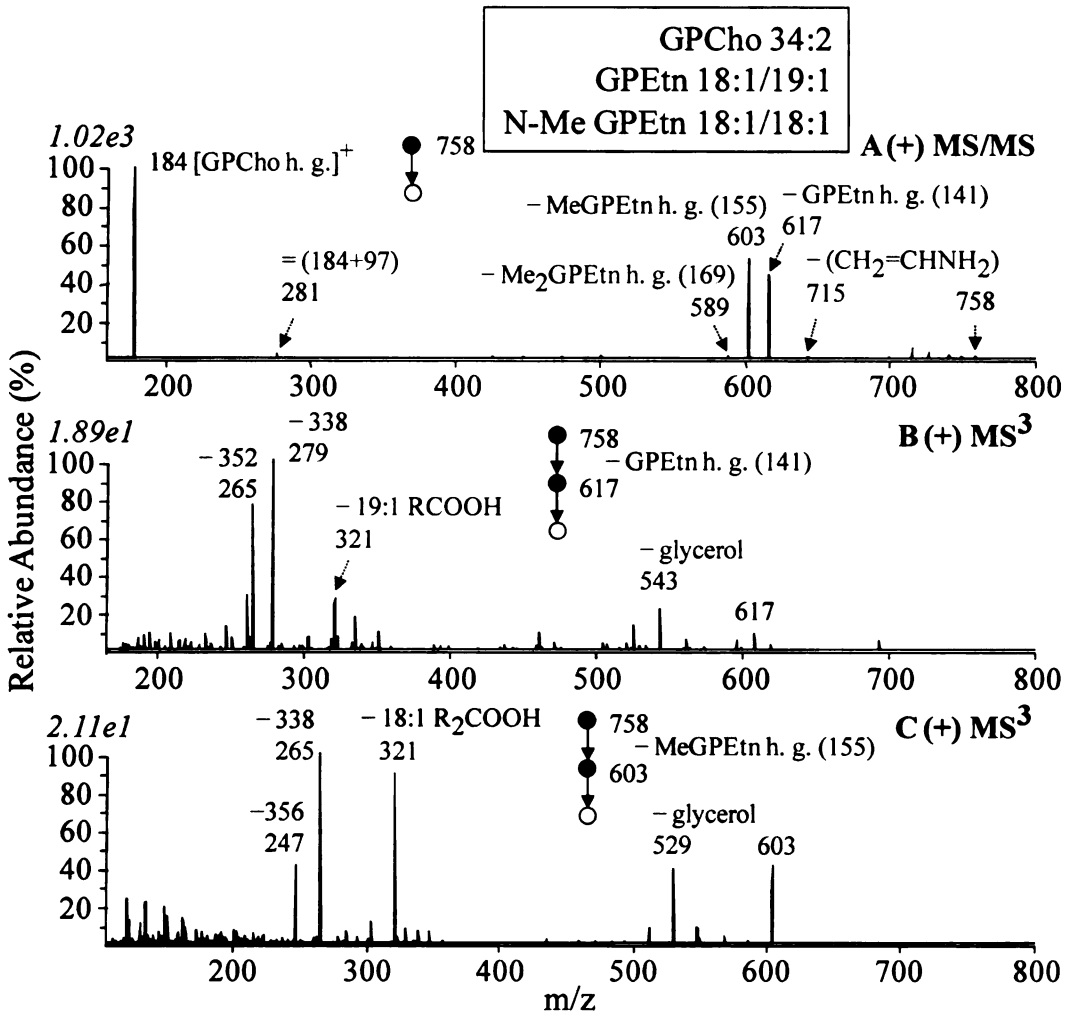


Figure 7.7 Positive ion mode ESI MS/MS and MS^3 spectra of m/z 758 in the MS of lipid extracts from the cell membranes of the wild type *R. sphaeroides* reveal that this isotopically isolated precursor ion contains multiple species, including the major components of GPCho 34:2, GPEtn 18:1/19:1 and N-Me GPEtn 18:1/18:1: A) MS/MS of m/z 758 from Figure 7.6A, B) MS^3 of m/z 617 from panel A, and C) MS^3 of m/z 603 from panel A.

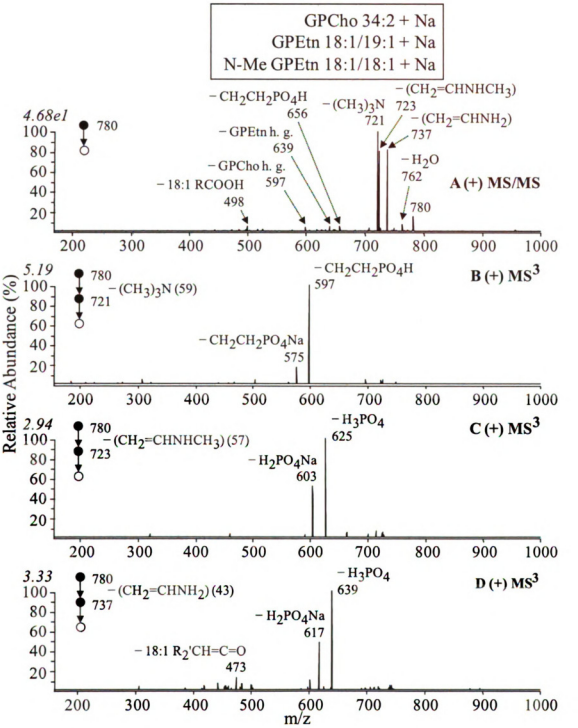


Figure 7.8 ESI MS/MS (A), and MS^3 spectra of m/z 780 from Figure 7.6A) revealing the overlapping of sodium adduct ions of GPCho 34:2 (B), N-Me GPEtn 18:1/18:1 (C), and GPEtn 18:1/19:1 (D).

The precursor ion at m/z 780 in the positive ion mode MS (Figure 7.8) is 22 Da higher than m/z 756, and might correspond to the sodium adduct ion. The ESI MS/MS and MS^n spectra (Figure 7.8) of m/z 780 in the lipid extract from the cell membranes of the wild type *R. sphaeroides* reveal that this isotopically isolated precursor ion again contains a mixture of GPCho 34:2, GPEtn 18:1/19:1 and N-Me GPEtn 18:1/18:1 in the sodium adduct form. In the MS/MS of the sodium adduct ions, while GPCho loses the head group as a neutral loss of 59 Da and GPEtn loses 43 Da, the N-Me GPEtn lipid loses the head group as a 57 Da neutral loss. In MS^3, the m/z difference between the two predominant product ions are 22 Da in each case (Figures 7.8 B-D) corresponding to the mass of (sodium-hydrogen), further confirming that the precursors ion are all sodium adduct ions.

The negative ion mode deprotonated ion corresponding to m/z 758, is m/z 756. The m/z 756 precursor ion was fragmented (Figure 7.9) and was found to contain the deprotonated ions of the GPEtn 18:1/19:1 and N-Me GPEtn 18:1/18:1 lipids, but not GPCho, which is not expected to be observed as a deprotonated ion.

Likewise, the other N-Me GPEtn and N,N-Me_2 GPEtn species shown in Tables 7.1-7.3 are identified by using MS/MS and MS^n.

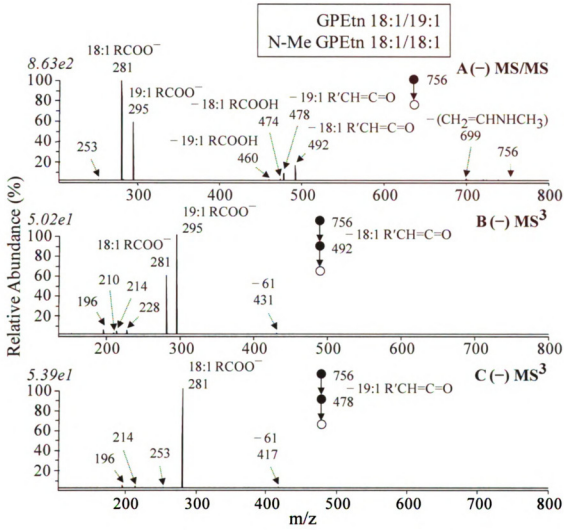


Figure 7.9 ESI MS/MS (A), and MS^3 spectra of m/z 756 from Figure 7.6B) in the negative ion mode, revealing the overlapping of the deprotonated ions of N-Me GPEtn 18:1/18:1 (B), and GPEtn 18:1/19:1 (C).

The situation of overlap revealed here raised an alarm against quantification by using MS peak abundance or area, even if an internal standard is included. It can be clearly seen that most peaks in MS actually contain overlapping multiple species, including both the protonated and deprotonated ions and adduct ions. However, quantification by MS peak intensity or peak area is not able to take this into

consideration. Therefore, before any quantification using MS, especially when dealing with lipid extracts from biological samples, the identity of the precursor ion should be examined at first for overlaps, and only those ions that are found to be dominated by one species can be quantified by MS using internal standard to yield convincing results.

These results also suggest that MS/MS quantification by using the characteristic fragmentations in MS/MS in a quadrupole ion trap mass spectrometer is sometimes necessary in order to achieve accurate lipid quantification from the complex biological lipid extracts, which is applied extensively in Chapter 10.

Therefore, in this chapter, only those MS peaks that have been determined to be predominantly one species by using MS/MS are shown for quantification. Only the GPEtn, GPCho, GPGro and CL phopholipids components, for which internal standards with the same head group are commercially available, are shown for absolute quantification. Since SQDG does not have an internal standard that is commercially available, it was relatively quantified between the strains by comparison to the GPGro 14:0/14:0 internal standard. The MS/MS quantification was only applied to the CL lipids in the wild type 2.4.1+C*c*O and the CL-deficient CL3+C*c*O strains for the lipid extracts from the membranes and from the purified C*c*O enzymes in this chapter.

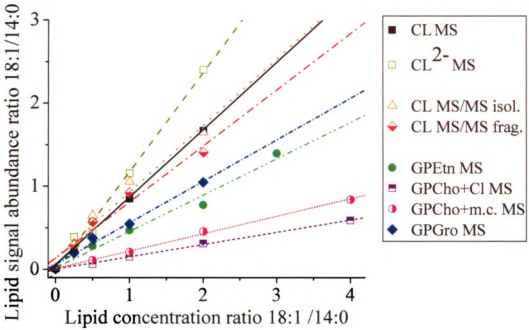
7.3.1.4 Changes in the lipid species in the mutants

In the membrane lipid extracts from the specific lipid-deficient mutants, other than those lipids that are genetically deficient, most of the other lipids seen in the wild type are also seen in the mutants, although at different relative ion abundances. The difference in the apparent ion abundance might reflect the actual concentration difference in solution, but may also arise due to a change in ionization efficiency affected by the missing types of lipids. Therefore, in order to perform a quantitative comparison of the lipid profiles in the mutants, proper internal standards have to be included.

7.3.2 Basis for absolute quantification by MS and MS/MS using internal standards

The ion forms observed and the ionization efficiencies are very different between different types of lipids in either ESI or MALDI, and are highly dependent on the polar head group of the lipids, the solvent conditions, and the other components in the solution (data not shown). However, lipids with the same head group are found to form the same types of ions in MS and have similar ionization efficiency, although the chain length may slightly affect the ionization. Therefore lipids from different samples can be quantified by incorporating an internal standard that has the same head group but differs in the chain length. In order to prove that the ion abundance ratio is linearly dependent on the concentration ratio, the relationship between the MS peak abundance ratio and the in-solution concentration ratio was first examined using a series of lipid mixture samples, by using 18:1/18:1 synthesized lipids at different concentration combinations as the models for the lipid extracts, and 14:0/14:0 synthesized lipids as the internal standards (see the table in Figure 7.10 for the specific sample compositions). Similarly the isolation and fragmentation of CL lipids by MS/MS were also examined.

The results represented in Figure 7.10 show that the relative peak abundance ratio against the internal standard in MS is a linear function of the relative concentration in solution for each lipid in the lipid mixture, within the range of concentrations examined. In addition to the MS peak abundance of the deprotonated ions of CL, GPEtn and GPGro, such linearity is also found for the doubly charged deprotonated CL, the non-covalent anionic adduct ions of GPCho formed with chloride or methyl carbonate, and more importantly, the isolation and fragment ions of CL in MS/MS (fragment ion m/z 699 from $CL(18:1)_4$ vs m/z 591 from internal standard $CL(14:1)_4$).



Sample (μM)	# 1	# 2	# 3	# 4	# 5	# 6
GPEtn 18:1/18:1	0	12	8	4	2	1
GPGro 18:1/18:1	0	0.5	4	2	1	8
GPCho 18:1/18:1	0	4	1	2	8	0.5
$CL(18:1)_4$	0	0.25	0.5	1	2	4
Internal standards						
GPEtn 14:0/14:0	4	4	4	4	4	4
GPGro 14:0/14:0	2	2	2	2	2	2
GPCho 14:0/14:0	2	2	2	2	2	2
$CL(14:0)_4$	1	1	1	1	1	1

Figure 7.10 Correlation between the peak abundance ratios in ESI MS and MS/MS spectra and the actual concentration ratios of GPEtn, GPGro, GPCho and CL lipid standards containing two 18:1 fatty acid chains and the lipid standards containing two 14:0 fatty acid chains, in the lipid mixture solutions prepared at random combinations of concentrations (0 – 12 μM). The compositions of the lipid standard mixtures used for constructing the quantification calibration plot are shown in the table (m.c.= methyl carbonate, isol.= isolation, frag.= fragmentation).

Such linearity can then be used as the basis to quantify lipid molecular species in a more complex lipid mixture by incorporating a lipid internal standard containing the same head group.

7.3.3 Quantitative lipid profiles of membranes from each mutant

The lipid quantification methods using MS and MS/MS developed above were then applied to the quantitative analysis of the membrane lipid extracts from the wild type and the GPCho, SQDG and CL specific lipid deficient mutants.

7.3.3.1 Quantitative lipid profiles of membranes: abundant membrane lipids using ESI MS

Figures 7.11 and 7.12 show the MS spectra of the membrane lipids extracts from the wild type and the specific lipid-deficient strains in positive and negative ion modes, respectively, with the incorporation of lipid internal standards. The lipid species to be quantified by MS here have each been determined to be the predominant component of the precursor ions by MS/MS (data not shown).

Figure 7.11 Positive ion mode ESI MS of lipids extracted from cell membranes of A) wild type (2.4.1+C*c*O) B) CL-deficient (CL3+C*c*O) C) SQDG-deficient (SB1K1+C*c*O) and D) GPCho-deficient (CHB20+C*c*O) mutants of *R. sphaeroides*, with the internal standards GPEtn, GPGro, GPCho and CL 14:0 at final concentrations of 4, 2, 2 and 1 μM, respectively.

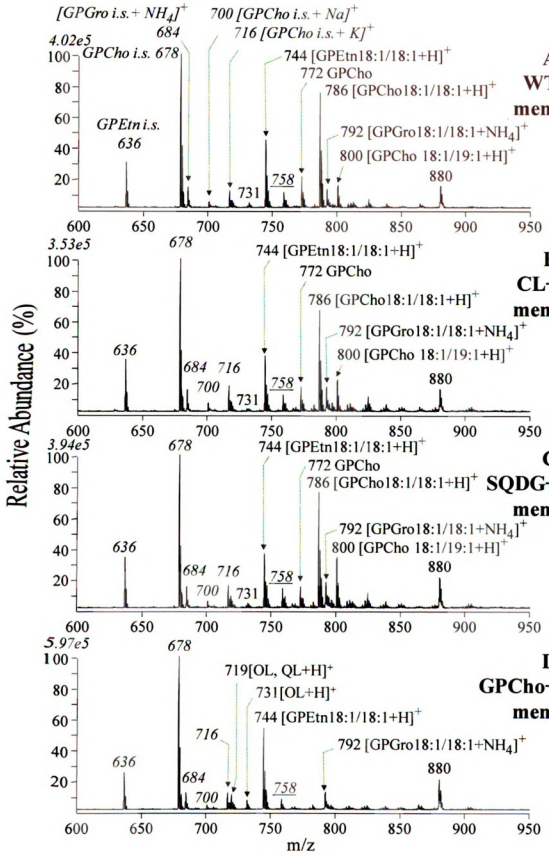
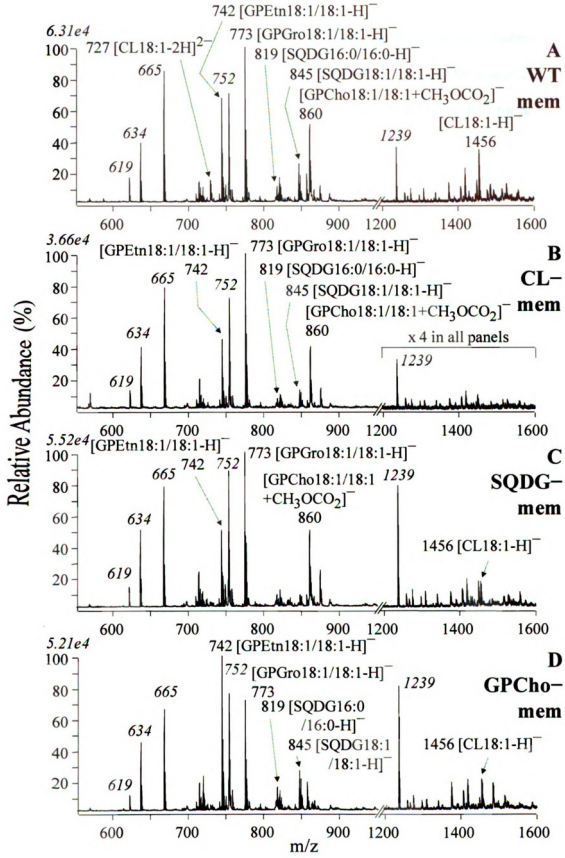

[GPGro i.s.+ NH4]+
684
700 [GPCho i.s.+ Na]+
716 [GPCho i.s.+ K]+
4.02e5
GPCho i.s. 678
744 [GPEtn18:1/18:1+H]+
772 GPCho
786 [GPCho18:1/18:1+H]+
A
WT
mem
GPEtn i.s.
636
792 [GPGro18:1/18:1+NH4]+
800 [GPCho 18:1/19:1+H]+
758
731
880
3.53e5
678
744 [GPEtn18:1/18:1+H]+
772 GPCho
B
CL–
mem
786 [GPCho18:1/18:1+H]+
792 [GPGro18:1/18:1+NH4]+
636
800 [GPCho 18:1/19:1+H]+
684 716
700
758
731
880
3.94e5
678
744 [GPEtn18:1/18:1+H]+
772 GPCho
C
786 [GPCho18:1/18:1+H]+
SQDG–
mem
792 [GPGro18:1/18:1+NH4]+
636
800 [GPCho 18:1/19:1+H]+
684 716
700
758
731
880
5.97e5
678
719[OL, QL+H]+
731[OL+H]+
D
744 [GPEtn18:1/18:1+H]+
GPCho–
mem
716
792 [GPGro18:1/18:1+NH4]+
636
880
684
700
758
Relative Abundance (%)
m/z

Figure 7.12 Negative ion mode ESI MS of lipids extracted from cell membranes of A) wild type (2.4.1+C*c*O) B) CL-deficient (CL3+C*c*O) C) SQDG-deficient (SB1K1+C*c*O) and D) GPCho-deficient (CHB20+C*c*O) mutants of *R. sphaeroides*, with the internal standards GPEtn, GPGro, GPCho and CL 14:0 at final concentrations of 4, 2, 2 and 1 μM, respectively.


Relative Abundance (%)
m/z
A
WT
mem
B
CL–
mem
C
SQDG–
mem
D
GPCho–
mem
6.31e4
3.66e4
5.52e4
5.21e4
742 [GPEtn18:1/18:1-H]−
773 [GPGro18:1/18:1-H]−
727 [CL18:1-2H]2−
819 [SQDG16:0/16:0-H]−
845 [SQDG18:1/18:1-H]−
[GPCho18:1/18:1+CH3OCO2]−
860
[CL18:1-H]−
1456
665
752
634
619
1239
x 4 in all panels
[GPCho18:1/18:1
+CH3OCO2]−
1456 [CL18:1-H]−
819 [SQDG16:0
/16:0-H]−
845 [SQDG18:1
/18:1-H]−

7.3.3.2 Summary of the quantification of membrane lipid species

Based on the MS peak abundance normalized to individual internal standards, the quantity of each lipid species observed by MS in the wild type and the specific lipid-deficient mutant was obtained, and the results are summarized in Figure 7.11 for positive ion mode and Figure 7.12 for negative ion mode.

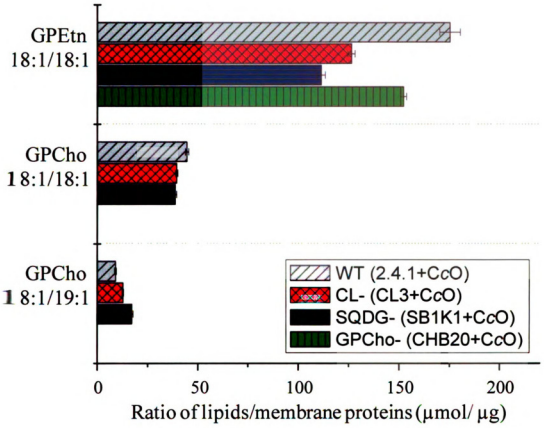
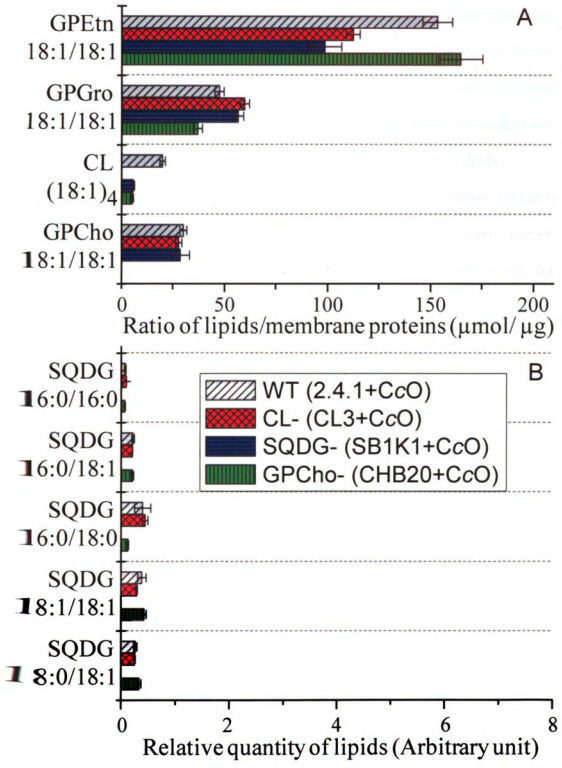


Figure 7.13 Summary of the quantification of the major phospholipid ions observed in the MS spectra of the membrane lipid extracts from the wild type and the specific lipid-deficient mutant in positive ion mode, based on triplicate extractions (except for duplicate for the CHB20 sample). The data shown are the mean values, and the error bar is the standard deviation (except for the CHB20 sample). The quantified lipids include GPEtn 18:1/18:1 (m/z 744), GPCho 18:1/18:1 (m/z 786), and GPCho 18:1/19:1 (m/z 800). For all of the phospholipids quantified here, the lipid concentrations in the ESI MS sample are within the linear range as shown in Figure 7.10.

Figure 7.14 Summary of the quantification of the major lipid ions observed in the MS spectra of the membrane lipid extracts from the wild type and the specific lipid-deficient mutant in negative ion mode, based on triplicate extractions (duplicate for the CHB20 sample).In panel A, the phospholipids GPEtn, GPGro, CL and GPCho are quantified against their individual14:0/14:0 internal standards, but in panel B, SQDG lipids are relatively quantified with reference to the GPGro 14:0/14:0 internal standard. The data shown are the mean values, and the error bar is the standard deviation (except for the CHB20 sample). For all of the phospholipids quantified here, the lipid concentrations in the ESI MS samples are within the linear range as shown in Figure 7.10.


A
GPEtn 18:1/18:1
GPGro 18:1/18:1
CL (18:1)4
GPCho 18:1/18:1
0
50
100
150
200
Ratio of lipids/membrane proteins (μmol/ μg)
B
SQDG 16:0/16:0
SQDG 16:0/18:1
SQDG 16:0/18:0
SQDG 18:1/18:1
SQDG 18:0/18:1
WT (2.4.1+CcO)
CL- (CL3+CcO)
SQDG- (SB1K1+CcO)
GPCho- (CHB20+CcO)
0
2
4
6
8
Relative quantity of lipids (Arbitrary unit)

The quantification results shown in Figures 7.13 and 7.14 provide a picture of the relative composition of different types of lipids in the membranes of the wild type and the mutants. Because the abundances of the SQDG lipids are normalized to the GPGro 14:0/14:0 lipids, the bar length in the figures should be be used for comparison between the wild type and the individual strains with caution, as they do not necessarily indicate their real concentrations, and should not be compared to other types of lipids.

Nonetheless, Figures 7.13 and 7.14 reveal that in all of the strains, GPEtn is the most abundant phospholipid, followed by GPCho (except for the GPCho-deficient strain), GPGro and then CL. The quantification results of GPEtn and GPCho (as methyl carbonate adduct in negative ion mode) lipids from the positive ion mode and negative ion mode MS are very similar, but the positive ion mode results show a smaller relative standard deviation, because the ion abundances of these species are higher, and there is less overlap at these m/z values in the positive ion mode than those in the negative ion mode. Figure 7.15 summarizes the relative quantity of lipids by the strains. In addition to the deficient lipids that are not detectable by ESI MS in these mutants, the most appreciable differences are: GPEtn increases significantly in the GPCho-deficient mutant, GPGro increases in both CL-deficient mutant and SQDG-deficient mutant, while GPCho remains relatively unchanged in these two mutants.

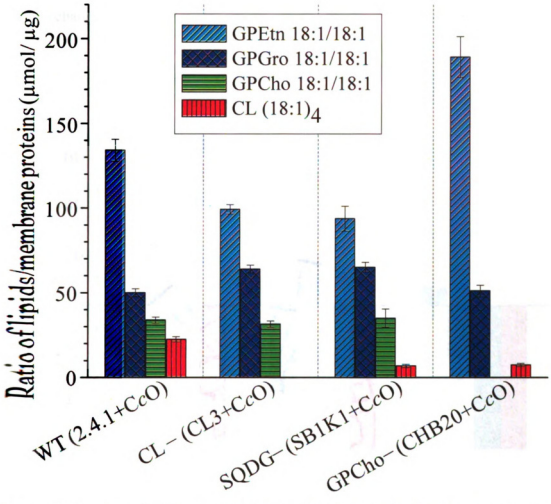


Figure 7.15 Quantitative phospholipid compositions in the membranes of in the wild type and the mutant strains, from negative ion mode MS analysis.

In order to display the changes more clearly, the percentage of change relative to those in the wild type are calculated and presented in Figure 7.16. Figure 7.16 shows that, compared to the wild type, the membrane from the cardiolipin-deficient mutant contains 30% more GPGro18:1/18:1, about the same level of GPCho 18:1/ 18:1 and GPEtn 18:1/18:1, and no cardiolipin within the limit of detection by MS, but not by MS/MS (see below section 7.3.3.3). The SQDG-deficient mutant also displayed a ~30% increase in

the amount of GPGro. The GPCho-deficient mutant has a 40% increase in GPEtn lipids and no change in GPGro.

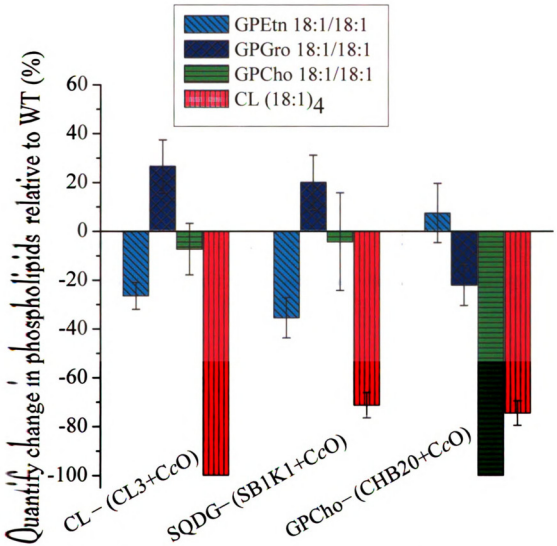


Figure 7.16 The percentage change in the quantity of each type of membrane lipid with available internal standards, relative to the wild type.

7.3.3.3 Quantification of the CL-deficient mutant: the low-abundance cardiolipin using ESI MS/MS

Although undetectable by MS, the presence of $CL(18:1)_4$ in the membranes from cardiolipin-deficient *R sphaeroides* cells was clearly revealed by MS/MS. Quantification by MS/MS using the internal standard $CL(14:0)_4$ further revealed that the quantity of $CL(18:1)_4$ in the membrane of the cardiolipin-deficient mutant was actually 2.4% of the quantity of $CL(18:1)_4$ in the wild type (Figure 7.17). The quantification result using MS/MS is similar to the result using MS for the wild type (Figures 7.17A and 7.17C). Table 7.6 summarizes the relative changes of the major phospholipids of the CL-deficient mutant compared to the wild type, by using the combination of MS and MS/MS quantification.

Figure 7.17 Negative ion mode nanoESI MS and MS/MS of lipids extracted from membranes of wild type (2.4.1+C*c*O) and cardiolipin-deficient (CL3+C*c*O) *R. sphaeroides* cells. A) MS of the wild type, B) MS of the cardiolipin-deficient mutant, C) MS/MS of m/z 1240 and 1456 from A, and D) MS/MS of m/z 1240 and 1456 from B. The internal standards mixture containing GPEtn, GPGro, GPCho and CL 14:0 at final concentrations of 4, 2, 2 and 1 μM, respectively, was included in the lipid extract for quantification. The MS mass range was broken down to m/z 600-900 and m/z 1200-1600, and the m/z 1200-1600 region in panels A and B was expanded 5 times in abundance to show the potential CL peaks more clearly.

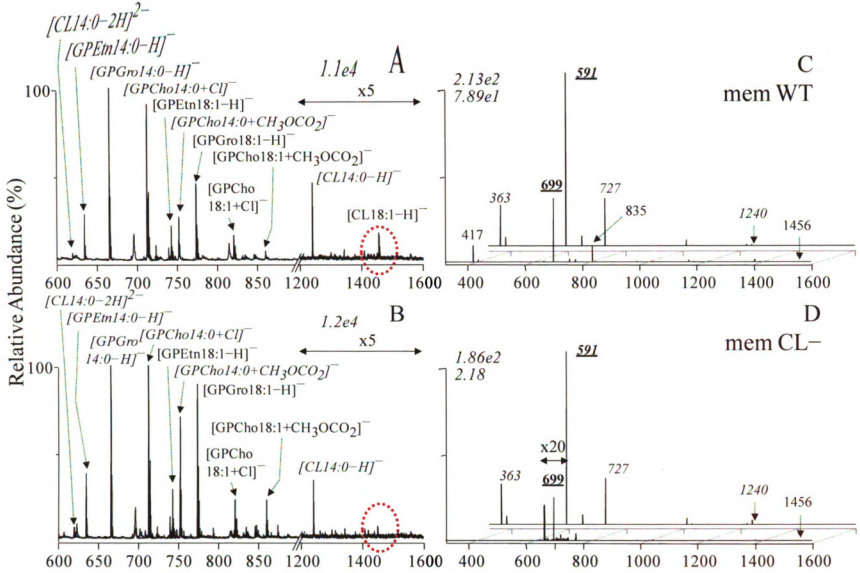

[CL14:0−2H]2−
[GPEtn14:0−H]−
[GPGro14:0−H]−
[GPCho14:0+Cl]−
[GPEtn18:1−H]−
[GPCho14:0+CH3OCO2]−
[GPGro18:1−H]−
[GPCho18:1+CH3OCO2]−
[GPCho 18:1+Cl]−
[CL14:0−H]−
[CL18:1−H]−
1.1e4
A
x5
2.13e2
7.89e1
C
mem WT
591
699
363
727
835
417
1240
1456
Relative Abundance (%)
100
600 650 700 750 800 850 1200 1400 1600
400 600 800 1000 1200 1400 1600
[CL14:0−2H]2−
[GPEtn14:0−H]−
[GPGro14:0−H]−
[GPCho14:0+Cl]−
[GPEtn18:1−H]−
[GPCho14:0+CH3OCO2]−
[GPGro18:1−H]−
[GPCho18:1+CH3OCO2]−
[GPCho 18:1+Cl]−
[CL14:0−H]−
1.2e4
B
x5
1.86e2
2.18
D
mem CL−
591
x20
363
699
727
1240
1456
100
600 650 700 750 800 850 1200 1400 1600
400 600 800 1000 1200 1400 1600

Table 7.4 Summary of lipids extracted from the membranes of wild type (2.4.1+C*c*O) and CL-deficient mutant (CL3+C*c*O), using MS and MS/MS: CL-deficient membranes are significantly depleted in cardiolipin.

Sample	nmol lipid*/ mg protein**				
	GPEtn 18:1	GPGro 18:1	GPCho 18:1	CL18:1 MS/MS	**Σ phospho-lipid**
WT mem (2.4.1+C*c*O)	111	33	18	13	176
CL- mem (CL3+C*c*O)	83	42	17	0.32	144
% lipid (CL- /WT) mem	75%	128%	98%	**2.4%**	82%

* nmol of lipid was determined by ESI MS and MS/MS of lipid extract using internal standards.

** mg of protein was determined by BCA assay using BSA as the standard.

7.3.4 Interpreting the physiological meaning of the specific lipid deficiency in membranes

An increase of GPGro but not GPCho in the SQDG-deficient mutant is in agreement with previous studies using TLC and ^{14}C-labelling experiments which found that the growth of the cells is not affected by the SQDG, but the cells became unviable when both SQDG and GPGro were depleted [14,16]. SQDG was thus proposed to be able to functionally replace GPGro [14,16], because both have a negatively charged head group [14], and together, they can meet the cells' requirement for a certain amount of

membrane lipids with negatively charged head groups. GPGro is not a major precursor for synthesizing SQDG [13], thus such an increase in GPGro production is probably due to the need for maintaining physiological function.

An increase in GPEtn, but not GPGro, was observed here and in the original GPCho-deficient mutant (CHB20), and it can be partially explained with regard to the biosynthetic pathways of GPCho from GPEtn [13,90], and it seems that this pathway is somewhat independent from the GPGro lipids (see Chapter 1 for a detailed description). Nonetheless, the consequence is that a GPCho-deficiency and abundant GPEtn did not affect the growth of the cells. Both GPEtn and GPCho carry a positive charge in the head group in addition to the negatively charged phosphate.

An increase in GPGro in the CL-deficient mutant can also be explained by considering the pathways used to synthesize CL from GPGro by the mutated cardiolipin synthase. The specific functional replacement of CL by GPGro has been proposed repeatedly in previous studies, particularly for C*c*O and other membrane-bound redox complexes [54].

In spite of the significant deficiency of the specific type of lipids in the membrane lipid profiles, no appreciable physiological defects are observed in the mutants. This suggests that none of the individual lipids are essential for the *R. sphaeroides* cells *per se*. The observed characteristic increase in other types of lipids, however, may suggest that these other lipids can replace the functions of the deficient lipids, such as was proved in the case of SQDG and GPGro [14,16], or each mutant must have developed mechanism to cope with the altered lipids. It is not likely that the cells would be indifferent to their

lipid profiles. Elucidating how the lipids can replace each other, can provide valuable insight into how and why the lipids may affect the membrane protein C*c*O.

The results here show that none of the individual types of deficient lipids are essential for the cells *per se*. The lipid profile characterizations of the membranes established the background to examine the C*c*O purified from these mutants, in order to gain further insight on the functional roles of lipids in the membrane protein C*c*O.

7.3.5 Profiles of the lipids maintained in the purified C*c*O: WT and CL−

Characterization of the properties of the C*c*O purified from the wild type and the specific lipid-deficient strains, showed no appreciable difference between these C*c*O (see the introduction), although their membrane lipid environments were shown to have been altered significantly. The possible reasons for the close-to wild type behavior of C*c*O from the CL, SQDG or GPCho-deficient mutant are: 1) The profiles of the lipids associated with the purified C*c*O are significantly different from those of the bulk membrane, due to preferential enrichment of the specific types of lipids by the C*c*O. For example, in the CL-deficient mutant, the C*c*O might accumulate all of the CL that it can from the depleted pool of CL in the membranes, to a level close to that in the C*c*O from the wild type, and thus guarantee its normal activity; 2) If the profile of the lipids associated with the purified C*c*O resembles that of the membrane and shows no dramatic enrichment of a specific type of lipid, then the cells and C*c*O must have developed mechanisms to compensate for its altered lipid profile; 3) The cells and the C*c*O are completely unaffected by the lack of lipids such as cardiolipin, which seems unlikely.

These possibilities can be distinguished by quantitatively examining the lipid components in the purified C*c*O. Therefore, the lipids in the purified enzymes from the CL-deficient mutant and the wild type were examined by using MALDI MS and MS/MS analysis directly on the purified enzymes (see Chapter 9 for some of the data), and quantitative ESI MS and MS/MS analysis of the lipids extracted from these purified C*c*Os following freeze-drying and cold anhydrous acetone-washing steps to remove the interfering detergents. ESI MS could not detect CL in the lipid extracted from C*c*O of the CL-deficient mutant, but MS/MS analysis reveals that there is still a low amount of cardiolipin in the C*c*O from the CL-deficient mutant, at 5% relative to that of the C*c*O from the wild type (Figure 7.18). This is about a two-fold enrichment of CL in the enzyme compared to the 2.4% in the membranes of the CL-mutant and the wild type, but 5% is still a low amount, and does not suggest a significant level of specific accumulation and enrichment of the depleted CL in C*c*O. The results from both quantitative ESI MS and MS/MS (for CL lipid) are summarized in Figure 7.19.

Figure 7.18 Negative ion mode nanoESI MS and MS/MS of lipids extracted from C*c*O purified from the wild type (2.4.1+C*c*O) and cardiolipin-deficient (CL3+C*c*O) *R. sphaeroides* membranes using a Ni-NTA gravity column. Lipid extraction was performed after freeze-drying and three repeats of cold anhydrous acetone-washing steps to remove detergents. A) MS of the lipids extracted from the wild type C*c*O (WT), B) MS of the lipids extracted from the cardiolipin-deficient mutant (CL^-), C) MS/MS of m/z 1240 and 1456 from panel A, and D) MS/MS of m/z 1240 and 1456 from panel B. The internal standards mixture containing GPEtn, GPGro, GPCho and CL 14:0 at final concentrations of 4, 2, 2 and 1 μM, respectively, was included in the lipid extract for quantification. The MS mass range was broken down to m/z 600-900 and m/z 1200-1600, and the region of m/z 1200-1600 in panels A and B was expanded 5 times in abundance to show the potential CL peaks more clearly.

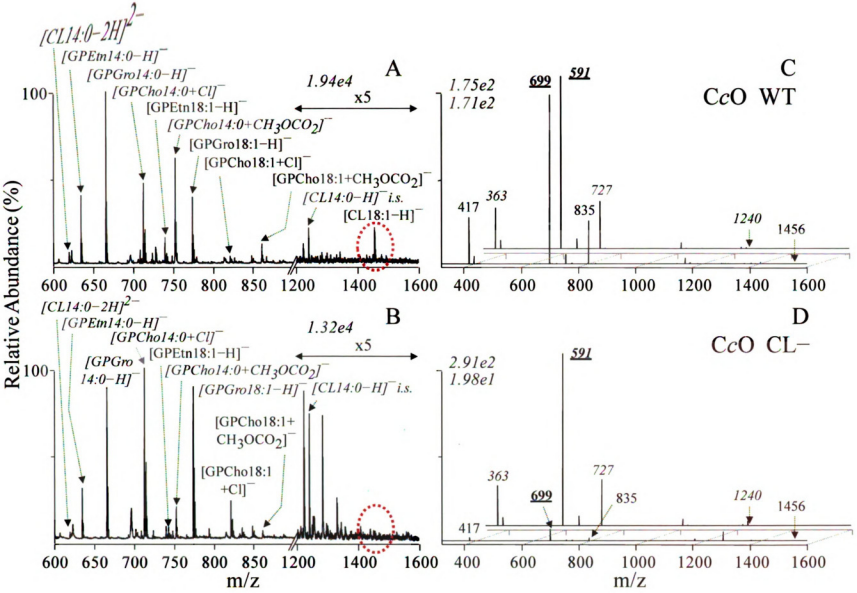

A
B
C
D
CcO WT
CcO CL−
Relative Abundance (%)
m/z
[CL14:0−2H]2−
[GPEtn14:0−H]−
[GPGro14:0−H]−
[GPCho14:0+Cl]−
[GPEtn18:1−H]−
[GPCho14:0+CH3OCO2]−
[GPGro18:1−H]−
[GPCho18:1+Cl]−
[GPCho18:1+CH3OCO2]−
[CL14:0−H]− i.s.
[CL18:1−H]−
[GPGro14:0−H]−
[GPCho18:1+ CH3OCO2]−
[GPCho18:1 +Cl]−
1.94e4
1.32e4
x5
1.75e2
1.71e2
2.91e2
1.98e1
591
699
363
727
835
417
1240
1456

Figure 7.19 The ratio of the numbers of moles of the lipids extracted from the purified C*c*O to the numbers of moles of the original purified C*c*O (moles/ moles), which should indicate the stoichiometric relationship of the lipids in C*c*O, and the relative quantification of other types of lipids. Only the CL-deficient mutant (CL3+C*c*O) and the wild type (2.4.1+C*c*O) are examined. The lipids are extracted using the methods described in Chapter 3, after freeze-drying and three times of acetone-washing, to remove the detergents. The results shown are the average of multiple repeats of extractions. In panel A, the phospholipids are quantified against their individual internal standards in MS and MS/MS; in panel B, the SQDG lipids are relatively quantified with reference to the GPGro internal standard in MS. The data shown are the mean values, and the error bar is the standard deviation. For all of the phospholipids quantified here, the lipid concentrations in the ESI MS samples are within the linear range as shown in Figure 7.10.

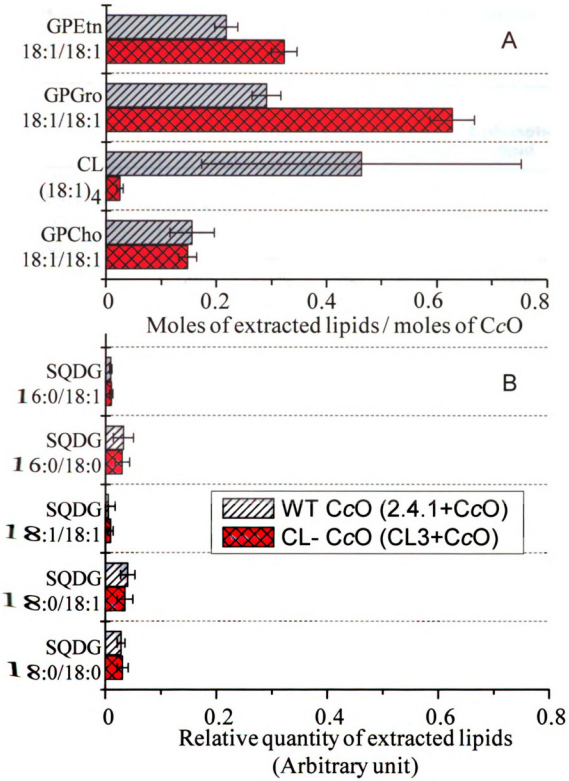

A
GPEtn
18:1/18:1
GPGro
18:1/18:1
CL
(18:1)4
GPCho
18:1/18:1
0
0.2
0.4
0.6
0.8
Moles of extracted lipids / moles of CcO
B
SQDG
16:0/18:1
SQDG
16:0/18:0
SQDG
18:1/18:1
SQDG
18:0/18:1
SQDG
18:0/18:0
WT CcO (2.4.1+CcO)
CL- CcO (CL3+CcO)
0
0.2
0.4
0.6
0.8
Relative quantity of extracted lipids
(Arbitrary unit)

Table 7.5 Summary of changes in the quantity of phospholipids from the lipid extracts of C*c*O purified from the wild type (2.4.1+C*c*O) and the CL-deficient strain (CL3+C*c*O), in comparison to the membranes as shown in Table 7.4.

Sample	mol lipid*/ mol C*c*O**				
	GPEtn 18:1	GPGro 18:1	GPCho 18:1	CL18:1 MS/MS	**Σ phospho-lipid**
WT C*c*O (2.4.1+C*c*O)	0.22	0.29	0.15	0.46	1.1
CL- C*c*O (CL3+C*c*O)	0.32	0.62	0.15	0.02	1.1
% lipid CL- vs WT C*c*O	149%	215%	95%	**5.4%**	100%
	nmol lipid*/ mg protein**				
WT C*c*O (2.4.1+C*c*O)	1.8	2.4	1.3	3.8	9.3
CL- C*c*O (CL3+C*c*O)	2.7	5.2	1.2	0.2	9.3
% lipid CL- vs WT C*c*O	149%	215%	95%	**5.4%**	100%

* mol of lipid was determined by ESI MS and MS/MS of lipid extracts using internal standards.

** mol of C*c*O protein was determined by UV-Vis spectroscopy, and converted to mg by using 120 kDa as the molecular weight.

Although no dramatic accumulation of CL is observed, the results in Figure 7.19 do show that the lipid composition in purified C*c*O are different from that of the bulk membrane in terms of the relative quantity of different types of lipids. In contrast to the membrane lipid extract that contains a predominant amount of GPEtn, the lipid extract from the purified C*c*O from the wild type contains GPEtn, GPGro, GPCho and CL at similar quantities, and it also contains a variety of SQDG, but the SQDG cannot be compared quantitatively to the phospholipids due to the lack of an internal standard of its own. The lipid extracted from the C*c*O from the CL-deficient mutant shows the same level of GPCho and all of the SQDG species, a slight increase in GPEtn, and a nearly two-fold increase in GPGro, compared to the wild type C*c*O. The fractional change in the lipid abundances extracted from the CL-deficient mutant and the wild type C*c*O are shown in Table 7.5 with comparison to the membranes.

The absolute quantification of phospholipids in the lipid extract by ESI, however, also reveals that the quantities of the phospholipids extracted from purified C*c*O, after acetone-washing to remove detergents, are significantly lower than the number obtained from the inorganic phosphate analysis, and are also lower than the expected stoichiometric composition of lipids per C*c*O molecule. Phosphorus analysis revealed that the Ni-NTA gravity column purified C*c*O from 2.4.1+CcO or from CL3+C*c*O strains each contain about 10 phosphates per C*c*O (Table 8.2 in Chapter 8) based on duplicate or triplicate experiments, and the FPLC purified C*c*O from 169-2.4.1 and 169CL3 strains contain 7-8 and 6-7 phosphates per C*c*O, respectively.

This suggests that the lipid extraction is not complete and the extraction efficiency is only 20-30%. This issue of incomplete lipid extraction from the purified C*c*O after

acetone-washing is confirmed by a more detailed examination described in Chapter 8, and the issues associated with membrane proteins lipid extractions are also discussed in Chapter 8.

Due to the incomplete extraction, it was important to substantiate the finding of low cardiolipin levels in the mutant C*c*O by another method. An independent non-chemical extraction method of releasing the lipids, by MALDI (matrix-assisted laser desorption/ ionization), can be used as a complement to chemical extraction. In the negative ion mode MALDI MS analysis of purified C*c*O, the CL lipid in the C*c*O from the CL-deficient mutant can be observed, but still at abundances much lower than that of the wild type.

These results ruled out the first possible reason described earlier that the C*c*O could accumulate CL to the wild type level from the depleted CL pool in the membrane, and support the second possibility proposed above that the C*c*O and the cells can adapt to the altered lipid profile *in vivo*. The C*c*O requirement for lipids is likely to be restricted to certain structural features of a few types of lipid, rather than being specific for an entire lipid structure. The *in vivo* nature of these studies on the lipid-deficient mutants seems to reveal a different level of flexibility in the lipid requirement of the membrane proteins.

In particular, the results from the C*c*O of the CL-deficient mutant of *R. sphaeroides* bring the previous conclusions drawn from the mammalian C*c*O and CL into question [8,54]. The two systems might have different mechanisms of CL lipid-protein interactions. The CL-deficient *R. sphaeroides* C*c*O is therefore being further pursued by using x-ray crystallography (Chapter 9), and by using a combination with the metabolic lipid profile modulation approach (Chapter 10).

7.4 Conclusions

The series of specific lipid-deficient mutants of *R. sphaeroides*, which are specifically deficient in CL, SQDG and GPCho lipids, respectively, were found to be not only viable under aerobic growth, but can also express the *R. sphaeroides* C*c*O at good yield and grow robustly. To understand the significance of these findings, the membranes isolated from these strains are analyzed by systematic mass spectrometry approaches.

MS/MS and MS^n analysis elucidated a number of lipid molecular species in the wild type and the specific lipid-deficient mutants, which were not identifiable by using MS, but could be physiologically important. The MS and MS/MS-based quantification method by incorporating a set of lipid internal standards is also shown to be amenable for quantitative lipid analysis of complex lipid mixtures. Quantitative analysis of the membrane lipid extracts of the wild type and the mutants reveals characteristic variations in the overall membrane lipid composition induced by the specific deficiency in certain lipid classes, and the relationship can be understood in the context of lipid biosynthesis, as well as potential physiological functional substitutions. In general, the CL-deficiency and the SQDG-deficiency caused significant increases in GPGro lipid, but did not affect the level of GPCho in the membranes, and the GPCho-deficiency caused increase in GPEtn lipids, but not GPGro lipids in the membranes.

The results here show that none of the individual types of deficient lipids are essential for the cells *per se*. The lipid profile characterizations of the membranes

estabh

gain fu

memb

yield.

charac

defici

tempe

defici

signif

MS a

show

SQD

have

sugge

CoO.

spina

using

chemi

established a background to examine the CcO purified from these mutants, in order to gain further insight on the functional roles of lipids in the membrane protein C*c*O.

The individual specific deficiencies in CL, GPCho, or SQDG lipids in the membranes of *R. sphaeroides* did not prevent the expression of C*c*O at close-to-wild type yield, and the C*c*O purified from these mutants displayed the close-to-wild-type spectral characteristics, subunit composition and steady state activity. The C*c*O from the CL-deficient mutant also displayed similar-to-wild-type activity stability with increasing temperature.

Quantitative ESI MS and MS/MS analysis of lipid extracts from C*c*O of the CL-deficient mutant revealed increased GPGro (~100%) and GPEtn (~50%) abundances, but significantly decreased CL (~95%), compared to the wild type enzyme. Direct MALDI MS and MS/MS analysis of the purified enzyme revealed similar results (data not shown).

The unaffected cellular and enzymatic properties suggest that none of the CL, SQDG or GPCho lipids are essential to the functions of C*c*O *per se*, although C*c*O might have a preference for CL. Furthermore, the altered lipid profiles in the C*c*O are suggestive of an *in vivo* adaptability/flexibility in the lipid requirement of *R. sphaeroides* C*c*O, in contrary to findings from mammalian C*c*O and its CL. The CL-deficient *R. sphaeroides* C*c*O therefore requires further investigation by x-ray crystallography, and by using the combination with the metabolic lipid profile modulation approach.

The quantitative analysis on the lipid extracts from the C*c*O also reveals low chemical extraction efficiency (20-30%) from the purified C*c*O after acetone-washing to

remove detergents. These issues of lipid extraction from membrane proteins are followed up in Chapter 8.

Chapter 8

Lipid Extraction from Membrane Proteins: Effects of Detergent and Detergent Removal Procedures on Extraction Efficiencies

8.1 Summary

As the presence of even the non-ionic detergents can introduce a serious challenge for lipid mass spectrometric analysis, particularly for ESI, the quantitative mass spectrometric analysis of the lipids from the purified C*c*O enzymes requires removal of interfering detergents down to a level that is compatible with the ESI ion source. However, the detergent removal procedure might further limit the extraction efficiency of the lipids from the membrane proteins. In this chapter, approaches to detergent removal from the highly hydrophobic and structurally sensitive C*c*O, and the effects of treatments of C*c*O on the lipid extraction efficiency from the purified protein, were examined.

The effectiveness of the approaches for detergent-removal, including cold anhydrous acetone-washing and dilution-filtration, was evaluated, mainly by using thin layer chromatography (TLC). Other potential approaches, such as protein digestion and the usage of a cleavable detergent, were also tested.

The extraction of the few lipids maintained by purified hydrophobic membrane proteins are known to be difficult, and the ESI quantification results in Chapter 7 have revealed sub-stoichiometric ratio of the lipids in the extracts. Here the exact phospholipid extraction efficiency was evaluated by quantitatively measuring the phosphate in the

purified C*c*O, in both the lipids extracts of the C*c*O, and in the residual protein after chemical extractions, and also examined was which step of C*c*O sample processing is detrimental, and what is beneficial for more efficient lipid extraction, and suggested directions for continued investigations in the future.

8.2 Introduction

Since the detergent that is required for the purification and solubilization of the membrane protein C*c*O was found to strongly interfere with lipid ESI ionization efficiency as well as TLC analysis [225], cold anhydrous acetone-washing, following lyophilization of the enzyme has been used to remove the detergent [225] in order to obtain acceptable ESI sensitivities for the lipids. However, previous ESI MS and MS/MS analysis of these lipid extracts as shown in Chapter 7 resulted in reproducible sub-stoichiometric ratios of different types of phospholipids including phosphatidylglycerol (GPGro), phosphatidylethanolamine (GPEtn), phosphatidylcholine (GPCho) and cardiolipin (CL) in the purified enzyme, which is contradictory to the current knowledge of the stoichiometry of lipids in the C*c*O enzyme by phosphorus analysis (Chapter 7).

MS quantification using lipid standards has showed that this problem was not due to the detection efficiency in MS. Such a low recovery of lipid extract potentially compromised the quantification results of the lipids, in particular the likely low-abundance cardiolipin in the cardiolipin-deficient mutant. Therefore the aim is to find the high-efficiency lipid extraction procedures for membrane protein C*c*O that are compatible with ESI MS and tandem MS analysis.

8.2.1 The need to remove detergent from membrane proteins for lipid analysis

Identification and quantification of lipids using ESI mass spectrometry has recently become more extensively applied to lipid mixtures extracted from tissues, cells, cellular organelles, lipid rafts and lipid-containing membrane proteins [229]. Surface-

active detergents are known to affect the mass spectrometric analysis of the lipids, peptides and proteins in a detrimental way by significantly suppressing their ionization efficiencies [85], probably due to their high tendency to ionize or form non-covalent adduct ions in both ESI and MALDI ionizations, although MALDI can generally be more tolerant of detergents than ESI, due to different ionization mechanisms (see Chapter 2 for a detailed description). Non-ionic detergents, such as the dodecyl maltoside (DDM) and the decyl maltoside (DM) applied in the C*c*O purifications (with molecular weights at 510 and 482 Da, respectively), are found to have the least detrimental effects [85]. In the MALDI analysis of the subunits that have molecular weights of several thousands, or several tens of thousands of Daltons, the detergents can improve the detection of these hydrophobic subunits by assisting with the dissociation from the rest of the proteins when applied at optimal concentrations (data not shown), but for the lipid analysis, which is the focus of the current study, these detergents strongly tend to form protonated or deprotonated ions and several types of adduct ions in the m/z range that overlaps with those of the common types of lipids, and significantly hampers the effective analysis of the lipids.

It is particularly challenging when the sample of interest is the few lipids maintained by the purified C*c*O, while the minimal detergent concentration that is required in the buffer in order to prevent the protein from precipitation and inactivation, is much higher than the lipids [75]. Therefore, in order to obtain accurate quantitative analysis of the lipids in the purified C*c*O enzymes, these detergents have to be removed at sufficient efficiency to make the samples amenable for mass spectrometry analysis.

8.2.2 The issue of incomplete extraction of lipids from membrane proteins

The quantification analysis of the lipid extracts from the purified C*c*O using mass spectrometry by incorporating appropriate lipid internal standards (Chapter 7) suggested that the lipid extracted from the purified protein C*c*O gives sub-stoichiometric ratios of phosphate/C*c*O, and it is much lower than the results from phosphate analysis of the purified C*c*O. All of these results suggest that the extraction methods that have been previously applied extensively in the lipid extraction from tissues, membrane pellets, and even membrane proteins [53,137,147], did not extract the lipids that remain bound to the purified membrane protein *CcO* at high yield.

Lipid extraction from purified membrane proteins is known to be much more difficult than from bulk tissue or membrane pellets [53], because the lipids that remain in the purified membrane proteins are more tightly bound to, or buried inside, the hydrophobic portion of the proteins. The extraction yield is often low, and requires additives such as salt to help remove the lipids through ionic pairing, and to prevent the proteins from denaturation and aggregation.

8.2.3 The variables that might affect the lipid extraction efficiency

The widely cited Bligh and Dyer extraction method was originally developed for lipid extraction from fish tissue that contains ~ 80% (m/m) water, and the extraction yield can reach above 90% [137-139]. The key point to such a high yield is the maximum contact between the solvent and the lipids in the tissue, which is achieved by suspending the sample in a mono-phase mixture of chloroform: methanol and water [137]. The Bligh and Dyer method has since then been applied extensively in all kinds of systems with slight modifications, and in most of the recent lipidomics analyses, the issue of extraction yield was typically not directly evaluated, but was bypassed by adding lipid internal standards to the tissues or cells prior to lipid extraction [111,140,141], assuming that the endogenous lipids will be extracted at the same efficiency as the spiked free lipids standards.

However, prior to the application of MS to lipid analysis, a series of papers had examined the effects of different extraction conditions and pre-extraction sample treatments on the efficiency of lipid extraction, and a number of variables have been reported to affect the extraction efficiency summarized as follows. Using lipid quantifications through ^{14}C-radioactive labeling [308], phosphate analysis [147], dry weight measurement [136-138] or ^{31}P-NMR analysis [89], several studies have found that the lipid extraction efficiency is highly dependent on the nature of the samples [89,147,309,310], such as the ratio of lipid to protein components, and the hydrophobicity of the samples, as well as several aspects of the operation conditions. More importantly, when it comes to samples that contain a high composition of membrane proteins, the maximum contact of the lipids with the solvent is not just a

matter of forming a mono-phase solution, but is significantly affected by the membrane proteins that many of the lipids are associated with. High extraction efficiency requires breaking the lipids free from the associations with other lipids and the hydrophobic proteins. The denaturation, aggregation, and the conformational changes in the folding of the membrane proteins, which are all very sensitive to the solvents, could significantly limit the solvent accessibility to the lipids and lead to a low lipid extraction efficiency.

1) Lipids/ membrane protein composition ratio. In the membrane-protein-rich bovine heart mitochondria, the lipid extraction efficiency is much lower than in the membrane protein-free phospholipid vesicles [147]. The extraction of lipids from purified membrane protein, however, would be considerably much more difficult, due to a tighter association, and a higher sensitivity, of the membrane protein to the extraction solvent. For example, cardiolipin associated with the bovine heart C*c*O has been shown to be difficult to extract, and needs the addition of ammonium hydroxide and several extraction steps [53].
2) Extraction temperature. Higher extraction temperatures (0 to 31 °C) lead to higher lipid extraction efficiency [147].
3) Counter ions. The extraction of charged lipids is often assisted by the addition of counter ions via forming neutral ion pairs or complexes. The addition of neutral salts [143,146], particularly the divalent salts, such as $CaCl_2$ and $MgCl_2$ (0-50 mM), are found to increase the phospholipid extraction efficiency from mitochondria, and the salt NaSCN can improve the extraction more efficiently than NaCl [147].

4) Solvent pH. The effect of solvent pH is variable depending on the samples [147]. The diluted acetic acid [311], HCl, or NH_4OH is often used to adjust the solvent pH in order to neutralize the charge states of the lipids and thus increase their solubility in hydrophobic solvents. However, some lipids [139] such as plasmalogens [117,132] that contain vinyl bonds are extremely sensitive to acidic pH and instantly decompose, and glyceride lipids, in general, tend to undergo hydrolysis in highly basic conditions [312].

5) Sample/ solvent size ratio. In general, a smaller sample size in a larger solvent volume can improve the extraction efficiency [138,149].

6) Polarity of solvent. Longer chain length in the alcohol solvent (C_1 to C_4) was found to have higher lipid extraction efficiency from mitochondria [147]. At individual optimal conditions, alcohols can reach over a 70% extraction efficiency from the mitochondria, but ethyl ether can only reach about a 30% extraction efficiency for the polar phospholipids [147]. Another complication is that a small portion of the mitochondrial proteins are soluble in the chloroform: methanol (2:1, v/v) extraction solvent of the Bligh and Dyer method [147]. In addition to the chloroform: methanol (2:1, v/v) solvent, chloroform: methanol (1:1, v/v), diethyl ether [146,309], hexane [148,310], benzene [308], i-propanol [309], t-butyl methyl ether [145], methanol only [89], and some other the nonhalogenated solvents (the Jenson method) [309] have also been applied in different systems, with comparable or slightly lower extraction efficiency [145,148,309,310]. While the chloroform: methanol solvent can efficiently extract most types of lipids [137], the ether and acetone solvents extract nonpolar lipids more efficiently

[147,308,313]. Lipid artifacts might also arise when the solvents are introduced to biological samples inappropriately, either through enzymatic action or chemical reaction, such as the generation of phosphatidylmethanol [314], and the formation of imine in plasmalogen by acetone [313].

7) Denaturing reagent. The addition of urea (0-6 M) generally decreases the extraction efficiency from mitochondria even in the presence of salt [147].

8) Lyophilization. The anti-denaturing lyophilization (freeze-drying) of mitochondria was shown to increase the lipid extraction efficiency [147]. Lyophilization of several other systems, such as brain tissue [315] , yeast cells [308] and oyster tissue [139], were also found to give a higher extraction efficiency than extracting from the aqueous solution. The contact of the membrane with chloroform: methanol: water solvent was found to instantly denature and destroy the activities of several membrane-associated proteins, whereas lipid extraction using anhydrous chloroform: methanol (or with less than 5% water, v/v) from the freeze-dried sample was found to maintain the enzymes' activities [315]. Removal of water is likely to weaken the hydrophilic interactions of the lipids with the proteins and other lipids and help release the lipids. However, drying using either heat or a vacuum was found to reduce extraction efficiency [139] or was less reliable [316]; therefore, it seems that the minimal degree of destruction to the protein structure by freeze-drying is the key reason.

9) Protein digestion. Digesting bovine heart mitochondria with pronase at 23 °C for 6 hours was found to appreciably increase the lipid extraction efficiency [147], probably by destructing the protein structures that associate with the lipids.

8.2.4 Approaches to improve the lipid extraction efficiency from C*c*O

Each individual membrane protein can be very different from another, and although some membrane proteins can be directly soluble in hydrophobic organic solvents, C*c*O instantly precipitates in chloroform and methanol, but it was found to be partially solubilized in the Bligh and Dyer mono-phase solvent mixture of chloroform, methanol and water, and form a light-green solution or fine suspension (data not shown). Nonetheless, the general variables that might affect lipid extraction from membrane proteins, summarized above, provide targets to address this issue. Some of the potential approaches, and general considerations to improve the lipid extraction efficiency from C*c*O are proposed in Table 8.1. Although only a few of these approaches were experimentally carried out in the current study, they can be helpful for further efforts in the future.

Table 8.1 Potential approaches to improve the lipid extraction efficiency from membrane proteins at different stages of lipid extraction.

detergent removal	
pre-extraction	• cold anhydrous acetone-washing following freeze-drying of C*c*O • dilution-filtration of C*c*O solutions with detergent-free buffer using filters with a molecular weight cutoff of 3 kDa • exchanging the DDM and DM detergents in the C*c*O solution into a cleavable detergent • adding biobeads to C*c*O solutions to absorb and remove the detergent
after extraction	• acetone-washing of dried lipid extract
extraction efficiency	
extraction	• freeze-drying of C*c*O prior to extraction • enzymatic digestion of C*c*O prior to extraction • keeping C*c*O in detergent during extraction • extraction solvent • ammonium hydroxide (ammonium cation, pH) • salt (cations to pair with anionic lipids) • extraction solvent volume

8.3 Results and discussions

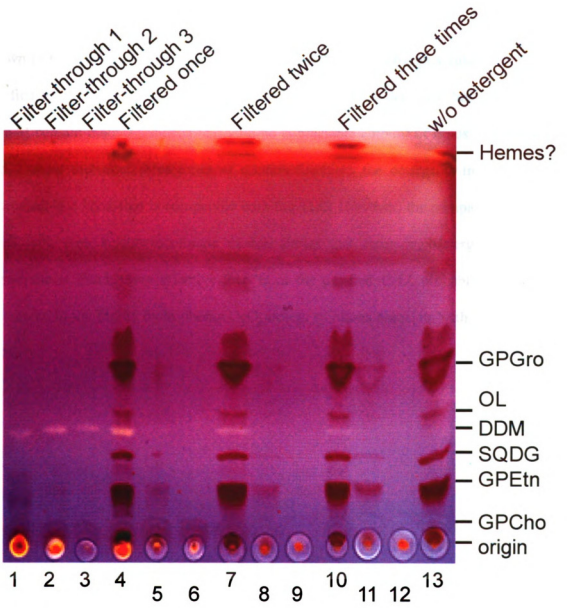
8.3.1 Evaluation of the efficiency of detergent removal methods

The presence of detergent affects the migration positions of lipids in thin-layer chromatography (TLC), but to a much less extent than it affects mass spectrometry analysis, thus, TLC was employed here to evaluate the efficiency of detergent removal using different methods.

8.3.1.1 Detergent removal by a dilution-filtration method

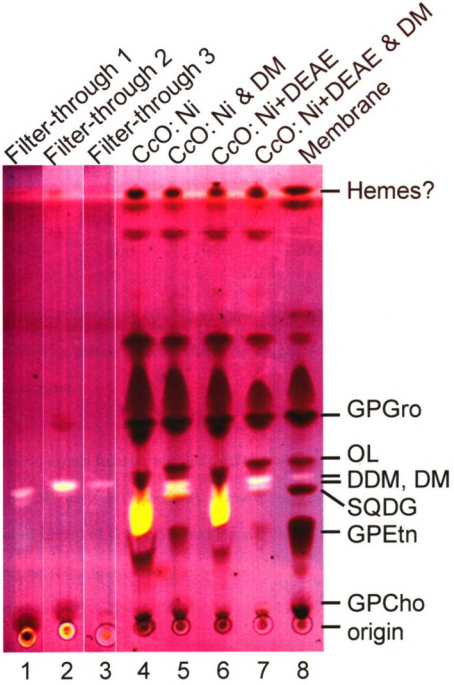
The dilution-filtration method is essentially using a detergent-free buffer to dilute the enzyme solutions that contain DDM or DM detergent, followed by using a small molecular weight cutoff filter to remove the free detergents by centrifugation. The dilution-filtration method for detergent removal was tested at first by using the membrane suspension, diluted in the detergent-containing buffer, as the model for the C*c*O enzyme solution (Figure 8.1). The samples were all freeze-dried prior to lipid extraction using chloroform: methanol or chloroform: methanol: ammonium hydroxide (see Chapter 2 for a detailed description). The first three lanes in Figure 8.1 show that the filter-through solution contains mainly the detergents, but most of the lipids are not lost. Lanes 4, 7 and 10 show that increasingly more detergents are removed from the model sample with the increase in the dilution-filtration steps. Lanes 10 and 11 show that after three cycles of dilution-filtration, most of the detergents are removed from the sample. Lanes 4, 5, and 6 shows that the first lipid extraction can get most of the lipids out, and the third time of extraction contains very few lipids, therefore extracting the lipids twice would be sufficient.

Figure 8.1 The efficiency of detergent removal by the dilution-filtration method (3 kDa molecular weight cutoff) from the detergent-containing membrane samples, displayed by thin layer chromatography (TLC) of the lipids, extracted from the resuspended membranes (8.7μL, 1.25 mg of total membrane proteins determined by BCA assay) of *R. sphaeroides* 169Δ4 strain, diluted with 104 μL of the FPLC buffer containing 0.05% DDM. Lanes 1, 2 and 3 are the first time, second time, and third time filter-through solutions, respectively; lanes 4, 5 and 6 are the first, second and third time lipid extracts from the enzymes, respectively, following one dilution-filtration step; lanes 7, 8 and 9 are the first, second and third time lipid extracts from the enzymes, respectively, following twice of the dilution-filtration step; lanes10, 11 and 12 are the first, second and third time lipid extracts from the enzymes, respectively, following three repeats of the dilution-filtration steps; lane 7 is the lipid extracted from the detergent-free membrane, for comparison. The silica gel TLC plate is treated with $(NH_4)_2SO_4$, developed by using acetone: toluene: water (91:30:7, v/v/v), and visualized by iodine vapor strain. Cardiolipin is not resolved using these conditions. The bright bands are the detergents.


Filter-through 1
Filter-through 2
Filter-through 3
Filtered once
Filtered twice
Filtered three times
w/o detergent
Hemes?
GPGro
OL
DDM
SQDG
GPEtn
GPCho
origin
1 2 3 4 5 6 7 8 9 10 11 12 13

The same dilution-filtration procedures were applied on the purified C*c*O solutions (wild type C*c*O from 169Δ4 strain, purified by FPLC), and the results are shown in Figure 8.2. Lanes 1 through 3 show that the filter-through solutions from C*c*O purified by a Ni-NTA column and exchanged into the DM detergent buffer (shown in lane 5) contain mainly the detergent with no appreciable amount of lipids. Lanes 4, 5, 6 and 7 show that after three times of dilution-filtration, the detergents in C*c*O can be decreased to a level that is compatible with the TLC. However, the comparison of these lanes with lane 8, the membrane model, shows that removing detergent from the membrane is much more effective than from the purified C*c*O, probably because the detergents in the highly hydrophobic C*c*O protein solutions associate with proteins more strongly.

Figure 8.2 The efficiency of detergent removal by the dilution-filtration method (3 kDa molecular weight cutoff) from the purified C*c*O enzymes is displayed using TLC of the lipids extracted from the purified C*c*O enzymes from the *R. sphaeroides* 169Δ4 strain, in buffers containing 0.05% DDM or 0.2% DM. Lanes 1, 2 and 3 are the first time, second time, and third time filter-through solutions, respectively; lanes 4 and 5 are the lipids extracted from C*c*O after Ni-NTA FPLC purification and concentration in DDM buffer, without and with exchange into the DM buffer, respectively; lanes 6 and 7 are the lipids extracted from C*c*O after Ni-NTA and a DEAE two-step FPLC purification and concentration in DDM buffer, without and with exchange into the DM buffer, respectively; lane 7 is the lipid extracted from the DDM detergent-containing membrane, for comparison. All the samples were treated by dilution-filtration three times and extracted twice. The silica gel TLC plate is treated with $(NH_4)_2SO_4$, developed by using acetone: toluene: water (91:30:7, v/v/v), and visualized by iodine vapor strain. Cardiolipin is not resolved using these conditions. The bright bands are the detergents.


Filter-through 1
Filter-through 2
Filter-through 3
CcO: Ni
CcO: Ni & DM
CcO: Ni+DEAE
CcO: Ni+DEAE & DM
Membrane
Hemes?
GPGro
OL
DDM, DM
SQDG
GPEtn
GPCho
origin
1 2 3 4 5 6 7 8

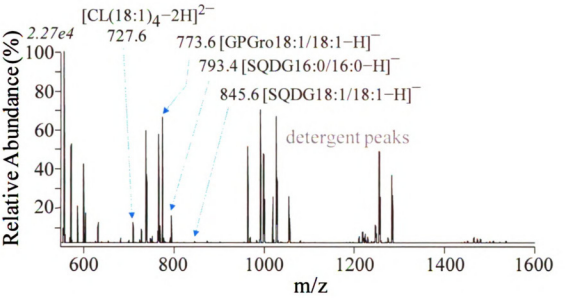


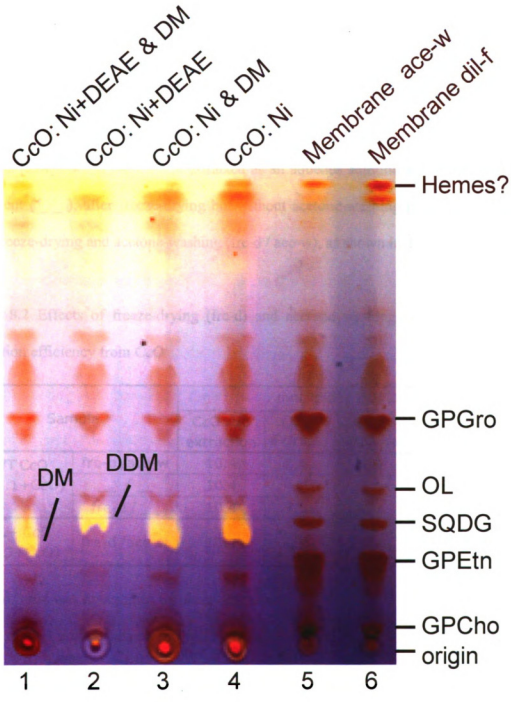
Figure 8.3 Negative ion mode ESI MS of lipids extracted from wild type C*c*O enzyme purified by Ni-NTA gravity column, after three cycles of the dilution-filtration steps to remove the detergent.

The lipid extract from the purified C*c*O after dilution-filtration treatment was then applied to ESI MS analysis (Figure 8.3). Figure 8.3 shows the ESI MS spectrum of the lipid extract of C*c*O (FPLC Ni-NTA purified and DM exchanged) after three cycles of dilution-filtering steps to remove the detergent. Although still present, the detergent peaks were significantly reduced, and the lipid peaks could be clearly observable in MS. It demonstrates that three cycles of dilution-filtration using a 3 kDa molecular weight cutoff filter can remove a significant amount of the detergents, and it is sufficient to obtain a practically useful spectrum using an ESI source.

8.3.1.2 Acetone-washing method to remove detergent

Membrane lipids are shown to have very low solubility in cold anhydrous acetone [225], but the non-ionic dodecyl maltoside and decyl maltoside detergents can be relatively more soluble, therefore anhydrous acetone washing of freeze-dried C*c*O enzyme under 4 °C was carried out to remove the detergent without losing the lipids [225]. Figure 8.4 shows the efficiency of detergent removal from purified C*c*O in the DDM and DM containing buffers using this approach. After three rounds of acetone-washing, the detergent was significantly reduced, but still showed a strong band in the TLC (the bright yellow bands are the detergent, the upper one is DDM and the lower one is DM). Again, the detergent removal from the membrane, suspended in the same detergent containing buffer, is much more efficient, and barely any detergent can be detected in the TLC (lane 5). This demonstrates that this method can remove detergent from purified C*c*O, but more importantly, it again reemphasizes the fact that the membrane proteins associate strongly with the lipids and the detergents, instead of having them loosely hanging around. Compared to Figure 8.3, the acetone-washing applied here was slightly less effective in detergent removal than the dilution-filtration method. The final lipid extract was also analyzed by ESI MS (data not shown), and lipid ions can be observed.

Figure 8.4 The efficiency of detergent removal by the acetone-washing method from the purified C*c*O enzymes, displayed by TLC of the lipids extracted from 0.68 μg purified C*c*O enzymes from the *R. sphaeroides* 169Δ4 strain. Lanes 1 and 2 are the lipids extracted from C*c*O after Ni-NTA FPLC purification and concentration in DDM buffer, without and with exchange into the DM buffer, respectively, after three acetone-washing steps to remove detergent; lanes 3 and 4 are the lipids extracted from C*c*O after Ni-NTA and DEAE two-step FPLC purification and concentration in DDM buffer, without and with exchange into the DM buffer, respectively, after acetone washing; lanes 5 and 6 are the lipid extracted from the DDM detergent-containing membrane after detergent removal using acetone-washing (ace-w) and dilution-filtration (dil-f), respectively, for comparison. All the samples were subjected to dilution-filtration three times and extracted twice. The silica gel TLC plate is treated with $(NH_4)_2SO_4$, developed by using acetone: toluene: water (91:30:7, v/v/v), and visualized by an iodine vapor stain. Cardiolipin is not resolved using these conditions. The bright bands are the detergents.


CcO: Ni+DEAE & DM
CcO: Ni+DEAE
CcO: Ni & DM
CcO: Ni
Membrane ace-w
Membrane dil-f
Hemes?
GPGro
DM
DDM
OL
SQDG
GPEtn
GPCho
origin
1
2
3
4
5
6

8.3.2 What affects the extraction of lipids from membrane protein C*c*O

The lyophilization (freeze-drying) of C*c*O and the acetone-washing of the dried C*c*O were the two major steps of sample treatment applied prior to lipid extraction in order to remove detergent; how each affects the extraction efficiency was thereby examined by comparing the phospholipid extraction efficiency (measured by phosphate analysis [224]), when the C*c*O is extracted as an aqueous solution with neither of these treatment (_/_), after freeze-drying but without acetone-washing (fre-d /_), and after both freeze-drying and acetone-washing (fre-d / ace-w), as shown in Table 8.2.

Table 8.2 Effects of freeze-drying (fre-d) and acetone washing (ace-w) on the lipid extraction efficiency from C*c*O

Sample		mol lipid*/ mol CcO**			
		CcO w/o extraction	lipid extract	CcO after extraction	**% extraction efficiency**
WT CcO (2.4.1+CcO)	fre-d /ace-w	10.4	2.4	0.9	**22.7%**
	__ / __	10.4	4.7	1.5	**43.2%**
	fre-d / __	10.4	7.1	2.1	**68.0%**
CL– CcO (CL3+CcO)	fre-d /ace-w	10.1	2.1	4.1	**21.1%**

* mol of lipid was determined by phosphorus assay [224].

**mol of C*c*O protein was determined by UV-Vis spectroscopy.

The results in Table 8.2 shows that the extraction efficiency from the acetone-washed C*c*O is the lowest at 23%, and it consistent with the results revealed by absolute lipid quantification using MS in Chapter 7, that from the wet enzyme is 43%, but it was increased by over 0.5 fold by lyophilization prior to the extraction and reached 68%.

8.3.2.1 Lyophilization of C*c*O prior to extraction

The lyophilization (freeze-drying) step of C*c*O samples was initially applied because the acetone-washing step requires anhydrous conditions to prevent loss of lipids, but a second consideration is that lyophilization would introduce the least degree of destructive conformational changes in C*c*O during solvent removal, which seems to be the case, and is demonstrated to improve the extraction efficiency from 43% for wet C*c*O, to 68% (Table 8.2).

The beneficial effect of lyophilization for lipid extraction efficiency has been observed in a few earlier applications, although not as significant as in the current case. An earlier study that examined the lipid extraction from yeast using methanol quantified by ^{14}C-labelling, also found that the extraction efficiency follows the order of freeze-dried cells> wet cells>acetone washed-dried cells [308]. chloroform: methanol (2:1, v/v) extraction of the freeze-dried brain tissue also has a higher lipid extraction yield than extracting the tissue using aqueous solution, and the proteins are often more stable to anhydrous organic solutions, and chloroform: methanol mixture acts as a strong denaturant for proteins only in the presence of water [315]. The rationale is that the non-aqueous extraction maintains the membrane protein activities and structure, and is therefore less denaturing than the chloroform: methanol: water aqueous solution [315].

Why does freeze-drying improve lipid extraction efficiency from mitochondria and brain? First of all, denaturation of the protein limits the contact of solvents with lipids, and hence decreases the extraction efficiency, but the freeze-drying can remove the water without significantly destroying the structure of the protein or causing

denaturation. Second, the removal of water eliminated the hydrophilic interactions between lipid and proteins, and other lipids.

These results suggest that, in contrast to the lipid extraction from bulk membranes and cells, in the extraction of lipids from membrane proteins or membrane protein-rich samples, the mono-phase solvent is not the only consideration to maximize the solvent contact with lipids. Protein denaturation and partial aggregation is a major reason that limits the extraction efficiency of lipids from the membrane protein C*c*O. Therefore, strategies should be developed to target the proteins and their associations with the lipids.

Extracting lipids while keeping the C*c*O in a native, or close-to-native, state might then improve the extraction efficiency. Detergent is often required by *R. sphaeroides* C*c*O to maintain its proper conformation and prevent aggregation, but the DDM and DM detergents interfere with mass spectrometry analysis. Therefore, a detergent that can be cleaved into less interfering pieces can potentially be applied during the extraction, and cleaved and removed after lipid extraction. Preventing, or minimizing the protein from denaturation in organic solution during extraction, by freeze-drying C*c*O and using anhydrous solvent is here proven to work.

8.3.2.2 Acetone washing of C*c*O prior to extraction

Acetone washing of the membrane protein C*c*O prior to lipid extraction is repeatedly shown to be detrimental to the extraction and gives the lowest lipid extraction efficiency at around 20-25% from both the wild type (2.4.1+C*c*O) and the cardiolipin-deficient (CL3+C*c*O) strains (Table 8.2), probably by causing severe denaturation of the

protein. In fact, acetone is a frequently used as the reagent to aggregate and precipitate proteins in proteomic experiments.

8.3.2.3 Partial digestion of C*c*O to assist with the lipid release during extraction

Digesting the proteins into smaller pieces can also potentially reduce the binding of lipids [147], and hence makes them more accessible to solvents. Initially the purified C*c*O was treated with trypsin digestion under 37 °C for 24 hours, but in this trial no peptides were detected in the final solution, using the linear ion trap mass spectrometer (m/z range 50-2000), and the protein was found to precipitate throughout the procedure. Therefore, the digestion conditions need to be further optimized. The effective digestion of a membrane protein often requires that it be more or less soluble and not aggregated, but the prevention of aggregation often requires the detergent to be present at a sufficiently high concentration [75]. Novel types of detergent that can improve the membrane protein digestion, and are compatible with peptide analysis, have become recently available and can potentially help to address this issue.

8.3.2.4 Addition of acid or base in the extraction solvent

Addition of acid or base is used to adjust the pH and act as ion pairs, although the buffer of C*c*O already has sufficiently high concentrations of salt. Ammonium hydroxide has been routinely included in the extraction methods employed throughout the current study, because previous reports showed that it can help with the extraction of cardiolipin [53]. Here, it was found to be able to slightly improve the overall extraction of all the major types of phospholipids, at the concentration of chloroform: methanol: 28% (m/v)

ammonium hydroxide (65:33:3, v/v/v) (data not shown). Also tested was replacement of the ammonium hydroxide with volatile acetic acid at concentrations from 125 mM to 500 mM under extraction temperatures of 4 °C or 20 °C, in triplicate, and no significant change in the overall phospholipid extraction efficiency was observed (data not shown).

8.3.2.5 Urea treatment of C*c*O

While acetone causes proteins to aggregate and precipitate, urea is a strong denaturing reagent that can keep the protein unfolded, so it should affect the C*c*O lipid extraction. In initial attempts, the addition of 6 M urea to the C*c*O after the acetone-washing step seemed to bring the extraction efficiency back up (data not shown), but more repeats would be needed in order to draw any meaningful conclusions.

8.3.2.6 Usage of cleavable detergent for detergent removal

A type of cleavable detergent made by the Anatrace company can be degraded into products that have a much smaller molecular weight through hydrolysis of a Schiff base functional group, under mild reaction conditions. Therefore, substituting the original DDM or DM detergent in the C*c*O buffer into this type of detergent, performing the lipid extraction, and then degrading the detergent contained in the lipid extracts, might be one approach to remove the interference of the maltoside detergent for the mass spectrometric analysis of the lipid extracts. However, this type of detergent was found to cause instant precipitation of C*c*O upon contact, probably due to the positively charged amino head group in the detergent. On the other hand, because of the positively charged amino group, in mass spectrometry, this detergent is the predominant ion species, even at the minimal

concentration required to solubilize membrane proteins, and it significantly suppressed the ionization of any other species, including lipids, and even the non-ionic maltoside detergents. The product ion carries the same head amino group, and is expected to cause similarly serious ionization suppression problems. Nonetheless, the strategy of using detergent during extraction, and removal after extraction, is promising.

8.3.3 Future directions

All of the experiments performed in this chapter were attempts to remove detergent prior to the lipid extraction, which almost inevitably causes denaturation of C*c*O, and decreases the efficiency of the following lipid extraction. The other approach is to extract the lipids with the detergent, and later separate the detergents from the lipid extract. In fact, liquid chromatography has been reported to be the only method currently available to effectively remove detergent from the lipid extracts of systems such as detergent-resistant microdomains, to make it amenable for mass spectrometric analysis.

8.4 Conclusions

Detergent removal and extraction efficiency are the two key issues in the application of quantitative lipid analysis of membrane proteins by mass spectrometry. By using the more detergent-tolerant method of TLC, the efficiency of detergent removal methods including the previously applied cold anhydrous acetone-washing, and a new dilution-filtration method were examined, and the results showed that both can bring the detergent in the extract down to a level that is amenable to the ESI ion source. However,

the acetone-washing step was found to severely decrease lipid extraction efficiency (20-25%), probably by denaturing and aggregating C*c*O proteins. On the other hand, freezing-drying of C*c*O prior to lipid extraction can improve the efficiency to 68%, probably by mainly preventing protein from aggregation. Initial experimental results, using other potential approaches to address both issues, have also been discussed.

While the traditional Bligh and Dyer based extraction methods [137], which were developed for lipid-abundant cells and tissues, emphasize the formation of a mono-phase extraction solvent to maximize lipid-solvent contact, the accessibility of solvent to lipids in the membrane protein lipid extraction seems to be more affected by the folding state of the membrane proteins. The promising solutions to improve lipid extraction efficiency should probably target on keeping the membrane protein from denaturation and aggregation during lipid extraction.

Chapter 9

Crystallization of Cytochrome *c* Oxidase Produced in a Cardiolipin-Deficient Mutant of *Rhodobacter sphaeroides* and its Lipid Profile Characterization [§]

9.1 Summary

The lipid environment of membrane proteins is critical for their function *in vivo*, and many studies indicate a role for lipids in their structure, function and assembly. High resolution crystals of membrane proteins further reveals specifically bound lipids, leading to the hypothesis that the proper lipid environment may be important for well-ordered crystal formation. To test a proposed requirement for cardiolipin in the function and crystallization of cytochrome *c* oxidase, a cardiolipin-deficient mutant of *Rhodobacter sphaeroides* was constructed. The cardiolipin synthase (*cls*) gene of *R. sphaeroides* was identified and disrupted, causing a greater than 90% reduction in cardiolipin content. The cytochrome *c* oxidase produced in the mutant strain was active, and analysis of its spectral characteristics and crystallized form indicated a normal assembly of the protein complex. Cardiolipin levels were similarly reduced in the membranes and in cytochrome *c* oxidase crystals derived from the cardiolipin-deficient mutant, as determined by mass

§ Part of the contents described in this chapter was prepared in the manuscript entitled "Cytochrome *c* Oxidase Produced in a Cardiolipin-Deficient Mutant of *Rhodobacter sphaeroides* is Fully Functional and Crystallizable" by Banita Tamot, Xi Zhang, Carrie Hiser, Gavin E. Reid, Shelagh Ferguson-Miller and Christoph Benning.

spectrometry. These data indicate that an altered lipid environment that includes very low cardiolipin levels does not impact cytochrome *c* oxidase function or its crystallizability.

9.2 Introduction

9.2.1 Why the focus of interest on CL in C*c*O

Lipid molecules are resolved in crystal structures of many membrane proteins, implying a significant role in protein structure and function. In fact, it has been shown that specific lipids are required for correct folding and assembly of some membrane proteins, such as the plant light harvesting complex [317] and the bacterial lactose permease [318-320]. Other studies on bovine and yeast cytochrome bc_1, bovine cytochrome *c* oxidase, and bacterial KcsA K^+ channel, indicate a requirement for specific lipids for full activity [52-54,321]. In some cases, complete removal of the bound lipid was found to abolish protein function, an effect that is reversible by adding back lipids [54,55,322]. In addition to their influence on assembly and function, bound lipids also stabilize the protein structure [73]. Since structural stability is a crucial factor for membrane protein crystallization, retention of lipid molecules during the purification steps has been emphasized for successful protein crystallization [6,35]. Supporting evidence for the role of lipids in the crystallization of membrane proteins includes the observation that the quality of *E. coli* lactose permease crystals can be controlled by changing the phospholipid levels [323]. A similar observation was made regarding the crystallization behavior of the cytochrome b_6f complex, in which the addition of lipids improved the crystallizability of the protein [73]. Such efforts, to obtain high resolution

structures of membrane proteins, have led to the need for closer scrutiny of the role of protein-associated lipid molecules.

Cytochrome *c* oxidase (C*c*O) has served as a model system for studying the involvement of lipid in membrane protein structure and function [324,325] because of its spectrally-accessible metal centers, which provide sensitive intrinsic probes for monitoring structural integrity as well as activity. As the terminal enzyme of the respiratory electron transport chain, C*c*O transfers electrons from cytochrome *c* to oxygen and acts as a proton pump [25,326]. Understanding the molecular mechanism of electron transfer and proton pumping requires developing reproducible methods for obtaining high resolution structures of the wild-type and mutant forms of C*c*O, including those from *R. sphaeroides*, a model system for the mammalian mitochondrial enzyme [33]. A number of lipid molecules co-purify with C*c*O from *R. sphaeroides* [34,35,37] and the lipid binding sites in the core subunits of C*c*O are highly conserved from bacteria to mammals, emphasizing the importance of lipids in the protein structure.

Cardiolipin (CL) is one lipid whose requirement has been established by biochemical studies in the function of several membrane proteins from bacterial and mitochondrial sources [1,53,54,327]. However, the molecular basis of its function in C*c*O is not understood. Although cardiolipin is found to be involved in the respiratory chain complexes, particularly C*c*O, in both bacterial and eukaryotic systems, the last step of cardiolipin biosynthesis from GPGro, and the following remodeling reactions, are totally different between the two systems [7,8,61], and the final composition of the cardiolipin molecular species are also very different. Therefore, it is conceivable that the mechanism

through which cardiolipin exerts its functional effects might be different as well, between the bacterial and mammalian systems.

Due to its unique structure, composed of two phosphates and one glycerol in the head group and four hydrophobic fatty acid chains, cardiolipin can bind to membrane proteins more tenaciously than lipids with two alkyl chains. It is perceived to act as a "super glue" to help maintain the integrity of multi-protein super-complexes [65,66]. Beyond that, cardiolipin has also been found to be specifically essential for the full activity of mammalian heart C*c*O [54,68]. In mammalian cells, cardiolipin can get peroxidized at its double bonds and form a complex with cytochrome *c*, which then triggers the release of cytochrome *c* from mitochondria under stress stimuli, leading to cell apoptosis [8,67-69]. Further investigation of the cardiolipin molecular species involved in various processes revealed that healthy mammalian systems mainly contain cardiolipin with unsaturated 18:2 chains, particularly $CL(18:2)_4$ [8,68,70]. Although CL containing 18:1 and 16:0, the dominant species in bacteria, are also found at much lower abundances [70], the critical roles of cardiolipin seem to reside in the unsaturated $CL(18:2)_4$ species through potential oxidation of its double bonds. A decreased fraction of $CL(18:2)_4$ leads to decreased activity of C*c*O down to about 40%, and causes mitochondrial dysfunction [68]. When adding back cardiolipins, $CL(18:2)_4$ is more effective in stimulating C*c*O than other cardiolipin species [60]. However, $CL(18:2)_4$ is not produced directly from the biosynthesis of lipids in mammalian cells, but is formed through the modification by acyltransferases of the initial cardiolipin species [8]. Interestingly, mutations affecting the assembly, but not the catalytic functions of C*c*O,

were found to decrease the biosynthesis of cardiolipin down to 50% to 60%, whereas mutations in complex III or complex V, the ATPase, did not display such effects on cardiolipin synthesis [62].

In stark contrast, *R. sphaeroides* was found to make mainly $CL(18:1)_4$, but no detectable levels of $CL(18:2)_4$, even when grown under aerobic conditions and survive via the respiratory chain complexes (Chapter 7). Likewise, yeasts predominantly produce cardiolipin containing 16:1 and 18:1 fatty acyl chains but not 18:2 [20] . Several studies, using genetic mutagenesis in bacterial and yeast systems, found that the deficiency in cardiolipin did not significantly affect the activity of C*c*O, nor did it alone cause the dysfunction of mitochondria in yeast [23,71,328], but the double deficiency in GPGro and CL resulted in very little C*c*O production and severely dysfunctional mitochondria [23], suggesting CL is not essential for C*c*O or mitochondria in yeast, but is functionally replaceable by GPGro lipids.

To test the role of CL in *R. sphaeroides* C*c*O, C*c*O was expressed in a CL-deficient mutant by the disruption of the *cls* gene encoding the enzyme CL synthase, which had been constructed earlier [15], and acetate ^{14}C-labeling revealed that the level of CL in the mutant was reduced to less than 10% of the wild type [15].

9.2.2 Effect of CL deficiency on *R. sphaeroides* cell growth

To analyze the effect of the decreased CL on the overall growth of *R. sphaeroides* cells, the photosynthetic and respiratory growth of the wild type and the mutant was compared. Under the conditions used in this study, no significant differences were

observed in the photosynthetic growth for both lines (Figure 9.1A). However, respiratory growth was slightly reduced in the mutant, as indicated by the increased lag time and lower final cell density (Figure 9.1B). The results suggest that there is a requirement of CL for optimal respiratory growth.

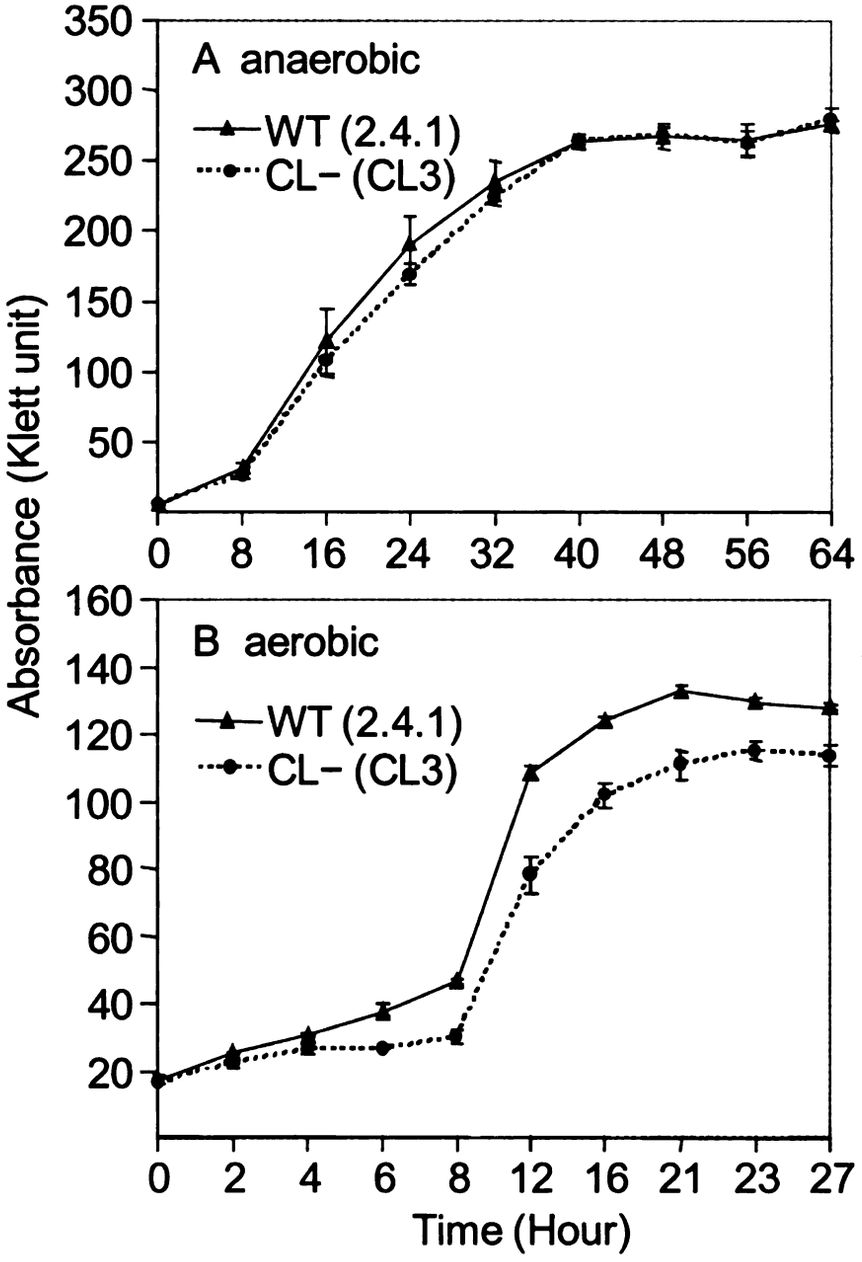


Figure 9.1 Growth curves of *R. sphaeroides* wild type (▲; WT; 2.4.1) and CL-deficient mutant (●; CL−; CL3, also called BC-m3) strains under A) anaerobic photoheterotrophic growth, and B) aerobic chemoheterotrophic growth conditions, both in Sistrom's media at 30 °C. The presented data are the average of three independent growth cultures and the error bars are the standard deviations (The experiments shown here were performed by Banita Tamot and Dr. Carrie Hiser).

9.2.3 Production of C*c*O in *R. sphaeroides* WT and CL− cells

The wild-type 2.4.1 strain of *R. sphaeroides* naturally produces a low level of C*c*O in its membranes when grown under aerobic conditions (Figure 9.2A). Since this strain has been used to produce a variety of lipid mutants [14,90,274], it was necessary to demonstrate that it was a suitable host for C*c*O overproduction, in order to provide a model system for testing the role of lipids in C*c*O activity. Optical difference spectra provide a facile method to calculate the concentration of C*c*O. In the difference spectrum of solubilized membrane proteins of the wild-type 2.4.1 strain (Figure 9.2A), the 606 nm peak, which indicates the presence of the *a*-type hemes of C*c*O, is small relative to the size of the 560 nm peak, which represents the level of *b*-type hemes of the bc_1 complex (complex III). After the C*c*O genes were introduced as part of the plasmid pRK-pYJ123H (2.4.1+C*c*O), the peak corresponding to the 606 nm peak strongly increased consistent with overproduction of C*c*O (Figure 9.2B). When this plasmid was introduced into the BC-m3 CL-deficient strain, the relative levels of C*c*O expression were variable depending on the culturing time and size of the culture (data not shown). High levels of C*c*O were produced in smaller cultures, while the levels of C*c*O were usually lower in larger cultures grown for longer times for the purposes of large-scale C*c*O protein production. This observation possibly indicates a greater sensitivity of the mutant to stress experienced during subculturing and dilution into larger flasks.

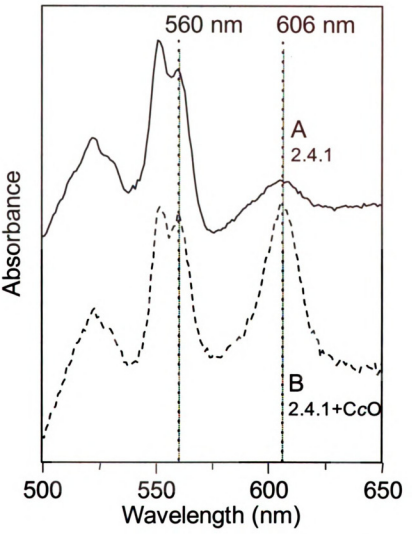


Figure 9.2 Optical difference spectra of dithionite-reduced minus ferricyanide-oxidized solubilized membranes from *R. sphaeroides* strains 2.4.1 (wild-type, graph A) and 2.4.1+C*c*O (with C*c*O plasmid pYJ123H, graph B), showing the levels of C*c*O (indicated by heme *a* peak at 606 nm) produced in *R. sphaeroides* 2.4.1 strains without C*c*O genes added on a plasmid. The spectra are normalized to the 560 nm (heme *b*) peak. The experiments shown here were performed by Dr. Carrie Hiser.

9.

9.2.4 Properties of C*c*O purified from wild type and *cls* mutant cell lines

Table 9.1 shows the spectral properties and enzymatic activities of C*c*O protein purified from four *R. sphaeroides* cell lines overproducing a subunit I-histidine-tagged wild-type version of C*c*O. The Soret and alpha bands in the optical (reduced-only) spectra are diagnostic for the native state and the amount of the heme centers of C*c*O. The positions of these maxima from the CL–deficient mutant cell line (BC-m3+C*c*O) and the CL-proficient control (2.4.1+C*c*O) were the same, indicating that the absence of the *cls* gene in BC-m3+C*c*O did not impair its ability to correctly assemble and insert the metal centers into C*c*O. Addition of a copy of the *cls* gene on a plasmid to either the mutant cell line (to create BC-m3+C*c*O+*cls*) or the control cell line (to create 2.4.1+C*c*O+*cls*) did not alter the difference spectra maxima of the purified enzymes.

The enzymatic activities of C*c*O purified from BC-m3+C*c*O and 2.4.1+C*c*O were also very similar, indicating that the enzyme purified from the CL-deficient mutant cells is as active as that purified from the control cells. The activities of the C*c*O proteins from the two cell lines with the *cls* gene added back were similar to each other, but slightly higher than the activities from the two lines without the added *cls* gene. The activities of all purified C*c*Os increased in the presence of externally-added lipids. This commonly observed phenomenon was somewhat variable and is generally related to the extent of delipidation of C*c*O during the purification process [33]. The percent increases with added lipids were similar for C*c*O from all cell lines.

Table 9.1 Spectral and enzymatic properties of CcO purified from *R. sphaeroides* wild-type and BC-m3 (also called CL3) cell lines ‡.

Cell Line	Genotype	Spectral Properties of Purified CcO (nm)	(nm)	Activity without Added Lipids (s^{-1})	Activity with Added Lipids (s^{-1})	Increase in Activity with Added Lipids
2.4.1+C*c*O	Wild Type	445	606	1050 ± 100#	1340 ± 50#	28 ± 2%#
2.4.1+C*c*O+*cls*	Wild Type with *cls* Gene Added	445	606	1300 ± 40*	1640 ± 110*	27 ± 4%*
BC-m3+C*c*O	Δ*cls*	445	606	1060 ± 109@	1410 ± 120@	33 ± 8%@
BC-m3+C*c*O+*cls*	Δ*cls* with *cls* Gene Added	445	606	1240 ± 100#	1530 ± 160#	24 ± 4%#

‡ All strains produced His-tagged C*c*O from pYJ123H. The positions of the Soret and alpha peaks from the optical spectra of dithionite-reduced C*c*O are listed. The molecular activity of purified C*c*O at pH 6.5 is presented as turnover number (moles cytochrome *c* oxidized per mole C*c*O per second) in the absence or presence of externally-added lipids. The number of independent measurements was 2*, 3#, or 5@. (The experiments shown here were performed by Dr. Carrie Hiser).

9.3 Results

9.3.1 MALDI analysis of the membrane lipids expressing C*c*O

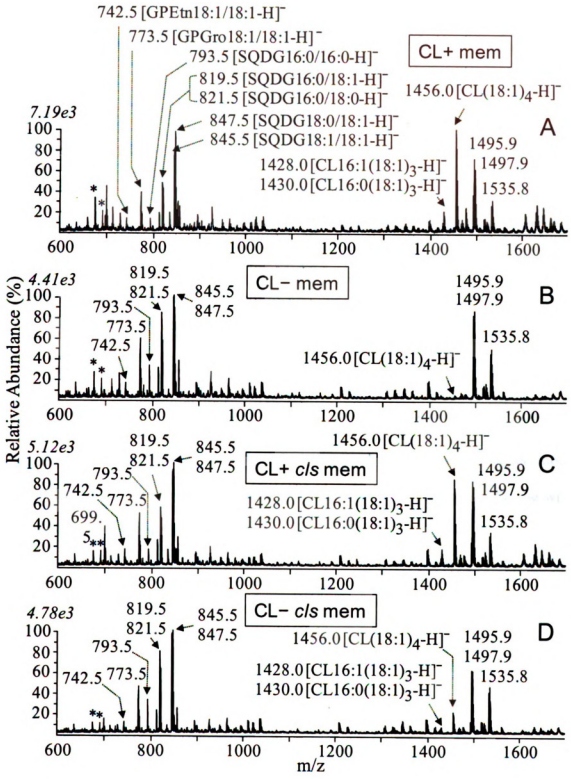
The negative ion mode MALDI MS spectra obtained by direct analysis of isolated membranes from the wild-type (2.4.1+C*c*O) and CL-deficient (BC-m3+C*c*O) strains of *R. sphaeroides* are shown in Figures 9.3A and 9.3B, respectively, and the MS spectra of the two with insertion of the CL synthase gene (2.4.1+C*c*O+cls and BC-m3+C*c*O+cls) are shown in Figures 9.3C and 9.3D, respectively. Note that while MALDI is not generally considered to be a rigorously quantitative method, due to issues associated with matrix/sample heterogeneity, when experiments on each sample are performed in parallel under identical sample handling and data acquisition conditions, with multiple replicates such as the experiments performed here, semi-quantitative information can be obtained. Similar lipids, including GPEtn, GPGro, SQDG, and CL, were observed in the isolated membranes of both strains (compare Figures 9.3A and 9.3B), albeit with different abundances. The major molecular species of lipids detected in these strains in negative ion mode MALDI MS include the phospholipids GPEtn 18:1/18:1 and GPGro 18:1/18:1, sulfolipids SQDG 16:0/16:0, SQDG 16:0/18:1, SQDG 16:0/18:0, SQDG 18:1/18:1 and SQDG 18:0/18:1, and cardiolipins $CL(18:1)_4$, $CL(16:1)_1(18:1)_3$, $CL(16:0)_1(18:1)_3$ and $CL(18:0)_1(18:1)_3$.

Notably, the relative abundance of CL in the CL-deficient mutant membrane was observed to be approximately 5% compared to the membrane sample from the CL-proficient strain, relative to the ion abundances of SQDG 18:1/18:1 and SQDG 18:0/18:1 lipids, the most abundant ions within the range of display. This is consistent with the

results obtained from radioisotope labeling data [15]. In contrast, the abundance of the GPGro 18:1/18:1, SQDG 16:0/18:1 and SQDG 16:0/18:0 lipid species appeared to increase in the *cls* mutant membrane. The identities of each of the membrane lipid species labeled in these figures were confirmed by tandem mass spectrometry (MS/MS) analysis (data not shown).

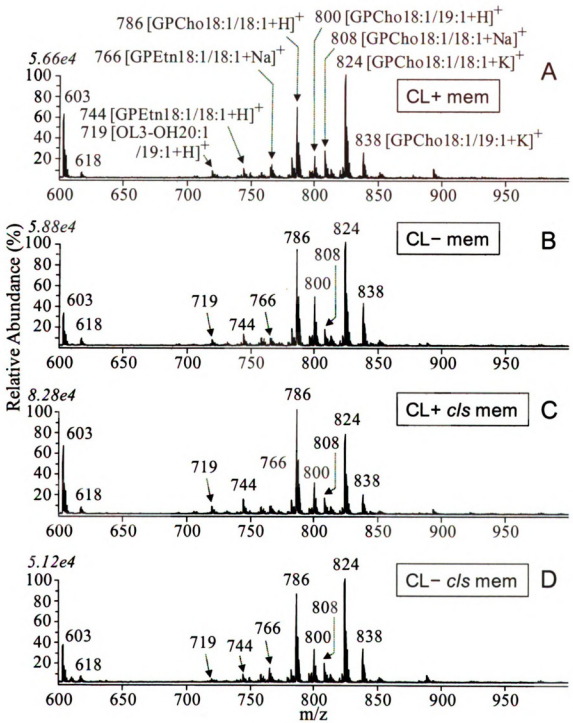
Figure 9.3C shows the mass spectrum of the wild type and *cls* mutant expressing C*c*O after insertion of the *cls* plasmid. As expected, the membrane lipid profile from the 2.4.1+C*c*O+*cls* strain shown in Figure 9.3C was very similar to that of 2.4.1+C*c*O shown in Figure 9.3A. Compared to Figure 9.3B, however, the addition of *cls* the CL-deficient mutant resulted in only a moderate increase in the CL abundance (Figure 9.3D).

Figure 9.3 Negative ion mode MALDI-MS spectra of isolated membranes from CL–proficient and CL-deficient *R. sphaeroides*. A) Wild type (2.4.1+C*c*O), B) CL-deficient mutant (BC-m3+C*c*O), C) Wild type with *cls* gene (2.4.1+C*c*O+*cls*) and D) CL-deficient mutant with *cls* gene (BC-m3+C*c*O+*cls*), each at 0.25 mg/mL membrane protein concentration. The identities of labeled ions in each spectrum were confirmed by MS/MS experiments. Ions labeled with asterisks were identified as 2,5-DHB matrix cluster adducts. All strains were produced from pYJ123H C*c*O.


742.5 [GPEtn18:1/18:1-H]⁻
773.5 [GPGro18:1/18:1-H]⁻
793.5 [SQDG16:0/16:0-H]⁻
819.5 [SQDG16:0/18:1-H]⁻
821.5 [SQDG16:0/18:0-H]⁻
847.5 [SQDG18:0/18:1-H]⁻
845.5 [SQDG18:1/18:1-H]⁻
1456.0 [CL(18:1)4-H]⁻
1428.0 [CL16:1(18:1)3-H]⁻
1430.0 [CL16:0(18:1)3-H]⁻
1495.9
1497.9
1535.8
CL+ mem
CL− mem
CL+ cls mem
CL− cls mem
A
B
C
D
7.19e3
4.41e3
5.12e3
4.78e3
Relative Abundance (%)
m/z

The positive ion mode MALDI MS spectra of the membranes of the wild-type (2.4.1+C*c*O) and CL-deficient (BC-m3+C*c*O) strains, and the strains with a *cls* insertion (2.4.1+C*c*O+*cls* and BC-m3+C*c*O+*cls*) of *R. sphaeroides* are shown in Figures 9.4. Abundant GPCho lipid species, as well as ornithine lipids (OL), and a novel type of glutamine lipids (QL) (Chapter 5), were observed. The positive ion mode MALDI MS mainly revealed GPCho lipids (GPCho 18:1/18:1, GPCho 18:1/19:1) and GPEtn lipids (GPEtn 18:1/18:1) as protonated ions and as non-covalent alkali adduct ions with sodium and potassium, and the lower-abundance ions of ornithine lipids (OL 3-OH 20:1/19:1) and glutamine lipids. Comparison of Figure 9.4A with Figure 9.4B suggested that the GPCho, GPEtn and ornithine lipids molecular species are not significantly affected by the *cls* mutation, either in molecular diversity or in relative quantity. A similar conclusion can be obtained after the *cls* gene insertion (Figures 9.4C and 9.4D). Note that, although not displayed in Figure 9.4, the cardiolipin $CL(18:1)_4$ can sometimes also be observed as singly positive-charged di-sodium adduct ions at m/z 1495.9 in the positive ion mode MALDI MS using 2,5-dihydroxyl benzoic acid (2, 5-DHB) as the matrix for the wild type (see Chapter 3 for a detailed description of methods).

Figure 9.4 Positive ion mode MALDI-MS spectra of isolated membranes from *R. sphaeroides* strains: A) wild type (2.4.1+C*c*O), B) CL-deficient mutant (BC-m3+C*c*O), C) wild type with *cls* gene insertion (2.4.1+C*c*O+*cls*) and D) CL-deficient mutant with *cls* gene insertion (BC-m3+C*c*O+*cls*), analyzed at 0.25 mg/mL protein concentration. All strains produce C*c*O from pYJ123H.


786 [GPCho18:1/18:1+H]+
800 [GPCho18:1/19:1+H]+
808 [GPCho18:1/18:1+Na]+
824 [GPCho18:1/18:1+K]+
766 [GPEtn18:1/18:1+Na]+
744 [GPEtn18:1/18:1+H]+
719 [OL3-OH20:1 /19:1+H]+
838 [GPCho18:1/19:1+K]+
5.66e4
CL+ mem
A
5.88e4
CL− mem
B
8.28e4
CL+ cls mem
C
5.12e4
CL− cls mem
D
Relative Abundance (%)
m/z

9.3.2 Purification and crystallization of C*c*O from *cls* mutant and wild type

Like the BC-m3+C*c*O (also called CL3+C*c*O) strain described earlier, the C*c*O prepared from the cardiolipin-deficient strain 169CL3 (with a genome containing wild type cox I, II, III and IV, and the deletion of *cls*, and a plasmid containing wild type cox I and III, histidine-tagged cox II and short cox IV), which is specially designed for crystallization, is also expressed at high yield, and the C*c*O purified by using the FPLC with Ni-NTA columns had UV-Vis spectral characteristics that closely resemble those of the wild type (Figure 9.5).

The purified C*c*Os all contain four subunits (I, II III and IV) as revealed by MALDI-TOF MS and SDS-PAGE analyses (see Chapter 10 for the SDS-PAGE of the purified 169-2.4.1 and 169CL3 C*c*Os; other data not shown). The relative expression levels of C*c*O, measured by UV-Vis spectroscopy, compared to the total membrane proteins measured by the BCA assay (see Chapter 3 for a detailed description of the methods) consistently indicated a higher level in the CL-deficient mutant than in the wild type, using the large-culture-volume growths, but seemed to be variable in small-culture growths. The FPLC-purified from cardiolipin-containing strains, 169WT and 169-2.4.1 C*c*Os (see Table 3.1 in Chapter 3 for detailed descriptions of the strains), were analyzed by phosphate analysis and found to contain 7-8 phosphates per molecule of C*c*O, and the purified cardiolipin-deficient 169CL3 C*c*O contained about 6-7 phosphates per C*c*O (Chapter 7).

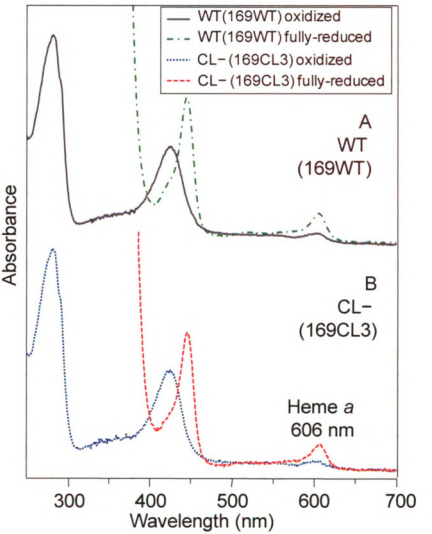


Figure 9.5 Oxidized and reduced spectra of FPLC-purified C*c*O from A) 169WT (WT) and B) 169CL3 (CL−) strains grown aerobically at 30 °C.

Using C*c*O purified from cardiolipin-containing (169WT and 169-2.4.1) strains and *cls* mutant (169CL3) strains, both four-subunit C*c*O crystals and two-subunit C*c*O crystals (subunit I and II) were obtained under the same range of crystallization conditions, as indicated by the X-ray crystallography analysis. Furthermore, the resolution obtained for the four-subunit C*c*O crystals from the CL-deficient mutant was

similar to that of four-subunit crystals (3.2 Å) from the CL-proficient strain (Table 9.2), based on dozens of purification repeats of the wild type and the mutant grown in parallel over two years' efforts. Thus, the strongly decreased levels of CL observed in the membrane lipid profile did not prevent the crystallization of four-subunit or two-subunit C*c*O. The four-subunit C*c*O crystals generated from 169WT and 169CL3 were further redissolved/resuspended and examined by MALDI analysis.

Table 9.2 Crystallography screening results of C*c*O crystals obtained from C*c*O expressed in the *R. sphaeroides* wild type (CL+) (169WT and 169-2.4.1) and c*ls* mutant (CL−) (169CL3) at different crystal growth temperatures.

C*c*O crystal resolution	4-subunit 4 °C	2-subunit (I and II) 20 °C
169WT (CL+)	3.4 Å	n/a
169-2.4.1 (CL+)	3.3 Å	2.9 Å
169CL3 (CL−)	3.2 Å	3.3 Å

9.3.3 MALDI analysis of the lipids in the re-dissolved four-subunit C*c*O crystals

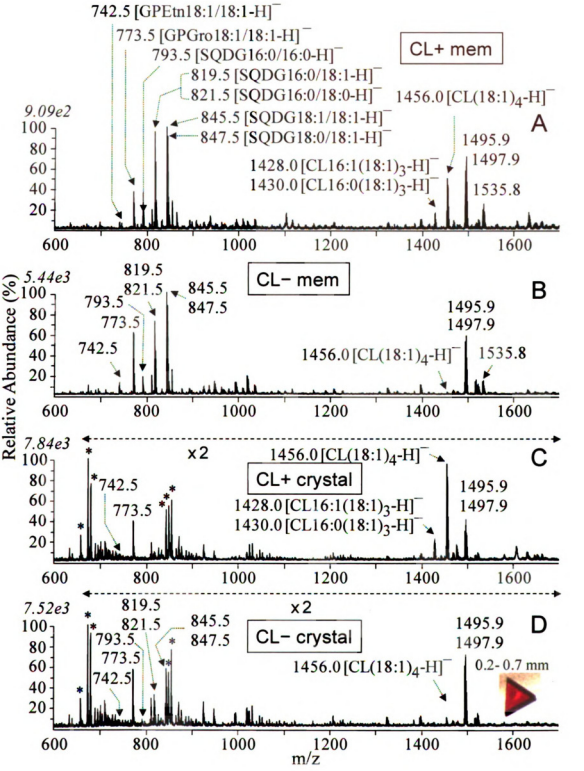
Figure 9.6 shows the negative ion mode MALDI MS spectra obtained by direct analysis of the isolated membranes of CL-proficient (169WT) and CL-deficient (169CL3) crystallography strains (Figures 9.6A and 9.6B, respectively) that were specially engineered and optimized for subsequent crystallization of the purified C*c*O enzyme, and the spectra obtained from the re-dissolved crystals grown from these strains

(Figure 9.6C and 9.6D, respectively). Figure 9.7 shows the MALDI MS of these samples in positive ion mode. The data in Figures 9.6A and 9.6B (negative ion mode) and Figures 9.7A and 9.7B (positive ion mode) indicate that these strains designed with optimization for crystallography had membrane lipid profiles that were similar to those strains used for all the other analyses (Figure 9.3A and 9.3B, and Figures 9.4A and 9.4B, respectively).

MALDI analysis of re-dissolved crystals of C*c*O produced from these two strains reveals that in the CL-proficient strain, 169WT (Figure 9.6C), abundant GPGro and CL lipid species were retained. The presence of these species, as well as GPEtn and all of the SQDG species observed in the membrane, albeit at low abundance, were confirmed by CID MS/MS (Figures 9.8 and 9.9A-C). In addition to the abundant $CL(18:1)_4$, minor species of $CL(16:1)_1(18:1)_3$ and $CL(16:0)_1(18:1)_3$ were also found to be retained in the protein crystals, introducing a potential source of heterogeneity. In the positive ion mode, GPCho18:1/18:1 and OL 3-OH 20:1/19:1 were also observed to be maintained in the four-subunit C*c*O crystals (Figures 9.7 and 9.9D).

In contrast, the re-dissolved C*c*O crystals from the CL-deficient mutant, 169CL3, (Figure 9.6D) clearly revealed significantly decreased levels of CL lipid species as well as higher abundances of the SQDG species, compared to those observed in the crystals from the CL-proficient strain. The GPGro lipid species were also observed to increase in abundance to some extent. GPEtn, GPCho and OL (positive ion mode) lipids were observed in the positive ion mode at similar levels compared to those in the crystal sample of the CL-proficient strain (Figures 9.7C and 9.7D).

Figure 9.6 Negative ion mode MALDI-MS spectra of isolated membranes and C*c*O protein crystals from CL-proficient and CL-deficient *R. sphaeroides*. A) Isolated membrane from CL-proficient *R. sphaeroides* (169WT), B) isolated membrane from CL-deficient mutant *R. sphaeroides* (169CL3), C) C*c*O protein crystals from CL-proficient *R. sphaeroides* (169WT), and D) C*c*O protein crystals from CL-deficient *R. sphaeroides* mutant (169CL3). All strains produce modified C*c*O from pCH169, and the crystal contains four subunits. Ions labeled with asterisks were identified as 2,5-DHB matrix cluster adducts. The identities of labeled ions in each spectrum were confirmed by MS/MS experiments (see Figures 9.8 and 9.9 for some of the spectra).


742.5 [GPEtn18:1/18:1-H]⁻
773.5 [GPGro18:1/18:1-H]⁻
793.5 [SQDG16:0/16:0-H]⁻
819.5 [SQDG16:0/18:1-H]⁻
821.5 [SQDG16:0/18:0-H]⁻
845.5 [SQDG18:1/18:1-H]⁻
847.5 [SQDG18:0/18:1-H]⁻
1456.0 [CL(18:1)4-H]⁻
1428.0 [CL16:1(18:1)3-H]⁻
1430.0 [CL16:0(18:1)3-H]⁻
1495.9
1497.9
1535.8
CL+ mem
A
9.09e2
5.44e3
CL− mem
B
Relative Abundance (%)
7.84e3
x2
CL+ crystal
C
7.52e3
CL− crystal
D
0.2- 0.7 mm
m/z

cell me

CL(18:

contain

much

found

ICL(18

cytoch

strains

molec

9.8 a

It is also noteworthy that the major molecular species of cardiolipin in the isolated cell membranes and the C*c*O crystals contains CL with four 18:1 fatty acyl chains $CL(18:1)_4$ (Figure 9.3, and Figures 9.8A-B). Two minor species of cardiolipin containing $CL(16:1)_1(18:1)_3$, $CL(16:0)_1(18:1)_3$ and $CL(18:0)_1(18:1)_3$ were detected at much lower abundances (Figure 9.8). However, the predominant cardiolipin species found in mammalian mitochondria containing tetralinoleoyl fatty acyl chains, L_4CL ($CL(18:2)_4$), which were proven to be essential for the normal function of mammalian cytochrome *c* oxidase and mitochondria [8,68,70], is not observed in MS of any of the strains of *R. sphaeroides* examined in the current study.

The CID MS/MS evidence for the identification of some of the major lipid molecular species that remain bound in the four-subunit C*c*O crystals is shown in Figure 9.8 and Figure 9.9.

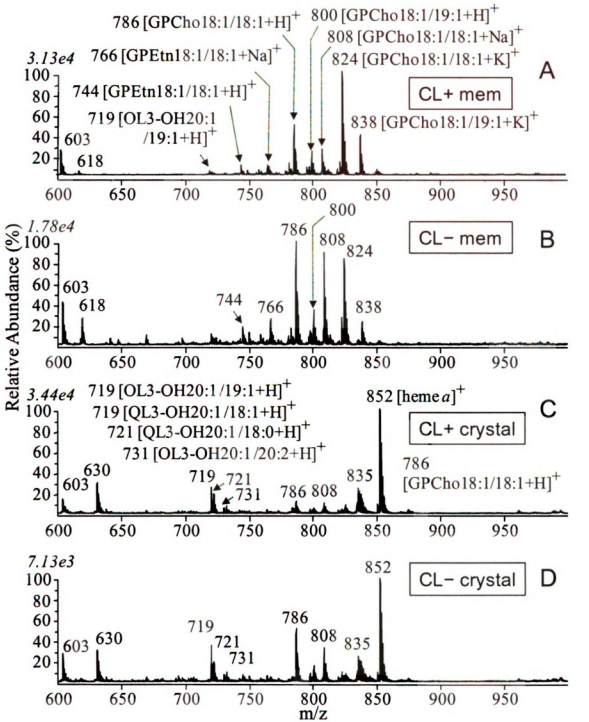


Figure 9.7 Positive ion mode MALDI-MS spectra of isolated membranes (A and B) and CcO crystals (C and D) from CL-proficient (169WT) and CL-deficient (169CL3) *R. sphaeroides*.

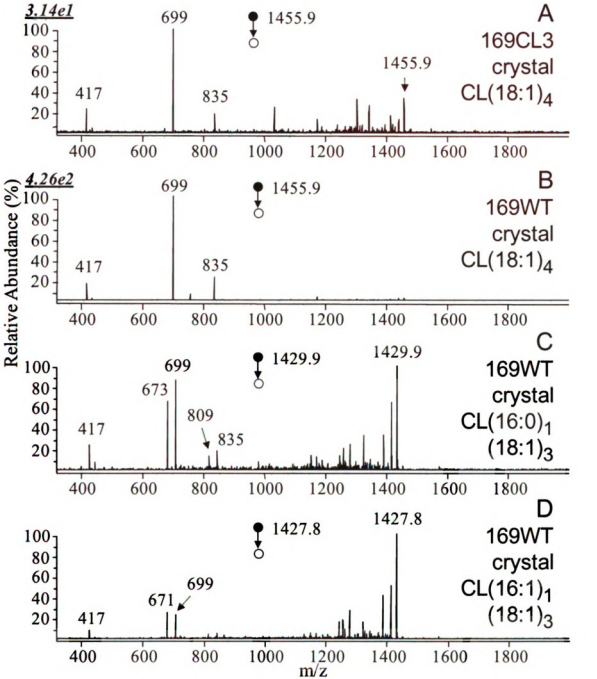


Figure 9.8 Identification of the cardiolipin molecular species in the four-subunit C*c*O crystals from CL-proficient (169WT) and CL-deficient (169CL3) *R. sphaeroides* using CID MS/MS in negative ion mode on a MALDI-linear ion trap mass spectrometer.

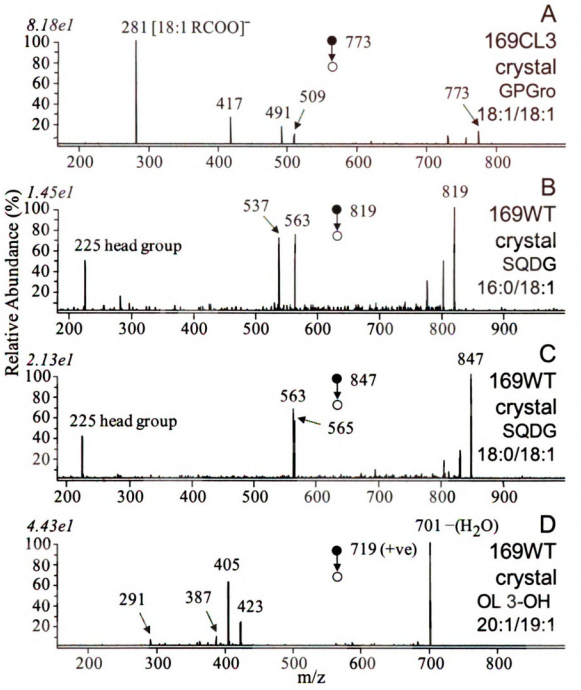


Figure 9.9 Identification of the major lipids ions in the CcO crystals from CL-proficient (169WT) and CL-deficient (169CL3) *R. sphaeroides* using CID MS/MS in positive and negative ion modes on a MALDI-linear ion trap mass spectrometer.

9.4 Discussions

9.4.1 Residual CL in the cardiolipin deficient mutant

To understand the role of CL in C*c*O of *R. sphaeroides*, the CL-deficient mutant BC-m3(also called CL3) was constructed by inactivation of the gene (*cls*) identified as encoding CL synthase by its ability to complement the *pss*-1 *cls* double mutant of *E. coli* [329]. The *cls*-encoded enzyme catalyzes the synthesis of CL from two GPGro molecules [330]. Lipid analysis showed a significant reduction in the level of CL in the mutant membranes (Figure 9.3 and Figure 9.6), but a low amount of CL (<10% wt) was detected by quantitative analysis of the lipids using radioisotope labeling and by mass spectrometric analysis of lipids in the membrane and re-dissolved crystals from the mutant (Figure 9.6 and 9.8). The source of this residual CL in the mutant still needs to be determined. Based on the observations made in the *E. coli cls* knock-out mutant, which shows a low amount of CL [331], it can be speculated that an alternative pathway for CL biosynthesis could also exist in *R. sphaeroides*. In the *E. coli cls* knockout mutant, overexpression of the *pss* gene led to an increase in the CL level [331], suggesting that phosphatidylserine synthase has CL synthase activity. In a similar experiment, it has been observed that the expression of the *pss* gene (GenBank protein ID YP_353797) from *R. sphaeroides* in the *E. coli* SD9 strain resulted in the synthesis of CL (up to 1%) which showed dependence on the level of expression of the gene [15]. Thus, as observed for *E. coli*, phosphatidylserine synthase may be the source of the residual CL in the BC-m3 mutant of *R. sphaeroides* [15].

9.4.2 Molecular components of CL species in *R. sphaeroides*

Further tandem mass spectrometry analysis revealed that the CL molecular species in the membrane, the purified C*c*O enzymes, and the C*c*O protein crystals, are mainly $CL(18:1)_4$, while much less abundant $CL(16:1)_1(18:1)_3$ and $CL(16:0)_1(18:1)_3$ are also present in all of the stages of purification and crystallization. In contrast to the mammalian mitochondria, where $CL(18:2)_4$ and not $CL(18:1)_4$ is the predominant and functionally essential species, the *R. sphaeroides* contained no $CL(18:2)_4$ detectable by MS in the membrane or in the purified and crystallized C*c*O protein complex.

One of the essential functional roles of cardiolipin for the respiratory chain complexes, in particular cytochrome *c* oxidase, and for the overall mitochondria in mammalian systems, has been proposed to be due to the peroxidizability of the 18:2 unsaturated fatty acyl chains, and the 18:1 acyl chain components [8,68,70]. $CL(18:2)_4$ is found to be the predominant CL species in healthy mitochondria, and a relative decrease of the 18:2 cardiolipin component has been correlated to failing mitochondria [68,70]. CL $(18:2)_4$ was also found to activate cytochrome *c* oxidase more efficiently than other lipids [60]. The 18:2 acyl chain is a sensitive target for peroxidation by reactive oxygen species produced mainly in the respiratory chain complexes; by forming a complex with cytochrome *c*, peroxidized cardiolipin triggers the release of cytochrome *c* from the mitochondria, leading to cell apoptosis [67]. Compared to the more unsaturated 18:2 acyl chains, the 18:1 fatty acyl chains produced predominantly in bacteria are less of a target for oxidation. The observed difference in cardiolipin molecular components implies fundamental differences in the functional roles that cardiolipin might play in the bacterial

or yeast system and in the mammalian systems, and this brings a cautionary note for interpreting the results obtained from bacterial systems, versus those from mammalian systems.

9.4.3 CL and growth of *R. sphaeroides*

The BC-m3 CL-deficient mutant showed some decreased growth under respiratory conditions, suggesting that a normal level of CL is important for robust respiratory growth. A similar effect of CL deficiency on respiratory growth has been observed in a *Saccharomyces cerevisiae crd1*Δ mutant, in which the loss of CL affects the stability of the respiratory chain complexes [65,66,332]. The photosynthetic growth of the BC-m3 mutant was not affected, probably because other lipids such as GPGro substituted for CL. It has been shown that GPGro is preferentially increased in purple bacteria during photosynthetic growth [333]. It is possible that the level of CL needed for photosynthetic growth is not as high as that needed for respiratory growth, and therefore the low level of CL retained by the BC-m3 mutant could be sufficient under photosynthetic conditions.

Alternatively, CL may be only required during stress situations. Osmotic stress during growth has been shown to increase CL synthesis in *R. sphaeroides* [334]. Variable, but often lower, levels of C*c*O production was observed from BC-m3 C*c*O overproducing cultures, a response which may be due to the added stress of subculturing, dilution and growth at high oxygen levels and high pH (approaching stationary phase). Determining a specific role of CL during respiratory growth in *R. sphaeroides* requires further analysis beyond the scope of this work.

9.4.4 A role for CL in the function or assembly of C*c*O of *R. sphaeroides*

Low levels of CL did not appreciably affect the assembly of C*c*O in the BC-m3 mutant or the activity of the purified enzyme (Table 9.2). This C*c*O also crystallized in the same manner as that purified from CL-proficient cells, producing four-subunit crystals that diffracted to the same level as crystals from the CL proficient strain. It was critical to determine whether, despite the low CL levels, C*c*O was able to preferentially sequester enough CL for its needs. However, the MS analyses reproducibly demonstrated that the purified enzyme and the crystals did not concentrate CL to any level above that found in the membranes. It is tempting to conclude that CL is not essential for the structure, function or crystallization of C*c*O, consistent with several previous studies using bacterial and yeast systems [23,71,328], despite numerous biochemical and biophysical studies in mammalian systems [8,54,57,68] which suggest otherwise. A low level of CL is still present in the purified C*c*O enzyme and crystals (Figures 9.6 and 9.8) from the mutant, and this small amount of CL must be more rigorously quantified to absolutely establish that it is not representative of a tightly and stoichiometrically bound CL that is not released by either solvent extraction or MALDI-MS methods.

Another possibility is that CL may only be required for maintaining supercomplexes between C*c*O and other membrane proteins of the respiratory chain, and not for the stability or activity of C*c*O alone. Experiments in yeast suggest that complexes III (bc_1) and IV (C*c*O) do not form the normal level of supercomplexes in the mitochondria of CL-deficient mutants, and CL-deficient yeast cultures also grew more

slowly and to a lower final density than wild-type yeast cultures [65]. Similarly, the BC-m3 mutant showed slower growth under respiratory conditions in this study (Figure 9.1).

When analyzing C*c*O directly, mass spectrometric data suggests that other lipids substitute for CL. A relative increase in the levels of SQDG and GPGro was observed in re-dissolved crystals from the 169/CL3 mutant strain (Figures 9.6C and 9.6D). The increase in GPGro in the CL-deficient mutant was also observed in the membrane samples by radioisotope labeling and mass spectrometry. Earlier studies comparing the yeast *cls* mutant (CL-deficient) and *pgs* mutant (GPGro and CL-deficient) suggested that CL is not essential for the functions of C*c*O or mitochondria in yeast [23,71,328], but can be functionally replaced by GPGro [23]. The difference in SQDG was not as obvious in membrane preparations analyzed by thin-layer chromatography or by mass spectrometry, implying that it may reflect the selectivity of C*c*O, not a general metabolic response at the cellular level. Specifically bound SQDG molecules had been previously resolved in the crystals of cyanobacterial photosystem II [335,336]. The increased abundance of SQDG in the re-dissolved C*c*O crystals suggests a possible compensatory role for SQDG during CL deficiency, since both are anionic lipids, and SQDG was found to increase in *R. sphaeroides* membranes under phosphate-limiting growth conditions [14]. Studies in *Rhodobacter capsulatus*, which has neither a CL nor an aa_3-type oxidase, have suggested a similar function for ornithine lipid [273]. This type of lipid is present in the *R. sphaeroides* membranes [184] but is not appreciably altered in BC-m3 membranes, as seen by thin-layer chromatography and mass spectrometry [184].

In a previous study [35] high resolution (2.0 Å), 2-subunit wild-type C*c*O crystals were obtained which appear to contain a potential CL binding site, based on homology

with the bovine enzyme, even though the head group was not resolved. It was also found in the current study that the 2-subunit crystal form of C*c*O can be produced from the enzyme purified from the 169CL3 mutant strain (Table 9.3). Analysis of these crystals showed that they diffract as well as the crystals from the CL-proficient strain, but further analysis will determine whether the putative CL binding site is occupied by CL or substituted by SQDG or GPGro.

While all the recent studies on cardiolipin in mammalian systems point towards an essential functional role for this lipid in the respiratory chain complexes and mitochondria, encoded in the polyunsaturated 18:2 fatty acyl chains, most studies with the yeast and bacterial systems using a genetic specific-lipid-deficiency approach for specific lipid deficiency, found that cardiolipin alone is not essential, and its functions can be replaced by lipids such as GPGro [23,71,328], whereas the combined CL and GPGro deficiency in yeast severely affects the activity of both C*c*O and mitochondria.

9.4.5 Lipid mutants of *R. sphaeroides* as tools for the study of membrane proteins

One of the motivations for studying the production, properties, and crystallization of C*c*O in the CL-deficient mutant of *R. sphaeroides* was to test the hypotheses that 1) CL is a necessary component of the fully functional enzyme in *R. sphaeroides*; and 2) the specific lipid composition of a membrane protein sample is an important factor in achieving high quality crystals. The basis for the first hypothesis was a wealth of biochemical evidence supporting a role for CL in C*c*O function in mammalian systems [1,324,325,337]. The basis for the second hypothesis was the observation of specifically bound and conserved lipids in high resolution crystal structures of membrane proteins. A

furth

over

prov

CL-

crys

start

com

whe

Sinc

com

pos

here

add

tha

cry

further motivation for these studies was to establish *R. sphaeroides* as a tool for the overproduction of membrane proteins, from many sources, for structural studies [338] by providing versions of *R. sphaeroides* with different and controlled lipid compositions.

The results shown herein demonstrate that it is possible to overproduce C*c*O in a CL-deficient mutant, and that the purified enzyme is fully active and gives well-resolved crystals, despite a very low CL content. These results argue strongly against both of the starting hypotheses. However, higher resolution crystal structures, and a more completely CL-deficient mutant, are needed to disprove these hypotheses, or to establish whether some of the roles of CL can be satisfactorily substituted by other lipid species. Since additional lipid mutants of *R. sphaeroides* are currently available [14,90,274], combining different lipid deficiencies into one expression strain, in principle, will be possible. This approach, in combination with the analytical techniques demonstrated here, will enable narrowing down of the specificity for CL replacement by other lipids. In addition, these mutants provide tools for the production of membrane protein complexes that possibly require specific lipid environments for their successful overproduction and crystallization.

Chapter 10

Characterization of a Cardiolipin-Deficient Mutant of *Rhodobacter sphaeroides,* under Phosphate-Limited and Phosphate-Rich Conditions, with Regard to Cytochrome *c* Oxidase Production, Activity and Lipid Profile Modification

10.1 Summary

In this chapter, a metabolic approach was employed to alter the lipid profiles of the C*c*O-expressing strains of *R. sphaeroides in vivo* by using a phosphate-limiting growth medium. The profiles of all the phospholipids and non-phospholipids are changed, in contrast to the results from the single specific lipid-deficiency approach applied in the previous chapters. Such alterations can provide further insight into the inter-changeability between the phospholipids and non-phospholipids, in addition to the single replacement possibilities proposed in previous chapters. The combination of the collective metabolic deficiency approach with the genetic specific lipid-deficiency approach also created a cleaner CL-deficient strain that contained a barely detectable level of CL even by using MS/MS. The cell growth, C*c*O expression, and C*c*O properties were characterized for the 169-2.4.1(WT) and 169CL3(CL−) strains aerobically grown under phosphate-abundant and phosphate-limiting conditions, respectively, and the lipid

profiles in the membrane and purified C*c*O from these four samples were examined by quantitative ESI or MALDI MS and MS/MS.

10.2 Introduction

10.2.1 Lipid profile modulation using phosphate-limiting growth media

The lipid biosynthesis of bacteria is highly sensitive and adaptable to the components in the growth media [11]. In addition to the genetic mutations described in Chapters 7 and 9, the lipid profile of bacteria can also be modulated through metabolic approaches such as using low-phosphate growth media [11,93,106].

Since limited phosphate in the growth media affects all types of phosphate-containing lipids, this experiment can be used as another tool to evaluate the functional significance of phospholipids, and the potential functions of non-phospholipids, *in vivo*, by examining whether and how the phospholipids and non-phospholipids display functional equivalence. Previous studies of both *R. sphaeroides* [11] and *Sinorhizobium melitoti* [93,106] found that the bacteria can be viable at phosphate concentrations as low as 0.1 mM (compared to the normal 20 mM [11]), but phosphate-limiting media significantly changed the overall membrane lipid profiles. The amounts of phospholipids are seen to be significantly reduced, and novel types of phosphate-free lipids are produced at high abundance [11].

Previous lipid biochemistry studies found that in growth media containing abundant phosphate [16,90], the membranes of the wild type *R. sphaeroides* strain 2.4.1 contain phosphatidylethanolamine (GPEtn), phosphotidylcholine (GPCho), phosphatidylglycerol (GPGro) and cardiolipin (CL), and the nonphospholipids such as sulfolipids sulfoquinovosyldiacylglyceride (SQDG) and ornithine lipids (OL), but phospholipids are the predominant components. Under phosphate-limiting growth

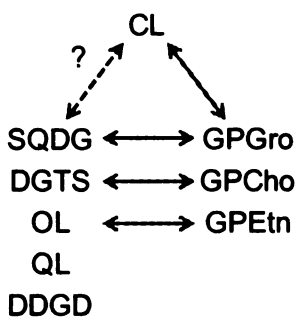
conditions, the novel non-phospholipids glycolipids glucosylgalactosyldiacylglyceride (GGDG) and diacylglyceryl-N, N, N-trimethylhomoserine (DGTS) started to be produced, and the production of SQDG and OL were increased [11]. DGTS is proposed to functionally compensate for GPCho, SQDG for GPGro, and OL for GPEtn, based on the similarity of the charge state in the head group [11,14,289]. DGTS was also found to be the predominant type of lipids in *Sinorhizobium melitoti* under phosphate-limiting growth [93].

10.2.2 Combining specific lipid-deficient mutation with phosphate-limiting growth

A mutation can cause a specific deficiency in a particular type of lipid, such as GPCho, cardiolipin (CL) or SQDG, but at the same time, the amount of some other types of lipids are often seen to increase, which is tempting to interpret as a compensatory mechanism to fulfill the required biological functions. For example, in the GPCho-deficient strain where the phosphatidylethanolamine methyl transferase is mutated, GPEtn significantly increases, and the GPEtn is rationalized to be able to functionally replace GPCho because both GPEtn and GPCho can carry a positive charge in the head group, and are highly similar in the rest of the structure [90]. A cardiolipin-deficiency which is often created by mutating the cardiolipin synthase [15,23], produced an increased level of GPGro lipids, and in that study when both GPGro and CL are genetically depleted, the strain is found not viable. Therefore it has been proposed that the high structural similarity of GPGro to CL makes GPGro the essential lipid that can functionally replace CL [23]. On the other hand SQDG and GPGro lipids appear to be inter-changeable in *R. sphaeroides* because both have negative charge in the head group,

and the depletion of both SQDG and GPGro is lethal [14]. An effect of GPEtn-depletion on some membrane proteins can be restored by a type of phospholipid containing a glyco head group due to similarity in the molecular shape [1].

One question raised from comparing these previous findings is, are such types of functional compatibility determined more by the phosphate group, by the phosphatidylglyceride structure, by the negative or positive charge state, by the head group functional groups, or by the molecular shape? If SQDG can replace GPGro due to the negative charge, and GPGro can replace CL likely due to the similar phosphate head groups, can the non-phospholipid SQDG then replace CL (Scheme 10.1)?



Scheme 10.1 Possible functional interchangeability between different types of lipids

Since metabolic phosphate-limiting growth can decrease the production of the entire set of phospholipids, and increase the relative amount of polar non-phospholipids, its combination with the genetically produced specific lipid-deficiency should be able to provide deeper insights into the functional substitutability between different types of lipids, and therefore a better understanding of the essentiality of a particular type of lipids, such as cardiolipin.

In this chapter, the wild type (169-2.4.1; WT) and the cardiolipin-deficient strain (169CL3; CL−) of *R. sphaeroides* grown in normal-phosphate and low-phosphate media were compared and the C*c*O expression level under these four conditions were examined. The enzymes obtained from these two different strains under these two different growth conditions were characterized in the membrane, and after FPLC purification, with respect to the UV-Vis spectroscopic properties, subunit-composition and enzymatic activity. The lipid profile of the membrane and the purified enzymes was analyzed by using quantitative ESI and MALDI MS and MS/MS, to relate the observed behaviors of C*c*O and the *R. sphaeroides*, to the lipid composition.

10.3 Results and discussions

10.3.1 Cell growth, C*c*O expression in membranes and purification stability

The wild type (169-2.4.1; WT) and the CL-deficient-mutant strain (169CL3; CL−) were grown in parallel with both phosphate-limiting and phosphate-rich conditions, as described in Chapter 3 and in the figure legend to Figure 10.1. No obvious difference was observed in the cell culture optical density that these cells reach at harvest. The UV-Vis spectroscopic analysis of the isolated membrane also shows very similar spectral characteristics for all of these four samples with no absorption peak shift (606 nm) observed (Figure 10.1). These findings indicate that the *R. sphaeroides* can make the C*c*O in normal amounts and levels of production, and with the normal structure as reflected in the native spectra of the redox active metal centers, even with both CL-deficiency and phosphate-deficiency. The purification profiles from Ni-NTA FPLC are also very similar

for

of t

the

or s

for these four samples, in term of the peak elution conditions and the relative abundances of the eluted peaks (data not shown), as well as purification yields. It appears that neither the CL-deficiency nor phosphate-deficiency, nor both, affects the production, assembly, or stability of the multi-subunit complex protein C*c*O, during enzyme purification.

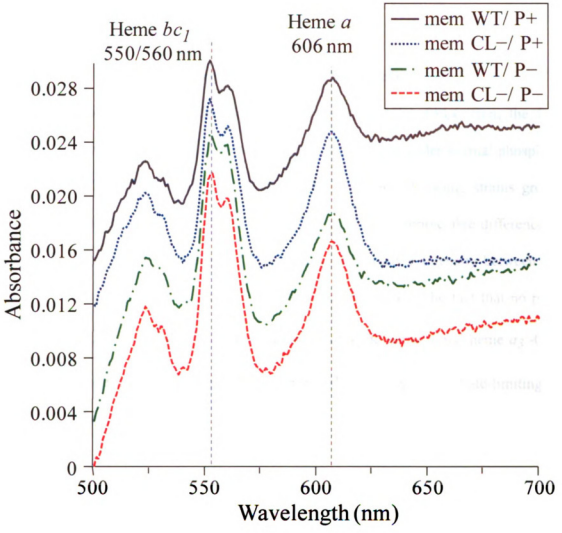


Figure 10.1 Reduced-oxidized UV-Vis spectroscopy of the resuspended membranes isolated from *R. sphaeroides* strains 169-2.4.1(WT) and 169CL3(CL−) grown under normal P (20 mM KH_2PO_4; P+), and low P (0.1 mM KH_2PO_4; P−) conditions. Spectra are offset to show characteristics more clearly. Gray = WT grown under normal phosphate (WT/ P+); Blue = CL− under normal phosphate (CL−/ P+); Green = WT under low phosphate (WT/ P−); and Red = CL− under low P (CL−/ P−). Purification was performed using Ni-NTA column on a FPLC system as described earlier (Chapter 3).

10.3.2

10.3.2

samp

cond

unde

term

Sore

shift

cata

pho

10.3.2 Characterization of C*c*O purified from the four cell samples

10.3.2.1 UV-Vis spectroscopic properties of the purified C*c*O

The reduced spectra of the C*c*O purified using Ni-NTA FPLC from the four samples are shown in Figure 10.2, as isolated from cells grown under normal phosphate conditions, 169-2.4.1 (WT/ P+) and 169CL3 (CL−/ P+), and the same strains grown under low phosphate (WT/ P− and CL−/ P−). They display no appreciable difference in terms of the absorption wavelength of the peaks, or the relative intensity between the Soret (445 nm) and alpha (606 nm) heme a/a_3 absorption peaks. The fact that no peak shift is observed, indicates that the coordination state of the heme *a* and heme a_3 -Cu_B catalytic center are not disturbed in the C*c*O purified from these phosphate-limiting or phosphate-rich conditions.

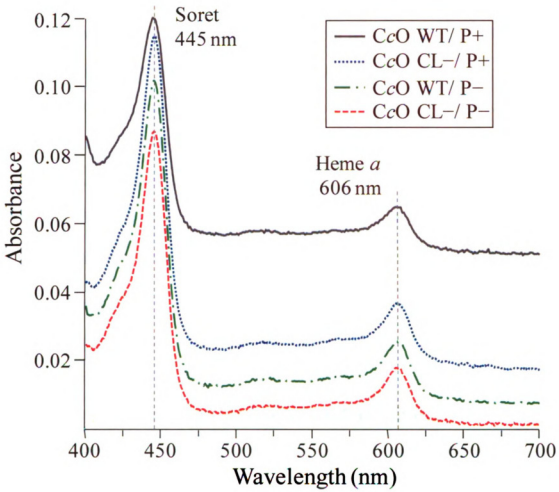


Figure 10.2 Reduced UV-Vis spectroscopy of CcO purified from *Rhodobacter sphaeroides* strains: Gray = 169-2.4.1 grown under normal phosphate (WT/ P+); blue = 169CL3 under normal phosphate (CL−/ P+); green = 169-2.4.1 under low phosphate (WT/ P−); and red = 169CL3 under low P (CL−/ P−). Purification was performed using Ni-NTA column on a FPLC system as described earlier (Chapter 3).

10.3.2.2 SDS-PAGE analysis of the purified C*c*O

SDS-PAGE analysis of the purified C*c*O from these four samples using urea as the denaturation reagent is shown in Figure 10.3. It is clear that each sample of C*c*O contains all of the four subunits, and there is no appreciable difference between the four samples in terms of subunit composition and the size of the subunits that are resolvable by the SDS-PAGE method. The SDS-PAGE analysis for the peak that eluted before the pure C*c*O in FPLC purification was also performed in the same gel (data not shown). This peak contains other respiratory complexes such as a cytochrome bc_1 (Complex III), which also seems to be unaffected by the growth conditions or the CL− mutation. Importantly, the combination of phosphate-deficiency and cardiolipin-deficiency did not cause the C*c*O subunits to dissociate from each other during purification. This is particularly interesting with respect to subunit IV (see Figure 1.5 in Chapter 1), which is connected to the rest of the enzyme via a layer of phospholipids, identified as 4 phosphatidylethanolamine molecules in the four-subunit *R. sphaeroides* C*c*O [34].

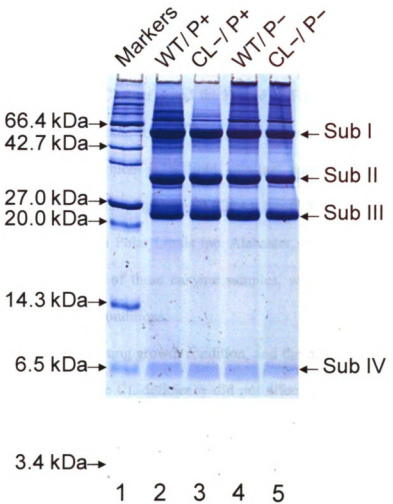


Figure 10.3 SDS-PAGE analysis of the C*c*O purified by Ni-NTA FPLC from the *Rhodobacter sphaeroides* strains 169-2.4.1 (WT) and 169CL3 (CL−) aerobically grown under normal P (20 mM KH_2PO_4) (P+), and low P (0.1 mM KH_2PO_4) (P−) conditions, using conditions described in Chapter 3 and Coomassie blue for the staining: lane 1 = molecular weight markers; lane 2 = 169-2.4.1 grown under normal phosphate (WT/ P+); lane 3 = 169CL3 under normal phosphate (CL−/ P+); lane 4 = 169-2.4.1 under low phosphate (WT/ P−); and lane 5 = 169CL3 under low P (CL−/ P−).

10.

ox

un

sh

ad

ph

lip

the

oxi

in

p

i

10.3.2.3 Activity analysis of the purified C*c*O

The steady state activities of the C*c*O from these four samples were evaluated by oxygen consumption measurements in the presence of cytochrome *c* as the substrate, under conditions described in Chapter 3 and the legend to Figure 10.4 [77]. The results shown in Figure 10.4 demonstrate that all four samples have similar activity, and the addition of soy asolectin, which is a lipid mixture containing GPEtn, GPCho, phosphatidylinositol (GPIns), phosphatidic acid (GPA), lysoGPCho and other unspecified lipids (information from Avanti Polar Lipids Inc. Alabaster, AL), in the assay increases the activity by 20-30% for all of these enzyme samples, which is typical for purified oxidase isolated under normal conditions.

Thus the phosphate-limiting growth condition, and the phosphate-limiting growth in combination with the genetic CL-deficiency did not affect the UV-Vis spectroscopic properties, the subunit composition, or the activity of the purified C*c*O enzymes, or, as indicated earlier, the cell growth and relative C*c*O expression level. However, the lipid profiles in the cells are expected to have changed [11]. Do these unaffected enzymatic properties come from an unaltered lipid profile, from the adaptability to the altered lipid background *in vivo*, or from the flexibility in the lipid structural requirement of C*c*O? To answer this question, the lipid profiles in the membrane and in the purified C*c*O enzymes were then examined by using quantitative ESI and MALDI MS and MS/MS methods, with the incorporation of lipid internal standards.

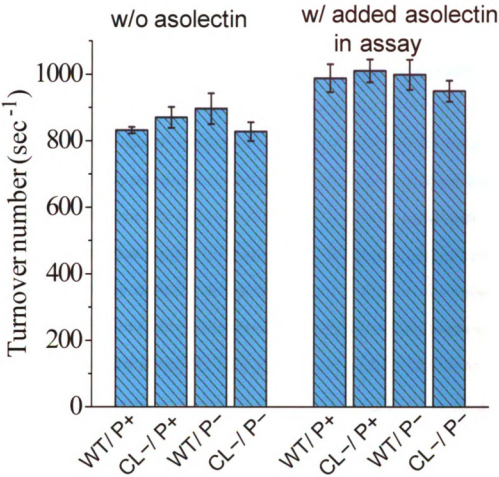


Figure 10.4 Steady-state oxygen consumption activity analysis of the CcO purified by Ni-NTA FPLC from *Rhodobacter sphaeroides* strains169-2.4.1 (WT) and 169CL3 (CL−) grown aerobically under normal P (20 mM KH_2PO_4) (P+), and low P (0.1 mM KH_2PO_4) (P−) conditions, before and after the addition of asolectin lipids in the reaction mixture: 169-2.4.1 grown under normal phosphate (WT/ P+), 169CL3 under normal phosphate (CL−/ P+), 169-2.4.1 under low phosphate (WT/ P−), and 169CL3 under low P (CL−/ P−). The data shown are the mean values from triplicate extractions, and the error bar is the standard deviation. Conditions for the assay are described in Chapter 3 and reference [77].

10.3.3

grow

from

P-.

cont

pho

(W

com

Fig

nov

(da

(Fi

for

18

ad

lin

re

(F

Fi

io

10.3.3 Quantitative analysis of the membrane lipids profile for low-phosphate growth

Figure 10.5 shows the positive ion mode ESI MS spectra of the lipids extracted from the membranes obtained from the four different conditions: WT/ P+, CL−/ P+, WT/ P−, and CL−/ P−. The internal standards were GPEtn, GPGro, GPCho and CL lipids containing 14:0/14:0 fatty acid chains at the final concentrations of 4, 2, 2 and 1 μM.

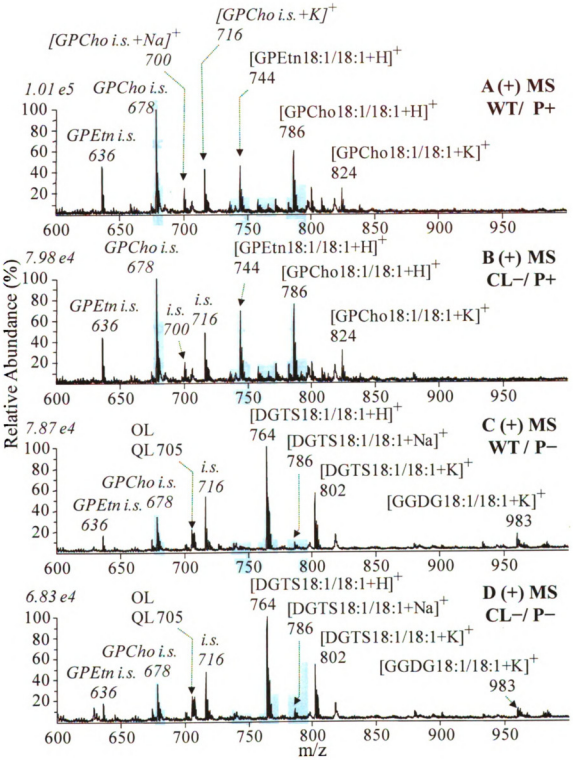
Figure 10.5A is the MS spectrum of the WT (169-2.4.1) grown under normal phosphate (WT/ P+). When compared to Figure 10.5C, WT grown under low phosphate (WT/ P−), a completely different lipid profile is seen. Neither of the predominant components in Figure 10.5A, the GPCho and the GPEtn lipids, are observable by MS in Figure 10.5C grown under phosphate-limiting conditions; instead, a new set of ions are now dominant. The identities of the lipid species were determined by MS/MS and MS^n (data not shown). The most abundant ion observed for the phosphate-limiting growth (Figure 10.5C) at m/z 764 was determined to be the polar phosphate-free lipid, DGTS. It forms a sodium adduct ion at m/z 786, the same m/z as the protonated ion of GPCho 18:1/18:1, but MS/MS analysis of m/z 786 revealed only a very low level of GPCho. In addition, the phosphate-free glycolipids GGDG were also observed in the phosphate-limiting growth membranes (Figure 10.5C).

The drastic change in the lipids observable by positive ion mode ESI, was also revealed in the CL-deficient mutant under high (Figure 10.5B) and low-phosphate (Figure 10.5D) growth conditions. A comparison of Figures 10.5A with 10.5B, and Figure 10.5C with 10.5D, however, shows that the lipid species detected by the positive ion mode ESI are very similar between the WT and the CL-deficient mutant, whether

they are grown with abundant-phosphate or limiting phosphate, although the exact quantity might differ. This might be expected since the major difference in levels of cardiolipin itself is typically not seen in the positive ion mode under these experimental conditions.

A clearer picture of the quantitative membrane lipid profile change in the positive ion mode MS can be derived from the quantification results summarized in Figure 10.6. Figure 10.6 only summarizes the dominant component if several species overlap at the same precursor ion m/z. The phospholipids GPGro, GPEtn, GPCho and CL can be quantified by their individual internal standards, but those lipids that do not have internal standards of their own can only be relatively quantified by referring to a phospholipid standard with the closest structural similarity, and should be interpreted with caution. Thus the quantity of the GPCho and GPEtn lipids shown in Figure 10.6 represent their absolute concentrations, and can be compared with each other. The DGTS lipid has a fixed positive charge and its ionization efficiency should closely resemble GPCho, and can therefore be relatively quantified by the GPCho internal standard, while the OL or glutamine lipids (QL) and the GGDG lipids are relatively quantified with reference to the GPEtn internal standard, and each can be compared within its own lipid type, but could not be compared to the phospholipids.

Figure 10.5 Positive ion mode ESI MS spectra of the lipids extracted from the same amount of isolated membranes of *R. sphaeroides* 169-2.4.1 grown under normal phosphate (WT/ P+), 169CL3 under normal phosphate (CL−/ P+), 169-2.4.1 under low phosphate (WT/ P−), and 169CL3 under low P (CL−/ P−), with the presence of the lipid internal standards of GPEtn 14:0/14:0, GPGro14:0/14:0, GPCho 14:0/14:0 and CL $(14:0)_4$ at final concentrations of 4, 2, 2 and 1 μM in the chloroform: methanol (1:1, v/v) solvent containing 40 mM ammonium hydroxide. Experimental conditions are described in Chapter 3 section 3.7.2.


[GPCho i.s.+K]+
716
[GPCho i.s.+Na]+
700
[GPEtn18:1/18:1+H]+
744
1.01 e5
GPCho i.s.
678
A (+) MS
WT/ P+
[GPCho18:1/18:1+H]+
786
GPEtn i.s.
636
[GPCho18:1/18:1+K]+
824
7.98 e4
GPCho i.s.
678
[GPEtn18:1/18:1+H]+
744
B (+) MS
CL−/ P+
[GPCho18:1/18:1+H]+
786
GPEtn i.s.
636
i.s.
700
i.s.
716
[GPCho18:1/18:1+K]+
824
Relative Abundance (%)
7.87 e4
OL
QL 705
[DGTS18:1/18:1+H]+
764
C (+) MS
WT / P−
[DGTS18:1/18:1+Na]+
786
i.s.
716
GPCho i.s.
GPEtn i.s. 678
636
[DGTS18:1/18:1+K]+
802
[GGDG18:1/18:1+K]+
983
6.83 e4
OL
QL 705
[DGTS18:1/18:1+H]+
764
D (+) MS
CL−/ P−
[DGTS18:1/18:1+Na]+
786
i.s.
716
GPCho i.s.
GPEtn i.s. 678
636
[DGTS18:1/18:1+K]+
802
[GGDG18:1/18:1+K]+
983
600
650
700
750
800
850
900
950
m/z

GPEt

incre

abun

GGD

defic

consi

defic

altho

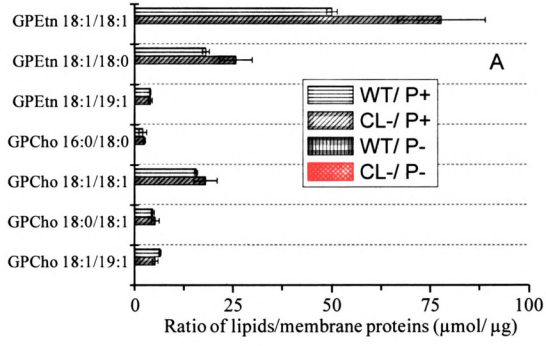
wild

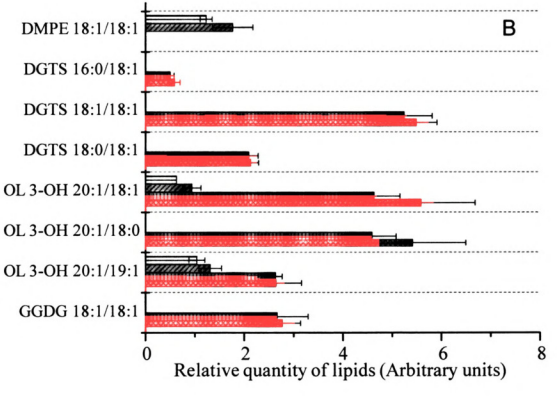
DDC

norm

Figure 10.6 shows that, in the phosphate-limiting growth, there is no GPCho or GPEtn lipids beyond 5% of normalized relative abundance in MS, but instead, there is an increased level of OL, and a high level of DGTS lipids as well as GGDG lipids. The most abundant dominant fatty acid composition for DGTS is DGTS 18:1/18:1. The DGTS and GGDG lipids are not detectable in the normal-phosphate growth conditions. The CL-deficient mutant has a slightly higher level of GPEtn lipids compared to the wild type, consistent with earlier findings (Chapter 7), but in the low-phosphate growth, the CL-deficient mutant did not contain an appreciably higher level of OL than the wild type, although OL has been proposed to be functionally substitutable with GPEtn. Between the wild type and the CL-deficient mutant, there is no significant difference in the DGTS, or DDGD level under low phosphate growth, and no difference in the GPCho level in the normal phosphate growth.

Figure 10.6 Summary of the quantification results from Figure 10.5 using positive ion mode ESI MS. The lipids are extracted from the membranes grown under normal phosphate (WT/ P+ and CL–/ P+), or under low phosphate (WT/ P– and CL–/ P–). In panel A, the phospholipids GPEtn and GPCho are quantified against their individual internal standards and expressed with respect to membrane protein measured by BCA assay (Chapter 3); in panel B, DGTS is relatively quantified with reference to the GPCho standard, and the OL, DMPE and GGDG are relatively quantified against the GPEtn standard. The data shown are the mean values from triplicate extractions, and the error bar is the standard deviation.


GPEtn 18:1/18:1
GPEtn 18:1/18:0
GPEtn 18:1/19:1
GPCho 16:0/18:0
GPCho 18:1/18:1
GPCho 18:0/18:1
GPCho 18:1/19:1
A
WT/ P+
CL-/ P+
WT/ P-
CL-/ P-
0
25
50
75
100
Ratio of lipids/membrane proteins (μmol/ μg)


DMPE 18:1/18:1
DGTS 16:0/18:1
DGTS 18:1/18:1
DGTS 18:0/18:1
OL 3-OH 20:1/18:1
OL 3-OH 20:1/18:0
OL 3-OH 20:1/19:1
GGDG 18:1/18:1
B
0
2
4
6
8
Relative quantity of lipids (Arbitrary units)

these

nearl

mode

revea

growt

growt

these

mainl

20:1

been

SQD

exc

ph

G

q

t

p

ph

Likewise, the negative ion mode ESI MS analysis of the lipids extracted from these four samples is shown in Figure 10.7 from m/z 600 to 1000. In contrast to the nearly complete apparent depletion (< 5%) in GPCho and GPEtn seen in positive ion mode, the negative ion mode MS and further identification using MS/MS and MS^n revealed that the GPGro lipids still remain at measurable levels under phosphate-limiting growth in both the wild type and the CL-deficient mutant; however, in the low-phosphate growth, appreciable increases in other types of non-phospholipids are observed. Among these is the peak at m/z 717 in Figures 10.7C and 10.7D, which was determined to be mainly the glutamine lipid QL 3-OH 20:1/18:1, with a low level of overlapping OL 3-OH 20:1/19:1. This is the first time that the recently discovered type of glutamine lipid has been found to vary under different growth conditions. The relative abundance of the SQDG ions also increased.

The quantification of the resolved species in negative ion mode MS (with the exception of CL; see below) are summarized in the bar graph in Figure 10.8, by using the phospholipid internal standards. SQDG lipids were relatively quantified by referring to GPGro internal standards, and QL, OL, GGDG, MMPE and DMPE lipids were relatively quantified by using the GPEtn standard. Now it is clearer that the phosphate-limiting growth causes the GPGro lipids to drop by ~50% for both the wild type and the CL-deficient mutant, in the species containing 18:1/18:1 and 18:0/18:1 fatty acids. However the saturated species GPGro 18:0/18:0, which was barely observable under normal-phosphate growth, was now observed as one of the main species of GPGro under phosphate-limiting growth conditions for both the wild type and the CL-deficient mutant.

Figure 10.7 Negative ion mode ESI MS spectra of the lipids extracted from the same amount of isolated membranes of *R. sphaeroides*: WT/ P+ and CL−/ P+ grown under normal phosphate, WT/ P− and CL−/ P−, grown under low phosphate, in the presence of the lipid internal standards of GPEtn 14:0/14:0, GPGro14:0/14:0, GPCho 14:0/14:0 and CL $(14:0)_4$ at final concentrations of 4, 2, 2 and 1 μM in the chloroform: methanol (1:1, v/v) solvent containing 40 mM ammonium hydroxide. The m/z range of 600-1000 is displayed.

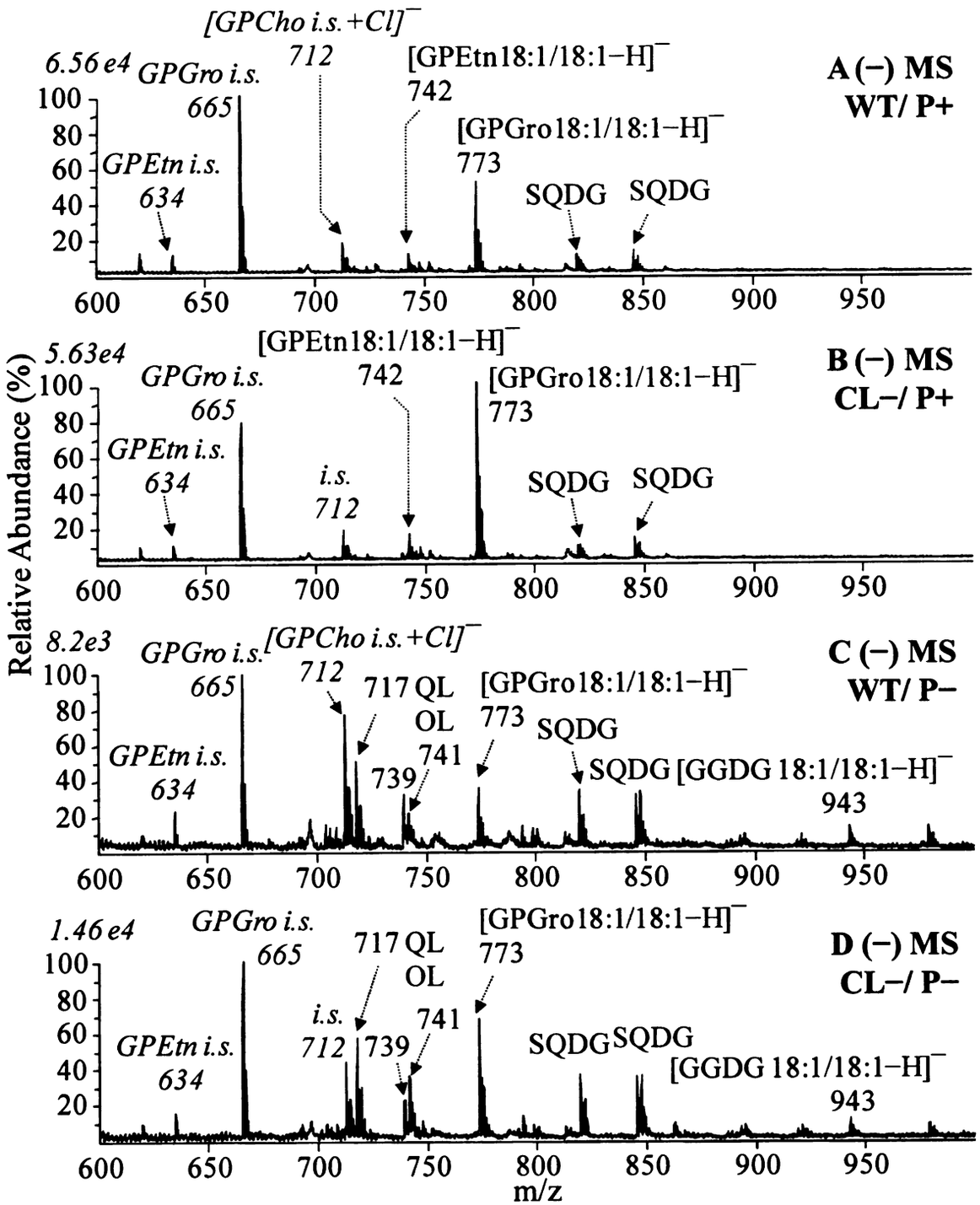
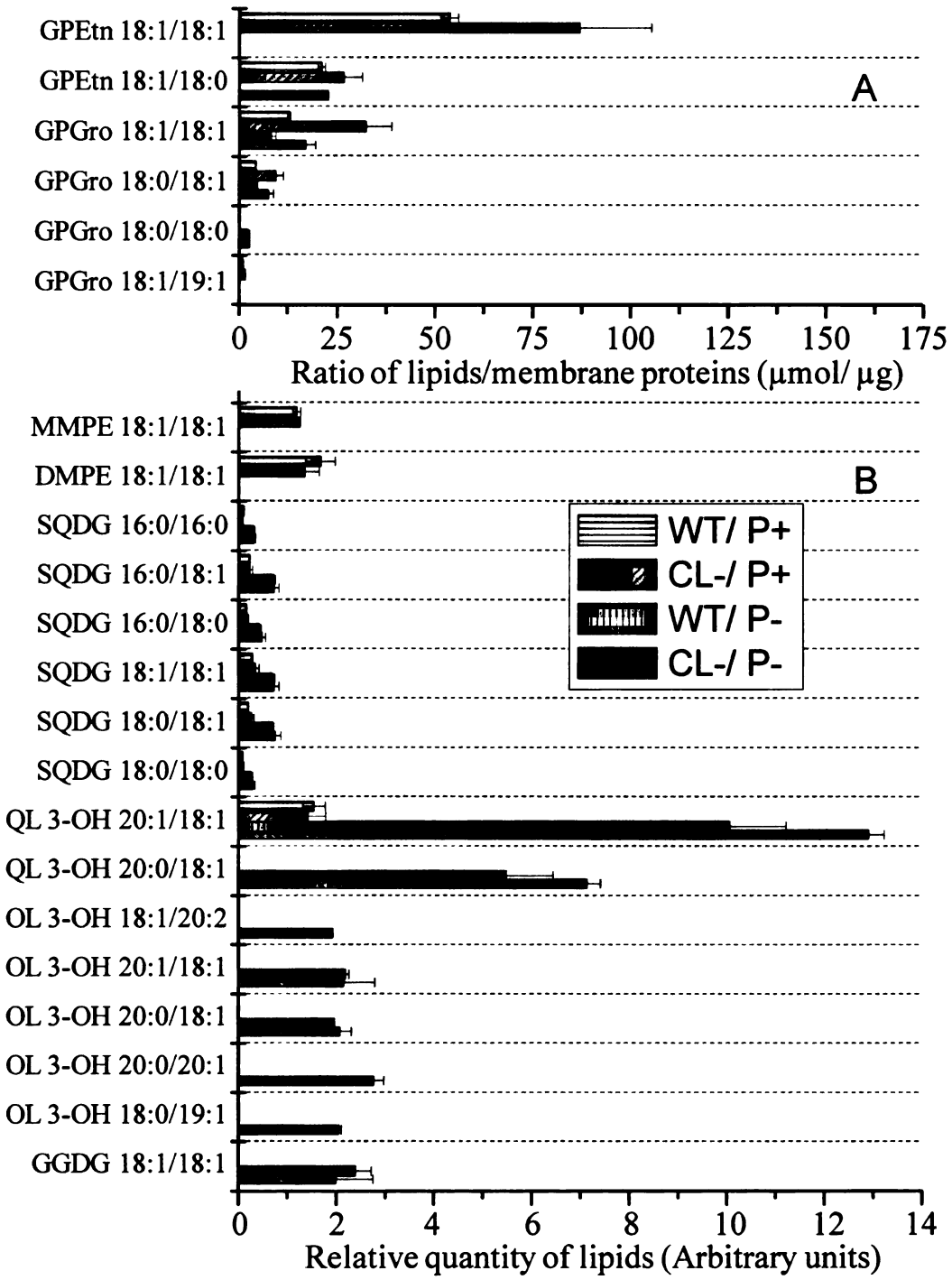

[GPCho i.s.+Cl]⁻
712
[GPEtn18:1/18:1−H]⁻
742
6.56 e4
GPGro i.s.
665
[GPGro18:1/18:1−H]⁻
773
A (−) MS
WT/ P+
GPEtn i.s.
634
SQDG
SQDG
5.63e4
[GPEtn18:1/18:1−H]⁻
742
GPGro i.s.
665
[GPGro18:1/18:1−H]⁻
773
B (−) MS
CL−/ P+
GPEtn i.s.
634
i.s.
712
SQDG
SQDG
Relative Abundance (%)
8.2e3
GPGro i.s.
665
[GPCho i.s.+Cl]⁻
712
717 QL
OL
[GPGro18:1/18:1−H]⁻
773
C (−) MS
WT/ P−
741
739
SQDG
SQDG
[GGDG 18:1/18:1−H]⁻
943
GPEtn i.s.
634
1.46 e4
GPGro i.s.
665
717 QL
OL
[GPGro18:1/18:1−H]⁻
773
D (−) MS
CL−/ P−
i.s.
712
741
739
SQDG
SQDG
[GGDG 18:1/18:1−H]⁻
943
GPEtn i.s.
634
100
80
60
40
20
600
650
700
750
800
850
900
950
m/z

Figure 10.8 Summary of the quantification results from Figure 10.7 using negative ion mode ESI MS. The lipids are extracted from the WT and CL– strains (WT/ P+) and (CL–/ P+), grown under normal phosphate, and (WT/ P–) and (CL–/ P–), grown under low phosphate conditions. In panel A, phospholipids GPEtn and GPGro are quantified against their individual internal standards; in panel B, DGTS is relatively quantified with reference to the GPCho standard, and the OL, QL, MMPE, DMPE and GGDG are relatively quantified against the GPEtn standard. The data shown are the mean values from triplicate extractions, and the error bar is the standard deviation. For all of the phospholipids quantified here, the lipid concentrations in the ESI samples are within the linear range as shown in Figure 7.10.



g negative ion
(WT/ P+) and
, grown under
are quantified
quantified with
nd GGDG are
e mean values
For all of the
, are within the

On the other hand, the SQDG lipids were found to increase by 2-3 fold in the phosphate-limiting growth for both the wild type and the CL-deficient mutant (Figure 10.8). The saturated molecular species of SQDG, such as the SQDG 16:0/16:0 (m/z 793) and SQDG 18:0/18:0 (m/z 849) showed an increase of nearly 3 fold, higher than the unsaturated SQDG 18:1/18:1 species. The QL lipids increased dramatically (over 5 fold) in the low-phosphate growth and the increase of QL 3-OH 20:1/18:1 (m/z 717) is slightly more appreciable in the CL-deficient mutant than in the wild type (Figure 10.8).

The negative ion mode ESI MS spectra of the membrane lipid extract showing m/z 1200-1600, the m/z range of the cardiolipin species, is displayed in Figure 10.9. Cardiolipin, the lipid that is of the most interest to our study, however, is roughly shown to decrease under low phosphate growth by only about 20% compared to levels in the normal-phosphate growth in the wild type (Figures 10.9A and 10.9C). For the CL-deficient mutant under normal phosphate growth, the CL is below the detection limit in ESI MS (Chapter 7; Figure 10.9B); therefore the quantification of CL is based on the wide band MS/MS isolation and fragmentation of the precursor ion m/z for $CL(18:1)_4$ and the $CL(14:0)_4$ internal standard, summarized in Figure 10.10. All of the ions above 5% in normalized relative abundance in MS have been quantified by MS/MS in this experiment, but only the CL MS/MS quantification results are going to be discussed here. Since CL is often proposed to be substitutable by GPGro, and GPGro has been shown to be functionally exchangeable with SQDG, the quantification of CL (by MS/MS) and GPGro, and relative quantification of SQDG lipids (by MS) are included in Figure 10.10.

Figure 10.9 Negative ion mode ESI MS spectra of the lipids extracted from the same amount of isolated membranes of *R. sphaeroides* 169-2.4.1 grown under normal phosphate (WT/ P+), 169CL3 under normal phosphate (CL−/ P+), 169-2.4.1 under low phosphate (WT/ P−), and 169CL3 under low P (CL−/ P−), in the presence of the lipid internal standards of GPEtn 14:0/14:0, GPGro14:0/14:0, GPCho 14:0/14:0 and CL $(14:0)_4$ at final concentrations of 4, 2, 2 and 1 μM in the chloroform: methanol (1:1, v/v) solvent containing 40 mM ammonium hydroxide. The m/z range of 1200-1600 is displayed for the cardiolipin.

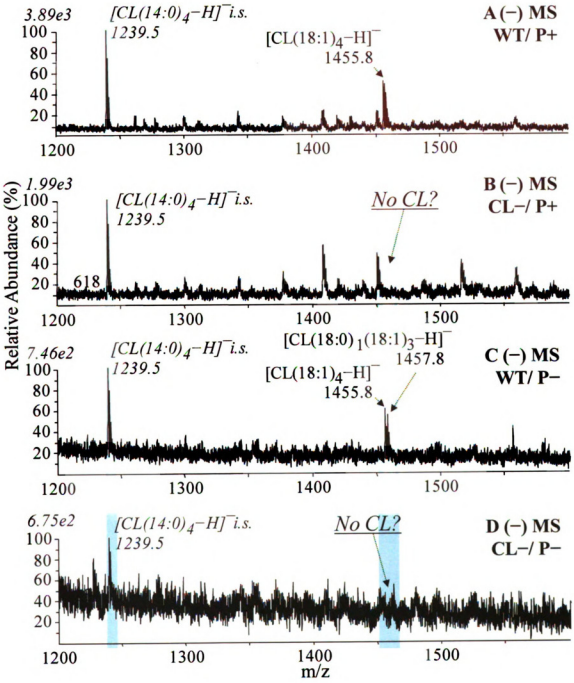
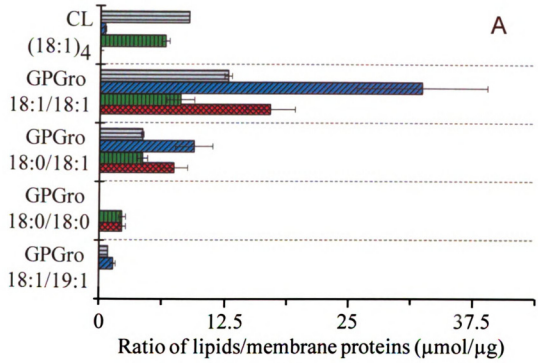
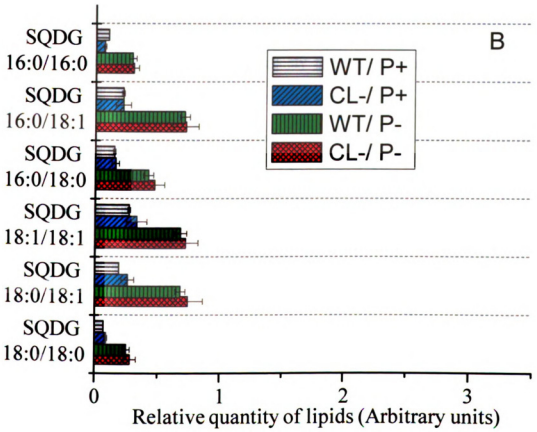

3.89e3
[CL(14:0)4–H]¯ i.s.
1239.5
[CL(18:1)4–H]¯
1455.8
A (–) MS
WT/ P+
1.99e3
[CL(14:0)4–H]¯ i.s.
1239.5
No CL?
618
B (–) MS
CL–/ P+
Relative Abundance (%)
7.46e2
[CL(14:0)4–H]¯ i.s.
1239.5
[CL(18:0)1(18:1)3–H]¯
1457.8
[CL(18:1)4–H]¯
1455.8
C (–) MS
WT/ P–
6.75e2
[CL(14:0)4–H]¯ i.s.
1239.5
No CL?
D (–) MS
CL–/ P–
100
80
60
40
20
1200
1300
1400
1500
m/z

Figure 10.10 Summary of the quantification results of CL using negative ion mode ESI MS/MS with wide band isolation and activation, and the quantification of GPGro and SQDG lipids by MS. The lipids are extracted from the 169-2.4.1 grown under normal phosphate (WT/ P+), 169CL3 under normal phosphate (CL−/ P+), 169-2.4.1 under low phosphate (WT/ P−), and 169CL3 under low P (CL−/ P−). In panel A, $CL(18:1)_4$ is quantified against the $CL(14:0)_4$ internal standard by the most abundant fragment ions (m/z 699 vs. m/z 591), GPGro lipids are quantified against their individual internal standards in MS; in panel B, SQDG is relatively quantified with reference to the GPGro standard in MS. The data shown are the mean values from triplicate extractions, and the error bar is the standard deviation. For all of the phospholipids quantified here, the lipid concentrations in the ESI samples are within the linear range as shown in Figure 7.10.


A
CL
(18:1)4
GPGro
18:1/18:1
GPGro
18:0/18:1
GPGro
18:0/18:0
GPGro
18:1/19:1
0
12.5
25
37.5
Ratio of lipids/membrane proteins (µmol/µg)


B
WT/ P+
CL-/ P+
WT/ P-
CL-/ P-
SQDG
16:0/16:0
SQDG
16:0/18:1
SQDG
16:0/18:0
SQDG
18:1/18:1
SQDG
18:0/18:1
SQDG
18:0/18:0
0
1
2
3
Relative quantity of lipids (Arbitrary units)

The MS/MS quantification of CL shown in the first row of Figure 10.10 clearly indicates that, first of all, the level of cardiolipin in the CL-deficient mutant was further decreased by the phosphate-limiting growth, and therefore, a five-fold "cleaner" CL-deficient sample is obtained by the combination of the CL-deficient mutation and the low-phosphate growth: CL−/ P− gave 0.95% vs. CL−/ P+ 5.5%, relative to the wild type WT/ P+ CL level, and an over-five-fold further depletion of the CL seen in the CL-deficient mutant CL−/ P+ is now seen in the combined depletion sample CL−/ P−. Secondly, the CL in the wild type under phosphate-limiting growth CL−/ P+, is maintained at 73% of the level in the normal-phosphate growth. This can be compared with GPEtn and GPCho which are found to be nearly completely depleted by the phosphate-limiting growth (0.1 mM phosphate vs. the normal 20 mM phosphate).

The limited phosphate seems to have priorities of destination for making lipids. The first priority is the cardiolipin (73% maintained), followed by GPGro (50% maintained), while GPEtn and GPCho probably have the lowest priority. While both GPGro and CL decrease by different degrees, the SQDG lipids increase significantly in the phosphate-limiting growth conditions. All of the SQDG, GPGro and CL lipids carry a negative charge in the head group. The sum of the negative charge from all the negatively charged lipids may be required to be maintained at a certain level for their physiological needs [14]. The nearly complete depletion in the positively charged GPCho lipids and the dramatic increase in the DGTS carrying the same zwitterionic center containing a fixed positive charge in the trimethyl amino group, however, suggest that zwitterionic center containing the fixed positive charge in the GPCho lipids is also essential, but not the

entire molecule; if the center can be provided by another type of non-phospholipid, the limited phosphate source will not be wasted to make the rest of the GPCho structure.

The appreciably increased amount of lipids with saturated fatty acid chains in the remaining GPGro and SQDG in the phosphate-limiting growth can probably be related to the membrane lipid interactions. The phosphate group, by forming hydrogen bonds and electrostatic interactions, is one of the forces that keep the membrane at the appropriate tightness and flexibility. The deficiency in phosphate, and the decrease in the total amount of phospholipids, limited the contribution by such interactions from phosphate groups. It is possible that the increase in the degree of saturation in the fatty acid chains helps to compensate for the loss by making the membrane tighter by increasing the rigidity and hydrophobicity of the lipid tail [339].

In summary, it was found that, in response to the limited phosphate concentration in the growth media, the lipid profile of *R. sphaeroides* membranes, both the wild type (169-2.4.1) and the CL-deficient mutant (169CL3), indeed changed drastically, therefore the close-to-wild-type behavior seen in the purified C*c*O and the cells are probably the result of adaptations of the lipid environment *in vivo*. In particular, the combination of CL-deficiency mutation and the phosphate-limiting growth can create a significantly cleaner (by 5 fold) CL-deficient strain. However, all the results discussed so far are obtained from extracts of *Rhodobacter* membranes. In order to understand more about the nature of the potential roles of CL for *R. sphaeroides* C*c*O, it is necessary to look directly at the lipids that are associated with the purified C*c*O, which can be done more readily using MALDI.

10.3.4 Quantitative analysis of the lipids in the membrane grown with low-phosphate using MALDI

Due to the detergent interference and incomplete chemical extraction efficiency issues with ESI analysis of the lipid extract from the membrane protein C*c*O, the direct MALDI MS and MS/MS analysis was used to obtain a relatively quantitative comparison of the lipids in the purified C*c*O, by incorporating a set of internal standards at appropriate concentrations. The same methods were applied to the analysis of resuspended membrane pellets, and the MALDI spectra were compared to those of the ESI spectra on the membrane lipid extract. Importantly, similar conclusions could be drawn about the relatively quantitative changes in the lipids as a result of the CL-deficiency or the phosphate-limiting growth. Figure 10.11 shows the MALDI MS spectra of the membranes from *R. sphaeroides* 169-2.4.1 (WT) and 169CL3 (CL−) grown under normal phosphate (WT/ P+), (CL−/ P+), and low phosphate (WT/ P−), (CL−/ P−), in the presence of the lipid internal standards of GPEtn 14:0/14:0, GPGro14:0/14:0, GPCho 14:0/14:0 and CL $(14:0)_4$. Figures 10.11C and 10.11D show that the DGTS is the predominant species observed in positive ion mode in the phosphate-limiting growth, and GPCho is nearly completely depleted, consistent with the ESI analysis.

Figure 10.11 Positive ion mode MALDI MS spectra of the same amount of isolated membranes (1 μL at 0.25 mg/mL final membrane protein concentrations determined by BCA assay) of *R. sphaeroides* 169-2.4.1 grown under normal phosphate (WT/ P+), 169CL3 under normal phosphate (CL−/ P+), 169-2.4.1 under low phosphate (WT/ P−), and 169CL3 under low P (CL−/ P−), with the presence of the lipid internal standards of GPEtn 14:0/14:0, GPGro 14:0/14:0, GPCho 14:0/14:0 and CL $(14:0)_4$ at final concentrations of 10, 5, 1.25 and 1.25 μM, respectively, in the mono-phase mixture with the sample. The m/z range from 600-1000 is displayed.

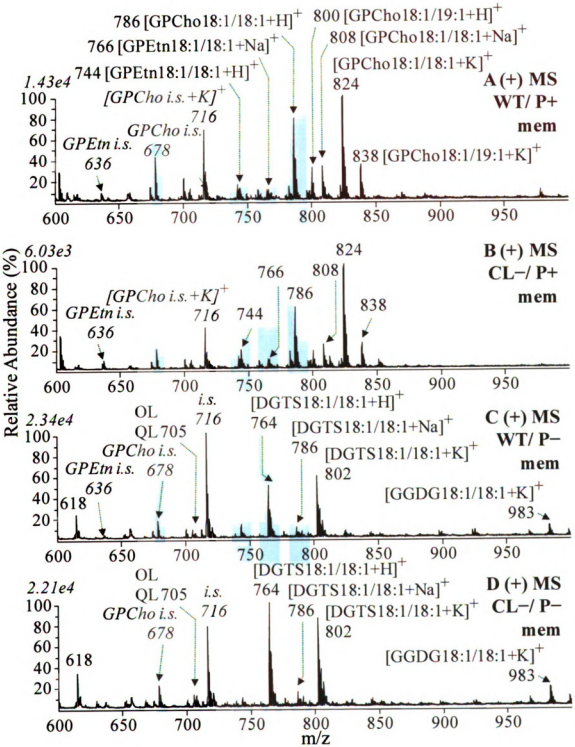

786 [GPCho18:1/18:1+H]+
800 [GPCho18:1/19:1+H]+
766 [GPEtn18:1/18:1+Na]+
808 [GPCho18:1/18:1+Na]+
744 [GPEtn18:1/18:1+H]+
[GPCho18:1/18:1+K]+
824
1.43e4
[GPCho i.s.+K]+
716
GPCho i.s.
678
GPEtn i.s.
636
838 [GPCho18:1/19:1+K]+
A (+) MS
WT/ P+
mem
6.03e3
824
B (+) MS
CL−/ P+
mem
766
808
786
[GPCho i.s.+K]+
716
744
838
GPEtn i.s.
636
Relative Abundance (%)
i.s.
716
[DGTS18:1/18:1+H]+
2.34e4
OL
QL 705
764
[DGTS18:1/18:1+Na]+
C (+) MS
WT/ P−
mem
GPCho i.s.
678
786
[DGTS18:1/18:1+K]+
GPEtn i.s.
636
802
618
[GGDG18:1/18:1+K]+
983
[DGTS18:1/18:1+H]+
2.21e4
OL
QL 705
i.s.
716
764
[DGTS18:1/18:1+Na]+
D (+) MS
CL−/ P−
mem
GPCho i.s.
678
786
[DGTS18:1/18:1+K]+
802
618
[GGDG18:1/18:1+K]+
983
m/z

Figure 10.12 Negative ion mode MALDI MS spectra of the same amount of isolated membranes (1 μL at 0.25 mg/mL final membrane protein concentrations determined by BCA assay) of *R. sphaeroides* 169-2.4.1 grown under normal phosphate (WT/ P+), 169CL3 under normal phosphate (CL−/ P+), 169-2.4.1 under low phosphate (WT/ P−), and 169CL3 under low P (CL−/ P−), with the presence of the lipid internal standards of GPEtn 14:0/14:0, GPGro14:0/14:0, GPCho 14:0/14:0 and CL $(14:0)_4$ at final concentrations of 10, 5, 1.25 and 1.25 μM in the mono-phase mixture with the sample. The m/z range from 600-1000 is displayed.

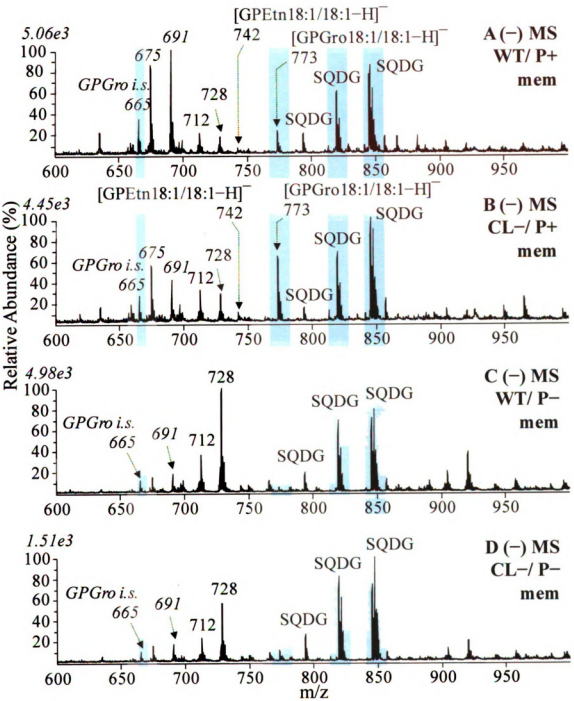
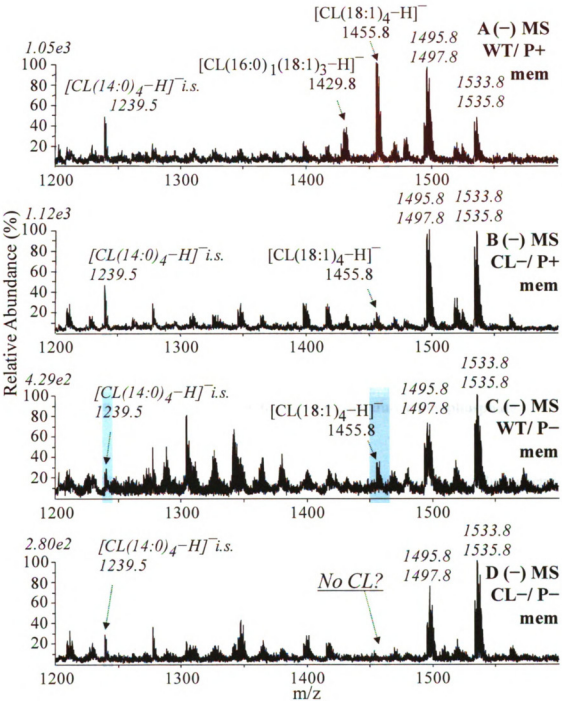

[GPEtn18:1/18:1−H]⁻
[GPGro18:1/18:1−H]⁻
5.06e3
691
742
675
773
SQDG
SQDG
GPGro i.s.
665
728
712
SQDG
A (−) MS
WT/ P+
mem
4.45e3
[GPEtn18:1/18:1−H]⁻
[GPGro18:1/18:1−H]⁻
742
773
SQDG
B (−) MS
CL−/ P+
mem
675
728
GPGro i.s.
691
712
665
SQDG
Relative Abundance (%)
4.98e3
728
C (−) MS
WT/ P−
mem
SQDG
SQDG
GPGro i.s.
665
691
712
SQDG
1.51e3
SQDG
D (−) MS
CL−/ P−
mem
SQDG
728
GPGro i.s.
665
691
712
SQDG
600
650
700
750
800
850
900
950
m/z

Figure 10.13 Negative ion mode MALDI MS spectra in the m/z range from 1200-1600, for the same amount of isolated membranes (1 μL at 0.25 mg/mL final membrane protein concentrations determined by BCA assay) of WT (169-2.4.1) and CL− (169CL3) *R. sphaeroides* grown under the same set of conditions as in Figure 10.12, with the lipid internal standards of GPEtn 14:0/14:0, GPGro 14:0/14:0, GPCho 14:0/14:0 and CL $(14:0)_4$ at final concentrations of 10, 5, 1.25 and 1.25 μM in the mono-phase mixture with the sample, respectively.


A (−) MS
WT/ P+
mem
B (−) MS
CL−/ P+
mem
C (−) MS
WT/ P−
mem
D (−) MS
CL−/ P−
mem
[CL(18:1)4−H]−
1455.8
[CL(16:0)1(18:1)3−H]−
1429.8
[CL(14:0)4−H]− i.s.
1239.5
1495.8
1497.8
1533.8
1535.8
No CL?
Relative Abundance (%)
m/z

Likewise, the negative ion mode MALDI MS (Figure 10.12) also reveals the partial retention of GPGro lipids, and the increase in SQDG, particularly in the saturated SQDG species, in response to the low-phosphate growth. The m/z 1200-1600 region of the MS in negative ion mode in Figure 10.13 shows that CL can be detected for the wild type sample grown under phosphate-limiting conditions (WT/ P−) at 64 % of the level of CL in WT/ P+, and in the CL-deficient mutant under normal phosphate growth conditions (CL−/ P+) at 21 % of the level of CL in WT/ P+ , but cannot be detected in the CL-deficient mutant under low-phosphate growth conditions (CL−/ P−), due to a much decreased quantity. This shows a higher sensitivity of MALDI for detection of cardiolipin, compared to the ESI, under the conditions applied.

10.3.5 MALDI analysis of lipids in purified C*c*O grown under low-phosphate conditions

The comparison of the MALDI MS spectra of the membrane including internal standards with those of the ESI MS and MS/MS shows that the MALDI analysis method can yield valid quantitative results by including internal standards, and running triplicate experiments. Furthermore, when working with purified enzyme with high levels of detergent, it offers a significant advantage.

The MALDI MS spectra of the C*c*O purified by Ni-NTA FPLC from the *R. sphaeroides* 169-2.4.1 and 169CL3 grown under normal phosphate (WT/ P and CL−/ P+), and under low phosphate (WT/ P− and CL−/ P−), containing phospholipid internal standards, are shown in Figure 10.14 (positive ion mode MS), Figure 10.15 (negative ion mode MS in the region of m/z 600-1000) and Figure 10.16 (negative ion mode in the

region of m/z 1200-1600). The interpretation of the MALDI is still made difficult by the detergent peaks, and the quantification capability is still low. Nonetheless, the inclusion of internal standards provides a relatively quantitative picture of the alterations in the lipid compositions in these four different samples.

Figure 10.14 Positive ion mode MALDI MS spectra of the same amount of purified C*c*O (1 μL at 0.5 mg/mL final C*c*O concentrations determined by UV-Vis spectroscopy) of WT (169-2.4.1) and CL− (169CL3) *R. sphaeroides* grown under normal phosphate (WT/ P+), (CL−/ P+), and low phosphate (WT/ P−), (CL−/ P−), with the presence of the lipid internal standards of GPEtn 14:0/14:0, GPGro 14:0/14:0, GPCho 14:0/14:0 and CL $(14:0)_4$ at final concentrations of 10, 5, 1.25 and 1.25 μM in a mono-phase mixture with the sample, respectively. The relative abundance in the m/z range of 706-830 is expanded 4 fold in all four panels for a clearer display of the lipids peaks.

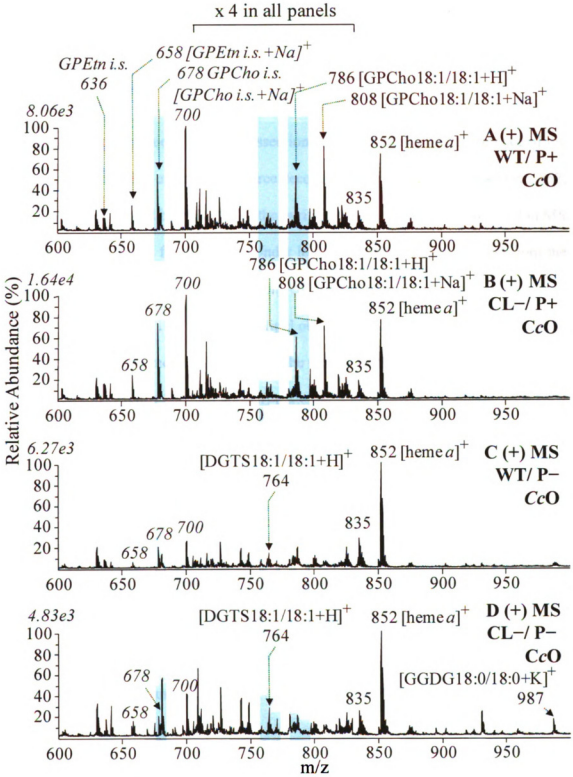

x 4 in all panels
GPEtn i.s.
636
658 [GPEtn i.s.+Na]+
678 GPCho i.s.
[GPCho i.s.+Na]+
786 [GPCho18:1/18:1+H]+
808 [GPCho18:1/18:1+Na]+
8.06e3
700
852 [heme a]+
A (+) MS
WT/ P+
CcO
835
1.64e4
B (+) MS
CL−/ P+
CcO
678
658
6.27e3
[DGTS18:1/18:1+H]+
764
C (+) MS
WT/ P−
CcO
4.83e3
D (+) MS
CL−/ P−
CcO
[GGDG18:0/18:0+K]+
987
Relative Abundance (%)
m/z

Figure 10.14 shows that in the positive ion mode MS of the purified CcO from the normal-phosphate growth of the WT (WT/ P+) (Figure 10.14A) and the CL-deficient mutant (CL−/ P+) (Figure 10.14B), the phospholipid GPCho 18:1/18:1 is the major component (shown as protonated ions and sodium adduct ions). The GPEtn lipid peaks are not observed partly due to the suppressed ionization efficiency in the presence of the detergents and the higher extent of in-source decomposition. The heme *a* peaks (m/z 852, 835; structures confirmed by MS/MS) of the purified C*c*O can be clearly observed in MS at high abundance for all four samples. Under low-phosphate growth, the C*c*O from the two strains (WT/ P+) and (CL−/ P+) displayed no detectable GPCho, but a new non-phospholipid DGTS 18:1/18:1 became the lipid observed at the highest ion abundance.

The negative ion mode MS spectra of the C*c*O from the normal-phosphate growth of WT (WT/ P+) (Figure 10.15A) and CL-deficient mutant (CL−/ P+) (Figure 10.15B) show that the GPGro 18:1/18:1 and a series of SQDG lipids are retained in the purified C*c*O, and by referring to the GPGro internal standard at m/z 665, the GPGro18:1/18:1 lipid level can be seen to increase in CL−/ P+, compared to WT/ P+, which is consistent with the results by ESI analysis following lipid extraction. However, under low-phosphate growth, C*c*O from WT/ P− still shows the existence of GPGro 18:1/18:1 at about 50% of the level of GPGro in WT/ P+, by referring to the GPGro 14:0/14:0 internal standard (Figure 10.15C), but it is not clearly resolved in the CL−/ P− sample (Figure 10.15D). SQDG lipids can be observed in both the WT/ P− and the CL− / P− C*c*O samples.

Figure 10.15 Negative ion mode MALDI MS spectra of the same amount of purified C*c*O (1 μL at 0.5 mg/mL final C*c*O concentrations determined by UV-Vis spectroscopy) from WT (169-2.4.1) and CL− (169CL3) *R. sphaeroides* grown as described previously, with the presence of the lipid internal standards of GPEtn 14:0/14:0, GPGro 14:0/14:0, GPCho 14:0/14:0 and CL $(14:0)_4$ at final concentrations of 10, 5, 1.25 and 1.25 μM in the mono-phase mixture with the sample, respectively. The relative abundances in the m/z ranges of 700-850 and 660-670, are expanded 4 fold in all four panels for a clearer display of the lipids and the internal standards peaks.

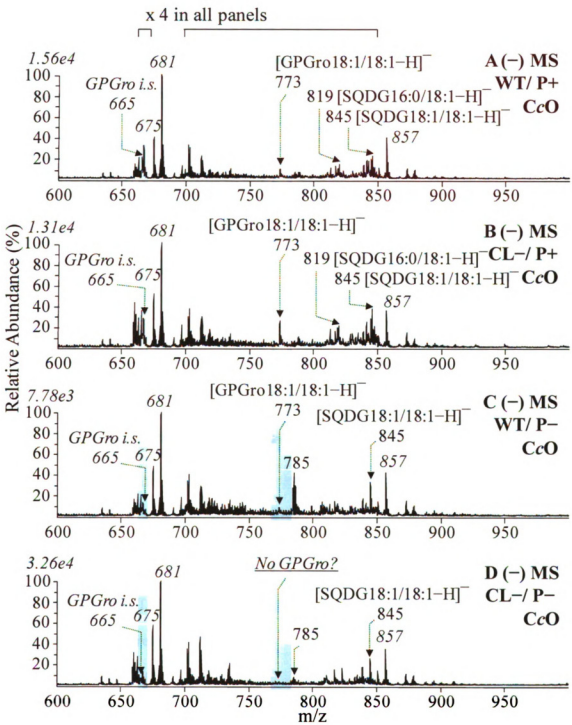
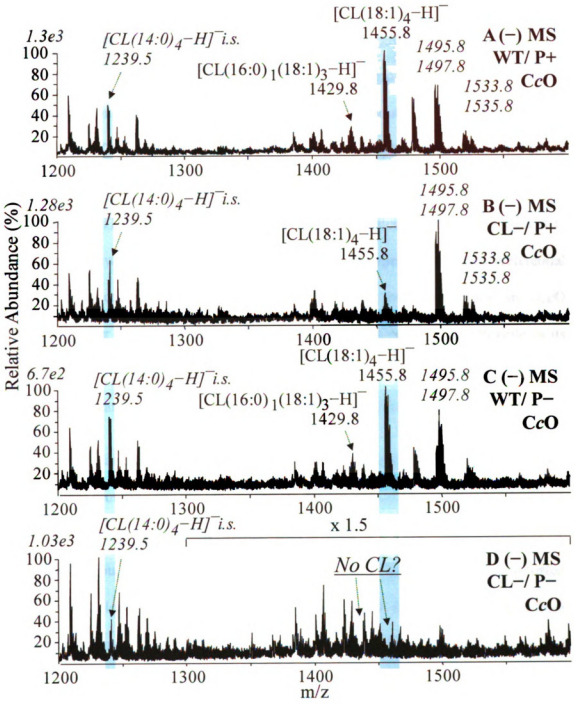

x 4 in all panels
1.56e4
681
[GPGro18:1/18:1−H]−
A (−) MS
WT/ P+
CcO
GPGro i.s.
665
675
773
819 [SQDG16:0/18:1−H]−
845 [SQDG18:1/18:1−H]−
857
1.31e4
681
[GPGro18:1/18:1−H]−
B (−) MS
CL−/ P+
CcO
GPGro i.s.
665
675
773
819 [SQDG16:0/18:1−H]−
845 [SQDG18:1/18:1−H]−
857
7.78e3
681
[GPGro18:1/18:1−H]−
C (−) MS
WT/ P−
CcO
GPGro i.s.
665
675
773
[SQDG18:1/18:1−H]−
845
785
857
3.26e4
681
No GPGro?
D (−) MS
CL−/ P−
CcO
GPGro i.s.
665
675
[SQDG18:1/18:1−H]−
845
785
857
Relative Abundance (%)
100
80
60
40
20
600
650
700
750
800
850
900
950
m/z

Figure 10.16 shows the negative ion mode MS spectra of the four C*c*O samples in the mass range of m/z 1200-1600 to display the CL species. In WT/ P+ C*c*O (Figure 10.16A), several CL species are detectable including the most abundant CL $(18:1)_4$ at m/z 1455.8, and the less abundant CL $(16:0)_1(18:1)_3$ at m/z 1429.8, but CL $(18:2)_4$ (expected m/z 1448.8) is not observed to be present here in the *R. sphaeroides* C*c*O. The negatively charged sodium or potassium adduct of CL $(18:1)_4$ could also be observed at m/z 1478.9 and m/z 1494.9, respectively. The abundant ions at 1495.8 and 1497.8, however, displayed characteristic fragmentation behaviors in MS/MS and MS^n that are not related to CL lipids or any known phospholipids (data not shown). In C*c*O from the CL-deficient mutant CL−/ P+ (Figure 10.16B), the level of CL is significantly reduced, but CL $(18:1)_4$ is still observable at low abundance, about ~30% of that in WT/ P+ C*c*O, (compared to 21% of that in WT/P+ for membranes determined by MALDI MS In the low-phosphate growth, however, the WT/ P− C*c*O (Figure 10.16C) contains abundant ions of CL 18:1/18:1 and CL $(16:0)_1(18:1)_3$. By referring to the CL$(14:0)_4$ internal standards, the CL in WT/ P− CcO (Figure 10.16C) is about 70% of the quantity of CL in the WT/ P+ CcO (Figure 10.16D), reflecting the relative CL level in the membranes. In stark contrast, the C*c*O from CL−/ P− contains no detectable CL ions (Figure 10.16D), also consistent with its membrane content of CL.

Figure 10.16 Negative ion mode MALDI MS spectra in the m/z range from 1200-1600, of the same amount of purified C*c*O (1μL at 0.5 mg/mL final C*c*O concentrations determined by UV-Vis spectroscopy) of *R. sphaeroides* 169-2.4.1 grown under normal phosphate (WT/ P+), 169CL3 under normal phosphate (CL−/ P+), 169-2.4.1 under low phosphate (WT/ P−), and 169CL3 under low P (CL−/ P−), with the presence of the lipid internal standards of GPEtn 14:0/14:0, GPGro 14:0/14:0, GPCho 14:0/14:0 and CL $(14:0)_4$ at final concentrations of 10, 5, 1.25 and 1.25 μM in the mono-phase mixture with the sample, respectively. In panel D, The relative abundance in the m/z range of 1300-1600 is expanded 1.5 fold for a clearer view of the CL region.


1.3e3
[CL(14:0)4−H]− i.s.
1239.5
[CL(16:0)1(18:1)3−H]−
1429.8
[CL(18:1)4−H]−
1455.8
1495.8
1497.8
1533.8
1535.8
A (−) MS
WT/ P+
CcO
1.28e3
[CL(14:0)4−H]− i.s.
1239.5
[CL(18:1)4−H]−
1455.8
1495.8
1497.8
1533.8
1535.8
B (−) MS
CL−/ P+
CcO
Relative Abundance (%)
6.7e2
[CL(14:0)4−H]− i.s.
1239.5
[CL(16:0)1(18:1)3−H]−
1429.8
[CL(18:1)4−H]−
1455.8
1495.8
1497.8
C (−) MS
WT/ P−
CcO
x 1.5
1.03e3
[CL(14:0)4−H]− i.s.
1239.5
No CL?
D (−) MS
CL−/ P−
CcO
m/z

Combining the results seen from both the positive and the negative ion mode MS of the WT and CL− C*c*O under normal and low-phosphate growth conditions, it is clear that, in the wild type sample (WT/ P−), the low-phosphate growth (P−) causes the nearly complete depletion of GPCho from the purified C*c*O, and about 50% depletion in GPGro, but maintained 70% of the level of CL in the normal-phosphate growth, similar to the membrane lipid composition as quantified earlier by ESI. On the other hand, the non-phospholipid DGTS increased and SQDG species can be detected in the C*c*O from WT/ P−. When only low-phosphate growth is applied, the wild type demonstrated preferential synthesis and incorporation of the phospholipid CL in both membrane and C*c*O compared to other lipids such as GPCho, suggesting that C*c*O is highly flexible in its requirement for GPCho or non-phospholipid DGTS, but is less flexible with respect to CL, and demonstrates a priority of CL synthesis and incorporation.

However, in the CL-deficient mutant enzyme sample (CL−/ P−), the combination of CL-deficient mutation and the low-phosphate growth caused nearly complete depletion of not only CL but also GPCho. It resulted in an increase in the non-phospholipid DGTS, depleted GPGro but clearly identifiable SQDG, along with, most importantly, depletion of CL down to below detectable levels. These results suggest that the C*c*O purified from the CL-deficient mutant from low-phosphate growth maintained its native activity and enzyme properties by a means other than the selective enrichment of CL in the isolated enzyme. Even at significantly depleted level of CL, GPGro, and GPCho, the increase in DGTS and SQDG (and probably also QL, which is typically more difficult to detect by MALDI) enables C*c*O to be fully functional.

Therefore, under normal supply of phosphate, C*c*O has preferential specificity for CL lipids. Such a preference can be substitutable by GPGro when CL is not able to be synthesized, but when both GPGro and CL are unavailable, the requirement for CL appears to be successfully replaced by negatively charged non-phospholipids such as SQDG.

10.4 Conclusions

Phosphate-limiting growth conditions caused significant selective changes in the lipid profiles of both the *Rhodobacter* membrane and purified cytochrome c oxidase. The bacteria under limited phosphate conditions display priorities for making different types of lipids. The first priority is the cardiolipin (73% maintained), followed by GPGro (50% maintained), and then GPEtn and GPCho. The latter two lipids probably have an option for substitution with the non-phospholipids DGTS that carry the same fixed positive charge center, suggesting that the fixed positive charge, not the entire molecule, is important. The appreciably increased amount of lipids with saturated fatty acid chains in the remaining GPGro and SQDG in the phosphate-limiting growth could be related to the requirement to strengthen the membranes by increasing the hydrophobic interactions. QL as well as SQDG were found to increase by 2-5 fold in the low-phosphate growth, suggesting their functional substitutability for other lipids. In the end, the phosphate-limiting growth combined with the *cls* mutation produced a much "cleaner" CL-depleted strain. ESI and MALDI MS revealed similar changes in the relative abundances of lipid

species between WT and the mutants in the membrane of the bacteria, the CL levels being reduced to 0-0.9% in the membrane and purified enzyme.

However, the purified bacterial *R. sphaeroides* C*c*O demonstrated limited sensitivity to the modified lipid environment, in terms of subunit composition, enzyme activity, expression level or stability during purification. While the wild type P− C*c*O maintained 70% of the CL level compared to normal-phosphate growth, reflecting significant selection ability of the bacteria for CL compared to other phospholipids level in the membranes, the combination of CL-deficiency with P− growth created a C*c*O that was essentially completely depleted in CL, but fully active. Therefore the significant lack of CL did not appreciably affect the assembly of C*c*O in the CL-deficient mutant or the activity of the purified enzyme.

These findings suggest that, first of all, CL is not essential for the active form of bacterial C*c*O *per se* even though C*c*O has a preference of incorporating CL. Instead, C*c*O displays some level of flexibility for a CL requirement, which can be fulfilled by GPGro, when available. Second, the requirement for CL is not only satisfied by GPGro lipids with high structural similarity to CL, but can also be satisfied with non-phospholipids such as SQDG, and potentially QL as well, when phospholipids are not available at sufficient amount.

CL in bacteria ($CL(18:1)_4$) seems to function via mechanisms different from mammalian systems ($CL(18:2)_4$) [8,21]. Further insight of the role of lipids in C*c*O might be gained from examination of the crystal structures (Chapter 9).

BIBLIOGRAPHY

BIBLIOGRAPHY

1. Palsdottir H, Hunte C. Lipids in membrane protein structures. *Biochim Biophys Acta, Biomembr* **2004**; *1666*: 2-18

2. Engelman DM. Membranes are more mosaic than fluidic. *Nature* **2005**; *438*: 578-580

3. IUPAC-IUB. IUPAC-IUB commision on biochemical nomenclature. The nomenclature of lipids. *Biochem J* **1978**; *171*: 21-35

4. Fahy E, Subramaniam S, Brown HA, Glass CK, Merrill AH, Jr., Murphy RC, Raetz CRH, Russell DW, Seyama Y, Shaw W, Shimizu T, Spener F, van Meer G, VanNieuwenhze MS, White SH, Witztum JL, Dennis EA. A comprehensive classification system for lipids. *J Lipid Res* **2005**; *46*: 839-862

5. Kaltashov IA, Doroshenko V, Cotter RJ, Takayama K, Qureshi N. Confirmation of the structure of lipid A derived from the lipopolysaccharide of *Rhodobacter sphaeroides* by a combination of MALDI, LSIMS and tandem mass spectrometry. *Anal Chem* **1997**; *69*: 2317-2322

6. Garavito RM, Ferguson-Miller S. Detergents as tools in membrane biochemistry. *J Biol Chem* **2001**; *276*: 32403-32406

7. Lopez-Lara IM, Sohlenkamp C, Geiger O. Membrane lipids in plant-associated bacteria: Their biosyntheses and possible functions. *Mol Plant-Microbe Interact* **2003**; *16*: 567-579

8. Chicco AJ, Sparagna GC. Role of cardiolipin alterations in mitochondrial dysfunction and disease. *Am J Physiol* **2007**; *292*: C33-C44

9. Schlame M. Cardiolipin synthesis for the assembly of bacerial and mitochondrial membranes. *J Lipid Res* **2008**; *49*: 1607-1620

10. Schlame M, Rua D, Greenberg ML. The biosynthesis and functional role of cardiolipin. *Prog Lipid Res* **2000**; *39*: 257-288

11. Benning C, Huang Z-H, Gage DA. Accumulation of a novel glycolipid and a betaine lipid in cells of *Rhodobacter sphaeroides* grown under phosphate limitation. *Arch Biochem Biophys* **1995**; *317*: 103-111

12. Schmid P, Kumar V, Weis B, Schmid H. Phosphotidyl Tris rather than N-acylphosphatidylserine is synthesized by *Rhodopseudomonas sphaeroides* grown in Tris-containing media. *Biochemistry* **1991**; *30*: 1746-1751

13. Tamot B, Benning C. Membrane lipid biosynthesis in purple bacteria. *The Purple Phototropic Bacteria* **2008**; *Springer Science and Business Media B.V.*: 119-134

14. Benning C, Beatty JT, Prince RC, Somerville CR. The sulfolipid sulfoquinovosyldiacylglycerol is not required for photosynthetic electron transport in *Rhodobacter sphaeroides* but enhances growth under phosphate limitation. *Proc Natl Acad Sci U S A* **1993**; *90*: 1561-1565

15. Tamot B. Construction and characterization of a cardiolipin-deficient mutant in *Rhodobacter sphaeroides*. In: M.S. Thesis MSU; **2006**

16. Benning C, Somerville CR. Isolation and genetic complementation of a sulfolipid-deficient mutant of *Rhodobacter sphaeroides*. *J Bacteriol* **1992**; *174*: 2352-2360

17. Benning C, Ohta H. Three enzyme systems for galactoglycerolipid biosynthesis are coordinately regulated in plants. *J Biol Chem* **2005**; *280*: 2397-2400

18. Benning C. Genetic mutant screening by direct metabolite analysis. *Anal Biochem* **2004**; *332*: 1-9

19. Dowhan W, Mileykovskaya E, Bogdanov M. Diversity and versatility of lipid-protein interactions revealed by molecular genetic approaches. *Biochim Biophys Acta, Biomembr* **2004**; *1666*: 19-39

20. Gaspar ML, Aregullin MA, Jesch SA, Nunez LR, Villa-Garcia M, Henry SA. The emergence of yeast lipidomics. *Biochim Biophys Acta, Mol Cell Biol Lipids* **2007**; *1771*: 241-254

21. Xu Y, Malhotra A, Ren M, Schlame M. The enzymatic function of tafazzin. *J Biol Chem* **2006**; *281*: 39217-39224

22. Xie J, Bogdanov M, Heacock P, Dowhan W. Phosphatidylethanolamine and monoglucosyldiacylglycerol are interchangeable in supporting topogenesis and function of the polytopic membrane protein lactose permease. *J Biol Chem* **2006**; *281*: 19172-19178

23. Chang S-C, Heacock PN, Mileykovskaya E, Voelker DR, Dowhan W. Isolation and characterization of the gene (CLS1) encoding cardiolipin synthase in Saccharomyces cerevisiae. *J Biol Chem* **1998**; *273*: 14933-14941

24. Garrett RH, Grisham CM. Biochemisry 2nd edition. *Harcourt, Inc* **1999**:

25. Hosler JP, Ferguson-Miller S, Mills DA. Energy transduction: proton transfer through the respiratory complexes. *Annu Rev Biochem* **2006**; *75*: 165-187

26. Schagger H. Respiratory chain supercomplexes. *IUBMB Life* **2001**; *52*: 119-128

27. Qin L, Mills DA, Buhrow L, Hiser C, Ferguson-Miller S. A conserved steroid binding site in cytochrome *c* oxidase. *Biochemistry* **2008**; *47*: 9931-9933

28. Shinzawa-Itoh K, Aoyama H, Muramoto K, Terada H, Kurauchi T, Tadehara Y, Yamasaki A, Sugimura T, Kurono S, Tsujimoto K, Mizushima T, Yamashita E, Tsukihara T, Yoshikawa S. Structures and physiological roles of 13 integral lipids of bovine heart cytochrome *c* oxidase. *EMBO J* **2007**; *26*: 1713-1725

29. Yoshikawa S, Shinzawa-Itoh K, Tsukihara T. X-ray structure and the reaction mechanism of bovine heart cytochrome *c* oxidase. *J Inorg Biochem* **2000**; *82*: 1-7

30. Qin L. X-ray crystallographic studies of cytochrome *c* oxidase from *Rhodobacter sphaeroides*. In, Ph. D. Dissertation MSU; **2005**

31. Mills DA, Ferguson-Miller S. Influence of structure, pH and membrane potential on proton movement in cytochrome oxidase. *Biochim Biophys Acta, Bioenerg* **2002**; *1555*: 96-100

32. Mills DA, Schmidt B, Hiser C, Westley E, Ferguson-Miller S. Membrane potential-controlled inhibition of cytochrome c oxidase by zinc. *J Biol Chem* **2002**; *277*: 14894-14901

33. Hosler JP, Fetter J, Tecklenburg MMJ, Espe M, Lerma C, Ferguson-Miller S. Cytochrome aa3 of Rhodobacter sphaeroides as a model for mitochondrial cytochrome c-oxidase. Purification, kinetics, proton pumping, and spectral analysis. *J Biol Chem* **1992**; *267*: 24264-24272

34. Svensson-Ek M, Abramson J, Larsson G, Tornroth S, Brzezinski P, Iwata S. The x-ray crystal structures of wild-type and EQ(I-286) mutant cytochrome *c* oxidases from *Rhodobacter sphaeroides*. *J Mol Biol* **2002**; *321*: 329-339

35. Qin L, Hiser C, Mulichak A, Garavito RM, Ferguson-Miller S. Identification of conserved lipid/detergent-binding sites in a high-resolution structure of the membrane protein cytochrome c oxidase. *Proc Natl Acad Sci U S A* **2006**; *103*: 16117-16122

36. Tsukihara T, Aoyama H, Yamashita E, Tomizaki T, Yamaguchi H, Shinzawa-Itoh K, Nakashima R, Yaono R, Yoshikawa S. The whole structure of the 13-subunit oxidized cytochrome *c* oxidase at 2.8 Å. *Science (Washington, D C)* **1996**; *272*: 1136-1144

37. Distler AM, Allison J, Hiser C, Qin L, Hilmi Y, Ferguson-Miller SM. Mass spectrometric detection of protein, lipid and heme components of cytochrome *c* oxidase from *R. sphaeroides* and the stabilization of non-covalent complexes from the enzyme. *Eur Mass Spectrom* **2004**; *10*: 295-308

38. Mills DA, Ferguson-Miller S. Proton uptake and release in cytochrome c oxidase: separate pathways in time and space? *Biochim Biophys Acta, Bioenerg* **1998**; *1365*: 46-52

39. Boekema EJ, Braun H-P. Supramolecular Structure of the Mitochondrial Oxidative Phosphorylation System. *J Biol Chem* **2007**; *282*: 1-4

40. Heinemeyer J, Lewejohann D, Braun H-P. Blue-native gel electrophoresis for the characterization of protein complexes in plants. *Methods Mol Biol (Totowa, NJ, U S)* **2007**; *355*: 343-352

41. Heinemeyer J, Braun H-P, Boekema EJ, Kouril R. A structural model of the cytochrome c reductase/oxidase supercomplex from yeast mitochondria. *J Biol Chem* **2007**; *282*: 12240-12248

42. Ferguson-Miller S, Hochman J, Schindler M. Aggregation and diffusion in the mitochondrial electron-transfer chain: role in electron flow and energy transfer. *Biochem Soc Trans* **1986**; *14*: 822-824

43. Dudkina NV, Heinemeyer J, Sunderhaus S, Boekema EJ, Braun H-P. Respiratory chain supercomplexes in the plant mitochondrial membrane. *Trends Plant Sci* **2006**; *11*: 232-240

44. Saddar S, Dienhart MK, Stuart RA. The F_1F_O-ATP synthase complex influences the assembly state of the cytochrome bc_1-cytochrome oxidase supercomplex and its association with the TIM23 machinery. *J Biol Chem* **2008**; *283*: 6677-6686

45. Shen H, Walters DE, Mueller DM. Introduction of the chloroplast redox regulatory region in the yeast atp synthase impairs cytochrome *c* oxidase. *J Biol Chem* **2008**; *283*: 6677-6686

46. Wittig I, Schagger H. Structural organization of mitochondrial ATP synthase. *Biochim Biophys Acta* **2008**; *1777*: 592-598

47. Stuart RA. Supercomplex organization of the oxidative phosphorylation enzymes in yeast mitochondria. *J Bioenerg Biomembr* **2008**; *40*: 411-417

48. Dudkina NV, Sunderhaus S, Boekema EJ, Braun H-P. The higher level of organiation of the oxidative phosphorylation system: mitochondrial supercomplexes. *J Bioenerg Biomembr* **2008**; *40*: 419-424

49. Schagger H, de Coo R, Bauer MF, Hofmann S, Godinot C, Brandt U. Significance of respirasomes for the assembly/stability of human respiratory chain complex I. *J Biol Chem* **2004**; *279*: 36349-36353

50. Schagger H, Pfeiffer K. Supercomplexes in the respiratory chains of yeast and mammalian mitochondria. *EMBO J* **2000**; *19*: 1777-1783

51. Wittig I, Carrozzo R, Santorelli Filippo M, Schagger H. Supercomplexes and subcomplexes of mitochondrial oxidative phosphorylation. *Biochim Biophys Acta* **2006**; *1757*: 1066-1072

52. Lange C, Nett JH, Trumpower BL, Hunte C. Specific roles of protein-phospholipid interactions in the yeast cytochrome bc1 complex structure. *EMBO J* **2001**; *20*: 6591-6600

53. Awasthi YC, Chuang TF, Keenan TW, Crane FL. Tightly bound cardiolipin in cytochrome oxidase. *Biochim Biophys Acta* **1971**; *226*: 42-52

54. Gomez B, Jr., Robinson NC. Phospholipase digestion of bound cardiolipin reversibly inactivates bovine cytochrome bc1. *Biochemistry* **1999**; *38*: 9031-9038

55. Schagger H, Hagen T, Roth B, Brandt U, Link TA, von Jagow G. Phospholipid specificity of bovine heart bc_1 complex. *Eur J Biochem* **1990**; *190*: 123-130

56. White SH, Ladokhin AS, Jayasinghe S, Hristova K. How membranes shape protein structure *J Biol Chem* **2001**; *276*: 32395-32398

57. Robinson NC, Zborowski J, Talbert LH. Cardiolipin-depleted bovine heart cytochrome *c* oxidase: binding stoichiometry and affinity for cardiolipin derivatives. *Biochemistry* **1990**; *29*: 8962-8969

58. Qin L, Sharpe MA, Garavito RM, Ferguson-Miller S. Conserved lipid-binding sites in membrane proteins: a focus on cytochrome c oxidase. *Curr Opin Struct Biol* **2007**; *17*: 444-450

59. Zhang M, Mileykovskaya E, Dowhan W. Cardiolipin is essential for organization of complexes III and IV into a supercomplex in intact yeast mitochondria. *J Biol Chem* **2005**; *280*: 29403-29408

60. Yamaoka-Koseki S, Urade R, Kito M. Cardiolipins from rats fed different dietary lipids affect bovine heart cytochrome *c* oxidase activity. *J Nutr* **1991**; *121*: 956-958

61. Schlame M, Greenberg ML. Cardiolipin synthase from yeast. *Biochim Biophys Acta* **1997**; *1348*: 201-206

62. Zhao M, Schlame M, Rua D, Greenberg ML. Cardiolipin synthase is associated with a large complex in yeast mitochondria. *J Biol Chem* **1998**; *273*: 2402-2408

63. Camara-Artigas A, Brune D, Allen JP. Interactions between lipids and bacterial reaction centers determined by protein crystallography. *Proc Natl Acad Sci U S A* **2002**; *99*: 11055-11060

64. Schagger H. Respiratory chain supercomplexes of mitochondria and bacteria. *Biochim Biophys Acta, Bioenerg* **2002**; *1555*: 154-159

65. Zhang M, Mileykovskaya E, Dowhan W. Gluing the respiratory chain together. Cardiolipin is required for supercomplex formation in the inner mitochondrial membrane *J Biol Chem* **2002**; *277*: 43553-43556

66. Pfeiffer K, Gohil V, Stuart Rosemary A, Hunte C, Brandt U, Greenberg Miriam L, Schagger H. Cardiolipin stabilizes respiratory chain supercomplexes. *J Biol Chem* **2003**; *278*: 52873-52880

67. McMillin JB, Dowhan W. Cardiolipin and apoptosis. *Biochim Biophys Acta, Mol Cell Biol Lipids* **2002**; *1585*: 97-107

68. Sparagna GC, Chicco AJ, Murphy RC, Bristow MR, Johnson CA, Rees ML, Maxey ML, McCune SA, Moore RL. Loss of cardiac tetralinoleoyl cardiolipin in human and experimental heart failure. *J Lipid Res* **2007**; *48*: 1559-1570

69. Huang Z, Jiang J, Tyurin VA, Zhao Q, Mnuskin A, Ren J, Belikova NA, Feng W, Kurnikov IV, Kagan VE. Cardiolipin deficiency leads to decreased cardiolipin peroxidation and increased resistance of cells to apoptosis. *Free Radical Biol Med* **2008**; *44*: 1935-1944

70. Sparagna GC, Johnson CA, McCune SA, Moore RL, Murphy RC. Quantitation of cardiolipin molecular species in spontaneously hypertensive heart failure rats using electrospray ionization mass spectrometry. *J Lipid Res* **2005**; *46*: 1196-1204

71. Jiang F, Rizavi HS, Greenberg ML. Cardiolipin is not essential for the growth of Saccharomyces cerevisiae on fermentable or non-fermentable carbon sources. *Mol Microbiol* **1997**; *26*: 481-491

72. Landau EM, Rosenbusch JP. Lipidic cubic phases: a novel concept for the crystallization of membrane proteins. *Proc Natl Acad Sci U S A* **1996**; *93*: 14532-14535

73. Zhang H, Kurisu G, Smith JL, Cramer WA. A defined protein-detergent-lipid complex for crystallization of integral membrane proteins: The cytochrome b6f complex of oxygenic photosynthesis. *Proc Natl Acad Sci U S A* **2003**; *100*: 5160-5163

74. Toyoshima C, Nakasako M, Nomura H, Ogawa H. Crystal structure of the calcium pump of *Sarcoplasmic reticulum* at 2.6 Å resolution. *Nature (London)* **2000**; *405*: 647-655

75. Thompson DA. Cytochrome *c* oxidase purified by affinity chromatography in laurylmaltoside: the effects of detergent, lipid depletion, and subunit III removal on function. In: Ph. D. Dissertation MSU; **1984**

76. Marone PA, Thiyagarajan P, Wagner AM, Tiede DM. Effect of detergent alkyl chain length on crystallization of a detergent-solubilized membrane protein: correlation of protein-detergent particle size and particle-particle interaction with crystallization of the photosynthetic reaction center from Rhodobacter sphaeroides. *J Crystal Growth* **1999**; *207*: 214-225

77. Hiser C, Mills DA, Schall M, Ferguson-Miller S. C-Terminal Truncation and Histidine-Tagging of Cytochrome c Oxidase Subunit II Reveals the Native Processing Site, Shows Involvement of the C-Terminus in Cytochrome c Binding, and Improves the Assay for Proton Pumping. *Biochemistry* **2001**; *40*: 1606-1615

78. Ferguson-Miller S, VanAken T, Rosevear P. Effects of alkyl glycoside detergents on the physical and kinetic properties of cytochrome oxidase. *Electron Transp Oxygen Util, [Int Symp Interact Iron Proteins Oxygen Electron Transp]* **1982**: 297-303

79. Thompson DA, Suarez-Villafane M, Ferguson-Miller S. The active form of cytochrome c oxidase. Effects of detergent, the intact membrane, and radiation inactivation. *Biophys J* **1982**; *37*: 285-293

80. le Maire M, Champeil P, Møller JV. Interaction of membrane proteins and lipids with solubilizing detergents. *Biochim Biophys Acta, Biomembr* **2000**; *1508*: 86-111

81. Luecke H, Schobert B, Richter H-T, Cartailler J-P, Lanyi JK. Structure of bacteriorhodopsin at 1.55 Å resolution *J Mol Biol* **1999**; *291*: 899-911

82. Kolbe M, Besir H, Essen L-O, Oesterhelt D. Structure of the light-driven chloride pump halorhodopsin at 1.8 Å resolution. *Science* **2000**; *288*: 1390-1396

83. Gordeliy VI, Labahn J, Moukhametzianov R, Efremov R, Granzin J, Schlesinger R, Bueldt G, Savopol T, Scheidig AJ, Klare JP, Engelhard M. Molecular basis of transmembrane signalling by sensory rhodopsin II-transducer complex. *Nature* **2002**; *419*: 484-487

84. Cohen SL, Chait BT. Mass spectrometry as a tool for protein crystallography. *Annu Rev Biophys Biomol Struct* **2001**; *30*: 67-85

85. Cristoni S, Bernardi LR. Development of new methodologies for the mass spectrometry study of bioorganic macromolecules. *Mass Spectrom Rev* **2003**; *22*: 369-406

86. Marsh D. Electron spin resonance in membrane research: Protein-lipid interactions. *Methods* **2008**; *46*: 83-96

87. Marsh D. Protein modulation of lipids, and vice-versa, in membranes. *Biochim Biophys Acta, Biomembr* **2008**; *1778*: 1545-1575

88. Schiller J, Zschornig O, Petkovic M, Muller M, Arnhold J, Arnold K. Lipid analysis of human HDL and LDL by MALDI-TOF mass spectrometry and ^{31}P-NMR. *J Lipid Res* **2001**; *42*: 1501-1508

89. Byrdwell WC, Sato H, Schwarz AK, Borchman D, Yappert MC, Tang D. ^{31}P NMR quantification and monophasic solvent purification of human and bovine lens phospholipids. *Lipids* **2002**; *37*: 1087-1092

90. Arondel V, Benning C, Somerville CR. Isolation and functional expression in *Escherichia coli* of a gene encoding phosphatidylethanolamine methyltransferase (EC 2.1.1.17) from *Rhodobacter sphaeroides*. *J Biol Chem* **1993**; *268*: 16002-16008

91. Wriessnegger T, Gübitz G, Leinter E, Ingolic E, Cregg J, de la Cruz B, Daum G. Lipid composition of peroxisomes from the yeast *Pichia pastoris* grown on different carbon sources. *Biochim Biophys Acta* **2007**; *1771*: 455-461

92. Cipak A, Jaganjac M, Tehlivets O, Kohlwein SD, Zarkovic N. Adaptation to oxidative stress induced by polyunsaturated fatty acids in yeast. *Biochim Biophys Acta* **2008**; *1781*: 283-287

93. Lopez-Lara IM, Gao J-L, Soto MJ, Solares-Perez A, Weissenmayer B, Sohlenkamp C, Verroios GP, Thomas-Oates J, Geiger O. Phosphorus-free membrane lipids of *Sinorhizobium meliloti* are not required for the symbiosis with alfalfa but contribute to increased cell yields under phosphorus-limiting conditions of growth. *Mol Plant-Microbe Interact* **2005**; *18*: 973-982

94. Cullen J, Phillips MC, Shipley GG. Effects of temperature on the composition and physical properties of the lipids of *Pseudomonas fluorescens*. *Biochem J* **1971**; *125*: 733-742

95. Taylor CJ, Anderson AJ, Wilkinson SG. Phenotypic variation of lipid composition in *Burkholderia cepacia*: a response to increased growth temperature is a greater content of 2-hydroxy acids in phosphatidylethanolamine and ornithine amide lipid. *Microbiology (Reading, U K)* **1998**; *144*: 1737-1745

96. Hara H, Cotter RJ. Assessment of the effect of growth temperature on the lipid composition of *Serratia marcescens* using laser desorption mass spectrometry. *Rapid Commun Mass Spectrom* **1987**; *1*: 103-104

97. Lopalco P, Lobasso S, Babudri F, Corcelli A. Osmotic shock stimulates de novo synthesis of two cardiolipins in an extreme halophilic archaeon. *J Lipid Res* **2004**; *45*: 194-201

98. de Leo V, Catucci L, Ventrella A, Milano F, Agostiano A, Corcelli A. Cardiolipin increases in chromatophores isolated from *Rhodobacter sphaeroides* after osmotic stress: Structural and functional roles. *J Lipid Res* **2008**: published online ahead of print

99. Rossak M, Schafer A, Xu N, Gage DA, Benning C. Accumulation of sulfoquinovosyl-1-O-dihydroxyacetone in a sulfolipid-deficient mutant of *Rhodobacter sphaeroides* inactivated in sqdC. *Arch Biochem Biophys* **1997**; *340*: 219-230

100. Lin YY. Chemical ionization mass spectrometry of steroids and other lipids. *Mass Spectrom Rev* **1984**; *3*: 319-355

101. Schiller J, Arnhold J, Benard S, Muller M, Reichl S, Arnold K. Lipid analysis by matrix-assisted laser desorption and ionization mass spectrometry: a methodological approach. *Anal Biochem* **1999**; *267*: 46-56

102. Tomer KB, Crow FW, Knoche HW, Gross ML. Fast atom bombardment and mass spectrometry/mass spectrometry for analysis of a mixture of ornithine-containing lipids from *Thiobacillus thiooxidans*. *Anal Chem* **1983**; *55*: 1033-1036

103. Cole MJ, Enke CG. Direct determination of phospholipid structures in microorganisms by fast atom bombardment triple quadrupole mass spectrometry. *Anal Chem* **1991**; *63*: 1032-1038

104. Heller DN, Murphy CM, Cotter RJ, Fenselau C, Uy OM. Constant neutral loss scanning for the characterization of bacterial phospholipids desorbed by fast atom bombardment. *Anal Chem* **1988**; *60*: 787-2791

105. Heller DN, Cotter RJ, Fenselau C. Profiling of bacteria by fast atom bombardment mass spectrometry. *Anal Chem* **1987**; *59*: 2806-2809

106. Geiger O, Rohrs V, Weissenmayer B, Finan TM, Thomas-Oates JE. The regulator gene phoB mediates phosphate stress-controlled synthesis of the membrane lipid diacylglyceryl-N,N,N-trimethylhomoserine in *Rhizobium* (*Sinorhizobium*) *meliloti*. *Mol Microbiol* **1999**; *32*: 63-73

107. Cerny RL, Tomer KB, Gross ML. Desorption ionization combined with tandem mass spectrometry: advantages for investigating complex lipids, disaccharides and organometallic complexes. *Org Mass Spectrom* **1986**; *21*: 655-660

108. Gage DA, Huang ZH, Benning C. Comparison of sulfoquinovosyl diacylglycerol from spinach and the purple bacterium *Rhodobacter sphaeroides* by fast atom bombardment tandem mass spectrometry. *Lipids* **1992**; *27*: 632-636

109. Riekhof WR, Ruckle ME, Lydic TA, Sears BB, Benning C. The sulfolipids 2'-O-acyl-sulfoquinovosyldiacylglycerol and sulfoquinovosyldiacylglycerol are absent from a *Chlamydomonas reinhardtii* mutant deleted in SQD1. *Plant Physiol* **2003**; *133*: 864-874

110. Han X, Gross RW. Shotgun lipidomics: electrospray ionization mass spectrometric analysis and quantitation of cellular lipidomes directly from crude extracts of biological samples. *Mass Spectrom Rev* **2005**; *24*: 367-412

111. Watson AD. Lipidomics: a global approach to lipid analysis in biological systems. *J Lipid Res* **2006**; *47*: 2101-2111

112. Manicke NE, Wiseman JM, Ifa DR, Cooks RG. Desorption Electrospray Ionization (DESI) Mass Spectrometry and Tandem Mass Spectrometry (MS/MS) of Phospholipids and Sphingolipids: Ionization, Adduct Formation, and Fragmentation. *J Am Soc Mass Spectrom* **2008**; *19*: 531-543

113. Marto JA, White FM, Seldomridge S, Marshall AG. structural characterization of phospholipids by matrix-assisted laser desorption/ionization Fourier transform ion cyclotron resonance mass spectrometry. *Anal Chem* **1995**; *67*: 3979-3984

114. Fujiwaki T, Yamaguchi S, Sukegawa K, Taketomi T. Application of delayed extraction matrix-assisted laser desorption ionization time-of-flight mass spectrometry for analysis of sphingolipids in tissues from sohingolipidosis patients. *J Chromatogr B* **1999**; *731*: 45-52

115. Schiller J, Suess R, Arnhold J, Fuchs B, Lessig J, Mueller M, Petkovic M, Spalteholz H, Zschoernig O, Arnold K. Matrix-assisted laser desorption and ionization time-of-flight (MALDI-TOF) mass spectrometry in lipid and phospholipid research. *Prog Lipid Res* **2004**; *43*: 449-488

116. Han X, Gross RW. Structural determination of picomole amounts of phospholipids via electrospray ionization tandem mass spectrometry. *J Am Soc Mass Spectrom* **1995**; *6*: 1202-1210

117. Pulfer M, Murphy RC. Electrospray mass spectrometry of phospholipids. *Mass Spectrom Rev* **2003**; *22*: 332-364

118. Schiller J, Suss R, Petkovic M, Zschornig O, Arnold K. Negative-ion matrix-assisted laser desorption and ionization time-of-flight mass spectra of complex phospholipid mixtures in the presence of phosphatidylcholine: a cautionary note on peak assignment. *Anal Biochem* **2002**; *309*: 311-314

119. Gusev AI, Vasseur OJ, Proctor A, Sharkey AG, Hercules DM. Imaging of thin-layer chromatograms using matrix-assisted laser desorption/ionization mass spectrometry. *Anal Chem* **1995**; *67*: 4565-4570

120. Guittard J, Hronowski XL, Costello CE. Direct matrix-assisted laser desorption/ionization mass spectrometry analysis of glycosphingolipids on thin layer chromatographic plates and transfer membranes. *Rapid Commun Mass Spectrom* **1999**; *13*: 1838-1849

121. McDonnell LA, Heeren RMA. Imaging mass spectrometry. *Mass Spectrom Rev* **2007**; *26*: 606-643

122. Puolitaival SM, Burnum KE, Cornett DS, Caprioli RM. Solvent-free matrix dry-coating for MALDI imaging of phospholipids. *J Am Soc Mass Spectrom* **2008**; *19*: 882-886

123. Caprioli RM. Perspectives on imaging mass spectrometry in biology and medicine. *Proteomics* **2008**; *8*: 3679-3680

124. Caprioli RM, Farmer TB, Gile J. Molecular imaging of biological samples: localization of peptides and proteins using MALDI-TOF MS. *Anal Chem* **1997**; *69*: 4751-4760

125. Schwartz SA, Caprioli RM. Molecular imaging by mass spectrometry. *Med Appl Mass Spectrom* **2008**: 533-554

126. Basile F, Beverly MB, Abbas-Hawks C, Mowry CD, Voorhees KJ, L. HT. Direct mass spectrometric analysis of in situ thermally hydrolyzed and methylated lipids from whole bacterial cells. *Anal Chem* **1998**; *70*: 1555-1562

127. Ishida Y, Nakanishi O, Hirao S, Tsuge S, Urabe J, Sekino T, Nakanishi M, Kimoto T, Ohtani H. Direct analysis of lipids in single zooplankter individuals by matrix-assisted laser desorption/ionization mass spectrometry. *Anal Chem* **2003**; *75*: 4514-4518

128. Smith PBW, Snyder AP, Harden CS. Characterization of bacterial phospholipids by electrospray ionization tandem mass spectrometry. *Anal Chem* **1995**; *67*: 1824-1830

129. Petković M, Schiller J, Müller J, Müller M, Arnold K, Arnhold J. The signal-to-noise ratio as the measure for the quantification of lysophospholipids by matrix-

assisted laser desorption/ionisation time-of-flight mass spectrometry. *Analyst* **2001**; *126*: 1042-1050

130. Sugiyama E, Hara A, Uemura K. A quantitative analysis of serum sulfatide by matrix-assisted laser desorption ionization time-of-flight mass spectrometry with delayed ion extraction. *Anal Biochem* **1999**; *274*: 90-97

131. Vaidyanathan S, Rowland JJ, Kell DB, Goodacre R. Discrimination of aerobic endospore-forming bacteria via electrospray-ionization mass spectrometry of whole cell suspensions. *Anal Chem* **2001**; *73*: 4134-4144

132. Han X, Holtzman DM, McKee DW, Jr. Plasmalogen deficiency in early Alzheimer's disease subjects and in animal models: molecular characterization using electrospray ionization mass spectrometry. *J Neurochem* **2001**; *77*: 1168-1180

133. Keller BO, Li L. Nanoliter solvent extraction combined with microspot MALDI TOF mass spectrometry for the analysis of hydrophobic biomolecules. *Anal Chem* **2001**; *73*: 2929-2936

134. Cheng C, Gross ML, Pittenauer E. Complete Structural Elucidation of Triacylglycerols by Tandem Sector Mass Spectrometry. *Anal Chem* **1998**; *70*: 4417-4426

135. Houjou T, Yamatani K, Imagawa M, Shimizu T, Taguchi R. A shotgun tandem mass spectrometric analysis of phospholipids with normal-phase and/or reverse-phase liquid chromatography/electrospray ionization mass spectrometry. *Rapid Commun Mass Spectrom* **2005**; *19*: 654-666

136. Folch J, Lees M, Stanley GGS. A simple method for the isolation and purification of total lipides from animal tissues. *J Biol Chem* **1957**; *226*: 497-509

137. Bligh EG, Dyer WJ. A rapid method of total lipid extraction and purification. *Can J Biochem Physiol* **1959**; *37*: 911-917

138. Iverson SJ, Lang SLC, Cooper MH. Comparison of the Bligh and Dyer and Folch methods for total lipid determination in a broad range of marine tissue. *Lipids* **2001**; *36*: 1283-1287

139. Katyal SL, Barilaro L, Hanin I. Lipid composition of different areas od murine brain: effects of lipid extraciton procedures. *Lipids* **1985**; *20*: 201-203

140. Han X, Gross RW. Global analyses of cellular lipidomes directly from crude extracts of biological samples by ESI mass spectrometry: A bridge to lipidomics. *J Lipid Res* **2003**; *44*: 1071-1079

141. Han X, Yang K, Cheng H, Fikes KN, Gross RW. Shotgun lipidomics of phosphoethanolamine-containing lipids in biological samples after one-step in situ derivatization. *J Lipid Res* **2005**; *46*: 1548-1560

142. Carrapiso AI, García C. Development in lipid analysis:some new extraction techniques and *in situ* transesterification. *Lipids* **2000**; *35*: 1167-1177

143. Poerschmann J, Carlson R. New fractionation scheme for lipid classes based on "in-cell fractionation" using sequential pressurized liquid extraction. *J Chromatogr A* **2006**; *1127*: 18-25

144. Rose HG, Oklander M. Improved procedure for the extraction of lipids from human erythrocytes. *J Lipid Res* **1965**; *6*: 428-431

145. Matyash V, Liebisch G, Kurzchalia TV, Shevchenko A, Schwudke D. Lipid extraction by methyl-tert-butyl ether for high-throughput lipidomics. *J Lipid Res* **2008**; *49*: 1137-1146

146. Parenti-Castelli G, Bertoli E, Sechi AM, Silvestrini MG, Lenaz G. Effects of soluble and membrane proteins upon diethyl ether extraction of aqueous phohpholipid dispersions. *Lipids* **1978**; *14*: 221-228

147. Lenaz G, Parenti-Castelli G, Sechi AM, Masotti L. Lipid-protein interactions in mitochondria. III. Solvent extraction of phospholipids from mitochondrial preparations. *Arch Biochem Biophys* **1972**; *148*: 391-399

148. Čertík M, Peter A, Ján Š. Effect of extraction methods on lipid yield and fatty acid composition of lipids classes containing γ-linolenic acid extracted from fungi. *J Am Oil Chem Soc* **1996**; *73*: 357-365

149. Ametaj BN, Bobe G, Lu Y, Young JW, Beitz DC. Effect of sample preparation, length of time, and sample size on quantification of total lipids fron bovine liver. *J Agric Food Chem* **2003**; *51*: 2105-2110

150. Keusgen M, Curtis JM, Thibault P, Walter JA, Windust A, Ayer SW. Sulfoquinovosyl diacylglycerols from the alga *Heterosigma carterae*. *Lipids* **1997**; *32*: 1101-1112

151. Sotirhos N, Herslöf B, Kenne L. Quantitative analysis of phospholipids by ^{31}P-NMR. *J Lipid Res* **1986**; *27*: 386-392

152. Karas M, Hillenkamp F. Laser desorption ionization of proteins with molecular masses exceeding 10,000 daltons. *Anal Chem* **1988**; *60*: 2299-2301

153. Zenobi R, Knochenmuss R. Ion formation in MALDI mass spectrometry. *Mass Spectrom Rev* **1998**; *17*: 337-366

154. Budnik BA, Moyer SC, Pittman JL, Ivleva VB, Sommer U, Costello CE, O'Connor PB. High pressure MALDI-FTMS: implications for proteomics. *Int J Mass Spectrom* **2004**; *234*: 203-212

155. Vorm O, Roepstorff P, Mann M. Improved resolution and very high sensitivity in MALDI TOF of matrix surfaces made by fast evaporation. *Anal Chem* **1994**; *66*: 3281-3287

156. Mann M, Fenn JB. Electrospray mass spectrometry: principles and methods. *Mass Spectrom* **1992**; *1*: 1-35

157. Fenn JB, Mann M, Meng CK, Wong SF, Whitehouse CM. Electrospray Ionization for Mass Spectrometer of Large Biomolecules. *Science (Washington, D C)* **1989**; *246*: 64-71

158. Fenn JB, Mann M, Meng CK, Wong SF, Whitehouse CM. Electrospray ionization-principles and practice. *Mass Spectrom Rev* **1990**; *9*: 37-70

159. Gomez A, Tang K. Charge and fission of droplets in electrostatic sprays. *Phys Fluids* **1994**; *6*: 404-414

160. Thomson BT, Iribarne JV. Field induced ion evaporation from liquid surfaces at atmospheric pressure. *J Chem Phys* **1979**; *71*: 4451-4463

161. Iribarne JV, Thomson BT. On the evaporation of small ions from charged droplets. *J Chem Phys* **1976**; *64*: 2287-2294

162. Wilm M, Mann M. Analytical properties of the nanoelectrospray ion source. *Anal Chem* **1996**; *68*: 1-8

163. Wiseman JM, Ifa DR, Zhu Y, Kissinger CB, Manicke NE, Kisinger PT, Cooks RG. Desorption electrospray ionization mass spectrometry: imaging drugs and metabolites in tissues. *Proc Natl Acad Sci U S A* **2008**; *105*: 18120-18125

164. Cornett DS, Reyzer ML, Chaurand P, Caprioli RM. MALDI imaging mass spectrometry: molecular snapshots of biochemical systems. *Nat Methods* **2007**; *4*: 828-833

165. Han X, Yang K, Yang J, Fikes KN, Cheng H, Gross RW. Factors Influencing the Electrospray Intrasource Separation and Selective Ionization of Glycerophospholipids. *J Am Soc Mass Spectrom* **2006**; *17*: 264-274

166. Thomas MC, Mitchell TW, Blanksby SJ. A comparison of the gas phase acidities of phospholipid headgroups: experimental and computational studies. *J Am Soc Mass Spectrom* **2005**; *16*: 926-939

167. McAnoy AM, Wu CC, Murphy RC. Direct qualitative qnalysis of triacylglycerols by electrospray mass spectrometry using a linear ion trap. *J Am Soc Mass Spectrom* **2005**; *16*: 1498-1509

168. Al-Saad KA, Zabrouskov V, Siems WF, Knowles NR, Hannan RM, Hill HHJ. Matrix-assisted laser desorption/ionization time-of-flight mass spectrometry of lipids: ionization and prompt fragmentation patterns. *Rapid Commun Mass Spectrom* **2003**; *17*: 87-96

169. Xu Y, Bruening ML, Watson JT. Non-specific, on-probe cleanup methods for MALDI-MS samples. *Mass Spectrom Rev* **2003**; *22*: 429-440

170. Douglas DJ, Frank AJ, Mao D. Linear ion traps in mass spectrometry. *Mass Spectrom Rev* **2005**; *24*: 1-29

171. de Hoffmann E, Stroobant V eds. Mass Spectrometry Principles and Applications 2nd ed: *John Wiley and Sons, New York*; **2002**

172. Glish G, Vachet R. Quadrupole Ion Trap Mass Spectrometry. In, ASMS lecture notes; **2007**

173. McLuckey SA, Goeringer DE. Slow heating methods in tandem mass spectrometry. *J Mass Spectrom* **1997**; *32*: 461-474

174. Reid GE, Simpson RJ, O'Hair RAJ. Gas phase ion chemistry of biomolecules. 17. Probing the fragmentation reactions of protonated glycine oligomers via multistage mass spectrometry and gas phase ion molecule hydrogen/deuterium exchange. *Int J Mass Spectrom* **1999**; *190/191*: 209-230

175. Thomas MC, Mitchell TW, Harman DG, Deeley JM, Nealon JR, Blanksby SJ. Ozone-induced dissociation: elucidation of double bond position within mass-selected lipid ions. *Anal Chem* **2008**; *80*: 303-311

176. Syka JE, Coon JJ, Schroeder MJ, Shabanowitz J, Hunt DF. Peptide and protein sequence analysis by electron transfer dissociation mass spectrometry *Proc Natl Acad Sci USA* **2004**; *101*: 9528–9533

177. ThermoScientific. Pulsed Q collision induced dissociation(PQD) on linear ion trap mass spectrometers. *Thermo Scientific Product Support Bulletin* **2006**; *124*: 62577-62578

178. Liang X, Liu J, LeBlanc Y, Covey T, Ptak AC, Brenna JT, McLuckey SA. Electron transfer dissociation of doubly sodiated glycerophosphocholine lipids. *J Am Soc Mass Spectrom* **2007**; *18*: 1783-1788

179. Schwudke D, Hannich JT, Surendranath V, Grimard V, Moehring T, Burton L, Kurzchalia T, Shevchenko A. Top-down lipidomic screens by multivariate analysis of high-resolution survey mass spectra. *Anal Chem* **2007**; *79*: 4083-4093

180. Leitner A, Foettinger A, Lindner W. Improving fragmentation of poorly fragmenting peptides and phosphopeptides during collision-induced dissociation by malondialdehyde modification of arginine residues. *J Mass Spectrom* **2007**; *42*: 950-959

181. Ahn YH, Ji ES, Lee JY, Cho K, Yoo JS. Arginine-mimic labeling with guanidinoethanethiol to increase mass sensitivity of lysine-terminated phosphopeptides by matrix-assisted laser desorption/ionization time-of-flight mass spectrometry. *Rapid Commun Mass Spectrom* **2007**; *21*: 2204-2210

182. Wysocki VH, Tsaprailis G, Smith LL, Breci LA. Mobile and localized protons: a framework for understanding peptide dissociation. *J Mass Spectrom* **2000**; *35*: 1399-1406

183. Eckersley M, Bowie JH, Hayes RN. Collision-induced dissociations of deprotonated alpha -amino acids. The occurrence of specific proton transfers preceding fragmentation. *Int J Mass Spectrom Ion Processes* **1989**; *93*: 199-213

184. Zhang X, Ferguson-Miller SM, Reid GE. Characterization of ornithine and glutamine lipids extracted from cell membranes of *Rhodobacter sphaeroides*. *J Am Soc Mass Spectrom* **2009**; *20*: 198-212

185. Zhang X, Reid GE. Multistage tandem mass spectrometry of anionic phosphatidylcholine lipid adducts reveals novel dissociation pathways. *Int J Mass Spectrom* **2006**; *252*: 242-255

186. O'Hair RAJ, Reid GE. The search for stable gas phase b1 ions derived from aliphatic amino acids: a combined experimental and ab initio study. *Rapid Commun Mass Spectrom* **2000**; *14*: 1220-1225

187. Griffiths WJ. Tandem mass spectrometry in the study of fatty acids, bile acids, and steroids. *Mass Spectrom Rev* **2003**; *22*: 81-152

188. Hsu F-F, Bohrer A, Turk J. Formation of lithiated adducts of glycerophosphocholine lipids facilitates their identification by electrospray ionization tandem mass spectrometry. *J Am Soc Mass Spectrom* **1998**; *9*: 516-526

189. Hsu F-F, Turk J. Charge-driven fragmentation processes in diacyl glycerophosphatidic acids upon low-energy collisional activation. A mechanistic proposal. *J Am Soc Mass Spectrom* **2000**; *11*: 797-803

190. Hsu F-F, Turk J. Charge-remote and charge-driven fragmentation processes in diacyl glycerophosphoethanolamine upon low-energy collisional activation: a mechanistic proposal. *J Am Soc Mass Spectrom* **2000**; *11*: 892-899

191. Hsu F-F, Turk J. Characterization of phosphatidylethanolamine as a lithiated adduct by triple quadrupole tandem mass spectrometry with electrospray ionization. *J Mass Spectrom* **2000**; *35*: 596-606

192. Hsu F-F, Turk J. Structural Determination of Sphingomyelin by Tandem Mass Spectrometry With Electrospray Ionization. *J Am Soc Mass Spectrom* **2000**; *11*: 437–449

193. Hsu F-F, Turk J. Studies on phosphatidylglycerol with triple quadrupole tandem mass spectrometry with electrospray ionization: fragmentation processes and structural characterization. *J Am Soc Mass Spectrom* **2001**; *12*: 1036-1043

194. Hsu F-F, Turk J. Characterization of cardiolipin as the sodiated Ions by positive-ion electrospray ionization with multiple stage quadrupole ion-trap mass spectrometry. *J Am Soc Mass Spectrom* **2006**; *17*: 1146-1157

195. Hsu F-F, Turk J, Rhoades ER, Russell DG, Shi Y, Groisman EA. Structural characterization of cardiolipin by tandem quadrupole and multiple-stage quadrupole ion-trap mass spectrometry with electrospray ionization. *J Am Soc Mass Spectrom* **2005**; *16*: 491-504

196. Zemski B, Karin A, Murphy RC. Electrospray ionization tandem mass spectrometry of glycerophosphoethanolamine plasmalogen phospholipids. *J Am Soc Mass Spectrom* **2004**; *15*: 1499-1508

197. Hsu F-F, Turk J. Studies on phosphatidylserine by tandem quadrupole and multiple stage quadrupole ion-trap mass spectrometry with electrospray ionization: structural characterization and the fragmentation processes. *J Am Soc Mass Spectrom* **2005**; *16*: 1510-1522

198. Hsu F-F, Turk J. Characterization of phosphatidylinositol, phosphatidylinositol-4-phosphate, and phosphatidylinositol-4,5-bisphosphate by electrospray ionization tandem mass spectrometry: a mechanistic study. *J Am Soc Mass Spectrom* **2000**; *11*: 986-999

199. Golik J, Dickey JK, Todderud G, Lee D, Alford J, Huang S, Klohr S, Eustice D, Aruffo A, Agler ML. Isolation and structure determination of sulfonoquinovosyl dipalmitoyl glyceride, a P-selectin receptor inhibitor from the alga Dictyochloris fragrans. *J Nat Prod* **2007**; *60*: 387-389

200. Hsu F-F, Turk J. Structural characterization of triacylglycerols as lithiated adducts by electrospray ionization mass spectrometry using low-energy collisionally

activated dissociation on a triple stage quadrupole instrument. *J Am Soc Mass Spectrom* **1999**; *10*: 587-599

201. Han X, Gross RW. Structural determination of lysophospholipid regioisomers by electrospray ionization tandem mass spectrometry. *J Am Chem Soc* **1996**; *118*: 451-457

202. Gross ML. Charge-remote fragmentation: an account of research on mechanisms and applications. *Int J Mass Spectrom* **2000**; *200*: 611-624

203. O'Hair RAJ, Reid GE. Neighboring group versus cis-elimination mechanisms for side chain loss from protonated methionine, methionine sulfoxide and their peptides gas phase ion chemistry of biomolecules. *Eur Mass Spectrom* **1999**; *5*: 325-334

204. Hvattum E, Hagelin G, Larsen Å. Study of mechanisms involved in the collision-induced dissociation of carboxylate anions from glycerophospholipids using negative ion electrospray tandem quadrupole mass spectrometry. *Rapid Commun Mass Spectrom* **1998**; *12*: 1405-1409

205. Murphy RC, Fiedler J, Hevko J. Analysis of nonvolatile lipids by mass spectrometry. *Chem Rev* **2001**; *101*: 479-526

206. Moe MK, Anderssen T, Strøm MB, Jensen E. Total structure characterization of unsaturated acidic phospholipids provided by vicinal di-hydroxylation of fatty acid double bonds and negative electrospray ionization mass spectrometry. *J Am Soc Mass Spectrom* **2005**; *16*: 46-59

207. Thomas MC, Mitchell TW, Harman DG, Deeley JM, Murphy RC, Blanksby SJ. Elucidation of double bond position in unsaturated lipids by ozone electrospray ionization mass spectrometry. *Anal Chem* **2007**; *79*: 5013-5022

208. Han X, Gross RW. Electrospray ionization mass spectroscopic analysis of human erythrocyte plasma membrane phospholipids. *Proc Natl Acad Sci U S A* **1994**; *91*: 10635-10639

209. Kim H-Y, Wang T-CL, Ma Y-C. Liquid chromatography/mass spectrometry of phospholipids using electrospray ionization. *Anal Chem* **1994**; *66*: 3977-3982

210. Ekroos K, Chemushevich IV, Simons K, Shevchenko A. Quantitative profiling of phospholipids by multiple precursir ion scanning on a hybrid quadrupole time-of-flight mass spectrometer. *Anal Chem* **2002**; *74*: 941-949

211. Houjou T, Yamatani K, Nakanishi H, Imagawa M, Shimizu T, Taguchi R. Rapid and selective identification of molecular species in phosphatidylcholine and

sphingomyelin by conditional neutral loss scanning and MS^3. *Rapid Commun Mass Spectrom* **2004**; *18*: 3123-3130

212. Busch KL. Chemical Noise, Part IV: Reduction of Noise through Informatics. *Spectroscopy* **2004**; *19*: 44-52

213. Busch KL. Chemical noise in mass spectrometry. Part I. *Spectroscopy (Duluth, MN, United States)* **2002**; *17*: 32-34, 36-37

214. Busch KL. Chemical noise in mass spectrometry. Part II - effects of choices in ionization methods on chemical noise. *Spectroscopy (Duluth, MN, United States)* **2003**; *18*: 56,58,60-62

215. Busch KL. Chemical noise in mass spectrometry. Part III - more mass spectrometry/mass spectrometry. *Spectroscopy (Duluth, MN, United States)* **2003**; *18*: 52-55

216. Benard S, Arnhold J, Lehnert M, Schiller J, Arnold K. Experiments toward quantification of saturated and polyunsaturated discylglycerols by matrix-assisted laser desorption and ionization time-of-flight mass spectrometry. *Chemistry and Physics of Lipids* **1999**; *100*: 115-125

217. Reid GE, Simpson RJ, O'Hair RAJ. A mass spectrometric and *ab initio* study of the pathways for dehydration of simple glycine and cysteine-containing peptide $[M+H]^+$ ions. *J Am Soc Mass Spectrom* **1998**; *9*: 945-956

218. Sistrom WR. A requirement for sodium in the growth of *Rhodopseudomonas spheroides*. *J Gen Microbiol* **1960**; *22*: 778-785

219. Sistrom WR. The kinetics of the synthesis of photopigments in *Rhodopseudomonas spheroides*. *J Gen Microbiol* **1962**; *28*: 607-616

220. Zhen Y, Qian J, Follmann K, Hayward T, Nilsson T, Dahn M, Hilmi Y, Hamer AG, Hosler JP, Ferguson-Miller S. Overexpression and purification of cytochrome c oxidase from Rhodobacter sphaeroides. *Protein Expression Purif* **1998**; *13*: 326-336

221. van Niel CB. The culture, general physiology, morphology, and classification of the non-sulfur purple and brown bacteria. *Bacteriol Rev* **1944**; *8*: 1-118

222. Kovach ME, Elzer PH, Hill DS, Robertson GT, Farris MA, Roop RM, 2nd, Peterson KM. Four new derivatives of the broad-host-range cloning vector pBBR1MCS, carrying different antibiotic-resistance cassettes. *Gene* **1995**; *166*: 175-176

223. Benning C. In, Genetic analysis of the pathway for the biosynthesis of the plant sulfolipid in the purple bacterium *Rhodobacter sphaeroides* Ph.D. Dissertation MSU **1991**

224. Bartlett GR. Phosphorus assay in column chromatography. *J Biol Chem* **1959**; *234*: 466-468

225. Hilmi Y. Use of mutagenesis, novel detergents, and lipid analysis to optimize conditions for achieving high resolution 3-dimensional crystal structure of *Rhodobacter sphaeroides* cytochrome *c* oxidase. Ph. D. Dissertation MSU; **2002**

226. Weissenmayer B, Geiger O, Benning C. Disruption of a gene essential for sulfoquinovosyldiacylglycerol biosynthesis in *Sinorhizobium meliloti* has no detectable effect on root nodule symbiosis. *Mol Plant-Microbe Interact* **2000**; *13*: 666-672

227. Tsukihara T, Shimokata K, Katayama Y, Shimada H, Muramoto K, Aoyama H, Mochizuki M, Shinzawa-itoh K, Yamashita E, Yao M, Ishimura Y, Yoshikawa S. The low-spin heme of cytochrome *c* oxidase as the driving element of the proton-pumping process. *Proc Natl Acad Sci U S A* **2003**; *100*: 15304-15309

228. Cartailler J-P, Luecke H. X-ray crystallographic analysis of lipid-protein interactions in the bacteriodopsin purple membrane. *Annu Rev Biophys Biomol Struct* **2003**; *32*: 285-310

229. Pike LJ, Han X, Chung K-N, Gross RW. Lipid rafts are enriched in arachidonic acid and plasmenylethanolamine and their composition is independent of caveolin-1 expression: A quantitative electrospray ionization/mass spectrometric analysis. *Biochemistry* **2002**; *41*: 2075-2088

230. Simons K, Vaz WLC. Model systems, lipid rafts, and cell membranes. *Annu Rev Biophys Biomol Struct* **2004**; *33*: 269-295

231. Pike LJ, Han X, Gross RW. Epidermal growth factor receptors are localized to lipid rafts that contain a balance of inner and outer leaflet lipids: a shotgun lipidomics study *J Biol Chem* **2005**; *280*: 26796-26804

232. Brugger B, Erben G, Sandhoff R, Wieland FT, Lehmann WD. Quantitative analysis of biological membrane lipids at the low picomole level by nano-electrospray ionization tandem mass spectrometry. *Proc Natl Acad Sci U S A* **1997**; *94*: 2339-2344

233. Zacarias A, Bolanowski D, Bhatnagar A. Comparative measurements of multicomponent phospholipid mixtures by electrospray mass spectroscopy: relating ion intensity to concentration. *Anal Biochem* **2002**; *308*: 152-159

234. Koivusalo M, Haimi P, Heikinheimo L, Kostiainen R, Somerharju P. Quantitative determination of phospholipid compositions by ESI-MS: effects of acyl chain length, unsaturation, and lipid concentration on instrument response. *J Lipid Res* **2001**; *42*: 663-672

235. Taguchi R, Houjou T, Nakanishi H, Yamazaki T, Ishida M, Imagawa M, Shimizu T. Focused lipidomics by tandem mass spectrometry. *J Chromatography B* **2005**; *823*: 26-36

236. Milne SB, Ivanova PT, DeCamp D, Hsueh RC, Brown HA. A targeted mass spectrometric analysis of phosphatidylinositol phosphate species. *J Lipid Res* **2005**; *46*: 1796-1802

237. Han X, Gubitosi-Klug RA, Collins BJ, Gross RW. Alterations in individual molecular species of human platelet phospholipids during thrombin stimulation: electrospray ionization mass spectrometry-facilitated identification of the boundary conditions for the magnitude and selectivity of thrombin-induced platelet phospholipid hydrolysis. *Biochemistry* **1996**; *35*: 5822-5832

238. Harrison KA, Murphy RC. Negative electrospray ionization of glycerophospho-choline lipids: formation of $[M-15]^-$ ions occurs via collisional decomposition of adduct anions. *J Mass Spectrom* **1995**; *30*: 1772-1773

239. DeLong CJ, Baker PRS, Samuel M, Cui Z, Thomas MJ. Molecular species composition of rat liver phospholipids by ESI-MS/MS: the effect of chromatography. *JLipid Res* **2001**; *42*: 1959-1968

240. Karlsson AA, Michelsen P, Odham G. Molecular species of sphingomyelin: determination by high-performance liquid chromatography/mass spectrometry with electrospray and high-performance liquid chromatography/tandem mass spectrometry with atmospheric pressure chemical ionization. *J Mass Spectrom* **1998**; *33*: 1192-1198

241. Lehmann WD, Koester M, Erben G, Keppler D. Characterization and quantification of rat bile phosphatidylcholine by electrospray-tandem mass spectrometry. *Anal Biochem* **1997**; *246*: 102-110

242. Kerwin JL, Tuininga AR, Ericsson LH. Identification of molecular species of glycerophospholipids and sphingomyelin using electrospray mass spectrometry. *J Lipid Res* **1994**; *35*: 1102-1114

243. Khaselev N, Murphy RC. Structural characterization of oxidized phospholipid products derived from arachidonate-containing plasmenyl glycerophosphocholine. *J Lipid Res* **2000**; *41*: 564-572

244. Uran S, Larsen Å, Jacobsen PB, Skotland T. Analysis of phospholipid species in human blood using normal-phase liquid chromatography coupled with electrospray ionization ion-trap tandem mass spectrometry. *J Chromatogr B* **2001**; *758*: 265-275

245. Pacetti D, Malavolta M, Bocci F, Boselli E, Frega NG. High-performance liquid chromatography/electrospray ionization ion-trap tandem mass spectrometric analysis and quantification of phosphatidylcholine molecular species in the serum of cystic fibrosis subjects supplemented with docosahexaenoic acid. *Rapid Commun Mass Spectrom* **2004**; *18*: 2395-2400

246. Larsen Å, Uran S, Jacobsen PB, Skotland T. Collision-induced dissociation of glycero phospholipids using electrospray ion-trap mass spectrometry. *Rapid Commun Mass Spectrom* **2001**; *15*: 2393-2398

247. Hsu F-F, Turk J. Studies on sulfatides by quadrupole ion-trap mass spectrometry with electrospray ionization: structural characterization and the fragmentation processes that include an unusual internal galactose residue loss and the classical charge-remote fragmentation. *J Am Soc Mass Spectrom* **2004**; *15*: 536-546

248. Hsu F-F, Turk J, Shi Y, Groisman EA. Characterization of acylphosphatidylglycerols from Salmonella typhimurium by tandem mass spectrometry with electrospray ionization. *J Am Soc Mass Spectrom* **2004**; *15*: 1-11

249. Mazzella N, Molinet J, Syakti AD, Dodi A, Doumenq P, Artaud J, Bertrand J-C. Bacterial phospholipid molecular species analysis by ion-pair reversed-phase HPLC/ESI/MS. *J Lipid Res* **2004**; *45*: 1355-1363

250. Jensen NJ, Tomer KB, Gross ML. Fast atom bombardment and tandem mass spectrometry of phosphatidylserine and phosphatidylcholine. *Lipids* **1986**; *21*: 580-588

251. Huang ZH, Gage DA, Sweeley CC. Characterization of diacylglycerylphosphocholine molecular species by FAB-CAD-MS/MS: a general method not sensitive to the nature of the fatty acyl groups. *J Am Soc Mass Spectrom* **1992**; *3*: 71-78

252. Hayashi A, Matsubara T, Morita M, Kinoshita T, Nakamura T. Structural analysis of choline phospholipids by fast atom bombardment mass spectrometry and tandem mass spectrometry. *J Biochem* **1989**; *106*: 264-269

253. Kayganich-Harrison KA, Rose DM, Murphy RC, Morrow JD, Roberts LJ, II. Collision-induced dissociation of F2-isoprostane-containing phospholipids. *J Lipid Res* **1993**; *34*: 1229-1235

254. Lee CY, Lesimple A, Larsen Å, Mamer O, Genest J. ESI-MS quantitation of increased sphingomyelin in Niemann-Pick disease type B HDL. . *J Lipid Res* **2005**; *46*: 1213-1228

255. Gronert S. Quadrupole ion trap studies of fundamental organic reactions. *Mass Spectrom Rev* **2005**; *24*: 100-120

256. Landin J, Pascher I, Cremer D. Effect of a Polar Environment on the Conformation of Phospholipid Head Groups Analyzed with the Onsager Continuum Solvation Model. *Journal of Physical Chemistry A* **1997**; *101*: 2996-3004

257. Pohle W, D.R.; G, Bohl M, Mrazkova E, Hobza P. Lipid hydration: headgroup CH moieties are involved in water binding *Biopolymers* **2004**; *74*: 27-31

258. Cai Y, Concha MC, Murray JS, Cole RB. Evaluation of the role of multiple hydrogen bonding in offering stability to negative ion adducts in electrospray mass spectrometry. *J Am Soc Mass Spectrom* **2002**; *13*: 1360-1369

259. James PF, Perugini MA, O'Hair RAJ. Sources of artifacts in the electrospray ionization mass spectra of saturated diacylglycerophosphocholines: From condensed phase hydrolysis reactions through to gas phase intercluster reactions. *J Am Soc Mass Spectrom* **2006**; *17*: 384-394

260. Streitweiser A. Solvolytic displacement reactions at saturated carbon atoms *Chem Rev* **1956**; *56*: 571-752

261. Ho T-L. The hard soft acids bases (HSAB) principle and organic chemistry. *Chem Rev* **1975**; *75*: 1-20

262. Gorchein A. The separation and identification of the lipids of *Rhodopseudomonas spheroides*. *Proc Roy Soc, Ser B* **1968**; *170*: 279-297

263. Shively JM, Knoche HW. Isolation of an ornithine-containing lipid from *Thiobacillus thiooxidans*. *J Bacteriol* **1969**; *98*: 829-830

264. Knoche HW, Shively JM. The structure of an ornithine-containing lipid from *Thiobacillus thiooxidans*. *J Biol Chem* **1972**; *247*: 170-178

265. Wilkinson BJ, Sment KA, Mayberry WR. Occurrence, localization, and possible significance of an ornithine-containing lipid in *Paracoccus denitrificans*. *Arch Microbiol* **1982**; *131*: 338-343

266. Kawai Y, Yano I. Ornithine-containing lipid of *Bordetella pertussis*, a new type of hemagglutinin. *Eur J Biochem* **1983**; *136*: 531-538

267. Minnikin DE, Abdolrahimzadeh H. Replacement of phosphatidylethanolamine and acidic phospholipids by an ornithine-amide lipid and a minor phosphorus-free lipid in *Pseudomonas fluorescens* NCMB 129. *FEBS (Fed Eur Biochem Soc) Lett* **1974**; *43*: 257-260

268. Weissenmayer B, Gao J-L, Lopez-Lara IM, Geiger O. Identification of a gene required for the biosynthesis of ornithine-derived lipids. *Mol Microbiol* **2002**; *45*: 721-733

269. Rojas-Jimenez K, Sohlenkamp C, Geiger O, Martinez-Romero E, Werner D, Vinuesa P. A CIC chloride channel homolog and ornithine-containing membrane lipids of *Rhizobium tropici* CIAT899 are involved in symbiotic efficiency and acid tolerance. *Mol Plant-Microbe Interact* **2005**; *18*: 1175-1185

270. Kawai Y, Akagawa K. Macrophage activation of an ornithine-containing lipid or a serine-containing lipid. *Infect Immun* **1989**; *57*: 2086-2091

271. Kawai Y, Nakagawa Y, Matuyama T, Akagawa K, Itagawa K, Fukase K, Kusumoto S, Nishijima M, Yano I. A typical bacterial ornithine-containing lipid Nalpha-(D)-[3-(hexadecanoyloxy)hexadecanoyl]-ornithine is a strong stimulant for macrophages and a useful adjuvant. *FEMS Immunol Med Microbiol* **1999**; *23*: 67-73

272. Kawai Y, Ishida Okawara A, Okuyama H, Kura F, Suzuki K. Modulation of chemotaxis, O_2^- production and myeloperoxidase release from human polymorphonuclear leukocytes by the ornithine-containing lipid and the serine-glycine-containing lipid of *Flavobacterium*. *FEMS Immunol Med Microbiol* **2000**; *28*: 205-209

273. Aygun-Sunar S, Mandaci S, Koch H-G, Murray IVJ, Goldfine H, Daldal F. Ornithine lipid is required for optimal steady-state amounts of *c*-type cytochromes in *Rhodobacter capsulatus*. *Mol Microbiol* **2006**; *61*: 418-435

274. Klug RM, Benning C. Two enzymes of diacylglyceryl-O-4'-(N,N,N,-trimethyl)-homoserine biosynthesis are encoded by btaA and btaB in the purple bacterium *Rhodobacter sphaeroides*. *Proc Natl Acad Sci U S A* **2001**; *98*: 5910-5915

275. Yasutaka T, Yuzi Y, Keiji K. A new lysine-containing lipids isolated from *Agrobacterium tumefaciens*. *Agric Biol Chem* **1976**; *40*: 1449-1450

276. Gao J-L, Weissenmayer B, Taylor AM, Thomas-Oates J, Lopez-Lara IM, Geiger O. Identification of a gene required for the formation of lyso-ornithine lipid, an intermediate in the biosynthesis of ornithine-containing lipids. *Mol Microbiol* **2004**; *53*: 1757-1770

277. Thiele OW, Biswas CJ, Hunneman DH. Isolation and characterization of an ornithine-containing lipid from *Paracoccus denitrificans*. *Eur J Biochem* **1980**; *105*: 267-274

278. Dees C, Shively JM. Localization and quantitation of the ornithine lipid of *Thiobacillus thiooxidans*. *J Bacteriol* **1982**; *149*: 798-799

279. Choma A, Komaniecka I. Analysis of phospholipids and ornithine-containing lipids from *Mesorhizobium spp*. *Syst Appl Microbiol* **2002**; *25*: 326-331

280. Linscheid M, Diehl BWK, Övermöhle M, Riedl I, Heinz E. Membrane lipids of *Rhodopseudomonas viridis*. *Biochim Biophys Acta, Lipids Lipid Metab* **1997**; *1347*: 151-163

281. Hilker DR, Gross ML, Knocke HW, Shively JM. The interpretation of the mass spectrum of an ornithine-containing lipid from *Thiobacillus thiooxidans*. *Biomed Mass Spectrom* **1978**; *5*: 64-71

282. Hilker DR, Knoche HW, Gross ML. Thermolysis chemical ionization of a complex polar lipid. *Biomed Mass Spectrom* **1979**; *6*: 356-358

283. Bowie JH, Brinkworth CS, Dua S. Collision-induced fragmentations of the $[M-H]^-$ parent anions of underivatized peptides: an aid to structure determination and some unusual negative ion cleavages. *Mass Spectrom Rev* **2002**; *21*: 87-107

284. Bowie JH. The fragmentations of even-electron organic negative ions. *Mass Spectrom Rev* **1990**; *9*: 349-379

285. Yalcin T, Harrison AG. Ion chemistry of protonated lysine derivatives. *J Mass Spectrom* **1996**; *31*: 1237-1243

286. Grogan DW, Cronan JEJ. Cyclopropane ring formation in membrane lipids of bacteria *Microbiol Mol Biol Rev* **1997**; *61*: 429-441

287. Reid GE, Roberts KD, Kapp EA, Simpson RJ. Statistical and mechanistic approaches to understanding the gas-phase fragmentation behavior of methionine sulfoxide containing peptides. *J Prot Res* **2004**; *3*: 751-759

288. Gueler S, Seeliger A, Haertel H, Renger G, Benning C. A null mutant of *Synechococcus sp.* PCC7942 deficient in the sulfolipid sulfoquinovosyl diacylglycerol. *J Biol Chem* **1996**; *271*: 7501-7507

289. Benning C. Biosynthesis and function of the sulfolipid sulfoquinovosyl diacylglycerol. *Annu Rev Plant Physiol Plant Mol Biol* **1998**; *49*: 53-75

290. Wenk M. The emerging field of lipidomics. *Nature Reviews* **2005**; *4*: 594-608

291. Kim YH, Yoo JS, Kim MS. Structural characterization of sulfoquinovosyl, monogalactosyl and digalactosyl diacylglycerols by FAB-CID-MS/MS. *Journal of Mass Spectrometry* **1997**; *32*: 968-977

292. Benning C. Questions remaining in sulfolipid biosynthesis: A historical perspective. *Photosynth Res* **2007**; *92*: 199-203

293. Ohta K, Mizushina Y, Hirata N, Takemura M, Sugawara F, Matsukage A, Yoshida S, Sakaguchi K. Sulfoquinovosyldiacylglycerol, KM043, a new potent inhibitor of eukaryotic DNA polymerases and HIV-reverse transcriptase type 1 from a marine red alga, Gigartina tenella. *Chem Pham Bull* **1998**; *46*: 684-686

294. Hanashima S, Mizushina Y, Yamazaki T, Ohta K, Takahashi S, Sahara H, Sakaguchi K, Sugawara F. Synthesis of sulfoquinovosylacylglycerols, inhibitors of Eukaryotic DNA Polymerase a and b. *Bioorg Med Chem* **2001**; *9*: 367-376

295. Cedergren RA, Hollingsworth RI. Occurrence of sulfoquinovosyl diacylglycerol in some members of the family *Rhizobiaceae. J Lipid Res* **1994**; *35*: 1452-1461

296. Sprott GD, Larocque S, Cadotte N, Dicaire CJ, McGee M, Brisson JR. Novel polar lipids of halophilic eubacterium *Planococcus* H8 and archaeon *Haloferax volcanii. Biochim Biophys Acta, Mol Cell Biol Lipids* **2003**; *1633*: 179-188

297. van Mooy BAS, Fredricks HF, Evans CT, Devol AH. Sulfolipids dramatically decrease phosphorus demand by picocyanobacteria in oligotrophic marine environments. *Proc Natl Acad Sci U S A* **2006**; *103*: 8607-8612

298. Naumann I, Darsow KH, Walter C, Lange HA, Buchholz R. Identification of sulfoglycolipids from the alga *Porphyridium purpureum* by matrix-assisted laser desorption/ionisation quadrupole ion trap time-of-flight mass spectrometry. *Rapid Commun Mass Spectrom* **2007**; *21*: 3185-3192

299. Imhoff JF. Polar lipids and fatty acids in the genus *Rhodobactor. Systematic and Applied Microbiology* **1991**; *14*: 228-234

300. O'Hair RAJ, Styles ML, Reid GE. Role of the sulfhydryl group on the gas phase fragmentation reactions of protonated cysteine and cysteine containing peptides. *J Am Soc Mass Spectrom* **1998**; *9*: 1275-1284

301. Cheng C, Gross ML. Applications and mechanisms of charge-remote fragmentation. *Mass Spectrom Rev* **2000**; *19*: 398-420

302. Domingues MRM, S.-Marques MGO, Vale CAM, Neves MG, Cavaleiro JAS, Ferrer-Correia AJ, Nemirovskiy OV, Gross ML. Do charge-remote fragmentations occur under matrix-assisted laser desorption ionization post-

source decompositions and matrix-assisted laser desorption ionization collisionally activated decompositions? *J Am Soc Mass Spectrom* **1999**; *10*: 217-223

303. Riekhof WR, Andre C, Benning C. Two enzymes, BtaA and BtaB, are sufficient for betaine lipid biosynthesis in bacteria. *Arch Biochem Biophys* **2005**; *441*: 96-105

304. Marsh D, Páli T. The protein-lipid interface: perspectives from magnetic resonance and crystal structures. *Biochim Biophys Acta, Biomembr* **2004**; *1666*: 118-141

305. de Matteis MA, Godi A. Protein-lipid interactions in membrane trafficking at the Golgi complex. *Biochim Biophys Acta, Biomembr* **2004**; *1666*: 264-274

306. van Dalen A, de Kruijff B. The role of lipids in membrane insertion and translocation of bacterial proteins. *Biochim Biophys Acta* **2004**; *1694*: 97-109

307. Lee AG. How lipids affect the activities of integral membrane proteins. *Biochim Biophys Acta, Biomembr* **2004**; *1666*: 62-87

308. Sobus MT, Homlund CE. Extraction of lipids from yeast. *Lipids* **1976**; *11*: 341-348

309. Jensen S, Lisbeth H, Jörundsdóttir H, Göran O. A quantitative lipid extraction method for residue analysis of fish involving nonhalogenated solvents. *J Agric Food Chem* **2003**; *51*: 5607-5611

310. Drouillard KG, Hagen H, Haffer GD. Evaluation of chloroform/methanol and dichloromethane/hexane extractablelipids as surrogate measures of sample partition capacity for organochlorines in fish tissue. *Chemosphere* **2004**; *55*: 395-400

311. Phillips F, Privett OS. A simplified procedure of the quantitative extraction of lipids from brain tissue. *Lipids* **1978**; *14*: 590-595

312. Silipo A, Lanzetta R, Amoresano A, Parrilli M, Molinaro A. Ammonium hydroxide hydrolysis: a valuable support in the MALDI-TOF mass spectrometry analysis of lipid A fatty acid distribution. *J Lipid Res* **2002**; *43*: 2188-2195

313. Helmy FM, Hack MH. An ethanolamine plasmalogen artifact formed by acetone extraction of freeze-dried tissue. *Lipids* **1966**; *1*: 279-281

314. Roughan PG, Slack CR, Holland R. Generation of phospholipid artefacts during extraction of developing soybean seeds with methanolic solvents. *Lipids* **1978**; *13*: 497-503

315. Kurihara T, Nishizawa Y, Takahashi Y. The use of nonaqueous chloroform/methanol extraction for the delipidation of brain with minimal loss of enzyme activities. *Biochem J* **1977**; *165*: 135-140

316. Salminen J-P. Effects of sample drying and storage, and choice of extraction solvent and analysis methods on the yield of birch leaf hydrolyzable tannins. *J Chem Ecol* **2003**; *29*: 1289-1305

317. Nussberger S, Doerr K, Wang DN, Kuhlbrandt W. Lipid-protein interactions in crystals of plant light-harvesting complex. *J Mol Biol* **1993**; *234*: 347-356

318. Bogdanov M, Sun J, Kaback HR, Dowhan W. A phospholipid acts as a chaperone in assembly of a membrane transport protein. *J Biol Chem* **1996**; *271*: 11615-11618

319. Bogdanov M, Dowhan W. Phospholipid-assisted protein folding: phosphatidylethanolamine is required at a late step of the conformational maturation of the polytopic membrane protein lactose permease. *Embo J* **1998**; *17*: 5255-5264

320. Bogdanov M, Umeda M, Dowhan W. Phospholipid-assisted refolding of an integral membrane protein. Minimum structural features for phosphatidylethanolamine to act as a molecular chaperone. *J Biol Chem* **1999**; *274*: 12339-12345

321. Valiyaveetil FI, Zhou Y, MacKinnon R. Lipids in the structure, folding, and function of the KcsA K^+ channel. *Biochemistry* **2002**; *41*: 10771-10777

322. Yu CA, Yu L. Structural role of phospholipids in ubiquinol-cytochrome c reductase. *Biochemistry* **1980**; *19*: 5715-5720

323. Guan L, Smirnova IN, Verner G, Nagamori S, Kaback HR. Manipulating phospholipids for crystallization of a membrane transport protein. *Proc Natl Acad Sci U S A* **2006**; *103*: 1723-1726

324. Marsh D, Horvath LI. Structure, dynamics and composition of the lipid-protein interface. Perspectives from spin-labelling. *Biochim Biophys Acta* **1998**; *1376*: 267-296

325. Powell GL, Knowles PF, Marsh D. Spin-label studies on the specificity of interaction of cardiolipin with beef heart cytochrome oxidase. *Biochemistry* **1987**; *26*: 8138-8145

326. Mills DA, Ferguson-Miller S. Understanding the mechanism of proton movement linked to oxygen reduction in cytochrome c oxidase: lessons from other proteins. *FEBS Lett* **2003**; *545*: 47-51

327. Fyfe PK, Isaacs NW, Cogdell RJ, Jones MR. Disruption of a specific molecular interaction with a bound lipid affects the thermal stability of the purple bacterial reaction centre. *Biochim Biophys Acta, Bioenerg* **2004**; *1608*: 11-22

328. Tuller G, Hrastnik C, Achleitner G, Schiefthaler U, Klein F, Daum G. YDL142c encodes cardiolipin synthase (Cls1p) and is non-essential for aerobic growth of Saccharomyces cerevisiae. *FEBS Lett* **1998**; *421*: 15-18

329. Shibuya I, Miyazaki C, Ohta A. Alteration of phospholipid composition by combined defects in phosphatidylserine and cardiolipin synthases and physiological consequences in Escherichia coli. *J Bacteriol* **1985**; *161*: 1086-1092

330. Hirschberg CB, Kennedy EP. Mechanism of the enzymatic synthesis of cardiolipin in Escherichia coli. *Proc Natl Acad Sci U S A* **1972**; *69*: 648-651

331. Nishijima S, Asami Y, Uetake N, Yamagoe S, Ohta A, Shibuya I. Disruption of the Escherichia coli cls gene responsible for cardiolipin synthesis. *J Bacteriol* **1988**; *170*: 775-780

332. Zhong Q, Gohil VM, Ma L, Greenberg ML. *Journal of Biological Chemistry* **2004**; *279*: 32294-32300

333. Russell NJ, Harwood JL. Changes in the acyl lipid composition of photosynthetic bacteria grown under photosynthetic and non-photosynthetic conditions. *Biochem J* **1979**; *181*: 339-345

334. Catucci L, Depalo N, Lattanzio VMT, Agostiano A, Corcelli A. Neosynthesis of cardiolipin in Rhodobacter sphaeroides under osmotic stress. *Biochemistry* **2004**; *43*: 15066-15072

335. Loll B, Kern J, Saenger W, Zouni A, Biesiadka J. Towards complete cofactor arrangement in the 3.0 Å resolution structure of photosystem II *Nature* **2005**; *438*: 1040-1044

336. Jones MR. Lipids in photosynthetic reaction centres: Structural roles and functional holes. *Progress in Lipid Research* **2007**; *46*: 56-87

337. Hunte C. Specific protein-lipid interactions in membrane proteins. *Biochem Soc Trans* **2005**; *33*: 938-942

338. Laible PD, Scott HN, Henry L, Hanson DK. Towards higher-throughput membrane protein production for structural genomics initiatives. *J Struct Funct Genomics* **2004**; *5*: 167-172

339. Cronan JE. Bacterial membrane lipids: Where do we stand? *Annu Rev Microbiol* **2003**; *57*: 203-224


MICHIGAN STATE UNIVERSITY LIBRARIES
3 1293 03063 4087